TAYLOR'S
SCHOOL OF
ENGINEERING

eureca 2013

Leadership through
Research & Innovation

engineering undergraduate research catalyst conference 2013

- **1 – 2 July 2013**
- **Taylor's University, Lakeside Campus**

cdio™

GRAND CHALLENGES
FOR ENGINEERING

FOREWORD BY PROFESSOR DATO' DR. HASSAN SAID

With the ever-increasing expectations of graduates to be industry-ready to address a variety of new world challenges, the requirements to equip these graduates, especially those in the field of engineering, science and technology, with research skills are more pressing. As such, Taylor's University through our School of Engineering, is proud to organise the inaugural EURECA 2013 conference, which is aimed at providing undergraduate engineering students the opportunity to develop their research skills and knowledge through intense sharing session with the industry and academic experts.

At Taylor's University School of Engineering, we place huge emphasis in educating our students through not only the acquisition of comprehensive discipline-specific knowledge, but also encourage them to develop key skills that will give our graduates an edge in pursuing their career in future.

With notable leaders in the engineering field presenting their research findings and sharing their valuable insights on the current global challenges of the world, participants of the EURECA conference will find this event a great platform to engage with these experts as well as their peers. The two-day conference will allow participants to hone their presentation and critical thinking skills, which are crucial in preparing them to become competent engineers.

This beyond-classroom learning experience will be an invaluable networking opportunities for our engineering students with experts and peers as the Taylor's University School of Engineering will witness its very first batch of students graduating this year.

I hope this conference will set another milestone for the school in creating moments of *eureka* – a celebration of important discovery or invention – in the field of engineering among its participants.

PROFESSOR DATO' DR. HASSAN SAID
Honorary Chairman of the EURECA 2013
Vice Chancellor & President
Taylor's University

FOREWORD BY PROFESSOR DR. MUSHTAK AL-ATABI

The 21st century is a very interesting time for engineers. It is a time that is filled with Grand Challenges that require serious reconsideration to the way we go about doing our business. With challenges such as depleting natural and energy resources, polluted environment, climate change, global security and health, the ability of engineers to conduct research is becoming more and more a requirement and an expectation.

At Taylor's School of Engineering, we are proud that besides Project Based Learning, our students perform real world research projects that are directly linked to the Grand Challenges for Engineering. Honing research skills of the engineers will, undoubtedly, enable them to develop sound judgment and propose viable solutions, qualities that are highly sought after by employers.

EURECA 2013 conference is aimed at giving graduating engineers with the opportunity to present their final year research work, emphasising the importance of building research skills as well as research culture. We hope that the skills developed by the students will go a long way to produce engineers who will be able to contribute to a sustainable future for all of us.

M. T. Al-

PROFESSOR DR. MUSHTAK AL-ATABI
Dean, School of Engineering
Taylor's University

TABLE OF CONTENTS

Numerical Simulation on Outsole of Basketball Shoes

A. T. Tan*, Alexander Chee H. C.

[1]*School of engineering, Taylor's University, Malaysia*

**E-mail: andre.tan6@gmail.com*

Abstract— **Numerical analysis simulation of linear finite element on basketball shoes has been conducted. The traction and durability analysis of the outsole has been tested, based on the various movements of the basketball players, such as cutting movement, shuffling movement, jumping, and etc. The materials used by the outsole are polyurethane outsole shoes. The results of the traction simulation are combined for durability of the outsole.**

Keywords— Finite Element Analysis, durability, biomechanics, sport engineering, traction

1. Introduction

Traction capabilities of a basketball shoes can affect the performance and safety of the player due to high excessive reaction force from the motion [1-2]. Traction occurs between playing surface and shoes outsole, therefore, the traction of each basketball shoes can be varied depending on the material of the outsole of the shoes and coefficient of friction of the playing surface [2]. There is a lot of movement in basketball games such as cutting movement, shuffling movement, and running movement (starting and stopping) [3]. There are numerous study have done in the past by various corporations, however, a large number of them are kept as trade secrets.

Fig. 1(a) Fig. 1(b)

Sample of Nike shoes for the experiment

Numerous study by using traction machine has been done in the past, including the various movement analysis, however, the technique used is based on traction testing machine which differentiate between playing surface, movements, and reaction force [1], [3]. Koike and Okina have done a modeling study, the model was divided into 4 parts on the plantar surface. The simulation was based on non-linear finite element analysis; it was assumed that the outsole as damper and spring (vibration), however, this method is not combining the various movements in basketball games [4]. Nevertheless, the finite element study on outsole shoes to determine the durability based on traction of the outsole of basketball shoes has yet to be established and it is the main objective of the current study.

Furthermore, the result from the finite element analysis on traction of the model will be extracted to conclude the stress concentration for determining the durability of the outsole.

In this paper, the numerical analysis simulation of finite element was conducted by using SolidWorks software to test the traction capabilities of the shoes. The durability will depend on the concentration force from traction simulation. Material specification was chosen according to the proper common material for basketball shoes outsole, which are polyurethane DP 9370 A.

2. Methodology

A finite element study was conducted by using SolidWorks, implementing the model technique of Koike and Okina [4]. The validation of the simulation boundary condition were initially followed the ASTM standard with Numerical simulation.

2.1 Boundary Condition

Numerical simulations were performed using SolidWorks static analysis. A virtual wall is defined as the playing surface with dry condition surface. At the top of forefoot area are subjected to fixed geometry condition and the forefoot area are subjected to the force with several directions depending on the movement of the player. The 3D model of the computational domain and implemented boundary condition are shown in Fig. 2.

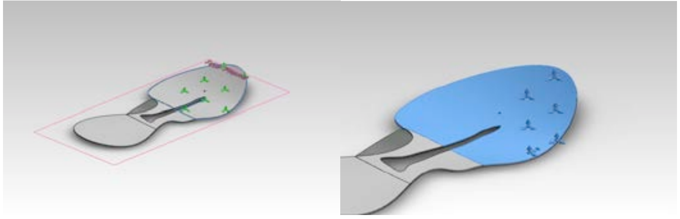

Fig. 2(a) Fig. 2(b)

Boundary Condition

Furthermore, in order to imitate the real condition of basketball movement, the force was force was subjected at X-direction and human body weight is assumed to be normally distributed load at plantar surface. The reaction force is based on the newton's third law of motion.

$$F = F_{reaction} \qquad (1)$$

Based on equation 1, the ground reaction force is accumulated to find the traction between the shoe surface and playing surface, and then the value of the maximum of reaction stress from the numerical simulation will be calculated to get the durability of the outsole of the shoes.

The coefficient of friction and condition of the playing surface are taken into consideration, which are 0.40 for wet condition and 0.60 for dry condition [5].

Table 1. Parameters Used in simulation

Parameters	Scheme
Virtual Wall	Top Plane
Force	Depend on the movement
Fixed Point	Forefoot Area

Table 1. Shows that the components used as the boundary condition of the simulation. Virtual wall contact acts as the playing surface, which have different coefficient of friction. The force acting on the outsole are determined from the movement condition such as, cutting movement, shuffling movement, and running (stopping and starting).

2.2 Shoes Model

The shoes model is divided by 3 parts, which are the forefoot, middle, and back. The shoes were modeled using solid works advance 3D surface modeling technique.

Fig. 3

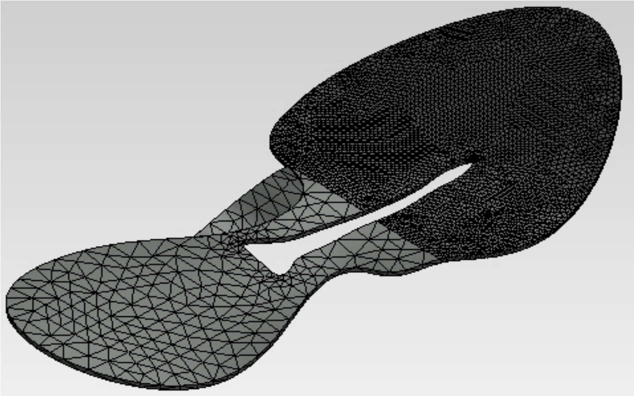

Mesh of the outsole model

Mesh parameters set up with 2 different mesh parameter. Forefoot area has smaller size for the mesh parameters in order to get more accurate result in the stress concentration. The minimum size is 0.178201 cm and the maximum is 0.891006 cm. The computational grid as shown in Fig 3 is set up using high quality meshing parameters. The resolution is higher in the forefoot area compare with the middle and back area. Shoes are divided based on a dynamic analysis [4].

3. Results and Discussion

3.1 Results

The study of traction of the outsole of basketball shoes will be presented in this section. Linear Finite Element Analysis method of the outsole during cutting movement analysis will be presented at this section. The traction result shows the concentration force to determine the durability of the shoes.

3.1.1 Traction

The numerical simulation obtains including the coefficient of friction of the playing surface, and cutting movement force analysis will be presented in this section.

Fig 4(a). Displacement

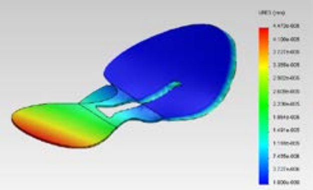

Fig 4(b). Strain

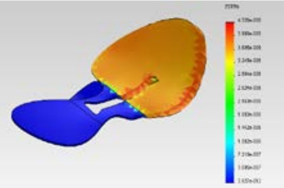

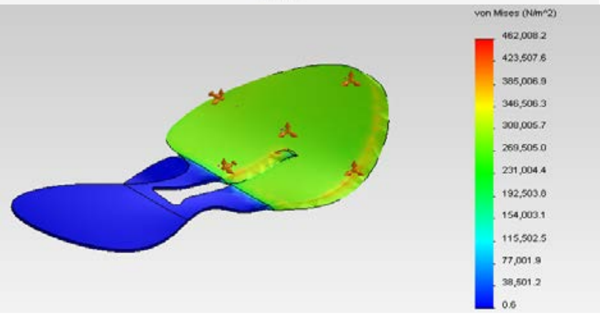

Fig 4(c). Stress distribution of cutting movement

Fig. 4 illustrated the result of cutting movement analysis of the simulation. It is shown in Fig. 4(c) that the highest stress is in the center of the forefoot area. The highest stress was 462.008 KPa located at the forefoot area of the outsole. The highest displacement (deformation) is found at the back of the shoes.

3.1.2 Durability

The material used in the experiment is polyurethane, which is classified as polymer material, with various material properties. Material properties used are based on the actual product data sheet.

Table 2.

Material Properties	Value
Shore hardness, method A	70
Ultimate Tensile Strength	26.1 MPa
Abrasion Resistance	69 mm^3
Density	1060 kg/m3
Poisson's ratio	0.49

Material Properties of polyurethane [6]

The elasticity of this model gives an impact to the final result [7]. Highest wear rate found at the middle of the forefoot area, shown in Fig. 4(c)

3.2 Discussion

The middle of forefoot area overcomes the highest concentration rate, due to the plantar distribution on human's foot [2],[3]. Nevertheless, there are maximum deformation occurs at the back of the shoes, due to the swing effect during the cutting movement.

Deformation of the shoes depends on both force acting on the forefoot and the materials properties, therefore large deformation will occurs in the numerical analysis simulation.

4. Conclusion and Recommendation

Wear rate of the shoes are found at specific location in cutting movement analysis. It is shown that the highest force concentrations are at middle part of the forefoot, which caused higher wear rate compared with another part.

Design improvement should be made for reducing the wear rate to improve the durability of the outsole. Increase the thickness of the material in the middle of forefoot area and improve the material abrasion resistance properties can be implemented.

Acknowledgement

I am very grateful to Mr. Alexander Chee Hon Cheong as my supervisor for his guidance during the experiment and to all my colleagues who help me with my project.

References

[1] B.S. Cooper, "*Traction characteristic of cleated athletic shoes at various angles of internal rotation on artificial turf",* Boise State University, May 2009.

[2] D. J. Rheinstein, C. A. Morehouse, and B. W. Nabiel, "Effects on traction of outsole composition and hardness of basketball shoes and three types of playing surface", *Medicine and science in sport*, vol. 10, no. 4, pp 282-288, 1987.

[3] Standard test method for traction characteristic of the athletic shoe-sport surface interface, F2333-02, 2011.

[4] S. Koike and S. Okina, "A modelling method of sport shoes for dynamic analysis of shoe-body coupled system", *International Sport Engineering Association*, pp. 272-277, 2012

[5] Flexcourt, "Basketball/multisport surface", 225 datasheet, 2013 [Revised May 2013]

[6] Bayer, "Desmopan product data range", 01.2010 data sheet, 2010 [Revised May 2013]

[7] N. J. Mills, C. Fitzgerald, A. Gilchrist, and R. Verdejo, "Polymer foam for personal protection", *Composite science and technology,* Vol. 63, pp. 2389-2400, 2002

Effects of Physical Properties on Resonance of Natural Fibers Panel

A.N. Rahman[1], M. H. Nassir[2]

[1,2]*School of Engineering, Taylor's University*

[1]*ahmad.nazri90@gmail.com* [2]*mohamedh.nassir@taylors.edu.my*

Abstract— **The maximum absorption of certain frequencies occurs at resonance frequency. It is widely accepted that the fibre is very common material to be employed in this matter. Studies on absorption resonance are varied from the use of fibre panel in rooms, theatres, factories, airplanes, or even in shuttles sent by NASA to the outer space. All previous studies focus on using a single chemically-fibre treated to serve the purpose. In this study, the focus is to investigate the role of modified physical properties on resonance frequency. Initial proposed models shows that the density of the panel and length of the fibre have real impact on the resonance of the natural fiber.**

Keywords— Resonance, density, radius, length, fibre panel.

1. Introduction

The resonance frequency is an old phenomenon in science which caught the attention of engineers. Resonance frequencies may be damage in nature such as the resonance frequency in bridges and constructions or it has another face where a great deal of benefits may obtained as in medical field, nuclear resonance, or absorbing unwanted sound which is the concern of this study. Extensive theoretical and experimental studies were conducted since 40's in last century [1], [2], [3], and [4]. A comprehensive review by Attenborough [2] was conducted and no reason to review both experimental and theoretical part here. Concerning the theoretical and modeling studies, both Walker [3] and Kawasima [5] expressed comparative results of their work. The main focus for my research paper is modeling an acoustical fibrous system in which the resonance will be studied extensively in order to provide deep picture to this phenomenon as parameters such as density, radius, and porosity changing.

2. Methods

Sound absorption inside the porous sound absorber occurs due to the attenuation of sound wave by viscous loss and thermal loss [6].The properties of the porous absorber which affects the sound absorption such as thickness, density, porosity, tortuosity, fiber size, characteristic length and flow resistivity are identified. There are also several macrostructure properties that affect the sound absorption such as the absorption coefficient, and normal surface impedance. Since there are no exact result that show how much these properties effect the resonance of the porous material, this research will be based on other researcher's results. For example, the experiment done by Biot [6] and Dahl, Rice and Groesbeck [10] shows the resonance frequency decreases as the length and the density of the porous material increase.

Resonance occurs when the frequency of the sound wave reaches near or equal to the natural frequency of the sound absorber, which is known as absorption coefficient as experimented by Housseini, Ayub and Jailani [7]; and shown by Wang, Kuo and Chen [8]. Fig. (1) shows the experimental results of Wang, Kuo and Chen [8] which proves the earlier statement. We can see from the line of best fit where the maximum absorption coefficient is at around 2500 to 3000 Hz and the resonance frequency lies between these frequencies.

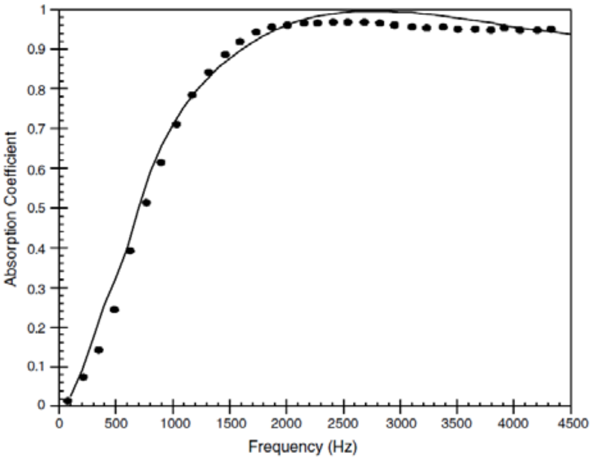

Fig. 1: Experimental results done by Wang, Kuo and Chen [8]

For this research, the porous material will only consist of one material. In the future, the material can be combined with two or more other porous material such as mixture of coir and corn fiber. To show the properties, first we model the equation by using Laplace's equation. There are two ways to solve the Laplace's equation. The first one is the standard way by introducing a boundary condition and solves it using differential equation. We will have no error when we solve the equation using this method because the equation has exact solution. However, some differential equations are impossible to solve because of the nature of these equations. The second method is also introducing boundary condition but we use numerical analysis to solve it. Although there are a percentage of errors when using this method, it can be negligible. Fig. (2) shows the imaginary set up is used in this research when modeling the formula where the natural fiber is set to be cylindrical shape and the sound wave will be projected at one of the flat face of the natural fiber.

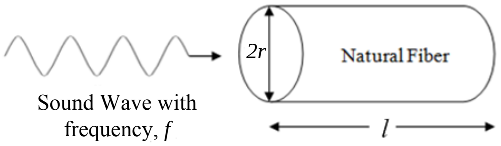

Fig. 2: The set up and dimensions of the natural fiber

3. Results& Discussion

In this study, three possible solutions will be proposed. The resonance function, φ will be proposed to three variables: density, of the fiber, length and radius of the fiber.

3.1 Density

According to Biot [6], due to the stress and strain or pressure difference in the porous material, the properties of the porous material will change. Biot also stated that as there is a pressure difference on the solid, the porosity of the solid will decrease. When the porosity of the solid decreases, it can tell us that either the void volume decreases and the total solid volume increases. When the total solid volume increases due to the flexible frame, the density of the solid will decrease. Based on this argument, the resonance frequency φ is inversely proportional to the density as shown in (1)

$$\varphi(\rho) \propto \frac{1}{\sqrt{density\ ,\rho}} \tag{1}$$

3.2 Length

Biot also stated in his book that the strain component is linearly related to the actual changes in the length of the material [9]. This can also be proven experimentally as in the work done by Dahl, Rice and Groesbeck [10]. The results explain that in viscous medium, the drag force and the pressure gradient across the length is created. For these reason, the second φ dependency is the length as shown in Fig.

$$\varphi(l) \propto \frac{1}{lengt\ h,l} \tag{2}$$

3.3 Radius

The resonance of the bulk natural fiber which we considered it to be cylindrical will also be influenced by resonance due to the flexible frame that is stated by Kawasima [5]. According to Kawasima's experiment, there are two waves that are similar to the two waves from Biot's theory where one can propagate in the frame set in vacuum which is called frame-borne wave while the other one propagates in the air which is called the airborne wave [11]. Although the fame-borne wave is generally negligible due to the stiffness and the density of the frame, the amplitude of this wave can increase considerably when the frequency of the sound wave approaches the resonant frequency. Therefore a third proposal could be set in which the resonance frequency φ is a function of the radius:

$$\varphi(r) \propto radius, r \tag{3}$$

3.4 Final Equation

From the three equations, we can combine into one equation that shows the properties that affects the resonance.

$$\varphi(\rho, r, l) \propto \frac{r}{l\sqrt{\rho}} \tag{4}$$

$$\varphi(\rho, r, l) = \frac{kr}{l\sqrt{\rho}} \tag{5}$$

The k the proportionality constant introduced for completing this equation. This equation needs to be solved further to show the resonance using Laplace's equation. Since the equation here is dimensionless, we can find the unit for the constant, k by using dimensional analysis to find the unit of the other properties.

$$\frac{L}{L*\sqrt{\frac{M}{L^3}}} \tag{6}$$

$$\frac{1}{\frac{\sqrt{M}}{\sqrt{L^3}}} \tag{7}$$

$$\frac{\sqrt{L^3}}{\sqrt{M}} \tag{8}$$

Equation (8) shows the unit for the properties in equation (4). By inversing the unit for the other properties, the unit for constant, k is;

$$\frac{\sqrt{M}}{\sqrt{L^3}} \tag{9}$$

$$\sqrt{\frac{M}{L^3}} \tag{10}$$

Equation (10) here shows the unit for the proportionality constant, k which can also be explained as the square root of the specific gravity for the natural fiber.

4. CONCLUSION

The present study shows that the effects of the physical properties of natural fibers on resonance are the density, porosity, length as well as the radius of the natural fiber. Equation (4) shows that the resonance is directly proportional to the radius and inversely proportional to the length and the square root of density. Equation (5) will be used to solve using Laplace's equation and the numerical method.

Acknowledgment

I would like to thank Dr. Nassir for his help and support in working this project with me. This work was supported by the School of Engineering, Taylor's University.

References

[1] Scott, R. A. (1946) The Absorption of Sound in a Homogeneous Porous Media. *Proc. Phys. Soc. London*, 58, 165-183

[2] Attenborough, A. (1971) The Influence of Microstructure on Propagation in porous Fibrous Absorbents. *J. Sound Vibration* 16, 419-442

[3] Hersh, A. S. & Walker, B. (1980, June) *Acoustic Behavior of Fibrous Bulk Materials*. AIAA 6thAeroacoustic Conference Papert AIAA 80-0980, Hartford, Connecticut, USA

[4] Lambert, R. F. (1979) Acoustical Properties of Highly Porous Fibrous Materials. NASA TM-80135

[5] Kawasima, Y. (1960) Sound Propagation in a Fiber Block as a Composite Medium. *Acustica* 10, 208-217

[6] Biot, M. A."The theory of propagation of elastic waves in a fluid-saturated porous solid, I. Low frequency range, II.Higher frequency range."*The Journal of the Acoustical Society of America*, vol. 28, pp.168-191, 1956

[7] Fouladi, M. H., Ayub, M., Jailani, M. "Analysis of coir fiber acoustical characteristics," *Applied Acoustic*, vol 72, pp. 35-42, 2011

[8] Wang, C. N., Kuo, Y. M., Chen, S. K. "Effects of Compression on the sound absorption of porous materials with an elastic frame," *Applied Acoustic* vol. 69, pp. 31-39, 2008

[9] Biot, M. A. *Mechanics of Incremental Deformations*. John Wiley & Sons, Inc. New York, 1965

[10] Dahl, M. D., Rice, E. J., Groesbeck, D. E. "Effects of Fiber Motion on the Acoustic Behavior of an Anisotropic, Flexible Fibrous Material" presented at the 113th Meeting of the Acoustical Society of America, Indiana, May 1987

[11] Allard, J. F., Herzog, P., Lafarge, D., Tamura, M. "Recent Topics Concerning the Acoustics of Fibrous and Porous Materials," *Applied Acoustics*, vol 39, pp. 3-21, 1993

Drag of Conical Nose at Supersonic Speeds

Arthur S.Q Saw*, Abdulkareem Sh. Mahdi Al-Obaidi

Department of Mechanical Engineering, School of Engineering, Taylor's University, Malaysia

**Corresponding author: arthursherqen.saw@sd.taylors.edu.my*

Abstract— **In designing a projectile, there are various configurations and designs that can be considered. Normally, the shape and design of the projectile are selected on the basis of the combined considerations of aerodynamic, guidance and structure. One of the main design factors that affect projectile configuration is the nose drag. In this study four widely known nose shapes are considered, pointed and blunted cone; pointed and blunt ogive. The drag of the configurations is considered with respect to the Mach number. As fineness ratio and Mach number increases the overall drag decreases. Each drag component behaves differently depending on the Mach number and fineness ratio. The drag is compared based on the 3 main drag components; skin friction drag, wave drag and base drag. For this paper only the conical nose shape is presented.**

Keywords— Skin friction drag, Base drag, Wave drag, Nose, Supersonic

1. Introduction

There are multiple configurations and designs of projectile noses that are taken into account during the design stage. The final nose design is selected after considering aerodynamic, structural and guidance as well as Tactical-Technical-Requirements (TTR) of the mission. The case considered in this study is a 300 km range supersonic surface missile. As a result of having different requirements and restrictions there is no perfect configuration and the design undergoes various design changes till an optimum compromise is reached with the requirements mostly met [1]. One of the key considerations or factors of a projectile's aerodynamic consideration is the nose drag which will be the focus of this study.

In general, there are three drag components, drag directly related to the cross-sectional of the projectile, skin-friction drag due to the contact between the surfaces of the projectile (roughness) with the surrounding air particles (viscosity), wave drag as a result of the shock wave and base drag as a result of bluntness and diameter of the base. In layman terms drag is a force which is parallel but in opposite direction to the direction of the velocity vector of an object and it is opposing the object's motion [2].

This paper focuses on the nose drag at supersonic speeds, taking speeds from Mach 2 to Mach 4. For this study a wingless body projectile, forebody with cylindrical afterbody considered. The drag will be studied on the aerodynamic aspect of the nose design.

This study is a section of an ongoing study which considers four common nose shapes to be analysed for their drag aerodynamic performance; pointed (Fig. 1) and blunt cone (Fig. 2); and pointed (Fig. 3) and blunt ogive (Fig. 4). This paper presents the results for one shape only, the pointed conical nose.

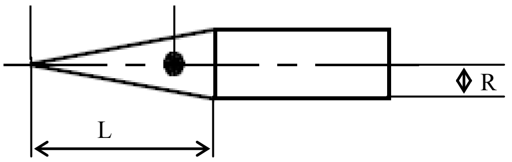

Fig. 1 Pointed Cone.

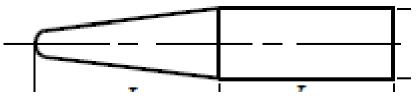

Fig. 2 Blunted Cone.

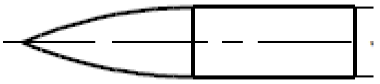

Fig. 3 Pointed Ogive.

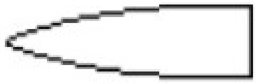

Fig. 4 Blunted Ogive.

2. Methodology

The aim of this study is to research what are the effects of a different nose configuration has on the drag of a projectile travelling at supersonic speeds. The goal is to produce a design table with selected parameters which would assist a projectile designer in selecting the optimum nose for the projectile. The parameters considered in the design table are drag coefficient and nose geometry.

The main approach used in this study is the analytical approach. The drag of the noses are analyzed with mathematical formulas to calculate the three main components of drag that forms the zero-lift drag coefficient (Eq. 1)[1]; skin friction drag (Eq. 2) [3], wave drag (Eq. 3) [4] and base drag (Eq. 4) [3].

$$C_{DO} = C_{Dsf} + C_{Dw} + C_{DB} \tag{1}$$

$$C_{Dsf} = \frac{4}{\pi} C_F S_w \tag{2}$$

where C_F represents the skin friction coefficient for a smooth/ flat plate and S_w the wetted area

$$C_{Dwv} = \frac{128 K_{vw} V^2}{\pi S L^4} \tag{3}$$

where, S is the wetted area, L is the length of the body, V is the volume and K_{vw} is a factor of geometry and Mach number

$$C_{DB} = \frac{2 d_B^2}{\gamma M_\infty^2}\left(1 - \frac{P_b}{P_\infty}\right) \tag{4}$$

where, d_B is the base diameter, M_∞ is the free stream velocity, γ is the ratio of specific heats, P_b and P_∞ are base pressure and free stream static pressure respectively

To be more specific, the zero lift drag coefficient (dimensionless) basically describes the resistance of a particular body in the direction of the moving force or motion. The equation makes use of the wetted area and viscosity to determine the drag and is measured at zero angle of attack.

Skin-friction drag is the result of viscous forces acting on the surface of the projectile. It is also very dependent on the wetted area.

Wave drag describes the drag due to the interaction of the body with the flow particles and is related to shockwave energy losses.

Base drag is the drag formed from the base pressure as a result of the bluntness at the object and is highly dependent on the size of the base.

A Matlab program is developed to run these formulas for all the different cases of the nose configuration. The results are tabulated in a graphical manner to demonstrate the relation and contribution of each component.

One important factor that affects drag under the nose geometry section is the fineness ratio. Fineness ratio is the ratio of the length of the nose divided by its diameter (Eq. 5) [5] and Fig. 1.

$$Fineness\ ratio = \frac{L}{2R} \qquad (5)$$

Next, semi empirical approach is used as a means to support the analytical approach. Values such as P_B from (Eq. 4) are acquired from graphs.

3. Results and discussion

The graphical results of the study are generated with Matlab, which is also used as a means of calculation to obtain the individual results.

Figure 6 shows the effects of the fineness ratio as the Mach number changes. At lower Mach number (e.g., Mach 2) the C_D exhibits a higher value although it decreases as the fineness ratio is increased. However, the rate of decrease of the drag reaches its maximum at fineness ratio 3 after that the change in C_D is not so apparent. Also increasing the Mach number also results in a noticeable decrease in the drag.

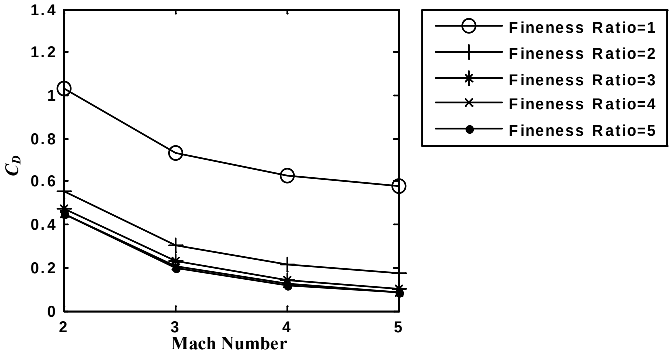

Fig .6 Total Drag Coefficient, C_D as a Function of Fineness Ratio and Mach Number.

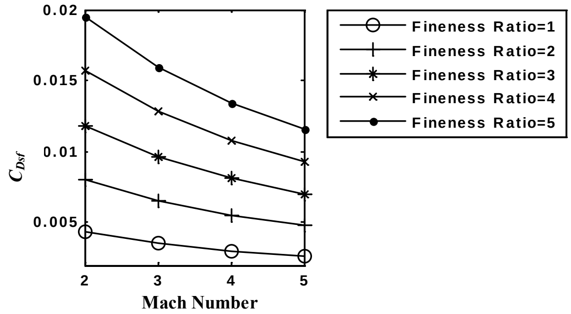

Fig .7 Skin Friction Drag, C_{Dsf} as a Function of Fineness Ratio and Mach Number.

Figure 7 displays the behavior of the skin friction drag that increases in proportion with the fineness ratio. This is consistent with Eq. 2 that contains the variable S_W which is the wetted area (area of reference). By increasing the fineness ratio, the geometry of the nose also increases and thus leads to an increase in surface area.

Next, based on (Eq. 4), it can be noted that the base drag is independent of the shape and fineness ratio of the nose. It is only affected by the base diameter and Mach number which also in turn influences the base pressure.

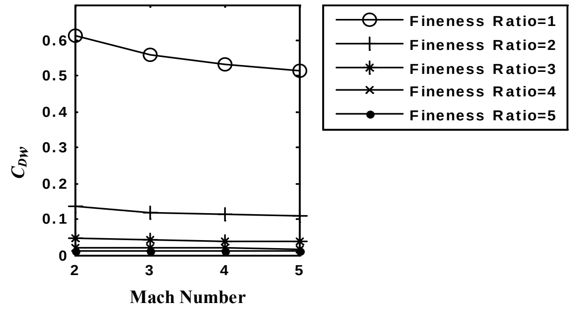

Fig. 8 Wave Drag, C_{dw} as a Function of Fineness Ratio and Mach Number.

Figure 8 demonstrates that the change in wave drag is mostly affected by the fineness ratio. As the fineness ratio increases the wave drag decreases. This agrees with the logic that an increased fineness ratio makes the nose more slender where it is able to stay in the Mach cone with minimal air disturbance. When compared to the skin friction drag, the drag coefficient values in general are much higher especially at low fineness ratios.

4. Conclusion and recommendation

By increasing the fineness ratio of the nose, it is possible to reduce the overall drag of the projectile. However, increasing the fineness ratio without proper study could possibly result in a higher drag coefficient. Increasing the fineness ratio in fact increases the skin friction drag, while it doesn't contribute much as seen with its small C_{Dsf} values compared to the total C_D but if the fineness ratio is increased beyond the values of the graph it may become more significant as the graph clearly shows an increasing trend.

Also it can be noted that the wave drag is the largest contributor especially at low Mach number and low fineness ratio due to more energy losses. While the base drag is only affected by the Mach number, however as it enters the supersonic speed range the base drag decreases as such it is less of a concern. From this study, a projectile designer aiming to reduce drag should focus more on the wave drag component as it is the largest contributor and care should be taken not to increase the fineness ratio without proper consideration as he may end up increasing drag instead.

For further study, it is recommended that Computational Fluid Dynamics (CFD) be used as an additional verification tool due to its current advancement and ease of use in providing and displaying graphics to help understand the airflow around the nose. CFD also allows multiple configurations to be tested initially without resorting to expensive wind tunnel testing.

References

1. Mahdi, A. and Al-Atabi, M. (2008) Effect of Body Shape on the Aerodynamics of Projectiles at Supersonic Speeds. *Journal of Engineering Science and Technology (JESTEC)*, 3 (3), 278-292.
2. Bertin, J.J., and Cummings, R.M., (2009). *Aerodynamics for engineers*. New Jersey, Pearson/ Prentice Hall.
3. Mccoy, R. (1981). *"MC DRAG"- A Computer Program for Estimating the Drag Coefficients of Projectiles.* [report] Maryland: US Army Armament Research and Development Command.
4. Sadreay, M. (2009). *Aircraft Performance Analysis*. Saarbrücken, VDM Verlag Dr. Müller.
5. Crowell Sr, G. (1996). *The Descriptive Geometry of Nose Cones*. Miscellaneous Paper.

Tribological Evaluation of Nano Graphene Platelets as an Additive to Biolubricant Base Fluid

Arwin Goo Zen[1], Rashmi G. W[1*]

[1] *Department of Chemical Engineering, Taylor's University Lakeside Campus, Malaysia.*

**Corresponding authoremail:rashmi.walvekar@gmail.com*

Abstract— **This paper presents a tribological evaluation of graphene nano platelets (NGPs) as an additive for two different biolubricant base stocks. Two biolubricant base stocks are prepared, (a) palm oil based trimethylolpropane (TMP) ester, and (b) a blend of 20% palm based TMP ester with 80% palm based cooking oil. NGPs were dispersed in each biolubricant proportionately from 0.01% to 0.1% by weight based on the total weight of the fluid and graphene platelets combined. With the addition of a thickener or a desired amount of NGPs, the lubricant becomes a grease composition. The evaluation of frictional coefficient was done using a four ball machine. Results showed that the addition of NGPs as an additive results in the reduction of coefficient of friction in biolubricants, achieving a reduction maximum reduction of 10% in palm oil TMP esters, and an impressive 17.9% reduction in the mix blend. However the effect of a higher temperature has a negative effect on the lubricating properties, and could be due to the failure of the graphene to form a protective film over solid surfaces at higher temperatures and the tendency to agglomerate at higher concentrations of NGPs.**

Keywords— Nanolubricant, Nano Graphene Platelets (NGPs), Trimethylpropane Ester, Friction coefficient

1. Introduction

The exponential growth in the field of nanotechnology has led to the development of carbon nanoparticles as lubricant additives. The current issue with conventional lubricants is the high amounts of sulphur and phosphorus contents which adversely affect the performance in diesel engines. Graphene exhibit unique properties that render them as suitable contact finish treatments that can reduce friction while still providing the potential benefit of stability in harsh environments such as high temperature or high vacuum when compared to liquid based lubricants. Thus the aim of this study is to investigate the combined properties of graphene nanoparticles with TMP ester and palm based cooking oil in a conventional bio-lubricant base as a potentially ground breaking nanolubricant with enhanced friction with low sulphur and phosphorus content by utilizing a four ball wear tester. The predicted results from this study would be a stable nanolubricant with enhanced tribological properties.

2. Experimental Procedure

2.1 Materials

The NGPs used are 12nm in diameter while the balls used for the experiment are the standard AISI E-52100 chrome alloy steel, with a diameter of 12.7mm; hardness 64-66 HRC (Rockwell C Hardness). Each test is conducted with a set of four new balls.

2.2 Lubricants

For the lubricants used in this experiment, palm oil trimethylolpropane ester and a mix blend of 80% Seri Murni double fractionated cooking oil with 20% palm oil trimethylolpropane ester was used. Palm based polyol esters have been touted as excellent biodegradable base stocks for lubricants. The TMP ester is derived from palm oil and has high lubricating properties, higher flash point and a higher viscosity index [1]. However the cost of synthesizing TMP esters involve a higher cost, hence a mix blend of TMP and palm based cooking oil is also prepared and evaluated. Palm based cooking oil consists mostly of palm olein, which has been researched on as a potential biolubricant stock. In fact, research has shown that vegetable cooking oils actually function as good as or better than mineral and synthethic oils, due to their long chain fatty acids [2].

2.3 Preparation of Nanofluids

For this study, the NGPs were added in three specific ratios (0.01 wt%, 0.05wt% and 0.1 wt%) to lubricant base. A crankcase lubricant additive, IPAC 1230A (Biogen Solutions) was added to each sample to increase the oxidative stability and viscosity index of the nanolubricant samples. The nanolubricant samples were first homogenized for 5 minutes by utilizing a high speed homogenizer (IKA-T18, ULTRA-TURRAXX, Germany) and then sonicated in a ultrasonic bath (Crest Ultrasonics, USA) for 4 hours at 50 C to ensure that the samples are well dispersed.

2.4 Test Procedure

Figure 1: Set up of the ball pot assembly

In order to set up the experiment, the three balls *were* assembled as shown *in **Fig 2***, and tightened using a torque wrench. The fourth ball is then locked inside the collector using a spindle. Then 10ml of the test sample is poured into the ball pot assembly. The assembled components are loaded into the four ball tester and the heater then heats the test fluid up to 40°C via the internal heater. Once the set temperature is achieved, the drive motor rotates the top ball at 1200 rpm at a load of 40 kg for 600 seconds. The test is repeated for different temperatures of 60˚C and 80˚C.

2.5 Set up for Tribology Testing

A specific data acquisition system connected to the four ball machine records down the frictional torque at specific time intervals. The coefficient of friction is then calculated according to IP-239, as following:

$$\mu = \frac{T\sqrt{6}}{3Wr}, \tag{1}$$

Where μ is the friction coefficient, T is the frictional torque (kg mm), W is the load in kg, and r, the distance from the contact surface of the lower balls to the axis of rotation. The friction coefficient was calculated by the computer automatically. This calculation method is similar to the one used by Thorp [3].

3. Results and Discussion

3.1. Tribological Evaluation for Friction

(a) NGP lubricant in TMP vs Temperature

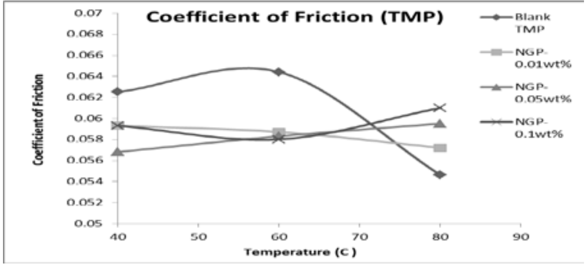

Fig. 2: Coefficient of Friction vs Temperature for NGP in TMP

From the results of the four ball tester, it can be observed that the addition of NGP to Palm Oil TMP esters lowered the coefficient of friction significantly . However, at higher temperatures, the nanolubricants fared worse off than the blank TMP esters. This is further elaborated on in the latter section of this paper . As seen in Fig 3, at 40C, the biggest improvement in lubricity is produced by the nanolubricant dispersion with 0.05wt% of NGP, approximately reducing the coefficient of friction by 9.12%. While at 60C, the most significant reduction in friction coefficient is induced by the TMP ester sample with 0.1wt% of NGP, reducing the friction coefficient by 10%. This observation strengthens the claims that the single layer graphene can strongly adhere to solid surfaces, hence producing a molecular scale lubricating film [4].

(b) NGP lubricant in Mix Blend of TMP and Cooking Oil

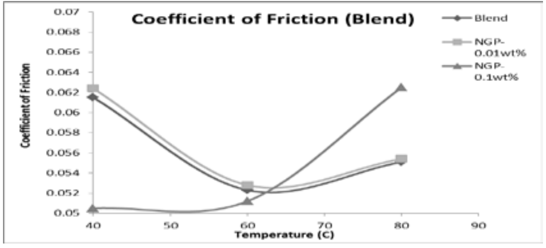

Fig. 3: Coefficient of friction vs Temperature for NGP in mix blend

From Figure 4, the addition of NGPs to a mix blend of cooking oil and TMP follows the same trend as the addition of NGP's to TMP, where a significant reduction in coefficient of friction is observed , but where at higher temperatures , the difference becomes insignificant . At 40C, the sample with 0.1wt% of NGP brings forth the biggest reduction in the coefficient of friction , at approximately 17.9%. At 60, the reduction for the same sample decreases to about 2%.

(c) Failure of NGPs at High Temperature

The failure of the NGP's as lubricant additive at higher temperature could be due to the damaging of the protective film formed by the graphene at higher temperatures. Furthermore, it could be possible that the single graphene layer does not adhere strongly to solid surfaces at higher temperatures. Studies have also indicated that higher concentrations of carbon nanoparticles, the friction and wear reducing properties decrease due to a significant increase in agglomerations within the lubricant [5]. A solution to this problem would be to add a dispersant or surfactant to the lubricant that will ensure agglomerations do not occur .

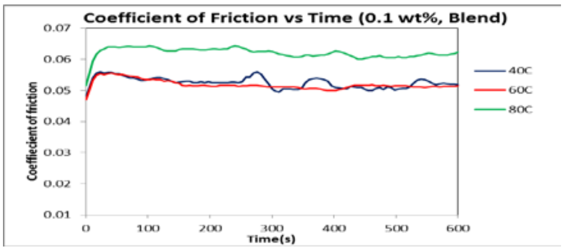

Fig 4: Coefficient of Friction vs Time

Conclusion

The role of NGPs as an additive is relevant in reducing the coefficient of friction in biolubricants, achieving a reduction maximum reduction of 10% in palm oil TMP esters, and an impressive 17.9% reduction in the mix blend. The mix blend has a better distribution of frictional coefficient across the different temperatures tested. However the effect of a higher temperature has a negative effect on the lubricating properties. The solution to this would be the addition of a dispersant or surfactant which will reduce the agglomerates in the lubricant.

References

[1] Shah S, Moser BR, Sharma BK. "Glycerol tri-ester derivatives as diluent to improve low temperature properties of vegetable oils". *J ASTM* Int, 2012;7.

[2] Kim, et al., 2009. "Correlation of fatty acid composition of vegetable oils with rheological behavior and oil uptake". *Food Chemistry*, 118: 398-402.

[3] Thorp, J.M. ''Four-ball assessment of deep drawing oils'', *Wear*, 33,pp. 93–108 (1975).

[4] H. Hong, et al., "Carbon Nanoparticle- Containing Lubricant and Grease," *US Publication* No. 2007/0158609 (Jul. 12, 2007)

[5] S. Bhaumik, et al., " Efficiency of Multiwalled Carbon Nanotubes in Nanolunricant," *Golden Research Thoughts,* Vol 2: 11 (May 2013)

Study of Spray Drying of '*Piper Betle L.*' Leaves Extract Using Whey Protein

Boey Kah Heng[1*], Tee Lee Hong[2], Masniroszaime[1], Rajesh Rajasekaran[1], Yus Aniza Yusof[3]

[1]*School of Engineering, Taylor's University, Malaysia,* [2]*School of Engineering, Monash University, Malaysia,*

[3]*Department of Process and Food Engineering, Faculty of Engineering, Universiti Putra Malaysia, Malaysia*

**Corresponding author: jasonboey90@hotmail.com*

Abstract— ***Piper betle Linn* is known as betel or local name 'Sirih' and is known to possess antimicrobial, anti-carcinogenic, and antioxidant properties. The objective of this study is to investigate the effects of whey protein isolate as an additive to the powder properties of the spray dried of *P.betle L.* leaves extract. The process parameters chosen in this study is the inlet hot air temperature (120° C to 160°C), feed flow rate (4 ml/min to 15 ml/min), and concentration of whey protein isolate (5 w/v% to 20 w/v %). The properties of the dried powder were investigated in terms of moisture content, powder yield and hygroscopicity. Response Surface Methodology (RSM) was used to optimize the spray drying process *of P. Betel L.* From RSM, the optimum process parameters to produce the highest yield, lowest moisture content and lowest hygroscopicty were 158.89 °C, 7.21 ml/min and 5.98 w/v% which will produced a powder with yield 3.34 g, moisture content of 0.99% and powder hygroscopicity of 12.87 g/100g.**

Keywords— Spray drying, Response surface methodology, *Piper Betle L*, Whey protein isolate

1. Introduction

Betel (*Piper betle Linn.*) belongs to genus *Piper* of Piperacea family. This plant originates from the central and eastern part of Peninsular Malaysia and locally called Sirih [1]. It is also cultivated in Sri Lanka, India, Philippine Islands and East Africa. This plant is well known for its medicinal application as well as for betel quid chewing.

Experimentally, leaves of *Piper betle* are shown to possess many beneficial properties which according to past studies, various phytochemicals were found present in betel leaves, however two of the major propenlyphenols, which are Hydroxychavicol (HC) and Eugenol (EU), contributed to the majority of the bioactivities in betel leaves [1]. It has been reported that Hyroxychavicol provides useful properties which includes anti-inflammatory, antibacterial activities [2]. It is found from previous studies that Hyroxychavicol is the major phenolic component isolated from aqueous extract of *Piper Betle L*, and therefore chosen as the main bioactive component in this study [3].

Spray drying enables the bioactive components to be produced in a powder form for ease of transportation and storage. In this study the inlet air temperature, feed flow rate, and concentration of Whey Protein isolate is varied to produce the best quality of spray dried betel leave extract. The powder is analyzed for its yield, moisture content, hygroscopicity and its hydroxychavicol content.

2. Experimental Section

2.1 Materials

Betel leaves was acquired from a large scale supplier at Jalan Morib, Banting to ensure continuous supply. Whey protein isolate was chosen as an additive. Whey Protein Isolate powder is obtained from Ultimate Nutrition, Subang Jaya, Selangor.

2.2 Preparation of Betel Leaves Extract

The betel leaves was first dried in an oven (FAC 350, Protech, Malaysia). The oven is set at 70 °C based on a previous study of the drying kinetics of betel leaves [4]. The dried betel leaves is then extracted using distilled water at 60 °C for 1 hour which are the optimum parameters of extraction of betel leaves [1].

2.3 Spray Drying

The spray drying is done on a laboratory scale spray dryer (SD-05, LabPlant, UK). A 200 ml mixture of betel leaf extract with whey protein solution (5 w/v% to 20 w/v% based on preliminary runs) at 1:1 ratio were mixed. The mixture is fed into the spray dryer through a peristaltic pump. The flow rate varies from 4 ml/min to 15 ml/min and the inlet air temperature is varied from 120 °C to 160 °C [5].

2.4 Powder Yield

The powder was collected in a cyclone separator after the spray drying process and weigh on a weighing machine (PA4101, Ohaus, USA).

2.5 Moisture Content

The moisture content in the spray dried powder is obtained gravimetrically by drying in an oven (FAC 350, Protech, Malaysia) at 105 °C until constant weight is achieved [6].

2.6 Hygroscopicity Test

The powder hygroscopicity was tested based on a proposed method from Tonon and with slight modification from Cai and Corke [7, 8]. This method requires about 1 g of spray dried powder to be placed in a weighing container and weighed. The spray dried powder is then placed in a closed container at 25 °C with saturation sodium chloride (NaCl) salt solution which provided a relative humidity of 75.3%. After one week, the samples were weighed again and the hygroscopicity was expressed as g of adsorbed moisture per 100g of dry solids (g/100g).

2.7 Experimental Design

The experiment was design with the aid of the software Design Expert, where Box-Behnken design of Response Surface Methodology (RSM) was chosen. The 3 process parameters (inlet drying temperature, feed flow rate and whey protein concentration) are varied at 3 levels to give 17 possible combinations.

3. Results and Discussion

A statistical analysis was performed on the experimental result and the regression models were obtained. Based on ANOVA, which evaluates the significance of each variable, linear model was significant for both the response of the moisture content and powder hygroscopicity. For powder yield however, the quadratic model was significant. The responses for the model are shown below:

$$\begin{aligned} Yield = {} & 7.58 + 0.19A - 0.47B + 4.46C - 0.46A2 - 0.66B^2 \\ & +0.057C^2 + 0.46AB - 0.13AC - 0.51BC \end{aligned} \qquad (1)$$

$$\text{Moisture Content} = +2.60 - 1.60A + 0.15B + 0.048C \qquad (2)$$

$$\text{Hygroscopicity} = +12.87 + 1.38A - 0.60B + 0.48C \qquad (3)$$

Where A is the inlet drying temperature, B is the pump flow rate and C is the concentration of whey protein solution

3.1 Powder Yield

The influence of the process parameters are shown in Fig. 1. The responses were only influenced by the feed flow rate ($P < 0.05$) and concentration of whey protein solution ($P < 0.001$). The decrease of flow rate shows an increase of yield due to the lower feed flow rates that facilitate higher heat and mass transfer during the spray drying process [7, 8]. The increase in whey protein concentration increased the yield of the powder due to the use of whey protein isolate that has modified the surface properties of the particles/droplets, which has increased the surface protein coverage of the particles [9]. This in turn has reduced the stickiness between the particles and between the particle and the dryer wall and increased the yield of the powder, as reported in the study of using whey protein isolate in bayberry juice [9].

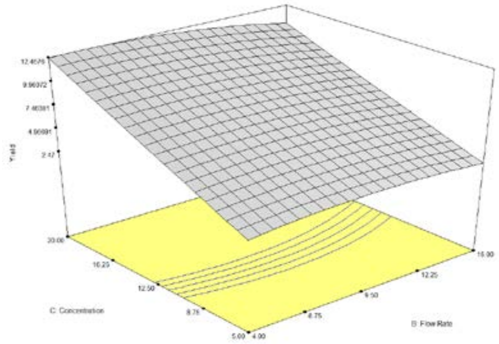

Fig. 1: Effect of flow rate and concentration to the powder yield

3.2 Moisture Content

Based on the results from the statistical analysis, only the inlet drying temperature affected the powder moisture content ($P < 0.05$). The increase in inlet drying temperature decreases the moisture content. This is because when the inlet air temperature increases, there is a larger temperature difference between the atomized feed and the drying air, which produced a greater driving force for water evaporation and produces powder with lower moisture content [7].

3.3 Hygroscopicity

Based on statistical analysis, no parameters were found to significantly affect the powder hygroscopicity (all parameters $P > 0.05$).This is because additive agents with low hygroscopicity are an effective carrier agent to produce low hygroscopic powders [7, 8]. Ordinary whey powders are fine, dusty and hygroscopic. The stickiness, caking and the associated issues of normal whey powder are mainly due to lactose being present [10]. However, whey protein isolate has been processed to remove lactose, and may have produced powders which are not hygroscopic.

4. Conclusion

Based on the results obtained by RSM it is observed that the powder yield increases with decreasing flow rate and increasing concentration of whey protein solution, the moisture content of the powder is affected by the inlet drying air temperature, and the powder hygroscopicity was not affected by any process parameters. From RSM, the optimum process parameters to produce the highest yield, lowest moisture content and hygroscopicty were 158.89 °C, 7.21 ml/min and 5.98 w/v%, which will produce powder properties with yield of 3.34 g, moisture content of 0.99% and powder hygroscopicity of 12.87 g/100g.

5. Acknowledgement

I would like to thank my supervisors for their support throughout the Final Year Project module as well as staff from UPM for their assistance.

6. Reference

[1] Pin K. Y., Chuah A. L., Rashih A. A., Mazura M. P., Fadzureena J., Vimala S and Rasadah M. A., "Antioxidant and anti-inflammatory activities of Extracts of betel leaves (Piper betle) from solvents with different polarities," *Journal of Tropical Forest Science, 22*(4), pp. 448-455, 2010.

[2] Sharma S., Khan I. A., Ali I., Ali F., Kumar M., Kumar A., Johri R. K., Abdullah S. T., Bani S., Pandey A. , Suri K. A., Gupta B. D., Satti N. K., Dutt P. and Qazi G. N., "Evaluation of the antimicrobial, antioxidant, and anti-inflammatory activities of hydroxychavicol for its potential use as an oral care agent," *Antimicrob Agents Chemother, 53*(1), 2009.

[3] Ali I., Khan F. G., Suri A. K., Gupta B. D., Satti N. K., Dutt P., Afrin F., Qazi G. N. and Khan I. A., "In vitro antifungal activity of hydroxychavicol isolated from Piper betle L," *Annals of Clinical Microbiology and Antimicrobials, 9*(7), 2010.

[4] Pin K. Y., Chuah T. G., Rashih A. A., Law C. L., Rasadah M. A. and Choong T. S., "Drying of Betel Leaves (Piper betle L.): Quality and Drying Kinetics," *Drying Technology: An International Journal,* 27, pp. 149-155, 2009.

[5] Tee L. H., Luqman C. A., Pin C. A., Abdull R. A. and Yusof Y. A., "Optimization of spray drying process parameters of Piper betle L. (Sirih) leaves extract coated with maltodextrin," *Journal of Chemical and Pharmaceutical Research, 4*(3), pp. 1833-1841, 2012.

[6] AOAC, "Official Methods of Analysis of AOAC International," no. 16, 1995.

[7] Tonon R. V., Brabet C. and Hubinger M. D., "Influence of process conditions on the physicochemical properties of acai (Euterpe oleraceae Mart.) powder produced by spring powder," *Journal of Food Engineering,* 1(88), pp. 411-418, 2008.

[8] Cai Y. Z. and Corke H., "Production and properties of spray-dried Amaranthus betacyanin pigments," *Journal of Food Science, 65*(6), pp. 1248-1252, 2000.

[9] Fang Z. and Bhandari B., "Comparing the efficiency of protein and maltodextrin on spray drying of bayberry juice," *Food Research International, 48*, pp. 478-483, 2012.

[10] Morgan F., Nouzille C. A., Baechler R., Vuataz G. and Raemy A., "Lactose crystallisation and early Maillard reaction in skim milk powder and whey protein concentrates," *2nd International Symposium on Spray Drying of Milk Products, 85*(4-5), pp. 315 - 323, 2005.

Effect of Condensate Inundation on Enhanced Tubes

Bryan C. W. Ng[1*], S. Namasivayam[2]

[1]*School of Engineering, Taylor's University, Malaysia*

**Email: bryan.ng7@gmail.com*

Abstract— **Enhanced tubes have effectively mitigated condensate inundation in tube bundles. This paper shows data mainly for wire-wrapped tubes but also includes data for smooth tubes, corrugated tubes and low-finned tubes. Thus far, results from previous researches have shown thatenhanced tubes not only prevent inundation, but enhances the heat transfer coefficient of the tubes.The experiment was conducted using simulated artificial inundation technique where the inundation rate is controlled to simulate a depth of up to 30 rows of tubes. The results from this experiment shows that enhanced tubes suffers less inundation compared to smooth tube and the fin tube was the best performing tube among corrugated and wire-wrapped tubes.**

Keywords— Condensation; Corrugated tube; Inundation; Low-finned tube; Tube bundle; Wire-wrapped tube

1.0 INTRODUCTION

The word inundation is used to portray the condensate falling from the upper tubes to the lower tubes of a horizontal condenser tube bundle. In the lower tubes, due to the increase of condensate film thickness by inundation, the heat transfer coefficient decreases. The condensate falls in various ways depending on the rate of condensation; droplets, columns or a continuous sheet. If steam is being pumped excessively into a shell and tube heat exchanger, the condensate would most probably flow from the upper tubes to the lower tubes in a continuous sheet; however, if steam is pumped in at a slow rate, the falling condensate would be in droplets [1,2].

The objective of this project is to study the effect of condensate inundation on enhanced tubes; wire-wrapped tubes, integral-fin tubes and corrugated tubes. By doing so, this research will aid in future designs of steam condensers to increase its efficiency.

There have been a number of researches done to evaluate the performance of wire-wrapped tubes in contrast to other enhanced tubes, namely horizontal integral-fin tubes (HIFTs), corrugated tubes and 3-Dimensional tubes. With this knowledge, wire-wrapped tubes can be utilized efficiently for applications such as condensers for Ocean Thermal Energy Conversion (OTEC) where finned tubes may not be so suitable [3].

The method of collecting data and analyzing results has much evolved since laminar film condensation for free-convection condensation was first investigated by Ernst Wilhelm Nusselt in 1916. The performance of a tube is measured in terms of heat transfer coefficient, α. The higher the heat transfer coefficient, the better the performance of the tube. The Nusselt formula is used to measure heat transfer coefficient.

2.0 METHODOLOGY

The experiment was conducted using simulated artificial inundation adapted from Murase [4], where water is pumped into an inundation supply tube from both ends. The water then drops through the supply tube through holes at the bottom of the tube. The water is collected in an inundation distribution tube where the top half is removed to collect water and overflow onto the test condenser tube made of copper. The inundation rates used in the experiment are 01.1l/min, 0.3l/min, 0.5l/min and 0.8l/min. The inundation rates are as such to simulate the effect of inundation in a tube bank of approximately 20-30 rows deep. The whole set up was condeucted over a measuring cylinder where water overflows from the tube into the cylinder. A stopwatch is used to time every minute to determine the inundation rate. The test condenser tubes used in the experiment consists of 1 smooth tube, 2 wire-wrapped tubes, 1 corrugated tube and 1 low-finned tube. The picture of the copper enhanced test condenser tubes and experimental set up is shown in the figures below. The specification of the 5 test condenser tubes are shown in the table below

Table 1. Specifications of test condenser tubes

Type of Tube	**Tube Geometry**
Plain copper tube	Length: 200mm, Outer Diameter: 12.7mm, Thickness: 1mm
Wire-wrapped tube	Length: 200mm, Outer Diameter: 12.7mm, Thickness: 1mm, Pitch: 4mm
Wire-wrapped tube	Length: 200mm, Outer Diameter: 12.7mm, Thickness: 1mm, Pitch: 8mm
Corrugated tube	Length: 200mm, Outer Diameter: 12.7mm, Thickness: 1mm, Loop: 8mm
Horizontal Integral-Fin Tube (HIFT)	Length: 200mm, Outer Diameter: 12.7mm, Thickness: 1mm, Fins density: 20fpi, Fin height: 1mm

3.0 RESULTS AND DISCUSSION

Results obtained from this experiment have shown that the heat transfer coefficient of enhanced tubes aresignificantly higher compared to smooth tubes in the graph below. Comparing the results of Murase et al. and the results obtained in this experiment, it is proven that enhanced tubes perform better than smooth tubes. Below are pictures of inundation on smooth tubes for 4 different inundation rates.

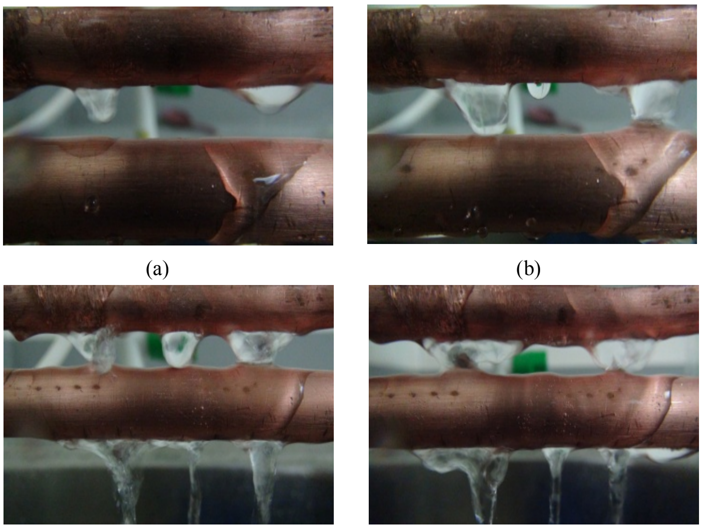

(a) (b)

(c) (d)

Figure 1. Photograph of simulated inundation on smooth tubes (a) Inundation rate: 0.1l/min; (b) inundation rate: 0.3l/min; (c) inundation rate: 0.5l/min; (d) inundation rate 0.8l/min

The figure above clearly illustrates the effect of condensate inundation on tubes and with it, the mode of falling condensates; (a) and (b) shows dropwise condensation while (c) shows column condensation and (d) shows a continuous sheet. As observed, the smooth tube is mostly covered in a film condensate preventing condensation whereas for enhanced tubes, the effect is much less. This can be seen in the pictures below. The results shown however, are only for 0.5l/min and 0.8l/min inundation rate, where the two highestrate tested in which the effect of condensate inundation is most apparent. This first set of results are pictures adopted from Murase et al. for wire-wrapped tube with winding pitch 4mm at 0.5l/min and 0.8l/min inundation rate.

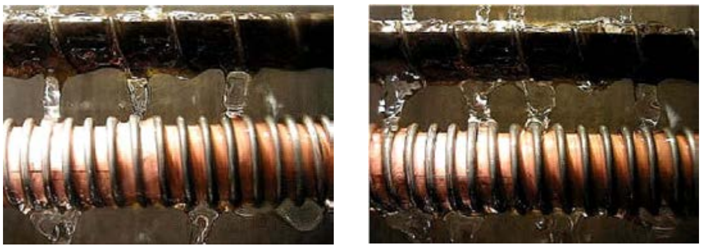

(a) (b)

Figure 2. Photograph of simulated inundation on enhanced tubes on wire-wrapped tubes with 4mm winding pitch. (a) Inundation rate: 0.5l/min; (b) inundation rate: 0.8l/min [1]

The second and third set of results shown below are obtained from the conducted experiment for 4 enhanced tubes for 0.5l/min and 0.8l/min inundation rates.

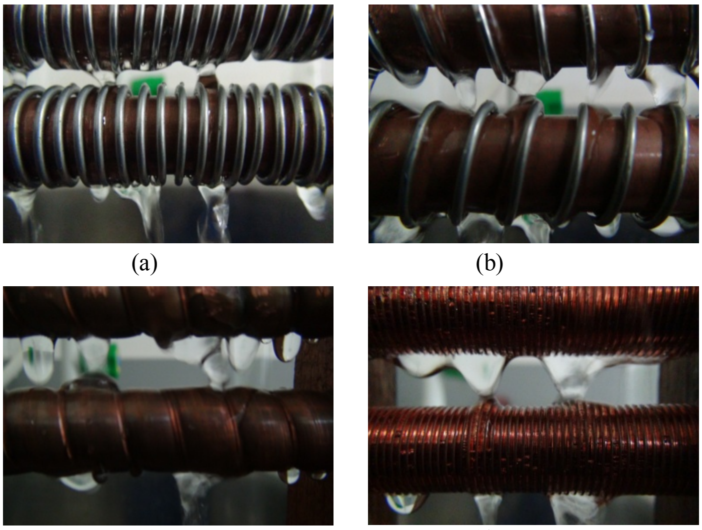

(a) (b)

(c) (d)

Figure 3. Pictures of simulated inundation on enhanced tubes at inundation rate of 0.5l/min where (a) Wire-wrapped tube 4mm pitch, (b) wire-wrapped tube 8mm pitch, (c) corrugated tube 8mm loop, (d) low-finned tube

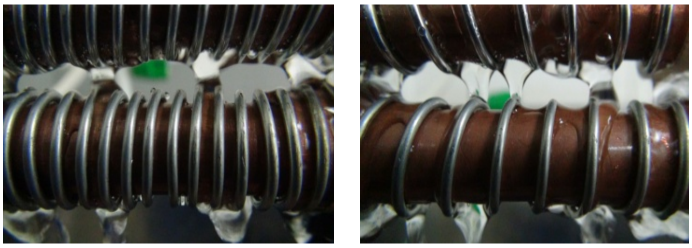

(a) (b)

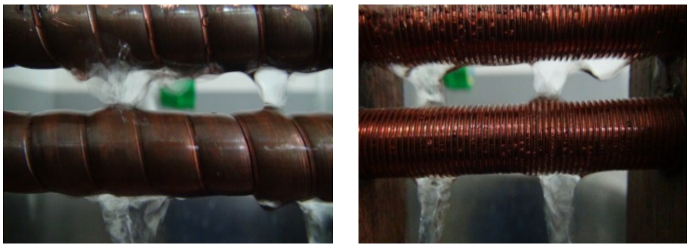

(c) (d)

Figure 4. Pictures of simulated inundation on enhanced tubes at inundation rate of 0.8l/min where (a) Wire-wrapped tube 4mm pitch, (b) wire-wrapped tube 8mm pitch, (c) corrugated tube 8mm loop, (d) low-finned tube

From the results above, it is clearly seen that the effect of inundation is less in enhanced tubes than smooth tubes. The results obtained in this experiment are similar to that done by Murase et al. for the wire-wrapped tube with 4mm pitch. In addition, in both experiments, it was found that the fin tube was the best performing tube. However, in this experiment, where a corrugated tube was tested, it was found that the corrugated tube does not perform as well as the other enhanced tubes.

4.0 ERROR ANALYSIS

The Kline and McClintock technique was used in this experiment. It was found that for a flow rate of 2l/min, there is a ±0.05l/min error. This would affect the outcome of the experiment.

5.0 CONCLUSION

The effect of condensate inundation was found to heavily affect the performance of a smooth copper tube. However, on an enhanced tube, this effect was less based on the results obtained even at a depth of 30 rows of tubes. The tube found with the least amount of condensate inundation was the low-finned tube. As for the wire-wrapped tubes, the performance of the tube improved when the winding pitch of the tube decreased. Lastly, the performance of the corrugated tube was almost similar to that of the wire-wrapped tube with 8mm winding pitch. However, results show that the heat transfer coefficient of corrugated tube is less than the wire-wrapped tube.

ACKNOWLEDGMENT

It is with immense gratitude that I acknowledge the support and help of my supervisor, Dr. Satesh Namasivayam whose patient guidance, steadfast encouragement and enthusiasm has made this research work possible.

REFERENCES

[1] T. Murase, H.S. Wang, J.W. Rose, Effect of inundation for condensation of steam on smooth and enhanced condenser tubes, International Journal of Heat and Mass Transfer 49 (2006) 3180-3189

[2] S. Namasivayam, Forced-Convention Condensation on Horizontal Integral-Fin Tube, University of London, Ph.D Thesis (2006)

[3] T. Murase, A. Briggs, H. S. Wang, J. W. Rose, Condensation on a horizontal wire-wrapped tube, Trans. ASME J. Heat Transfer 127 (11) (2005) 1207-1213

[4] T. Murase, Surface tension effects in condensation heat transfer: condensation on wire-wrapped tubes and Marangoni condensation of mixtures, PhD Thesis, University of London, 2006

Aerodynamic Loads on Trees During Storms

C. J. Gan*, S. M. Salim

School of Engineering, Taylor's University, Malaysia

**E-mail: gan.edwardchernjinn@sd.taylors.edu.my*

Abstract— **Fluid-structure interaction of trees during a typical storm is evaluated using Computational Fluid Dynamics (CFD). Velocity and pressure profiles with resulting mechanical effects are produced and compared between gentle breeze and severe tropical storm conditions where it is observed that tree damage is most likely to occur for the latter.**

Keywords— Aerodynamic loads, CFD, fluid-structure interaction, trees, turbulence, uprooting, windthrow

1. Introduction

Significant economic losses due to reduction of timber value and destruction of public amenities, fatalities, and the upset of balance of ecosystems in forests have long been a problem attributed by windthrow [1]. Windthrow occurs predominantly during storms therefore it is important to establish the key factors during its occurrence. Majority of previous investigations on windthrow have been performed using wind-tunnel (WT) experiments taking into account mechanical stability and other factors such as geographical, topographical, and seasonal and meteorological influences [2], [3]. However, numerical studies to investigate the imposed aerodynamic loads and the resulting mechanical effect on trees during storms have yet to be established. This is the main aim of the present research undertaking.

Velocity and pressure fields around a tree are numerically predicted using Reynolds Stress Model (RSM) turbulence closure scheme based on steady-state Reynolds-averaged Navier-Stokes (RANS) equations. A baseline (*gentle breeze*) wind speed of 4.7 ms^{-1} and extreme wind speed of 24 ms^{-1} (for a severe tropical *storm*) are investigated while accounting for typical Malaysian meteorological conditions [4] and tree species [5]. Aerodynamic effects between *tropical storm* conditions are then compared against *gentle breeze* conditions to allow qualitative conclusions to be drawn.

The imposed aerodynamic loads i.e. pressure fields on a tree obtained using CFD simulation are extracted from ANSYS FLUENT and implemented into ANSYS Mechanical in order to examine the resulting mechanical effects using structural analysis based on the Finite Element Method (FEM). This would give better insight into the aerodynamic ramifications leading to a possible windthrow during storms.

2. Methodology

Numerical flow simulations are performed in ANSYS FLUENT, adopting the simulation techniques and best practices of Salim *et al.* [6].

An inlet boundary condition is defined at the entrance while a pressure outlet is imposed at the exit of the domain to evacuate air. The top and sides of the computational domain behave as symmetry to represent a slip condition while the floor is considered as non-slip to correspond to typical conditions in open space. A summary of the 3D computational domain and employed boundary conditions are illustrated in Fig. 1.

In order to mimic a typical urban atmospheric boundary layer flow, the inlet wind is assumed to follow the power law profile

$$u(z) = u_H\left(\frac{z}{H}\right)^{\alpha} \tag{1}$$

where u is the vertical velocity profile, z is the vertical distance and the profile exponent, $\propto = 0.3$ while u_H is the free-stream velocity (= 4.7 ms^{-1}, 24 ms^{-1}) at reference height, $H = 0.12$ m for gentle breeze and storm inlet conditions, respectively. This follows the established settings used in [6] validated against WT experiments.

The computational grid illustrated in Fig. 1 is achieved using approximately 455K hexahedral elements. Resolution is progressively enhanced at the vicinity of the tree (at the center) to maximize numerical accuracy and reduce computational cost.

2.1. Tree Modeling

Idealization of the tree geometry is performed with 5 separate cuboids as illustrated in Fig. 2 with aim to resemble the Acacia Mangium, a common roadside tree in Malaysia [5]. The tree trunk is modeled as a solid body while the crown is set to be permeable with a porosity of $P_{vol} \approx 96$ %. The tree specifications are summarized in Table 1.

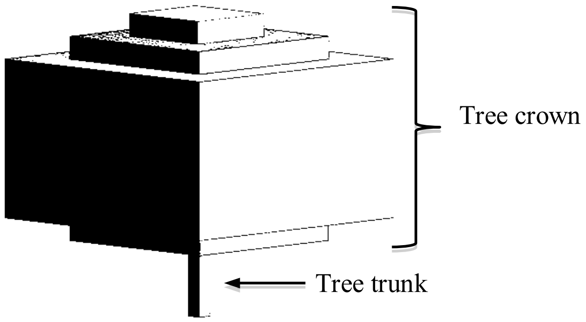

Fig. 2. Isometric view of tree geometry used in present study

Table 1. Tree Specifications

Parameter	**Value**
Tree species	Acacia mangium
Largest width of crown (m)	27
Largest height of crown (m)	27
Trunk height (m)	9
Trunk diameter (m)	2.8
Tree crown porosity, P_{vol} (%)	96
Flexural modulus, E (MPa)	5828[a]
Modulus of rupture, R (MPa)	62.28[a]

[a] Mechanical properties of tree are obtained from field measurements [5]

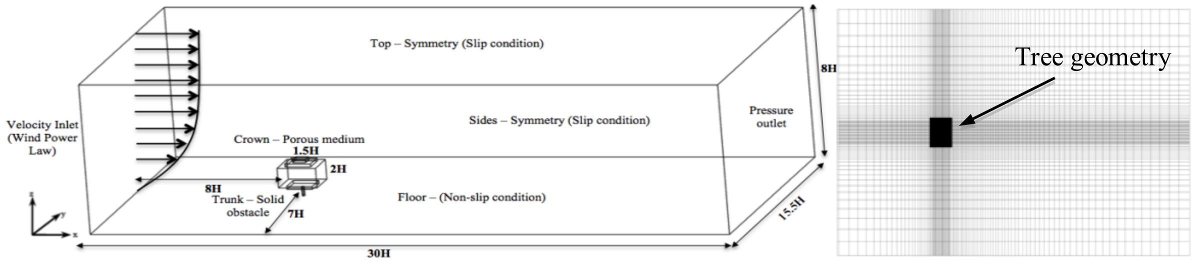

a) b)

Fig. 1. Configuration of a) computational domain, setup, and b) grid

2.2. Numerical Setup

The steady-state RANS solutions are obtained using RSM turbulence model and the convergence criterion (numerical precision) for all flow properties are set to 1 x 10^{-6} in ANSYS FLUENT for both the *gentle breeze* and *storm* inlet conditions.

The resulting imposed aerodynamic loads obtained from ANSYS FLUENT are mapped, interpolated, and exported to ANSYS Mechanical as face pressures. The material of the tree trunk is defined to match the mechanical specifications from Table 1 while the crown is assumed to be rigid. In order to solely investigate the aerodynamic effects resulting from interaction between the wind flow and structural behavior, the tree is assumed to be massless.

3. Results and Discussions

Fig. 3 presents the velocity contours for *gentle breeze* and *storm* conditions respectively. Airflow is observed to have a tendency to go around the tree rather than through it. The magnitudes of the flow field and resulting recirculation region are greater for the *storm* condition in comparison to the *gentle breeze.*

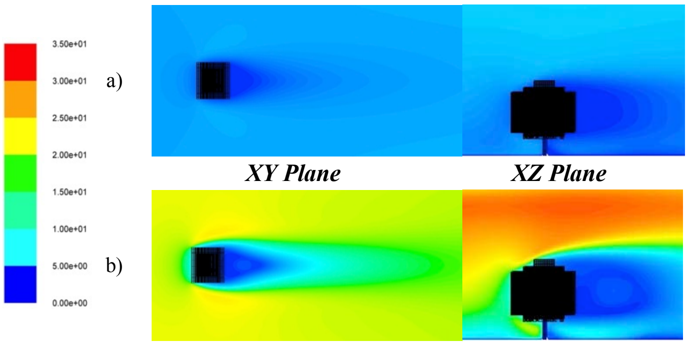

Fig. 3. Contours of the velocity magnitude (Pa) for a) 4.7 ms^{-1} *(gentle breeze)* and b) 24 ms^{-1} *(storm)*

The larger velocity drop that is generated by the *storm* condition presents a bigger pressure difference, which as a consequent implies higher aerodynamic loads are experienced by the tree. It is observed that the velocity difference between the windward and leeward sides of the *gentle breeze* (i.e. 4.7 ms^{-1}) are negligible compared to the *storm* (24 ms^{-1}) wind.

In fact, just behind the tree (at $x/H \approx 10$), the *storm* condition experiences a drop in velocity, indicating a very strong recirculation region, which is observable in the velocity contours of Fig. 3.

The profiles of static pressure for the two wind conditions are presented in Fig. 4. These supports the observations derived from the velocity fields, where it is deduced that the pressure difference experienced during the *storm* conditions are far greater than those during *gentle breeze*, resulting in greater aerodynamic forces on the tree.

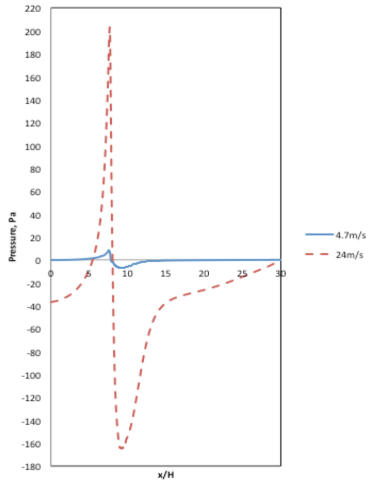

Fig. 4. Profiles of static pressure (Pa) 1H above ground along symmetry axis for 4.7 ms^{-1} *(gentle breeze)* and 24 ms^{-1} *(storm)* conditions

Winds typically induce a turning moment hence the flexural modulus rather than Young's modulus is considered. For the purpose of this investigation, failure by virtue of breakage of trunk is assumed to occur when the imposed stresses from the aerodynamic loads exceed the modulus of rupture. The resulting static stresses from the imposed aerodynamic loads are shown in Fig. 5.

Generally, it is seen that the stresses are at a minimum at the core of the trunk and increases outward. This suggests that at the time of trunk damage resulting from wind loads, failure is most likely to first occur on the outside and gradually spreads inwards. On the leeward side of the trunk (i.e. back of tree), the stresses can be seen to progressively increase as it moves farther from the ground (fixed support); where the magnitude of deflection is proportional to the resulting stresses.

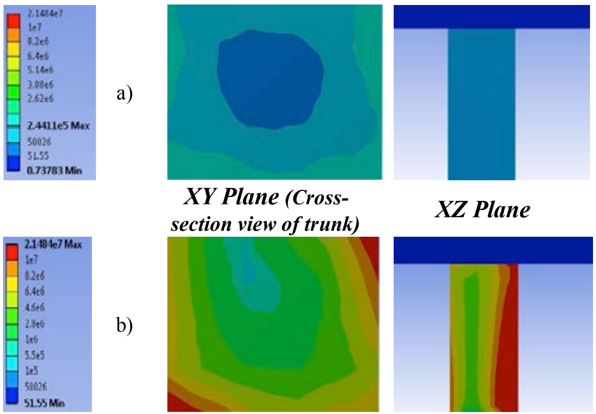

Fig. 5. Contours of the equivalent stress (Pa) of trunk for a) 4.7 ms^{-1} *(gentle breeze)* and b) 24 ms^{-1} *(storm)*

From the simulated results, during a storm condition, windthrow by trunk breakage is likely as resulting mechanical stresses closely matches the modulus of rupture for the given material.

4. Conclusion

During the *storm* condition, the pressure difference between the windward and leeward sides of the tree are much larger than during the *gentle breeze* due to a more prominent recirculating region which produces a negative flow field. This implies that the aerodynamic forces experienced by the tree are larger during stronger winds, which as a consequent results in higher deformation and stresses and increasing the possibility of structural failure.

Windthrow by damage to tree trunk is demonstrated to likely occur for *storm* conditions as the maximum equivalent stresses due to bending exceeds the rupture modulus of the material. Tree damage is highly unlikely for *gentle breeze.*

References

[1] Nina G. Ulanova, "The Effects of Windthrow on Forests at Different Spatial Scales: A Review," *Forest Ecology and Management*, vol. 135, pp. 155–167, 2000.

[2] Heli M. Peltola, "Mechanical Stability of Trees Under Static Loads," *American Journal of Botany*, vol. 93, no. 10, pp. 1501–1511, October 2006.

[3] Erk Brudi and Philip van Wassenaer, "Trees and Statics: Non-Destructive Failure Analysis," in *How Trees Stand Up and Fall Down*, Illinois, 2002, pp. 53–70.

[4] M. S. Sapuan, A. M. Razali, and K. Ibrahim, "Forecasting and Mapping of Extreme Wind Speed for 5 to 100-years Return Period in Peninsula Malaysia," *Australian Journal of Basic and Applied Sciences*, vol. 5, no. 6, pp. 1204–1212, 2011.

[5] M. H. Sahri, Z. Ashaari, R. A. Kader, and A. L. Mohmod, "Physical and Mechanical Properties of Acacia mangium and Acacia Auriculiformis from Different Provenances," *Pertanika Journal of Tropical Agricultural Science*, vol. 21, no. 2, pp. 73-81, 1998.

[6] S. M. Salim, A. Chan, and S. C. Cheah, "Numerical Simulation of Atmospheric Pollutant Dispersion in Tree-lined Street Canyons: Comparison between RANS and LES," *Building and Environment*, vol. 46, pp. 1735–1746, 2011.

CFD Application on Cleanrooms Design

C.Y.Chuah[1], Salim.M.Salim[1], H.G Low[2]

jeffersonchuah@gmail.com

[1]School of Engineering, Taylor's University, Malaysia

[2]EMS Design and Consultation department, Toptrans Engineering Sdn.Bhd, Malaysia

Abstract - **Cleanroom is a facility desirably for the manufacturing or scientific research that has a lower level of environmental pollutants or particles where it has a controlled level of contamination. Clean rooms have evolved into two major types which are also known as non-unidirectional (turbulent) and unidirectional (laminar) clean rooms. This study therefore analyses, simulates, and compares two types of non-unidirectional (turbulent) clean rooms which are also known as locally balanced and wall-return turbulent clean rooms, by Computational Fluid Dynamics analysis (CFD). Comparison has been made between all the different turbulence models to determine which set of turbulence model is suitable for the cleanroom CFD modelling. LES model shows a drastically different results where it is believed that LES model has a better accuracy however high computational cost.**

Keywords— Air recirculation; CFD (Computational Fluid Dynamic); Cleanroom; HVAC; Non-unidirectional

1. Background

There are two major types of cleanrooms and they are categorized by their method of different ventilation configuration. These are unidirectional flow and non-unidirectional flow cleanrooms. Unidirectional flow cleanrooms were originally known as 'laminar flow' cleanrooms. Besides that, the non-unidirectional flow cleanrooms were also known as 'turbulent flow' cleanrooms. The two major types of cleanrooms are shown diagrammatically in Figure 1. Figure 1a shows a non-unidirectional cleanroom receiving clean filtered air through air diffusers in the ceiling. Figure 1b shows a unidirectional cleanroom [1].

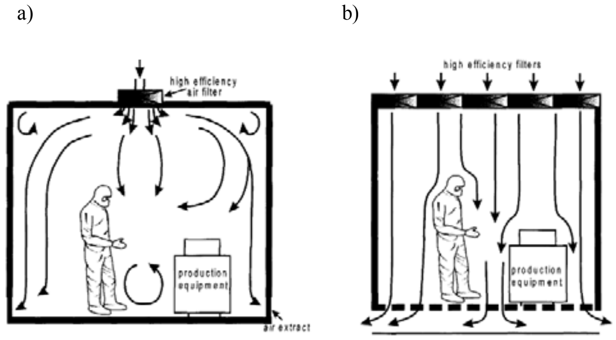

Figure 1: Two major types of clean rooms, a) non unidirectional, b) unidirectional [1].

2. Introduction

Non-unidirectional cleanrooms are used in many areas such as high-technology industries, hospitals, precision machine assembly lines and so on. Understanding the flow pattern is important to achieve contamination control when designing a cleanroom [1]. A clean room with supply air opening on the ceiling and exhaust air opening on the wall hereafter referred as a wall return type cleanroom (figure 2b), is traditionally assumed to facilitate particle exhaust, because the direction of airflow is consistent with the movement of particle settling. Installing supply as well as exhaust openings on the ceiling is common in office buildings (figure 2a). However, from the view point of ordinary contamination control in a clean room such an arrangement is not recommended [2].

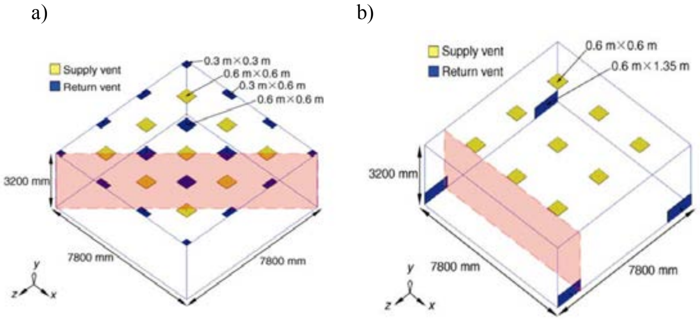

Figure 2: Computational domain of two different ventilation arrangements cleanroom, a) Locally Balanced, b) Wall-Return [3].

2.1. Literature Review

Murakami *et al.* [4] studies the effect of changes in arrangement or in the number of exhaust openings in the cleanroom. The study found out that such change will affect the flow field drastically as it affects the pressure gradient of the cleanroom and hence will greatly affect the particle escape ratio. Shimida *et al.* [5] investigated a study in theoretically the change in concentration distribution of particulate contaminants emitted in a laminar flow type cleanroom.

2.2. Objective

This study aimed to examine and compare the performance of two types of non-unidirectional cleanrooms in order to identify viable solutions to effective contamination control. We developed CFD models to simulate the air in the cleanroom. The objectives of present study are summarized following:

a) To increase confidence in using CFD for industrial cleanroom engineering application.
b) Investigate the numerical behavior of CFD turbulence models with ANSYS Fluent v14.0, and hence improve flow prediction in cases where reliable experimental data are unavailable.
c) Ultimately, to obtain the best practice guideline for the CFD study of cleanroom.

3. Research Methodology

This study used the Lagrangian approach to study to model the particle transport. The Lagrangian method considers particles as a discrete phase and tracks the pathway of each individual particle. Equation 3.1 shows the Lagrangian and Eulerian specifications of the flow field are sometimes denoted as the Lagrangian and Eulerian frame of reference. Both can be applied in any observer's frame of reference.

$$\bar{a}(x,y,z,t) = \frac{Du}{Dt} = \frac{\partial \rho u}{\partial t} + u\nabla\rho u \qquad (3.1)$$

For numerical modeling, one steady Reynolds-Average Navier-Stoke (RANS) turbulence model and a Large Eddy Simulation (LES) were performed in present study:

a) Renormalization Group kε – Model (RNG)(RANS)
b) Large Eddy Simulation (LES)

CFD Approach	Differences
RANS	All turbulent scales on time-averaging and transport equations of mean flow quantities are solved.
LES	Only resolves the energy-containing eddies and filters out the smaller universal eddies that are modeled.

Table 1: Types of CFD approaches [6].

4. Simulation Results

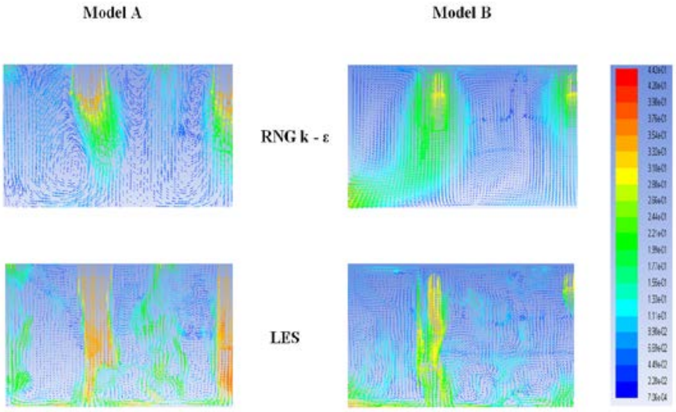

Figure 3: Streamlines of velocity vectors obtained in Model A: Locally Balanced cleanroom, Model B: Wall-return cleanroom.

In Figure 3, model A with RNG k- ε model shows the inlet supply air flow down towards the floor direction and circulate up back to the exhaust grille because of pressure gradient. There were huge recirculation airflows and swirls generated between the falling and the rising airflows, and resulted in stagnation regions. In the other hand, model B shows the supply air from the inlets pushes the airflow and hit the top part of the tools and the airflow was spread into two direction left and right. There were two swirls created before the left airflow get exhausted out from the room through the outlet exit from the bottom corner of the wall. The right airflow hit the airflow from the middle supply grille and several swirls and air recirculation were generated in between the tools and particles can be easily trap here. The LES result for both models showed a significant difference compared with the RANS turbulence results. The LES results showed more swirls created everywhere. It is believed that LES has a better accuracy in results because the main advantage of LES over RANS is that deterministic unsteadiness of large eddy motions can be resolved. In LES the transport equations are filtered such that only the larger eddies need be solved, whereas the smaller eddies are modeled.

5. Graph

In figure 4, the gravitational forces of 100 µm were too dominant. Therefore, there are no particles in this large size being ventilated from both the cleanrooms. The percentage of the escaped particles ≤ 1.0 µm diameter in model A and B was 12% and 24%. In the other hand, particles of 10 µm diameter in models A and B was 2% and 16%. As predicted, the wall-return type cleanroom has better cleanliness efficiency in terms of particles removal than the locally balanced type cleanroom.

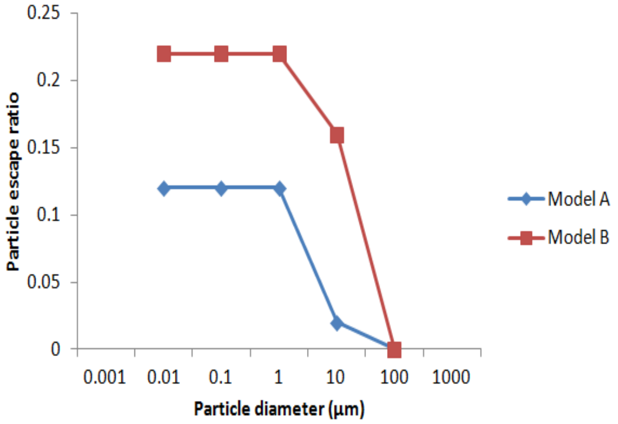

Figure 4: Ratios of the escaped particles in Model A and B.

6. Conclusions

LES model showed significant different results compared with the RANS turbulence models in both the cleanrooms. More swirls are generated in LES model hence more particles are predicted to be trapped in the rooms. The layout of exhaust openings greatly influences particle trajectories. Wall-return cleanroom has a better efficiency in particle removal compared to locally balanced cleanroom because less swirls that will trap particles are generated in the room as shown in figure 3.

Acknowledgment

Special credits to the following main contributors of the research:

1) Supervisor: Dr. Salim Mohammed Salim

2) Industrial Supervisor: Ir. Den Low Han Guan

References

[1] William Whyte, *Cleanroom Technology: Fundamentals of Design, Testing and Operation*. United Kingdom: Wiley, 2010.

[2] S.C.Hu and Y.C.Tung, "Performance Assessment for Locally Balanced and Wall-Return Turbulent Clean rooms by the Stochastic Particle Tracking Model," *International Journal on Architectural Sciences*, vol. 3, pp. 146 - 162, 2002.

[3] Yun-Chun Tung, Shih-Cheng Hu, Tengfang Xu, Ren-Huei Wang, "Influence of ventilation arrangements on particle removal in industrial cleanrooms with various tool coverage," *Building Simulation*, vol. 3, pp. 3 - 13, 2010.

[4] S.Murakami, S.Kato and S.Nagano, "Numerical study on diffusion in a room with a locally balanced supply-exhaust airflow rate system," *ASHRAE Transactions*, vol. 98, pp. 218 - 238, 1992.

[5] Shimida M, Okuyama K, Okazaki S, Asai T, Matsukura M, Ishizu Y, "Numerical simulation and experiment on the transport of fine particles in a ventilated room," *Aerosol Science and Technology* , vol. 25, pp. 242 - 255, 1996.

[6] H K Versteeg and W Malalasekera, *An Introduction to Computational Fluid Dynamics, The Finite Volume Method*: Pearson, Prentice Hall, 2007, pp 40 – 101.

Controller Tuning for a Nonlinear Liquid Level System

Chan Woei Shyan[*], TVN. Padmesh , K. Suresh Manic

School of Engineering, Taylor's University, Malaysia

**Corresponding email: chan.woeishyan@sd.taylors.edu.my*

Abstract— **Nonlinear system is due to the variation of cross section area correspond to the level system with change in shape. Hopper tank, for instance. Controlling the process parameters for nonlinear process is one of the important issues identified in literature. Firstly, Identification of process transfer function is done through the real time implementation experiment and it is applied to a conventional PID (proportional, integral and derivative) controller. Followed by tuning method has been proposed including Cohen-Coon (C-C), Ziegler & Nichols (Z-N), Internal Model Control (IMC) and Tyreus & Luyben (T-L) into PID controller. These tuning methods are design using computer simulation in MATLAB under Simulink software and error integral (ISE, IAE, ITAE) has been used as the criterion for comparison. From the result, it is observed that, T-L and Z-N provides better result compared to other methods considered in this study.**

Keywords— Nonlinear Process; PID Controller; Hopper Tank; Tuning Method;

1. Introduction

A process performance in an industrial are mainly depends on effective use of process control. This process control can be included in a unit operation that controlling such system in order for maintaining it operation condition [1]. Pumps, valves, pipes and other process equipment, for instance. There are two categories system that can be found in industrial segment such as linear and nonlinear system. For you information, nonlinear behavior is typically exhibit in most process control industries [2].

Nonlinear system exists is due it cross section area vary toward the height. For example, a spherical tank, cyclone, hopper tank, as well as a conical tank. Control system goal is to maintain the process variable (PV) at or near the set point (SP) in the presence of any load changes, disturbances or SP changes [3]. Conventional PID (proportional, integral, and derivative) controllers are used to control highly nonlinear process. By many process control research has been largely emphasized on the tuning parameters. PID controllers are tune to achieve a good control that provides stable behavior over the entire range of operating conditions.

Several controller tuning rules are used in PID controller and it performance will be analyzed and compared in this work. This paper has been carry out in a hopper tank which has a nonlinear behavior. Controller tuning rules are included C-C (Cohen-Coon), Z-N (Ziegler & Nichols), IMC (internal model control) and TL (Tyreus & Luyben) in order to makes the process operational and meet the performance criteria with minimum error.

2. Methodology

For this research, a Hopper Tank will be fabricated with height of 100cm. Experiment set up can be seen in Fig. 1, it consist of pump, water storage tank, PID tuning controller, pneumatic valve, pressure regulator, air compressor, I/P convertor, and the hopper tank.

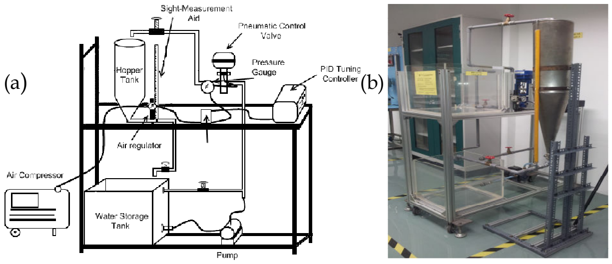

Fig. 1: (a) Experimental setup for nonlinear liquid level system
(b) Real time impletation of PID tuning with hopper tank

2.1. System Identification and Modeling

Identifying the process has to be done before proceed to tuning method. The process of identification has deals with the process gain (K_m), time constant (τ_m), and time delay (θ) that can be determined by an experimental result of single step change on process input. Process parameters can be calculated from equation 1-3 as follows [4]:

The process gain:

$$K_m = \frac{\Delta input}{\Delta output} \tag{1}$$

The time constant:

$$\tau_m = 1.5(t_{63.2\%} - t_{28.3\%}) \tag{2}$$

Time delay:

$$\theta = t_{63.2\%} - \tau_m \tag{3}$$

System testing here is considered the first order system with dead time (FOPDT) according to the laboratory results obtain. Determination of process parameters are clearly shown in Fig. 2.

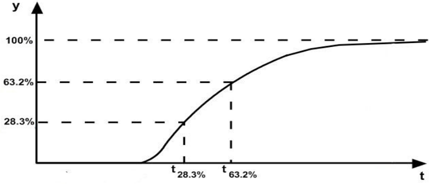

Fig. 2: First-order system response to a unit step [4].

Process of nonlinear system here is known as FOPDT model by the following transfer function:

$$G_m(s) = \frac{K_m e^{-\theta s}}{(\tau_m s + 1)} \tag{4}$$

2.2. Controller Identification

PID controller tuning methods are classified into four categories as follows:

- Cohen-Coon
- IMC (internal model control)
- Ziegler and Nichols
- Tyreus and Luyben

Tuning technique, Cohen – Coon can be fit to a FOPDT model with the advantages that the procedure does not involve trial and error with only a single experiment is necessary [5]. As for Ziegler-Nichols method, is one of the popular methods among others in tuning PID controllers. It controller settings are easily calculated and a process model is not necessary [5]. For IMC tuning method, it involves “lambda tuning (λ)” which obtain by trial-and-error. Lastly, Tyreus & Luyben is an alternative method as Ziegler-Nichols but with modified formulas for the controller parameters that provide better performances [5].

2.3. Simulation

MATLAB will be used to stimulation each of the step input from 40% valve opening to a 100% fully opened valve. In order to get this complete, Simulink has been applied. Simulink is software that runs under MATLAB which provide blocks to represent operations [6]. For this research, a block of operation is shown in Fig. 3.

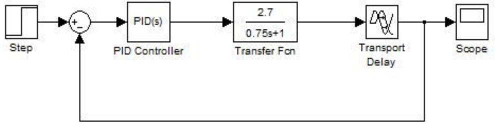

Fig. 3: Simulink diagram for the simulation of the nonlinear process

2.4. Real Time Implementation

After the simulation, two of the best tuning methods with good performance are chosen to be tested at real tank. Ziegler & Nichols tuning method and Tyreus & Luyben (1997) has shown less overshoot, minimum offset with fast response time as compared to others tuning method. At 80% step input, Tyreus & Luyben tuning result can be seen in Fig. 4.

2.5. Criteria of Error Integral Analysis

Selection for a best controller by using three different tuning criteria: IAE (integral of absolute error), ISE (integral of square error) and ITAE (integral over time of the absolute error) [3]. So, there will no excessive response to a SP (set point) changes given by the controller. Each of this error integral is a form of penalty function representing the size and duration of error [7]. Figure 3 gives details of the tuning methods that aim to minimize the penalty.

3. Results and Discussions

From the system identification, process parameters of different operating regions are obtained and can be seen in Table 1.

Table 1: Process Gain, Time Constant and Time delay at different valve opening operating condition.

Valve Opening	K_m	τ_m	θ
at 40%	2.7	0.75	0.15
at 60%	0.68	1.50	0.70
at 80%	0.18	0.78	0.22
at 100%	0.09	0.30	0.30

In real time experimental result, it exhibits an oscillatory response by which it has shown an overshoot at 5 minutes time and then slowly settling down to the set point (SP) which is at 10cm after 5 minutes. There is no overshoot that exceed the set point in simulation result unlike experimental result. In addition, simulation has slow response to achieved SP. Besides, TL is also considered a best tuning where steady state can be achieved within 3 minutes as step input added. Comparison between simulation and real time implementation is shown in Fig 4.

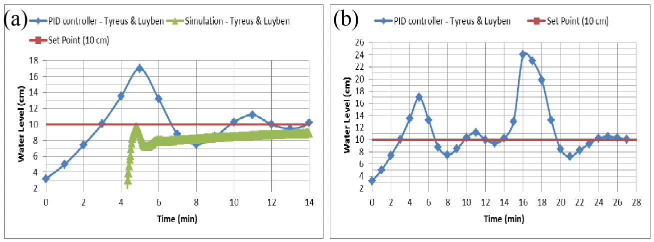

Fig. 4: (a) Comparison between simulation and real time experimental result.
(b) Response of step input (load) in real time experimental result.

For TL tuning method, it has shown the least error integral value that can be applied for PID tuning controller. ZN tuning will be chosen as second selection where error integral value is much lesser than error integral method (ISE, IAE and ITEA), as shown in Table 2.

Table 2: Minimum error integral value for different tuning method

Method	Error Integral Value
ISE	27.86
IAE	26.01
ITEA	25.44
Z-N (Ziegler & Nichols)	21.38
T-L (Tyreus & Luyben)	17.55

4. Conclusion

Tuning method of Tyreus & Luyben in PID controller has given good and acceptable performance with less aggressive oscillation as well as fast settling response. Besides, it also shows good result for disturbance rejection with fast settling response. In addition, it has the minimum error integral value and followed by Ziegler & Nichols method. This concludes that both Tyreus & Luyben and Ziegler & Nichols method are applicable for most system control in nonlinear process. In future, both tuning can be applied in nonlinear control of hopper tank as well as continual exploration needed to meet the process requirements.

Acknowledgment

I would like to thanks my course mates who have helped in completing this research including Boey Kah Heng and Song Cher Pin who has supported me in all doubt. Finally, thanks to my family for their continued encouragement of completing this research.

References

[1]Bela G. Liptak. (2012). *Instrument Engineer’s Handbook: Process Control.* United State of America: CRC Taylor & Francis.

[2]Micheal A. Henson., & Dale E. Seborg. (1997). *Nonlinear Process Control.* Upper Saddle River, New Jersey: Prentice Hall PTR.

[3]Carlos A. Smith, Armondo B. Corripio. (1985). *Principles and Practice of Automatic Process Control-3rd ed.*United States of America: John Wiley & Son.

[4]Sakthivel G., Anandi T. S. and Natarajan S. P. (2011). Modelling and real time implementation of digital PI controller for a non linear process. *Journal of Innovative Research in Engineering and Sciences 2(5), 274-290.*

[5]Jose A. Romagnoli, Ahmet Palazoglu. (2012). *Introduction to Process Control.*Boca Raton, London: CRC Press.

[6]Manjita Srivastava, Srivastava M. C., & Smriti Bhatnagar. (2009). *Control System – MATLAB and Simulink Tutorial.*7 West Patel Nagar, New Delhi: Tata McGraw-Hill

[7]Myke King. (2011). *Process Control - A Practical Approach.*Whitehouse Consulting, Isle of Wight, United Kingdom: WILEY.

MEMs Biosensor: the Electromagnetism Approach

Chan Ching Hong[1], Edwin C.Y. Chung and Kandasamy Pirapaharan[2*]

[1]*chan.chinghong@sd.taylors.edu.my*

School of Engineering, Taylor's University, Malaysia

Abstract— **Traditional method for the detection of pathogens requires culturing to increase the density of pathogen for clearer observation. However, culturing is inefficient as the entire process take days to complete. This paper summarises the concept and theory for a MEMs biosensor that utilises electromagnetic inductance as a detection method. Hypothesis of the concept is supported by mathematical derivation and further verified by computational simulation and experiments.**

Keywords— Biosensor, Electromagnetic, Inductance, Permeability, MEMs.

1. Introduction

Biosensor, as an emerging technology, has advanced recently due to the ability to improve health screening and the fight against Bioterrorism [1]. Different approaches [2-4] have previously been proposed as a means to overcome several weaknesses in current biosensor technology. Top of this list of weaknesses are accuracy, efficiency and user-friendliness. This paper present a study conducted to investigate the possibility of detecting the presence of a specific pathogen via changes in mutual inductance of VLSI coils immersed in a solution of magnetic nanoparticles coated with receptors targeting specific pathogen.

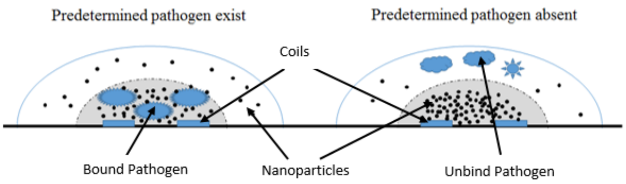

Fig. 1 Illustration of the operational principle of biosensor, showing the difference in response with respect to the present of pathogens.

It is theorized that magnetic nanoparticles, coated with biochemical to create receptors on a surface of these nanoparticles that bind with a specific strain of pathogens, will changes the magnetic properties if the specific strain of pathogen is present. It is assumed that when appropriate magnetic force is applied, pathogens that bound with nanoparticles will clump close together near the energized coils. In that finite volume, density of nanoparticles will be low as part of the volume is occupied by pathogens. However, if the predetermined strain of pathogen does not exist, these nanoparticles will occupy most of the volume near the energized coils. The difference density is detected via a change in mutual inductance in VLSI coils.

2. Literature Review and Methodology

In order to gain comprehensive understanding in the changes of properties of mixtures due to different mixture ratio, literature related to how inclusions influence effective permeability were reviewed. Moreover, a numerical model of electrostatic analysis is completed to study the behavior of resultant output with respect to several parameters.

2.1. 2-Dimensional Electrostatic Analysis

2-Dimensional Electrostatic Analysis is done with respect to its relationship to several design parameters, referring Fig. 2a, in order to determine optimum configuration for sensor design.

$$B = \frac{\mu_0 IR(N_1)(N_2)}{4\pi}\int_0^{\pi}\frac{(R+d)\cos\emptyset - R}{[(d+R)^2+R^2+2(d+R)(R)\cos\emptyset]^{\frac{3}{2}}}\cdot d\emptyset$$

Equation above is derived with respect to Bio-Savart law (applicable for Magnetostatic analysis) and geometrical analysis. Although the accuracy of first order equation is greatly reduced due to 2-dimensional approach and simplified modelling, it is however able to show that the resultant of mutual inductance will be somewhat response linearly due to changes of permeability.

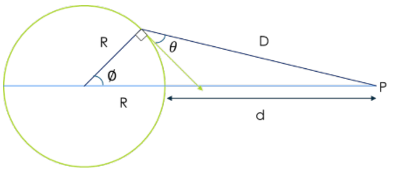

Fig. 2a Geometry of analyzing B generated by coil at point P with distance d.

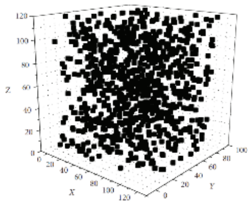

Fig. 2b Studies [7] shows that random distribution of inclusion possesses only 0.5% deviation of permeability

2.2. Effective Permeability of Mixture (Maxwell-Garnett Model)

Different Models [5] are used to demonstrate the nature of permeability changes of material in different concentration and different geometrical representations. In this study, Maxwell-Garnett Mixing model [6] is used as a benchmark for implementing into the equation derived earlier, due to the lack of other mixing models demonstrating in study of dielectric mixtures and electromagnetism properties.

$\mu_{eff} = \mu_0 + 3\mu_0 \frac{f\frac{\mu_1-\mu_0}{\mu_1+2\mu_0}}{1-f\frac{\mu_1-\mu_0}{\mu_1+2\mu_0}}$	f: Filling factor of the inclusion μ_0: Permeability of background material μ_1: Permeability of inclusion.

The equation shown above, is the generalized equation for sphere inclusion. Modelled equation above prove that density of inclusion will result in linearly increment in overall permeability.

However, a study done by B. Hallouet and R. Pelster [7] using computational domain evidently demonstrated that random distribution of inclusion in a finite volume possesses negligible effect on the overall permeability of composite mixtures. If such case holds, the required sensitivity and accuracy of the approach proposed in this paper will be difficult to achieve.

3. Practical Result

In order to verify such uncertainty, an experiment was performed whereby a sensor is designed using 2 coils placed next to each other. The resultant waveform at the secondary coil was observed while the primary coil energized by a sinusoidal waveform for various density and distribution of inclusions (mild steel powder).

70 samples for each combination of density and input RMS were recorded against the induced voltage. It is observed that there is a correlation between the induce voltage and the density of inclusion. There is approximately 5% - 17% increment in voltage with each increment in density of inclusion. It is also noticed that there is very little difference in induced voltage between scattering and concentrating inclusions.

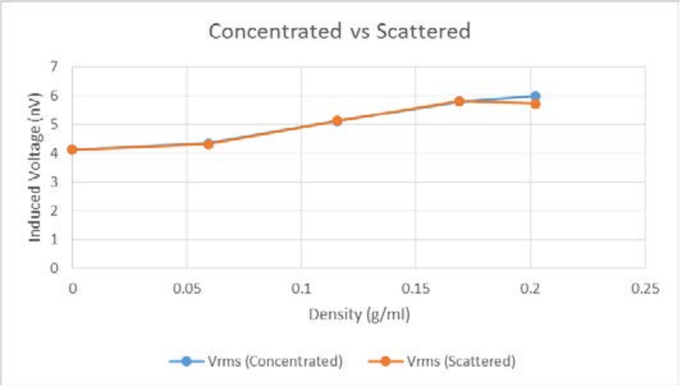

Fig. 3 Result of practical test, showing the relationship of increment in density versus resultant induced voltage.

4. Computational Simulation

Table 1. Setups and Boundary Conditions of Simulation

Items	Description
Domain	10mm x 10mm x 10mm
Coils	0.5mm radius, 12 segments polygon, 1mm separation
Background	4mm x 4mm x 0.25mm
Inclusions	Volume Fraction: 5%
Voltage Input	15V, 600Hz
No. of Elements	150000 – 200000 meshes
Simulated Time	0.05s, 0.0001s interval

Similarly, a computational simulation is carried out to examine the accuracy of the predicted behavior. Several cases which manipulate the distribution of inclusion, effective permeability of domain have been simplified and modelled, simulated using transient magnetic solver. Basic design characteristics and boundary conditions are listed in Table 1.

5. Result Discussion

In both practical and simulation result, the influence of material property toward the changes of resultant induced magnetic flux is obvious. However, results obtained indicate the lack of sensitivity and accuracy. Moreover, the distribution of inclusions doesn't have much effect towards the overall induced magnetic flux. From Fig. 4, for concentrated and conc.div case, resultant voltage drop immensely due to the slight separation distance between inclusions. It can be deduced that it will further decrease if the number of divisions increases.

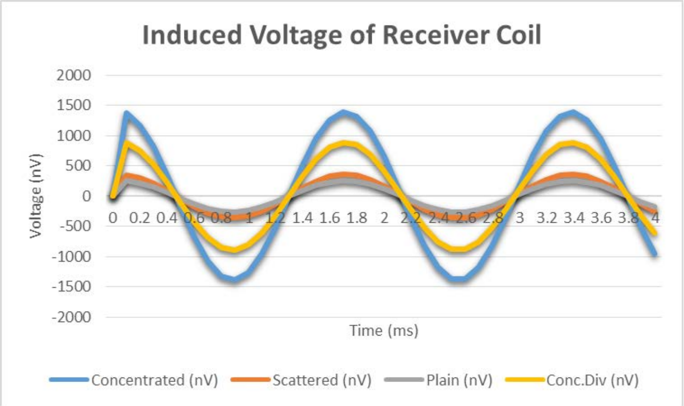

Fig. 4 Part of the result from simulation demonstrating the difference of resultant voltage in difference cases. Plain – simulation without high permeability inclusions; Concentrated – simulation with 5% volume fraction (VF) metal inclusion concentrated; Scattered – simulation with 5% VF inclusions, randomly distributed; Conc.Div – simulation with 5% VF inclusions, concentrated with minor separation.

6. Conclusion

The result from this research indicates that the proposed approach is fairly plausible. However, several limitations were noticed need to be improved for the sensor to be accurate and practical. Smart algorithm is necessary for noise cancelling. The smaller the sensing coils, the higher the saturation of noise once amplified. It is believed that the solution may lie in the configuration of multiple coils and the way these coils are energized and sensed.

Acknowledgment

I would like to thank my supervisor, Dr. Edwin Chung for this project concept and along with my co-supervisor, Dr. Kandasamy Pirapaharan, for sacrificing precious time to guide me through the project.

I would also like to thank all my fellow colleagues who had lend me their helping hand in sharing knowledge and discussed with me for better understanding in this study.

References

[1] B. Hoyle, "Bioterrorism," 2012. [Online]. Available: http://science.jrank.org/pages/918/Bioterrorism.html.

[2] Alexander D Rosenstein, David Carroll, Journal of Biosensors & Bioelectronics, OMICS Publishing Group, 2010.

[3] M. Berger, "Nanotechnology sensor detects living bacteria at ultralow concentrations." 2009. [Online]. Available: http://www.nanowerk.com/spotlight/spotid=12906.php .

[4] Yong-Ho Kim, Eun-Soo Hwangm and Yong-Jun Kim, "Polymer/Metal Based Flexible MEMS Biosensors for Nerve Signal Monitoring and Sensitive Skin," Journal of Semiconductor Technology and Science, vol. 5, pp. 11-16, 2005.

[5] A. H. Sihvola and I.V. Lindell, "Effective Permeability of Mixtures," in Electromagnetic Mixing Formulas and Applications, IET, 1999, p. 153-180.

[6] G. W. Milton, The Theory of Composites (eds. Ciarlet, P. G., Iserles, A., Kohn, R. V. & Wright, M. H.), Cambridge University Press, 2002.

[7] B. Hallouet and R. Pelster, "3D-Simulation of Topology-Induced Changes of Effective Permeability and Permittivity in Composite Materials," Journal of Nanomaterials Volume 2007, p. 8, 2007.

Investigation of Flow Profile in Spray Drying Process

Cher Pin Song[1*], Rashmi Gangasa Walvekar[1], Lee Hong Tee[2]

[1]School of Engineering, Taylor's University, Malaysia, [2]School of Engineering, Monash University, Malaysia

**Corresponding author: songcherpin@gmail.com*

***Abstract*— The flow pattern inside the spray dryer during the drying of betel leaf extract at different initial droplet size, hot air temperature and feed rate was simulated using ANSYS FLUENT v14.0. In this study, standard k-ε was selected and the flow was assumed to be steady flow. Four different initial droplet sizes (36, 79, 123, 166μm) were tested with four sets of combination of hot air temperature (140, 160℃) and feed rate (4, 9.5, 15ml/min). The predicted flow profiles were compared and analyzed. Results showed that smaller initial droplet size at the temperature of 160℃ and a feed rate of 9.5 ml/min is the optimum drying condition.**

Keywords— Spray Drying, CFD, Flow Profile, Initial Droplet Size, Hot Air Temperature, Feed Rate

1. Introduction

Studies have proven that betel leaf possess beneficial effect such as antioxidant properties, antidiabetic activity and antimicrobial which improve human health. There is a great potential to extract the phytochemicals within the leaf and introduced into consumable food product. Spray drying technique can be used to convert the extract into powder to increase the life span of the extract [1].

The quality of the spray drying dried product is directly affected by the air flow pattern [2]. However, the modeling of the flow profile in the spray dryer at different operating parameters is inadequately developed [3]. CFD can be used to predict the complex flow behavior during the spray drying process by solving the governing equations numerically [4].

The objective of the current study is to present and discuss the flow profiles for different initial droplet size at different hot air temperatures and feed rates. The results are compared with the drying kinetics studied by Roustapour et al. [5].

2. Methodology

2.1. Geometry and Meshing

The simulations were conducted in a lab scale cylinder-on-cone spray dryer as shown in Fig. 1. The heating medium and the feed are flowing concurrently. Its characteristics are shown in Table 1.

Fig 1. Geometry of the lab scale spray dryer

In this study, the analysis was conducted using 2-D and the flow behavior inside the dryer was assumed to be axisymmetric. This is to reduce the complexity of the air flow pattern inside the spray dryer by assuming the swirl angle is zero [5].

The geometry of the spray dryer was created using Design Modeler. 3 different fineness meshes as shown in Table 2 were generated for grid independency test. No significant difference was obtained for the velocity profile between 0.01 m and 0.005 m mesh size. However, the flow profile obtained from 0.01 m was more detail than 0.015 m mesh size. Hence, 0.01 m was used in this study as it provides precise flow profile and requires lesser time to compute a simulation. Fig. 2 shows the geometry with mesh size of 0.015m.

Table 1. Characteristics of spray dryer

Part	Length (m)
Cone Height	0.4900
Cylinder Height	0.1100
Cone Diameter	0.0800
Air Inlet Diameter	0.0400
Nozzle Diameter	0.0070
Outlet Diameter	0.0175

Table 2. Meshing for grid independency test

Type	Mesh Size (m)	No. of Mesh
1	0.015	10300
2	0.010	35442
3	0.005	128879

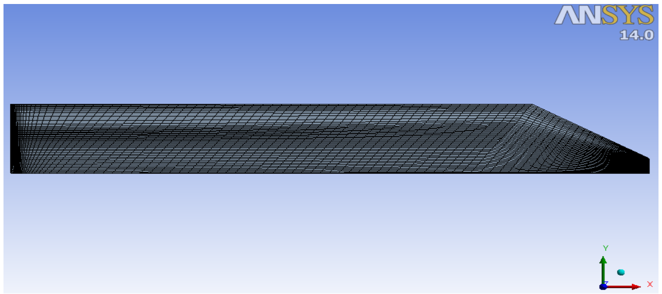

Fig 2. Geometry of spray dryer with 0.015m mesh size

2.2. Boundary Conditions

An injection point was created at the feed inlet of the geometry. The velocities of the hot air and the feed were 0.003257 kgs^{-1} and 0.41 ms^{-1} respectively. The outlet pressure was set to be 4415 Pa. For pressure-velocity coupling, SIMPLEX was chosen for this study and the turbulence intensity was set to be 9%.

Four initial droplet sizes (36, 79, 123, 166μm) were tested at four combinations of hot air temperature and feed rate as shown in Table 3 to determine the flow profile.

Table 3. Operating parameters combination

Set	Hot Air Temperature (℃)	Feed Rate (ml/min)
1	160	9.5
2	140	4.0
3	140	15.0
4	160	15.0

The flow in the dryer is two-phase. Therefore, a coupling between continuous and discrete phase was required to model this type of flow. The continuous phase calculation was performed to model the air and discrete phase was used to model the droplets [6]. The governing equations for continuous and discrete phases are shown as below:

Continuous Phase – Momentum Equation

$$\frac{\partial(\rho u_i u_j)}{\partial x_i} = -\frac{\partial P}{\partial x_j} + \frac{\partial}{\partial x_i}\left[\mu\left(\frac{\partial u_i}{\partial x_j} + \frac{\partial u_j}{\partial x_i}\right) - \rho\overline{u_i' u_j'}\right] + M_F \qquad (1)$$

Discrete Phase

$$\frac{du_{pi}}{dt} = C_D \frac{18\mu}{\rho_p d_p}\frac{Re}{24}\left(u_i - u_{pi}\right) + g_i \frac{\rho_g - \rho}{\rho_g} + F_{xi} \qquad (2)$$

For turbulence model, standard k-ε was chosen as it converges better than other models. In addition, it requires less computational effort to generate a simulation result which is similar when other models are applied but require much more computational effort.

3. Results and Discussion

ANSYS FLUENT solved the complex governing equations of each mesh iteratively to predict the flow structure and its properties. The residuals set for continuity and energy were 0.000001 while x-velocity, y-velocity, k, epsilon and H_2O were set to be 0.001. Generally, the iteration required for the numerical solution to converge was approximately 1100 to 1300.

Each droplet with 4 different initial sizes would have to feed into the spray dryer at 4 different sets of operating parameters setting as shown in Table 3. The velocity profiles predicted using CFD for initial droplet size of 36 μm at different hot air temperature and feed rate were shown in Fig. 2a–d. The results obtained were very similar to the velocity streamline produced by Roustapour et al. [5].

The air flow had only axial velocity at the inlet. The velocity of air was very high at the point where it contacted with the feed. Then, the velocity decreased as it moved down to the bottom of the spray dryer and it increased tremendously just before it left the dryer. Besides, the recirculation of the flow was formed around the inlet and the core. At the outlet, small vortexes were also observed.

The particles flight paths will be affected by the air flow profile. This will also affect the drying rate of the spray dryer. High recirculation will enhance the mixing between the hot air medium and the feed and increase the contact time. The longer the contact time between these two phases will increase the drying rate. This result was supported by Tee et al. [7].

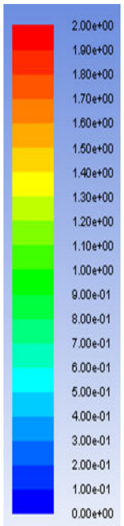

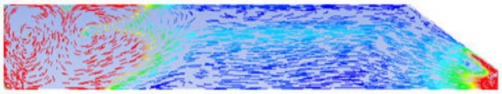

Fig. 2a 36 μm under Set 1 Operating Parameters

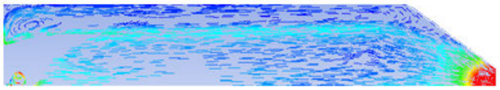

Fig. 2b 36 μm under Set 2 Operating Parameters

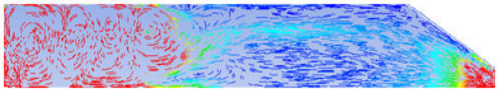

Fig. 2c 36 μm under Set 3 Operating Parameters

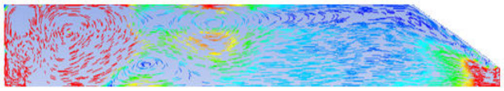

Fig. 2d 36 μm under Set 4 Operating Parameters

The velocity profile for different initial droplet sizes under Set 1 operating parameters were shown in Fig. 3a–c. From the result, it illustrated that the bigger the initial droplet size, the further it traveled away from the core flow.

Small droplets follow the air flow pattern as they have insufficient momentum to escape from the core flow. However, as the droplet size increases, the momentum of the droplet will also increase. Therefore, larger droplet will have higher chance to escape from the core flow. This will result the formation of wall deposition [5].

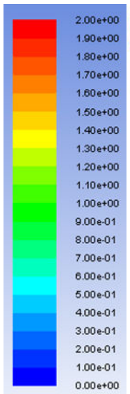

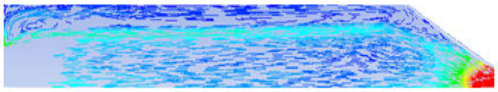

Fig. 3a 79 μm under Set 1 Operating Parameters

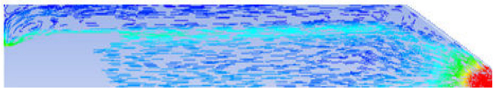

Fig. 3b 123 μm under Set 1 Operating Parameters

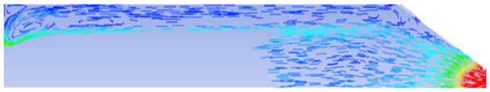

Fig. 3c 166 μm under Set 1 Operating Parameters

4. Conclusion

In conclusion, at a hot air temperature of 160℃ and a feed rate of 9.5 ml/min have the optimum drying rate compared to the other sets of combination. This is because the contact time for the hot air medium and the feed is higher. As a result, more water is evaporated from the feed.

Moreover, larger droplet size will have greater momentum which can escape from the core flow. These droplets will have least drying and tend to deposit at the side wall of the dryer. Therefore, it is recommended that the initial droplet of the feed to be small.

Despite that, the simulation results are not completely validated by experimental data. Therefore, more experiments and numeric are needed in order to have more precise findings in future.

Acknowledgment

I would like to thank my main supervisor, Dr. Rashmi Gangasa Walvekar for giving me all the supports throughout the whole research. In addition, I would like to show my gratitude to Ms. Tee Lee Hong, Dr. Harun Mohamed Ismail and Dr. Woo Meng Wai for assisting me in order to complete my research.

References

[1] L. S. R. Arambewela, L. D. A. M. Arawwawala, and W. D. Ratnasooriya, "Antidiabetic Activities of Aqueous and Ethanolic Extracts of Piper Betle Leaves in Rats," *Journal of Ethnopharmacology*, no. 102, pp. 239-245, 2005.

[2] F. G. Kieviet, J. Van Raaij, P. P. E. A. De Moor, and P. J. A. M. Kerkhof, "Measurement and Modeling of the Air Flow Pattern in a Pilot-plant Spray Dryer," *Institution of Chemical Engineer*, no. 75, pp. 321-328, 1997.

[3] D. Fletcher et al., "What is Important in the Simulation of Spray Drying Performance and How Do Current CFD Models Perform?," in *Third International Conference on CFD in the Minerals and Process Industries*, Melbourne, Australia, 2003.

[4] T. A. G. Langrish and D. F. Fletcher, "Spray Drying of Food Ingredients and Applications of CFD in Spray Drying," *Chemical Engineering and Processing*, no. 40, pp. 345-354, 2001.

[5] O. R. Roustapour, M. Hosseinalipour, B. Ghobadian, F. Maheghegh, and N. M. Azad, "A Proposed Numerical Experimental Method for Drying Kinetics in a Spray Dryer," *Journal of Food Engineering*, no. 90, pp. 20-26, 2009.

[6] L. Huang, K. Kumar, and A. S. Mujumdar, "Simulation of a Spray Dryer Fitted with a Rotary Disk Atomizer Using a Three-Dimensional Computational Fluid Dynamic Model," *Drying Technology*, vol. 22, no. 6, pp. 1489-1515, 2004.

[7] L. H. Tee, C. L. Chuah, K. L. Pin, R. A. Abdull, and Y. A. Yusof, "Optimization of Spray Drying Process Parameters of Piper Betle L.," *Journal of Chemical and Pharmaceutical Research*, vol. 4, no. 3, pp. 1833-1841, 2012.

Development of Modal Test Fixtures for Multi-bent Copper Tubes

J. Tyng Cheok [1*], M. Hosseini Fouladi[1], K. Haw Yap [2],

[1]*School of engineering, Taylor's University, Malaysia,*
[2] *Research and Development Department, Panasonic Appliances Air-Conditioning R&D(M) Sdn Bhd, Malaysia*
* *albert_cheok@live.com*

Abstract-This project was conducted to design an EMA test fixture design for impact hammer modal testing on multi-bent oxidized phosphorus copper tube within the interesting frequency range of 1Hz to 200 Hz. The test fixture is needed to be designed in order to alter the resonances out of the range of testing and with the free vibration's background theory. The designed model of fixture is set up via finite element modeling method by using the 3D elements' meshes of FEA (finite element analysis) software (Nx-Nastran) and doing the simulation of the free vibration analysis in solver SEMODES 103. The FEA results show the different stage improvements' designs' natural frequencies and mode shapes. Improve the performance of the current design fixture to the final design of the fixture by analyzed mode shapes and natural frequencies via topology optimization. Topology optimization is to reduce the mass as low as possible of the fixture and increase its rigidity as high as possible, in material choosing aspect and structure shape aspect. The final design of the fixture gives 5 times greater than the current used design in terms of natural frequencies by increasing the mass of the fixture by 37%.

Keywords- EMA (experiment modal analysis), resonances, Nx-Nastran software, finite element analysis (FEA), natural frequencies, mode shapes, topology optimization.

1. Introduction

The main problem is the excitation of the uneven road surface that generated vibration and transmit its' vibration (1Hz-200 Hz) via transportation's vehicles to the attached multi-bent copper tubes from the compressor. When the huge magnitude of vibration is experienced by copper tubes, it is concerned about the durability of the products consumers buy. If the design is not to be concerned about this factor, the copper tubes will fail during the transportation. By studying and applying the free vibration theory to this study to solve this transportation problem. And, test engineers complained that they can't get a desirable and accurate results from the test specimen with the utilizing of current fixture no matter how they managing and controlling the experimental modal analysis (EMA).
The paradox idealized principle to design a test fixture is to maximize its' stiffness at all frequencies where the mass is approaching to zero. This approach will not be achieved in real life circumstances, but it is an ultimate goal for designing vibration test fixture. This statement implies that the fixture would be resonances free, especially for the range of interesting testing frequency. For this testing an impact hammer modal testing was done for a multi-bent copper tube in an interest frequency range of 1 Hz to 200 Hz. The resonances occurred are due to the mass over stiffness characteristic of the test fixture
Free Vibration of multi-degree of freedom (n-DOF) system is governed by a system which consists of n differential equations. If the system is linear, the differential equations would be expressed in a matrix form. For the free vibration paradox equation, [1]

$$M\ddot{x} + Kx = 0 \tag{1}$$

Symbol x is the vector of node displacements, M is the mass matrix of the system, K is stiffness matrix of the system and C is damping matrix. For the free vibration with linear undamped n-degree of system, which is $C = 0$ and obtain. By assuming that free vibration of an n-DOF system is initiated by inputting potential or kinetic energy. If the system is undammed, there would not be dissipated energy mechanism. Therefore, the normal mode solution of equation (1) in the form of [1]

$$x(t)= Xe^{i\omega t} \tag{2}$$

Symbol ω is the frequency of vibration, X is mode shape, t is instantaneous time, x is nodal displacement. [1]
[2, 4]

2. Fixture Design Methodology

The fixture should go for as high as infinity stiffness at any frequencies over a zero mass. It is a paradox for designing EMA test fixture. In order to fulfill this contradictory goal, an optimization methodology is used in this project. In a good design of test fixture, any resonances do not exist within the range of testing frequencies. The materials that are commonly used in building a vibration test fixture are such as steel, aluminum and magnesium which are the most common. The ratio of Young's Modulus to density (E/ρ) is a controlling factor natural frequency of building a fixture. Materials chosen and considered for the fixture design were looked in terms of cost efficiency and the ratio (E/ρ) of the material which in this case was higher than steel; AA6061-T6 aluminum alloy is the most suitable for this case. By designing different designs of the test fixtures, it had to be compared it to each other and to the current using test fixture. Sketching them by using Nx-Nastran Modeling and using FEA advanced simulation of Nx-Nastran by utilizing SEMODES 103 solver (free vibration analysis). The boundary condition of the solution used Lanczos for eigenvalues method, by utilizing the interest frequency from 1 to 200Hz, for the test range of the test specimen in this case. [2, 3, 4]

3. Fixtures Topology Optimization FEA Results

Firstly, studying and simulating the current used test fixture by using computational tools (in this case is Nx Nastran). By doing modeling and simulations of the different stage of fixtures' design, obtain the simulation results' and studying the parameters from the simulations, namely mode shapes, natural frequencies, nodal displacements and mass. Via topology optimization, the current design (Refer to Fig1.) is optimized to different stages (Refer to Fig1 till Fig4) until the last stages (Refer to Fig4.)

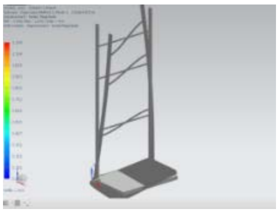

Figure1. The first step mode shape for current design

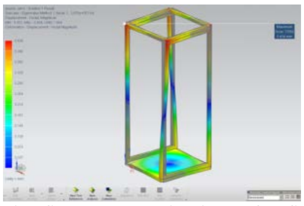

Figure2. The first step mode shape for first design

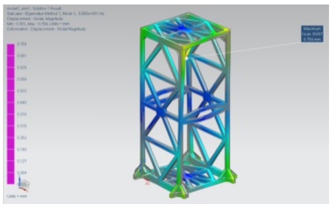

Figure3. The first step mode shape for third design

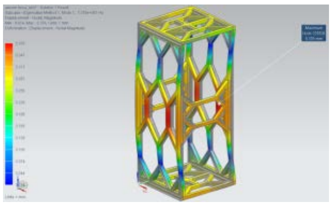

Figure4. The first step mode shape for forth design

Table1. The natural frequencies, mass and the vibrant mode about first 3 steps in the FE mode of the EMA test fixtures.

Type of Designs	Mass, kg	Mode no	Natural frequency, Hz	Nodal Displacement, mm
Current	9.8	1	14.2	1.241
		2	16.5	1.156
		3	32.4	1.112
First	15.0	1	26.7	0.434
		2	37.4	1.419
		3	38.3	0.335
Second	12.5	1	29.1	0.182
		2	32.2	0.132
		3	62.5	0.226
Third	13.4	1	73.8	0.378
		2	77.9	0.533
		3	86.5	0.465

4. Analysis and Discussion

From the current fixture which is used by test engineer currently (Refer to Fig1), there are less bracing bars, bars and ribs. In a practical manner, adding bracing bars and certain bars to the fixture in order to increase the fixture's rigidity means to increase its' stiffness by adding a small amount of mass. Basically, the natural frequency is the function of mass and stiffness. Natural frequencies are directly proportional to the stiffness whereas the natural frequencies are inversely proportional to the mass. For the first design, the mass is a lot of larger comparatively but just increasing two times of the natural frequencies and the nodal displacements about the same (Refer to table 1.) And for the third and fourth design, by increasing 28% and 37% of the mass and increasing the natural frequencies by 2 times and 5 times separately and the nodal displacements are reduced to 10 multiples. From the results at section 3, modifying the fixtures by changing its configurations of the bars, according to the mode shapes of every design (Refer from Fig1 till Fig4.). The red colored zone implies the weaker part of the bar configurations which can be solved by adding braces symmetrically and so on. All the designs use the same cross section bar which is a 36mm×36mm, 1mm wall thickness hollow square bar which is according to the current design and the overall dimension as well. [2, 5]

5. Conclusion

Mainly, the best EMA test is to be done with resonances-free test fixture which can get the least error of the modal readings. An EMA test fixture is designed with the material of AA6061-T6 aluminum alloy. It is designed with symmetrical and hexagonal bars configurations. This design will give a higher stiffness to the fixture and lightweight properties which can be shown by possessing higher natural frequencies, which is five times greater than the current used design. However, it doesn't achieve the first natural frequency of 200 Hz. (Refer to Table 1.).In other way, it can alter the mounting way of the test piece in hanging by bungee cord in free-free condition in order to minimize these unavoidable resonances.

6. Acknowledgements

I would like to thank Panasonic Appliances Air-Conditioning R&D (M) Sdn Bhd, Malaysia for funding me with the FEA tools and software. I would like to thank Mr Yap Kim Haw and Dr. Mohammad Hosseini Fouladi who gave me guidances and advices.

7. Reference

[1] S.Graham Kelly(2012), *Mechanical Vibration Theory and Applications*, Stamford, United States: Cencage Learning

[2] (1987)Fixture for B&K exciters, Bruel&Kjaer.

[3] G.Phani Sowjanya, P.Divakara Rao, Dr. C. Udaya Kiran (2013, January), *Finite Element Analysis of Vibration Fixture Made of Aluminum and Magnesium Alloys.* International Journal of Latest Trends in Engineering and Technology (IJLTET)

[4] Y.B. Autger, S.S Khandagale, R.S. Bindu, *Vibration Analysis of Propellant Actuated Devices.* International Journal of Modern Engineering research (IJMER) Vol.2, Issue.4, July-Aug 2012 pp-2897-2902

[5] Fabien PONCELET, Frédéric MARIN. Claude FLEURY and Jean-Claude GOLINVAL (2005), *Optimal Design of Fixtures for Vibration Testing of Structures on Electro-Dynamic Shaker.* Twelfth International Congress on Sound and Vibration ICSV12 Lisbon 11-14 July.

Investigation of Wing Tip Sails

Chin Jitve, Mushtak al-Atabi

Mechanical Engineering, Taylor's University, Malaysia

jitve.chin@hotmail.com

***Abstract*— An example of mimicking nature is the adaptation of wing tip feathers of birds into the tips of airplanes' wings. This paper describes the use of computational fluid dynamics (CFD) technique to analyze the subsonic flow over NACA0012 wing tip sails attached to a NACA4412 wing. The lift coefficient of 3D wing simulation is about 30% different from the 2D wing simulation. On the other hand, the lift coefficient for 3D wings with wing tip sails is similar to the one without wing tip sails.**

Keywords— Computational Fluid Dynamics (CFD), Wing Tip Sails, Induced Drag, Wing Tip Vortices, Wing Tip Devices

1. INTRODUCTION

One of the foremost important aerodynamic force is induced drag, which is a drag caused by lift. It takes up approximately 33% of the total drag of the aircraft when in cruise and it is even more significant at low speed, accounting for 80%-90% of the aircraft drag, especially during landing and taking off situations[1]. Streamline over an airfoil causes pressure difference between the top and bottom surface. However, on a finite wing, there is a leakage of air molecules at the wing tip which causes downwash, thus generating vortices at the trailing edge of the wing. Wing tip sails are attached to the wings in such a way they use local airflows about the wing tips induced by the generation of lift on the wing to produce trust[2].

The core objective of this project is to study the effect of subsonic flow across NACA0012 wing tip sails on NACA4412 (shown in Figure 1) wing on the role of reducing induced drag. It is conducted numerically using ANSYS FLUENT 14.0 software. The result of this project is mainly compared with data from Mushtak[3] Abbott et al[4] and Saraf A.K, Singh M., & Kumar A. [5].

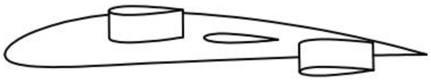

Figure 1: Wing Tip Sail Assembly

2. RESEARCH METHODOLOGY

There are three cases of simulation. First being simulation of 2D NACA4412 with three turbulence model: standard k-e, standard k-w and Spalart Allmaras. Second is simulation of 3D NACA4412 using standard k-w turbulence model. Lastly, third is the simulation of NACA0012 wing tip sails on NACA4412 wing using Large Eddy Simulation (LES) turbulence model.

There will be a total of three sails of NACA0012 wing of chord length 175mm and span of 262.5mm. These sails are attached on NACA4412 at 30%, 52.5% and 75% of the chord length and at dihedral angle of $+15^{O}$, 0^{O} and -15^{O} from the horizontal (shown in Figure 1). These sails are configured in three arrangements: Configuration 1(-10^{O}, 5^{O}, 0^{O}), Configuration 2(-15^{O}, -10^{O}, -5^{O}) and Configuration 3(-20^{O}, -15^{O}, -10^{O}). All these sails pitched down to recover the sails' undersurface separation at an angle of attack of the wing about 1^{O} [3].

The simulation is conducted on NACA4412 wing of chord length 1000mm and semispan of 1500mm. Velocity of 50m/s is used, similar to the experimental data from Abbott et al [4]. The free stream temperature is 300K whereas the density of the air is $1.225 kg/m^3$ and its viscosity is $1.7894x10^{-5}kg/ms$. This corresponds to Reynolds number of $3.42x10^{6}$. The flow can be considered to be incompressible.

The NACA4412 and NACA0012 profile is generated through a online website[6]. The profile is then imported into ANSYS Fluent for modeling and simulating. The domain is 20m from the back of the wing and 15 m semi-circle radius from the front of the wing. The domain of 2D and 3D are shown in Figure 2. The 2D domain is meshed in quadrilateral whereas the 3D domain is meshed in tetrahedral due to complications of the geometry when wing tip sails are included. After that, the boundary conditions are set up. This includes pressure outlet, velocity inlet, wall of wing surfaces, and symmetry of domain faces. The model is then simulated until convergence is achieved.

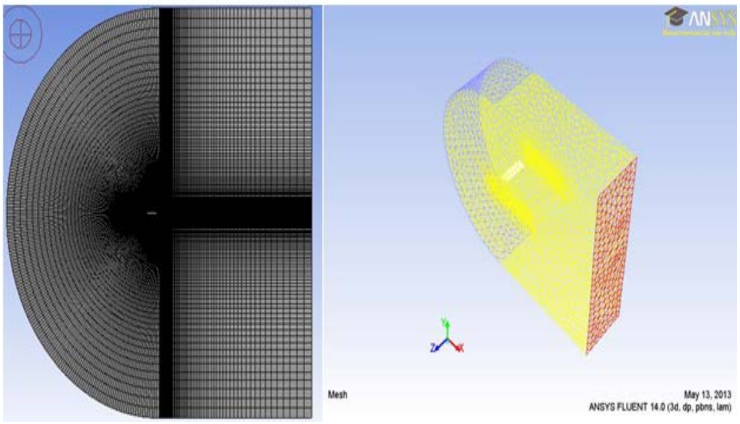

Figure 2: 2D and 3D domain mesh

3. RESULTS AND DISCUSSIONS

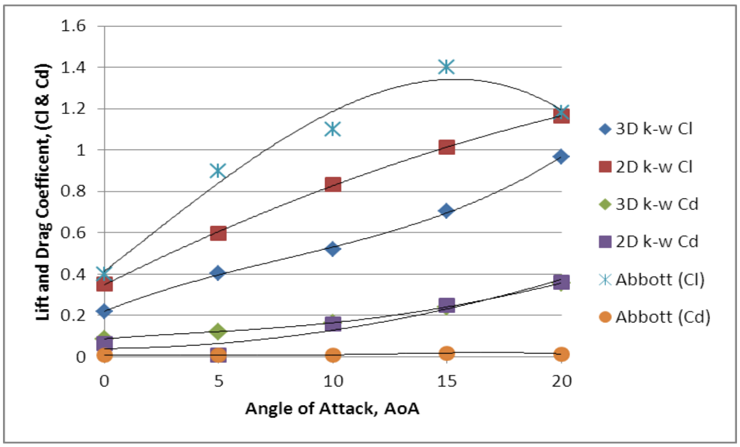

Figure 3: Lift and drag Coefficient, C_L& C_D, against angle of attack, AoA

Figure 3 shows the comparison of lift and drag coefficient of 2D and 3D NACA 4412 wing by increasing angle of attack using standard k-w turbulence model. It can be seen that C_L for 3D wing is significantly low whereas the C_D has some minor differences from the 2D wing. The lift coefficient of 2D wing appeared to be higher than 3D wing due to the flow not accounting for the spanwise direction, but only the top and bottom surface of the wing. Conversely, 3D wing involve the flow in all three x,y,z dimensional axis taking additional account of the flow in finite span of the wing. However, both 2D and 3D data obtained are slightly different from Abbott et al experimental data due to many factors such as domain size and turbulence model used.

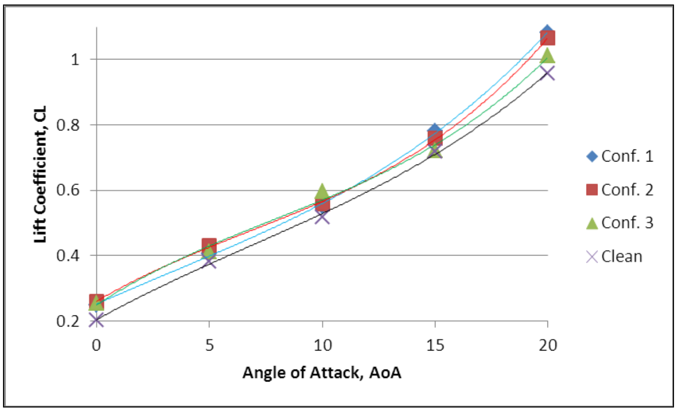

Figure 4: Lift Coefficient, C_L of different configuration of wing tip sails with increasing angle of attack, AoA of the wing

Figure 4 shows that the lift coefficient of every configuration is similar to one another with increasing angle of attack. All configurations have higher lift coefficient than the clean wing without wing tip sails. Configuration 3 has higher lift coefficient, followed by Configuration 2 and Configuration 1 at AoA between 0^{O} to 10^{O}. However, Configuration 1 has the highest lift coefficient followed by Configuration 2 and Configuration 3, relatively close at AoA between 10^{O} to 15^{O}.

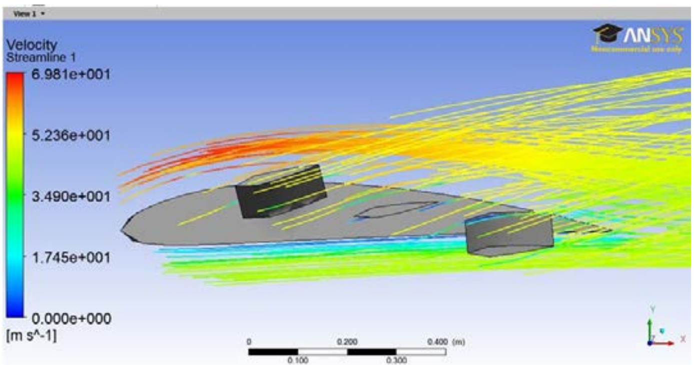

Figure 5: Velocity Magnitude of Configuration 2 at AoA 15^{O}

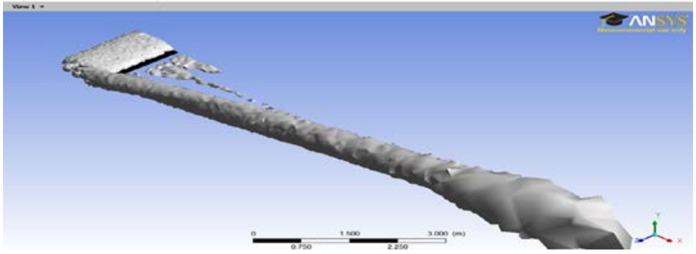

Figure 6: Vortex of Configuration 2 at AoA 15^{O}

Figure 5 and Figure 6 illustrates the velocity magnitude of streamline and the vortex formed using LES turbulence model at AoA 15^{O}. Pressure and velocity plays an important role for the generation of lift of a wing. Air travels faster at the top surface of the wing compared to the bottom surface of the wing, thus having pressure difference in accordance to Bernoulli's principle where pressure is inversely proportional to velocity. . Following the ideal gas law, air flows from area of higher pressure to area of lower pressure, thus in this case, lift is generated. Wing tip sails helps in taking advantage of the leakage of air molecules at the wing tip to generate local lift force as well as seen in Figure 5. The leakage of air molecules at the wing tip from outside to inside towards the root chord in circular pattern forms vortex at the trailing edge of the wing as shown in Figure 6.

4. CONCLUSION

The results obtained are less accurate and far from the experimental data. This can be clearly seen from Figure 3 and Figure 4, where lift coefficient obtained appears to be increasing up to AoA 20^{O}. This is not right as maximum lift coefficient is expected at critical AoA 15^{O} to 16^{O} for NACA4412 as shown in Figure 3. Beyond this point, the wing will experience stall and lift coefficient decreases with increasing AoA [2].

There are many factors of these inaccuracies such as meshes, turbulence model, boundary conditions and so on. Moreover, the simulation only can process one type of flow at a time. In this case, turbulent flow is used throughout the experiment although there is laminar flow at the early stage as flow passes through the wing. The simulation cannot take in account for both flow regimes, which in reality; both laminar and turbulent regimes are always present.

Generally, the lift and drag coefficient for 2D NACA 4412 airfoil is almost the same as the numerical analysis done by others [5] and also Abbott experimental data [4] at about 20-25% error. As for 3D NACA4412 wing, the difference margin for lift coefficient is wide, around 30% from the 2D airfoil whereas difference margin for drag coefficient is around 10%. For wing tip sails, results are suspected to be inaccurate as ANSYS could not register the force vector relative to the angle of attack of the sail.

Wind tunnel testing of wings with wing tip sails is suggested to study the flow and performance of it and also to compare the data with the numerical results.

ACKNOWLEDGMENT

I would like to take thank my supervisor, Prof. Dr. Mushtak for his guidance and support and my fellow course mates for their endless help throughout my project.

REFERENCES

[1] Samal S., undated, 'Computational Study of wing tip vortex control by blowing at Wingtip', [online] Accessed on 1st December 2012 from http://ficta.in/attachments/article/55/05%20Computational%20Study%20of%20wing%20tip%20vortex%20control%20by%20blowing%20at%20Wingtip.pdf

[2] Spillman. J.J, 1978, 'The Use of Wing Tip Sails to Reduce Vortex Drag', *Aeronautical Journal*, Vol. 82, No. 813, pp. 387-395

[3] Al-Atabi M., 1996, *Experimental Investigation of Wing Tip Sails Using Vortex Scanning and Forces Measurements*, University of Baghdad, Baghdad

[4] Abbott, I. and A. Von Doenhoff ,1959, *Theory of Wing Sections*, Dover Publications

[5] Saraf A.K., Singh M., & Kumar A., 2012, 'Analysis of the Spalart-Allmaras and k-ω standard models for the simulation of the flow over a National Advisory Committee for Aeronautics (NACA) 4412 airfoil', International Journal of Scientific & Engineering Research, Vol 3., Issue 8, ISSN 2229-5518

[6] Trapp J. and Zores R., undated, 'NACA 4 Digits Series Profile Generator', [online] Accessed on 7th October 2012 from http://www.ppart.de/aerodynamics/profiles/NACA4.html

Removal of $PM_{2.5}$ and PM_{10} using Palm Shell as Activated Carbon

Christopher M. K. Chew[1]*, Ralina Shirin Akbar, Nurhazwani Ismail, TVN Padmesh

[1]*School of Engineering, Taylor's University, Malaysia*

**Corresponding author email: christophermunkit.chew@sd.taylors.edu.my*

Abstract—**Particulate matter is a complex mixture of small particles and liquid droplets, which can be a serious health threat when inhaled. An adsorption column utilising activated carbon is used to study the effectiveness of removing particulate matter from gaseous pollutant stream. Activated carbon prepared from palm shell showed a particulate matter removal effectiveness of 83% as compared to 75% using commercial coal activated carbon.**

Keywords— Activated carbon; Particulate matter; Adsorption; Palm Shell

1. Introduction

Activated carbon is a highly adsorbent granular carbon made by carbonization and chemical activation and is mainly used for purification by adsorption. The conventional activated carbon that is widely used in the market is coal. In Malaysia, there is presently an abundance of palm shell waste materials which can be used to produce activated carbon. Presently the usage of activated carbon for adsorption is mainly for the removal of gaseous pollutants. Particulate matter is a rising health treat with many adverse health effects including major respiratory disorders including asthma and lung cancer [1]. Therefore a demand is present for the effective removal of particulate matter from gaseous emissions to ensure that the air quality in Malaysia is within the acceptable level [2]. This research studies the effectiveness of the removal of particulate matter using palm shell activated carbon in an adsorption column setup.

2. Methodology

The research consists of the production of activated carbon from palm shell that is discarded as waste materials [3], followed by an experiment devised to compare particulate matter removal effectiveness.

2.1. Activated Carbon Preparation

Palm shells used in this research are obtained from Felda Palm Industries Sdn. Bhd in Negeri Sembilan, Malaysia. Palm shells obtained were dried in the oven at 110°C for 24 hours. The dried palm shells were then crushed and sieved to obtain a size between the ranges of 1.0 - 2.0mm. The crushed palm shell granules were then carbonized in the furnace at a temperature of 700°C for 20 minutes, to burn off all of its fatty acids. The furnace was momentarily turned off to reduce the smoke emission. The palm shells were then continued to be carbonized for another 100 minutes at the same temperature of 700°C, under constant nitrogen flow. The resulting char was left to cool and then soaked in a 0.1M Potassium Hydroxide (KOH) solution with an impregnation weight ratio of 1:1, for the chemical activation portion of the preparation. The mixture was then placed in the oven for further dehydration at a temperature of 105 °C for 24 hours. The chemically activated palm shells are then subjected to physical activation. The palm shells were then carbonized at a temperature of 850°C for 4 hours in the furnace, under constant nitrogen flow. The resulting palm shell activated carbon would have undergone both chemical and physical activation [4].

2.2. Experimental Setup

The research was done through experimental laboratory scale setup in order to obtain data of adsorption capabilities to make deductions and inferences. The size of the particulate matter measured would be in the range of 2.5 to 10 micrometers, as it is known that particulate matter are most harmful in these sizes [5]. The experimentation was conducted twice, once on commercial activated carbon in the form of coal and the second using activated carbon prepared from palm shell. In this research, the adsorption capacity of the respective activated carbon is the parameter of study that is found through experimentation. Further research would be conducted to determine the effect of flow rate and bed height to the adsorption capacity.

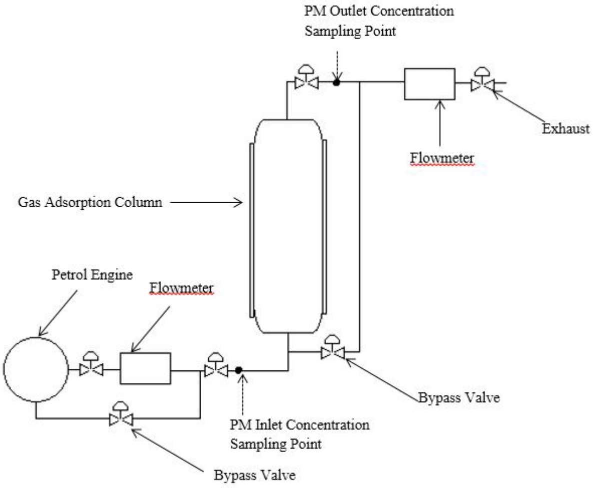

Fig. 1 Experimental Setup

Figure 1 depicts the experimental setup of the analysis. The sample polluted gas would be in the form of emission from a petrol engine. The experiment was conducted with commercial activated carbon, coal as the adsorbent, with a bed height of 30 cm and a flow rate of polluted gas of 5 l/min. The experiment was then repeated with palm shell activated carbon in the same conditions. The adsorbent with the higher adsorption capacity was used to study the effects of varying polluted gas flow rate in the inlet of the adsorption column, and the varying bed height of the adsorbent. The flowrate of the polluted gas was varied at 10 l/min and 15 l/min while keeping the bed height constant. The research was then continued with keeping the flow rate at 5 l/min while varying the bed height at 5 cm and 15 cm. Each adsorption process is a batch process hence the adsorbent would be replaced to ensure that it is not saturated. The particulate matter in the gas sample was measured using a particulate matter analyser, TSI Optical Particle Sizer (OPS) Model 3300.

3. Results and Discussion

The concentration of particulate matter in ambient air is 0.175 mg/m3, and the concentration of particulate matter in the exhaust of a petrol engine is 150 mg/m3. Coal showed a 75% particulate matter removal from the exit stream while palm shell shows a higher removal rate of 83%. Furthermore, from Figure 2, it can be observed that palm shell has a consistently higher removal percentage at any sampling point as compared to coal. It can also be observed that the usage of activated carbon prepared from palm shell has a better adsorption capacity as compared to commercial activated carbon, coal. This is due to the better porosity in palm shell activated carbon as opposed to coal.

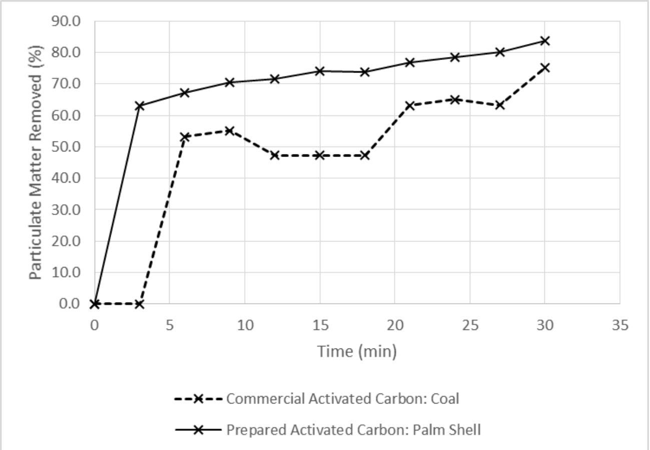

Fig. 2 Particulate Matter Removal using Coal and Palm Shell Activated Carbon

Figure 3 depicts the concentration of particulate matter is lowest by using a lower gas inlet flowrate. This is due to the increase in contact time between the gaseous pollutants and the activated carbon, which allows the activated carbon to capture more particulate matter.

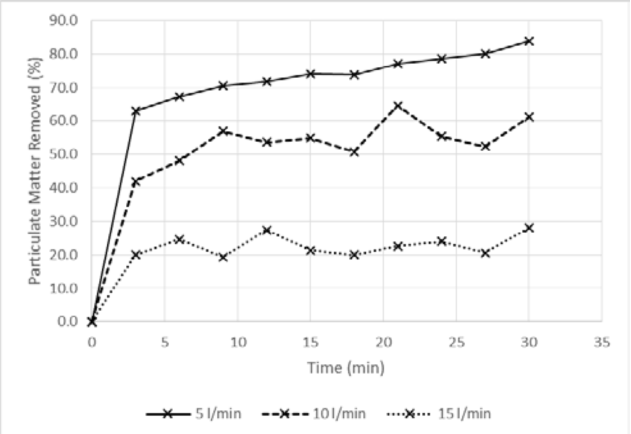

Fig. 3 Effect of Flowrate on Particulate Matter Removal

Figure 4 indicates that the higher the bed height, the lower the concentration of particulate matter in the exit stream. This is because of the increase in amounts of activated carbon being used, would have an increase in the adsorption capacity. It was also noted that by using a 5 cm bed height, it can be observed that the activated carbon was saturated at 27 minutes.

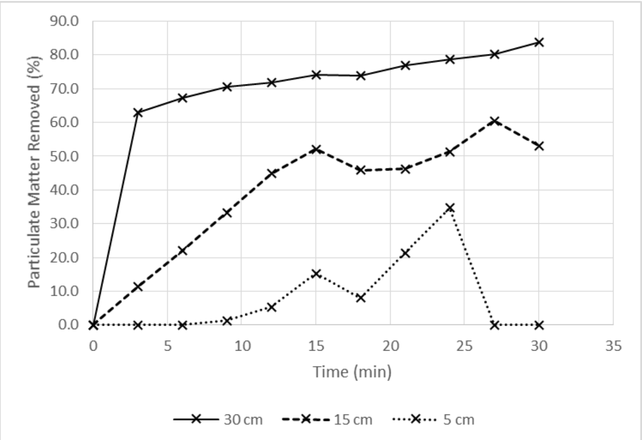

Fig. 4 Effect of Bed Height on Particulate Matter Removal

Palm shell is a waste material that is discarded regularly after palm oil is extracted. Hence as palm shell clearly shows a higher adsorption rate over coal, this waste materials have beneficial properties in the field of pollution control.

3. Conclusions

The usage of palm shell activated carbon as adsorbent is highly effective in the removal of particulate matter as compared to current commercial activated carbon, coal. It is also concluded that the removal of particulate matter is more effective at a lower gas inlet flowrate and a higher adsorbent bed height.

Acknowledgment

I would like to acknowledge Taylor's University School of Engineering for their continuous support in providing the funding and necessary facilities to carry out this research. I would also like to acknowledge all the support and guidance that was provided by my colleagues to accomplish this research.

References

[1] M. Kampa & E. Castanas (2007). Human Health Effects of Air Pollution. *Environment Pollution.*

[2] R. Afroz, M. N. Hassan & N. A. Ibrahim (2007). Review of Air Pollution and Health Impacts in Malaysia. *Environmental Research.*

[3] J. M. Dias, M. C. M. Alvin-Ferraz, M. F. Almeida, J. Rivera-Utrilla & M. Sanchez-Polo (2007). Waste Materials for Activated Carbon Preparation and its Uses in Aqueous-phase Treatment: A Review. *Journal of Environmental Management.*

[4] Wan Nik, W.B., et al, (2006). Production of activated carbon from palm oil shell waste and Its Adsorption Characteristics. Putrajaya, Malaysia: 646-654.

[5] R. M. Harrison & J. Yin (2000). Particulate Matter in the Atmosphere: Which Particle Properties are Important for its Effects on Health. *Science of Total Environment*

Calculation and Optimization of the Aerodynamic Drag of An Open-Wheel Race Car

Chung Sun Lee*, Abdulkareem Sh. Mahdi Al-Obaidi

Department of Mechanical Engineering, School of Engineering, Taylor's University, Malaysia
**Corresponding author: chungsun.lee@sd.taylors.edu.my*

Abstract— **Aerodynamic drag reduction is one of the important factors to make a race car achieve a faster lap time. Additional drag is produced due to the air channel for radiator cooling of the student designed open-wheel race car. This paper presents the aerodynamic drag optimization of the race car through studying the effect of the angle of the radiator air channel. A reduction of 23.8% in drag coefficient compared to the current setup is achieved by tilting the angle of cooling channel to 72.5 degree.**

Keywords— Aerodynamic drag, Drag reduction, Drag optimization, Automobile drag, CFD

1. Introduction

A number of students from Taylor's University had conceived, designed and built an open-wheel race car to participate in the national competitions. Due to the competition rules and constrains, the radiator is placed directly at the back of the driver which blocks most of the cooling air from entering the radiator. Thus, an air channel is fabricated to direct the air above the driver's head into the radiator which results in additional aerodynamic drag. The cooling of the engine is extremely important during the endurance race. Overheated engine will affect the efficiency of the engine or even engine failure might occur during the race.

The objective of this paper is to find an optimum solution for drag reduction of the race car by studying the effect of the angle of the radiator cooling channel on aerodynamic drag.

2. Theoretical Approach

The total drag of an automobile can be separated into two major components; the skin-friction drag and pressure drag.

$$C_D = C_{Df} + C_{Dp} \tag{1}$$

where C_D is total drag coefficient, C_{Df} is the skin-friction drag coefficient and C_{Dp} is the pressure drag coefficient.

2.1. Skin-Friction Drag

Skin-friction drag is mainly caused by the fluid viscosity, surface area, and surface roughness of the body. Theoretical relations for skin-friction drag at different Reynolds numbers are obtained experimentally. The Reynolds number is calculated using the reference length of the race car which is in the range of 10^6 at the operating speed. Prandtl and Von Karman suggested an empirical formula for skin-friction coefficient for Reynolds number at the range of 10^6 [1]. Skin-friction can be estimated using the coefficient of flat plate multiplied by the wetted area over the reference area. Viscosity of the fluid (air) is the main source of skin-friction which produces itself in form of a very thin layer adjacent to the surface, boundary layer.

$$C_f = \frac{0.455}{(\log R_l)^{2.58}} \tag{2}$$

where C_f is the skin-friction drag and R_l is the Reynolds number.

2.2. Pressure Drag

Pressure drag is caused by the pressure differential throughout the automobile. It is mainly caused by the shape and design of the vehicle. As fluid (air) flows through a body, there will be a change in pressure and velocity thus causing momentum changed [1].

$$D_p = \int P\cos\theta \, dA \tag{3}$$

where D_p is the pressure drag force, P is the pressure, θ is the angle between relative velocity to the normal pressure force and A is the frontal area [2].

Numerical Approach Using Computational Fluid Dynamic (CFD)

Ansys Fluent 14 software is used to simulate the aerodynamics of the automobile to obtain the drag coefficient numerically. A simplified vehicle shape called Ahmed Body was used for verification and validation of the software [3]. It is also used to determine the proper meshing, turbulence model and CFD solver input settings for the external flow simulation for the race car model. Table 1 shows three different simulations on Ahmed Body using different turbulence models; Realizable *k-ε* solves two transport equations to obtain turbulent kinetic energy, k and dissipation rate, ε. Reynolds Stress Model (RSM) solves 6 components of Reynolds stresses and dissipation rate, ε and Large Eddy Simulation (LES) solves the large eddies and model the smaller eddies [4]. LES Smagorinsky-Lilly model was used for the simulation. The results don't differ much from experimental value [3, 5, 6]. Hence, using less computational time to obtain similar results is highly recommended.

The results from Table 1 shows that the numerical results is in acceptable range hence the similar meshing and solver input methods were used for the external flow race car simulations.

Table 1. Comparison of CFD results of Ahmed Body.

	Realizable k-ε	RSM	LES
Drag coefficient (C_D)	0.316	0.316	0.284
Experimental Drag Coefficient	0.299	0.299	0.299
C_D accuracy (%)	5.3	5.3	5.2
Computational Time (hours)	0.5	3	8

3.1 Geometry and Meshing

Figure 2 shows a full-scale simplified drawing of Taylor's University Race Car named Imperica in Solidworks 2011. A computational domain similar to a wind tunnel test section is created around the car. A domain of 3 car lengths upstream and 5 car lengths downstream is created to accommodate for the flow development at the front and turbulence formation at the rear end. A hybrid meshing approach tested using Ahmed Body is also used on Imperica. Prismatic layers are created near the surface of the body and also the road. This type of meshing is suggested by Marco Lanfrit using inflation of first aspect ratio of 5, growth rate of 1.2 and a total of 5 layers [7]. A rectangular box mesh with smaller element size is created near the body to capture the flow condition near the surface body and also the wake region at the rear end [7]. Figure 3 shows the mesh condition near the surface body of the car.

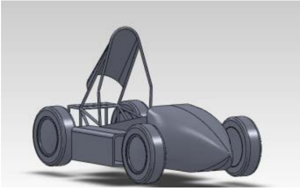

Fig. 2 Simplified full scale CAD drawing.

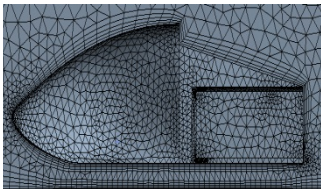

Fig. 3 Mesh condition near the surface body.

3.2 Turbulence Model

Realizable k-ε with non-equilibrium wall function is recommended in this external flow simulation and it is also tested using Ahmed Body. Non-equilibrium wall function is highly recommended for near wall modeling as it can capture and predict near wall boundary flow condition and also flow separation [7].

4.0 Results and Discussions

The first CFD simulation was conducted to obtain the total drag coefficient of the current basic setup on the race car with the radiator cooling channel relative to velocity. Figure 4 shows the relationship of the drag coefficient relative to velocity obtained through CFD. The figure shows that the drag coefficient doesn't vary much when the velocity increases. The total drag coefficient obtained is approximately 0.624 with the current race car setup. The results also match with theory where the drag coefficient doesn't vary much when velocity increased at subsonic speed [1].

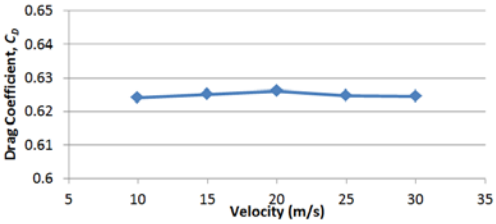

Fig. 4. Variation of drag coefficient, C_D, with velocity.

From the graph shown in Fig. 4, a velocity of 18.3 m/s is chosen as an overall average speed for next simulation by considering the race car is maintained at an average speed of 18.3 m/s throughout the Melaka International Motorsport Circuit (MIMC). The effect of the angle of radiator cooling channel is investigated through CFD at the mentioned speed. The original setup of the cooling channel is angled at 36 degree where it completely directs the flow into the radiator to cool the engine. Multiple simulations were conducted to analyse the effect of increasing the angle of the radiator cooling channel. The effect of drag coefficient by varying the angle of the cooling channel is plotted in Fig. 5.

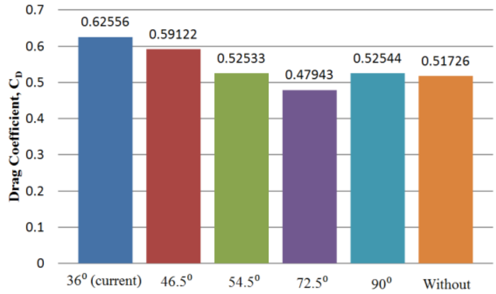

Fig. 5 Drag coefficient as a function of angled radiator cooling channel.

The race car without any radiator cooling attached shows a drag coefficient of 0.517. Malcolm Campbell's "Blue Bird" achieved drag coefficient of 0.45 for an open-wheel race car [1]. The result obtained shows some similarity in drag coefficient. The current setup of the race car which attached the radiator cooling channel at 36 degree produces a drag coefficient of 0.625 which increased the drag coefficient by 20.8% compared to the one without. Attaching the radiator cooling channel produced negative pressure region at the rear of the car which increases the drag coefficient. The cooling channel is then angled to reduce the drag coefficient but on the other hand it reduces the air flowing into the radiator. Increasing the angle of the cooling channel actually reduces the drag coefficient towards the drag coefficient of the race car without the cooling channel. The radiator cooling channel angled at 90 degree shows similarity in drag coefficient with the one without the cooling channel which is in the range of 0.51 to 0.52. There was less resistance of air when the radiator cooling channel is angled at 90 degree similar to the one without.

When the radiator cooling channel is angled at 72.5 degree, the drag coefficient is 0.479 which is lower than the one without the cooling channel attached. A reduction of 23.4% in drag coefficient compared to the current setup is achieved. The drag coefficient after this angle returns towards to the one without the cooling channel. This phenomenon might be caused by the turbulence created from the cooling channel. This particular angle introduced turbulence into the negative pressure region at the rear end of the car which increases the pressure coefficient, C_p at the rear reducing the pressure difference. 72.5 degree cooling channel setup has a C_p of -1.5 at the rear whereas the current setup has a C_p of -2.0.

5.0 Conclusions

Based on this simulation, 72.5 degree cooling channel produced least drag but the cooling of the engine need to be compromised. Hence, an automated system with temperature sensor can be implemented to optimize the drag produced and cooling of the engine. When the temperature of the engine increases, the angle of the cooling channel will be properly changed to direct more air into the radiator to cool the engine and vice versa. Heat transfer effects from the radiator could be taken into considerations for future work.

Acknowledgment

I would like to thank my colleagues for giving me valuable help and support throughout this final year project.

References

1. Hoener, S. F. (1958). *Fluid Dynamic Drag*. New Jersey.
2. Zala, B. (2012). Comparative Assessment of Drag Force of Hatchback and Sedan Car Model by Experimental Method. *International Journal of Advanced Engineering Research and Studies*. Volume 1, Issue 3, pp. 181-183.
3. Ahmed, S. R. (1984). Some Salient Features of the Time Average Ground Vehicle Wake in Detroit. *SAE International Congress and Exposition*. SAE paper 840300.
4. Versteeg, H. K., and Malalasekera, W. (1995). *An introduction to Computational Fluid Dynamics*. Harlow: Person Limited.
5. Drage, P., Hormann. T., Meile. W., Gabriel. A., Brenn. G., and Lindbichler. G. (2008). Efficient Use of Computational Fluid Dynamics for the aerodynamic Developmet Process in the Automotive industry. *26th AIAA Applied Aerodynamics Conference*. AIAA 2008- 6735.
6. Lienhart, H., and Becker S. (2003). Flow and Turbulence Structure in the Wake of a Simplified Car Model in Michigan, USA. *SAE 2003 World Congress,* SAE Paper 2003-01-0656.
7. Marco, L. (2005). *Best practice guidelines for handling Automotive External Aerodynamics with Fluent*. Birkenweg: Fluent Deutschland GmbH.

Ultrasonic Recordings and Signal Processing of Bats

D.J.H.Wong[1], M. Hosseini Fouladi[2*]

[1]*Mechanical Engineering, Taylor's University, Malaysia,* [2]*Mechanical Engineering, Taylor's University, Malaysia*

**darrenwong91@hotmail.com*

***Abstract*— the research topic being studied in this project is a bat target tracking approach for tracking preys which will then be implemented in a collision avoidance system. Bats track the prey or target by emitting signals and by receiving its signals in the form of echo to give information on the location of the preys which are in the clutter environment. The principle behind the emission of the bat signals is known as echolocation. Since, bat emits ultrasonic signals, the appropriate frequency component needed to be obtained will determine the accuracy of locating the prey by means of target tracking.**

Keywords— Target tracking, collision avoidance, ultrasonic signals, echolocation, clutter environment

1. Introduction

The research objective in the Ultrasonic frequency of bats in locating prey location is to implement it on a vehicle collision avoidance system. Bats are blind therefore; it needs guidance in avoiding obstacles along its path as well as to track down preys. The guidance that will provide the bat with information will be its mouth which acts as a sensor by emitting out ultrasonic signals and ears to receive its signals. One of the main ideas to understand the concepts of sound is to apply binary acoustics. This idea will give information of bats as role in hunting down preys [1]. The idea of the binary acoustics gives rise to a process called echolocation whereby it is the process of emitting ultrasonic signals and by receiving the reflected signals in the form of echo by the bats ear. Based on recent research, bats can only determine the location of the target by hearing the change of pitch of about 10 kHz and above [2]. Higher frequency sounds will provide a higher resolution of reflected echo back to the ear of the bats auditory system. This will provide more detailed information about the target size and shape. When bats emit its signals to the prey, there will be a certain time delay before the echo is received by the bats [2]. The time delay is important to determine the range of the prey from the bats.

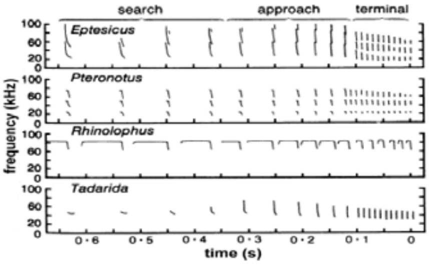

Figure 1: Schematic illustrations of sonograms of echolocation signals of different bats. [1]

Figure 1 above represents the types of ultrasonic signals emitted by the bats for four different bat species with the time duration and frequency obtained.

2. Research Methodology

The main objectives of the project are to perform simulations of target tracking on a prey by using Matlab software. In order to carry out the target tracking simulations, equations are derived based on the principle of echolocation. The equations will be used as part of the Matlab command to plot the path of the bat as well as the target. Based on the path line plotted, this will give an indication on the accuracy of the tracking results. In the simulation, two scenarios are being analyzed which is firstly to track a stationary target and secondly to track a moving target. Assumptions are made in this process to obtain the equation. By assuming that the bat emits constant waveform ultrasonic frequency, time delay can be obtained which is represented in Figure 2 below. However due to limited information such as the noise bandwidth, signal level, transmission losses etc, results by simulation will not be able to produce.

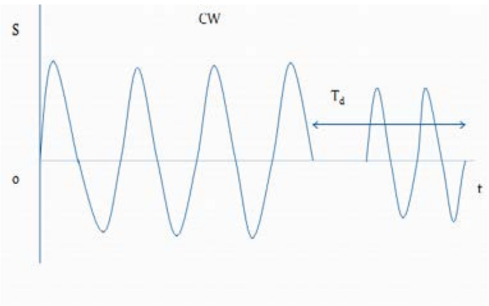

Figure 2: Constant waveform signals and its returning echo by a bat species.

Based on Figure 2 above, the distance between the bats and the target can be derived as

$$2d = V_u T_d \qquad (1)$$

Whereby,

D: the distance between the bat and the target

V_u: Ultrasonic speed of the signals

T_d: Time delay between the call emissions and returning echo

Based on equation 1 above, the distance between the bat and target, d can be obtained since the ultrasonic speed of the signals is known as 365 m/s and the time delay can be obtained in the real environment.

Besides having found the distance, the angle between bat and the target is also important to obtain the exact location of the prey. A schematic diagram of the bat representation with respect to its prey is as shown below.

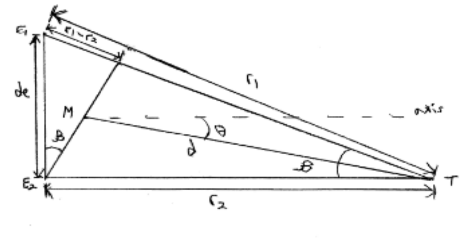

Figure 3: Bat representation with respect to the target

Based on the geometric representation above,

D: Distance between bats to the target

θ: Angle between bat mouth axis and the distance between bat's mouths to the target

D_e: The distance between $E_1$and E_2

β: The angle between d_e and the axis which is aligned with the bat's mouth.

By referring to figure 3 above,

$$\theta = \frac{1}{2}\beta \qquad (2)$$

β Can be calculated based on trigonometry as

$$\sin\beta = \frac{r_1 - r_2}{d_e} \qquad (3)$$

Since r_1 and r_2 are unknown, these unknowns can be calculated from equation 4 below

$$r_1 - r_2 = ut_{12} \qquad (4)$$

By substituting equation 4 into equation 3, equation 5 is formed

$$\sin\beta = \frac{ut_{12}}{d_e} \qquad (5)$$

β Can be calculated from this equation and therefore θ can be obtained based on equation 2 above.

3. Results

The results obtained will display how the bat tracks the position of the prey and to capture the prey when the prey it's in a stationary state and when the prey is moving. The results will be represented as shown in the graphs below

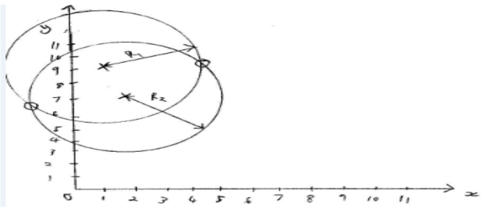

Figure 4 a) Detection of target by bat using the reflected distance R1 and R2 on a cartesian coordinate system.

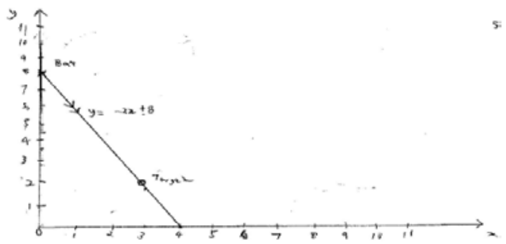

Figure 4 b) Target tracking of bat onto a stationary target in a cartesian coordinate system

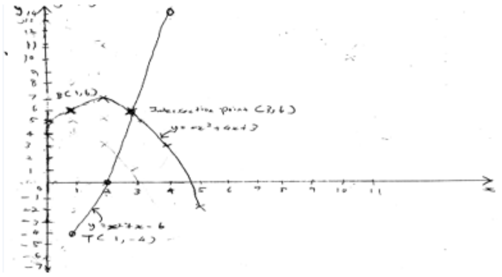

Figure 4 c) Target tracking of bat onto a moving target in a cartesian coordinate system

4. Discussions

The results obtained from Figure 4 a) determine how the bat tracks the target. Assumptions are taken in order to calculate R_1 and R_2 at which the intersection of the both radiuses provides the target location. In Figure 4 b) and 4 c), the target tracking path is obtained from the bats towards the target when the target is stationary and when it's moving. For the stationary case, the bat will travel in a linear path towards the target and for the moving case; the bat will travel in a curvilinear path to intercept the target as it travels in its own path.

5. Conclusion

The result obtained from Figure 4 c) is a simplified version of the trajectory of bats and its target. In the real case however, bats do move in all kinds of path such as path based on a cubic equation, orbital path, etc. Therefore, its accuracy of target tracking in this scenario can be further improved and in future research, comparisons can be made between simulation and experiment to compare on its accuracy of the target tracking results done by Fujioka .E [3].

Acknowledgement

I would like to thank my project supervisor, Dr Hosseini for giving me support and encouragement throughout the progress of my Final Year Project.

References

[1] Fernandez.J (2012) "IDBR: Bat mounted recording and wireless transmission of ultrasonic calls" viewed on 11th May 2013.

[2] Cotzin, M., Dallenbach, K. (1950). "Facial Vision: the role of pitch and loudness in the perception of obstacles by the blind". *The American Journal of Psychology*, **63**: 485-515.

[3]Fujioka.E, Mantani.S, Hiryu.S, Riquimaroux.H, Watanabe.Y (2010) "Echolocation and flight strategy of Japanese house bats during natural foraging revealed by a microphone array system" viewed on 11th May 2013.

Investigation of Mixing Using Synthetic Jets

Ferng Lin Ooi*, Mushtak Al-Atabi

School of Engineering, Taylor's University, Malaysia

**Corresponding author: mic3060@gmail.com*

Abstract— **Mixing is a crucial process in the industry and it is usually attained by means of mechanical agitators which are versatile but also attributed with high power requirements, blind spots and high shear rates. This paper studies the use of synthetic jets as a mechanism for mixing in tanks which can potentially solve the issues faced by mechanical agitators. The performance of synthetic jet mixing was assessed by means of particle image velocimetry and coefficient of variance via flow visualisation. It is found to be a potentially viable alternative to mechanical agitators.**

Keywords— Mixing, Process Engineering, Particle Image Velocimetry, Synthetic Jet, Flow Visualisation

1. Introduction

In the context of process engineering, mixing is defined as the operation of obtaining homogeneity in a heterogeneous physical system through some physical manipulation which in the industry, are typically agitators such as impellers and blades. [1]

Fluid mechanics define jet flows as an efflux of fluid that has been forced through a nozzle or restrictor into an ambient medium and it typically has a mass inflow or fluid influx which is the source for projection. [2] However, a synthetic jet has its flow generated from the ambient fluid instead of a fluid influx. [3][4]

In contrast to conventional mixers that create currents and vortices in the fluid using blades and impellers, synthetic jet mixers induce fluid flows through the synthesised flow from an aperture in the mixer. This induced flow is ejected from the orifice at considerable velocity hence it entrains the surrounding fluid causing vortices to propagate throughout the mixer space allowing mixing to occur. [1][2]

A typical synthetic jet contains an enclosed space called the cavity and an orifice on one side of the enclosed space and a flexible diaphragm on the other side. The diaphragm is displaced in an oscillating manner which will vary the volume in the enclosed space causing fluid to be ejected from the space through the orifice when the volume decreases and pulled in when the volume returns to normal. When this motion is repeated, a jet flow will be created at the orifice. A cross-sectional view of the synthetic jet can be seen in Fig. 1. [5]

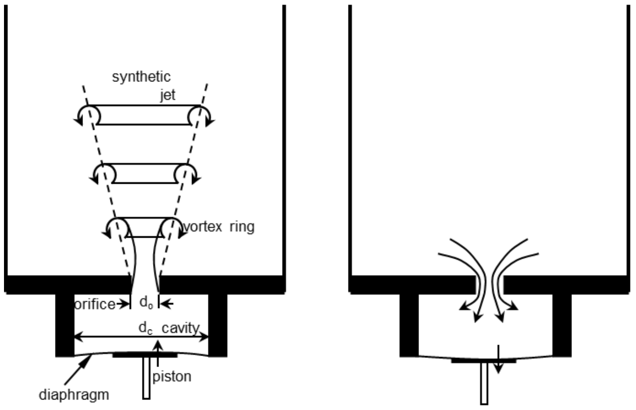

Fig. 1. Cross-sectional View of a Synthetic Jet.[5]

2. Methodology

A synthetic jet mixer was constructed that consist of an orifice of 4mm, a cavity of 80mm and a mixing space dimension of 170mm height and 150mm diameter. The mixing performance is assessed by means of coefficient of variance analysis via flow visualisation and 2D particle image velocimetry.

2.1. Coefficient of Variance Analysis

To gauge the effectiveness of a mixing technique, a typically used method in the industry, is the calculation of the Coefficient of Variance. Which statistically represents the degree variance among a number of samples from the mean of those samples. This can be used to calculate degree of homogeneity of a mixture by diving the mixture into a series of zones and adding a tracer into the system. In essence, the lower the CoV value, the more homogeneous the mixture is. The ideal CoV for industrial mixing applications is 0.2 where a mixture is assumed to be homogenous. [1] In this research, the amplitude and frequency of the oscillation is manipulated and the effects on the time taken to attain a stable CoV is observed.

The analyses were carried out using a digital camera that is capable of taking photographs at 5 frames per second (FPS). A laser sheet was used to illuminate a 2-dimensional plane in the mixer and 10 micron silver-coated hollow glass beads were used as tracers. The photographs taken were broken down into 100 individual zones (Fig. 2) and processed in Matlab using the CoV equation (Eq.1).

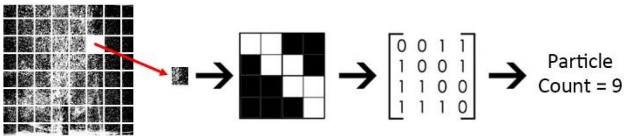

Fig. 2 CoV analysis processing flow

$$CoV = \frac{Standard\ Deviation}{Average} \qquad (1)$$

2.2. Particle Image Velocimetry Analysis

In addition to CoV, particle image velocimetry (PIV) analysis was also performed on the mixer to quantitatively determine the flow field within the mixer. PIV analysis allows the properties such as vorticity and both instantaneous and averaged velocities to be measured within a flow field. PIV analysis involves the use of a setup similar to CoV analyses with the exception of the camera being replaced with a special monochromatic camera that is extremely high speed and has low signal noise. Additionally, the laser is also replaced with a water-cooled microsecond pulse laser. [6]

The laser is pulsed twice in quick succession where a pair photographs are taken as well. The positions of individual particles are compared and the velocities for each particle are computed through the software which will build a velocity map of the region of interest. PIV analyses can be performed as a 2D or stereoscopic PIV where the analysed region is either a sheet or a 3 dimensional region. Stereoscopic PIV require multiple cameras whereas 2D require only one camera. [6]

The PIV analysis in this study was a 2D PIV study where the flow structure centre cross section of the synthetic jet mixer was analysed. The region of interest is the mixer region above the cavity. The laser pair was pulsed at 133ms intervals with 350μs delay between the pulse pairs. The images are exposed for 400μs.

3. Results & Discussion

The experimental sets that has been tested in this research are summarised in Table 2. The reference set of 15Hz and 1.5mm was chosen based on previous work. [7]

Table 2. Tabulation of experimental sets

	Amplitude (mm)					
Frequency	0.5	1.0	1.5	2.0	2.5	3.0
5Hz			●			
10Hz			●			
15Hz	●	●	●	●	●	●
20Hz			●			
25Hz			●			
30Hz			●			

Fig. 3 and Fig 4 show how the oscillation amplitude and frequency affects the time required for complete mixing. It can clearly be seen that the mixing time will decrease with increasing amplitude and oscillating frequency. However, from the trend, further increasing the amplitude or frequency will eventually not bring anymore improvement to the mixing time.

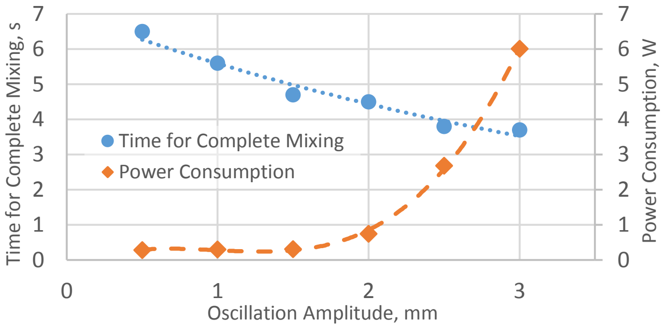

Fig. 3 Effects of oscillation amplitude on power and mixing time.

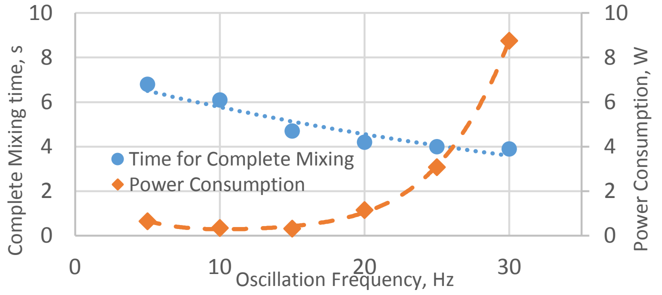

Fig. 4 Effects of oscillation frequency on power and mixing time.

In addition to not having further benefits, increasing the frequency and amplitude will also cause the power consumption to increase exponentially which can also be seen in Fig.3 and Fig. 4.

From the experiments, it is determined that at 15Hz and 1.5mm oscillating amplitude, the mixer has a good efficiency and power consumption.

The PIV analysis results for the 15Hz, 1.5mm amplitude set, both at time averaged and instantaneous (eject cycle) can be seen in Fig. 5 and Fig. 6. The results show a good agreement with previous works and clearly shows the formation of vortices. [7]

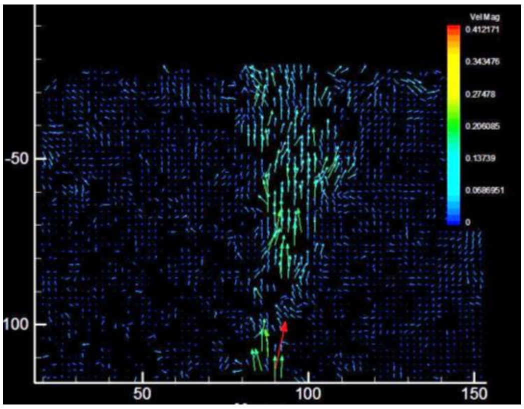

Fig. 5 Instantaneous velocity during an eject cycle at 15Hz, 1.5mm

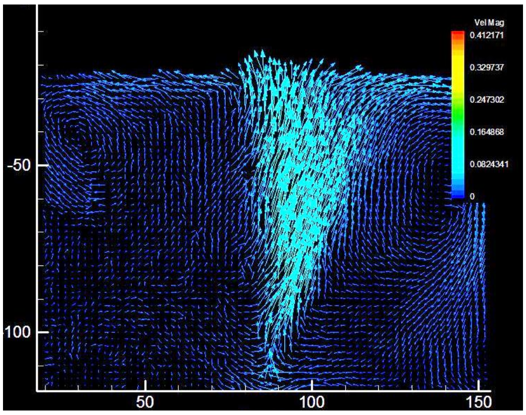

Fig. 6 Time averaged velocity at 15Hz, 1.5mm

4. Conclusions

The mixing performance of a synthetic jet mixer have been analysed and it is found to be a feasible alternative to conventional mixing. Power consumption is shown to rise exponentially when both frequency and amplitude are increased while the mixing time is decreased exponentially. However, the trend indicates that the mixing time will be constant after a certain amplitude and frequency.

Acknowledgment

The authors wish to convey their appreciation to Taylor's University School of Engineering for funding this project to enable its successful completion. Additionally, we would also like to acknowledge Professor Mark Simmons of the University of Birmingham for providing the particle image velocimetry apparatus for this project.

References

[1] Paul E., Atiemo-Obeng V., & Kresta S. (2004). *Handbook of Industrial Mixing*. New Jersey, USA. John Wiley & Sons, Inc.
[2] Kundu P. K., Cohen I. M., & Dowling D. R. (2012). *Fluid Mechanics*. 5th ed. Oxford, UK. Elsevier.
[3] Glezer A., & Wiltse J. W. (2000). *Synthetic Jet Actuators for Mixing Applications*. Patent No. 6056204, United States.
[4] Glezer A., & Amitay M. (2002). Synthetic Jets (Review Paper). *Annual Review of Fluid Mechanics*, Volume 34, pp. 503-529.
[5] Al-Atabi M., & M. Shamel. M. (2010). *Mixing in Tanks Using Synthetic Jets*. Daegu, ISFV 14.
[6] Raffel M., Willer C., Wereley S., & Kompenhans J. (2007). *Particle Image Velocimetry: A Practical Guide*. 2nd Ed. New York, US. Spinger.
[7] Al-atabi M., Liang H. C., Ng K. K., Hia I. L., Chin J. J., Ooi F. L. (2011). *Particle Image Velocimetry Study of Mixing in Tanks Using Synthetic Jets*. Kuantan, ICCEIB 2011.

Effect of Wing Configuration on Lift at Supersonic Speeds

Eric T.N.K*, Abdulkareem Sh. Mahdi Al-Obaidi

Department of Mechanical Engineering, School of Engineering, Taylor's University, Malaysia,

Corresponding author: ericnankui.tan@sd.taylors.edu.my

Abstract— **This paper is to discuss the effect of each wing parameter on the lift-curve slope, based on the results of a parametric study conducted using both analytical and semi-empirical approaches. This paper also serves as a tool to evaluate these two approaches in order to gauge their respective feasibility and to use the most appropriate method to generate a design table that correlates the investigated parameter.**

Keywords— supersonic, wing, configuration, lift coefficient, Mach number

1. Introduction

Supersonic wings are generally used in flying bodies as a means of control and stability as well as to maintain flight much like a subsonic wings; however, there are multiple configurations to design a supersonic wings to which must be taken into account during the design process as each configuration has its own strength and weaknesses and are only suited for a particular scenario based on a set of Tactical-Technical Requirement (TTR)

On the very fundamental level, wings are designed and developed solely to produce lift whether it is in the supersonic regime (Mach 1.2~4) or subsonic region. The aim of this paper is to discuss the effect of several wing parameters and their configurations to develop a design table that will instrumental for preliminary wing design.

2. Methodology

The variables that are investigated in this study are the wing geometrical characteristics and flight conditions. These variables are:

a. Airfoil shape
b. Relative thickness, t
c. Aspect ratio, A
d. Leading edge sweep angle, Λ_{LE}
e. Taper ratio, λ
f. Mach number, M
g. Lift Coefficient, C_L

In order to simplify the analysis, the angle of attack is assumed to be zero or small (below the stall angle) and the lift coefficient is expressed in terms of C_{L_α} or lift force curve slope per radians. The objective is to correlate the effect of these parameters on the generated lift. It is postulated that some of these parameters have a greater effect on the generated lift compared to others. Hence for the purpose of this study, four types of wing plan forms were studied as shown in Fig.1

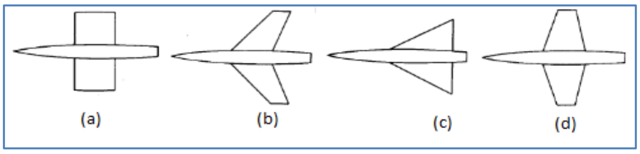

Fig. 1 The investigated wing planforms (a) rectangular unswept (b) swept (c) delta (d) trapezoidal

The effect of airfoil shapes were also taken into consideration in which two shapes, biconvex and double wedge were considered as shown in Fig. 2

Fig. 2 The investigated airfoils (a) biconvex (b) double wedge

There are 2 main approaches discussed within this paper, which are:

a. Analytical/ Theoretical Approach
b. Semi-Empirical Approach

2.1 Analytical Approach

The first method is to use existing theoretical formulations based on the *Linearized Supersonic Theory* [1] and the *Busemann's Second Order Approximation* [1]. Based on these two theories, two models were obtained:

$$C_{L\alpha} = \frac{4}{\sqrt{M^2 - 1}} \tag{1}$$

Equation (1) is the simplified equation obtained from the linearized theory. On the fundamental level, this theory only considers C_{L_α} as a function of Mach number, and it does this by assuming the wing to be of infinite span and of infinitesimally small thickness.

The Busemann's approximation expands Eqn. (1) by stating that the wing is of finite span and of finite thickness as expressed by Eqs (2) to (3)

$$C_{L\alpha} = \frac{4}{\sqrt{M^2 - 1}}[1 - \frac{1}{2(A(\sqrt{(M^2 - 1)})}(1 - C_3 A')] \tag{2}$$

$$C_3 = \frac{\gamma M^4 + (M^2 - 2)^2}{2(\sqrt{(M^2 - 1)})^3} \tag{3}$$

Equations (2) and (3) also takes into account the aspect ratio as well as the airfoil shape which is denoted by A' which are either two-thirds or half of the relative thickness corresponding to biconvex and double wedge respectively.

Analytical equations (1) and (2) were tested based on a series of cases based on Table 1 and benchmarked against wind tunnel results [2] for the purpose of validation.

Table 1. Wing characteristics and flight conditions

Design Parameter	*Range*
Aspect ratio, A	$2 \leq A \leq 4$
Taper ratio, λ	$0 \leq \lambda \leq 1$
Thickness ratio, t	3% , 5%, 8%
Mach Number, M	$1.2 \leq M \leq 4$
Leading Edge Sweep angle, Λ_{LE}	$0^\circ \leq \Lambda_{LE} \leq 70^\circ$

2.2 Semi Empirical Approach

The semi-empirical approach is the utilization of existing graphs [3] to generate a matrix array which is to be incorporated into a MATLAB sub-routine (MATLAB program). The sub-routine utilizes the interpolation method to determine the C_{L_α} based on the same set of parameters as outlined in Table 1.

The semi empirical approach is to serve as an alternate means to determine the values of C_{L_α} in which will later be used to compare with results obtained from analytical formulations. This is to validate the results obtained throughout the study.

3. Results and Discussions

Initially it is suspected that the aspect ratio, *A*, taper ratio, λ and leading edge sweep angle, Λ_{LE} would have a more prominent effect on C_{L_α} compared to the other parameters [5]. However based on the results shown in Table 2, it was found that one of these parameters which is the taper ratio has no significant impact on the lift.

Table 2. Aerodynamic Design table

Design Parameter		1.2 ≤ M ≤ 2.0	2.1≤ M ≤ 4.0
		$C_{L\alpha}$	$C_{L\alpha}$
Aspect Ratio	↑	↑	↑
	↓	↓	↓
Taper Ratio	↓	X	X
	↑	X	X
Relative Thickness	↓	X	X
	↑	X	X
Leading Edge Sweep Angle	↑	↓	↑
	↓	↑	↓
Airfoil	Biconvex	X	X
	Double Wedge	X	X

This discovery was an anomaly considering that taper ratio plays an important role in determining the shape of the wing, especially the trapezoidal planform, however it was later found that the taper ratio and leading edge sweep angle are highly coupled. This implies that the taper ratio cannot be changed without changing the leading edge sweep angle at the same time which means the effect of taper ratio is somewhat tied to the effect of the leading edge sweep angle. However the anomaly here is that the leading edge sweep angle can be changed freely without altering the taper ratio. This indicates that the taper ratio is dependent on the sweep angle whereas the sweep angle itself is independent of the taper ratio.

The leading edge sweep angle itself also has a profound effect on the lift, which is that at low Mach numbers, an increase in swept angle would degrade the performance of the wing; however at higher Mach numbers, the increase in swept angle has a positive effect. The reason for such behavior still requires further investigation.

The relative thickness and airfoil shape were also found to have no significant effect on the lift although it is speculated that these two parameters influences the drag instead [3,4]; however this effect was not studied as it was beyond the scope of the study. Further investigation was conducted to determine the effect of the airfoil shape on C_{L_α}. As seen in Fig.3, there are no clear indication that either of the airfoil shapes considered has any advantage over each other, however at low Mach numbers the biconvex airfoil delivers a slightly better performance compared to the double wedge profile. Although in spite of this performance gain, the double wedge profile is more commonly used compared to the biconvex as it is easier to manufacture a double wedge airfoil compared to a biconvex airfoil[5].

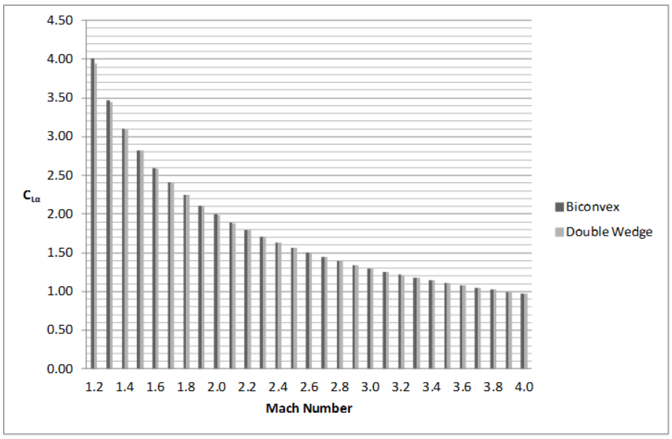

Fig. 3 Comparison of airfoil shape performance

Based on Fig. 3, it is indicated that as Mach number increases, the value of C_{L_α} decreases. This shows that as speed increases, the effect of the shock waves becomes less prominent, hence reducing the pressure difference over the upper and lower surface of the wing . This phenomenon can be described as the shock-waveless effect [6]. However this only applies to rectangular unswept wings.

4. Conclusion and Recommendations

Based on the outlined parameters in Section 2, a comprehensive study has been conducted based on two main approaches and the results have been tabulated into a design table shown in Table 2. It is evident that only the aspect ratio, *A* and leading edge sweep angle, Λ_{LE} have an impact on lift. However the credibility of the results is still questionable and is only suitable for preliminary design.

Further study using other methods such as numerical approach and experimental approach are still required to further validate the effect of each parameter as well to understand the coupled effect of both taper ratio, λ and leading edge sweep angle, Λ_{LE}.

References

[1] J. Anderson, Fundamentals of Aerodynamics, 3rd Ed., New York: McGraw Hill,2001.

[2] C. Hall, "Lift, Drag and Pitching Moment of Low Aspect Ratio Wings at Subsonic and Supersonic Speeds", National Advisory Committee for Aeronautics, Washington, 1953.

[3] Mahdi, A. Sh. Al-Obaidi,"The Influence of Configuration Design on Aerodynamics and Stability of SSM at Supersonic Speeds", Al-Rasheed College of Engineering and Science, University of Technology, Baghdad, Iraq, 2005.

[4] E. Bonney, " Aerodynamics Characteristics of Solid Rectangular Airfoil at Supersonic Speeds", Silver Spring MD: The John Hopkins University, Georgia Ave., 1945.

[5] Kermode A. C., Mechanics of Flight, New Jersey: Pearson Prentice Hall, 2006.

[6] Bensiger S.S.B., Prasanth N. "Analysis of Bi-convex Aerofoil using CFD Software at Supersonic and Hypersonic Speed," *Elixir International Journal of Mechanical Engineering*, vol. 53, 2012.

Drying Kinetics of Pesticide Droplets

Hiong Guo Naik[1], Meng Wai Woo[2], Jerry Y. Y. Heng[3], Rashmi W.[1], Chien Hwa Chong[1]

[1]*Department of Chemical Engineering, Taylor's University, Lakeside Campus, Subang Jaya, Selangor, Malaysia,*

[2]*Department of Chemical Engineering, Monash University, Clayton Campus, Victoria, Australia,*

[3]*Department of Chemical Engineering, Imperial College London, South Kensington Campus, London SW7 2AZ, U.K.*

Abstract— **Pesticides are widely used in the agricultural industry to control pests and prevent losses of crops. The objective of this paper is to investigate of the drying kinetics of pesticide droplets. The pesticide samples were applied on the target surface and placed into a drying chamber. The evaporation profile was plotted from the data obtained. It was found that the droplet exhibited a linear drop in drying rate at very low concentrations. Further investigation revealed that the pesticide used in the experiment is a surface active compound and alters the drying kinetics of the droplet with low concentrations.**

Keywords— Drying Kinetics, Pesticide, Surface Active, Surface Tension, Droplet

1. Introduction

Pesticides have been widely and extensively used for various purposes in agricultural activities. It is classified based on two main criteria: structural basis and mode of action. Discovered since 1945, pesticides in use today are labeled as organic synthetic pesticides, a label which includes pesticide families such as organophosphorus, carbamated and organochlorided insecticides [1]. Among the few families listed above, neonicontinoids are the latest and most rapidly-growing class of pesticides, representing almost 24% of the global market in 2008 [2]. Neonicotinoids are systemic pesticides that act on the central nervous systems of insects, a selectivity trait that makes it a potent hazard towards insects, without presenting threat towards mammals. This mode of action has resulted in a pesticide that is target specific, and has almost no cross-resistance towards older pesticides that have been stated above. Hence, neonicotinoids have been replacing older variants of pesticide on the field [3, 4].

In view of the low solid concentration in typical pesticides (10mL in 3000mL, roughly 0.33% v/v), the pesticide droplet is expected to have a drying profile that is similar to a pure water droplet. Many authors have done research on pesticide droplets, most of which used pesticides of the organophosphorus family, or were otherwise not stated. The variables that were frequently tested and studied were the effects of droplet size, addition of adjuvants and target surface morphology on the drying times, wettability, and deposition efficiency [5, 6, 7]. However, research on the drying kinetics is rather scarce. The purpose of this study is to study the drying kinetics of pesticide droplets. This will provide evidence if the drying of pesticide resembles water droplets or otherwise.

2. Methodology

A schematic of the apparatus used for measuring drying kinetics is shown in Fig. 1. The apparatus consists of a digital flow meter, a dehumidifier, a water bath, a coil and a drying chamber. The gas flow is regulated by the digital flow meter, which introduces the gas into a dehumidifier which removes any humidity present in the gas. The coil is immersed in the water bath, which serves to heat up the gas and regulate gas temperature into the drying chamber.

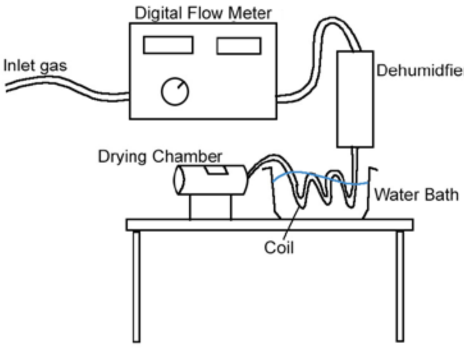

Fig. 1: Schematic of drying apparatus used in this study.

The variables controlled in the experiment are based on real-time environmental data. Weather data of the target area was collected from the Malaysian Meteorological Department. Data such as wind speed and temperature were collected and tabulated for the month of March, and the average values were selected to be the environmental variables of the investigation. Tomatoes were obtained from local market. The pesticide (15g/L Imidacloprid) was obtained from Hortico, a company which produces garden care products. The concentrations studied were the recommended concentration by the manufacturer, with ±5mL samples.

Glass slides that were used to hold the samples were weighed and labeled. The target surface was prepared by removing a section of 1.5 cm x 1.5 cm skin off a tomato and placing it onto the glass slide. The tomato skin was washed gently to avoid abrasion to the surface and to ensure that there is no residue from previous pesticide applications. The pesticide was prepared in sample vials using tap water, and was mixed by shaking to simulate the procedure done in the field. Using a syringe, nine 1μL droplets were placed onto the sample. The prepared slide with tomato skin was weighted, before and after applying the pesticide droplet. A control set (tomato skin only) was also prepared, to be run side-by-side with the experiment set. The drying chamber was set according to the collected variables. The samples were put into the chamber and weighed at 30 second intervals.

For each set of the experiment, the data collected was then compared between the sample set and the control set that were run concurrently. By running the control set in parallel with the sample set, both skins were exposed to similar drying conditions, which can be used to determine drying kinetics of pesticide droplets. All experiments were done in triplicates to avoid any error introduced.

In addition to that, further investigation was carried out to determine the surface tension of the samples, by using the capillary rise method. A petri dish was filled with water, and a capillary filled with water was inserted. The water is allowed to recede till it reaches a constant level, where the water level is noted. The same procedure is carried out in triplicates for each sample, and the surface tension is then derived from the data collected.

3. Results and Discussion

Fig. 2 shows drying rate of a sample studied at 24°C. Notice that the drying profile shows a linear progressive reduction in reduction rate. This profile contradicts with literature hypothesis. It is widely accepted that at low initial solid concentration, the activation energy for evaporation is very low, and should produce a profile that resembles pure water droplet drying, where a constant rate period would be observed followed by a drop at the end. A question then arises: Why is there a progressive reduction in evaporation rate even at such low solute condition at 0.167 %v/v concentration? In addition, within the resolution of the experiments, the initial constant rate period was also not observed. These observations suggest that significant solute already accumulated on the surface of the droplet even at the initial stage of drying.

The pesticide solute could have transported onto the droplet surface due to its surface activity. Fig. 3 shows a schematic diagram of this phenomenon. The molecules take up space on the surface of the droplet, reducing the available area for evaporation to take place. This effect is intensified as the droplet becomes smaller, since the pesticide molecules do not evaporate, making the surface of the droplet more saturated.

Therefore, to verify this claim, the surface tension of water and the samples are measured using the capillary rise method [8]. Fig. 4 shows the height liquid travels due to adhesion forces between the liquid and solid interface. It compares the relative effect of lactose and the pesticide towards surface tension of water. Surface tension of pesticide droplets relatively low compared to lactose. Lactose reduces the height travelled by water from 24.9 mm to an average of 23.7 mm for all concentrations tested. The pesticide used, however, reduced the height travelled by the water from 24.9 cm to an average of 13.8 mm. Even at concentrations as low as 0.167% v/v, the height travelled was reduced from 24.9 mm to 17.8 mm. This indicated that the pesticide is very surface active, even at very low concentrations which supports the explanation given above on the retardation of evaporation rate observed.

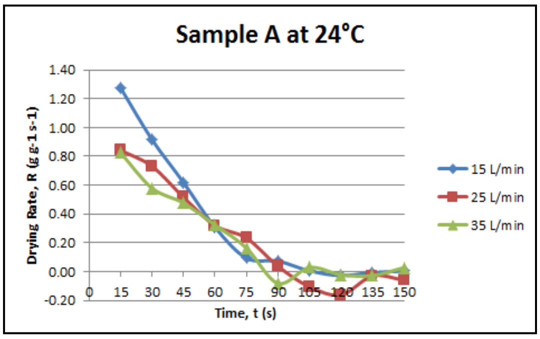

Fig. 2: Drying rate of sample A at 24°C

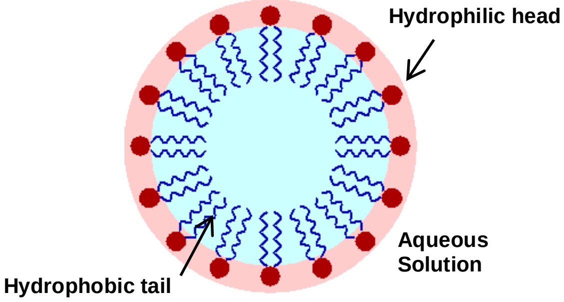

Fig. 3: Schematic showing the effect of surface active compounds on a water droplet.

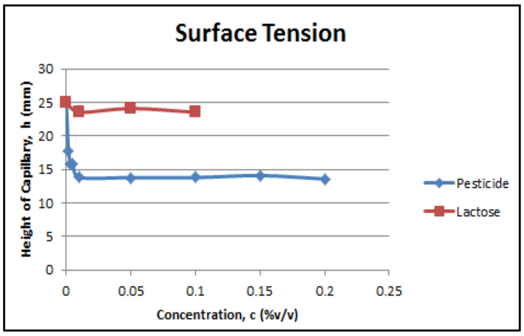

Fig. 4: Surface tension as a function of concentration.

4. Conclusions

Imidacloprid is a surface active compound, which affects the drying rate of a pesticide formulation at extremely low concentration which is 0.167 %v/v. The progressive retardation of the drying rate even at very low concentration is due to the accumulation of dissolved pesticides on the air-droplet interface via the surface activity mechanism. This provides an interesting insight into understanding the drying kinetics of pesticides, which may contribute into the development of newer and more efficient formulations and delivery of active ingredients for crop protection.

Acknowledgment

This work has received financial support from Dr. Woo Meng Wai of Monash University, Clayton Campus, Victoria, Australia, who provided access to the facilities and apparatus used in the experiment. Special thanks is also given to Prof. Wei Shen of the Australian Pulp and Paper Institute for his help in the method of measuring the surface tension of the samples studied.

References

[1] Zhang, W., Jiang, F., & Ou, J. (2011). Global pesticide consumption and pollution: with China as a focus. *Proceedings of the International Academy of Ecology and Environmental Science*, vol. 1(2), 125-144.

[2] Jeschke, P., Nauen, R., Schindler, M., & Elbert, A. (2011). Overview of the status and global strategy of neonicotinoids. *Journal of Agricultural Food Chemistry,* vol. 59, 2897-2908.

[3] Jeschke, P., & Nauen, R. (2008). Neonicotinoids – from zero to hero in insecticide chemistry. *Pest Management Science*, vol 64, 1084-1098.

[4] Nauen, R., & Denholm, I. (2005). Resistance of Insect Pests to Neonicotinoid Insecticides: Current Status and Future Prospects. *Archives of Insect Biochemistry and Physiology*, vol. 58, 200-215.

[5] Salyani, M. (1988). Droplet Size Effect on Spray Deposition Efficiency of Citrus Leaves. *Transactions of the ASAE,* vol. 31(6), 1680-1684.

[6] Smith, D., Askew, S., Morris, W., Shaw, D., & Boyette, M. (2000). Droplet Size and Leaf Morphology Effects on Pesticide Spray Deposition. *Transactions of the ASAE*, vol. 43(2), 255-259.

[7] Xu, L., Zhu, H., Ozkan, H.E., Bagley, W.E., & Krause, C.R. (2011). Droplet Evaporation and Spread on Waxy and Hairy Leaves Associated with Type and Concentration of Adjuvants. *Pest Management Science*, vol. 67, 842-851.

[8] Arbatan, T., & Shen, W. (2011) Measurement of the Surface Tension of Liquid Marbles. *Langmuir: the ACS Journal of Surfaces and Colloids,* vol. 27(21), 12923-12929.

Design & Analyses of a six-legged robot simulating bug movement

Imad Fahim[1]

[1]School of Engineering, Taylor's University, Malaysia,

Abstract — **A lot of research has been done in the past in relation to the construction of this project. Such works have proven to boost the manipulation of robots greatly; especially when biological principles are incorporated into its mechanical design. Raibert and colleagues have been credited with the construction of a highly successful robot by incorporating biologically-inspired dynamics into their designs. This paper, though, focuses on the design and analyses of the locomotion utilizing a six-legged robot; showcasing the attributes of a coccinellidae, commonly known as the ladybug or ladybird. It discusses a unique way of utilizing cams to obtain locomotion. The movement was triumphantly observed using ANSYS and SolidWorks. Furthermore, any obstructions caused by the joints on the assembly were also noted. Therefore, in the current text, we outline the observations made for replicating the insect, past literature on hexapods and literature entailing to the utilization of cams as primary mechanism. The above mentioned software's were employed in the preliminary stages of this project to formulate the design and initiate analyses, before an actual construction of the bug could be carried out.**

Keywords— Ladybug, hexapod, coccinellidae, ladybird, six legged robot

1. Introduction

As the field of robotics is progressing, apprehension of incorporating biological principles with mechanical designs is becoming more popular. This is carried out with a vision of creating mechanisms which could not only help humans with their work in dangerous environments; but innovate products which would be useful in daily activities, more efficient and reliable. Therefore, inventions of these robots have influenced human lives tremendously.

Classification of these robots, irrespective of their tasks, can be made simpler by associating them into either being stationery or mobile. This distinguishing factor is based the robots ability to displace from its residing position.

Amongst the mobile robots, six legged robots, also known as Hexapods, are robots whose design is based on insects. Such an intricate design is mostly inspired by small insects like ants and cockroaches. Though in the real world, these insects only use legs for locomotion; robotic designs of these creatures have incorporated proper utilization of mechanical legs, wheels and the combination of two.

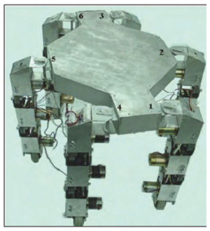

Figure 1Cassino Hexapod Robot at LARM [2]

Figure 2 Photograph of SLAIR2 [3]

Various researches has been conducted before the fabrication of such robots. Chica-Bug has been designed based on the anatomy of coccinellidae. Such a replication has never been done before, as nearly all of the literature researched had been based on the anatomy of a cockroach. These species of beetles are less than a quarter of an inch long, are round shaped and have six short legs [4].There are eight major parts of the ladybug, each with its individual purpose serves a unique purpose. From engineering perspective, the most important features are

a) Body structure b) Leg structure c) Leg movement

The major aspect before designing the leg is to set an objective for the number of DOF. The more the DOF, the more flexibility and agility the robot will contain and the more accurately it can imitate the insect. This paper discusses the utilization of only 1 DOF with cams. This bug has two various cam shafts, each controlling one side of the leg. This arrangement is compared with the mechanism used by H.Alli & S.Soygudder (2007) [10].

Table 1 Robots and the respective DOF

DOF	Robots
1	Roach [4], RHex [5]
2	HAMR [6]
3 or more	Cassino [7], Robot III [8], Gregor I [9]

Figure 3 Robot Design

2. Methodology

Once the design was finalized in SolidWorks, it was imported in ANSYS for structural analyses. These analyses were carried out based on the leg contact with ground – three legs signifying motion, while all six representing stationery. Furthermore, for the solution setup, joint method was simulated to attribute an actual connection. It was done the relative degree of freedom for each individual part; translational and rotational. Furthermore, the entire assemble was finely meshed with element size up to 0.05cm.

Table 2 Joint specification between parts

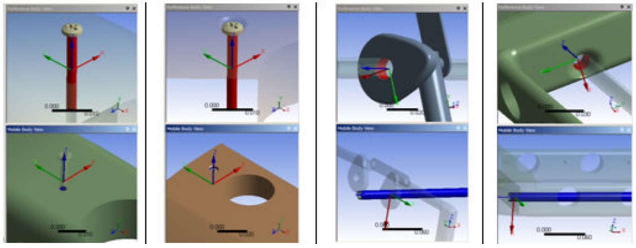

The structural integrity of the structure during the two states was later conduced with forces of varying magnitude subjected on the shell of the robot. This was done to work out the endurance of the assembly parts. The results calculated were based of shear stress and deformation.

3. Results

Results obtained clearly showed the difference of stress and corresponding deformation between the two states of motion. It even highlights the obvious relation of stability with the applied force. As the force is increased, we can notice the stress distribution on the legs in the ratio of their contact with ground – 2:1.

Table 3 Results obtained when in stationery state

Loads	Deformation (m)	Maximum Shear Strain	Maximum Shear Stress (Pa)	Strain Energy (J)
0	2.23E-08	1.41E-07	3.77E+03	3.22E-13
10	2.23E-05	1.41E-04	3.77E+06	3.22E-07
50	1.11E-04	7.06E-03	1.89E+07	8.05E-06
100	2.23E-04	1.41E-03	3.77E+07	3.22E-05
200	4.46E-04	2.83E-03	7.54E+07	1.29E-04
500	1.11E-03	7.06E-03	1.89E+08	8.05E-04

Table 4 Results obtained when in motion

Loads	Deformation (m)	Maximum Shear Strain	Maximum Shear Stress (Pa)	Strain Energy (J)
0	3.86E-08	2.36E-07	6.30E+03	1.02E-13
10	3.86E-05	2.36E-04	6.30E+06	1.02E-06
50	1.93E-04	1.18E-03	3.15E+07	2.55E-05
100	3.86E-04	2.36E-03	6.30E+07	1.02E-05
200	7.72E-04	4.72E-03	1.26E+08	4.08E-04
500	1.93E-03	1.18E-02	3.15E+08	2.55E-04

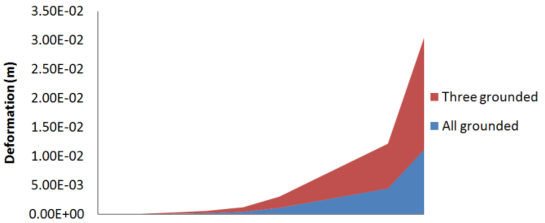

Figure 4 Graph of deformation at varying loads

4. Discussion

From the obtained results, it is evident that the design assembly has sufficient endurance to withstand loads beyond the targeted 500N. Furthermore, the design dimensions make it suitable for manufacturing using CNC machines.

As viewed in the work of by H.Alli & S.Soygudder (2007) [10], in which they utilized a transmission bar to obtain displacement for the robots locomotion, this robot makes use of a connection rod. The rod is attached to the two cams, perpendicular to the surface geometry and is subjected to translational motion. But, on the contrary, the transmission bar in the referred paper is connected in parallel and has various other links, which adds on to the weight and hinders motion

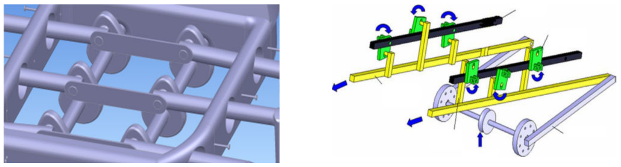

Figure 5 Comparison of the cam arrangement

In spite of having this difference in arrangement, both the mechanism obtained motion using the coordinated movement shown in Figure 6. The front leg and the rear leg on one side propel the robot, while the centre leg, on the opposite side, provides stability to the entire robot.

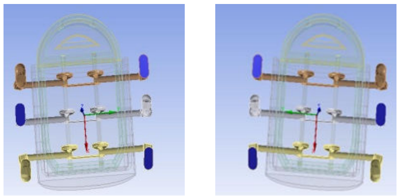

Figure 6 Mechanism coherent to the robot movement.

5. Conclusion

As signified in the above analyses, the components design is suitable to withstand the robots weight. The mechanism utilized for this bug has no corresponding benchmark. It serves merely to give analyses of the design. It is recommended to actually construct the robot in the near future to distinguish between the cam arrangement used by H.Alli & S.Soygudder (2007) in their paper against one developed in this one. The only limitation to these designs, lie in their degrees of freedom, as the movement is restricted to just backward and forward

References

[1] R. Q. R. B. W. F. G.M. Nelson, "Design and Simulation of a Cockroach-like Hexapod Robot," in IEEE International Conference on Robotics and Automation, Albuquerque, New Mexico, 1997.

[2] G. C. a. M. Ceccarelli, "A Low-Cost Easy-Operation Hexapod Walking Machine," International Journal of Advanced Robotic Systems, vol. 5, no. 2, pp. 161-166, 2008.

[3] P. A. S. B. T. M. Dzhantimrov J., "HIL/SIL by Development of a Six," in 10th International Conference on Climbing and Walking Robots CLAWAR, Singapore, 2007.

[4] R. Jones, "Ladybug Anatomy," [Online]. Available: http://www.ladybug-life-cycle.com/ladybug-anatomy.html. [Accessed 12 12 2012].

[5] E. S. R. S. F. Aaron M. Hoover, "RoACH: An autonomous 2.4g crawling hexapod robot," in International Conference on Intelligent Robots and Systems, 2008.

[6] M. B. a. D. E. K. Uluc. Saranli, "RHex - A Simple and Highly Mobile Hexapod," The International Journal of Robotics Research, vol. 20, no. 7, pp. 616-628, 2001.

[7] ,. C. H. M. K. R. J. W. Andrew T. Baisch, "HAMR: An Autonomous 1.7g Ambulatory Robot," in IEEE/RSJ International Conference on Intelligent Robots and Systems, San Francisco, 2011.

[8] Y. A. C. M. Y. S. CARBONE G., "Design and Simulation of Cassino Hexapod Robot," International Journal of Mechanics and Control, vol. 10, no. 2, pp. 27-34, 2009.

[9] P. A. a. L. P. M. Pavone, "An Innovative Mechanical and Control Architecture for a Biomimetic Hexapod for Planetary Exploration," in 56th International Astronautical Congress, Fukuoka, 2005.

[10] S. S. a. H. Alli, "Design and prototype of a six-legged walking insect robot," Industrial Robot: An International Journal, vol. 34, no. 5, pp. 412-422, 2007.

Numerical Analysis: The Effect of Composite Material on Insole Sport Shoe on Foot Pattern

John Whaley[1], Mr. Alexander Chee Hon Cheong[2*]

[1]*Mechanical Engineering, Taylor's University, Malaysia,* [2]*Mechanical Engineering, Taylor's University, Malaysia*

**john.whaley@hotmail.com*

Abstract— **Different type of foot pattern can deliver various impact to shoes. The composite material which constructive the insole shoe with specifically in basketball shoe will be tested with the different kinds foot patterns in terms of durability. The selected material that has been used is basically made from synthetic material such as polyethylene. The simulation of insole shoe will be compare to three different kinds of foot patterns to analyze the durability. All of these will be tested in the simulation to determine the impact to that insole shoe.**

1. Introduction

A sport shoe is a footwear design to comfort and protect athlete's foot while doing various activities [1]. However, the insole shoe has a huge impact for people footwear. Typical material like synthetic material is selected to give a suitable place for foot in the insole shoe. Different shoe has different type of materials for insole. For example, in sports game, insole shoe is created base on particularly sport that people do such as basketball, football, running, and so on. In basketball, insole shoe is made by using synthetic materials [1]. Viscoelastic materials are often characterized in the literature by an engineering measurement which is the ratio of the viscosity of material to its elasticity [2]. Thermoplastic materials are the material which can become ductile when the particle heated and will remain to the same configuration when cooled [2]. This why polyethylene thermoplastics are one of the most commonly used in insole basketball shoe because it designed to deliver comfortable to the people's foot and hold to the position where the weight and forces are being applied to the insole [3]. In insole design, they are divided into flat and heel cup insoles. In particular basketball insole design, heel cup is normally being used. There is a purpose of designing heel cup to basketball insoles because they provides a protection to ankle and reduce the forces during the impact loads that applied to the insole during walking and jumping. The heel cup insole is taken in order to investigate by using the Nike zoom basketball from Kobe Bryant. Figure 1. is the sample which taken from the right and the top view.

Figure 1. Original Basketball Shoe and Shoe Ins

In addition, the component that needs to evaluate to suit the insole shoe is by looking for the types of foot pattern. Foot pattern is divided by three pattern: normal/neutral foot, high arch/supination foot, and flat foot/pronation foot.

(a) (b) (c)

Figure 2. Foot Patterns: (a) neutral; (b) flat ; (c) High- arc

The three patterns of foot will be evaluated and make the accuracy for athletes so that it can fit to the foot. All of this will be tested of their durability.

2. Methodology and Experimental Work

2.1. Shoe Insole Modeling & Foot Pattern

The material for the shoe insole will be selected properly due to simulation later after the modeling. Polyethylene is chosen due to the configuration of stability and possesses adequate flexibility and strength [3]. The basketball insole will be modeled with 7.5 cm length. This modeling is done by solidworks software.

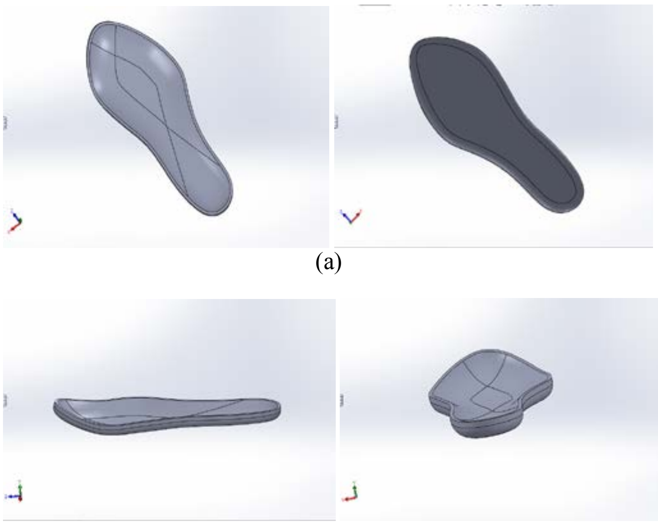

(a)

(b)

Figure 3. (a) Top View Model of Shoe Insole ; (b) Side View of Shoe Insole

Foot patterns are studied and tested to identify the different pressure at the insole to produce results in stress, displacement, and deformation. First, the experiment was started with taking three sample feet to wet and stick their foot to A4 paper as called foot printing. After three sample of foot printing are collected then the simulation will be run.


(a) (b) (c)

Figure 4. (a) Normal foot ; (b) High –arc foor ; (c) Flat foot [4]

2.2 Durability

Sport shoes should provide durability during the support phase of a lateral maneuver because of the large forces transmitted to the ground as player transition from lateral jump vertical to the ground [4]. The purpose is to investigate the barefoot pattern as perform the vertical jumping for evaluating lateral durability of insole shoe.

3. Results and Discussion

The results of the insole in the simulation will be resulted when the external loads were applied to the insole. For example, The external load/pressure is taken which applied to the insole is 20 N/m^2. This pressure will applied to each surface of the insole.

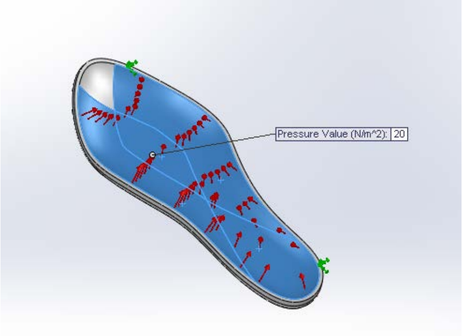

Figure 5. External Load on Shoe Insole

After the load was being applied, the insole will deform and results the stress, displacement, and deformation. Figure 6 is the statistic of the stress to the Shoe Insole and the displacement:

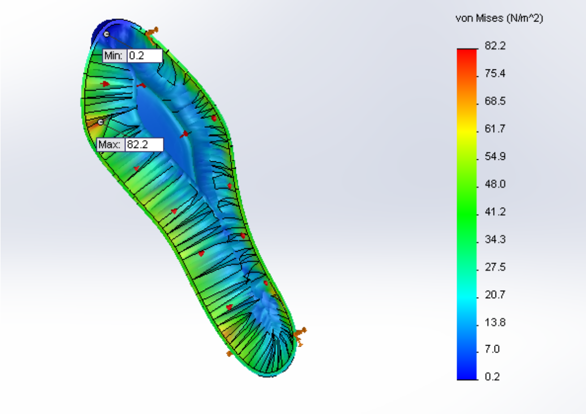

(a)

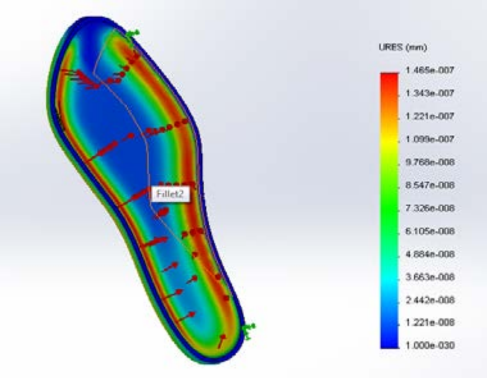

(b)

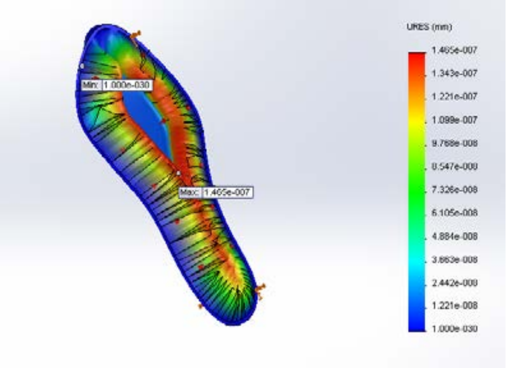

(c)

Figure 6. (a) Stress ; (b) Deformation; (c) Displacement

In stress, maximum stress is shown in red color with 82.2 N/m^2 and minimum stress is 0.2 N/m^2. In addition, the deformation is decompressed to 1.455 (10)$^{-7}$ mm. It caused of the movement of the foot that contact to the insole shoe which can deform slowly. In displacement, the maximum displacement happened in the middle of insole with 1.45 (10)$^{-7}$ mm and then slowly decreasing along the foot movement to the side part.

5. Conclusion

Shoe insole will affect by human foot based on the weight supply which will create pressure to the insole to analyze the durability. All in all, the testing in the simulation delivers the different pressure that result in stress, deformation, and displacement due to foot contact to the insole.

Acknowledgment

I personally would like to thank especially to my supervisor and friends who give support and motivation for my final year project

References

[1] H. Andrew, A.M. Roger. ‘Foot and Ankle’. Chapter 2. Pp. 1894-1896

[2] W.W. Michelle (2009). ‘The Use of Viscoelastic Materials in Shoes and Insoles’.Applied Mechanics and Materials. Pp 110-116

[3] W.C. Mark, M. Kristy May, L.B. Kim (2011). ‘Insole Effects on Impact Loading during Walking’. Centre Health, Exercise, and Sport Medicine

[4] A.K. Ramanathan, E.J. Parish, G.P. Arnold, T.S. Drew. (2011) ‘ The Influence of Shoe sole’s varying Thickness on Lower Limb Muscle Activity.’ Pp 218-223.

Biodiesel Production by Ethanolysis of Palm Oil with Immobilized Lipase

Joo Buan Yeow*, Marwan M. Shamel

School of Chemical Engineering, Taylor's University Lakeside Campus, 47500 Subang Jaya, Selangor Malaysia

**joyeow_89@hotmail.com*

Abstract— **Biodiesel synthesis by enzymatic ethanolysis of palm oil with *Aspergillus oryzae* lipase immobilized on ceramic honeycomb was studied. The effect of operating temperature, ethanol to oil molar ratio and water content on the reaction was experimental tested and compared to that of free lipase. The tested conditions were found to be at 45 °C, 3:1 and 5 % (v/v) respectively. Moreover, the conversion of fatty acid ethyl esters (FAEEs) using immobilized lipase through immersion pre-treatment in palm oil increased by approximately 18%.**

Keywords— Fatty Acid Ethyl Esters, Ethanolysis, Palm Oil, Ceramic Honeycomb, *Aspergillus oryzae* lipase

1. Introduction

Biodiesel is an alternative fuel derived from renewable resources such as vegetables oil and animal fats can replace petroleum-based diesel. It is renewable, biodegradable and non-toxic source of energy [1]. Biodiesel is obtained via the process of transesterification of triglyceride (fats and oils) with an alcohol in the presence of a catalyst with glycerol as a by-product. Ethanol is preferable to be used as an alcohol in biodiesel synthesis because it can be produced from various kind of biomasses by fermentation, which makes the process more eco-friendly [1]. In recent years, enzymatic production of biodiesel has drawn the attention due to several drawbacks caused by the conventional chemically catalyzed transesterification, such as the formation of soap, undesired by-products, difficulties in recovery of catalyst and glycerol, complicated product separation, waste water treatment and high energy requirements [2]. Lipase catalyzed reaction eliminates these problems, allows mild condition reaction and obtains higher grade of glycerol. However, there are limitations to use lipase as catalyst such as high catalyst cost, longer reaction time, low stability and easy inactivation by the alcohol [2]. These problems can be solved by immobilizing the enzyme to increase its stability and catalytic activity. In the present work, *Aspergillus oryzae* lipase was immobilized onto ceramic honeycomb carrier and used in the transesterification of palm oil with ethanol. The operating parameters affecting the enzymatic ethanolysis reaction were studied.

2. Materials and Methods

2.1. Materials

Refined palm oil (829 g/mol) was obtained from Sime Darby Foods and Beverages Marketing Sdn Bhd. Lipase from *Aspergillus oryzae* with activity of 100 KLU/mL was a kind gift from Novozymes. Ceramic honeycomb (2.0 cm diameter, 5.0 cm long and porosity of 0.37) was supplied by Acichemshun Industry (Jiangxi, China). Analytical grade of ethanol (95% v/v), glutaraldehyde (25% in water), tributyrin and other chemicals used were purchased from Merck.

2.2. Lipase Immobilization by Chemical Adsorption

Ceramic honeycomb was activated by soaking in glutaraldehyde (2.5% in H_2O) for 1 hour and followed by washing with distilled water (10 times of the soaking volume) for 5 times. Activated ceramic carrier was then fixed it in a column and circulating with enzyme solution at 25°C for 3 hours for immobilization. The activity of the enzyme used was 13500 LU that was measured by pH-stat method. This method is based on the hydrolysis of tributyrin by enzyme and titrating butyric acid produced with 0.05M of sodium hydroxide in distilled water [3]. One unit of lipase activity (LU) corresponds to the amount of enzyme needed to liberate 1μmol of butyric acid per minute [3].

2.3. Ethanolysis of Palm oil and Analysis of Ethyl Esters

After the immobilization process, the enzyme solution in the column was removed. A total of 800 mL substrate mixture containing palm oil and ethanol was fed into the column to the ceramic support by peristaltic pump at a constant flow rate of 25mL/min. The column was jacketed with water that was circulated from the bottom of the jacket at 70mL/min to maintain the operating temperature as illustrated in Fig. 1. The reaction of free lipase was conducted in a beaker which was filled with 800 mL of substrate mixture and placed in a water bath with the temperature required. 13500 LU of free lipase was added to the mixture and stirred with agitator at 200 rpm. Both reactions were carried out in 4 hours of reaction time. The effects of temperature (35 and 45°C), ethanol to oil molar ratio (3:1 and 6:1) and water content (5 and 10% v/v) on ethyl esters production were investigated in both reaction systems. Samples were collected at specific intervals and immersed in water bath adjusted to 70°C for 15 minutes to stop the enzyme reaction. 10mL of the reaction mixture was then centrifuged at 15000 rpm for 30 minutes. 1 mL of the aliquots was withdrawn and the glycerol content was analyzed using the spectrophotometric method described by Bondioli and Della Bella, 2005 [4]. The conversion of ethyl esters from 1 mole of palm oil was determined using the formula in Eq. 1 and Eq. 2.

$$Conversion\ (\%) = (No.of\ mole\ of\ ethyl\ esters/3)\ x\ 100\% \ldots\ldots (Eq.1)$$

$$No.of\ mole\ of\ ethyl\ esters = No.of\ mole\ of\ glycerol\ formed\ x\ 3 \ldots\ldots (Eq.2)$$

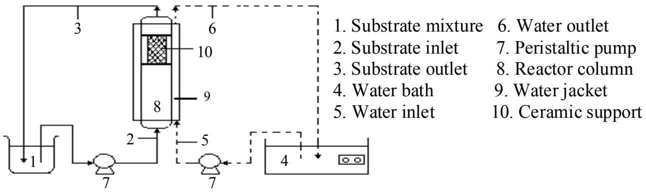

Fig. 1 Fixed Bed Reactor for Ethyl Esters production from Palm oil.

3. Results and Discussions

3.1. Operating Temperature

The influence of temperature on the lipase-catalyzed ethanolysis was examined at 35 °C and 45 °C with both free and immobilized enzyme. Fig. 2 shows that the highest ethyl esters conversion was at 45 °C in both cases with the same enzyme activity. However, the rate of ethyl esters formation was observed to be higher significantly when immobilized lipase was used at the same temperature. This proves that the immobilized lipase has a higher temperature resistance than free lipase due to the thermal stability given by the bound support. These results agree with Iso et al. (2001) [5]. Raita et al. (2010) stated that higher optimal temperature of immobilized enzyme is beneficial as it enhances the transesterification of oil with high saturated fatty acid content such as palm oil [6].

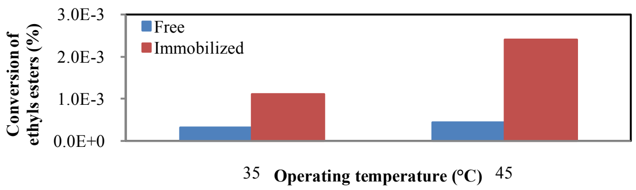

Fig. 2 Effect of operating temperature on the reaction (Both systems contain 3:1 of ethanol to oil molar ratio, 13500 LU of lipase and 5% (v/v) of water)

3.2. Ethanol to Oil Molar Ratio

The effect of ethanol molar ratio on the ethanolysis reaction is shown in Fig. 3. Increasing the ethanol to oil molar ratio from 3:1 to 6:1 led to a decrease in the conversion of ethyl ester. However, the conversion catalyzed by immobilized lipase is higher than the free lipase. The reduction in conversion is due to the deactivation of the lipase by exposure to ethanol. From the stoichiometric of the reversible transesterification reaction, 3 moles of alcohol are required for complete biodiesel conversion. According to Le Chatelier's equilibrium principle, excess of alcohol pushes the reaction to the right towards higher amount of product formation [7]. However, this rule does not apply in this reaction because of the high polarity of short chain alcohol, ethanol that inhibits the activity of the enzyme. The surplus ethanol which is insoluble and remained as droplets in the oil distort the water layer around the enzyme and thus decrease the enzyme catalytic activity and oil diffusion rate [7].

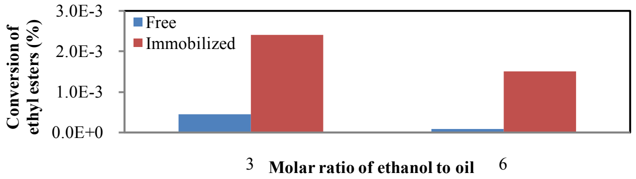

Fig. 3 Effect of ethanol to oil molar ratio on the reaction (Both reaction systems contain 13500 LU of lipase and 5% (v/v) of water at 45 °C)

3.3. Water Content

Lipase is well known for its unique feature to act at the interface between water and oil [8]. Lipase activation, which involves unmasking and restructuring of enzyme molecules, requires the presence of the interface [8]. Hence, with increased amount of water, the size of oil-water interfacial area formed increases. As a result, the catalytic activity of enzyme improves. However, excess water triggers the hydrolysis reaction that competes with transesterification to produce fatty acids. Hence, the water content in the reaction must be controlled in the range of favoring the enzyme activity and minimizing the hydrolysis reaction. The amount of water added was specific to each lipase and in this experiment the optimal water content obtained for *A. oryzae* lipase is 5% (v/v) as shown in Fig. 4.

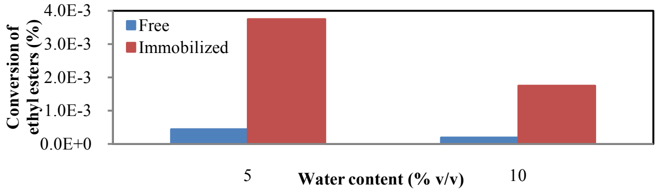

Fig. 4 Effect of water content present on the reaction (Both reaction systems contain 3:1 of ethanol to oil molar ratio and 13500 LU of lipase at 45 °C)

3.4. Pre-treatment of Immobilized Lipase

The pre-treatment method used was a modified of Chen and Wu (2003) method [9]. After immobilization, the ceramic honeycomb was immersed in palm oil for 15 hours. The pre-treated immobilized lipase was then used in the reaction with excess ethanol (6 molar ratios) to produce ethyl esters. From the results shown in Fig. 5, the ethyl esters conversion using pre-treated lipase was about 18 % higher than the lipase without pretreatment. This is because palm oil intrudes in the immobilized lipase during the immersion. As a result, the enzyme pore spaces were shielded from the excess inhibiting ethanol and thus improved the enzyme activity.

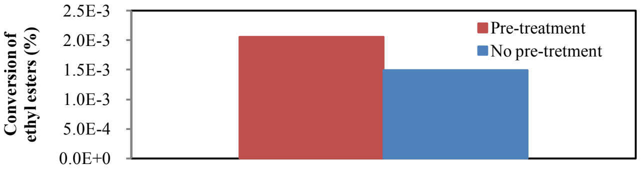

Fig. 5 Effect of the immersion pre-treatment (6:1 of ethanol to oil molar ratio, 13500 LU of lipase and 5% (v/v) of water at 45 °C for 8 hours)

4. Conclusions

Present research demonstrated the ethyl esters production from palm oil and ethanol catalyzed by immobilized lipase was higher than that found by reaction catalyzed by free lipase. The effect of the reaction parameters for the enzymatic process was tested. In addition, the activity of the immobilized lipase that was pre-treated by immersing in palm oil was found to be higher than that without the pre-treatment process. However, the conversion of palm oil to ethyl esters obtained was extremely low (less than 0.005 %). The reason for this is because the ethyl esters were calculated from the determined value of the glycerol. Triglycerides may partially transesterify to mono- and di-glycerides and still form ethyl esters. The reaction may not produce any glycerol, and yet considerable amount of biodiesel would have been formed. To further improve the study, it is suggested to determine the actual fatty acids ethyl esters using gas chromatograph. Moreover, the low conversion might be due to the low catalytic activity performed by the *Aspergillus oryzae* lipase in the ethanolysis reaction. To improve the experiment, the lipase may be replaced with other lipases that have shown high activity in catalyzing the transesterification of oils such as *Candida antarctica*.

Acknowledgement

Thanks to Ms. Farihah, Ms. Masni and Ms. Wani for their guidance in conducting the experiment.

References

1. Tan, T., Lu, J., Nie, K., Deng, L., Wang, F. (2010). Biodiesel production with immobilized lipase: A review. *Biotech. Advances*, 28 (5), 628- 634.
2. Talukder, M.M.R., Das, P., Tan, S.F., Jin, C.W. (2011). Enhanced enzymatic transesterification of palm oil to biodiesel. *Biochemical Engineering Journal*, 55(2), 119-122.
3. Salis, A., Bhattacharyya, M.S., Monduzzi, M., Solinas, V. (2008). Role of the support surface on the loading and the activity of *Pseudomonas fluorescens* lipase used for biodiesel synthesis. *Journal of Molecular catalysis B: Enymatic*, 57(1-4), 262-269.
4. Bondioli, P., & Bella, L.D (2005). An alternative spectrophotometric method for the determination of free glycerol in biodiesel. *European Journal of Lipid Science and Technology,* 107(3), 153-157.
5. Iso, M., Chen, B., Eguchi, M., Kudo, T. (2001). Production of biodiesel fuel from triglycerides and alcohol using immobilized lipase. *Journal of Molecular catalysis B: Enymatic*, 16(1), 53-58.
6. Raita, M., Chamreda, V., Laosiripojana, N. (2010). Biocatalytic ethanolysis of palm oil for biodiesel production using microcrystalline lipase in tert-butanol system. *Process Biochemistry*, 45(6), 829-834.
7. Aryee, A.N.A., Simpson, B.K., Cue, R.I., Philip, L.E. (2011). Enzymatic transesterification of fats and oils from animal discards to fatty acid ethyl esters for potential fuel use. *Biomass and Bioenergy*, 35(10), 4149-4157.
8. Moreno-Pirajan, J.C., & Giraldo, L. (2011). Study of immobilized candida rugosa lipase for biodiesel fuel production from palm oil by flow microcalorimetry. *Arabian Journal of Chemistry*, 4(1), 55-62.
9. Chen, J.W., & Wu, W.T. (2003). Regeneration of immobilized *Candida antarctica* lipase for transesterification. *Journal of Bioscience and Bioengineering*, 95(5), 466-469.

Biosorption of Dyes onto Mango Seed and Pineapple Peel

Keshminder Singh*, T.V.N Padmesh

School of Engineering, Taylors University, Malaysia

* *Corresponding authors email: s.keshminder@gmail.com*

Abstract— **In this study, the optimization of parameters was studied by adsorbing mixed dyes from the printer ink industry onto mango seed (MS) and pineapple peel (PP). Pineapple peel proved to be a better adsorbent in comparison to the mango seed. The effects of size, dosage, concentration and pH were studied closely batch wise. The optimum pH PP is 8. The optimum size for PP is 0.5mm. The dosage that shows the highest adsorption rate is 0.4g. The study shows that with increasing initial concentration adsorption capacity increases. The Langmiur plot best fitted the experimental data hence suggestion monolayer adsorption. The Q_{max} obtained in the plot was 16.02(mg/g).**

Keywords—biosorption, printer dye, isotherm, optimization

1. Introduction

In many industries such as textiles, paper, rubbers, leather tanning, food, ink and cosmetics wastewaters generated contain dyes and pigments. These dyes and pigments are sometimes carcinogenic or mutagenic and pose a threat to the environment. Hence, it has proven to be one of the serious environmental problems [1]. The adsorption process has proven to be as excellent process in terms of removal of substances and will prove to be a suitable process in the removal of dyes and pigments in this case. The novel adsorbent used during this process is the pineapple peel and the mango seed. Most agricultural wastes are relatively cheap, abundant and easily available. This has caught the attention of many researches due to its feasibility and its low-cost using it to remove various dyes, pollutants and heavy metals [2]. Currently the most popular type of adsorbent used in industries are coal and coconut shell [3].

This study is an attempt to use granulated mango seed kernel and pineapple shell to investigate the possibility of using these adsorbents to remove printer dye dyes. The study will include the influence of operational parameters such as pH, initial dye concentration, dosage and size of biosorbent to be studied closely. An isotherm is described as the functional expression for the variation of adsorption with respect to the concentration of adsorbate in the bulk solution at constant temperature [4]. Freundlich and Langmuir isotherms were looked at closely in this research to see which isotherm fits the adsorption behavior best.

2. Materials and Method

2.1 Preparation of Adsorbent

Pineapple peel and mango seeds are collected and washed. The grinder then grinds the adsorbents into powder. The powder is then treated with 0.1N HCL for 24 hours to remove and remaining impurities. The samples are then dried again at 70 ˚C in an oven for 48 hours. The dried sample is sieved to obtain different sizes of samples 0.5mm, 0.8mm, 1.0mm, 1.25mm and 1.6mm.

2.2 Adsorbate

Printer dyes are used as the adsorbate, where an acid yellow ink(uni yellow) is used and an alkali blue dye is used (cyan). The azo pigments present in the yellow ink solution and the copper panthalocyannine pigment present in the cyan ink solution is to be removed when they are mixed together to form a green solution. The residual dye concentration was estimated using a UV spectrometer where the maximum adsorption wavelength for λmax= 389nm.

2.3 Mixed Dye Adsorption

The adsorption capacities experiments where all carried out in batch mode to optimize each parameter. The effect of pH was also analyzed by manipulating the pH between the ranges of 2-12. The pH was adjusted using a HCL (0.1N) solution and NaOH (0.1N) solution. Other parameters such as size (0.5mm-1.6mm), dosage (1g-5g) and concentration (2ppm-10ppm) were analyzed for optimization. The batch solutions are placed onto a shaker at 150 rpm, where it is constantly being shaked for approximately 8 hours. The solution was then filtered and the absorbance of the solution was noted down. The amount of dye adsorbed was calculated using following equation [2]:

$$q_t = \frac{(C_o - C_t)V}{m} \qquad (1)$$

where C_o and C_t(mg/L) are the concentrations of dye at the beginning and time (t) of the experiment respectively. V is the volume of the solution (l) and *m* is the mass of adsorbent (g). The Langmuir and Freundlich isotherms were looked at closely to see which isotherm would fit the experimental values best. The equation used for Langmuir is:

$$Q = \frac{Q_{max} b C_f}{1 + bC_f} \qquad (2)$$

and the equation used for Freundlich is the following:

$$Q = kC_f^{\frac{1}{n}} \qquad (3)$$

where C_f is the final concentration (mg/g). Q_{max}, b, k and *n* are constants to be determined.

3. Results and Discussion

3.1 Effect of Size and Dosage

The highest adsorption capacity is obtain when a size of 0.8mm is tested in the case of pineapple peel and 1.5mm in the case of the mango seed. The increase in size for mango seed corresponds to a higher adsorption capacity this may be caused due to the fibrous properties of the mango seed which may have given rise to better adsorption surface area [6]. Pineapple show a sudden change when the size changes from 1.25mm-

1.6mm, this may be due to over saturation of pore sites or high competition for available sites.

The effect of dosage clearly plays a significant role on the ability of the pineapple peel powder and mango seed powder to remove dye from the solution. Increasing dosages brings about higher dye uptake. A dosage increase of 1g-4g gives a capacity increase from 43% to 67% for pineapple peal powder. As for the mango seed powder and increase from 1g-5g brings about an increase in adsorption capacity from 46% to 63%. This is an indication that an increase in dosage, more surface area is made available hence the total number of sites increases as well [7]. Pineapple adsorption capacity drops when the adsorbent size dosage was increase to 5g, this may have occurred due to experimental error as this behavior has not been reported before. A further study of surface morphology and surface composition may shed some light on the occurrence of such discrepancies.

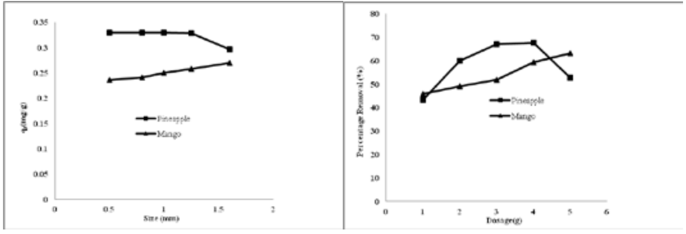

(a) **(b)**

Fig. 2. The effect of size and dosage on the uptake of dyes: (a) size, (b) dosage

3.2 Effect of Concentration and pH

Increase in concentration for both types of adsorbents brings about an increase in the capacity of dye removal Fig.3 (a). The higher concentration of mixed dyes causes an increase in the concentration gradient between the adsorbent and the solution hence increasing its adsorption capacity and also the complete utilization of all the active sites which is not possible at low concentrations.

The effect of pH on the mango seed powder adsorbent is very little creating almost no change at all when it was manipulated as it is shown in Fig.3 (b). Hence, it can be said that the surface charge of mango is neutral. On the other hand the effect of pH on pineapple peal powder shows significant effect at lower pH, this point out that the adsorption capacity is weak when the solution is acidic, where once the pH begins to move into the alkali region it increases and stables out. Fluid pH affects the surface charge of adsorbents, hence the low adsorption capacity in the acidic region may be due to surface charge of the pineapple peel powder where the surface repels the dye pigments making it difficult for adsorption to occur.

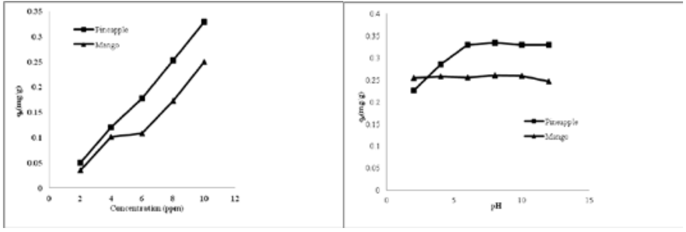

(a) (b)

Fig. 3. Effect of concentration and pH on dye uptake, (a) concentration, (b) pH

3.3 Isotherms

A comparison was made between the two models with respect to the experimental data. This relationship is shown in Fig. 4. It is seen that the Langmuir model fits best in the graph since it has a higher R^2 value (0.978) when compared to the R^2 value of the Freundlich plot (0.8164). The Langmuir model is basically an expression based on the assumption of monolayer onto adsorbent surface, where there is a finite capacity of adsorption and also the occupation of dye molecules on one site [8].

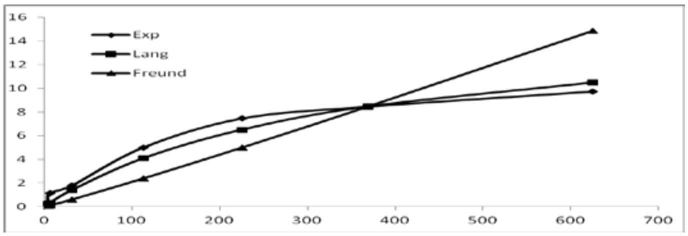

Fig. 4. Comparison between isotherms and experiment

4. Conclusion

The study shows that the acid treated mango seed powder and the pineapple peel powder can be considered as a cheap source of adsorbent for the removal of mixed dyes in waste water streams. The batch studies carried out has shown success in optimizing the parameters to be used. In comparison to the experimental data the Langmuir isotherms fits best in the giving a Q_{max} value of 16.01(mg/g). It also shows that surface charge effects adsorption of pineapple peel at lower pH values.

5. Acknowledgment

I would like to show my utmost gratitude towards the school of engineering for providing the necessary tools for me to successfully complete this project.

6. References

[1] O.Gercel, H.F. Gercel, A.S. Kooparal, U.B. Ugutveren, "Removal of disperse dye from aqueous solution by novel adsorbent prepared from biomass plant material," J. Hazrdous. Mate, Vol. 160, pp.668-674, 2008.

[2] Mohd Rasool, Salman Masoudi, Sara Kazemi Yazdi and Soraya Hosseini, "Equilibrium and Kinetic Studies of Safranine Adsorption on Alkali-Treated Mango Seed Integuments," International Journal of Cgemical Engineering and Applications, Vol. 3, pp.160-166, 2012.

[3] Itodo AU, Itodo HU, Gafar MK, Journal of Applied Sciences & Environmental Management, Vol 14(4), pp. 163-168, 2012.

[4] A.U.Itodu, H.U.Itodu, F.A.Atiku, R.A.Koko and A.A.Kwaido, "Dyes Uptake onto Processed and Raw Mango seed Back," Asian Journal of Plant Science and Research, Vol. 1(1), pp. 57-66, 2011

[5] Claudia Dittmer, Dirk T.Mayer, Prof. Dr. Faigle, *Printing Inks.* Stuttgard, Germany: University of Printing and Media Stuttgard, Germany.

[6] Kittiphoom. S, "Utilization of Mango Seed," International Food Research Journal, Vol. 19(4), pp. 1325-1335, 2012.

[7] N. Yeddou, A. Bensmaili. "Kinetic models for thesorption of dye from aqueous solution by clay-woodsawdust mixture", Desalination, Vol. 185, pp. 499-508, (2005).

[8] S.Sohn and D.Kim, "Modification of Langmuir isotherm in solution systems-definition and utilization of concentration dependent factor," *Chemosphere*, vol. 58, pp. 115-123, 2005.

Linear Flux Switching Induction Actuator

Khumira I[1], Aravind CV[2*], R.N. Firdaus[3], F.Azhar[3]

[1,2]*Applied Electromagnetic and Mechanical Cluster,*
Computer Intelligence Applied Group, Taylor's University, Malaysia
[3]University Teknikal Melaka, Malaysia
**aravindcv@ieee.org*

***Abstract*--A number of variable speed applications require linear actuation such as in linear compressors, wave trap etc. In this research a flux switching induction actuator is built and the variations in the height to width of the permanent magnet used in the flux switching on the torque characteristics is analysed. Finite Element Method is used to investigate the effect of the variation to the thrust characteristics. Analysis on the effect of changing the magnet ratio on the cogging force is also reported in this work.**

Keywords— Linear actuator, thrust, cogging force, flux analysis

1. Introduction

Linear actuators are machines that develop the linear force along its length (linear thrust) [1, 2]. Linear motor covers a wide range of applications from as cliché as transportations [3] to its utilization in medical field such as linear actuator syringe pump. Linear motor is preferred compared to rotary motor due to the relative speed accuracy, better positioning, and fast acceleration response characteristics [2-3]. This motor eliminates the mechanical components used to convert the rotation as it requires no mechanical transmission thereby reducing the flux density. Flux switching technique is whereby the flux in the coil is switched by varying the operation through control element. The control element significantly controls the electro-magnetic energy inside the machine thereby increasing the thrust. A high power control module is essential for these types of machines. In this paper the developed linear flux switching machine is analysed using Finite Element methods to optimize the thrust characteristics to be of sinusoidal under static conditions.

2. Methodology

The overall research design is a quantitative study; where magneto-static analysis is applied on the design by implementing FEM. This analysis is accomplished with two significant steps—the first one is to design the actuator by varying the height to width ratio using and the next step is to import the design to FEM tool to analyze. Results of this step demonstrate the flux flow, magnetic flux density, magnetic field intensity and its thrust. Data obtained from the original design is compared with different height-to-width ratios of its permanent magnet size to show the effect of varying the parameter to the motor's performance characteristic. The original design has the height to width ratio of 2.5 with 15mm height and width of 6mm. In this research, the ratio will be varied to 2.7 and 2.9 by keeping the original width as it is and varying the height of the pole magnet. In order to keep the total length of moving part fixed (which consists of the magnet and moving yoke) in any increasing value of magnet's height results in decreasing value the moving yoke's height. Three different design structures with varied h/w ratio as shown in Table 1 are analysed. Magneto-static analysis is applied to each design. The main objective of the analysis is to obtain the motor's thrust characteristics by getting the thrust value at every 1mm distance along its linear movement. The same simulation is repeated at 3 different current values; 0A, 1A and 5A. The thrust values obtained are plotted and compared so that the design with the best sinusoidal waveform can be sent for fabrication.

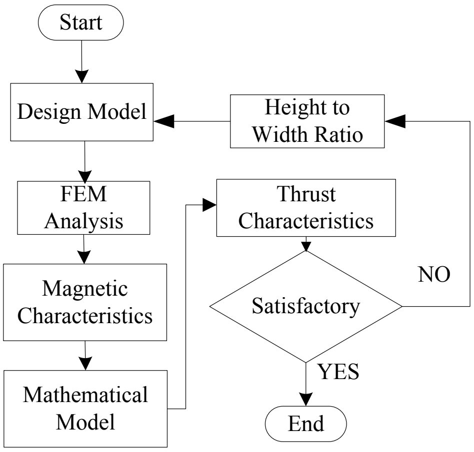

Fig. 1 Design Methodology

Table 1. Dimension of Permanent Magnet

	Height to Width Ratio		
Stack Length = 92.5mm	**2.5**	**2.7**	**2.9**
Height of Permanent Magnet (mm)	15.00	16.25	17.50
Height of Moving Yoke (mm)	6.50	5.50	4.50
Width of Permanent Magnet (mm)	6.00	6.00	6.00
Width of Moving Yoke (mm)	6.00	6.00	6.00

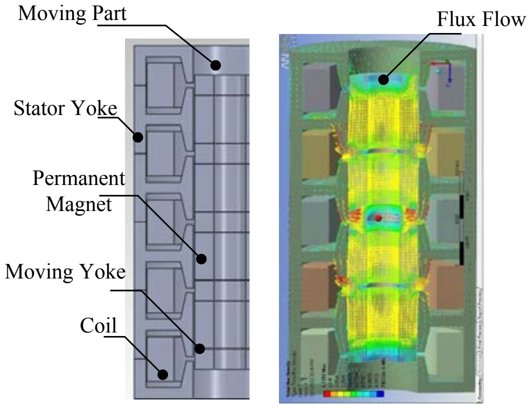

(a) (b)

Fig. 2 Linear Flux Switching Induction Actuator
(a) Model of induction actuator (b) Flux flow from FEA tool

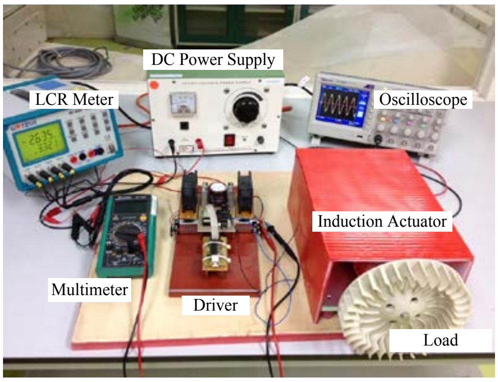

Fig. 3 Final setup of fabricated induction actuator and its driver

3. Results and Discussion

From Fig 4, Fig. 5 and Fig 6, design with 2.9 h/w ratio has the most stable sinusoidal waveform at all current conditions simulated. All designs at all current conditions showed a normal pattern of sinusoidal waveform with different thrust values according to their h/w ratio as well as their current condition. However, design with h/w ratio of 2.5 at current condition 5 A shows unexpected results at its 1mm displacement where its thrust dropped to 160 N when it is expected to increase to more than 220 N. Fig. 7 shows a comparison of all the three designs to determine which design has the least cogging force.

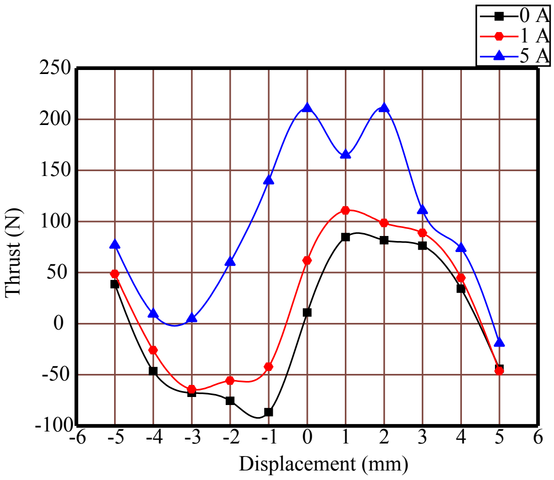

Fig. 4 Thrust characteristics with 2.5 h/w ratio at I = 0A, 1A and 5A

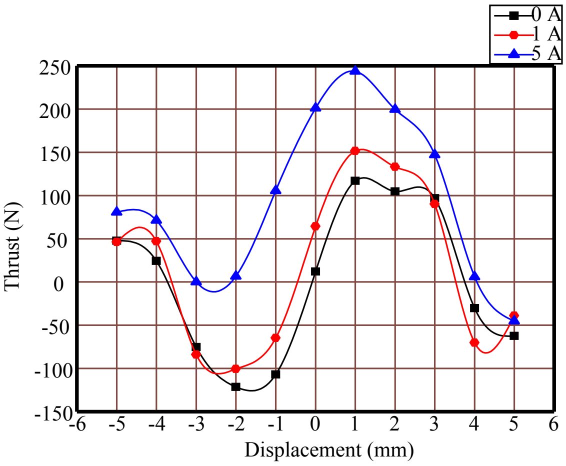

Fig. 5 Thrust characteristics with 2.7 h/w ratio at I = 0A, 1A and 5A

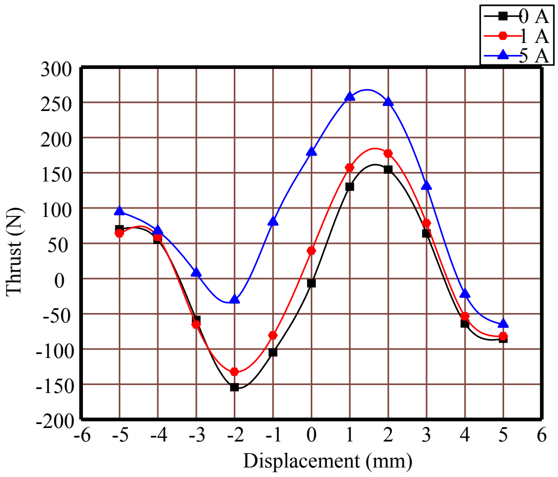

Fig. 6 Thrust characteristics with 2.9 h/w ratio at I = 0A, 1A and 5A

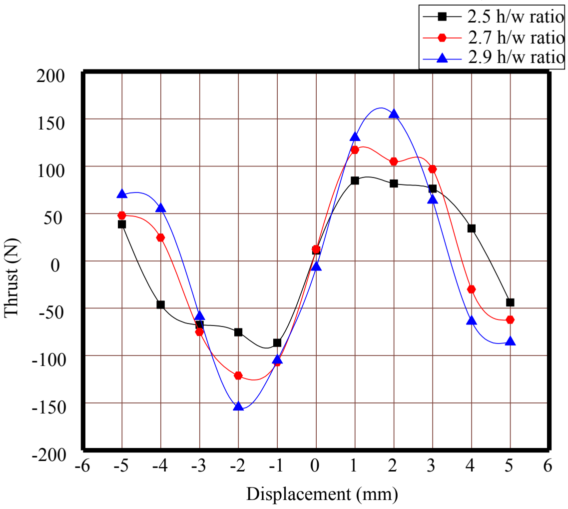

Fig. 7 Thrust characteristics of all designs at I = 0A

4. Conclusions

Induction actuator with height to width ratio of 2.9 has the best thrust characteristics where it is shown through the almost perfect sinusoidal. This design is better compared to previous two designs especially at position 1 mm and 2 mm for both designs with 2.5 and 2.7 h/w ratio where distorted waveform is detected. In Fig. 7, it shows that the actuator with 2.5 h/w ratio has the least cogging force compared to the other two designs.

5. References

[1] C. Myung-Jin, G. Dae-Gab, "Design Optimization and Development of Linear Brush-less Permanent Magnet Motor," in *International Journal of Control, Automation, and Systems*, Vol. 1, No. 3, pp. 351-357, September 2003

[2] J. F. Cui, L. L. Jiang, Y. M. Guo, H. Wu, C. Y. Wang, "Analytical Research for Permanent Magnet Linear Synchronous Motor," pp. 468-470

[3] H. Rolf, M. Peter, "Linear Motor-Powered Transportation: History, Present Status, and Future Outlook," in *Proceeding of the IEEE*, Vol. 97, No. 11, pp. 1892-1900, November 2009

Fluctuating Inlet Flow Conditions for Use in Urban Air Quality Studies

S. M. Kwa[1*], S. M. Salim[1]

[1]*School of Engineering, Taylor's University, Selangor, Malaysia,*
**Email: kwa.szemeng@sd.taylors.edu.my*

Abstract—**Fluctuating Wind Boundary Conditions (FWBC) profiles are used to model air flow and pollutant dispersion in urban street canyons using Computational Fluid Dynamics (CFD). The results obtained from FWBC are compared with the conventionally employed Steady Wind Boundary Conditions (SWBC). In FWBC, temporal variations are taken into account while SWBC assumes constant wind velocity profile. The simulations are run using Large Eddy Simulation (LES). It is observed that FWBC produces different outcomes as compared to wind tunnel (WT) experiments and SWBC. The FWBC developed produces more realistic results mimicking real urban conditions as meteorological data show fluctuations in wind speed and direction at all times, further proving the importance of selecting the more accurate FWBC in pollutant dispersion studies.**

Keywords—Computational Fluid Dynamics (CFD), Fluctuating Wind Boundary Conditions (FWBC), Large Eddy Simulation (LES), pollutant dispersion, urban street canyon.

1. INTRODUCTION

Air quality in urban and industrial complexes is of utmost importance given its massive implications to the health of public. In order to investigate the governing physics of air flow and pollutant dispersion, there are three approaches that can be adopted. These include the traditional on-site full-scale experiments, model-scale experiments usually in the form of wind tunnel investigations as well as numerical modeling using Computational Fluid Dynamics [1]. CFD is slowly developing to be an attractive tool for investigating fluid flow problems due to their large savings in resources and time while at the same time, providing sensible solutions to the problems being investigated.

The main aim of this study is to investigate air flow and pollutant dispersion in urban street canyons under Fluctuating Wind Boundary Conditions (FWBC). The fluctuating profiles differ from the conventional Steady Wind Boundary Conditions (SWBC) often adopted as the temporal variations in the wind velocity are taken into account. These temporal variations in wind velocity led to the flow being more turbulent than that constructed under SWBC [2] and further proven from meteorological data of wind velocities which change significantly over time.

2. RESEARCH METHODOLOGY

Majority of existing studies on air flow and pollutant dispersion have often employed SWBC [3], [4]. However, this method used provides a major source of inaccuracy when compared to realistic urban environments as it assumes constant wind velocity and turbulence kinetic energy. This is not always consistent with on-site field and wind tunnel measurements [2]. Accurate simulation of atmospheric boundary layer is crucial in order to obtain more realistic prediction of air flow and pollutant dispersion.

Fluctuating wind profile is to be developed and three-dimensional (3D) numerical simulations are carried out using ANSYS FLUENT, specifically Large Eddy Simulations (LES) model. LES was found to perform considerably better than Reynolds-averaged Navier-Stokes (RANS) model as LES is able to resolve fluctuations in the flow field which changes over time. As a result of this, it is able to capture the transient mixture which increases the accuracy in prediction of pollutant dispersion [3].

Wind tunnel and field measurements are often used to validate results of CFD simulations. Salim *et al.* [3] performed numerical simulation based on SWBC which were validated against experimental studies carried out by Gromke and Ruck [5] and wind tunnel experiment from online database www.codasc.de [6]. This study implements the same computational domain for validation purposes. Fig. 1 demonstrates the summary of computational domain and boundary conditions employed in the simulation. The total number of elements used to discretize the computational domain is 1.2 million with more refined cells placed within the vicinity of the buildings and street canyons.

The FWBC profile is developed from initial simulation based on SWBC. The velocity profiles at the outlet are shown to change considerably even with the smallest variation in time at the end of the simulation. The difference in the velocity profiles between CODASC wind tunnel (WT) database, SWBC and FWBC are shown in Fig. 2.

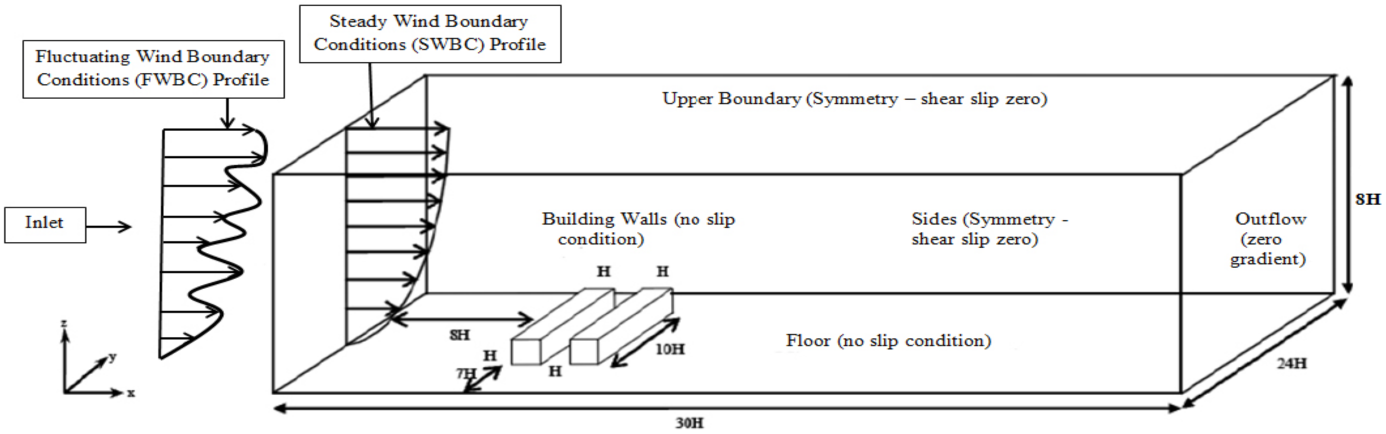

Fig. 1. Computational domain and boundary conditions for CFD simulation setup in ANSYS FLUENT

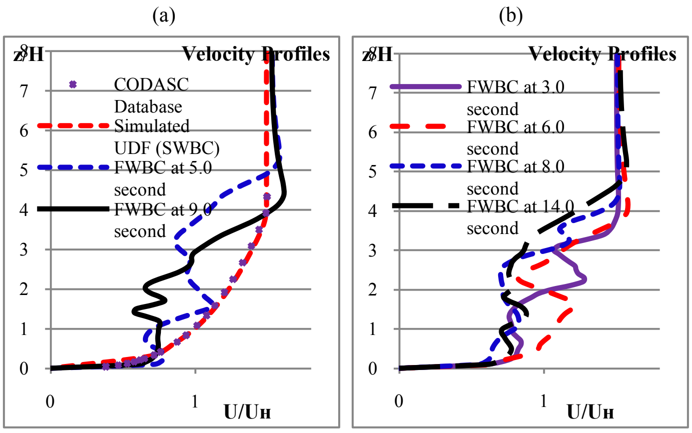

Fig. 2. Velocity profiles based on CODASC database [6], SWBC [3] and FWBC (at outlet)

3. RESULTS AND DISCUSSIONS

Dispersion of the sulphur hexafluoride pollutants applied in the simulation are observed through species concentration contours on the leeward (Wall A) and windward (Wall B) walls. Leeward wall refers to the upwind side of the canyon while windward wall refers to the downwind side of the canyon. Table 1 below shows the different fluctuating profiles used to obtain different set of results in this study.

TABLE 1. FLUCTUATING PROFILES USED IN SIMULATIONS

Simulations	Fluctuating Profiles from Fig. 2
Simulation 1	5.0 second
Simulation 2	9.0 second
Simulation 3	0-10 second flow-time in ANSYS FLUENT = 3.0 second
	10-20 second flow-time = 6.0 second
	20-30 second flow-time = 8.0 second
	30-40 second flow-time = 14.0 second

Fig. 3 below shows the results of mean concentration contours at the canyons leeward (Wall A) and windward (Wall B) walls. The numerical results clearly show the differences between SWBC and FWBC. SWBC reproduces pollutant concentration distribution similar to WT, particularly in the vicinity of the centerline ($y/H = 0$) at both Wall A and Wall B, underlining them as the most critical zone where maximum pollutant concentration occurs [3]. On the other hand, the results from 5.0 second and 9.0 second fluctuating profiles show pollutant concentration to be more prominent at the region to the right of the centerline ($y/H \approx 1.5$) and to the left of the centerline ($y/H \approx -1.3$), respectively. Besides, the results from multiple fluctuating profiles again show pollutant concentration to be more prominent at the region to the right of the centerline ($y/H \approx 0.6$). These events occur due to the use of fluctuating profiles which cause the velocity profiles along both the leeward and windward walls to vary significantly as compared to SWBC, which show similar velocity profile that is defined at the inlet. On top of that, it can be seen that the magnitude of pollutants formed with FWBC profiles are significantly lesser compared to that of in SWBC and WT. Different FWBC produces different outcomes. Therefore, use of FWBC based on real-time meteorological data is imperative to be able to predict accurate pollutant dispersion in urban street canyons.

4. CONCLUSIONS

FWBC velocity profiles are used to study their suitability in studying air flow and pollutant dispersion in urban street canyons. This study illustrates the importance of implementing the more realistic FWBC in characterizing pollutant dispersion as different FWBC profiles employed showed different results compared to that of in SWBC. In future studies, it is important to use real-time meteorological data that shows fluctuations in wind velocity and direction in order to obtain more accurate predictions. On top of that, wind tunnel testing could also be replicated following fluctuating velocity profiles based on the data collected to obtain better experimental data for future validations.

REFERENCES

[1] N. Nikolopoulos, A. Nikolopoulos, I. Papadakis and K. –S. P. Nikas, “CFD Applications in Natural Ventilation of Buildings and Air Quality Dispersion,” *CFD Applications in Energy and Environment Sectors, volume 1*, pp. 53-100, 2011.

[2] Y. W. Zhang, Z. L. Gu, Y. Cheng and S. C. Lee, “Effect of real-time boundary wind conditions on the air flow and pollutant dispersion in an urban street canyon – Large eddy simulations,” *Atmospheric Environment, volume 45*, pp. 3352-3359, 2011.

[3] S. M. Salim, A. Chan, R. Buccolieri and S. Di Sabatino, “Numerical simulation of atmospheric pollutant dispersion in an urban street canyon: Comparison between RANS and LES”, *Journal of Wind Engineering and Industrial Aerodynamics, volume 99*, pp. 103-113, 2011.

[4] Y. Tominaga and T. Stathopoulos, “CFD modeling of pollution dispersion in a street canyon: Comparison between LES and RANS”, *Journal of Wind Engineering and Industrial Aerodynamics, volume 99, issue 4*, pp. 340-348, 2011.

[5] C. Gromke and B. Ruck, “Influence of trees on the dispersion of pollutants in an urban street canyon – experimental investigations of the flow and concentration fields,” *Atmospheric Environment, volume 41*, pp. 3287-3302, 2007.

[6] CODASC, Concentration Data of Street Canyons, Laboratory of Building and Environmental Aerodynamics, IfH, Karlsruhe Institue of Technology, 2008.

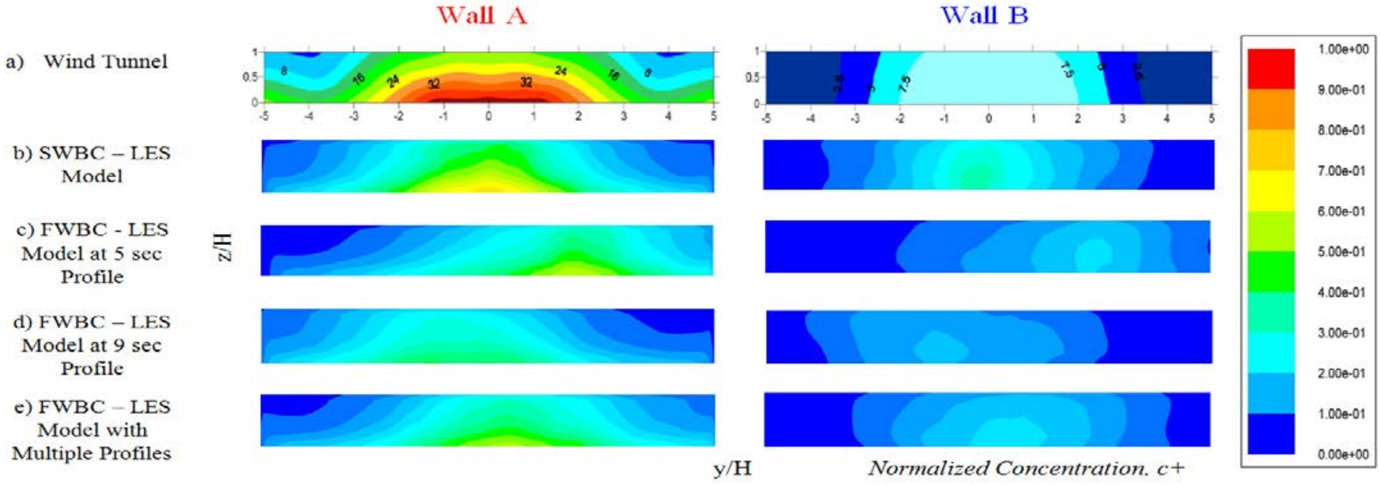

Fig. 3. Mean normalized concentration on Wall A (leeward) and Wall B (windward) for (a) wind tunnel CODASC database [6] (b) SWBC (c) FWBC at 5 second (d) FWBC at 9 second and (e) Multiple FWBC profiles

Experimentation and Simulation on the Design of Intake Manifold Port on Engine Performance

Y.K. Loong[1], Salim M. Salim[2]

[1]*School of Engineering, Taylor's University, Malaysia,*
**loongyunkit@gmail.com*

Abstract— **The aim of this project is to increase the performance of the engine by improving the design of the intake manifold port. Computational Fluid Dynamics (CFD) using k-epsilon model with standard wall function was applied to simulate and quantify the improvements of the new design by benchmarking against the original intake. It was found that the original intake manifold from the manufacturer could be improved by more than 79% by changing the geometry, shape and surface finish.**

Keywords— Intake Manifold, Computational Fluid Dynamics (CFD), Volumetric Efficiency, Pollution, Performance

1. Introduction

In today's world, there is a massive increase in the number of vehicle on the road in term increases the pollution level. Ironically, the internal combustion engine is highly inefficient. The internal combustion engine power output and volumetric efficiency is highly dependent on the amount of air being ingested into the combustion chamber which is then discharged by the exhaust system [1].

With more air in the cylinder, more fuel can be added into the combustion chamber hence increasing the peak pressure which will increase the performance of the engine. There are many parameters of the intake system that can massively influence this. All mass produced engine can be improved further as manufacturer have many constraints when designing an engine's intake system [2]. The manufacturer's constraints are usually cost, manufacturing difficulty, time and many others. Therefore, by using FLUENT commercial software, the design of the intake port can be investigated, evaluated and improved upon.

The objectives of the research project are as follow:

- To simulate different design parameters to obtain an improved intake system of an internal combustion engine for better performance and efficiency.
- To obtain valid intake gas condition such as gas temperature and pressure from a running internal combustion engine.
- To validate CFD simulation against experimental setup on engine.

2. Research Methodology

An investigation using CFD simulation is only valid if it is validated against experimental data. For this project, a S4PH Campro, 4 stroke, 1.6L, 4 cylinder engine from a Proton Satria Neo is the engine used as shown in Fig 1. A Haltech Platinium Sport 1000 engine control unit was used to measure the data from the running engine. Two sensors were connected to the engine control unit using a wiring harness. The two sensors are Air Temp Sensor and Manifold Air Pressure Sensor from Haltech.

Figure 1: Campro S4PH Engine

Intake Air Pressure and Temperature is measured at the base of the intake manifold as near as possible to the outlet as shown in Fig 2. Table 1 shows the data collected from the running engine. The frequency of the sensor coupled with the engine control unit is 20Hz. Therefore, an average gauge pressure of -6300Pa is obtained.

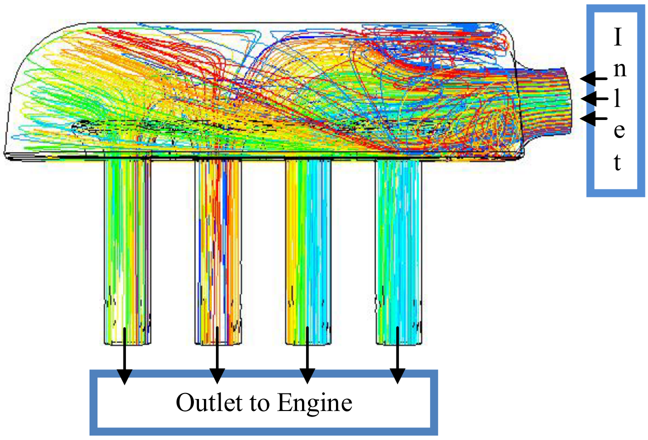

Figure 2: Computational Domain of Intake Manifold

Table 1: Data from Experimental Setup

Throttle Position	100% Open
Engine Speed	6000 rpm
Vacuum Level	-6300Pa
Temperature	313K
Pressure at Inlet	101300 Pa
Pressure at Outlet	95000 Pa

A Computer Aided Drawing (CAD) of the original intake was first drawn. After that, a mesh is created using Ansys Mesher as shown in Figure 3. Once done, a CFD simulation is done on it. The boundary conditions inputted based on the recorded data from the running engine. Table 2 shows the specifics of the CFD simulation based on Jiyuan Tu *et al* [4].

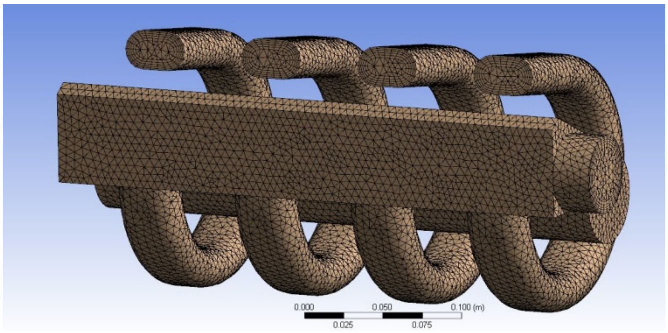

Figure 3: Meshing of Intake Manifold

Table 2: Specifics of CFD Simulation

Number of Cells	650,000 to 680,000
Type of Mesh	Pure tetrahedral with near wall mesh
Orthogonal Ratio	0.4 or higher
Maximum Aspect Ratio	2.9 and below
CFD Model	Standard k-epsilon
Near Wall Treatment	Standard wall treatment
Wall Roughness Constant	0.5= cast finishing, 0.1= mirror finish

A steady flow study is done and the results were recorded and compared against theoretical calculation. The summary of the CFD simulation is shown in Table 3.

Table 3: Results Comparison

Mass Flow Rate (CFD)	0.1899 kg/s
Mass Flow Rate (Theoratical)	0.07928 kg/s
Percentage Error	134%

Once the CFD simulation is validated against the Experimental Setup, many design parameters were tested using CFD as shown below.

- Intake Runner Length and Dimension
- Intake Runner Opening Shape
- Inlet to Plenum Angle
- Surface Finish

3. Results

By simulating all the various design parameters, a significantly improved design was obtained as shown in Table 4. The improved design has a much higher mass flow rate which in turn helps increase the performance of the engine. Furthermore, the flow distribution between all four cylinders is near equal which will also help improve the volumetric efficiency of each cylinder as shown in Fig 4.

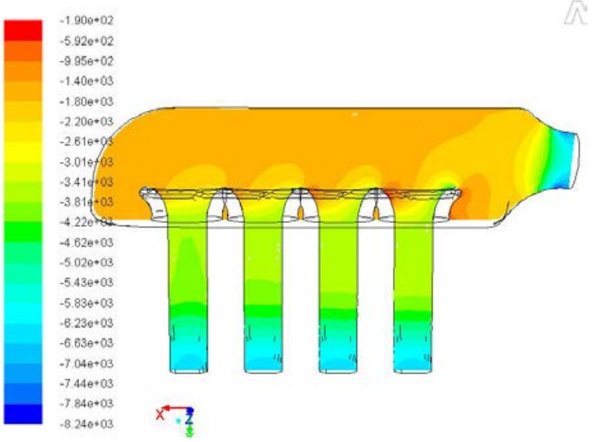

Figure 4: Velocity Contours of Final Iteration

Table 4: Summary of Results

Intake Volume	9.418 liters
Inlet to Plenum Angle	5 degrees upwards
Runner Opening Shape	Bellmouth [2]
Runner Length	200mm [3]
Surface Finish	Mirror Finish
Mass Flow Rate	0.3557 kg/s
Variance Difference Between Cylinders	3.27 X 10^{-6}
Percentage Improvement Over Original	79%

4. Conclusion

Based on the results, it can be seen that the new and improved intake manifold port has a much higher mass flow rate capacity based on CFD simulations. The main reasons for the improvement are due to the surface finish and geometry of the intake manifold. The distribution balances between all 4 cylinders are also is almost equal which helps in providing a proper air fuel mixture which in turn will increase the performance and efficiency of the engine. Even though the improvement over original is high, it does not signify a 79% improve in performance as other components of the engine will be the limiting factor.

The accuracy of the experimental setup can be improved further by using a data acquisition system along with sensors that has logging frequency of 200 Hz or higher in order to measure the proper trace of the pressure and temperature variation with respect to piston position. In the future, different CFD models can be used to simulate the accuracy of the k-epsilon model used in this investigation.

Reference

[1] John B. Heywood, “Exhaust Gas” in *Internal Combustion Engine Fundamentals*, McGraw-Hill Book Company, 1987

[2] Alexander Graham Bell, “The Cylinder Head”, *in Four Stroke Performance Tuning*, 2nd Edition, Somerset, United Kingdom, Haynes, 1998, pp7-13.

[3] Gordon Blair, W. Melvin Cahoon, *Special Investigation: Design of Intake Bellmouth*

[4] Jiyuan Tu, Guan Heng Yeoh and Chaoqun Liu. *Computational Fluid Dynamics A practical Approach*, Elsevier, First Edition, 2008, pg53-398

Effects of Xanthan Gum Concentration on Spray Drying of *Piper betle* L. Leaves Extract

X. K. Lim[1]*, L. H. Tee[2], Y. A. Yusof[3], C. H. Chong[1]

[1]*Department of Chemical Engineering, School of Engineering, Taylor's University, Malaysia*

[2]*Department of Chemical Engineering, School of Engineering, Monash University, Malaysia*

[3]*Department of Process and Food Engineering, Faculty of Engineering, Universiti Putra Malaysia, Malaysia*

**Corresponding author: lim.xikai@gmail.com*

Abstract — **The purpose of this study is to optimize the concentration of xanthan gum solution as the carrier during the spray drying process. Effect of concentration of carrier solution, extract concentration and extract to carrier solution ratio were investigated. Samples were dried and extracted before subjecting to spray drying (xanthan gum solution with concentrations 0.5, 0.6, 0.7, 0.8, 0.9 and 1.0 %w/v were prepared and mixed with the extract at a ratio of 1:1). It was found that limited spray dried samples can be obtained because samples were extremely hygroscopic.**

Keywords— *Piper betle* L., spray drying, spray-dried extract, xanthan gum concentration, hygroscopicity.

1. Introduction

Nowadays, there is an increasing demand in traditional remedies and medicine for diseases and sicknesses around the world due to the increasing awareness of potential danger and side effects of synthetic drugs [1]. In 2008, WHO estimated that 80% of the population in some Asian and African countries relies on herbal medicine for their primary healthcare needs [2]. Previous research conducted on the betel leaves shows that the leaves contain two bioactive components, namely Hydroxychavicol (HC) and Eugenol (EU). Both of these propenylphenols have many beneficial effects on human health, such as antimicrobial [3], antioxidant [5], [6], anti-diabetic [7], anti-carcinogenic [8], anti-depressant, wound healing and gastro-protective properties. Therefore, there is a potential for the betel leaves to be marketed as a health supplement due to its beneficial properties. In order to do that, the leaves must first be dried so that extraction can be done. Then, the extract has to be spray dried to form spray dried extract (SDE) powder, and finally compacted into tablets for easier administration into the body. The first stage drying of the leaves is to increase the HC content present in the leaves [4]. The extraction process is essential to obtain only the bioactive components and remove unnecessary solids that increase the mass. The spray drying of the extract serves as a method of preservation for the bioactive compounds. The betel leaves extract should be spray dried under optimum conditions to produce betel leaves extract powder with the best properties [3]. To ensure the safety and efficacy of the supplements produced, standardization and development of the processing aspects for the supplements are of utmost importance [1].

The optimization of HC and EU extraction process from betel leaves [4] and the optimization of spray drying process of betel leaves extract [3] have previously been conducted. However, the concentration of xanthan gum solution used as the carrier in the spray drying process has only been studied preliminarily and was not optimized [3]. This area was chosen to be studied again because the SDE powder obtained under optimum conditions stated readily absorbs moisture from the air. The hygroscopicity of the powder obtained, which is the ability to readily absorb moisture from the atmosphere, is too high. Without substantial resistance to the moisture in the air, the powder cannot be handled and preserved properly. Since the function of the carrier in the spray drying process is to reduce the hygroscopicity of the powder, the amount of xanthan gum may not be sufficient to encapsulate the betel leaves extract fully during the atomization process in the spray dryer. Therefore, the objective of this research is to study the effect of different concentration of the xanthan gum solution in the spray drying process of *Piper betle* L. extract.

2. Methodology

2.1. Materials

The betel leaves were obtained from a betel plantation owned by Mr. Gyanasuntharam at $25\frac{1}{2}$ mile along Jalan Morib, Banting to ensure that the leaves are continuously available from the same supply. Food grade xanthan gum (Xantham Gum from *Xanthomonas campestris*, Sigma) was used as the carrier during the spray drying process.

2.2. Preparation of Samples

Once the betel leaves were collected from the supplier, it should be dried in the oven as soon as possible. Before the drying process, the leaves were washed with clean water and wiped with a napkin to remove excess water.

2.3. Oven Drying

The betel leaves were dried in an forced air convection oven (FAC-350, Protech, USA) for at least 2.1 hours at 70°C to allow the leaves to reach equilibrium moisture [9]. Then, the dried betel leaves were crushed using a pin roller and grinded using a household blender until it becomes fine powder.

2.4. Extraction

Distilled water was used as the extraction solvent [11]. The dried betel leaves powder and distilled water was mixed with a solvent-solid ratio of 30mL:1g [11]. The mixture was poured into a beaker and placed in a water bath for 1 hour to maintain its temperature strictly at 60°C to avoid degradation of HC at high temperatures [10]. After the extraction, the extract was filtered using a clean cloth filter to eliminate the solid dried leaves powder so that blockage of the nozzle of the spray dryer can be prevented.

2.5. Concentration of Extract

The extract was concentrated in a water bath to 10°Bx. The approximate dissolved solid content is measured using a portable refractometer (Pocket Refractometer, Atago, Japan). After the extract reaches 10°Bx, the extract was filtered again using a clean cloth filter.

2.6. Preparation of Xanthan Gum and Feed Solution

Xanthan gum was used as an additive during the spray drying process to protect the bioactive components against severe heat and reduces the hygroscopicity of the powder. Food grade xanthan gum from *Xanthomonas campestris* (G1253 SIGMA, Sigma Aldrich, Malaysia) was progressively added into distilled water at 90°C and mixed thoroughly using a homogenizer (Ultra-Turrax T18, IKA, Malaysia) to ensure the solution was completely homogeneous (no lumps are present). Xanthan gum solution of concentration 0.5, 0.6, 0.7, 0.8, 0.9 and 1.0% w/v were prepared separately.

Prior to spray drying, the xanthan gum solution and betel leaves extract were mixed together in a conical flask with a ratio of 1:1 and stirred well using a magnetic stirrer. For each run, 50mL of xanthan gum solution and 50mL of betel leaves extract were mixed together to form 100mL of feed solution. The samples prepared were labeled as shown in Table 1.

2.7. Spray Drying

The feed solution was spray dried using a laboratory scale spray dryer (SD-05, Lab-Plant, UK) with an air inlet temperature of 160°C, a feed flow rate of 4mL/min and an aspirator rate of 86% with the compressed air pressure set to 3 bar.

After the spray drying process, the cyclone was left to cool down to room temperature because the powder tends to absorb moisture when hot. Then, the powder was collected into heat-sealable plastic bags to prevent exposure to the atmosphere. The plastic bags were then kept inside an air tight container with silica gels.

3. Results and Discussion

3.1. Comparison of Colour

The samples with 1°Bx of estimated dissolved solid content were compared with the samples with 10°Bx of estimated dissolved solid content. By comparing spray dried samples of A1 and B1, the powder from A1 shows a lighter colour compared to B1. This may be explained by the original colour of the samples before spray drying since the amount of dissolved solids inside sample A1 is less B1.

In addition, it could be due to the amount of xanthan gum present in sample B1 is not sufficient to encapsulate the dissolved solid content during the atomization of the spray drying process. Since xanthan gum exhibits a white-yellowish colour, the colour of the resulting spray dried samples should also be similar to the xanthan gum colour if the dissolved solids were completely encapsulated within the xanthan gum shell. Therefore, the darker brown colour of the spray dried sample B1 showed that the dissolved solids were exposed to the atmosphere.

Table 1. Labelling of Different Samples.

Concentration of Xanthan Gum Solution (%w/v)	**Approximated Dissolved Solid Content of Extract (°Bx)**	
	1	10
0.5	A1	B1
0.6	A2	B2
0.7	A3	B3
0.8	A4	B4
0.9	A5	B5
1.0	A6	B6

3.2. Comparison of Hygroscopicity

The spray dried samples A1 and B1 obtained fresh from the spray drying process were dry. However, after leaving the powders inside the cyclone and collector for the duration of the spray drying process, the powders absorb moisture from the air and become sticky and difficult to collect. This could be caused by the failed encapsulation of the solids due to lack of amount of xanthan gum in the feed solution. The spray dried sample B1 absorbed moisture more rapidly than A1 and this shows that insufficient xanthan gum contributes to the hygroscopicity. Powders with such high hygroscopicity easily stick to the wall of any container and difficult to handle.

4. Conclusions

The effect of concentration of xanthan gum used in the spray drying process of *Piper betle* L. leaves extract was investigated based on hygroscopicity of the resulting powders. The results showed that adequate amount of xanthan gum is required to fully encapsulate the dissolved solid (HC) content to prevent absorption of moisture from the atmosphere. The minimum concentration of xanthan gum increases with the dissolved solid content inside the solution. However, homogeneous xanthan gum solutions with concentration higher than 1%w/v are generally difficult to prepare without proper equipment due to its high viscosity and low mixing ability, and therefore should be avoided.

Acknowledgment

The authors would like to thank Faculty of Engineering, UPM for their support and technical assistance.

References

[1] S Gopalakrishnana, R Rajameena, and E Vadivel, *Journal of Chemical and Pharmaceutical Research*, vol. 4, no. 1, pp. 788-794, 2012.

[2] World Health Organisation. (2012) Traditional medicine. [Online]. http://www.who.int/mediacentre/factsheets/fs134/en/

[3] A R Fathilah, M M Bakri, and Z H A Rahim, "Proceeeding of Third National Symposium Health Sciences," in *Universiti Kebangssan Malaysia*, 2000, pp. 216-219.

[4] L Arambewela, M Arawwawala, and D Rajapaksa, "Piper betle: A Potential Natural Antioxidant," *International Journal of Food Science and Technology*, vol. 41, pp. 10-14, 2006.

[5] S Sharma et al., "Evaluation of the Antimicrobial, Antioxidant, and Anti-Inflammatory Activities of Hydroxychavicol for Its Potential Use as an Oral Care Agent: Antimicrobial Agents and Chemotherapy," *American Society for Microbiology*, pp. 216-222, 2009.

[6] L S R Arambewela, L D A M Arawwawala, and W D Ratnasooriya, "Antidiabetic activities of aqueous and ethanolic extracts of Piper betle leaves in rats," *Journal of Ethnopharmacology*, vol. 102, pp. 239-245, 2005.

[7] P R Padma, V S Lalitha, A J Amonkar, and S V Bhide, "Anticarcinogenic effect of betel leaf extract against tobacco carcinogens," *Cancer Letters*, vol. 45, pp. 195-202, 1989.

[8] Kar Yong Pin et al., "Drying of Betel Leaves (Piper betle L.): Quality and Drying Kinetics," *Drying Technology*, vol. 27, pp. 149-155, 2009.

[9] Lee Hong Tee, A. Luqman Chuah, Kar Yong Pin, A. Abdull Rashih, and Yus Aniza Yusof, "Optimization of spray drying process parameters of Piper betle L. (sirih) leaves extract coated with maltodextrin," *Journal of Chemical and Pharmaceutical Research*, vol. 4, no. 3, pp. 1833-1841, 2012.

[10] K Y Pin et al., "Aqueous Extraction of Hydroxychavicol from Piper betle L. Leaves," in *1st International Conference on Natural Resources Engineering & Technology*, Putrajaya, Malaysia, 2006, pp. 146-152.

Develop an Integrated Approach to FE Model Correlation on Multi-bent Deoxidised Copper Phosphorus Tubes

D.Z. Lim[1*], M. Hosseini Fouladi[1], K.H. Yap[2]

[1]School of Engineering, Taylor's University, Malaysia, [2]CMD/CAE, Panasonic Appliances Air-Conditioning R & D (M) Sdn. Bhd. (PAPARADMY 1), Malaysia

**dengzhaolim@gmail.com*

***Abstract*— Finite element model correlation of the dynamic properties of a multi-bent deoxidised Copper discharge tube for outdoor air-conditioning unit is numerically investigated. The processes for modelling, solving, pre-test and correlation using Siemens NX Nastran are presented. This feasibility study helps integrate new testing methods into existing structural design procedures in PAPARADMY 1. The processes will then be incorporated into a Standard Operating Procedure (SOP) for further applications in Computer Aided Engineering (CAE) such as transient and frequency response analyses.**

Keywords — Numerical Study, Modal analysis, NX Nastran, FE Model Correlation, Copper Tube

1. Introduction

PAPARADMY 1 has undertaken a new development process to apply finite element (FE) model correlation. Correlation is a pre-requisite for model validation which updates dynamic properties of FE models to closely represent physical prototypes. This initiative is to replace traditional design-to-production methods that are costly, time consuming and unsustainable. Traditionally, model validation has been implemented in the aerospace and automobile industries but the increased computational power of computers has made its application more economical for other structural design related industries [1]. FE model correlation compares the dynamic properties of a structure obtained through Analytical Modal Analysis (AMA) to Experimental Modal Analysis (EMA).

An outdoor air-conditioning unit's multi-bent deoxidised Copper Phosphorus discharge tube is studied. An 11 bent discharge tube from a 1.5 Hp air-conditioner is chosen for preliminary study. This paper describes the modeling, solution, pre-test planning and correlation processes using Siemens PLM Software's NX Nastran. Successful correlation is crucial for Copper tube design optimization processes to avoid resonances in outdoor air-conditioning units.

2. Background and Framework

2.1. Modal Analysis with the Siemens NX Nastran Solver

Dynamic properties of a structure are its natural frequencies and mode shapes. These are obtained through AMA using FE codes such as NX Nastran. AMA solves a structure's equation of motion, Eq. (1) in an un-damped free vibration state.

$$[M]\{\ddot{x}\}+[K]\{x\}=0 \tag{1}$$

where:

$[M]$= Mass Matrix, $[K]$= Stiffness Matrix, $\ddot{x}$ = Acceleration Vector and x = Displacement Vector.

The solution to Eq. (1) takes the form of harmonic motion in Eq. (2) and yields an eigenvalue problem Eq. (3). The Lanczos method is then used to extract a set of eigenvalues (ω^2) and eigenvectors (ψ) that corresponds to the structure's natural frequencies and mode shapes respectively. An important assumption in modal analysis is that the structure is linear and time-invariant [2].

$$\{x\}=\{X\}e^{i\omega t} \tag{2}$$

$$-\omega^2[M]\{X\}+[K]\{X\}=0 \tag{3}$$

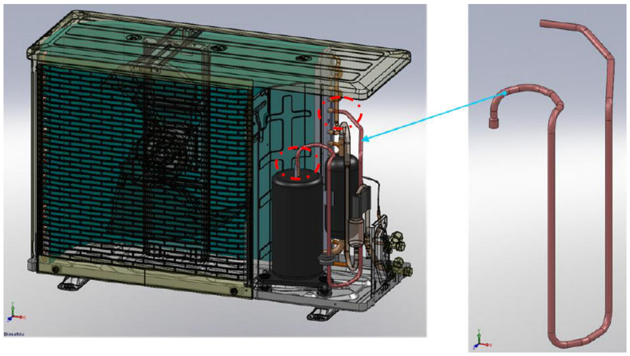

Fig. 1 3D model of a 1.5 Hp outdoor unit air-conditioner and a magnified view of the 11 bent discharge tube understudy from PAPARADMY 1

2.2. Pre-test Planning

Pre-test planning is performed after obtaining the mass and stiffness matrices but precedes modal testing. Pre-test helps determine measurement locations and creating a Test-Analysis Model (TAM). TAM is a reduced degree of freedom (DOF) representation of the actual model. This provides simpler test geometry without compromising modal data. Optimum measurement points can then be located on the TAM so that all desired modes can be captured.

Required DOFs are pre-selected to create an Analysis Set (A-SET) DOF. The A-SET shows clearly identified modes by evaluating the Automatic Modal Assurance Criterion (Auto-MAC) plot. Auto-MAC is a square matrix that compares a set of mode shape vectors to itself using equation Eq. (4) [3]. All diagonal terms are a scalar value of 1 and off-diagonal values of less than 0.1 is accepted [4]. An analysis-analysis correlation can then be used to verify the TAM [5]. Fig. 1b shows the TAM created after running the pre-test process

$$AutoMAC(A_1,A_2)=\frac{\left|\sum_{j=1}^{N}\psi_{A1j}\psi^{*}_{A2j}\right|^{2}}{\sum_{j=1}^{N}\psi_{A1j}\psi^{*}_{A1j}\sum_{j=1}^{N}\psi_{A2j}\psi^{*}_{A2j}} \tag{4}$$

where:

$\psi_{A1j}=j^{th}$ value of mode ψ_{A1}, $\psi_{A2j}=j^{th}$ value of mode ψ_{A2} and

* denotes the second set of mode matrix

Optimum measurement points are chosen from the TAM by choosing the number of required uni-axial or tri-axial accelerometers. A Min-MAC algorithm will choose the best DOF by minimizing the amount accelerometers needed to capture all desired modes [6]. A minimum of two required DOFs are compulsory and each additional DOF will be added until the best Auto-MAC plot is obtained.

2.3. FE Model Correlation

Mode vector comparison metrics and frequency differences are evaluated in the correlation process. In NX FE Model Correlation, the four metrics used are Modal Assurance Criterion (MAC), Modal Scale Factor (MSF), Coordinated MAC (COMAC) and Crossorthogonality (X-ortho). Application of the MAC will be illustrated as it is the principal metric to evaluate correlation results [4].

The Auto-Mac in Eq. (4) was adapted from the MAC equation [7]. The difference is changing the A_2 term with X, which represents the reference or test mode shapes. MAC compares AMA mode shape vectors to EMA mode shape vectors. A good correlation has diagonal terms of 0.9 or more and off-diagonal terms of 0.1 or less [7].

3. Application and Results

3.1. AMA of Multi-bent Copper Discharge Tube

The discharge tube was meshed with CQUAD4 (quadrilateral) elements of 1 mm size. A total of 24,449 CQUAD4 elements were recorded. This configuration proved optimum for modal analysis solution for torsional and incompressible materials [8]. C10100 Copper material with Young's modulus of 114 GPa was assigned.

Frequency range was limited between 0 - 300 Hz as the air-conditioner operating frequency is less than 200 Hz. An extra 100 Hz was chosen as tolerance limit. Eigenvalues were extracted using the Lanczos method in NX Nastran Sol 103. The natural frequencies and percentage error are compared to experimental values in Table 1.

3.2. Pre-test Planning Configuration

Fig. 2 shows the resulting TAM consisting of 24 DOFs for excitation and 7 DOFs for sensor placement. The effectiveness of pre-test planning can be further validated by verifying that most of the off-diagonal values of the final MAC plot in Fig. 3 are less than 0.1.

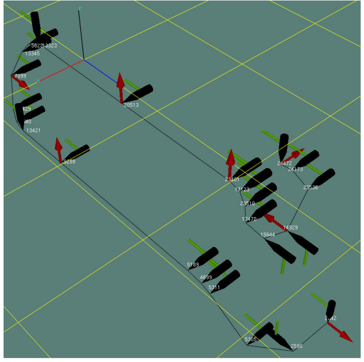

Fig. 2 Pre-test results for sensor (arrows) and excitation (hammer tip) points

3.3. Modal Test Results

Impact hammer testing was performed. Natural frequencies obtained from modal test data is compared to AMA data from section 3.1. The testing frequency range was set from 0 - 300 Hz for improved resolution. The results from EMA are compared to AMA in Table 1.

Table 1. AMA and EMA Natural Frequencies Comparison

Mode	Natural Frequencies (Hz)		% Difference
	AMA	EMA	
1	21.3	22.7	6.2
2	29.9	30.3	1.4
3	69.2	70.1	1.3
4	80.9	81.3	0.6
5	100.6	103.5	2.8
6	147.9	147.8	0.1
7	160.5	161.9	0.9
8	225.3	224.6	0.3
9	277.1	278.3	0.4
10	297.8	297.8	0.0

3.4. Test-Analysis Correlation

The pre-requisites to model correlation in NX require the importing of EMA results, alignment of TAM and FE model followed by mode pairing. The degree of agreement between test and FE model mode shape vectors can then be assessed using the MAC plot in Fig. 3.

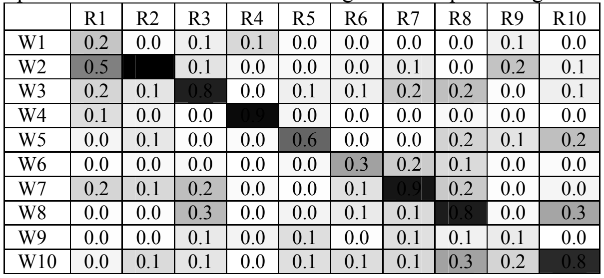

	R1	R2	R3	R4	R5	R6	R7	R8	R9	R10
W1	0.2	0.0	0.1	0.1	0.0	0.0	0.0	0.0	0.1	0.0
W2	0.5	[illegible]	0.1	0.0	0.0	0.0	0.1	0.0	0.2	0.1
W3	0.2	0.1	0.8	0.0	0.1	0.1	0.2	0.2	0.0	0.1
W4	0.1	0.0	0.0	0.9	0.0	0.0	0.0	0.0	0.0	0.0
W5	0.0	0.1	0.0	0.0	0.6	0.0	0.0	0.2	0.1	0.2
W6	0.0	0.0	0.0	0.0	0.0	0.3	0.2	0.1	0.0	0.0
W7	0.2	0.1	0.2	0.0	0.0	0.1	0.9	0.2	0.0	0.0
W8	0.0	0.0	0.3	0.0	0.0	0.1	0.1	0.8	0.0	0.3
W9	0.0	0.0	0.1	0.0	0.1	0.0	0.1	0.1	0.1	0.0
W10	0.0	0.1	0.1	0.0	0.1	0.1	0.1	0.3	0.2	0.8

Fig. 3 MAC matrix plot of the understudy Copper tube, where R refers to the reference modes (EMA) and W refers to the work modes (AMA)

4. Discussion

Analysis of the MAC plot showed that modes 2, 3, 4, 7 and 8 correlate well (diagonal values > 0.8) but modes 1, 6 and 9 were poor. Frequency difference values for all modes were desirable (<5%) [9], except for mode 1. Poor correlation was caused by insufficient measurement DOFs where sensors were limited. Test model might not have been excited properly as the sensors can only capture measurements in the X, Y and Z DOFs. Besides that, test setup errors could have caused poor correlation in local DOFs. These can be identified from the COMAC metric in subsequent post-processing.

Off-diagonal terms below 0.1 in the MAC proved that individual modes were clearly distinguished. The low percentage error of frequency difference verifies the accuracy of assigning C10100 Copper to FE model. Validation of EMA results is required to identify the discrepancies of low correlation in modes 1, 6 and 9.

5. Conclusions

The modeling process was accurate in producing a quality FE model. Implementing the pre-test process improved the efficiency of modal test by deriving TAM and choosing optimum measurement and impact points. Initial results showed reasonably good correlation of a multi-bent Copper Phosphorus discharge tube. Different Copper tube designs (lengths, routings and bends) are to be tested to validate the proposed processes before developing the SOP.

Acknowledgement

PAPARADMY 1 General Managers Mr. Low Seng Chok and Mr. Cheng Chee Mun of Cost Management Department (CMD) is greatly acknowledged for authorising the use of FEA-Project Team's NX CAE Software, B&K test equipment and Copper tube specimens.

References

[1] W. Ren, X. Peng and Y. Lin, "Experimental and analytical studies on dynamic characteristics of a large span cable-stayed bridge," *J. of Eng. Struc.,* vol. 27, 2005, pp.535-548.

[2] J. He and Z.F. Fu, "Modal Analysis of MDOF Systems," in *Modal Analysis*, Butterworth-Heinemann, pp. 94-97, 2001.

[3] D.J. Ewins, "Applications," in *Modal Testing: Theory, Practice and Application*, Second Edition, Research Studies Press Ltd., Baldock, England, 2000, pp. 428-432.

[4] L. Burns, "MAC evaluation utilized in FEA analysis for mode identification," *Proc. IMAC XXII,* 2004.

[5] J. Maly, W. Gibson and C. Chang, "Experimental Modal and Finite Element Analyses, Model Correlation and Model Tuning for an Aircraft Brake Component," *Proc. IMAC XIII*, 1995.

[6] *NX 8 Documentation*, Siemens PLM Software Inc., TX, 2011.

[7] R.J. Allemang, "The Modal Assurance Criterion: Twenty Years of Use and Abuse," *Proc. IMAC XX*, pp 14-23, 2002.

[8] S. Benzley, E. Perry, K. Merkley and B. Clark, "A comparison of All Hexagonal and All Tetrahedral Finite Element Meshes for Elastic and Elasto-plastic Analysis", *Proc. 4th Int. Meshing Roundtable*, 1995.

[9] M. Radeq, "Comparison of Modal properties," in *Comparison of Vibration properties*, Academic Press, Bucuresti, Romania, 2001.

CFD Simulation of Forced Convection Nanofluid Flow inside a Circular Conduit

Lup Kwan Low[1], Rashmi G. Walvekar[1*], Salim Mohamed Salim[1]
[1]*Department of Chemical Engineering, Taylor's University Lakeside Campus, Malaysia.*
**Corresponding author email: rashmi.walvekar@gmail.com*

Abstract—**This research aimed to analyse numerically the heat transfer enhancement in a turbulent flow circular conduit with respect to different nanoparticle concentration and Reynolds number including the effect of drag and lift forces, respectively. Single-phase model and two-phase (Mixture and Eulerian) models were employed to simulate the nanofluid flow behaviour in 3-D geometry. It was found that heat transfer of nanofluids is greater than that of the base liquid, and it increases with increasing particle volume concentration and Reynolds number, respectively. There was a good agreement between the present study results with the experimental correlations, especially for single-phase model (<9% difference). Among two-phase models, mixture model (<14% difference) showed better prediction compared to Eulerian-dispersed model (<18% difference).**

Keywords— Nanofluid, heat transfer, turbulent, forced convection, Computational Fluid Dynamics (CFD).

1. Introduction

During the past few decades, many investigations have been made to enhance the heat transfer. Based on the studies, solid metallic materials suspended in fluid increases the thermal conductivity, however large sized particles (millimeter- and micrometer-sized particles) causes abrasion, channel clogging and additional flow resistance due to poor suspension ability [1]. Nanofluid is the suspension of nanoparticles in base fluid. Nanoparticles are fine metallic particles of sizes less than 100nm such as Al_2O_3, CuO, TiO_2, Cu, Fe and carbon-based material such as carbon nanotubes (CNTs). Nanofluids exhibit great potentials to enhance heat transfer compared to conventional heat transfer fluids [2]. With small quantity of high thermal conductivity solid nanoparticles added in the base fluid, the overall thermal conductivity increases, thus increasing the heat transfer rate.

2. Mathematical Modeling

The physical parameters, such as particle size, concentration, heat load, and flow rates of the fluid are obtained from the benchmark research paper Bianco et al [3]. The geometrical configuration is shown in Fig. 1. Half tube with symmetrical with respect to the vertical plane along the tube main axis is considered. The grid size used is 20, 24, and 400 in the radial, circumferential, and axial directions respectively.

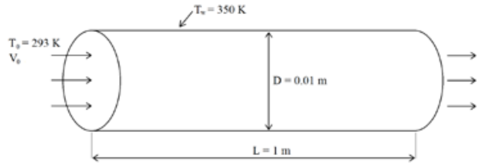

Fig. 1 Geometrical configuration for simulation

2. Governing Equations

The governing equations are described as follow [4]:
Mass Continuity equation:

$$\frac{\partial u_i}{\partial x_i} = 0 \tag{1}$$

Momentum equation:

$$F = -\frac{\partial P}{\partial x_i} + \frac{\partial u_i}{\partial x_j} = \frac{\partial \rho u_i}{\partial t} + u_j \frac{\partial \rho u_i}{\partial x_j} \tag{2}$$

Energy equation:

$$\frac{\partial \rho i}{\partial t} + u_j \frac{\partial \rho i}{\partial x_j} = k \frac{\partial^2 T}{\partial x_i^2} - p \frac{\partial u_i}{\partial x_j} + \Phi + Si \tag{3}$$

2.1. Turbulence Modeling

In present study, the Launder and Spalding (1972) k-ε model (standard k-ε model) is used to simulate turbulence flow for nanofluids. The turbulence kinetic energy, k, and its rate of dissipation, ε are as follow [4]:-

$$\frac{\partial}{\partial t}(\rho k) + \frac{\partial}{\partial x_i}\rho k u_i = \frac{\partial}{\partial x_j}\left[\left(\mu + \frac{\mu_i}{\sigma_k}\right)\frac{\partial k}{\partial x_j}\right] + G_k - \rho\varepsilon + S_k \tag{4}$$

$$\frac{\partial}{\partial t}(\rho \varepsilon) + \frac{\partial}{\partial x_i}\rho \varepsilon u_i = \frac{\partial}{\partial x_j}\left[\left(\mu + \frac{\mu_i}{\sigma_\varepsilon}\right)\frac{\partial \varepsilon}{\partial x_j}\right] + C_{1\varepsilon}\frac{\varepsilon}{k}G_k - C_{2\varepsilon}\rho\frac{\varepsilon^2}{k} + S_\varepsilon \tag{5}$$

2.2. Boundary Conditions

Uniform axial velocity and temperature are assumed at velocity inlet. At pressure outlet, the static (gauge) pressure is set to zero. The wall boundary is assigned with no-slip wall boundary conditions with uniform wall temperature.

2.3. Physical Properties of Fluids

The properties of water and nanofluid are obtained from the benchmark research paper Bianco et al. [3]. The nanofluid used is water suspended with Al_2O_3 nanoparticles with particle diameter of 38nm. For single-phase model, the properties of nanofluid are calculated as effective properties calculated using equations provided in Bianco et al. [3]. For two-phase model, the respective properties for the water phase and nanoparticle phase are input accordingly.

2.4. Numerical Method and Validation

The finite-volume solver FLUENT is used to solve the governing equations, appropriate boundary conditions and constitutive relations. The semi-implicit method for the pressure linked equations (SIMPLE) scheme is used to solve the pressure-velocity decoupling. The numerical results are validated with correlations and benchmark paper. Reynolds number and Nusselt number defined respectively as follow:-

$$Re = \frac{\rho V D}{\mu} \tag{6}$$

$$Nu = \frac{hD}{k} \tag{7}$$

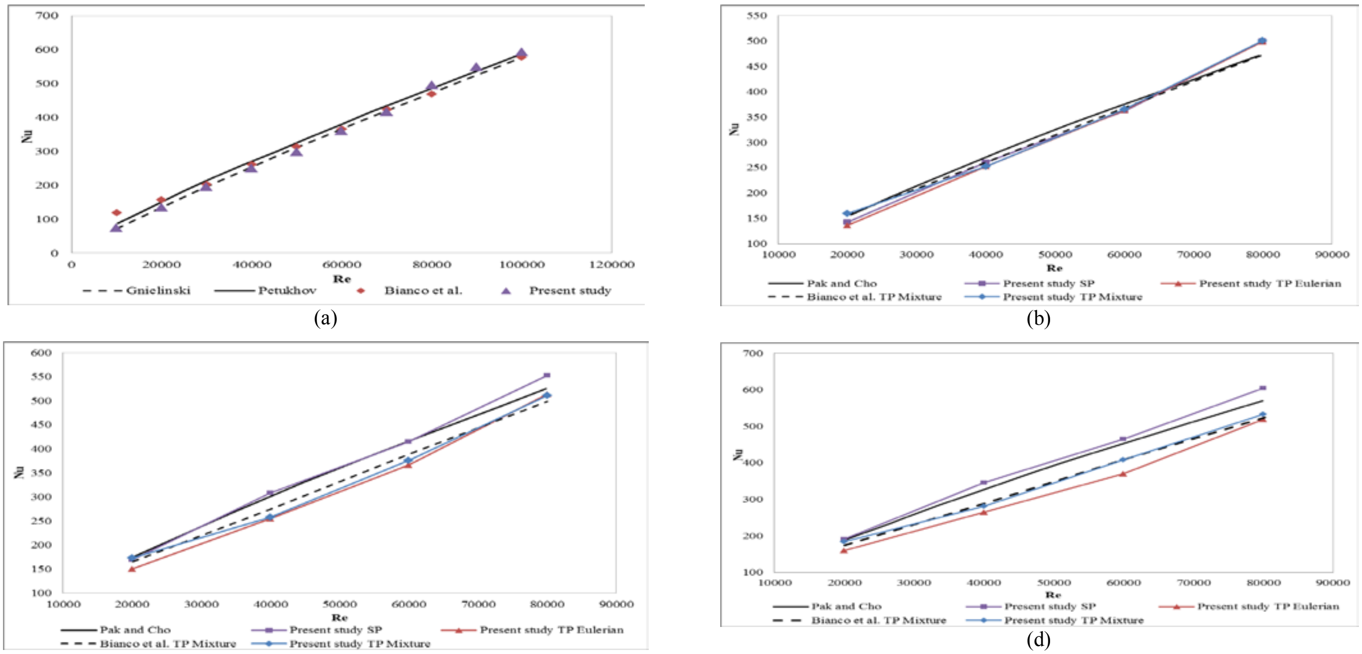

(a) (b) (c) (d)

Fig.2 Graph of average Nusselt number with respect to Reynolds number for: (a) base fluid (ϕ = 0%); (b) ϕ = 1%; (c) ϕ = 4%; (d) ϕ = 6%.

3. Results

In Fig. 2, the average Nusselt numbers for each particle concentration are reported with benchmark paper Bianco et al. [3] and correlation by Gnielinski [5] and Petukhov [6] for base fluid and Pak and Cho [7] for nanofluid. Nusselt number for Pak and Cho [7] correlation is a function of Reynolds number and Prantdl number. It is observed that heat transfer of nanofluid is higher than that of base fluid. The heat transfer increases with the increase in Reynolds number and particle volume concentration of nanoparticles.

For base fluid, there is strong agreement between the present study and the correlations and the benchmark. For nanofluids, single phase model has close agreement with Pak and Cho [7] at low concentrations, however it slightly overestimates the Nusselt number at ϕ = 6%. Therefore, it can possibly over predict the Nusselt number at particle concentration higher than 6%. This may be due to the assumption of single-phase model to treat nanofluid as homogeneous fluid with effective properties.

For two-phase models, mixture and Eulerian models are studied. Mixture model includes the drag force, while Eulerian model include both drag and lift forces. Overall, mixture model gives close agreement to both the correlation and benchmark, however it slightly underestimates the Nusselt number as particle concentration increases. The same pattern was observed between the correlation and benchmark. The percentage difference could be reduced by using temperature-dependent nanofluid properties. In the case of Eulerian model, although it includes the lift force in the simulation process, it further underestimates the Nusselt number as compared to mixture model, with higher percentage difference.

4. Conclusion

The results showed that nanofluid heat transfer increases as Reynolds number and particles volume concentration increases. There is a good agreement between the present study results and experiment correlation by Pak and Cho [7] and the benchmark paper Bianco et al. [3]. Single-phase model has strong agreement with Pak and Cho [7]. As for two-phase models, mixture model is satisfactory, while Eulerian model gives higher percentage difference when compared to Pak and Cho [7]. Temperature-dependent nanofluid properties could be used to improve the results. Moreover, heat transfer of nanofluid particle volume concentration of more than 6% could be further studied.

References

[1] He, Y., Jin, Y., Chen, H., Ding, Y., Cang., D. & Lu, H. (2007). Heat transfer and flow behaviour of aqueous suspensions of TiO_2 nanoparticles (nanofluids) flowing upward through a vertical pipe. *International Journal of Heat and Mass Transfer* 50, 2272–2281.

[2] Wang, X.Q. & Mujumdar, A.S. (2008). A review on nanofluids - Part I: theoretical and numerical investigations. *Brazilian Journal of Chemical Engineering* 25, 613-630.

[3] Bianco, V., Manca, O. & Nardini, S. (2010). Numerical simulation of water/Al2O3 nanofluid turbulent convection. Advances in Mechanical Engineering 2010, 1-10.

[4] Versteeg, H.K. & Malalasekera, W. (2007). *An introduction to computational fluid dynamics: the finite volume method*. 2nd ed. Harlow, Essex: Longman Group Ltd.

[5] Gnielinski, V. (1976). New equations for heat and mass transfer in turbulent pipe and channel flow. *International Chemical Engineering* 16, 359–368.

[6] Petukhov, B.S. (1970). Heat transfer and friction in turbulent pipe flow with variable physical properties. In J. P. Hartnett and T. F. Irvine (Eds.), *Advances in Heat Transfer* (pp. 504–564). New York, USA: Academic Press.

[7] Pak, B.C. & Cho, Y.I. (1998). Hydrodynamic and heat transfer study of dispersed fluids with submicron metallic oxide particles. *Experimental Heat Transfer* 11(2), 151-170.

The Effect of Frequency change on Transmission Losses in Low Frequency Resonator Tubes

Low Zhi Weng and Yousif Abdalla Abakr*
Department of Mechanical, Materials and Manufacturing Engineering, The University of Nottingham Malaysia Campus, Jalan Broga 43500 Semenyih, Selangor Darul Ehsan, Malaysia
**yousif.abakr@nottingham.edu.my*

Abstract — **Many thermoacoustic engines are designed to operate at atmospheric pressure with a relatively low frequency, therefore there was always a concern about the losses encountered through the bends in the loop of the engine. This paper investigates the transmission loss when travelling waves propagate through straight tubes or curved bends of different radii. This work is mainly focusing on travelling waves propagating in the loop with low frequency range and low pressure amplitude (25 – 95Hz and 7.1 Pa). The four-microphone method has been used to determine the sound pressure wave that propagates in the tube then the decomposition theory is used to calculate the transmission loss through the curved bends or the straight tube. From the results of this work, it is found that, all the curved bends and the straight tube have a maximum transmission loss at a frequency value between 30Hz to 35Hz for all cases. After the frequency of 35Hz, a constant rate of decrease of the transmission loss was observed for all frequencies larger than 35 Hz.**

1. Introduction

This paper investigates the transmission loss of the travelling wave when it propagates through a straight tube or curved bend tube. This research mainly focuses on the low frequency range of sound with low sound pressure amplitude which is a typical situation in low pressure thermoacoustics engine operating at atmospheric conditions. Transmission loss is a natural acoustic phenomenon; it is the loss of sound intensity as the sound waves passes through a medium. These losses are due to the attenuation and spreading of the sound waves. It is important to know sufficient information about the transmission loss for each different radius of curved bends for a proper design of the thermoacoustic engine; although this knowledge has been widely used in ducting systems, mufflers and thermoacoustic engines, but the concentration of most of the previous studies focus on high frequency ranges. A typical thermoacoustic engine consists of many curved bends, resulting in significant losses of sound pressure in these curved bends, therefore it is required to minimize the losses to improve the efficiency of the engine.

2. Objectives

The main objective of this work is to investigate the acoustics losses when a travelling wave passes through a curved bend at low frequency range and low pressure amplitude. This investigation covers two cases of transmission loss; one of a curved tube and one of a straight tube, both are of the same total length. The transmission loss for each case is calculated by using the decomposition theory [1], [2]. The decomposition theory has been described by Sybert and used to measure the acoustic properties of materials such as impedance and the intensity of the incident and reflected components.

The four-microphone method has been used by Yunseon [3] to determine the transmission loss coefficient of the exhaust system but he has used the full transfer function. This full transfer function is an alternative method for the decomposition theory but both methods can be used to calculate the transmission loss. The transmission losses of materials that have been measured by Yunseon are operated under a high frequency range of sound and high sound pressure amplitude.

3. METHODOLOGY

The apparatus is separated into two parts; upstream and downstream. The upstream part is where the sound wave coming from driving speaker before it enters the bend; the downstream is the part after the bend. Two microphones are positioned at each one of the upstream and downstream parts. Each two microphones are positioned 30 cm apart. The four microphones and amplifier are connected to the PXI system. This PXI system is used to record and analyse the signal measured by each one of the four microphones. Besides, it is also used to send the signal to the speakers to generate a travelling wave at a specific frequency. The amplitude of the travelling wave is controlled by the amplifier. In this experiment there are two speakers, one is the driving speaker and the other one is the attenuation speaker. The attenuation speaker is used to attenuate the reflected component, β2 at the downstream so that the transmission loss in the curved bends and straight tube can be calculated. Both of these speakers are generating sound waves with the same frequency but of a different phase angle which is controlled by the PXI system. The dimensions of each of the curved tube and the straight tube are shown in Table 1. The details of the whole system are shown schematically in Figure 1.

Table 1: Detail of each curved bend and the straight tube

	Length (m)	Radius of Curvature (m)
Curved Bend	0.550	0.115
Straight Tube	0.550	-

4. RESULTS AND DISCUSSION

The results of transmission loss for the curved bend and straight tube is shown in figures 2, 3 and 4. These transmission loss values are calculated by using the decomposition theory and two-port s-parameters theory [4]. In figure 2, the transmission loss is plotted against the frequency in order to show the transmission loss values for each case at different frequencies. Based on the trend lines shown figure 2, the transmission loss for the curved tube and the straight tube were observed to have a peak at a frequency ranging between 30Hz to 35Hz at the constant amplitude of 7.1Pa for the incident component at the upstream. The maximum transmission loss was observed ranging between 0.83 dB for the curved tube to a value for 0.53 dB for the straight tube. The transmission loss is generally decreasing at a constant rate of 0.01dB/Hz in the range between 35Hz to 95Hz. That means the transmission loss values are dependent on the frequency value since the amplitude of the incident component at the upstream was fixed at a constant value for all frequencies, this may be due to the dependence of the thickness of the acoustic boundary layer on the frequency, resulting in lower viscous losses as the frequency increases.

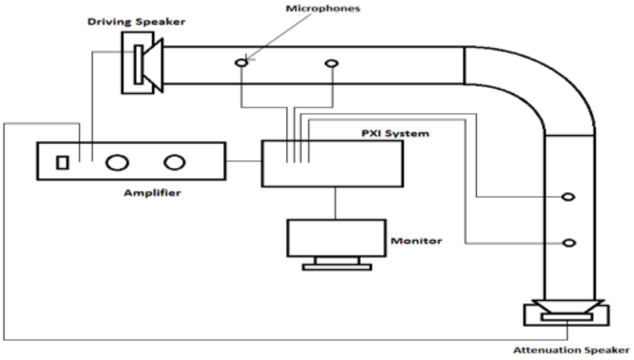

Figure 1: Schematic diagram for the whole system

The straight tube has the lowest transmission loss compared to the curved tube as shown in Figure 2. This is partially due to the reflection at the bend of the curved tube as well as loss of momentum loss due to direction change in the curved tubes. When the travelling wave passes the curved surface, part of the wave will be reflected and the rest will pass through the bend. So, this has caused the incident component of the wave at the downstream to be lower than the incident component at the upstream. Therefore, bends have higher transmission loss compared with straight tubes.

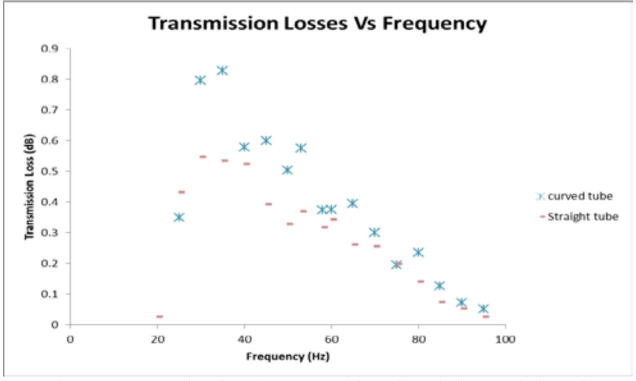

Figure 2: Results for the curved bend and the straight tube

The transmission loss can be represented in a non-dimensional form by dividing the loss at each frequency by the straight tube loss at the same frequency. A plot of the non-dimensional loss against frequency is shown in Figure 3, the non-dimensional loss of the curved tube was consistency has a higher value of about 1.6 up to a frequency of about 70Hz, after which the non-dimensional loss starts to increase linearly. This is believed to be due to the dominant viscous loss at the lower frequency, while the influence of turbulence and reflection starts to be stronger after the 70 Hz limit.

The results of each bend and straight tube are plotted in the form of percentage transmission loss against frequency as shown in Figure 4. It is observed that there is a peak of percentage transmission loss within the range of 30Hz to 35Hz for both of the curved tube and the straight tube. The maximum percentage transmission loss at this peak ranges between 11.85% for the straight tube and 17.26% for the curved tube. The percentage transmission loss in figure 4 is generally decreasing at a constant rate of 0.21%/Hz between the ranges of 35Hz to 95Hz.

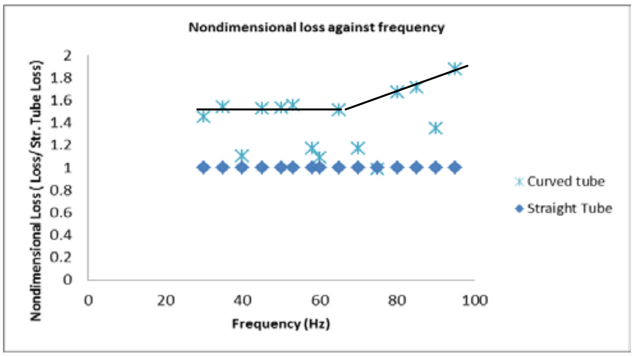

Figure 3: Comparison of the non-dimensional loss of the curved and the straight tubes

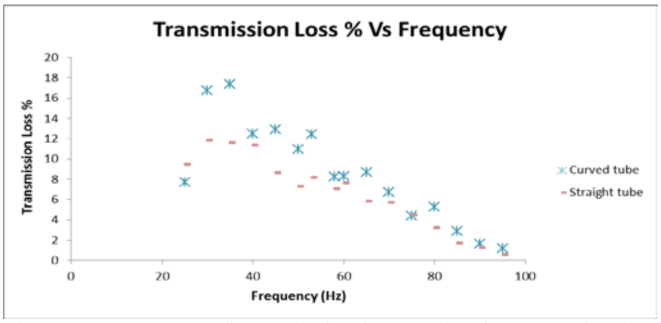

Figure 4: Percentage of transmission loss against frequency for the curved and the straight tubes

5. CONCLUSIONS

In this work, the decomposition theory and four-microphone method are used to investigate the transmission losses for a curved tube a straight tube. The investigation is focused on low frequency range of sound waves. There is a maximum of transmission loss within the range of 30Hz to 35Hz for both of the curved bend and the straight tube. The transmission loss was found to decrease at a constant rate with the increasing frequency. The curved tube exhibited higher losses compared to the straight tube; this is due to the reflected component from the curved surface giving a constant loss increase for all frequencies. Based on these results it is recommended avoid designing a thermoacoustic engine operating at the frequency range of 30-35Hz, the recommended frequency will be between 90-100 Hz.

Acknowledgment

The authors would like to thank MOSTI Science fund for providing the financial support for this research work. The authors would also like to thank the SCORE project, UK, for providing technical support for this research work.

References

[1] Ross, A. F. Seybert and D.F., “Experimental determination of acoustic properties using a two-microphone random-excitation technique,” J. Acoust. Soc. Am, pp. 1362-1370, May 1977.
[2] A. Seybert, “Two-sensor methods for the measurement of sound intensity and acoustic properties in ducts,” J. Acoust. Soc. Am, pp. 2233-2239, June 1988.
[3] RYU, Yunseon and Choi, Man-Rim, “Transmission Loss Measurement of the Exhaust system using 4-microphones with impedance tube,” AVISS korea.
[4] Sung Soo Jung et al, “Measurement of Sound Transmission Loss by Using Impedence Tubes,” *Journal of the Korean Physical Society,* pp. 596-600, August 2008.

The Effect of change of Radius of Curvature on Transmission Losses in a Low Frequency Resonator Tubes

Low Zhi Weng and Yousif Abdalla Abakr*
Department of Mechanical, Materials and Manufacturing Engineering, The University of Nottingham Malaysia Campus, Jalan Broga 43500 Semenyih, Selangor Darul Ehsan, Malaysia
yousif.abakr@nottingham.edu.my

Abstract — **This work investigates the transmission loss of curved bends of different radii and a straight tube at low frequency region (35Hz and 80Hz). This paper has shown the losses of sound power when specific frequency of travelling waves propagates through the different radius of curved bends and straight tube. In this work a four-microphone method has been used to measure the loss of sound pressure when travelling waves propagate through the curved bends and a straight tube. Then, the decomposition theory and two-port s-parameter theory are used to calculate the transmission loss of these bends and straight tube. Based on the result, it is noticed that the straight tube has the lowest transmission loss as it doesn't have any curved surface to create the reflection or turbulence losses. All bends exhibited higher transmission loss compared to the straight tube at frequencies below 55Hz, in frequency range higher than 55Hz there was no clear dependency on curvature on transmission loss.**

1. Introduction

This paper investigates the transmission loss when a travelling wave of specific frequency propagates through a curved bend. Bends of different radius of curvature were considered for investigation. The transmission loss through the bends was investigated at a low frequency value (80Hz) with a low sound pressure amplitude of 7.0882Pa. The values of the radii of curvature are similar to the values used in the thermoacoustic engine developed by the SCORE project. The thermoacoustic engine consists of multi-bends, believed to result in significant losses. There is no sufficient information about the order of magnitude of the losses as the radius of curvature changes. This is required to improve the efficiency of the engine. The transmission loss is one of the acoustic losses of sound intensity when sound waves propagate through a medium.

In this research, the main objective is to evaluate the transmission loss of curved bends of different radius of curvature compared to a straight tube, when a low frequency sound wave propagates through the tubes. So, the losses of sound pressure amplitude in the curved bends are measured by using the four-microphone method. Then, the transmission loss value of each bend and the straight tube is determined by using the decomposition theory and the two-port s-parameters theory. The decomposition theory has been described in detail by Sybert [1],[2]. To find the acoustic properties of materials by using the sound pressure amplitude that is measured by the microphones. Furthermore, there is another group led by Soo Jung, et al [3] have used the four-microphone method to investigate the transmission loss of absorbent materials. They have used an alternative way to calculate the transmission loss which is using a full transfer function. The full transfer function method is an alternative method that is used to determine the transmission loss property.

2. THEORETICAL BACKGROUND

In this work, the decomposition theory [1], [2] is applied in the upstream and downstream independently. Using the four-microphone method, it is possible to separate the sound pressure wave into an incident component and a reflected component for the upstream and downstream, as shown in Figure 1. The upstream is before the sound wave passes through the bend. By using the decomposition method the incident and reflected components are found and defined as α_1 and β_1. For the downstream where the sound wave has passed through the bend and its incident and reflected components are defined as α_2 and β_2. The decomposition theory is to decompose the wave matrix which involves the incident and reflected components of the wave that is multiplied with the coefficient matrix [A] to form the original wave matrix which involves the original values of the sound pressure as measured by the microphones. This is shown in equation 1 below:

$$[A]\ [S_{AA}\ \ S_{BB}\ \ C_{AB}\ \ Q_{AB}]^T = [S_{11}\ \ S_{22}\ \ C_{12}\ \ Q_{12}]^T \quad \text{…. (1)}$$

The coefficient matrix, [A] above can be inverted to form δ [B] as shown here:

$$[S_{AA}\ \ S_{BB}\ \ C_{AB}\ \ Q_{AB}]^T = \delta[B]\ [S_{11}\ \ S_{22}\ \ C_{12}\ \ Q_{12}]^T \quad \text{…. (2)}$$

The δ [B] matrix is shown given by the following matrix:

$$\delta\,[B] = \delta \begin{pmatrix} 1 & 1 & -2a_{32} & -2a_{42} \\ 1 & 1 & -2a_{31} & -2a_{41} \\ -a_{23}/2 & -a_{13}/2 & a_{33} & a_{43} \\ -a_{24}/2 & -a_{14}/2 & a_{34} & a_{44} \end{pmatrix}$$

The equations above are used to determine the incident and reflected component for the upstream. To determine the incident and reflected component for the downstream, it is required to carry out the decomposition theory again. So the equation for the downstream can be written as:

$$[S_{CC}\ \ S_{DD}\ \ C_{CD}\ \ Q_{CD}]^T = \delta[B]\ [S_{33}\ \ S_{44}\ \ C_{34}\ \ Q_{34}]^T \quad \text{…. (3)}$$

In order to calculate the transmission loss, the two-port S-parameters theory has been used. The S-parameter matrix can be defined as follows [4]:

$$\begin{pmatrix} b_1 \\ a_2 \end{pmatrix} = \begin{pmatrix} S_{11} & S_{12} \\ S_{21} & S_{22} \end{pmatrix} \begin{pmatrix} a_1 \\ b_2 \end{pmatrix} \quad \text{…...... (4)}$$

In this matrix, the a_1 and b_1 elements are the incident and reflected components for upstream and the elements a_2 and b_2 are the incident and reflected components for downstream. In this paper, the value of the reflected component, b_2 at the downstream is set to be zero by tuning the attenuation speaker to cancel the reflected component at the downstream. Therefore, the S-parameter matrix can be simplified as:

$$a_2 = S_{21}\ X\ a_1 \quad \text{…………………………….(5)}$$

The S_{21} variable is the forward gain, which is the loss factor. The transmission loss can be determined by the logarithmic loss factor and this is shown as:

$$TL = 20 \log (S_{21}) \quad \ldots\ldots\ldots\ldots\ldots\ldots\ldots\ldots\ldots\ldots (6)$$

$$P_{aa} = (S_{AA} \text{ X FreqRes X } 3)^{1/2} \quad \ldots\ldots\ldots\ldots\ldots\ldots\ldots (7)$$

The transmission loss value that calculated by using equation 6 will be in decibel, dB. The FreqRes is the sampling frequency over the number of samples. In order to have generalized transmission loss value, the percentage transmission loss has been used as shown below:

$$TL = \frac{P_{aa}^{2} - P_{cc}^{2}}{P_{aa}^{2}} \text{ X } 100\% \quad \ldots\ldots\ldots\ldots\ldots\ldots (8)$$

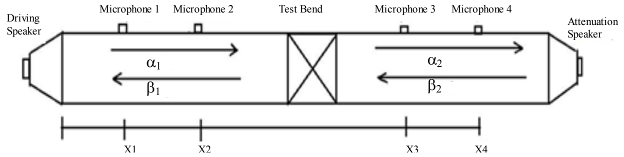

Figure 1: Schematic diagram of the apparatus

3. METHODOLOGY

In this work, the apparatus is divided into two parts that are upstream and downstream. Two microphones are positioned at each one of the upstream and downstream parts and with a distance of 30cm apart. A PXI computing system is used to record and analyse the signals measured by the microphones. It is also used to control the frequency and phase angle of the sound wave that generated by the driving and attenuation speakers. An amplifier is used to control the amplitude of the sound wave. The purpose of the attenuate speaker is to attenuate the reflected component, β_2 at the downstream and force it to a nearly zero value. Table 1 shows the number of bends used and its radius of curvature,

Table 1 specifications of bends used in the experiment

Curved Bend	Length (m)	Radius of Curvature (m)
A1	0.565	0.058
A2	0.578	0.098
A3	0.550	0.115
A4	0.550	0.139
A5	0.530	0.167
A6	0.530	0.193
A7	0.530	0.205
Straight Tube	0.550	-

4. RESULTS AND DISCUSSION

The results of the transmission loss of each curved bend and straight tube at the frequency of 80Hz are shown in this section. In Figure 2, the actual values of transmission loss in decibels are plotted against the radius of curvature; it is noticed that the transmission loss values for all bends and straight tube are quite consistent based on the trend-lines. It is also noticed that the straight tube has the lowest transmission loss values compared to all bends; this is partially due to the reflected component from the curved surface of the bend.

Figure 2: Results of transmission loss versus radius of curvature for a frequency of 80Hz

The transmission loss can be represented in non-dimensional form by dividing the loss of each bend by the straight tube loss at the same frequency. Figure 3 shows the result of non-dimension loss against the radius of curvature. There is no strong dependency of transmission loss on radius of curvature at this low frequency

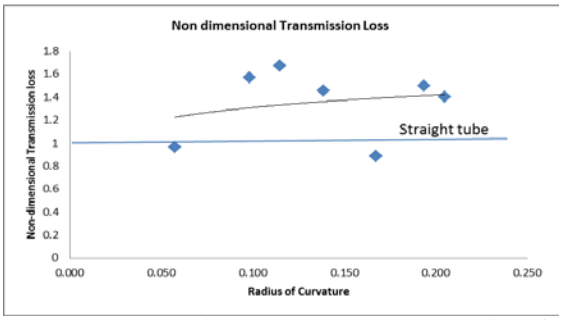

Figure 3 Non- dimensional transmission loss versus Radius of curvature at a frequency of 80 Hz

5. CONCLUSIONS

Basically, this research is mainly focused on the transmission loss through bends of different radii of curvature compared to a straight tube at a low frequency of 80Hz, as it is the case in a typical thermoacoustic engine. The results indicated no strong influence of the magnitude of the radius of curvature on the transmission loss, a slight increase of the loss was observed as the radius increases, generally most of the curved tubes indicated higher losses compared to the straight tube. This behavior is due to the high influence of the acoustic boundary layer effect on the loss value, the component of the loss due to reflection is relatively small at low frequencies. The influence of turbulence is also very limited resulting in lower effect of the sharp bends. In this work, the four-microphone method has been used to measure the losses of sound pressure then the decomposition theory and two-port s-parameter theory are used to calculate the transmission loss. The straight tube has the lowest transmission loss value in all conditions; this is due to the absence of the small reflected component from the curved surface.

Acknowledgment

The authors would like to thank MOSTI Science fund for providing the financial support for this research work. The authors would also like to thank the SCORE project, UK, for providing technical support for this research work.

References

[1] Ross, A. F. Seybert and D.F., “Experimental determination of acoustic properties using a two-microphone random-excitation technique,” J. Acoust. Soc. Am, pp. 1362-1370, May 1977.

[2] A. Seybert, “Two-sensor methods for the measurement of sound intensity and acoustic properties in ducts,” J. Acoust. Soc. Am, pp. 2233-2239, June 1988.

[3] Sung Soo Jung, Yong Tae Kim, Yong Bong Lee, Seung Il CHo and Jong Kyu Lee, “Measurement of Sound Transmission Loss by Using Impedence Tubes,” *Journal of the Korean Physical Society,* pp. 596-600, August 2008.

[4] S. Dequand,S. J. Hulshoff , “Acoustics of 90 degree sharp bends. Part II:Low-frequency aeroacoustical response,” *ACTA ACUSTICA UNITED WITH ACUSTICA,* vol. Vol. 90 , p. 13 – 23, 2004

The Dynamic response of Static Pressure Sensors when used on Acoustics Measurement Applications

Low Zhi Weng and Yousif Abdalla Abakr*

Department of Mechanical, Materials and Manufacturing Engineering, The University of Nottingham Malaysia Campus, Jalan Broga 43500 Semenyih, Selangor Darul Ehsan, Malaysia

yousif.abakr@nottingham.edu.my

Abstract — **Many researchers used to use ordinary pressure transducers to measure the acoustic pressure in ducts and mufflers, noting that most of these transducers are calibrated basically to measure static pressure rather than dynamic pressures, there was always a concern about the validity of such measurements. This work investigates the dynamic response behaviour of the pressure sensor at different frequencies (25Hz – 95Hz). This paper mainly focuses on the sound pressure amplitude that measured by each pressure sensor at a fixed position in the impedance tube. An attenuation speaker is used to attenuate the reflected component at the downstream, in a dynamic attenuation technique, in order to improve the reliability of the results. Based on the results, it is noticeable that the sound wave pressure amplitude and phase difference are dependent on the frequency. But, the phase difference and the pressure amplitude of sound wave are not interrelated at such small frequency range. Also it is noticed that there is a maximum of sound pressure amplitude reading at the frequency of 52Hz, indicating an existence of a resonance frequency of the pressure sensor at this value of frequency.**

1. INTRODUCTION

This paper investigates the dynamic response of the sound pressure sensor that is used to measure the sound wave pressure amplitude that propagating in the impedance tube. This work mainly focuses on the low frequency region (25Hz-95Hz), as this is the frequency range for the thermoacoustic engine under investigation by our research group. In thermoacoutic engine, the engine loop consists of many bends and the sound pressure sensors are used to measure the sound wave that is generated by the engine. This work is used as a validation of the readings of these pressure sensors which were originally calibrated by the manufacturer at constant pressure values.

A sound wave of constant amplitude and is produced by the driving speaker, an amplifier is used to keep the amplitude of the sound wave constant. Losses may occur when sound waves travel in a tube; this is due to several reasons such as viscosity losses, reflection of waves and others, but due to the short distance between the source and the sensor, losses can be considered negligible.

The variation of sound pressure amplitude in the impedance tube is measured by each pressure sensor at a fixed position. The results will be compared to the different frequency of sound used, there should be a certain correction value for the sensor readings based on the frequency applied by the driving-speaker.

According to previous research, the four-microphone method was used several researchers to investigate the acoustic properties of different materials and muffles. Yunseon [1] has used an impedance tube with four-microphone method to determine the transmission loss coefficient of the exhaust system. There is a group of researchers led by Soo Jung to develop a robust methodology for the application of the four microphone method [2], this group has also used the four-microphone method and an impedance tube to measure the acoustic properties of different materials with a particular focus on the transmission loss property. Other than that, there is another method that is the three-microphone method and its working principle is quite similar to the four-microphone method. In addition, Sybert [3] has used the three microphone technique to determine the transmission loss of the mufflers. Lastly, Yousif, et al [4] has also used the four-microphone method and decomposition theory to determine the transmission loss property of different radius of curved bends and straight tube at low frequency region.

2. METHODOLOGY

In this work, the apparatus consists of two speakers that are the driving speaker and the attenuation speaker. The driving speaker is used to generate the sinusoidal waves that will propagate through the impedance tube. Next, the attenuate speaker is used to attenuate the reflected component at the downstream. The position of both speakers in the apparatus is shown in Figure 1. In Figure 1 there is a schematic diagram that shows the detail of the whole system with clear symbols for illustration. Furthermore, the apparatus is divided into two parts which are upstream and downstream as shown in Figure 1. The upstream part is where the sound waves pass before entering the second section which consists of the third and the fourth pressure sensors. For the downstream part, the sound waves are attenuated dynamically by the attenuation speaker at the end of the second section. The two pairs of pressure sensors are positioned at each of the upstream and downstream parts at a fixed separating distance between each two pressure sensors of 30cm. All pressure sensors are connected to the PXI system(National Instruments NI PXI-1042Q). This PXI system is used to record and analyse data that is measured by the pressure sensors at a sampling rate of 1kHz. Besides, it is also used to control the phase angle and frequency of the sound waves that is generated by both speakers. The amplitude of the travelling wave is controlled by the amplifier and kept constant throughout the experiment.

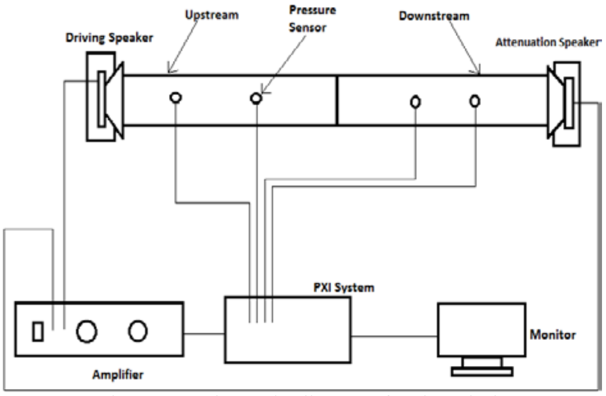

Figure 1: Schematic diagram for the whole system

In order to get accurate and consistent results, all the pressure sensors need to be calibrated every time before the experiment started. In this work, four pressure sensors have been used but we were only concentrating about the reading recorded by the first pressure sensor which has the nearest position to the driving speaker. After completing the readings of the first pressure sensor, covering all the frequency range, the position of the first pressure sensor is replaced by the second pressure sensor. This step was repeated until the entire pressure sensors have undergone the test. All the pressure sensors are tested with a range of frequency from 25Hz to 95Hz, with an interval of 5Hz. The attenuation speaker will not affect the accuracy of the result since it is used to attenuate the reflected component at the downstream. The attenuation can be done by adjusting the amplitude and phase angle of the sound waves that generated by the attenuation speaker continuously until a near zero value of the reflected wave component is found.

3. RESULTS AND DISCUSSION

The results of sound pressure amplitude measured by each pressure sensor fixed at the same position are plotted against the frequency as shown in Figure 2. According to Figure 2, the amplitude of the sound wave measured by each pressure sensor is different even at the same frequency because the initial sound pressure value is not fixed at a constant value and these amplitude is controlled by the amplifier. Although the amplitude values are different but the trend-line of the sound pressure amplitude is still the same for the entire pressure sensors as shown in Figure 2. It shows the sound pressure increase when the frequency increase but this stops in a frequency of 50Hz. After the 50Hz maxima, the sound pressure starts to decrease.

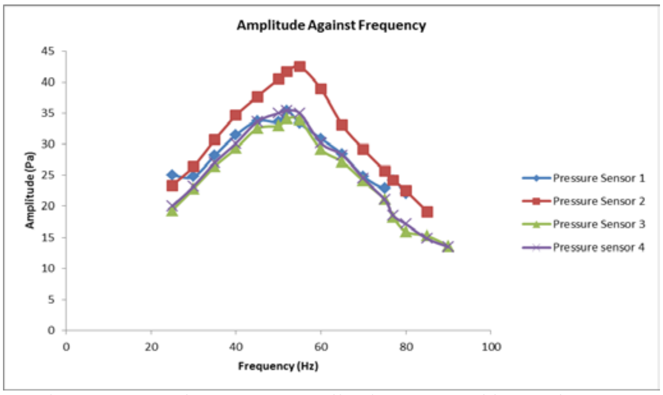

Figure 2: Sound Pressure Amplitude Measured by Each Pressure Sensor against Frequency

The reading of the pressure sensor 2 are found to be higher than all the other sensors at all frequencies, this is due to a constant error due to the original calibration of the sensor. The results indicate that the pressure transducers should be subjected to a dynamic calibration process or the readings will be strongly affected by the operating frequency.

In Figure 3, the phase difference of the sound wave that emitted by the attenuation speaker is shown. Based on Figure 3, it is noticed that the phase difference in the response of the pressure sensor relative the generated sound signal is increasing gradually from nearly zero value indicated by 360˚ at the low frequency near the zero frequency, which is the original static pressure frequency. The maximum phase difference is observed at about 52Hz where the value becomes nearly 180˚, indicating complete off the phase condition, after this the phase difference of the pressure sensor's response is decreasing again relative to the generated sound signal until it reaches a zero degree (or 360˚) as shown by the sudden jump (noting that zero and 360˚ are the same point). It is also interesting to notice that the biggest sensor's response was at the biggest phase angle difference with respect to the original exiting signal. The maximum reading was noticed to be about 10-15 Pa higher than the lower reading of the sensor.

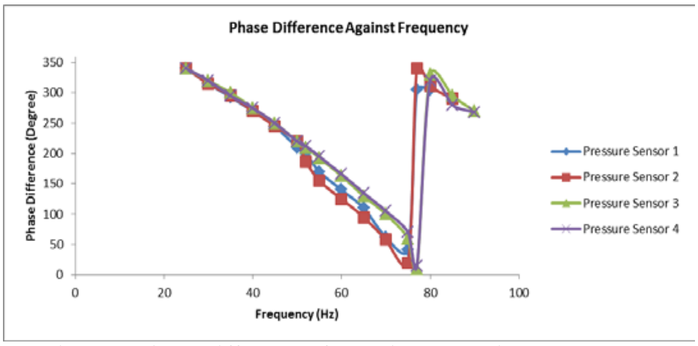

Figure 3: Phase Difference of Sound Wave against Frequency

The sound pressure amplitude is unstable at 50Hz is due to mains hum or electric hum. This electric hum happens when the audio system is running the same frequency with the alternative current frequency which is 50Hz. So, it is better to record the sound pressure amplitude at 52Hz compare to 50Hz.

4. CONCLUSIONS

Basically, this research mainly focused on the dynamic response behaviour of the pressure sensor at low frequency region (25Hz-95Hz). From the results it is concluded that static pressure transducers will not give an accurate sound pressure reading, when used to measure sound pressure, especially if the frequency is near to the natural frequency of the sensor. The pressure sensors were found to give higher values compared to the static reading of the sensor, the reading error can be close to the double in value of the original static reading (at about 52 Hz). It is also found that pressure sensors will not give an accurate estimate of the actual phase angle of the original excitation sound wave; the difference in phase angle can be as large as 180˚, indicating completely opposite direction. These results are very useful to understand the dynamic response of sensors and will help to estimate a correction factor based on the working frequency.

Acknowledgment

The authors would like to thank MOSTI Science fund for providing the financial support for this research work. The authors would also like to thank the SCORE project, UK, for providing technical support for this research work.

References

[1] RYU, Yunseon and Choi, Man-Rim, “Transmission Loss Measurement of the Exhaust system using 4-microphones with impedance tube,” *AVISS Korea, 2004.*

[2] Sung Soo Jung, Yong Tae Kim, Yong Bong Lee, Seung Il CHo and Jong Kyu Lee, “Measurement of Sound Transmission Loss by Using Impedence Tubes,” *Journal of the Korean Physical Society*, pp. 596-600, August 2008.

[3] Ross, A. F. Seybert and D.F., “Experimental determination of acoustic properties using a two-microphone random-excitation technique,” *J. Acoust. Soc. Am*, pp. 1362-1370, May 1977.

[4] B. Yousefzadeh, M. Mahjoob,N. Mohammadi,A. Shahsavari, “An experimental study of Sound Transmission Loss (STL) measurement techniques using an impedance tube,” *Acoustics 08 Paris*, pp. 965-968, 2008.

Numerical Analysis of Sport Shoes Ankle Protection

M.N. Jalil[1*], C.H. Alex[2]

[1,2]*Mechanical Engineering, Taylor's University, Selangor, Malaysia*

**Email: nazymjalil@gmail.com*

Abstract— **Ankle injuries are prudent among athletes especially basketball players. High ground reaction force during athletic movement is one of the factors that can result to ankle injuries such as sprain and fracture. ANSYS software is used to model the Nike zoom midsole and simulates it under vertical landing and cutting movement. Finite element analysis is used to analyze the effects of stress (σ), strain (ε), displacement and strain energy on static loading. The results show that highest stress located at heel region. Besides that, midsole's air gel provides 39% maximum stress reduction. The midsole also provide 2.24 Joules energy absorption during vertical landing which reduces shock transmitted to the ankle. Thus, the results prove that midsole provide cushioning as well reduce the risk of ankle injuries.**

Keywords— Ankle injuries, midsole, finite element analysis (FEA), ground reaction force (GRF), shock attenuation

1. Introduction

Ankle injuries usually correlate with ankle sprain which govern 80% of ankle injuries [1]. Ankle sprain will result to the rapture of the ligaments which susceptible to functional instability (FI). Ankle sprain is caused by the excessive pronation and supination at the subtalar joint of ankle. The purpose of this movement is to attenuate the ground reaction force (GRF) during biomechanics movements. Therefore, higher ground reaction force will cause greater pronation and supination. Besides that, high stress intensity will also result to the weakening of the biomechanical structure [2].

Studies have been done to analyze the GRF during various athletic movements. Vertical landing and cutting movement have resulted to high peak pressure compared to running movement [3]. Midsole, which is one of the shoe's components is designed to provide cushioning to the lower extremity. EVA midsole provide increasing elastic energy absorptions when increasing force is applied [4]. Besides that, higher elastic midsole will provide higher energy absorptions thus will attenuate the force intensity at the subtalar joint.

This study is to analyze the performance of EVA midsole during vertical loading and cutting movements. A Nike Zoom midsole is modeled and simulated using finite element method to analyze the efficiency of midsole in ankle protection.

2. Methodology

Finite element analysis has been applied to provide a computational framework on analyzing the effect of midsole to ankle protections. A computational software ANSYS is used to model and simulate the midsole.

3D scanning method on the Nike Zoom midsole was applied to have the actual midsole design. The hyper-elastic material EVA is modeled using Ogden strain energy function. The material was set to have function of N= 2, shear modulus $\mu 1$=1000kPa, $\mu 2$=50kPa, Poisson's ratio v1=0, v2=0 and exponential value of $\alpha 1$=10, $\alpha 2$= -4 [4]. The air gel also has a non-linear elastic property and has higher elasticity compared to the EVA foam.

In order to analyze the performance of the midsole, the boundary condition for plantar region was split into 7 regions which are the great toe, 1st metatarsal head, central forefoot, 5th metatarsal head, media mid-foot, lateral mid-foot and heel. Based on study that has been done by Orendurff etl al., different pressures were applied to the plantar regions [3]. The midsole being tested on static structural analysis and the applied pressures are perpendicular to the applied regions.

Vertical landing and cutting movements have been chosen since it resulted to high peak pressure. Therefore, by using ANSYS simulation, the performance of the EVA midsole in providing ankle protection was analyzed.

3. Result

Appended below data represent maximum stress, strain, displacement and elastic strain at different plantar regions during vertical loading and cutting movements. The results also provide the total energy absorption by the midsole during both movements.

Table 1. Analysis of Stress, Strain, Displacement and Strain Energy Density during Vertical Loading

Region	Stress,σ (Mpa)	Strain,ε (m/m)	Displacement (mm)
Great Toe	0.8656	0.04893	1.3935
1st metatarsal	0.7104	0.05521	0.9243
Central forefoot	0.6036	0.04077	0.8774
5th metatarsal	0.5117	0.02540	0.9184
Medial midfoot	0.3905	0.03091	1.4943
Lateral midfoot	0.5465	0.03100	1.4930
Heel	1.4637	0.10073	2.1617

Table 2. Analysis of Stress, Strain, Displacement and Strain Energy Density during Cutting Movement

Region	Stress (MPa)	Strain (m/m)	Displacement (mm)
Great Toe	0.5543	0.03409	0.9310
1st metatarsal	0.4661	0.04460	0.3823
Central forefoot	0.3561	0.03802	0.8098
5th metatarsal	0.5170	0.03057	0.8679
Medial midfoot	0.4529	0.01908	1.0200
Lateral midfoot	0.5063	0.03280	1.1280
Heel	1.0431	0.09053	1.6957

Table 3. Total Stain Energy Absorptions during Vertical landing and V-cutting Movements

Movements	Total Strain Energy Absorptions (J)
Vertical landing	2.24
V-Cutting	1.27

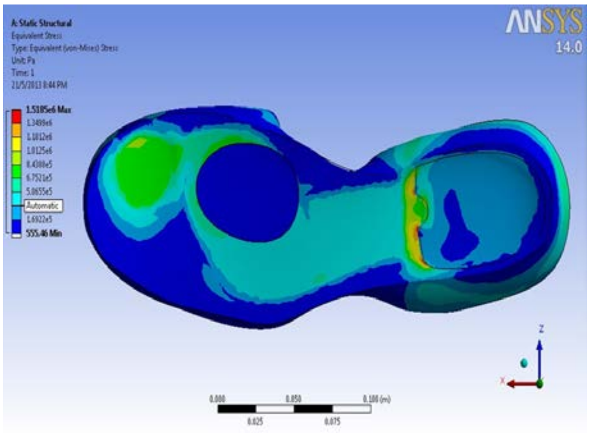

Fig. 1 Stress Intensity at Midsole during Vertical Landing

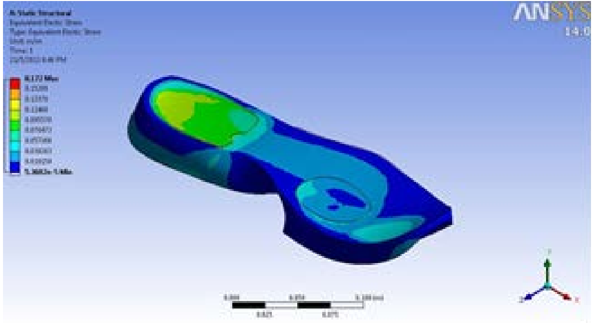

Fig. 2 Strain Intensity at Midsole during Vertical Landing

4. Discussion

The results indicate that heel region have highest amount of stress during vertical landing and cutting movements. However, larger amount of stress were analyzed during vertical landing. Based on Figure 1 and 2, the red color indicates high amount of stress and strain. Data is tabulated in Table 1 and 2 for maximum stress and strain at each region. The amount of stress correlate with the reaction force transmitted to the ankle. Based on Newton's third law, there will be opposing force to the direction of the applied force. Substantial amount of stress intensity will result to the rapture of the collagen threads which will cause swelling [1]. Besides that, high stress intensity can also cause micro damage which will result to stress fracture [5]. Figure 1 show the stress intensity during landing when plantar pressure is applied. This figure shows that the air gel encapsulated at the heel reduces the maximum stress at that region by 39%. This proves that higher elastic material will moderate the shock transmitted to the ankle region as well reduces the risk of ankle injuries.

The results of elastic deformation shows that almost 7.7% of deformation was observed at heel region during vertical landing while 6% during cutting movement. Elastic strain deformation is vital for energy absorption as higher deformation will provide greater energy attenuations. Higher elastic modulus (λ) will have lower strain which reduce the cushioning. The result of elastic strain during vertical landing is almost identical with past study that had been done where 0.129 elastic strain were recorded during vertical landing [6]. The minor differences are due to the different materials, pressure applied and midsole designs.

$$\lambda = \frac{\sigma}{\varepsilon} \quad (1)$$

Besides that, greater elastic displacement will reduce the average force transmitted to the lower extremity. Based on Newton's 2nd law of motion, longer impact time will yield to lower average force. Hence, higher elastic material will have greater force attenuation during impact loading.

Impulse momentum,

$$\sum F\Delta T = m(v_f - v_i) \quad (2)$$

The midsole is capable to absorb 2.24 J during vertical landing and 1.27 J during cutting movement. High energy absorption will result to smaller fraction of energy transferred to the lower extremity during impact. This data shows greater energy absorption compared to other research related to the energy absorption of EVA foam. The predicted energy absorption when applying similar peak pressure during vertical landing is only 1.8 J [4]. These are due to the different designs of the midsole as well with the additional energy absorption capabilities that have been introduced by the air gel.

5. Conclusions

In conclusion, the results show that elastic properties of midsole provide protection to ankle injuries. Vertical landing will result to higher stress intensity compared to the cutting movement. The hyper-elastic material of the air gel provides maximum stress reduction by 39%. The deformation at the midsole will increase the impact time as well will result to lower average force transmitted to the ankle. Besides that, midsole also provide 2.24 J of energy absorption during vertical landing and 1.27 J during cutting movement. The elastic material of the air gel subsequently increases the energy absorptions during rapid athletic movements as well providing shock attenuation.

Acknowledgment

The author would like to express his gratitude to Taylor's School of Engineering for providing financial support and the necessary facilities to complete this thesis. The author would also take this opportunity to convey sincere appreciation to Mr Alex for his guidance and support throughout the completion of this thesis.

References

[1] Fong, D et al. (2009) Understanding Acute Ankle Ligamentous Sprain Injury in Sports. *Sports Medicine, Arthroscopy, Rehabilitation*, Therapy and Technology 1, 14

[2] Susan J.H. (2012) *Basic Biomechanics*. 6th ed. New York: McGraw Hill, p.258-259

[3] Orendurff, M.S., & Rohr, E.A. (2008). Regional Foot Pressure during Running, Cutting, Jumping, and Landing. *American Journal of Sports Medicine, 36*(3), 248-253.

[4] Verdejo, R. and Mills, N., 2004. Heel–shoe interactions and the durabilityof EVA foam running-shoe midsoles. *Journal of Biomechanics* , 37 (9), p.1379-1386.

[5] Coventry, E. et al. (2006) The Effect of Lower Extremity Fatigue on Shock Attenuation during Single-leg Landing .*Clinical Biomechanics*, 21 (10), p.1090-1097

[6] Cho, J.R., & Park, S.B. (2009). Landing Impact Analysis of Sports Shoes using 3-D Coupled Foot-shoe Finite Element Model. *Journal of Mechanical Science and Technology, 23*(10), 2583-2591

Sport Shoes Traction Testing Device

Malvinder Singh[1], Mr. Alexander Chee Hon Cheong[2]

School of Engineering,Taylor's University,Malaysia , [2]School of Engineering, Taylor'sUniversity, Malaysia

Abstract— **Footwear traction is essential for sports like basketball in order to perform swift changes of directions. A huge amount of traction in basketball shoes is one of the factors that may contribute to more non-contact injuries. Therefore the experimenting of many different types of basketball sport shoes traction on the same gaming surface will be tested. The aim of this research is to study the traction of the basketball sport shoes on one type of playing surface to mainly reduce injuries like ankle injuries. A device is built to test the traction, and an experiment is conducted to obtain particular results.**

Keywords— Sport shoe traction, sport shoe testing device, traction testing device, pneumatic traction testing, basketball shoe.

1. Introduction

Traction is very important in sport shoes, but the right amount of traction is more important and too much or too little will cause injuries to athletes. Traction is the amount of maximum frictional force that can be produced between surfaces without slipping [1]. This project particularly is going to be tested only on basketball shoes. The main factors for a traction is a fast start and stop movements or performing a quick step in changing movement of direction for the participation in today's basketball games. Thus, in the industry today there are many different outsole design which promise an athlete to a huge amount of traction. However, excessive amount traction can be equally dangerous and the factor for injuries.

The study on human movement is part of this project as it deals with movement. Human movements relate to gait cycle. Gait cycle is a medical term to describe the way we walk [2]. Every human has a unique way of walking. A person's gait can be affected by injury or disease. This cycle describes the motion from initial placement of the supporting heal on the ground to when the same heal contacts the ground for the second time.

A device is needed to calculate the amount of traction in a particular shoe depending on the type of surface or ground it is used on..This device is running on pneumatic principles. This device is quite simple to operate. It can be easily pushed anywhere around to test. Any type of shoe can be tested on this device.

2. Theoretical Framework

2.1 Sport Shoes Traction Effect on Athlete

Traction of sport shoes is important for the performance and safety of an athlete. Excessive amount of traction increases the risk of foot fixation. Different amount of traction is required for different types of shoes available in the market. The right amount of traction is very important to avoid injuries during sport activities.

There are four main types of traction which is static, dynamic, translational and rotational. The translational traction basically is the amount of traction that is being resisted for the particular shoe that is being tested to slide. A typical example is that, high translational traction has more traction and low translational traction has less traction, for an athlete. Traction that resists rotation movement when any steps are taken is known as rotational movement. When an athlete is involved in a sport game, having large amount of rotational traction has a higher tendency for foot injury, whereas for small amount of rotational traction will have much lower tendency for foot injury because the amount of grip of the outsole to the ground is less and easier for the athlete to make the next move.

Besides that, static and dynamic traction explains how it contacts with the shoe outsole and the ground. Static traction is the traction that is resisting for motion when there is zero movement between the shoe outsole and the ground. For example, this type of movement resists the first move of an athlete. Dynamic traction is the traction that is resisting for motion during movement. For example, this type of traction resist for the next movement after one movement is completed.

Thus building a device to test the amount of traction in a particular brand or type of shoe outsole is very important to avoid injuries and to ensure the amount of traction is sufficient and not too much [3].

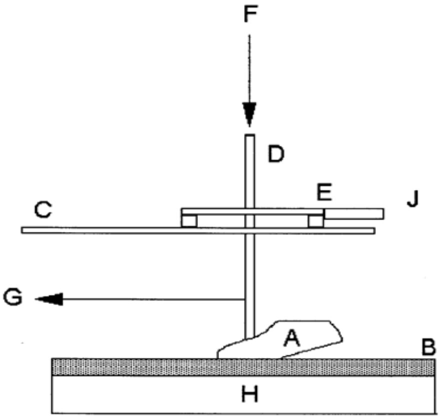

Figure 1 *Schematic Diagram of a Generic Device for measuring Translational Traction [4]*

3. Research Methodology

Building a sport shoe traction testing device was studied. There were many aspects that have been studied and it provided a lot of insight in building a sport shoe traction testing device. The device that is available in current market and information that is available is mainly on football and soccer shoes. The similar concept was used to build this device to test basketball shoes.

It can be seen that different turf and different amount of load exerted by a players affects in the cause of injuries during sport activities. Sometimes this injuries might lead athlete to lose their ability to play sports either for a long time or lifelong. Thus the studies on human gait cycles (human movement) were very vital to understand the main aspects that are connected to building this sport shoe traction testing device.

From all the studies and finding, solution to build a traction testing device has been achieved. A clear understanding on how will the sport shoe traction testing device works. It is simple and results should be accurate.

In building a traction device it is important to have a pressure regulator. This is because it independently regulates the force going to the two actuator cylinders. These two actuator cylinders are the vertical and the horizontal cylinders. The vertical cylinder forces to the vertical motion to test the surface, whereas the horizontal cylinder forces it to slide.

The vertical force is pressured externally. The force stays constant during the test. The force amount can be seen from the air pressure gauge. For horizontal force the pressure in converted into force taking consideration of the pneumatic cylinder diameter and stroke distance.

$$\boxed{\text{Resistance of shoe} = \frac{\text{Horizontal force}}{\text{Vertical force}}}$$

Figure 2 Sport Shoe Traction Testing Device

4. Results

Horizontal Force(N)	Vertical Force(N)	Slip Resistance(N)
277.33	544.63	0.51
554.63	544.63	1.00
831.93	544.63	1.52
1109.26	544.63	2.04

Table 1 Slip resistance results

5. Discussion

From the results above it can be seen that the vertical force is constant thorough out the experiment as it significant as human weight during sport activities. As for the horizontal force it can be seen that it is being changed. As this force signify the amount of force needed to move the shoe.

The amount of traction need to be significant, which is not too much or too little to reduce the number of injuries that, happens during basketball sport activities.

Slip resistance is calculated by horizontal force divided by the vertical force. The ideal amount of slip resistance should be around 1.5 to 3.0.

Different types of shoes have different amount of traction, thus shoes makes an important factor to avoid injuries. Different types of outsole of a particular shoe is usually made for particular sports where is has the right amount of traction on the particular ground where the sport is being played.

The amount of human weight also plays a big different for shoe traction as more weight can reduce the amount of traction in a particular ground. Thus, for many times of sports there are different shoes used that is suitable for the particular sport which in return will reduce the cases of injuries to the athlete.

6. Conclusions

In conclusion, traction testing device is important in order to avoid injuries during sport activities. As too much or too little amount of traction both can cause injuries or foot fixation which can lead to other health or medical problems. The study on the background of sport shoes and human movement is important in order to relate how to avoid injuries. This traction device works on pneumatic principle. Two pneumatic cylinders are connected for the vertical and horizontal movement. The amount of traction can be calculated, the vertical force divided by the horizontal force.

Acknowledgment

I am grateful and thankful to my supervisor Mr Alexander Chee Hon Cheong who gave me full support and a lot of insight in making this sport shoe traction testing device successful. This project would not have been possible with the help of my supervisor. Besides that, I would also like to thank my family, friends and other School of Engineering, Taylor's University staff that helped me indirectly in making this project a success.

References

[1] Thomas Grund, Veit Senner: Traction behavior of soccer shoe stud designs under different game-relevant loading conditions. Technische Unidersitat Munchen:2783-2788,2010

[2] Ashutosh Kharb, Vipin Saini, Y.K Jain, Surender Dhiman: A review of gait cycle and its paramters. Deptt. Of ECE, BMIET, Sonipat, Haryana, India: pp78-83,2011

[3] C.Alec Cheng, Ming-Chyuan Lin: Building an expert system for the design of sport shoes. University of Missouri-Comulbi,pp.72-77,1988

[4] ASTM International, Standard Test Methods for Traction Characteristics of the Athlete Shoe-Sports Surface Interface, ASTM International, USA:2011

[5] Martyn Shorten, Bret Hudson, Jennifer Himmelsbach: Shoe-surface traction of conventional and in-filled synthetic turf football surfaces. BioMechanica LLC, Portland, Oregon, USA

Aerodynamic Investigation of a Solar Car Body

Mark Darwin A/L Partap Singh*, S. M. Salim

School of Engineering, Taylor's University, Selangor, Malaysia

**Email: markdarwin15@gmail.com*

Abstract— **Aerodynamic forces are being investigated to provide a higher efficiency solar car. The investigation on various body designs is performed to achieve low drag coefficient and negative lift coefficient. CAD tool is used to generate various body designs while taking into account the functionality of the design. CAD drawing is then transferred to CFD for numerical solution. The outcome of this project is low drag and negative lift coefficient solar car body.**

Keywords— Solar Car, Aerodynamics, Computational Fluid Dynamics (CFD), Automotive, Drag Coefficients, Lift Coefficients.

1. Introduction

Depletion of the world's petroleum will soon force the automotive industry to change their direction in search for an alternative source of energy to power vehicles. According to a study, 80% of the world's crude oil level will be depleted by year 2050 [1]. To diminish this issue, automobiles are forced into R&D for new energy as a replacement of crude oil. Promising latest technologies, automotives are moving into the direction of using solar technology to generate power. The power generated will be relatively much smaller compared to the power output from crude oil. Therefore the aerodynamics forces, which are the drag and lift forces, need to be investigated in order to increase the efficiency of the car. There are 2 methods that can be used to investigate drag and lift coefficients of a car, a full-scale wind tunnel investigation or numerical modeling using Computational Fluid Dynamics (CFD). CFD provides an interactive tool to the user, which uses powerful computer and applied governing mathematics to model different kind of engineering fluid flow problems. This tool is gaining popularity due to the large saving in resources and time by performing the analysis without the having to build the actual end product. CFD provides easy modification to the problem by just editing through the simulation tool.

The aim of this study is to investigate various body designs of the solar car and fluid flow parameters such as low drag coefficient and low negative lift coefficient for the final design of the solar car body. The design of the solar car is in accordance to the practicality, functionality, design constraint, and rules & regulation of the race.

2. Methodology

NACA profile is always known to have low drag coefficient and this provides the backbone of this design. NACA 2420 is selected, as it is the smallest profile that is able to fit onto the underbody and the driver's knee roll hoop. The coordinates of NACA 2420 profile are generated from a NACA profile coordinate generator software, which edited its format in order for ANSYS software to be able to read the coordinates. As the backbone of the design (NACA 2420) is been selected, the canopy will be the manipulating design factor. Enhancement of the canopy is being done from the first to the last design, to provide better results.

Fig 1. Computational Domain for CFD Simulation Setup (Front View)

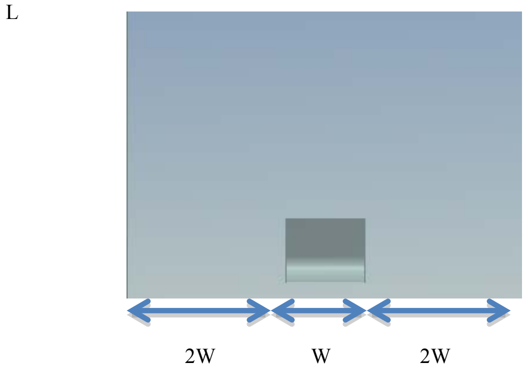

Fig 2. Computational Domain for CFD Simulation Setup (Side View)

This experiment uses the same computational domain as the Middle East Technical University solar car project [2]. This known computational domain will provide a benchmark when comparing the results generated. Fig 1. and Fig 2. provides the dimensioning of the computational domain that is being used throughout this study. At the inlet to the beginning of the body, it's given a length (2.2 meters) of the body. As for this study, the air inlet speed is defined as 8.33 m/s, which is equivalent to 30 km/h [3]. This air speed is defined due to the data gained from the average speed required during the race. Reynolds's number used in this experiment is defined as $125.49*10^4$. The density value used is 1.225 kg/m^3. A study has been done on manipulating the area behind the body, by replacing it from 8L to 3L. Table 1. shows the results generated have very minimal differences between them.

Table 1. Difference in Drag and Lift Coefficients With the Change of the Computational Domain

4th Design	Drag Coefficient	Lift Coefficient
8L (17.6 meters)	0.297	0.101
3L (6.6meters)	0.298	0.105
Differences	0.001	0.004
% Of Differences	0.34%	3.87%

After completing the design of the solar car body in the Design Modeler, it then moves on to the Meshing stage; to produce the mesh for the body and its computational domain. The meshes are being concentrated more on the body to ensure higher accuracy of results. The number and size of meshes have been altered to ensure it produces a good mesh with a high mesh quality ratio. The total number of elements used for the computational domain is 710 thousand. There is no need for a higher amount of element as the area of the computational domain is not large.

Turbulences model of RKE (Realizable k-ε) is used. The basic model of a standard k-ε is being modified in order to overcome its weakness and the outcome of the modification Realizable k-ε is achieved [4]. Turbulences model of RKE is used based on the study done on “Computation of Drag Force on Single and Close-Following Vehicles” [5].

3. Results & Discussion

Table 2. below shows the data generated from the simulation done in CFD to generate drag and lift coefficients. A total of 8 solar car body designs were investigated throughout this project period. The design results are tabulated in the table below.

Table 2. Drag and Lift Coefficient for the Various Design (1st-8th) of the Solar Car Body

Design	Drag Coefficient	Lift Coefficient
1st	0.103	-0.0285
2nd	0.374	0.0527
3rd	0.310	-0.00335
4th	0.297	0.101
5th	0.265	-0.365
6th	0.277	-0.00415
7th	0.235	-0.0752
8th	0.305	0.1523

The 1st design was the design of just the airfoil of NACA 2420. The simulation is performed to provide a baseline idea of the lowest possible drag coefficient. The 2nd design had the largest surface area of all the designs. With this maximum and minimum drag coefficient data gain, all designs should fall within this range. Improvements have been done on the canopy height, canopy profile, starting point of the canopy, and the gradient of the canopy. These improvements are done from the 3rd design to the 7th design. On the 8th design, improvements have been done to the diffuser angle of the undercarriage of the body. This improvement showed high lift coefficient as the diffuser slows air velocity and increased the pressure acting upwards. This pressure directly lifts the body up, creating a positive lift.

The best overall design is the 6th design, even though when compared to the 5th design it did not have the lowest drag coefficient, it had a much lower negative coefficient of lift. The higher amount of coefficient of lift will create rolling resistances for the car during the race hence decreasing the overall efficiency of the car. Nevertheless, improvements have been done to the 6th design in order to lower the value of negative coefficient of lift.

Table 3. below shows the improvement done to the 6th design. This design tweaked the angle of attack (AoA) to eliminate the negative lift coefficient of the solar car body. From the table, it shows that the AoA that produces the lowest negative lift is when the AoA is at 0.5 degree. We do not want to have a high positive lift as well as this will compromise the safety and stability level of the solar car during the race.

Table 3. Varying of the Angle of Attack Changes the Drag and Lift Coefficients.

Angle of Attack	Drag Coefficient	Lift Coefficient
0	0.277	-0.00415
0.5	0.272	0.000643
1	0.267	0.00956
2	0.2592	0.0277

Therefore, the final drag coefficient is 0.272 and 0.000643 for the lift coefficient. The drag coefficient of this body is lower as compared to the wining team from the Middle East Technical University, which has a drag coefficient of 0.366 [2]. The lift coefficient for the Queenís University Solar Vehicle Team was close to 0 lift coefficient and this was the wining factor for the particular race [6]. With this parameter taken into account it provides a solid ground on the success of the Taylor's University solar car performances.

4. Conclusions

In total 8 designs were produced. The best design is the 6th design, which is being investigated further in term of tweaking on the Angle of Attack (AoA). The study showed that the size of the computational domain does not affect the outcome of the results. Once the body is manufactured, it can be tested in a full-scale wind tunnel in order to validate the results generated from ANSYS FLUENT. The results generated from the simulation tool were compared with other wining universities that participated previously in the World Solar Car Challenge. With almost similar data results as the other teams, Taylor’ are confident we are able to lead Taylor’s Shell Eco-Marathon Solar Car team to greater heights.

Acknowledgment

I would like to thank my present mentor, Salim Mohamed Salim and my former mentor, Harun Muhammad Ismail for their guidance throughout this project. I’m also grateful to work alongside my team members, Teh Ren Yu, the chassis department and Navid Toosi, the leader of the Taylor’s Shell Eco-Marathon team. Last but not least I would like to thank my classmate Loong Yun Kit support and motivated me throughout this project.

References

[1] David Moo, *“Statically Crude Oil Production Handbook”*. Version 2, 2008

[2] Ethem Ersoz. (Sept 2006). Development of a Racing Strategy for a Solar Car, 47-55.

[3] Norman, K., (2013). *Shell Eco-marathon Official Rules 2013,* Chapter 2, pp 11.

[4] Shih T. H., Liou W. W., , Shabbir A. , Zhu J. (1995). *A new k-ε eddy – viscosity model for high Reynolds number turbulent. Computers Fluids*, 24: pp 227-238.

[5] Orselli, E., (2006), “Computation of Drag Force on Single and Close-Following Vehicles,” M. S. Thesis, Middle East Technical University, Turkey.

[6] Susan, Y., Michael, D., (April 2000). *Queenís University Solar Vehicle Team*, pp. 1-3.

Design and Evaluation of Enhanced Handheld Hydraulic Wrench

Mohamad Fadhlan Aziim M.N.*, Mohammad Hosseini Fouladi

Department of Mechanical Engineering, Taylor's University, Malaysia

** Corresponding Author: parklan_symphonyz@yahoo.com*

***Abstract*— This document gives information about design, evaluation and fabrication of a portable wrench powered by fluid power system. The wrench is designed to be a substitute to a conventional wrench for opening wheel nuts. The design of the portable wrench has gone through three stage of design process; initial, intermediate and final. A prototype to test the mechanism was built with some limitations. The design was modeled using modeling tool and a structural analysis has been done using a simulation tool. Torque of 120 Nm was taken as the baseline for the amount of tightening torque of wheel nuts. The safety factor of the assembly is 1.35 based on the lowest safety factor of the part in the assembly.**

Keywords—Hydraulic, Portable Wrench, Torque Wrench, Fluid Power System, ANSYS Static Structural Analysis

1. Introduction

Wrench comes in different sizes and designs. For conventional wrench, the bigger the size of the wrench, the greater the torque it can produce due to having longer arm to apply force. However, in the case where size is the limiting factor, the amount of torque can be increased by increasing the applied force.

Based on car owner's manual, the value of tightening torque of wheel nuts for sedan-type vehicles is in the range of 100 Nm to 110 Nm. The baseline output torque for the final product was set at 120 Nm, which is higher than the average value.

This project focuses on the idea of a compact and portable wrench powered by hydraulic which minimizes human effort to open wheel nuts of sedan-type vehicles. The wrench which is called as Enhanced Handheld Hydraulic Wrench (EHHW) was designed to be user friendly, compact and portable.

2. Fluid Power System (FPS)

There are seven basic components in FPS; a tank, pump, power source to drive the pump, control valves, actuators, hose line and the working fluids. Fluids can be categorized as gases and liquids. Because EHHW uses hydraulic fluid, the working fluid here refers to the hydraulic fluid.

The work is carried out by the pump that sends pressurized fluids into hydraulic actuators which drive the final mechanism to perform useful work. The system could produce very high horsepower and have tolerances up to one tenth-thousands of a centimeter at the same time, making it a very versatile system [1]. In addition, the force multiplication can be done without the use of gears, pulleys and levers. With less moving parts in the system, the chance of failure is minimal. Not only that, it is also capable of producing constant output torque regardless of speed changes [2].

3. Research Methodology

The design of EHHW has been through three phases of design stages; initial, intermediate and final stage. A stress analysis using ANSYS has been done on the final design. A prototype to test the workability of the mechanism was built.

3.1 Design Stages (Initial, Intermediate and Final)

The design of EHHW in the initial stage was inspired from the most basic shape of a bell crank which is a triangle. The main frame was designed in triangular shape which has two mounting points; one for the wrench and the other for the hydraulic cylinder. Two design constraints were introduced to ensure the final product to be compact in size; the length of the handle must not exceed 200 mm and the height of the triangle must not be higher than 90 mm.

In the intermediate stage, important design parameters which have great effect on the output torque were identified and a new design was drawn. It was found that the length of the handle has the least effect to the output torque produced. However, some of the parts were found in interference of each other. Therefore, to avoid complications, the design has been changed.

With the changes made, the EHHW has now entered the final stage of the design process. As a whole, EHHW has all the seven components of FPS. The pump and tank come together with a manual hydraulic pump. Hydraulic cylinder as the actuator is linked to the wrench that will do the opening of wheel nuts. The whole components are connected together with hydraulic hoses and human force will be used to power the pump which drives the whole system. A single mounting frame will hold the entire parts together as shown in Fig. 1. EHHW has user friendly features like adjustable stopper which its position can be adjusted and multiple size sockets can be used on the same wrench to accommodate different sizes of wheels.

Fig. 1 Complete EHHW assembly without hydraulic pump

3.2 Stress Analysis of EHHW in ANSYS Simulation

The stress analysis of the design has been done in ANSYS Workbench. A free body diagram was drawn to determine all the forces acted on the EHHW during operation. The loadings were configured as Fig. 2 to copy the actual operation. The direction of the forces from the hydraulic are labeled as D and E while C is pretension bolt loading of 60000 N. The bolt pretension load resembles a nut that has been tightened with 120 Nm of torque. The magnitude of loads D and E are

833 N. The stopper is fixed at the bottom (A) because in the real operation, it will rest in between the gap inside the wheel. Fixed points B and F resemble the wheel and wheel bolt.

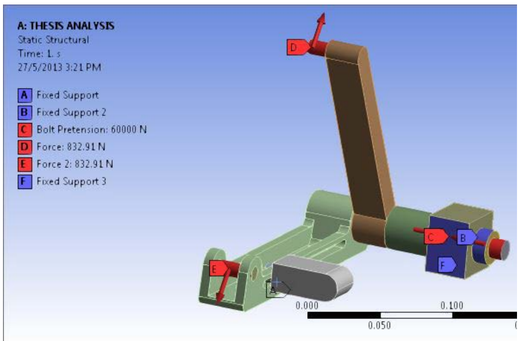

Fig. 2 EHHW Loadings and Supports Setup in ANSYS

The method used for the meshing was automatic. The size of the meshing for the stopper, wrench, main frame and holding bolt was controlled. A total of four simulations were done and the size of the meshing was different for every run. The size of the meshing was set to be default for the first run followed by 5 mm, 4 mm, and 3 mm for second, third and fourth run respectively.

3.3 EHHW Prototype

A prototype of EHHW has been made to test out the workability of the opening mechanism (Fig. 3). The design, materials and equipment used for the prototype are altered due to limited material and apparatus. However, the alterations are acceptable because the prototype is only tested on its mechanism only. The prototype was not tested for actual operation.

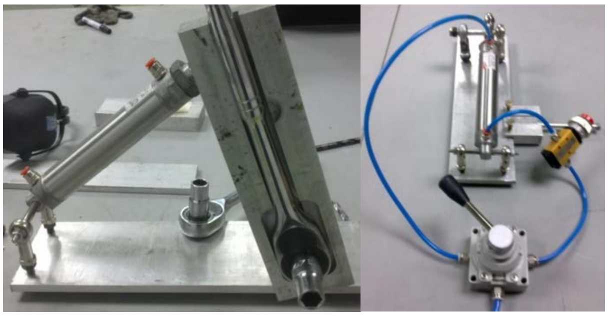

Fig. 3 EHHW Prototype

4. Results

The results of the simulations for the wrench, main frame, stopper and holding bolt are tabulated according to the different meshing size in Table 2.

The opening mechanism tested using the prototype worked finely as there is no parts interference. The wrench turns accordingly as the piston extends. However, because the prototype uses pneumatic cylinder as oppose to hydraulic cylinder, the wrench turns with high speed.

5. Discussion

Based on Table 1, the highest value of stress can be seen on the wrench. Compared to the wrench, the other parts experienced significantly lower stress. The material selection process was done based on the result of the stress analysis with more attention towards the wrench.

Aluminum alloy 2011-T3 with yield strength of 295 MPa was selected as the material for the wrench. The alloy was chosen over steel because the EHHW will be self-fabricated using university facility where there is a limitation of equipment which makes other materials not feasible to be used. In addition, lightweight is a very important design factor for EHHW and aluminum alloy has a good strength to weight ratio even though yield deformation can be a concern. However, if the yield strength of the material (YSTOM) is higher than the maximum stress value, the part would not deform permanently. The same alloy is also used for the main frame.

Table 1. Maximum Stress Value

Parts	Max. Stress according to mesh size (MPa)			
	Default	**5 mm**	**4 mm**	**3 mm**
Wrench	154.0	184	197.6	218.9
Main frame	65.0	172	116.5	129.8
Stopper	40.5	72.1	49.9	61.4
Holding Bolt	10.6	15.4	10.7	10.8

Factor of Safety (FOS) is another important factor that needs to be taken into consideration while designing. FOS is defined as, given the YSOTM, the ratio of maximum load over operational load [3]. FOS of the wrench is 1.35. That means the wrench can take up to 35 percent more load. Because the value of FOS for the wrench is the lowest for the EHHW, it can be said that the FOS of the whole assembly to be 1.35. It is important to consider having FOS to be more than one so that the assembly would not fail when overload.

When fully retract, EHHW is 200 mm in length, 150 mm in height and 100 mm width and becomes longer by 30 mm when it fully extend. Pressurized hydraulic fluid is supplied to the hydraulic cylinder by hydraulic pump which is manually operated by human. The wrench turns as the hydraulic piston extends. For a 32 mm diameter piston, a pressure of 1.1 MPa is needed to provide the required force to produce 120 Nm of output torque. Given the stroke of 125 mm, the volume of hydraulic fluids required is 0.1 litre. Therefore, any hydraulic pump that can provide the required pressure and any reservoir that has a capacity of at least 0.1 litre can be used for EHHW. However, a small hydraulic pump is preferred for portability purpose.

5. Conclusion

Aiming to minimize human effort to open wheel nuts, EHHW was design to be user friendly, compact and portable. The human force is amplified with the use of the hydraulic pump. Aluminum alloy was chosen over steel so that the final product will be lightweight. The stopper which its position can be changed can accommodate different size of wheels. With minimum FOS of 1.35, EHHW could withstand 35 percent more loads which means it can also open over tightened wheel nuts.

Acknowledgment

I would like to thank my supervisor, Dr. Mohamad Hosseini Fouladi, for all of his support and guidance.

References

[1] Sullivan, J. A. (1997). *Fluid Power Theory and Application*. New Jersey, United States: Prentice-Hall.

[2] Esposito, A. (2009). *Fluid Power with Applications*. Location, State: Prentice Hall.

[3] Juvinall, R.C.,&Marshek, K.M. (2012). *Machine Component Design*.5th Edition. Singapore: John Wiley & Sons, Inc.

Design and Analysis of A Thermo-Acoustic Refrigerator

Mohamed Gamal Mekdad*, Abdulkareem Sh. Mahdi Al-Obaidi

Department of Mechanical Engineering, School of Engineering, Taylor's University, Malaysia

**Corresponding Author: al-hoet1988@hotmail.com*

Abstract— **The design and functionality of thermo-acoustic refrigerator have been the focus of considerable attention from the research community since 1980. This environmental friendly technology has the potential to replace conventional refrigerator once the improvements in design and technology are realized. Thermo-acoustic is a term used to describe the effect arising from sound waves creating a heat gradient, and vice versa. In this paper, a typical modified thermo-acoustic refrigerator (TAR) consisting of acoustic driver (loudspeaker), resonator tube, thermocouple, stack, and a heat exchanger is designed. The effects of some design parameters such as wave patterns, frequency, and heat exchanger of thermo-acoustic refrigerator system were studied. It was found that a sine wave pattern lead to superior cooling effects compared to other wave patterns tested. Also adding the heat exchanger contributes significantly in increasing the temperature drop achieved by the modified TAR.**

Keywords— Thermo-Acoustic refrigerator, Sound wave, Cooling system, Wave pattern, Frequency, Stack

1. Introduction

From creating comfortable home environments to manufacturing fast and efficient electronic devices, air conditioning and refrigeration still expensive, yet essential, services for both homes and industries. However, in an age of energy and environmental development, conventional cooling devices continue to generate greenhouse gases with high energy costs [1]. As the technology and knowledge improve year by year, a new innovative method has come to minimize the effect of global warming and at the same time has a low cost and long life usage. This innovation is the thermo-acoustic refrigerator (TAR). TAR was first discovered by European glass blowers 200 years ago when it was noticed sound generated when a cold glass tube was placed next to a hot glass stem.TAR uses the sound effect to convert temperature differential into mechanical energy or mechanical energy into temperature differential. The advantages of using TAR are simple and clean mechanical system which doesn't use pistons, cranks and lubricants as the conventional refrigerator or air condition cooling systems. Moreover, thermo-acoustic refrigerators consider environment friendly and clean products since they don't produce harmful gases that cause global warming or stratospheric ozone depletion.

2. Theoretical Background

Thermo acoustic refrigerator uses standing waves to generate pressure difference along the resonator tube. Normally, waves do not reflect uniformly, resulting in constantly shifting gradients. However, in TAR the sound waves are reflected in such a way that they become standing waves, or waves that are self sustaining and steady. This behaviour generates a pattern of points that have alternating pressure maximums and velocities.

One of the important fundamental sciences behind thermo-acoustic refrigerator is thermodynamics, in specific the study of heat transfer. The ideal gas law states that

$$PV= \rho RT \tag{1}$$

where P, ρ, and T are the pressure, density, and temperature of the gas, respectively, and the R is the gas constant (for air R=287 J/kg·K). This law states that changes in gas pressure is directly proportional to changes in temperature, as the pressure of gas increases, the gas temperature also increases.

2.1. Frequency

Any sound wave has a specific number of oscillations per second, called the wave's frequency, and it is measured by the unit Hertz. In thermo-acoustic refrigerator closed tube, the required resonant frequency needed to get the maximum heat transfer rate is defined by the formula shown below.

$$F=a/(2L) \tag{2}$$

where a is the speed of sound and L is the resonator tube length. The temperature T_m is given by,

$$a = \sqrt{\gamma R T_m} \tag{3}$$

2.2. Penetration depth

Thermal penetration depth is one of the critical variables in designing thermo-acoustic refrigerator – in particularly the stack design. Thermal penetration depth is the spacing between stack walls. This variable helps to design the space between stack walls in a way that the spaces are not too close or too far,. According to G.W. Swift, the ideal spacing in a stack is 4 thermal penetration depths [2]. The Thermal penetration depth δ_k is given by the formula shown below:

$$\boldsymbol{\delta}_k= \sqrt{\frac{2k}{\rho c_p \omega}} \tag{4}$$

where k, ρ, c_p are the thermal conductivity, density and constant-pressure (isobaric) of the working fluid within the pore, respectively, and ω is the angular acoustic frequency.

3. Experimental Design

The thermo-acoustic refrigerator was constructed using the following materials (Fig.1):

1) Resonator tube 2) Stack 3) Rubber plug
4) Loud speaker (1000watt) 5) Box
6) Thermo-couple 7) Multi-meter

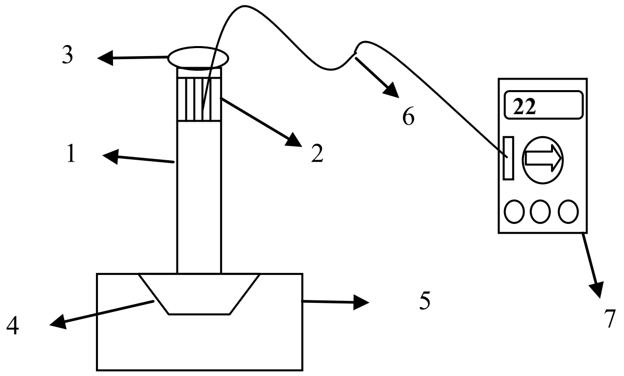

Fig. 1. Schematic of the thermo-acoustic refrigerator.

4. Result and Discussion

Once the thermoacoustic refrigerator is constructed, it was tested using a frequency of 260 Hz. Based on this frequency, the position of the stack was adjusted to reach the maximum temperature difference. Figure 2 shows the different stack positions and its corresponding temperature. The maximum temperature difference occurs when the stack position at 55 mm from the end of stack to the closed end of the resonator tube.

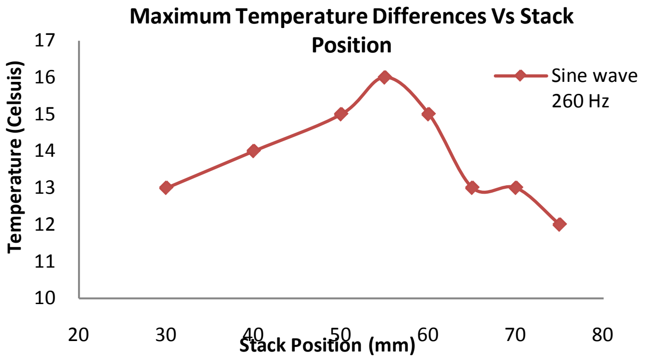

Fig. 2. Maximum temperature difference versus stack position.

From the optimum stack position found, a result was conducting to find the effect of frequency and wave pattern on the TAR. A range from (230 -300) Hz of frequency and three different wave patterns (sine, square and triangle) were used in the experiment. Figure 3 shows the result of maximum temperature difference obtained by the three wave patterns.

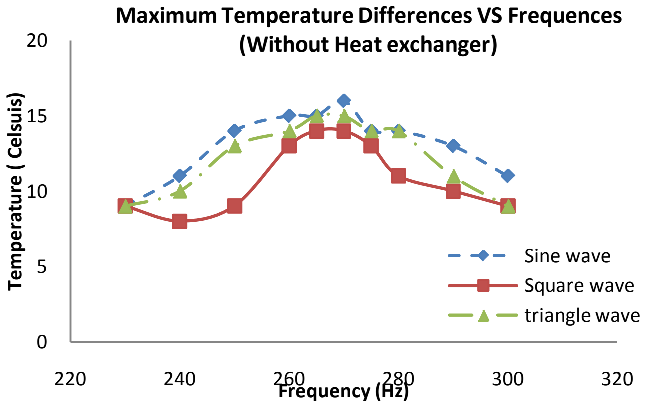

Fig. 3. Maximum temperature difference versus frequencies.

The maximum temperature difference occurs when the frequency is 270 Hz for the three different wave patterns; however sine wave pattern generates the highest temperature difference compare to square and triangle wave patterns. It has a temperature difference of 16°C, followed by the triangle wave which has 15°C and lastly is the squared wave which has 14°C. Similar behavior and trend but with different temperature drop have been achieved by Abakr et al. [3].

A significant improvement has been achieved in the current work to obtain more temperature difference by adding some sort of heat exchanger to the stack. Heat exchanger is one of the important methods that used to improve the performance of TAR. This method was used in Hofler's thermo-acoustic refrigerator. Hofler used rectangular copper strips as a heat exchanger [4]. The idea of heat exchanger is that the cold heat exchanger removes heat from a cold temperature reservoir and supplies it to the cold side of the stack. Figure 4 shows the new modification of the stack.

Fig. 4. A photograph of the modified stack.

Using the new stack modification, a result was conducted to analyze the effect of the heat exchanger on the thermo-acoustic refrigerator. Figure 5 shows the result of temperature difference corresponding to three different wave patterns and the new modification of the stack.

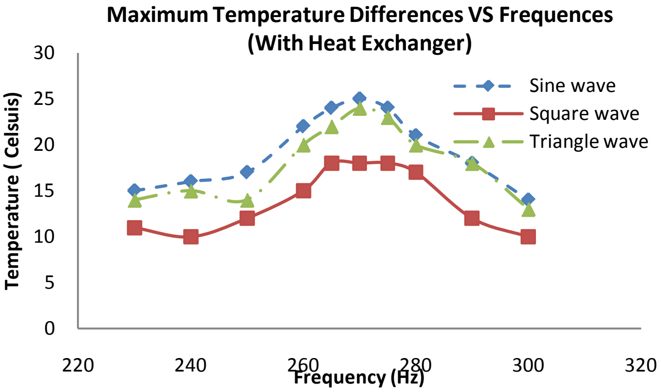

Fig. 5. Maximum temperature difference versus frequencies.

The heat exchanger improved the performance of the TAR, as the temperature difference increases compare with the old design (no heat exchanger). At 270 Hz sine wave pattern achieved the highest temperature difference of 25°C, followed by is the triangle wave which has 24°C and lastly is the squared wave which has 18°C.

5. Conclusion and recommendation

In conclusion, the influence of parameters such as stack position, stack heat exchanger, frequency and wave patterns were studied. It was found that sine wave gives the highest temperature difference; also adding heat exchanger improves the total performance of TAR. The current study is just one part of an ongoing overall study and analysis of the effect of other parameters such as geometry of resonator tube and stack.

Acknowledgment

I would like to take this opportunity to thank Dr. Abdulkareem for his guidance in developing this project, and also Dr. Yousif Abakr, university of Nottingham, Malaysia for his valuable advices.

References

1. Newman, J.; Cariste, B.; Queiruga, A.; Davis, I.; Plotnick, B.; Gordon, M.; and San Martín, S. (2006). Thermoacoustic refrigeration. *GSET Research Journal*, 1-9.
2. Swift, G.W. (1995). Thermoacoustic engines and refrigerators. *Physics Today*, 48, 22-28.
3. Abakr, Yousif A.; Al Atabi, Mushtak; and Baiman, Chen (2011). The influence of wave patterns and frequency on thermo-acoustic cooling effect. *Journal of Engineering Science and Technology* (*JESTEC*), 6(3), 392-396
4. Hofler, T.J. (1986). *Thermoacoustic refrigerator design and performance*. PhD. Dissertation, University of Calfornia, San Diego.

Design and Implementation of a Micro Scale Radio Frequency Energy Harvester

Bashir Beikzadeh[1],

[1]*School of Engineering, Taylor's University, Malaysia*
Corresponding author bashir.beik@gmail.com

Abstract— **This paper discusses the design and implementation of a Radio Frequency (RF) energy harvester from ambient sources. Frequency of 1800 MHz was found to be suitable for harvesting as it contains the highest energy levels. A system design consisting of antenna, matching circuit and voltage multiplier is presented. An array antenna with 8 arrays is simulated for the targeted frequency. The voltage multiplier is simulated and it is concluded that 3 stages of multipliers is the optimum value for a 100 load with a voltage of 748 mV. A circuit was constructed with 3 voltage multiplier stages outputting a total ambient power of 3.60 ± 2.4nW, and 24.01 ± 1.96 µW when fed with external RF source. The power levels, when fed, where enough to power a LED and a small digital clock**

Keywords— Radio frequency, harvester, energy, micro-power, antenna

1. Introduction

The environment contains many different forms of ambient energy including mechanical and electromagnetic. These can be harvested and utilized for conversion into electrical power for applications in devices which use them. [1] Benefits of such ambient energy harvesting comes with replacing the need for batteries which can be both economical and reduce waste created by disposing batteries. This project targets ambient energy in form of electromagnetic waves in the Radio Frequency range which is defined as frequencies in range of 3kHz to 300 Ghz[2].

The benefits of targeting RF ambient energy are due to its advantages over other types of ambient energy sources such as solar cells and wind turbines. These include the fact that RF waves exist in virtually all populated areas, that they are present at all times of the day and year, and that they can be made in smaller sizes as the only required part are an antenna of a few cm long and a circuit. The major drawback however is that the energy acquired is very small and can only be used for low-powered applications [1].

2. Theory

Array antennas are used for capturing RF energy due to their benefit of being directional and beam-forming. The Array Factor for the array antenna is given by $AF = \dfrac{\sin(N\beta d \cdot \cos\phi + N\alpha/2)}{\sin(\beta d \cdot \cos\phi + \alpha/2)}$ where N is the number of arrays, β is 2pi/wavelength, and d is the distance between arrays, and α is the phase shit. [3][4].

3. Methodology

First stage of research involves finding out the sources of RF energy in an urban area and take into account their frequency ranges, power levels and reliability factors. Once the optimum frequency is decided a circuit is designed to simulate the antenna and other circuits associated with the circuit.

3.1 Sources of RF Energy

Table 1 shows the major sources of RF energy in a typical populated area. These are categorized based on their frequency ranges, typical power densities [5], and reliability which is how likely they are to transmit at all times of the day and year.

Source	Frequency	Power Density ($\mu W/cm^2$)	Reliability
FM Radio	87.7-107.5 MHz	0.005	Not around the clock
TV	200-500 MHz	0.005	Not around the clock
Mobile Phone Base Tower	900 MHz, 1800 MHz	30-10000	Full reliability
Wifi router	2.4G Hz	10-20	Not reliable

Table 1 shows the different sources of RF radiation and their characteristics

From the table it was concluded that the optimum frequency range was in the range of 900 MHz or 1800 MHz. The frequency of 1800 Mhz was selected as the target frequency as the majority of cellular providers were operating at that frequency in Malaysia and the world [2].

3.2 System Design

The system was designed to be able to convert RF energy of 1800 Mhz into a DC voltage large enough to power a small device. It consists of a receiving antenna which is designed to capture the target frequency, a matching circuit that increases the power acquired from the antenna, and voltage multiplier which also acts as a AC to DC rectifier [1][7]. The rectifier is needed to convert the sinusoidal waveform into steady direct current for use in a device. The voltage multiplier is needed because the devices cannot function without high enough potential difference. This is done at the expense of lowering the current [6]. Figure 2 shows the system overview.

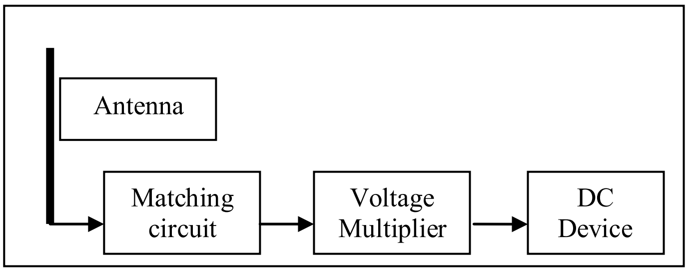

Fig. 2 shows the system overview of the RF Energy Harvester

4. Results and Discussion

Simulations were conducted for antenna and voltage multiplier circuits

4. 1 Antenna

The antenna can be of different types such as a simple dipole antenna which is not directional and therefore receives equal amounts of energy from all angles. For a frequency of 1800 MHz the optimum antenna length was calculated to be 7.94 cm. A more efficient antenna is an array antenna which can be pointed at the source (in this case cellphone base tower) to harvest more power. Using a Java-based antenna simulator [8] array antennas with different array numbers where simulated showing greater gain with more arrays in Fig. 3.

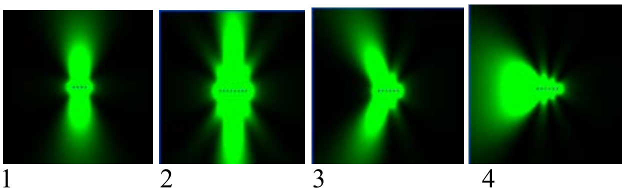

Fig. 3 An antenna array directional intensity with 4 arrays (1), 8 arrays (2), phase shift of 30 deg (3), and phase shift of 60 deg (4)

As observed the gain of the antenna can be increased by increasing the number of arrays. Beam forming may be done by adjusting the phase shift. This way the antenna would only capture RF energy from one particular direction and would therefore be more efficient.

4. 2 Voltage Multiplier

A voltage multiplier was simulated in Multisim to determine the optimum number of stages that would result in maximum voltage with minimum power loss.

The multiplier consists of schottky diodes which are chosen due to their low forward voltage for operation. This is important due to the very low power derived from the antenna. The circuit also uses ceramic capacitors. The value of capacitance controls the ripple voltage of the DC output. The relationship between ripple voltage and capacitance is that they are inversely proportional therefore to minimize ripple 100nF capacitors are chosen. Figure 4 shows the circuit design in Multisim.

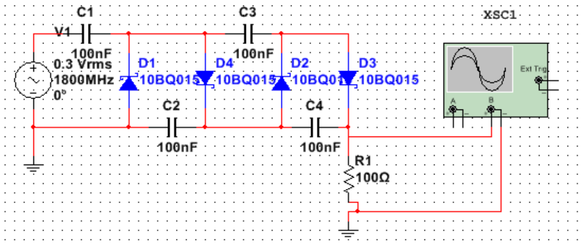

Fig. 4 Design of the Voltage Multiplier in Multisim

Figure 5 shows the results of the voltage obtained versus number of stages.The simulation showed that the output voltage of the multiplier increased with increasing stages reaching a peak at 3 stages for 100 ohm load, and at stage 4 for 1k ohm and open circuit loads. After that as more stages were added the output results in a drop in voltage. The explanation for this is that more components create more energy loss in the system [6] and therefore the optimum number of stage is found to be 3. Since the power is fixed, the voltage drops with decreasing load resistance. A 1 k ohm load produced a maximum of 1.029 mVoutput voltage.

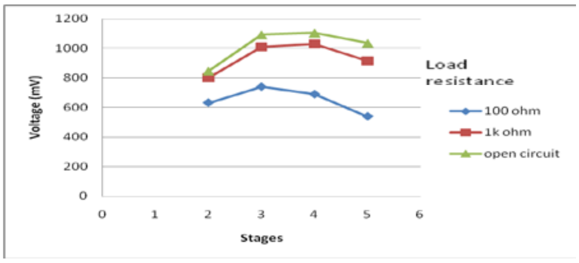

Fig. 5 The maximum voltage obtained from the output of the voltage multiplier versus the number of the stages for different types of load resistance.

4. 3 System Construction

A circuit was constructed with 3 voltage multiplier stages outputting a total ambient power of 3.60 ± 2.4nW, and 24.01 ± 1.96 uW when fed with external RF source through the dipole antenna with 2dB gain. The power levels, when fed, where enough to power a LED and a small digital clock. Figure 6 shows the circuit implementation.

Fig. 6, RF Energy harvester construction

5. Conclusions

Overall it was found that the frequency to target which corresponds to mobile phone base tower frequency of 1800 MHz is the most suitable due to its power and reliability. The antenna is more suitable to be an array antenna instead of a dipole antenna due to its higher gain and directionality. The voltage multiplier would have the most efficient operation at 4 stages with a value of 1.029 mV at 1k ohm load.

Acknowledgment

I would like to thank my supervisor Dr Pirapaharan Kandasamy for his help and guidance.

References

[1] D. Bouchouicha. et al (2010). *Ambient rf energy harvesting.* Manuscript submitted for publication, Retrieved from http://www.icrepq.com/icrepq'10/652-Bouchouicha.pdf

[2] GSM frequency bands by country, http://www.worldtimezone.com/gsm.html

[3] PowerCast. (2009). *Rf energy harvesting and wireless power.* Manuscript submitted for publication, Retrieved from http://powercastco.com/PDF/2009SensorsExpo1.pdf

[4] Li Bom .(2009). *Multiband radio frequency energy harvester*. Retrieved from http://www.isr.umd.edu/research/posters/2010_posters/Goldsman_Multiband_RF_Energy_Harvester.pdf

[5]Thomas Hauman et al (2009). *HF-radiation levels of GSM cellular phone towers in residential areas*

[6] H. Yan . (n.d.). An integration scheme for rf power harvesting. Manuscript submitted for publication

[7] Minhong Mi et al (2005). *RF Energy harvesting with multiple antennas in the same space*

[8] Java Antenna Simulator http://www.falstad.com/antenna/

Computer Intelligent System for Control and Collision Avoidance at Auto-landing Using the Mammal (e.g. bat) Intelligence and Signals.

M.H.Sharifi[1*]

[1,] *School of Engineering, Taylor's University, Malaysia*
sharifi.mohammadhossein@sd.taylors.edu.my

Abstract — **Nowadays most of the aircrafts are equipped with automatic landing system and they rely on Instrument landing system. Limitations of commercial control system and auto landing systems have led us to use artificial intelligence system inspired by bat's behavior to control auto landing. In order to develop such system, studies are done numerically. By using MATLAB software, the aircraft motion is simulated and developed neural network systems is expected to be trained by bats intelligence.**

Keywords— Collision avoidance, bat's intelligence, auto landing intelligent system, neural networking control

1. Introduction

Landing and approaching are the most challenging stage of flight. In order to have a smooth and safe landing, the aircraft wheels must make contact with the ground in a satisfying way within the defined surface of the runaway. Other factors such as six degrees of freedom of the aircraft must be attributed in the kinematics of the airplane. Commercial control theory's limitations have left no other ways but using computational intelligence. Intelligent control systems namely neural network, derive control patterns where the regime is unknown and it operates over large range of uncertainties. [5] The fascinating phenomenon of echolocation in mammals especially bats has raised hope in different field of science such as signal processing and intelligent control among researchers to improve reliability.

Training the neural network by bats intelligence is unique method that has been proposed and the applications has been discussed here for controlling the auto pilot system. The document is organized as follow: Part 2 presents particulars of the background and information on common auto landing problems, whereas part 3 provides the model used for the simulations of aircraft flight. Part 4 defines the application of bats intelligence on training neural network. Part 5 presents discussion and results and finally part 6 is the conclusions along with ongoing work in progress and future research.

2. Auto landing problem

In conditions when visual references are not reliable enough, landing aids should be used. Hence, in almost every airport Instrument Landing System (ILS) is extensively operated which helps pilots to make decision during landing [3]. At the point of height decision, the pilot should be able to clearly observe the runway to continue the approach and proceed; otherwise the pilot should take over the aircraft. [2] This procedure has been proven and it is reliable however, it's still not widely applicable due to the costs involved for required on board equipment.

According to Federal Aviation Admiration's regulations, there are certain dispersion limits levied by the environment which are: headwinds up to than 25 knots (28.75 mph); tailwinds of up to 10 knots and crosswinds less than 15 knots. Plus, a moderate turbulence and a wind shear of 8 knots per 100 ft from 200 ft to touchdown. Outside of these flight conditions, the Auto Landing System (ALS) must be deactivated and the pilot takes over. National Transportation Safety Board has reported that 36.4% of the flight safety events are due to wind disturbance [3]. Hence, having a developed intelligent ALS that operates in more flexible range of envelope would lead to safer response in wider range of conditions.

3. Equation of motion in auto landing

Although a linearized model has been used, the model responds realistically. The motion is represented by the linearized model in the vertical and longitudinal planes. The aircraft motion equations given below are used to simulate aircraft motion [1] [4]:

$$\begin{aligned} u(t+1) = {} & u(t) + \Delta\{X_u(u(t) - u_d) + \\ & X_W\ (w(t) - w_d) + X_q\, q(t) - \\ & g \cos \gamma\theta(t)\pi/180 + X_e\delta_E + X_T\ \delta_T\} \end{aligned} \tag{1}$$

$$\begin{aligned} w(t+1) = {} & w(t) + \Delta\{Z_u\,(u(t) - u_d) + \\ & ZW\ (w(t) - wd) + (Zq\ - U0\,\pi/180)q(t) + \\ & g\ \sin \gamma\theta(t)\,\pi/180 + Z_E\,\delta_E + Z_T\,\delta_T\} \end{aligned} \tag{2}$$

$$\begin{aligned} q(t+1) = {} & q(t) + \Delta\{M_u\,(u(t) - u_d) + \\ & M_W\,(w(t) - w_d) + M_q\, q(t) + \\ & M_E\,\delta_E + M_T\,\delta_T\} \end{aligned} \tag{3}$$

$$\theta\,(t+1) = \theta(t) + \Delta q(t) \tag{4}$$

$$\dot{h} = U0\,\pi/180\ \theta(t) - w(t) \tag{5}$$

$$h\,(t+1) = h(t) + \Delta\dot{h} \tag{6}$$

$$V_g = U_0 \cos\gamma + u_{gc} \tag{7}$$

$$x\,(t+1) = x(t) + \Delta V_g \tag{8}$$

u=longitudinal velocity (ft/sec), w =vertical velocity, q=pitch rate (degrees/sec), θ = pitch angle, h = altitude (ft), x = horizontal position as negative of ground distance to desired touchdown position (ft). Δ = 0.01sec sampling interval rate. [1]The incremental elevator angle δE , is given by:

$$\begin{aligned} & K1(\theta c\,(t) - \theta(t)) - K2\, q(t), \qquad h(t) \geq hf \\ & K3(\theta c\,(t) - \theta(t)) - K4\, q(t),\ h(t) < hf \end{aligned} \tag{9}$$

δ_T is the auto throttle setting (ft/sec) and u_T is updated by:

$$\delta_T = K_5\,(u_c - u(t)) + K_5\,\omega u_T\,(t) \tag{10}$$

$$u_T\,(t+1) = u_T\,(t) + \Delta(u_c - u(t)) \tag{11}$$

$\dot{h}_{TD} = -1.5$ft/sec is the altitude rate and θ_c is the ideal elevator angle:

$$-10^o \leq \theta_c \leq 5^o \tag{12}$$

Autopilot and auto throttle parameters: $K_1 = 2.8$, $K_2 = 2.8$, $K_3 = 11.5$ $K_4 = 6.0$, $K_5 = 3.0$, $\omega = 0$.

The values of constants used in equations can be found below:

Aircraft response		
X_u -0.038	X_w -0.0513	X_q 0.00152
X_E 0.00005	X_T 0.158	Z_u 0.313
Z_w -0.605	Z_q -0.0410	Z_E -0.146
Z_T 0.031	M_u -0.0211	M_w 0.157
M_q -0.612	M_E 0.459	M_T 0.0543

Table 1 Aircraft response parameters used for the equations.

Other parameters	
u_c 0ft/sec	throttle command
u_h 20ft/sec	wind speed at 510ft altitude
U_0 235ft/sec	nominal speed
γ -3^o	flight path angle
h_f 45ft	altitude at which flare begins
g 32.2ft/sec^2	acceleration due to gravity

Table 2 Additional parameters used for the equations of motion.

4. Bats intelligence and neural network approach

In nature, there are several animals using echolocation for purposes of collision avoidance and localization. Bats have made echo detection their primary sensory for guiding flight [8].Coordinate mapping relation is a method that bats use to calculate all the dimensions with knowing the initial position of receivers (bat's ears) and transmitter (bat's mouth)[7].As it is demonstrated in figure 1b, if the data is attained for one coordinates, others can be obtained as well.The overall reflection time(Rt) can be measured, however the travel time of each receiver(Rr1 and Rr2) should be found by triangular method to have a very accurate position of object. The hyperbolic linear frequency modulation used by echo locating bats would help the system to have a 3D map of environment. The equations are simulated in MATLAB software and the result is indicated in figure3a and 3b.

$$s(t)=rect(t/T)exp[j2\prod(-f1f2T)/(f2-f1)\ ln(1-(f2-f1)/f2T) \qquad (13)$$

Frequency illuminating center is fc and band width B=(f2-f1)

Neural network technique is used more often for intelligent control. NN works has two main phases, the learning process and pattern recognition [6].

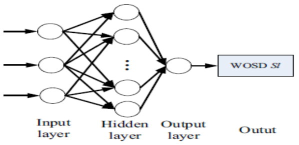

Figure 1a Neural Network structure

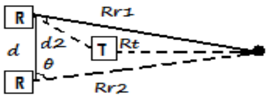

Figure 1b localization process

An algorithm to find the error is developed using multilayered NN shown in figure 2d by MATLAB software, samples for different assumed values are taken and the signal helps to locate and track path way and possible obstacles. The closest one to the ideal function is closer to the bottom surface. The NN model used is shown in figure1a, and three hidden layers with 10000 epochs are considered to train the system manually using MATLAB software and later on by considering the information obtained from bats localization. By setting initial random values for weights and knowing equation 14, predicted error is found.

$$H(s)=sgn((\square w1xi)-threshold) \qquad (14)$$

Figures2a,2b and 2c demonstrates NN control system at different point of training, developed in MATLAB software. It can be seen that the more system is trained the less fluctuation and error is given.

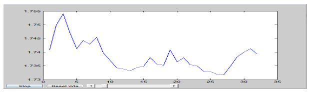

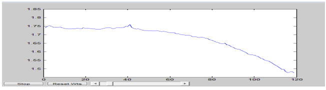

Figure 2a Untrained system

Figure 2b Not enough trained

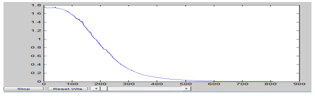

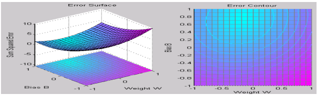

Figure 2c Well trained system

Figure 2d Diagram for errors

5. Results and Discussions

The emitted wave form as a function of target localization has been simulated using MATLAB software and NN is trained by. The chirp signal used by bat is simulated and the short Fourier transform indicates the change in the frequency with respect of time in figure 3b.

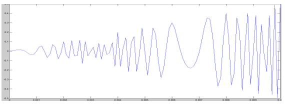

Figure 3a generated signal by bats

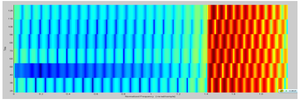

Figure3b short time Fourier transform

Figure4a and 4b, are showing the result of localization using bats signal. As it can be seen, the distance from the target and in auto landing case the runway can be identified. This data should be used to train the NN system.

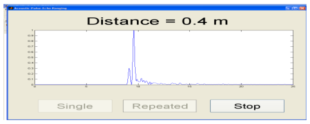

Figure 4a measured distance

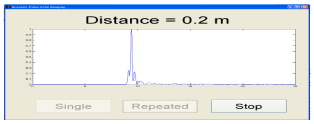

Figure 4b measured distance

6. Conclusion and further research

The NN approach trained by bats intelligence for auto landing of a commercial aircraft is discussed. The result shows that this approach could be considered as a satisfactory control of aircraft. The existing work in progress scrutinizes whether bats intelligence can help auto landing to handle wind disturbance with greater magnitude by training NN, applying actual information gained by bats localization and train the system by gained information. Considering the potential, this work can be seen as a long term project for future research which should cover two element antenna beams and signal processing and transmission of bats signal plus applying microwave signals for real life applications**.**

References

[1] Dimitris C.Dracopoulos, Auto landing of commercial aircraft by genetic programming, Proceeding of the world congress on engineering2007,U.K.
[2] Tiago F. Gonc¸alves, Jos´e R. Azinheira IDMEC, Vision based autonomous approach and landing for an aircraft using direct visual trackingmethod,N.1,1049-001Lisboa.
[3] Jih-Gau Juang and Kai-Chung Cheng, Application of Neural Networks to Disturbances Encountered Landing Control, IEEE Transactions on intelligent transportation systems,vol 7.No,4,Dec 2006
[4] Charles W. Anderson ,W. Thomas Miller III.Sutton Miller and Werbos, Neural Networks for Control.MIT Press, 1990.
[5] Karl Johan Astrom ,Bjorn Wittenmark., Adaptive Control. Addison-Wesley,firstedition,1989.
[6] Bhaskar Prasad Rimal, Hyoim Shin and Eunmi Choi ,Simulation of Nonlinear Identification and Control of Unmanned Aerial Vehicle: An Artificial Neural Network Approach, 978-1-4244-4522-6/09.
[7] sung-Ying Sun,Tsai, Jiun-Yuan Tseng, ,"The Study on Intelligent Vehicle Collision-Avoidance System with Vision Perception and Fuzzy Decision Making", IEEE international conference 2004.
[8] Michele Vespe, Gareth Jones and Chris J. Baker, Lessons for radar waveform diversity in echo locating mammals, IEEE signal processing magazine,2009

Numerical Simulation of Light Sport Aircraft Structure

Mohammed Hasan Al-Amoudi*, Alexander Chee Hon Cheong

Department of Mechanical Engineering, School of Engineering, Taylor's University, Malaysia

**corresponding Author: mooh_89@hotmail.com*

Abstract— **Light sport aircraft (LSA) is a small aircraft that can only fly in a short distance with capacity of two passengers. Fuselage is the main structural component that carries most of the weight and provides the connection to other component. Buckling analysis was carried out by using numerical simulation to test different loadings on different types of fuselages. Carbon Fiber Reinforced Plastic (CFRP) was tested by introducing Kevlar material and the results were compared with Aluminum Alloy. It was found that semi-monocoque structure that uses CFRP has the best weight to strength ratio. The project offers wide scope in terms of structural design; hence engineers who are designing this type of aircraft will be benefited in the choice of the best design and material for the fuselage of the LSA.**

Keywords— Light Sport Aircraft, Fuselage Structure, Carbon Fiber Reinforced Plastic, Aluminium Alloy, Liner Buckling Test.

1. Introduction

Light Sport Aircraft (LSA) is a small aircraft that flies in a small range with maximum of two passengers [1]. It has less weight and low speed compared to other commercial aircrafts [1]. LSA became more popular and more needed as traffic is increasing due to the increase of word population. Nowadays, many researches are being carried out to improve this kind of aircraft. The design of LSA contains of wings, nose, tail and fuselage [1].

Fuselage is the main body of the plane that carries most of the weight, and provides the structural connection to the wing and tail [4]. The fuselage of any aircraft undergoes different types of stresses so it has to be built properly with reasonable safety factor. The process of designing a fuselage has different types of structure tests. Buckling test is considered to be an important test that shows how strong and stiff the structure is [6]. It is considered a structural failure or deflection that occurs when the applied load exceeds the critical load which is the maximum load that body can withstand without being deformed [5].

Carbon fiber reinforced plastic (CPRP) is a group of composite material which has good weight to strength ratio [3]. CFRP seems to be suitable for aircraft structures due to their mechanical properties. It has been used in many aerospace and automobile applications [3]. However, this kind of material is still unknown on LSA. Most of the light sports aircrafts are using Aluminum as main material for its structure [4]. So the purpose of this project is to compare between the results of the two materials in terms of buckling, stress, weight.

2. Methods

There were some processes that have been done until the final results were obtained. The reason of doing buckling analysis is to test some different fuselages structure with different materials to analyze how these fuselages perform against the applied load. Weight to strength ratio is a very important factor that can show how good the structure is. The idea of buckling test was obtained from the behavior of the column under compression force. Fig1 shows numerical simulation which was done in the column to have better understanding of the buckling test.

Fig. 1. Buckling on column

In addition, the differences between LSA and the normal commercial aircraft had to be understood to avoid error in designing as the LSA should have maximum takeoff weight of 650 kg only [1].There are three different types of fuselage which are truss, monocoque and semi-monocoque [4]. Truss is the first type of the fuselage and it is still being used till today. It contains a welded tube which can be made from different materials such as aluminum or steel. The second type of the fuselage is monocoque. In this type of fuselage, the skin carries the entire load so it has to be thick and strong enough to keep the fuselage rigid. The third type of fuselage is semi-monocoque. It is a new design of monocoque, however it has extra components added to the skin which are; stringers which give more resistance against deformation and formers which help to maintain the shape rigid and strong [4].

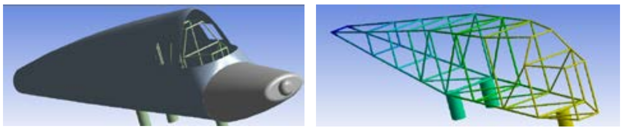

Fig. 2. Truss structure

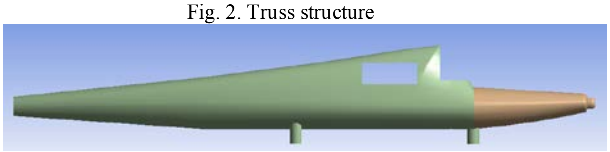

Fig. 3. Monocoque structure

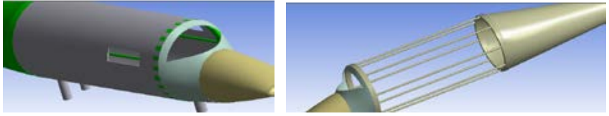

Fig. 4. Semi-monocoque

As weight to strength ratio is considered to be an important factor in designing fuselage, CFRP was introduced in this simulation to be compared with Aluminum Alloy. The CRFP material that been used in this simulation is Kevlar which has lower density than Aluminum Alloy and higher tensile strength [3]. The table below shows mechanical properties of Kevlar.

Table 1 Mechanical properties of Kevlar [3]

Mechanical properties	Kevlar
Density (kg/m^3)	1400
Young modules (GPa)	30
Poisson's ratio	0.20
Ultimate tensile strength (MPa)	480
Ultimate Compressive tensile strength (MPa)	190

3. Results and Discussion

Numerical simulation tests were done on the three types of fuselage using two different materials. Wings and tail were assumed to be neglected in these simulations. Each structure had different performance against the load, also the materials affected the total deformation and deflection as each material has different tensile and compressive strength. Table 2 below shows the results of the deflection in meter for each design and each materiel.

Table 2 Buckling test with load of 5000 N to 30,000 N

fuselage structure	**Deflection min- max (m)**	
	Aluminum Alloy	**CFRP (Kevlar)**
Truss	1.0853-1.0875	1.0817- 1.0834
Monocoque	1.3735- 1.3775	1.3536-1.3755
Semi-monocoque	1.0154- 1.0155	1.0104- 1.0105

As shown in the table above, the results of semi-monocoque are better than the other two structures as it has less deflection and it performed more stable. Also it can be noticed that the deflection of Aluminum Alloy is more than deflection of CFRP in all structures. After the results of deflection were obtained, it is also important to get the results of stress as it's considered to be important to determine if there is an elastic or plastic deformation occurring in the structure. In addition, calculating the stress will help in making decision of the best structure that can withstand more weight. The two graphs below show the stress on each structure against the load.

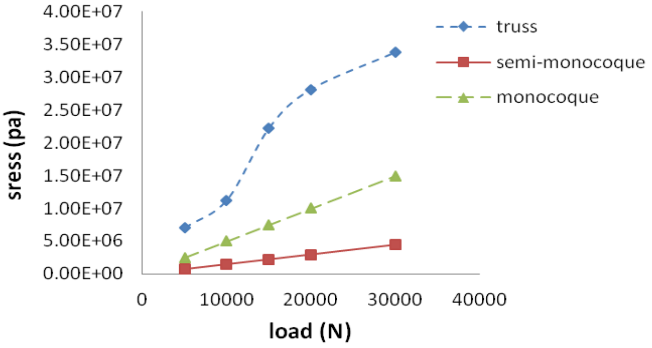

Fig. 5. The results of the three structures using Aluminum Alloy

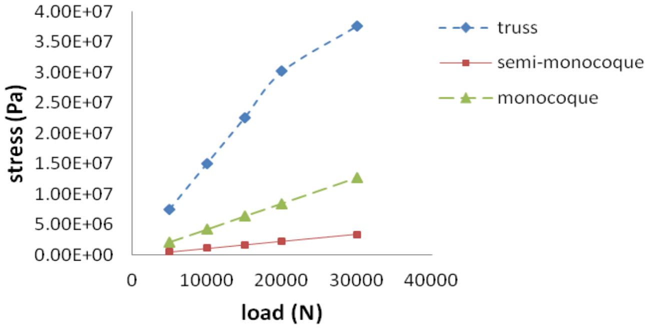

Fig. 6. The results of the three structures using CFRP (Kevlar)

In both graphs, semi-monocoque shows better results in terms of stress versus load, so it needs more force than other two designs to be deformed.

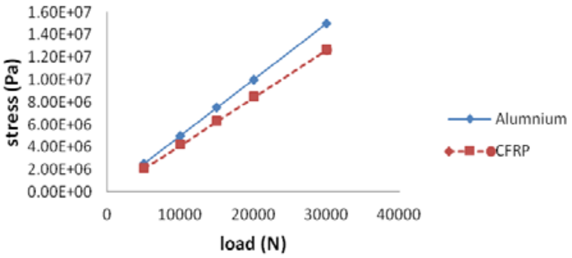

Fig. 7. Stress of semi-monocoque with two materials

This graph is to show the normal stress results of one structure by using two different materials. CFRP (Kevlar) shows better results in normal stress as less stress means more strong body, which can withstand more loads. However, Aluminum Alloy will be deformed faster than CFRP as it has less tensile strength.

Table 3 Weigh of the fuselages

fuselage structure	**weight (kg)**	
	Aluminum Alloy	**CFRP (Kevlar)**
Truss	325.61	164.57
Monocoque	259.64	131.22
Semi-monocoque	386.61	195.4

The table above shows the weight differences between Aluminum Alloy and Kevlar. The structures with CFRP have less weight of around 49% difference. So we can conclude that CFRP (Kevlar) has better weight to strength ratio compared to Aluminum Alloy and that will help the future application and the new aircraft generation to produce aircraft which has less fuel consumption.

4. Conclusions

Numerical analysis was carried out to test different loading on different types of fuselage. The application of CFRP provides better weight to strength ratio compared with Aluminum Alloy. Among all the structures, the semi-monocoque shows the best results in terms of stress over strength and in terms of weight and ability to resist the deflection and deformation. As CFRP considered being an expensive composite material compared to Aluminum Alloy, it is recommended advised to apply this material for only for some components and not for the whole structure, so a compromise solution between the materials is achieved in order to balance and optimize the cost and the weight.

References

[1] N. Probert, "LIGHT SPORT AIRCRAFT CERTIFICATE OF AIRWORTHINESS," September 2005.

[2] M. Achternbosch, "MATERIAL FLOW ANALYSIS - A COMPARISON OF MANUFACTURING, USE AND FATE OF CFRP- FUSELAGE COMPONENTS VERSUS ALUMINIUM-COMPONENTS FOR COMMERCIAL AIRLINERS," 2006.

[3] D. D. L. Chung, Carbon Fiber Composites, Belfast: ELSEVIER , 1994.

[4] Federal Aviation Administration, Pilot's Handbook of Aeronautical Knowledge, New York : Skyhorse Publishing Inc., 2009.

[5] S. DESHPANDE, "BUCKLING AND POST BUCKLING OF STRUCTURAL COMPONENTS," Texas, 2010.

[6] J.-P. D. Richard DEGENHARDT, "BUCKLING AND POSTBUCKLING ANALYSIS OF A CFRP STIFFENED PANEL FOR A BETTER MATERIAL EXPLOITATION," 2007.

Heat Transfer in a Typical Malaysian Room

Mohanad Yahya*, Mohamed H. Nassir

[1]*School of Engineering, Taylor's University, Selangor, Malaysia,*

**m.mihrabi@gmail.com*

***Abstract*— The lack of consistent studies of heat transfer through walls, doors, and windows of typical Malaysian constructions urges us to conduct this study for deep and accurate vision regarding this matter. To achieve this purpose a typical Malaysian room was scaled down and made of cement walls then data was collected by measuring temperature outside and inside the room for ample period of time. Windows are modified to serve as a single, double, and triple layer of glass at 10 mm gap. Initial results show significant reduction in heat transfer as the number of layers increases.**

Keywords— Heat Transfer, House Architecture, Malaysian Construction, Cement Wall, Window's Thickness

1. Introduction

The heat transfer through walls and composite layers has been a subject of significant investigations [1], [2]. Despite the availability of huge number of studies, the information in a certain and specific field is widely spread over almost unlimited various cases. Studies of heat transfer through walls and windows have considerable discrepancies due to huge number of structures, conditions of experimental work, and the widespread setting of experiments [3]. As another depth, studies in heat transfer through basic constructions in Malaysia are minimal. This project provides very essential knowledge equipped with physical data on a scaled-down Malaysian room. The room is fabricated using cement walls and roof with two windows and a door with both were scaled down similarly. The windows, as essential parts in the construction, are made of a single layer, which could be extended to a double and triple layer with 10 mm gaps. Armando Gallegos and his colleagues [4] investigated the thickness of the air layer and found that the heat transfer is significantly reduced as the number of the layers increases or the gap between layers increase.

The theoretical part includes the modes of heat transfer, thermal conductivity, and the methodology of solving equations [5], [6]. The heat transfers in conduction mode ($\dot{Q}$) through a single layer of thickness *x* is given by Fourier's law of heat conduction

$$\dot{Q} = -kA\frac{dT}{dx} \quad (1)$$

where T is temperature and *k* is thermal conductivity. The conduction equation could be written in 2 or 3 dimensions. For more than one layer, the system will be analogous to resistors connected in series [5], [6]. There are two other modes for heat transfer, namely convention and radiation. The convention mode is explained by Newton's Law of Cooling,

$$\dot{Q} = hA(T_w - T_\infty) \quad (2)$$

where h is the connective heat transfer, and by radiation mode which is known by Stefan-Boltzman law,

$$E = \sigma T^4 \quad (3)$$

where σ is Stefan-Boltzman constant.

To study the parameters of heat transfer in a typical Malaysian room under natural conditions and to map the temperature variation inside the room by examining these parameters as a function of a single, double, and triple glass window layers. Having measured these parameters, the best design will serve as better energy saving.

2. Experimental

Regarding the experimental part, the scaled-down room was fabricated as shown in Fig. 1 using CAD. The walls, roof, and the door are made of cement board because of easy to maintain, its affordability, and easy to handle. The size of the room is 1x1x1 m^3 and 20mm-wall thickness. It is placed in an open field on campus as shown in Fig 2.

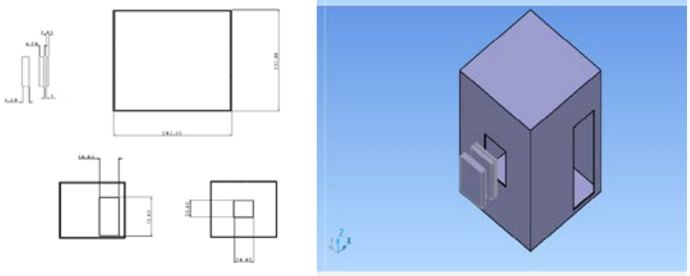

(a) (b)

Fig 1 CAD Drawing for the Room with Dimensions

The room was mounted such that one of its glass windows is oriented to the east direction and the second towards west as shown in Fig 2. The windows, which are crucial part of the study, were equipped with capability to handle a single, double, or triple glass layer. There are three types of glass layer with thickness, namely 2mm, 4mm and 6mm. The gap between the layers is 10mm. To measure temperature, four thermocouples were used and mounted outside and inside the room. The data was collected during day time and then repeated throughout night time until a constant temperature difference is achieved. Data collection was repeated for several days and results were averaged.

Fig 2 The Fabricated Room of 1x1x1 m and 2mm Wall Thickness

3. Results and Analysis

All measurements were taken simultaneously during day time measurements between 10 am and about 3 pm are shown in Fig 3. Temperature difference was measured in the vicinity of the windows (location A facing east and location B facing west) with a single and double layer (A1, B1 and A11, B11); respectively and the difference of temperature between **outside and inside** was reported. The single layer measurements shows very low maximum difference of 1.5 degrees compared to 3 degrees for double layer. For east-ward location A, the single layer measurements fluctuate to achieve maximum difference between the inside and outside (1.5 degrees) about noon while the double layer shows constant behavior until 1 pm where both layers have their minima of 0 degree and a half degree; respectively. For west-ward location B, the single layer shows very small difference of about 1 degree while the double layer shows 3 degrees maximum at noon time. The results for all cases show almost no difference in temperature about 3 pm except the B-double layer location of about half a degree. The data of east-ward, single-layer window shows fluctuation with two maxima one about 12 noon and another about 2.30 pm.

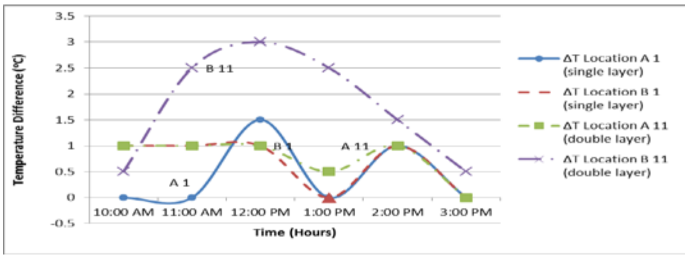

Fig 3 Temperature Difference versus Time during Daytime

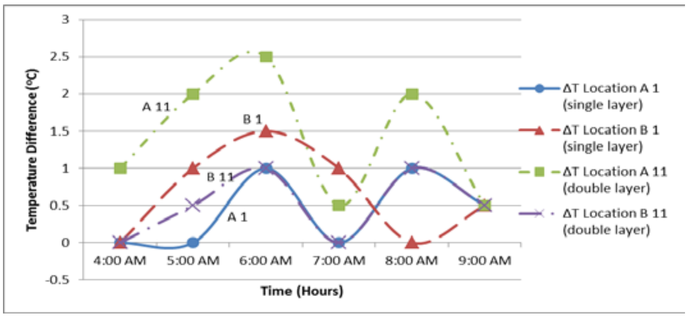

Fig 4 Temperature Difference versus Time during Nighttime

Similarly, the same procedure of the experiment has been followed during the night time. Temperature measurement were taken from 4 pm to 9 pm are represented in Fig 4. The single layer measurements on location B shows 1.5 degrees as the maximum difference reached. However, in comparison with the double layer on location B, the maximum difference is almost 2.5 degrees. Location B results tend to have fluctuation in the measurement as shown in Fig 4. This is because location B has more sun exposure during this time since the window is located on east side of the room. On the other hand, location A shows steadiness in the measurement as they almost follow the same trend as shown in Fig 4, since they have started the cooling down phase. Moreover, using single layer window on location B shows no difference in temperature at 7 pm, whilst the double layer window shows 2 degrees difference in temperature. At 9 pm, the data for all the cases shows almost half a degree difference. Particularly, this behavior shows the rate of dissipating the heat in the double layer and maintaining a cool climate inside the room.

4. Discussion

The results signify the role of the double layer glass as the results has shown significant difference between the single and double layer. Based on research done by Daikin [private interview with Mr. Chow at Daikin conducted on 23/04/2010], one degree Celsius reduction of the atmosphere temperature leads to 3% improvement of the energy efficiency. The temperature difference (ΔT) is obtained by measuring the temperature inside and outside the room. This small reduction in temperature difference has its own impact on two important issues, saving energy and greener environment. The difference of temperature at location A for double layer during the day time is about 3 degrees compared to about 1.5 degrees during night time. The trend of difference of temperature for all cases is almost same except the double layer at location B. The night time measurements, where the difference of temperature is measured between the outside and inside, show similar trend with lower maxima. Almost all measurements show a kind of fluctuation where the maximum appears more than once. This behavior may reflect very important result of temperature reduction that may lead to improve the energy efficiency; however, it is too early to confirm such a finding or the extent of it. Overall result are promising and encouraging for further studies not only about the double layer but also to include triple layer as well as to map the interior temperature distribution inside the room.

5. Conclusions

The lack of scientific and reliable studies on the heat transfer in a Malaysian typical room has supported the necessity of conducting this experiment as well as extending the investigation for further studies. Based on Daikin's results of a single temperature reduction could result in 3% reduction of energy which reflects an important impact on the environment. The experimental results show that the reduction was about a degree and a half based on single to double layer. Despite the slightly high cost of the two layers, the gained that comes from saving energy and friendly impact on environment is, by no means, comparable. It is important to note that the double layer is 50% more efficient than it's a single layer, which corresponds to the maximum temperature difference (ΔT) using double layer. However, when the single layer window glass is used, the maximum temperature difference is 1.5 degrees as show in Fig 3, which represents the daytime results. It is also important to take the reading for few times to ensure accurate results and avoid the sudden changes effects of the Malaysian weather. The hope is that this study becomes a corner stone and bench marking to similar studies in order to have better and higher energy saving.

References

[1] Frank, P. I. (2012), Principles of heat and Mass Transfer. Los Angeles, California: John Wiley & Sons, Inc. Seventh Edition.

[2] Michael, H. N. & Moran, J. (2008) USA: John Wiley & Sons, Inc. 6th Edition

[3] Van Dusen M. S. & Fink, J. L. (1931). Heat Transfer through Building Walls. Stds. J. Research.

[4] Armando Gallegos M., Christian Violante C., José A. Balderas B., Víctor H. Rangel H. and José M. Belman F.(2011)Analysis of the Conjugate Heat Transfer in a Multi-Layer Wall including an Air Layer. In Aziz Belmiloudi (Ed.), Heat Transfer, Mathematical Modelling, Numerical Analysis and Information Technology (pp. 553-565). INTECH, Europe.

[5] Bockh, P.V. & Wetzel, T. (2011) *Heat Transfer: Basics and Practice* , Germany, Springer.

[6] Cengel, Y. (2011) Heat and Mass Transfer fundamentals and Applications, USA, McGraw Hill, 4th Edition.

Noise Reduction at Taylor's Temptation restaurant

Mohd Afiq Bin Mohd Saleh, Mohammad Hosseini Fouladi

School of Engineering, Taylor's University, Malaysia

Abstract— **The research was carried out on engineering noise control in the Temptation restaurant. Extensive research and literature review which were done in the areas of sound control, room acoustics and material types as well as calculation for reverberation time. The use of modelling simulation was used to visualize the sound dispersion as well as calculate the reverberation time. Whether dining, waling or talking, the problem faced by the restaurant is the noise dispersion which causes echoes due to the open spaces and lack of sound absorbers. The appropriate solution to control noise in the restaurant is with the placement of sound diffusors and absorbers of ceiling baffles which decreases reverberation time to less than 2 seconds.**

Keywords— Sound absorption panel, sound absorbers, sound diffusers, sound control, room acoustics, reverberation time

1. Introduction

Noise is undesirable sound which causes sound pollution and makes patrons dinning feel uncomfortable when it becomes too noisy and loud. In order to overcome the problem is by installing acoustic panels and by controlling the noise within the room. As sound are energy waves that reflect to hard surfaces reverberation and echoes, fabric type materials are use as sound absorption panel as the multitude of air pockets have the sound waves bounce and loose its energy. Studies of sound control in offices have been done by Tugrul *et al.* [1] and Keranen *et al.* [2] with similar scope as this study but different approach and model of study. This study aims to design and soon install acoustic panels to construct an atmospheric and quiet restaurant where customers feel comfortable dining and conversing.

Fig.1 The interior of the Taylors' Temptation restaurant

2. Methodology

The research began with extensive exploring on the fundamentals of acoustics, noise control and acoustic panels. According to Cromption *et al.* [3] noise frequency are compellingly observed at 500 Hz and below as it contains less of a problem and also that average human speech are around that range [4].

Measurements of the Temptation restaurant as well as a layout plan of the interior of the restaurant. Readings of noise level from various sources were taken by a sound level meter to distinguish of the sources that create noises in the restaurant. The sound level meter used was standard IEC651 type 2, ANSI SI.4 type 2 and the sources of noise in decibels are shown in Figure 2.

The room temperature is measured at 21˚C where the sound travel is slower then compared to outside as at lower temperature the particles are denser which slows down the speed of sound. The speed of sound in the room is measured at 343.6 m/s while outside which is 31˚C is at 349.6 m/s.

The sound readings were taken at an interval of 2 hours starting from 10 am to 4 pm. These noise sources are taken from patrons, the air conditioner, and the fans and from the kitchen. The noise from the fans and air condition are constant.

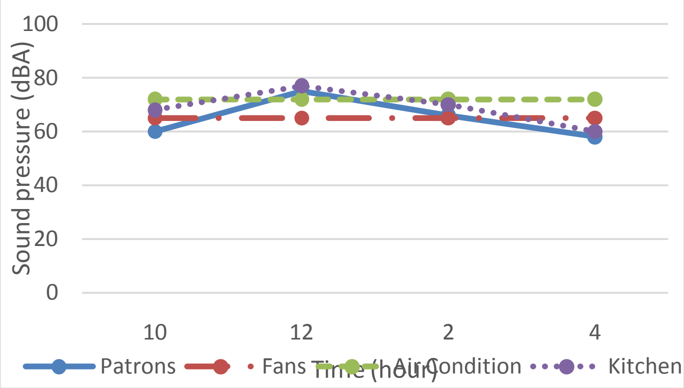

Fig.2 The sources of noise in the restaurant

The type of material used for the walls and panels are list down since each material type consists of their own absorption coefficient. By calculating the average noise level by the following formula [5];

$$L_{AV} = 10\, log_{10}\left(\frac{10^{\frac{L1}{10}} + \cdots . 10^{\frac{L5}{10}}}{n}\right) \qquad (1)$$

Using the noise reduction coefficient (NRC) to calculate the reverberation time as follows [5];

$$\text{RT(60)} = \frac{0.05V}{(\sum S\alpha)} \qquad (2)$$

The calculated reverberation time of the restaurant is around 2 seconds in which an appropriate reverberation time needed for that of a restaurant is 1 second where sound should decay or be below 60 dB

3. Results

Two different types of sound control is calculated, one being a ceiling baffle which is an absorber type and the other is a diffusor which disperse sound. The room is considered a cuboid shaped with 15.51 m x 24.43 m x 245 m to ease of calculating the reverberation times. The material type included in the room are also calculated by calculating the absorption coefficient. The ceiling baffles were calculated by using 3 different types of materials; vinyl, quilted and fabric to identify the differences in material absorption type. As for the diffusors, only one common type is used to distinguish its characteristics and differentiate with other sound controlling types. The sizes of these baffles are 1.2 m in length, 0.6 m in width and 0.6 m in height. The result gained if for a single baffle where it is multiplied by 5 or 5 piece of baffle as the total size of the room is at 928 m^2 and each baffle covers roughly 100 m^2. Therefore, an appropriate amount of 5 piece of baffle and 5 diffusers are calculated with each type.

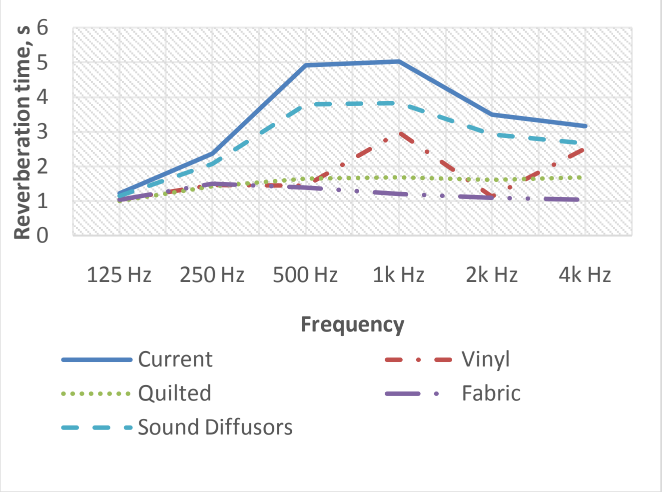

Fig. 3 Comparisons of all the calculated reverberation time

The comparisons in Figure 3 shows the calculated reverberation time for the current restaurant with no absorbers, the ceiling baffles of 3 different material types; vinyl, fabric and quilted; also the sound diffusors calculated at 125 Hz, 250 Hz, 5 00Hz, 1 kHz, 2 kHz and 4 kHz. The simulation done is by using Autodesk Ecotect where it is drawn in 3 dimensional with the exact scale of 1:1 including the pillars, furniture and specified materials for each.

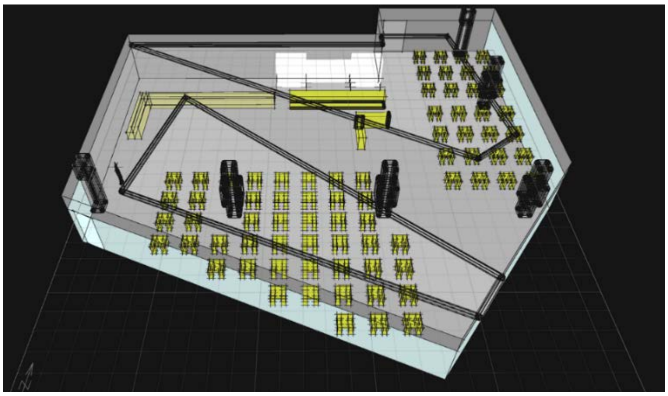

Fig. 4 The model of Temptations for simulating acoustics using Ecotect

As sound travels in the room at 343 m/s the sound dispersion in Figure 5 shows how sound is dispersed at 500 ms which is half a second from a sound source situated at the left of the room as shown in Figure 5. The reverberation time from the simulation by applying the sound treatment is as shown in Figure 6 where a previous reading of beyond 2.4 seconds now reads below 2 seconds.

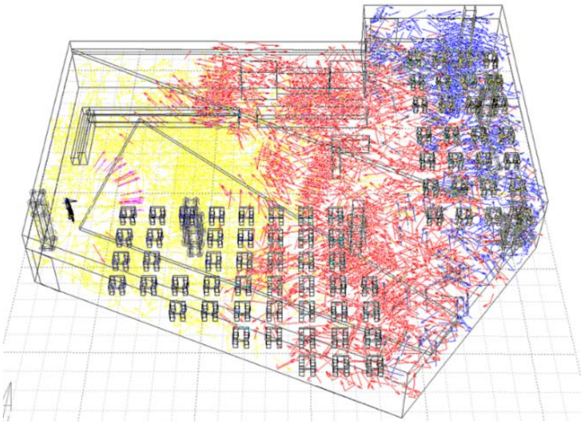

Fig. 5 The noise dispersion for speech at 500ms

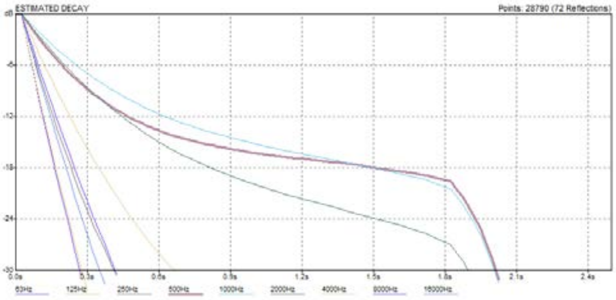

Fig. 6 The reverberation time of the applied treatment

4. Conclusions

By using compound panel absorbers, noise within the room can be control within the range of 500 Hz. This strategy aims to give an ambient feel for the patrons dining in terms of acoustically and aesthetically as it maintains the looks and overall interior of the restaurant. Using fabric as a material for ceiling baffle and sound diffusors, the reverberation time of sound travelling in the restaurant can decrease to below 2 seconds which is the recommended reverberation time for speech in restaurant around 1.5-2 s. Thus, without altering the image of the restaurant interior, the sound can be controlled within the restaurant.

Acknowledgment

Many thanks to Dr. Mohammad Hosseini Fouladi for the guidance and opportunity. Honourable mention goes to the engineering lectures for holding talks related to FYP and Mr. Tengku Murad, the manager of Taylors Temptation restaurant.

References

[1] Tugrul, Arzu, et al. "Exploring the role of simulation in room acoustical retrofit of office spaces: a case study." *Fourth German-Austrian IBPSA Conference* (2012): p.53-57.

[2] Keranen, Jukka S., Petra Virjonen, and Valtteri O. Hongisto. "Characterization of acoustics in open offices-four case studies." *Journal of the Acoustical Society of America* 123.5 (2008): 2971-2971.

[3] J.S. Crompton, L.T. Gritter, S.Y. Yushanov, K.C Koppenhoefer, D. Magyari (2010). Analysis of Acoustic Response of Rooms. *COMSOL Conference 2010 Boston,* 1-4.

[4] H.V. Fuchs, X. Zha, X. Zhou, H. Drotleff (2001). Creating low-noise environments in communication rooms. *Applied Acoustics 62*, 1375–1396.

[5] Randall McMullan. (2002). *Environmental science in building.* New York: Palgrave, pp. 247

Vibration isolation for machinery

MohdRosyazrilAisyamRusly, Mohammad HosseiniFouladi

Mechanical Engineering, Taylors University, Malaysia,

Abstract— **this research is about suppressing vibration for machinery at Taylors University's lab. Vibration is undesirable and is to be suppressed because vibration can contribute to undesirable circumstance to machinery for example mechanical failure in the machinery system. Here, this research is focus to develop skills and determine ways of adjusting physical parameter of the machinery in such a way that vibration response meets some specified criteria.**

Keywords: vibration, isolation, damping, frequency, and displacement

1. Introduction

Vibration is the sub-discipline of dynamics that deal with repetitive motion. In most mechanical system and structure, vibration is unwanted and even destructive. First of all, human will experience vibration in their daily routine and therefore engineer will always try to mitigate vibration in order to keep the human safeties. Hence, it becomes a most concern element in most of engineering field. For example in the manufacturing sector, vibration can cause fatigue and mechanical failure in machinery. As an effect, it will risk of injury to human who handle the machine. In the other hand, vibration also become the destructive element as it stimulates fatigue to the airplane structure and contributes to air crash. Besides, undesirable vibration fails the electronic component and withdraws the function of all system. Plus, undesired vibration creates unwanted noise to surroundings.[1]

The question here is who will benefit for this research. As a matter of fact, all industries will benefit this research because almost industries experience this kind of problem which is undesired VIBRATION problem. In fact, isolating vibration will increase the efficiency of systems and reduce the maintenance cost. For example in the automotive industries, vibration is the serious problem because it will contribute customer discomfort and mechanical failure for parts of automobile. Therefore, they design of isolation of a car or airplane body from engine vibrations. [1]In the other hand, suspension systems of vehicles also are a vibration isolation system. Plus, photographic field, vibration will contribute to blur image and shaky video. For the reason of that, vibrations will also trigger problems for surveying or surveillance applications. In the electric and electronic field, undesired vibration can cause of malfunction of the electronic device. Hence, this research has a potential to be part of the solution to the most industrial problems.

2. Design parameter

In fact, vibration experiment method depends on several assumptions and those are:

1. Lumped parameter describe effectively for the tested machine.
2. Test input drive the system under test only in linear range
3. Ignore the relativistic effect
4. Physical system can be treated as continuous piece of matter
5. Newton's law motion can be applied.[2]

3. Objective

Doing a research and analysis to design and adjusting system's physical parameter of diesel motor in Taylors University lab to caused it vibration response to behave in desired fashion. The desired vibration for the diesel motor is determine from figure 1 which is the displacement magnitude for vibration response must achieve the range of 0.001 to 0.01mm and the frequency must achieve 10Hz to 100Hz.this is equivalent to the ISO standard for machinery.

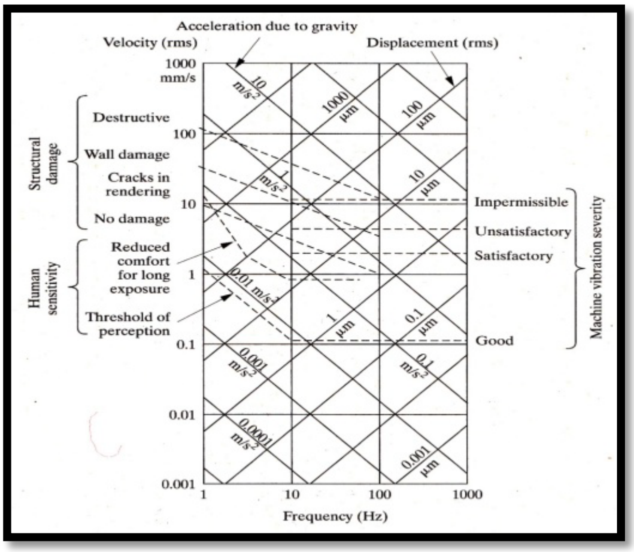

Figure 1: Acceptable level of vibration [1]

3. Detailed experiment

Modal testing is widely accepted for activities involving the characterization of mechanical and structural vibration through testing and measurement. (H.J.Hsueh, 1998)

The main reasons of conducting a vibration experiment are to determine the value of natural frequency, to determine durability of the structure in specific dynamic environment and for maintenance diagnostic. [3]

The device and software involve in this experiment are:

- Accelerometer (4507b)
- DAQ device
- Labview software

Source vibration⟶ accelerometer⟶DAQ⟶Labview

Important details for this experiment are:
Mass of the engine= 48kg
Rotational speed of the engine = 3000-3600RPM

In order to achieve an accurate result, the accelerometer must be set according to the right technique. The techniques are:

1. Make sure accelerometer is oriented correctly. - The signal produced by the accelerometer is dependent on the orientation in which the accelerometer is mounted, since the amplitude of vibration varies in different directions.
2. Mount the accelerometer in the same location. – in order to get consistent result

4. Experiment analysis

The equation of the vibration will be performed by this equation:

$x(t) = X\sin(\omega_n t+\varphi)$ (1)
$y(t) = Y\sin(\omega_n t+\varphi)$

T is the period of the oscillation response which can be determine through the graph from the result of experiment.

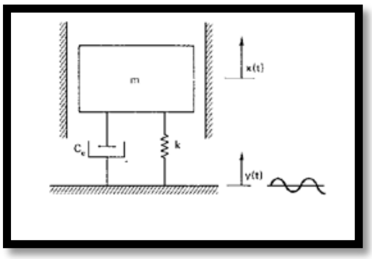

Figure 2: Displacement transmissibility diagram.[4]

Form figure 2, m is representing the mass of the diesel engine. x(t) represent the vibration response for the engine whereas the y(t) function represent vibration response of the casing of the engine and in this case it remarks as basement. Plus, c and k is the damping value and stiffness of the isolator in order to suppress vibration from the engine to the casing (basement).

Therefore, from the vibration isolator catalog, I just find and compare the value of damping value (c) and stiffness (k) of the isolator in order to achieve the target vibration response.

5. Experiment result

The result of the experiment will be shows in three types of graph which are in the acceleration versus time, magnitude versus time and magnitude versus frequency.

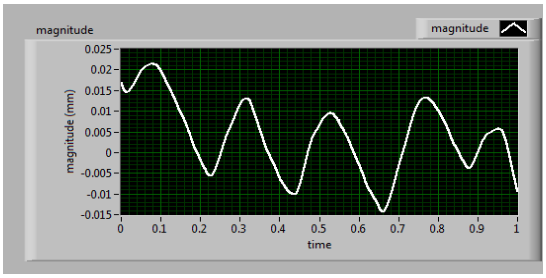

Figure 3(a): Experimental result for magnitude vs time

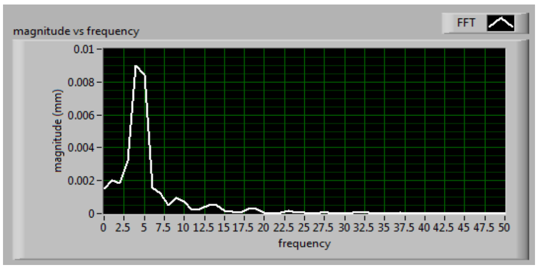

Figure 3(b): xperimental result in frequency domain

Figure 3(a) shows that the result for the amplitude in milimeter for the vibration versus time in labview fron panel. Thus, in order to analyse the vibration, the result will be convert into the frequency domain using FFT function and the result in figure 3(b) shows the vibration response in frequency domain.

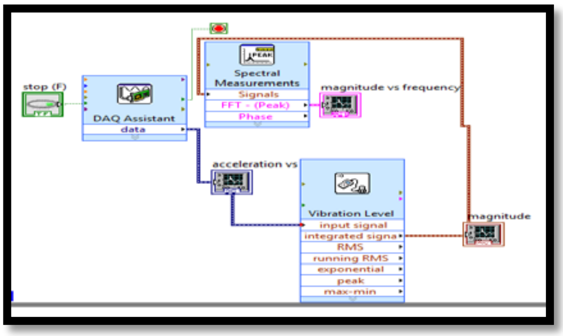

Figure 4: Block diagram for the experiment

Figure 4 shows the block diagram which represent the program to control this experiment.
Then, the formula for displacement transmissibility is:

$$X/Y = TR = F_t / F_0 = \{[1 + (2\zeta r)^2\ ] / [\ (1-r^2)^2 + (2\zeta r)^2]\}^{1/2} \quad (4)$$

0.028mm is the magnitude of the vibration occurs at the engine which is remark as source of vibration and 0.01mm is the ideal magnitude of vibration which is obtained from figure 1 in objective section.
TR = 0.028/0.01
= 2.8

Thus, from the formula $c= 2\zeta m\omega_n$,as the mass of the engine is around 50kg, thus the damping value is equal to 929.81 Ns/m

Conclusions

This work generalizes the theoretical and experimental procedure in order to analyze vibration. The measuring procedures mostly handle by experimental work using a specific device and for this research consist of accelerometer 4507b model, DAQ analyzer and LABVIEW software. LABVIEW use to control the parameter and FFT function in LABVIEW to change the unit of result.Whatever design that we work on must have calculation to support our result. Therefore, in order to isolate vibration, I need to determine what is the value of undesired vibration from the source and how much vibration need to suppress in order to get the desired vibration range. All of the analysis procedure required theoretical and mathematical understanding about vibration knowledge.

Acknowledgement

DrHosseini – Project supervisor
Mr. Douglas Tong KumTien – Final Year Project coordinator
Miss Sumaiyah – National Instrument representative
Mr Rahim – Lab assistant

Reference

[1]Inman, D. J. (2001). *Engineering Vibrations*. New Jersey: Pearson Education International.

[2]Adhikari, S. (2000). *damping model for structural vibration*

[3]Furman, B. (2005). Vibration Measurement. *ME 120 Experimental Methods*

[4]Frankovich, D. (1996*). The Basics of Vibrati*

Efficient Air-Condition Unit By Using Nano-Refrigerant

Muhammad Abbas[1], Rashmi G. Walvekar[2], Mohammad Taghi Hajibeigy[3], Farhood S. javadi[4]

[123]*School of Engineering, Taylor's University, Malaysia,* [4]*Department of Mechanical Engineering, University of Malaya, Malaysia.*

**Corresponding Author email: RashmiGangasa.Walvekar@taylors.edu.my*

Abstract— **This research mainly focuses on CNT-based nanolubricant in the refrigeration system. CNT Nanoparticles introduced into the system through lubricant to improve its heat transfer performance. A concentration of 0.01-0.1wt% of CNT-Polyester Oil was tested along with suitability and environmental friendly refrigerant R134a. Results show that CNT nanoparticle concentration of 0.1wt% is optimal and gives highest heat transfer enhancement and improve the coefficient of performance (COP) by 4.2%.**

Keywords— nanolubricant, refrigeration, heat transfer, coefficient of performance, polyester oil.

1. Introduction

Concept of Nano-lubricant came from the idea of Nano refrigerants which are a relatively new category of refrigerants consist of a conventional refrigerant with Nano-sized particles mostly (range between 1nm to 100nm) suspended within them. Nano refrigerant is also called Nanofluid; Nanofluid is famous because of its unique type with remarkable thermal conductivity in refrigeration and air-conditioning systems. Nanofluid was first proposed by Choi [1].

Carbon Nanotubes (CNT) are famous because of its great thermo-physical properties and extremely high thermal conductivity reported by researchers recently. Extensive research in the last two decades shows that nanofluids are a new generation of heat transfer fluids. Due to small size and large specific area of nanoparticles, nanofluids holds superior properties such as high thermal conductivity, minimal clogging in flow passage, long-term stability and homogeneity [2].

Refrigerants are widely used in refrigeration and air-conditioning equipment in industries, offices and domestic & commercial buildings, consuming huge amount of energy. Nano-refrigerants have potential to enhance heat transfer rate thus making heat exchanger of air-conditioning and refrigeration equipment compact. This, consequently, will reduce energy consumption in these sectors along with reduction in emission, global warming potential and greenhouse-gas effects [3].

CNT were observed to have relatively high thermal conductivity (~3000W/mK) over other nanoparticles such as CuO, Al_2O_3, SiO_2 diamond and TiO_2 [4]. Patel et al.[5] used R113a as a base refrigerant and significant evidences of performance improvement of the system was observed in the extensive research using CNT nanoparticles. The recent studies have found that the CNT based nanofluids have higher thermal conductivity compared to conventional refrigerants [5].

Recently, several research studies conducted on a refrigeration system using different refrigerants, lubricants and nanoparticles showed significant reduction in power consumption and improvement in coefficient of performance (COP) of the system. Sendil et al. [6] used hydrocarbon refrigerant and mineral lubricant suspended with Al_2O_3 nanoparticles and showed better lubrication and heat transfer performance. Furthermore study shows that 60% R-134a and 0.1 wt % Al_2O_3 nanoparticles were optimal. Hence, the power consumption drops by 2.4% and COP increased by 4.4% [6].

2. Methodology

2.1. Preparation of Nano lubricants

CNT nanoparticles are added to refrigerant by dispersing in the host lubricant POE (Poly Ester) in the compressor of the air-condition unit. POE is widely used in the industry for refrigeration and air-condition. CNT Nanoparticles with concentration of 0.01wt%, 0.05wt% and 0.1wt% were measured by digital weight balance. Each mass fraction of nanoparticles is mixed with base lubricant and the amount of each sample of nanolubricant prepared was 700 grams. Resultant nanolubricant was homogenized for 15 minutes followed by sonication for up to 4 hours using a water bath sonicator.

2.2. Charging of the system

A Refrigeration laboratory unit (R713) purchased from P. A. Hilton Ltd was used for the conduction of experiments for this research. First of all, system was isolated from electricity. Existing refrigerant and lubricant was evacuated from the system by the service ports provided in the compressor using vacuum pump. 650gm of nanolubricant oil was filled in the compressor through the service port. Then the refrigerant gas of 550g in the system was recharged by using precision electronic balance. The same procedure was followed for all mass fractions of CNT nanoparticle in lubricant.

2.3. Performance Test

The performance test was conducted for all samples of CNT-Lubricant oil mixture of 650gm and pure R-134a of 550g, which are treated as the basis for comparison with other results. In order to obtain repeatability each experiment was conducted 3 times.

3. Results and Discussions

To evaluate the efficiency of refrigeration cycle is the main objective of this research and it is expressed in terms of coefficient of performance (COP). The main purpose of refrigerator or air-condition is to remove heat, Q_L from the refrigerate space. In order to accomplish the heat removal it requires a work input $W_{net.in}$ [7]. Then COP of a refrigerator can be expressed as in equation 1.

Table 1. Temperature and Enthalpy reading in 3 different regions of refrigeration cycle with different concentration of nanoparticles.

T°C	POE Oil with CNT and without CNT			
h kJ	**Pure**	**0.01%**	**0.05%**	**0.1%**
1	18.86	18.85	19.26	19.68
	260.99	260.98	261.2	261.42

2	72.73 280.68	69.28 280.34	70.5 280.5	73.1 280.68
3	10.83 190.05	10.91 189.98	10.58 190.25	10.43 190.37
COP	3.60	3.66	3.67	3.757

Table 1 show that there are three readings for each nanoparticle concentration in lubricant. Reading 1 and 2 are the inlet and outlet temperature of the compressor unit and reading 3 is in the evaporation region of the system where heat has been rejected thus, temperature drops in this region.

Temperature readings converted to enthalpy values by using saturated refrigerant R-134a - Temperature Table. Therefore, enthalpy values of these three regions were used to calculate heat rejection from the system and work input to the system. Hence, COP was calculated using equation 1 as shown in section 3.1 below.

3.1. Formulas and Equations

The coefficient of performance of the refrigeration cycle can be calculated by using the equation 1.

$$COP = \frac{Q}{W} \tag{1}$$

where,

Q is the heat supplied to or removed from the reservoir.

W is the work done by the compressor.

Data reveals that, when nanoparticles are introduced in the open (reciprocating compressor or driven belt compressor) it travels into the whole system along with refrigerant due to miscibility between refrigerant and lubricant oil. Therefore, CNT nanoparticles improved the heat transfer performance of the system because of its remarkable thermo-physical properties due to their large surface area.

COP is related to power consumed by the system, higher the COP of the system lesser the power consumption of the system. It was found that, as the concentration of the CNT in lubricant increases the COP will also increase. Highest COP value was obtained at 0.1wt%, which was highest nanoparticle composition of this study.

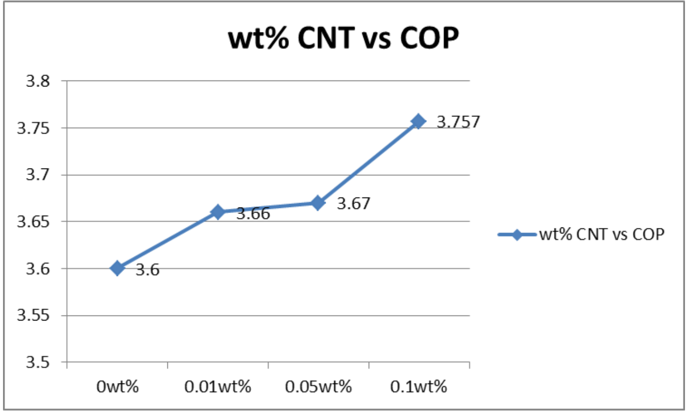

Fig. 1 CNT concentration in Lubricant vs. Coefficient of Performance COP

Fig. 1 illustrates that higher the concentration of CNT higher will be the efficiency of the system. However, more research need to be carried out to determine the optimum concentration of CNT nanoparticle which can show highest efficiency.

4. Conclusions

Addition of CNT nanoparticles into POE lubricant reveals improvement in coefficient of performance (COP) of the refrigeration system. Using nanoparticles reduce the power consumption and cost effective. COP of the system increase with increase of CNT weight percent in base lubricant. The highest COP value obtained was 3.757 at 0.1% of CNT.

Apart from that, Preparation of homogeneous suspension remains a technical challenge since the nanoparticles always form aggregates due to very strong van der Waals interactions.

Acknowledgment

First, I would like to thanks to Taylor’s University for providing me the platform for the research and all the facilities in the laboratory. Secondly, I would like to thanks to University of Malaya for their assistance during my research and I really admire their commitment for the enhancement of the technology.

References

[1] Choi SUS. 1995. Enhancing thermal conductivity of fluids with nanoparticles. In Developments and Applications of Non-Newtonian Flows. FED-vol. 231/MD-vol.66. Edited by: Siginer DA, Wang HP. New York: The American Society of Mechanical Engineers; 1995:99.

[2] Chandrasekar, M., Suresh, S. & Chandra Bose, A. 2010. Experimental investigations and theoretical determination of thermal conductivity and viscosity of AL2O3/water nanofluid. Experimental Thermal and Fluid science. 34(2):210-216.

[3] I.M. Mahbuhul, R. Saidur and M.A. Amalina. 2011. Pressure drop chracteristics of TIO2-R123 nanorefrigerant in a circular tube. Engineering e-transaction (ISSN 1823-6379). Vol. 6, No.2, December 2011.pp 124-130.

[4] Xuan Y, and Li Q. 2000. Heat Transfer Enhancement of Nanofluids, Int. J. Heat Fluid Flow.. 21M:58–64.

[5] Patel H. E, Das S. K., Sundararajan T, Nair A.S, George B, Pradeep T. 2003. Thermal Conductivities of Naked and Monolayer Protected Metal Nanoparticle Based Nanofluids: Manifestation of Anomalous Enhancement and Chemical Effects. J. Appl. Phys. Lett.. 83M:2931–2933.

[6] D. Sendil Kumar, R. Elansezhian. 2012. Experimental Study on Al2O3-R134a Nano Refrigerant in Refrigeration System: International Journal of Modern Engineering Research (IJMER) Vol. 2, Issue. 5. pp-3927-3929

[7] Yunus A. Cengel, Michael A. Boles. 2007. Thermodynamics an Engineering Approach. Sixth Edition. McGraw Hill.

Design an Experiment for Hydrostatic Force Measurements

Muhammad Azim Mohd Shariffuddin[1], Mohamed Nassir[2]

[1]*School of Engineering, Taylor's University, Malaysia,* [2]*School of Engineering, Taylor's University, Malaysia*

[1]*muhammadazim.ms@gmail.com,*[2]*mohamoski@yahoo.com*

Abstract— **In hydrostatics, the pressure depends on the depth of the water from the free surface. Students have difficulty in visualizing the line of action of the hydrostatic force acting on submerged surfaces. The project will serve the educational purpose as it takes aim at the learning process by using a survey and questionnaire in order to implement the fact that the design, the methodology, and the theoretical part of the experiment will serve the educational process.**

Keywords— hydrostatic force, experimental design, educational survey.

1. Introduction

Typically in Fluid Mechanics, topics regarding hydrostatic force usually being explained directly in class without approach to any laboratory exercises. However, there were some students having problems to understand as a whole on what has been thought in class. As a senior student, a hydrostatic force measuring apparatus is required to be design or re-design to help students understand on hydrostatic force and the line of action of the resultant force on the submerged surface. Although many sophisticated design of hydrostatic pressure measuring instrument are already available, a simple and basic measuring apparatus is desired and does not rely much or on electrical power, sensors, computers, etc. Ideas from the existing apparatus was used as a concept and guidelines to design or re-design the hydrostatic force measuring apparatus.

A simple design for hydrostatic force measuring apparatus is designed so that users can understand the concept of determining hydrostatic force on a submerged surface based on Pascal's Law.

2. Methods

2.1. Balance moment of force

This project is designed based on the guidelines of existing designs available. The project is designed based on the application of moment of force. The system of this project must be in balance state in order to conduct the experiment with minimum errors. The tendency of a force to cause rotation about an axis or a point is called the *moment,* M, of the force, F, with respect to that axis or point [1]. To maintain balance, the moments of two forces must be equivalent and opposite in the tendency to rotate a balance arm or beam. The resultant moment about a point can be determined by finding the summation of moments caused by all the forces in the system [2].

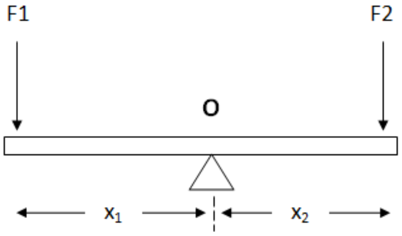

Fig.1 Equilibrium moment of a force

Fig. 1 shows the body of diagram of equilibrium moment of force for the lever arm component . Hence, the resultant moment to balance the lever arm can be determine by

$$\sum M = F_1 d_1 \times F_2 d_2 \tag{1}$$

F_1 and F_2 are the forces or loads applied on the lever arm while x_1 and x_2 are the distance between the loads and the center point O. The system is in equilibrium state when the moment left side is equivalent to right side.

2.2. Bearing Loads and Actual Shaft Loads

Since the application of balancing at hinge point involved rotating shafts and stationary housing, for such a configuration an approved interference fit should be specified between the shaft at the mounting site and the inner race bore of bearing itself. A close push fit should be also should be specified between the bearing's outer diameter and the housing bore (inner diameter) [3].

The basic arrangement for typical application is to support a rotating shaft on two bearings located at the end of the shaft. Fig.2 shows the part of illustration for the shaft and bearings arrangement

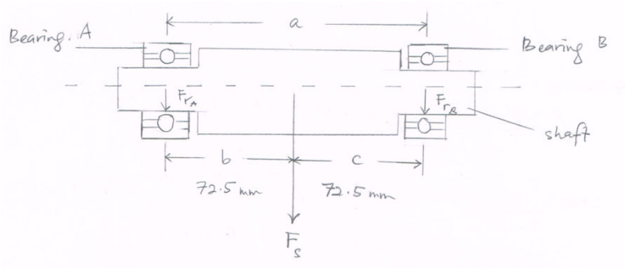

Fig.2 Illustration of the shaft and bearings arrangement

For shafting, the static tension is considered to be supported by the bearings, and any loads acting on the shaft are distributed to the bearings. Based on Fig.2, Equation (2) and (3) shows the calculation method for bearing load distribution on bearings

$$F_{rA} = \frac{c}{b+c}(F_s) \tag{2}$$

$$F_{rB} = \frac{b}{b+c}(F_s) \tag{3}$$

where F_{rA} and F_{rA} are radial load on bearing A and B, while F_s is radial load on shaft.

There are many factors that cause the actual shaft load during operation compared to calculated shaft load due to vibration or shock. Usually the actual shaft load will be much greater than the calculated load. Hence, the actual shaft load can be determine by

$$K = f_w \cdot K_c \tag{4}$$

Where K is actual shaft load, is load factor, is theoretically calculated load value. The load factor chosen for this project is around 1.0 ~ 1.2 since the application is related to measuring instrument.

2.3. Computer Aided Design (CAD) of Apparatus

The design for this project was inspired from three types of existing designs. The final design was based on combination of three existing designs. Using Solidworks software, the final design model was constructed as a method to save cost before the actual implementation of project. In the first design, the quadrant acts as water vessel where water is inserted inside the hollow quadrant. In the first design the quadrant is adjustable, enable to measure hydrostatic pressure at different angle of surface plane. While in second design [4], the quadrant is immersed in the water tank to measure the hydrostatic pressure acting on it. The third design is the improvement from the second design to look more sophisticated.

In the end, the final design consist of all characteristics where quadrant will be immerse inside a water tank and the shaft that mount the quadrant is adjustable enable to measure hydrostatic force at different angle of submerged plane. The lever arm in the final design is improved parallel to available tools and materials in the campus. Figure 6 shows the final design inspired by designs in Figure 3, 4 and 5 .

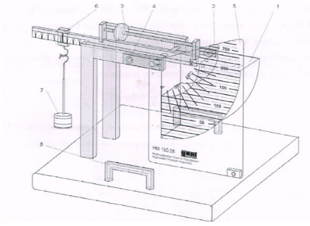

Fig. 3 First design given by supervisor as a guideline

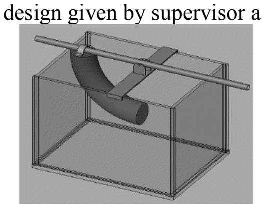

Fig. 4 Second design from existing design [9]

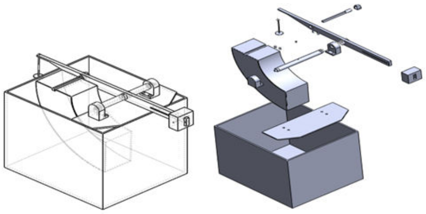

Fig. 5 Third design using Solidworks CAD software

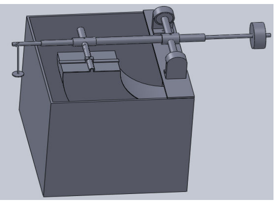

Fig. 6 Final Design

2.4 Resultant Hydrostatic Force and Center of Pressure

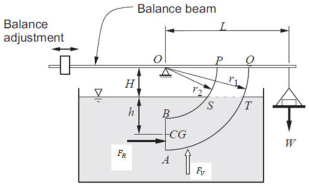

Fig. 7 Illustration of apparatus for hydrostatic force measurements

There can be four types of surfaces used to measure hydrostatic force on a submerged surface plane which are horizontal, vertical, curved, and incline surfaces [5]. However for this project, the vertical surface and incline surface plane are used to measure hydrostatic force. In this project, the resultant hydrostatic force can be determine by

$$F_T = \sqrt{F_H^2 + F_V^2} \tag{5}$$

where F_H is the horizontal force perpendicular to vertical surface plane and F_V is the magnitude of vertical force. The distance of center of pressure from free liquid surface can be determine by [5]

$$h_p = h_c + \frac{I_G}{A h_c} \tag{6}$$

where I_G is the moment of inertia of a surface plane about an axis passing through the centroid and parallel to the free surface [5].

3. Results and Discussions

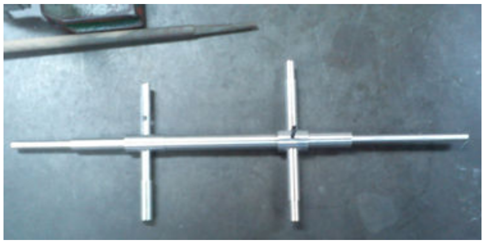

Fig. 8 Lever arm component

Fig. 8 above shows the outcome one of the component for the project apparatus. Using a lathe machine to cut and shape the raw material into aluminium rod is much convenient compared to other methods. The quadrant or quarter circle is outsourced to get an accurate and perfect outcome. The weight hook applied on lever arm is set to be 5N to overcome 6N of load on the opposite side during operation. The remaining 1 N of load is calibrated by the counter weight balance along the threaded lever arm.

4. Conclusions

Overall the design apparatus is manufactured based on the concept balance moment of force. The total amount of force in the system can be determine by the summation of vertical and horizontal force acting on the surface planes of quadrant [6]. Counter weight is used to overcome the force from opposite side of lever arm.

References

[1] Eide, A. et al. (2008) Engineering Fundamentals & Problem Solving. 5th ed. New York: McGraw-Hill, p.218 -219.

[2] Hibbeler, R. (2010) Engineering Mechanics Statics. 12th ed. Singapore: Prentice Hall, p.118.

[3] Collins, J. (2003) Mechanical Design of Machine Elements and machines. New York: John Wiley & Sons, p.436

[4] Atiqullah, M. and Russell, N. (2010) "Design, Building and Teaching with a Hydrostatic and Buoyancy Apparatus", paper presented at Fall 2010 Mid-Atlantic ASEE Conference, Villanova University, 15-16 October. Marietta, GA.: Southern Polytechnic State University, p.1-6

[5] Singh, S. (2009) Experiments in Fluid Mechanics. New Delhi: PHI Learning Private Limited, p.10.

[6] Cengel, Y. and Cimbala, J. (2006) Fluid Mechanics Fundamental and Applications. New York: McGraw Hill, p.86

Effect of Viscosity on Impedance Pump Performance

Muhammad Hamri bin Ibrahim*, Mushtak Al-Atabi

School of Engineering, Taylor's University, Malaysia

**antakimate@yahoo.com*

Abstract — **This study investigates the principle of impedance pump which made of an elastic tube filled with fluid that is connected at both ends to more rigid tube. The study show that the flow can be attained by introducing a periodic pinching applied at an asymmetrical location along the elastic tube. The effect of viscosity on impedance pump performance was experimentally investigated. The results show that as viscosity increases the mass flow rate through the pump decreases, while keeping the tapping frequency constant. The effective range for impedance pump operation was also identified.**

Keywords— impedance pump, viscosity, flow rate

1. Introduction

The impedance pump principle can be demonstrated by using an elastic tube filled with fluid which connected at its ends to more rigid tubing of different impedance [1]. By periodically pinching the elastic tube with an active element at an asymmetric position relative to its ends, a complex series of waves is produced. Traveling waves emitted from the compression of the elastic tube will combine with reflected waves at the impedance-mismatched positions. As the result of these wave dynamics, a net flow in a specific direction is observed. The impedance pump develops the net flow by imparting the kinetic energy from the compression of the elastic tube and transmitting that energy into the fluid through surface waves [2].

1.1. Impedance Pump Mechanism

The impedance pump consists of an elastic tube which functions as compressible section and connected at both ends to a more rigid tube with different impedance. The compression section is suitable for any material that allowing for wave propagation because impedance based pumping dependents on wave reflection. Impedance mismatch is created by connecting the elastic tube at both ends to another materials with different mechanical and geometries properties and therefore will generate the net flow. Figure 1 below shows a schematic of different impedance which represented by Z0 and Z1.

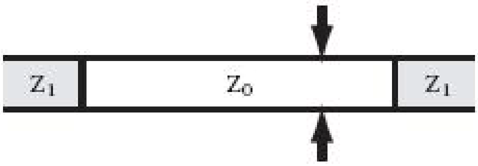

Fig. 1 A schematic of an impedance pump. The impedances are represented by Z0 and Z1. The two arrows show the pinch location [3].

The pinch location is the fundamental principle of the impedance pump mechanism. The pinch location must be asymmetrically from the center of the elastic tube in order to produce a flow. Periodic pinching at an offset center location results in a pressure builds up from wave interference and generate a flow. The direction of flow inside the tube can be reversed by changing pinch location, frequency and duty cycle [3].

2. Methodology

An experimental approach was chosen to investigate the impedance pump's behavior. The objective of the experiment is to identify the best range of fluid viscosity that impedance pump can operate effectively. This project also involves the modeling of experiment setup to examine the behavior of the impedance pump using different fluid viscosity. There are several data to be taken from the experiment in order to obtain the result.

2.1. Experiments

Experiments are conducted to investigate the effect of viscosity on impedance pump. All experiments were done in a controlled room temperature approximately 28°C. The volume inside the setup is kept constant for every experiment with tapping frequency at 5 Hz.

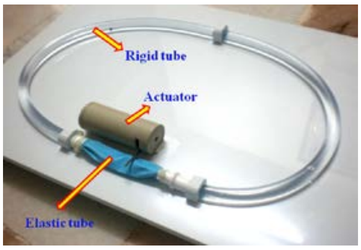

Fig. 2 The experiment setup of impedance pump

Impedance pump consist of elastic tube, rigid tube and actuator as the main components as shown in the Fig 2. The elastic part made of a latex tube with thickness of 0.4 mm and length of 0.15 m was used for the closed loop model. Another PVC tube, with diameter 0.077 m and length 0.8 m was used as the rigid tube. While the actuator was carried out using a direct current (DC) motor with a metal rod attached at the tip. An alternating current (AC) was supplied to the DC motor with adjustable frequency causing the metal rod to oscillate back and forth continuously using the function generator as shown in the Fig. 3a. Function generator used to generate sinusoidal function which allows the pincher to move back and forth continuously. To improve the frequency and amplitude of the actuator, amplifier was introduced to the system as shown in the Fig 3b. This mechanism was observed to be a reliable way to power the pump in the closed loop model.

Fig. 3a The function generator

Fig. 3b The amplifier

The effect of the fluid viscosity is tested using eleven different water-glycerol mixtures. The viscosity is adjusted by adding the percentage of glycerol inside the water solution. The eleven solutions are water with 0% volume glycerol, a 10% volume glycerol, 20% volume glycerol until 100% volume glycerol with 0% volume water. Stop watch is used to measure the time needed for the tracer inside the setup to complete one revolution.

3. Results

Table 1 shows the data collected from the viscosity experiment through the impedance pump with constant tapping frequency 5 Hz at 28 ^{o}c. The viscosity of the solution was converted from percentage of glycerol to viscosity value in centipoise (cP) based on data in the Viscosity of Aqueous Glycerine Solutions table [4].

Table 1. Experiment result for viscosity

Viscosity, ν		Density, ρ (kg/m³)	Area, A (m²)	Velocity, v (m/s)	Mass Flow Rate, ṁ (kg/s)
%	cP				
0	0.84	1000	0.0047	0.106	0.494
10	1.09	1101	0.0047	0.086	0.441
20	1.35	1127	0.0047	0.073	0.383
30	2.05	1145	0.0047	0.056	0.299
40	2.92	1177	0.0047	0.043	0.236
50	4.57	1200	0.0047	0.032	0.179
60	7.91	1216	0.0047	0.024	0.136
70	15.78	1233	0.0047	0.0056	0.032
80	39.14	1247	0.0047	0.0033	0.019
90	131.03	1262	0.0047	0.0019	0.011
100	771.62	1315	0.0047	0.0011	0.007

Density of the solution, area of the tube and velocity of the solution are used to calculate the mass flow rate of the fluid.

$$\dot{m} = \rho A v \quad (1)$$

where $\dot{m}$ is mass flow rate
ρ is density of the solution
A is area of the tube
v is the velocity of the solution

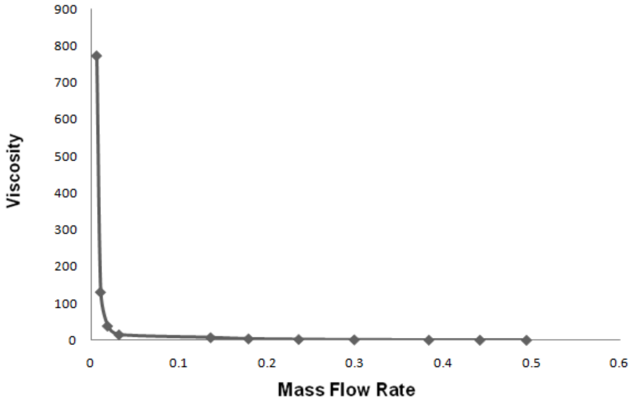

Fig. 4 Effect of viscosity on the mass flow rate through the impedance pump with constant tapping frequency 5 Hz

Fig. 4 above shows the effect of viscosity on the mass flow rate through the impedance pump with constant frequency 5Hz. Glycerol solutions with different fractions of glycerol to water were used to investigate the effects of viscosity on the performance of impedance pump. The solutions tested were 0%, 10%, 20%, 30%, 40%, 50%, 60%, 70%, 80%, 90% and 100% volume glycerol by mass corresponding to relative viscosities of 0.84 cP, 1.09 cP, 1.35 cP, 2.05 cP, 2.92 cP, 4.57 cP, 7.91 cP, 15.78 cP, 39.14 cP, 131.03 cP and 771.62 cP respectively.

4. Discussions

The results in Fig. 4 show that as viscosity increases the mass flow rate of glycerol-water solution through the pump decreases, while keeping the tapping frequency constant at 5 Hz. The mass flow rate consistently decreases from 0% to 70% volume glycerol solution with average of 0.066 kg/s. However, from 70% to 100% volume glycerol shows a very small decrease of mass flow rate with average of 0.008 kg/s. Small change in mass flow rate indicates the higher time needed for impedance pump to perform its application.

Therefore, the best range that impedance pump can operate effectively is from 0% volume glycerol which is 0.84 cP until 70% volume glycerol which is 15.78 cP. Every fluid with the viscosity within this range, 0.84 – 15.78 cP is suitable for impedance pump. It also can be concluded that gasoline (0.5 cP), water (1.0 cP), methanol (0.6 cP), ethanol (1.2 cP), mercury (1.5 cP) and milk (3.0 cP) are suitable as the working fluid for impedance pump.

This range gives people a better understanding on the fluid viscosity that supposed to use for impedance pump. This result also gives people a new perspective of impedance pump and leads to a new application in fluid transportation field.

5. Conclusions

The impedance pump can be demonstrated by an elastic tube filled with fluid and connected at its ends to more rigid tube of different impedance. By periodically pinching the elastic tube with an active element at an asymmetric position relative to its ends, a complex series of waves is developed. Presented in this study are the experimental results of the viscosity effects on the impedance pump performance. The experimental results show that the impedance pump was capable to pumping the fluid effectively within a certain range of fluid viscosity. The results indicate that as viscosity increases the mass flow rate through the pump decreases, while keeping the tapping frequency constant at 5 Hz. The mass flow rate is consistently decreases as the fluid viscosity increases from 0% to 70% volume glycerol solution. However, the mass flow rate shows a small change from 70% to 100% volume glycerol solution. Therefore, the best range that impedance can operate effectively is from 0% volume glycerol which is 0.84 cP until 70% volume glycerol which is 15.78 cP. Every fluid with the viscosity within this range, 0.84 – 15.78 cP is suitable for impedance pump.

Acknowledgment

I would like to thank all people who supported me throughout my final year project. Special thanks and deep acknowledgement go to my supervisor, Dr. Mushtak Al-Atabi for his insight, inspiration, motivation and providing me continuous support for this entire project. Thanks also to Mr. Douglas and other lectures in Taylor's University for providing me necessary support throughout the project.

References

[1] Avrahami, I., and Gharib,M., "Computational studies of resonance wave pumping in compliant tubes," *Journal of Fluid Mechanics*, 608:139-160, 2008.

[2] Hickerson, A. I., *An Experimental Analysis of the Characteristic Behaviors of an Impedance Pump*. PhD thesis, California Institute of Technology, 2005.

[3] Rinderknecht, D., Hickerson, A.I., and Gharib, M., "A Valveless Micro Impedance Pump Driven by Electromagnetic Actuation," *Journal of Micromechanical Microengineering*, 15:861-866, 2005.

[4] Bingham, E. C., and Jackson, R. F., *Bull. Bur. Standards*, 14, No. 298, 59-86 (1917).

Evaluation of CFD Sub-Models for the Intake Manifold Port Flow Analysis

M. M. Khan*, S. M. Salim

School of Engineering, Taylor's University, Selangor, Malaysia

**Email: mohsenkhan82@yahoo.com*

Abstract—**The purpose of this research is to appraise and simulate computational fluid dynamics (CFD) models, with respect to computing time, which can predict the flow conditions in an Intake Manifold (IM) of naturally aspirated Spark ignition (SI) engine by using flow analysis numerical model from ANSYS CFD software (FLUENT 14.0). The simulations are carried out by using different steady state Reynolds Averaged Navier Stoke (RANS) turbulence models such as Standard k-epsilon (k-ε) Re-Normalization Group k-ε (RNG), Realizable k-ε, k-omega (k-ω) and Reynolds Stress Model (RSM). Initial Boundary conditions and validation of simulation results based on experimental data are used. It is observed that each model produces almost similar results when it comes to pressure drop inside plenum and inlet velocity. However, RNG k- ε accounts for swirl dominated flow, predicting better flow conditions inside the manifold. Therefore, RNG k- ε is best to capture intake manifold flow turbulent conditions.**

Keywords— Fluent, Computational Fluid Dynamics (CFD), Intake Manifold, Realizable k-ε, k-omega (k-ω), Re-Normalization Group k-ε (RNG), Reynolds Stress Model (RSM), Turbulent flow.

1. Introduction

The engine of a car needs air for the combustion process in the cylinders. Air Intake Manifold (IM) has an important role in getting desirable amount of air into automobile engine by improving the combustion efficiency and reducing air pollution [1]. The main purpose of an air IM is to provide the engine with constant amount of required clean air to burn in the combustion chamber. The air enters the combustion chambers through IM, in which plenum box distributes the flow uniformly into the respective ports which goes to the combustion chamber. To optimize the flow inside intake system, thorough understanding of flows, inlet velocity and pressure drop through the system is essential [2].

The main objective of this study is to analyze different Reynolds Averaged Navier Stoke (RANS) turbulence models for better flow prediction of Intake Manifold. The numerical model of Proton Satria Neo 1.6L Air IM (Fig. 1) is used for the simulations. FLUENT is used to analyze the internal flow of air intake manifold and to get the results which are validated from the data collected from experiment.

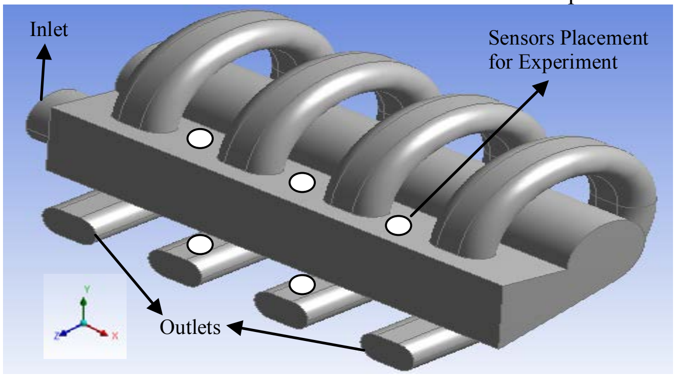

Fig 1: Computational Domain of Intake Manifold.

2. Research Methodology

Numerous studies on IM optimizations have been conducted. Kale et al. [3] analyzed the steady flow inside the IM of a S.I engine using STAR-CD but only considered Standard k-ε model to analyze optimum flow conditions inside IM. David et al. [4] studied the flow characteristic of flow inside the swirl helical IM port and concluded that CFD has high tendency on providing ways to design high swirl generating capacity intake ports which can help to reduce NOx emissions. However, little research has been done regarding the testing of CFD models which can analyze the flow inside IM accurately.

A three dimensional (3-D) geometry of IM consisting inlet, plenum and 4 outlet ports is developed. The mesh generated consists of 348,730 numbers of tetrahedral cells. To verify the adequacy of the grid, grid independent test was conducted [5]. Pressure based boundary conditions (from experiment, Fig 2) are assigned to the inlet and outlets of IM. 3-D, steady state numerical simulations are carried out using Reynolds Averaged Navier Stoke (RANS) Standard k-ε, RNG k-ε, Realizable k-ε, k-ω and RSM. It is noted that RNG performed exceptionally well as it accounts for swirl dominated flows [6]. RSM under relaxation factor also shows desirable results but due to higher computing time (Table 1) and cost it is less feasible.

Table 1: Computational Time Taken To Run Each Model

	Models	Estimated Computational Time (Hour)
1	Standard k-ε	2.5
2	Realizable k-ε	3
3	RNG k-ε	3.5
4	k-ω	3
5	RSM	4.5

Experimental Setup (Fig. 2) is developed for the initial boundary conditions and validation of CFD simulations. Pressure sensor is placed at the exit of outlet ports and at the plenum of IM to measure the pressure difference (Placement indicated in Fig. 1). The signals from pressure sensor are recorded by Engine Control Unit (ECU) of the car which is capable of data logging up to 200 Hz. The plots of static pressure and velocity magnitude of each model and experimental data are drawn and the difference in the discretization of each model is shown in the Fig. 3.

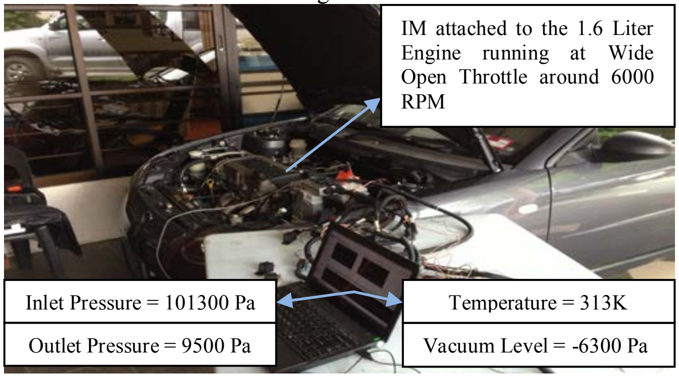

Fig 2: Experimental Setup and Calculated Data for Boundary Conditions

3. Results and Discussion

The velocity magnitude and static pressure profiles of the IM plenum chamber of all the models are shown in Fig. 3a and Fig. 3b respectively. It is observed that velocity magnitude discretization of each model differs greatly while static pressure drop has almost the same results with minor fluctuations. The theoretically calculated inlet velocity (using the piston swept volume of 1.6L) is well predicted by RNG k- ε and Standard k- ε with up to 5 percent error while Realizable, k- ω and RSM shows discrepancies giving up to 10 percent error. For static pressure all model shows larger deviation in the pressure drop compared to experimentally calculated values. It is observed that the experimental data gathered also have uncertainty when it comes to sensor effectiveness and leakages. Furthermore, the piston movement causes fluctuating backflow velocities and pressure changes inside the ports, making it difficult to get accurate boundary conditions which are used to predict the flow inside the manifold using RANS steady state models.

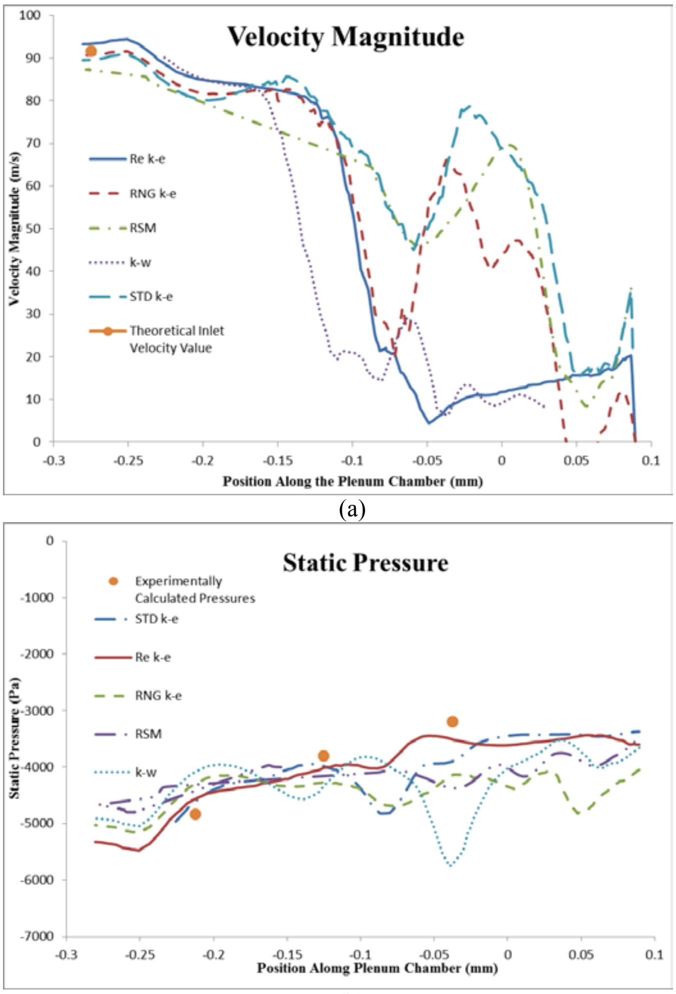

(a)

(b)

Fig 3: Velocity Magnitude and Static Pressure

The velocity vector and streamlines plots (Fig. 4a & Fig. 4b) obtained from the analysis shows the better prediction of the high turbulent flow inside the ports and plenum chamber of the IM, as found in other literature reviews [2] [3] [4] [5]. Beside the graphical results, vortices formed in RNG k- ε shows proper distribution of the flow in all the ports and plenum chamber. Hence making it better choice to analyze the flow inside intake manifold.

4. Conclusion

The investigation of the flow regime, within the intake manifold, using CFD analysis is possible. However, applying the correct parameters and CFD models, which can provide economical simulated results, is highly important. This study appraises different CFD turbulent models and the importance of realistic parameters to successfully predict the flow inside IM. It is noticed that each model shows variation with the experimental results. While, RNG and RSM shows promising results with lower margin of error compared to standard k- ε and k- ω.

For future studies, it is important to analyze each model using transient flow conditions for better accuracy and predictability of the flow inside IM with part throttle conditions. Furthermore, for future validations high calibrated sensors should be used to improve the accuracy of experimental data obtained.

References

[1] R. Rajput, Internal Combustion Engine, Laxmi Publications, 2007.

[2] M. Safwan, "Pressure Drop Analysis of 1.6l Car Air Intake System," Faculty of Mechanical Engineering, Universiti Malaysia Pahang, November 2009.

[3] S. Kale and V. Ganesan, "Investigation of the flow field in the," *Indian journals of Engineering and Material Sciences,* 2004.

[4] D. R. Jebamani and T. M. N. Kumar, "Studies on Variable Swirl Intake System for Di Diesel Engine Using Computational Fluid Dynamics," *Thermal Science*, vol. 12, no. 1, pp. 25-32, 2008.

[5] B.M.Angadi, A. S. Malipatil, V.V.Nagathan and R.S.Kattimani., "Modelling and Analysis of Intake manifold of a Multi-cylinder SI engine," in *& 4th International Conference on Fluid Mechanics and Fluid Poweer*, Madras, Chennai, 2010.

[6] H. K. Versteeg and W. Malalasekera, An Introduction to Computational Fluid Dynamics, The Finite Volume Method, Pearson Prentice Hall, 2007.

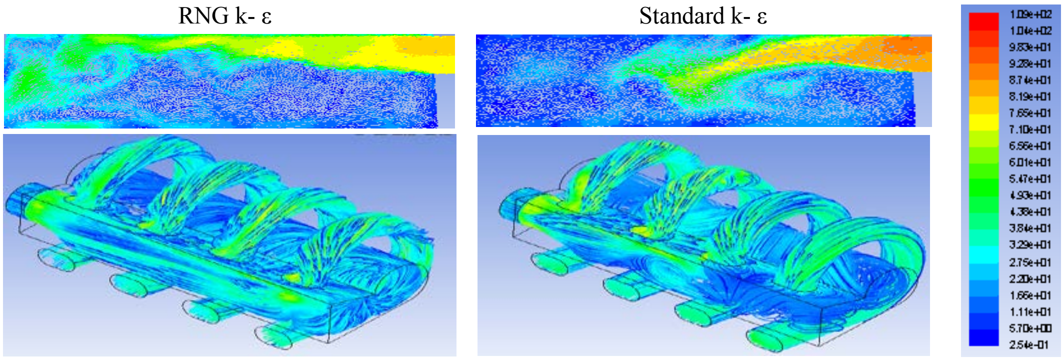

a) Velocity Vectors (Plenum xy plane cut)

b) 3D Streamlines

Fig 4: Plenum Chamber XY Plane Cut Velocity Vectors and 3D Streamline Flow

Performance Analysis of Variable Pitch Helicopter Rotor

Muhammad Firdaus Abu Bakar, Abdulkareem Sh.Mahdi Al-Obaidi

Department of Mechanical Engineering,School of Engineering, Taylor's University, Malaysia.

**Corresponding author: muhammadfirdaus_abubakar@live.com*

Abstract – **Applying the concept of airplane wing, rotating helicopter rotor blade is what is called rotary wings. Among many others, lift generation depend on 3 parameters; angle of attack, air speed, and area of the rotor blades. Excessive input of these parameters does not contribute to the lift optimization. It's been concluded that increasing blade length did not bring any limitation to the aerodynamic performance. However the other 2 parameters do have limitation in lift production.Experimental approach taken in this study had led to find the limiting state and identify the position of the blade section length as the absolute air velocity vector to be used in calculating the lift force analytically.**

Keywords— Helicopter,Lift force, Airfoil, Rotor, Pitch angle.

1. Introduction

Helicopter is among the most useful kind of air transportation ever invented today. The ability of helicopter to take off and landing vertically in limited space differentiate it from other types of aircraft. An airplane for example is needed to have certain amount of air flow moving around the airfoil shaped wing to generate lift [1]. The flight criteria of a helicopter is nothing like the airplane wing in generating lift force. Thus, make it able to hover in one place without the needs of moving forward. However people may not notice that helicopter blades are actually the wings that generate lift which are in the form of rotary wing.

Rather than having air velocity by moving forward in the case of airplane, the lift force can also be generated with rotating helicopter blades. Using the same concept as airplane wing to generate lift, helicopter blades are the rotating wings that strike the air circularly in order to generate thrust [2]. These rotary wings of helicopter are the main component in providing the lift force. It is true that the speed is important parameters in lift generation, but depending only upon the speed alone does not mean we can have an efficient method of lift generation. Therefore like the airplane wing, the angle of attack of the wing also can vary the amount of lift generated by the airfoil shape of the wing. Angle of attack is defined as the angle between air velocity vector and the central line of the airfoil chord. In the construction of helicopter variable pitch rotor head, the rotor blade angle can be varied to adjust the angle of attack.

Hence, in the design of a helicopter, the way it propels itself up is basically depend on these 2 essentialdesign components of the rotor blade; rotational speed and the angle of attack. This study is aiming to correlates the relationship between these 2 designs to optimize the helicopter performance. However, The entire project scope did not cover other aerodynamics factor such as airfoil profile drag, pitching momentsand fuselage drag effect.

2. Airfoils Aerodynamics Properties.

Figure 1 shows a typical wing airfoil and the forces and moment acting during the flight. This study is focuses on the lift force only as it is the most essentials forces which affecting the helicopter performance. While this study considers only the lift force, one should not completely neglect the effect of the drag and pitching moments. These two other components built up should bring towards further study.

The formula for lift force in general can be written as;

$L=0.5\rho C_L\, v^2 S$

$L= 0.5\rho C_L\, (\omega R)^2 \pi R^2$

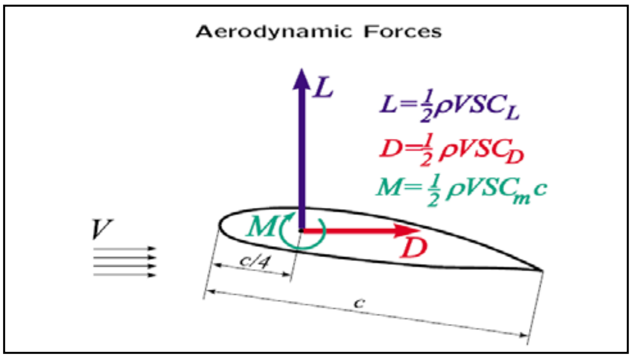

Fig. 1 Illustration of aerodynamics forces develop in an airfoil [3].

The important aerodynamic parameter which is the lift coefficient $C_L$for a given inflow velocity and airfoil profile depends on the angle of attack. Wing area, S in the formula is defined by the helicopter rotor disk area, A which in relation with the blade span, R. Rotational speed, v depends on the angular velocity, ω and radius of blade, R. Because of the rotational movement of the airfoil, the air velocity on each blade section is different. One of the objectives of this study is to identify the section of the blade length that represents absolute air velocity vectorto be used in the formula.

3. Lift Characteristics of an Airfoil Section

Figure 2 showsthat lift coefficient is directly proportional to the angle of attack for a typical airfoil. The lift coefficient keeps on increasing up to one point known as stall angle. The stall angle happened when the boundary layer of the flow at the upper surface starts to separate from the airfoil surface. The flow separation is the reason of the inability of an airfoil generating the effective lift.

The stall angle varies by different types of airfoil.

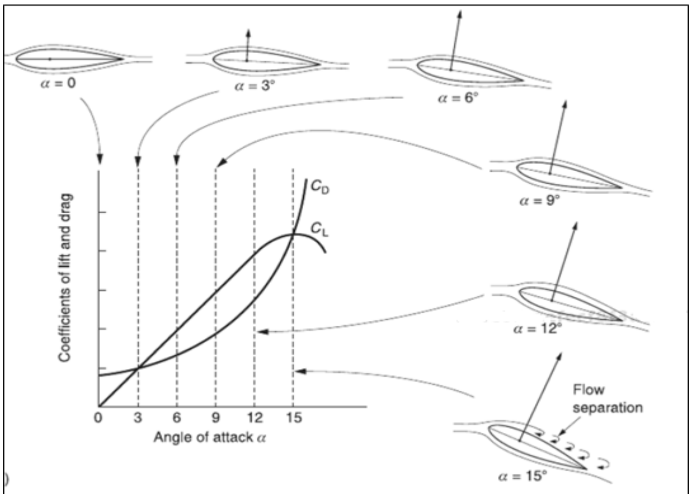

Fig. 2Lift coefficient and drag coefficient general relationship towards continuous increment angle of attack [2].

4. Detailed Experiment

A model scale helicopter is used to find the amount of lift force generated at specific combination of blade RPM and blade angle of attack. The objective of the experiment is to correlates these 2 performing parameters in production of lift force and identify the limiting state. The amount of lift force generated by the model scale helicopter will be measured using a specifically constructed device called “Lift Measurement Rig” as shown in Fig. 3.

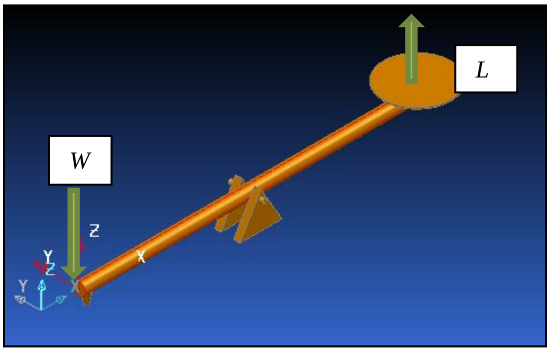

Fig. 3 3D drawing of conceptual design “Lift Measurement Rig”

5. Experiment Result and Discussions

The experiment was conducted using 4 different angles of attack with 5 different RPM ranges. The amount of lift produced in each combination are measured with the digital scale and recorded and tabulated in Table 1 and plotted in Fig. 4.

The figure shows that the trend of lift force produced are increasing exponentially over the RPM increment for all angle of attack. However, it is noticeably to mention that the lift curve slope angle of attack of 12 degree is start to decreasing at high RPM.

While this study is conducted under experimental approach, the comparison of the data obtained with analytical calculation is analysed to find the section of the blade length that represents an absolute air velocity vector for the formula. It is expected to define the position of the blade that will be used as the velocity vector components in calculating the lift force using the formula. Unlike the airplane, the helicopter rotor blade is having different velocity, *v* at every blade length point due to its circular movement.

Table 1Lift Force Generation.

Blade Angle	RPM	Lift Force Generated
3	864	43
	1215	72
	1488	110
	1820	154
	2023	193
6	881	86
	1087	150
	1320	238
	2050	312
	1980	390
9	870	131
	1105	220
	1400	318
	1800	470
	2016	579
12	872	168
	1136	278
	1403	440
	1890	570
	2006	680

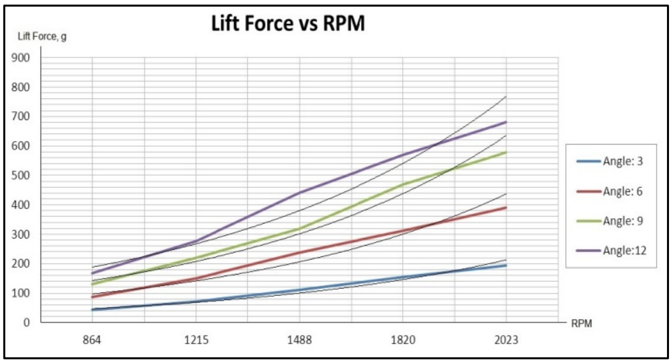

Fig.4Graph of lift force generated measured with the rig for various combinations of RPM& angles of attack based on NACA 0012 airfoil.

6. Experimental Error Analysis

To ensure that the readings of the digital weigh scale really represent the amount of lift generated, the lift measurement rig has went a calibration process by matching the standard weight block with the weight measured. The calibration was made physically on the mechanical design by moving the digital weight scale contact point accordingly. It is also important to test the model under the operating condition as close as possible to real helicopter in such way the aerodynamic properties equally matched. As to avoid the premature separation in very low Reynolds number, a rectangular blade shape will be used. Rectangular tip blade does not affect much in tip flow separation compared to tapered tip [4].

7. Conclusions and Recommendations

From the gathered experiment result, the first conclusion can be made is that the effective lift force generated is limited by the pitch angle of the blade. The lift-curve-slopes for angles of attack 3, 6 and 9 look similarly to each other. Interestingly to notice, there is slight difference in lift-curve-slope at 12 degree angle of attack under the same RPM range where it starts to decrease at blade rotational speed about 2000rpm. The justification on this scenario is due to the flow separation starts to develop at that high angle of attack. Another conclusion can be made is the location of blade section that can be taken as the air velocity vector in calculating the lift force analytically. From the comparison between the lift force measured and calculated, the matching absolute air velocity vector is concluded at the position of 0.5 of the blade length section.

Things to note, helicopter blade can experience a partial stall with the blade tip tends to stall earlier than the blade root due to higher rotational speed. Blade rotational speed and helicopter flight speed can contribute to supersonic flow at the blade tip, which greatly degrades the helicopter performance. Last but not least, this study only focuses on the lift force as the main key point in determining the performance. Other parameters such as blade airfoil geometry and the tip losses may also affect the generation of the lift force

Acknowledgment

A big acknowledgement goes directly to supervisor, Dr.Abdulkareem Sh.Mahdi and Malaysia Radio Control Club.

References

1. Bielawa, R. L. (1992). Rotary Wing Structural Dynamics andAeroelasticity. AIAA Education Series.
2. Watkinson,J. (2004). Art of Helicopter. Butterworth-Heinemann.
3. Petrovic, Z. (2002). Elements of Semi-Empirical Aerodynamics. Private documents.
4. Singleton, J. D.: and Yeager, W. T., Jr (1998). Important Scaling Parameters for Testing Model-Scale Helicopter, AIAA-98-2881.

Semi-Empirical Model for Forced-Convection Condensation on Integral Finned-Tubes

Muhammad Habib Zaid*, S. Namasivayam

Mechanical Engineering, Taylor's University, Malaysia
**muhammadhabibzaid@gmail.com*

Abstract— **Main reason why integral-fin tubes are enhanced over smooth tubes is because of the added surface area presented by the fins that increases the area for heat transfer. The major objective of this project is to develop a semi-empirical model that can prove all the data collections of previous studies are in the mean deviation of ± 25% using engineering and scientific formulas and methods.**

Keywords— Semi-Empirical Model, Forced Convection Condensation, Finned Tubes, Condenser, Heat Exchanger

1. Introduction

The use of horizontal, integral-fin tubes as shown in Figure 1 to enhance condensation is quite common in the design of surface condensers in the refrigeration and power generation industries such as steam turbine. Integral-fin tube is a tube with circumferential fins on its outside, manufactured by machining the material between the fins away. Main reason why integral-fin tubes are enhanced over smooth tubes is because of the added surface area presented by the fins that also increases the area for heat transfer as given by equation 1. [1]

$$Q = hA\Delta T \tag{1}$$

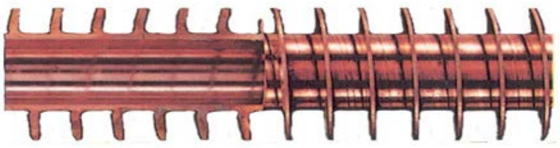

Figure 1: Horizontal Integral-Fin Tube [2]

Figure 2 shows how the condensation on integral-fin tube works where high temperature steam will make contacts with the fin-tube that contains low temperature of condensate. The temperature differences will result for the condensation process and liquid will be formed. A bundle of horizontal integral-fin tube is used in heat exchanger of a steam turbine such as the shell and tube heat exchanger. As the efficiency of condensation process is increasing, thus more liquid can be formed in a certain time and the heat exchanger efficiency will also increase that can also results for the increasing efficiency of a steam turbine.

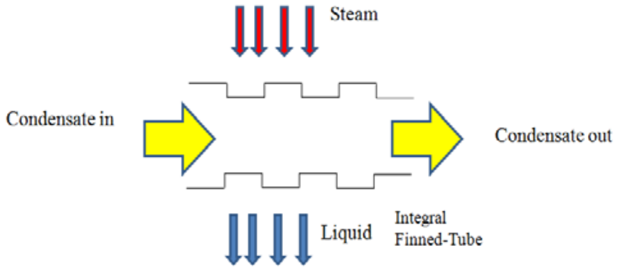

Figure 2: How Integral-Fin Tube Works

2. Methodology

Cavallini et al. (1996) developed a semi-empirical model for forced-convection condensation on integral-fin tubes. The following equation is proposed for the vapour-side, heat transfer coefficient.

$$\propto = \left[\propto_{st}^{n} + \propto_{fc}^{n}\right]^{\frac{1}{n}} \tag{2}$$

$\propto_{st}$ denotes the vapour-side, heat transfer coefficient under stationary vapour conditions and obtained from the model of Briggs and Rose (1994). denotes the vapour-side, heat transfer coefficient when forced-convection dominates and the effects of gravity and surface tension become negligible [3]. This was found from the following correlation.

$$Nu_{fc} = CRe_{eq}^{0.8}Pr^{\frac{1}{3}} \tag{3}$$

where,

$$Re_{eq} \approx \left(\frac{\rho_V U_{max}\, d_0}{\mu}\right)\left(\frac{\rho}{\rho_V}\right)^{0.5} \tag{4}$$

$$C = 0.03 + 0.166\left(\frac{t}{p}\right) + 0.07\left(\frac{h}{p}\right) \tag{5}$$

The values of C and n were obtained from the best fit procedure using the data of Bella et al. (1993) and Cavallini et al. (1996) for R-11 and R-113 condensing on 3 tubes.

Comparison was made between the model of R-11 and R-113 data of Cavallini with R-113 data of Honda et al. (1989, 1991). The model is able to predict the experimental data for forced-convection condensation of R-11 and R-113 occurring on horizontal integral-fin tubes with a margin of ±20%. In conclusion, Cavallini et al. successfully predicts forced-convection condensation data for R-11 and R-113 as test fluids but gives less accurate data for steam. Cavallini et al. (1998) modified the previous model and produced a model for forced-convection condensation on a single horizontal pin-finned tube. The model was able to predict the data within an absolute mean deviation of 7.6% [4].

For this project, a semi empirical model involving assumptions, approximations, or generalizations designed to simplify calculation. Dimensional analysis and best fit procedure will be used to generate the model where it reduces the difficulties of having many variables by simplifying the expressions into dimensionless product which means the results will be independent from the system of units. There are some factors that need to be considered such as the selection of variables, geometry, material properties and external effects.

This semi-empirical model will be developed for the heat transfer of the condensation process involving dimensionless Nusselt number using dimensional analysis techniques involving some dimensionless parameters which are Reynold's numbers and Prandtl numbers which represent the factors affecting the condensation which are the vapour velocity and condensate properties inside the finned-tubes respectively.

For Reynold number, the number is dimensionless relationg the condensate density, viscosity, diameter of the tube and vapour city as shown in Equation 6 below.

$$Re = \frac{\rho UD}{\mu} \tag{6}$$

Another dimensionless parameter to be consider is Prandtl number where the number relates the heat capacity and condensate viscosity.

$$Pr = \frac{C_p\mu}{k} \tag{7}$$

There is also a ratio of the geometry of the fins to be consider which are the ratio of fin spacing and fin height where

$$X = \frac{s}{h} \tag{8}$$

Finally, the dimensionless Nusselt number equation considering most of the important properties for the heat transfer inside the fin tube.

$$\frac{Nu}{Re^{0.5}} = 0.64[1 + (1 + 1.69F)^{0.5}]^{0.5} \tag{9}$$

Where,

$$F = \mu g d h_{fg}/kU_v^2\Delta T \tag{10}$$

The dimensionless parameter F quantifies the relative importance of gravity and vapour velocity for the motion of the condensate film.

Generally, the semi-empirical model should be looked like the equations below:

$$N_u = CRe^nPr^mX \tag{11}$$

3. Model Development

The method to develop the model is similar with Cavallini et al. (1996) First of all; sets of data from previous experiments are extracted. For this project, data is taken from Namasivayam (2006) [1]. There are sets of experiments using three different types of condensate which are steam at low pressure, steam at near atmospheric pressure and ethylene glycol at low pressure. The experiments are tested with different vapour velocities and different geometries of the fins. Figure 3 shows one of the experiments with fin spacing of 0.25 mm for steam at near atmospheric pressure tested with different values of vapour velocities.

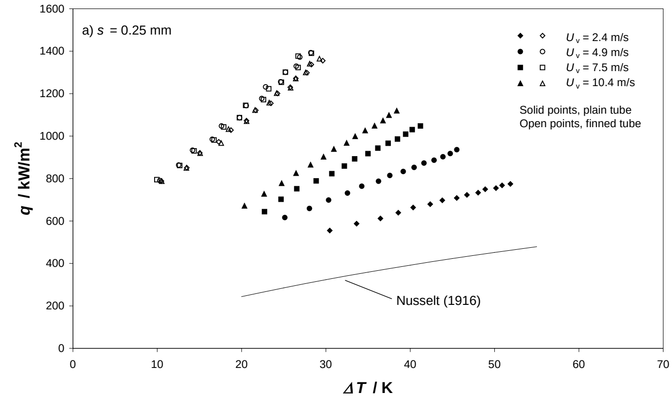

Figure 3: Variation of Heat Flux with Vapour-Side Temperature Difference for Fin Tubes (Set A, $h = 1.6$ mm, $t = 0.25$ mm, $d = 12.7$ mm) – Effect of Vapour Velocity (steam at near atmospheric pressure)

After the data is extracted, data correlation is done and values for dimensionless properties which are Nusselt number, Reynold number and Prandtl number are calculated from the theoretical formulas. The values are then plotted into the graph of Nusselt number vs combination of Reynold number, Prandtl number and geometry ratio of fin height and fin spacing based on previous studies and best fit procedure is done to get the equation of the graph to complete the empirical model of this project as shown in Figure 4 below.

From the linear model, the equation relating all the dimensionless number which is the semi-empirical model developed is

$$N_u = 2.2(Re^{1.2}Pr^{0.7})(\frac{s}{h})^{0.3} \tag{12}$$

4. Results and Analysis

After the model is developed, it is important to validate the model. In this project, the model is required to give the data within 25% range of deviation.

4.1. Model Validation

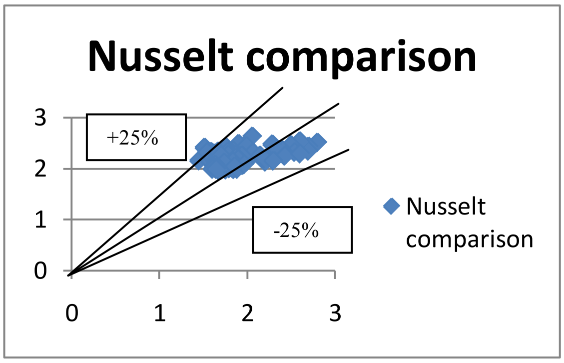

Figure 4: Comparison of the Model with Experimental Data on Nusselt Number

From the graph, it is found that the model is able to predict 1328 points from 1560 points tested which means that the model can predict for 85.1 % from the whole data. It is also noted that the points above the +25 % is where the steam experiment is conducted with high vapour velocity.

5. Error Analysis

The Kline and McClintock technique was used in this model development. It was found that for a flow rate of 2l/min, there is a ±0.05l/min error. This would affect the outcome of the model development.

6. Conclusions

Heat transfer measurement for forced-convection condensation is influenced by vapour velocity, condensate properties and fin geometry. The semi-empirical model considering all this properties is able to predict the collections of the experimental data within the range of 25%. This model is also based on some engineering assumptions that can be modified for the improvement of the model.

Acknowledgment

I would like to acknowledge my supervisor, Dr. Satesh Namasivayam whose patient guidance, encouragement and enthusiasm has made this research work possible.

References

1. Namasivam, S. “Effect of Vapour Velocity on Condensation of Atmospheric Pressure on Integral-Fin Tubes”, Applied Thermal Engineering, 2006
2. Virgil J. Lunardini and Abdul Aziz, “Effect of Condensation on Performance and Design of Extended Surface”, CRREL Report, November 1995.
3. Briggs, A. “Effect of Fin Efficiency on a Model for Condensation Heat Transfer on a Horizontal Integral-Fin Tube”, International Journal of Heat and Mass Transfer, 1994
4. Briggs A. “Condensation of Steam in the Presence of Air on a Single Tube and a Tube Bank”, International Journal of Energy Research, 2003

Calculation of Aerodynamic Drag of Human Being in Various Positions

Mun Hon Koo*, Abdulkareem Sh. Mahdi Al-Obaidi

Department of Mechanical Engineering, school of Engineering, Taylor's University, Malaysia,

**Corresponding author: mun-hon000@hotmail.com*

Abstract— **This paper studies the aerodynamic drag of human being in different positions through numerical simulation using CFD with different turbulence models. The investigation considers 4 positions namely (standing, sitting, supine and squatting) which affect aerodynamic drag. Standing has the highest drag value while supine has the lowest value. The numerical simulation was carried out using ANSYS FLUENT and compared with published experimental results. Aerodynamic drag studies can be applied into sports field related applications like cycling and running where positions optimising are carried out to reduce drag and hence to perform better during the competition.**

Keywords— Turbulence Models, Drag Coefficient, Human Being, Different Positions, CFD

1. Introduction

The performance of human being in various positions is strongly affected by the resistance they experience in which the resistance consists of aerodynamic drag. Aerodynamic drag, a resistance force that acts upon a body moving through fluid like air and that is opposite to the direction of motion of the body [1, 2]. In sports field that competing with speed, aerodynamic drag is one of the important factors. The lower the value of drag coefficient, the lower the aerodynamic drag of the positions.

The main idea of this paper is to investigate the effects of aerodynamic drag of human in different position theoretically and numerically. The total drag is majorly formed by pressure drag and friction drag due to the skin friction of the human body. In speed performing sports like cycling, cyclist often optimize the positions to reduce their drag by conducting experiment using wind tunnel. The measurement of human body flow can be said is time consuming and field tests are very difficult to set up. Even the experts in the related field can only optimize the positions to reduce drag by trial and error Therefore, computational fluid dynamic (CFD) is one of the alternative techniques to be carried out to investigate the aerodynamic drag. However, since the accuracy of numerical simulation method needs to be verified, published experimental data are used to compare and to justify the CFD results. Usually the maximum allowable errors in predicting the drag can range between10-12%. The wind tunnel experiment investigation of various positions of human was published by Schmitt [3]. The results can be used to validate the values obtain from CFD simulation. Fig. 1 shows the 4 body positions to be studies during the research.

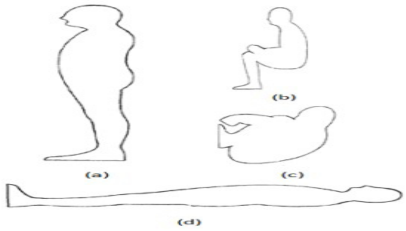

Fig.1 (a) Standing (b) Sitting (c) Squatting (d) Supine. [4]

2. Methods

2.1. Theoretical Analysis

According to Hoerner [4], the total aerodynamic drag of human body can be classified into 2 components which are:

$$C_{Dtotal}=C_{Dfriction}+C_{Dpressure}$$

Where $C_{Dpressure}$ is pressure drag coefficient and $C_{Dfriction}$ is friction drag coefficient. Pressure drag is formed from the distribution of forces normal .to the human body surface [5]. The effects of viscosity of the moving fluid (air) may contribute to the rising value of pressure drag. Drag that is directly due to wall shear stress can be knows as friction drag as it is formed due to the frictional effect. The friction drag is the component of the wall shear force in the direction toward the flow, and it depends on the body surface area and the magnitude of the wall shear stress.

2.2. Numerical Simulation

The numerical simulation in the present work is carried out using ANSYS FLUENT 14.0. According to Chowdhurry [6], the human body parts can be simplified due to the configuration and size of human body is way too complex. Therefore, a simplified model of human body with the average height and frontal area was drawn using SolidWorks as shown in Fig. 2 (a). The model is then imported into the virtual wind tunnel for computational studies as shown in Fig. 2 (b)

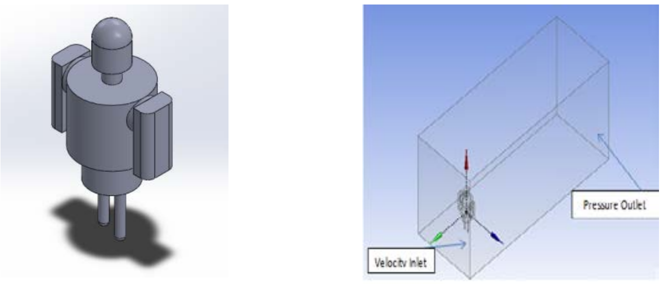

2 (a)

2 (b)

Fig. 2 (a) Simplified Human Body (b) computational domain and boundary condition.

Steady 3D Reynolds-averaged Navier-Stokes (RANS) is used in combination with turbulence models such as k-ε and k-ω with the low-Reynolds number modeling (LRNM) together is used. The four turbulence model to be carried out in the study is standard k- ε model, realizable k-ω model, standard k-ω model and lastly shear stress transport (SST) k-ω model. There is no universally proved that which turbulence model is the most accurate flow for every study case [7]. Only steady flow is performed as the studies of flow of transient can be very complicated and hard to predict. In this study case, the velocity inlet will be set at 10 m/s which is almost equivalent to 38 km/h as this input boundary condition is the normal speed for a casual cycling speed.

3. Results

3.1 Comparison of Introductory Test

The value of drag coefficient is dimensionless. Fig. 3 shows the values of drag coefficient of various positions using various turbulence models.

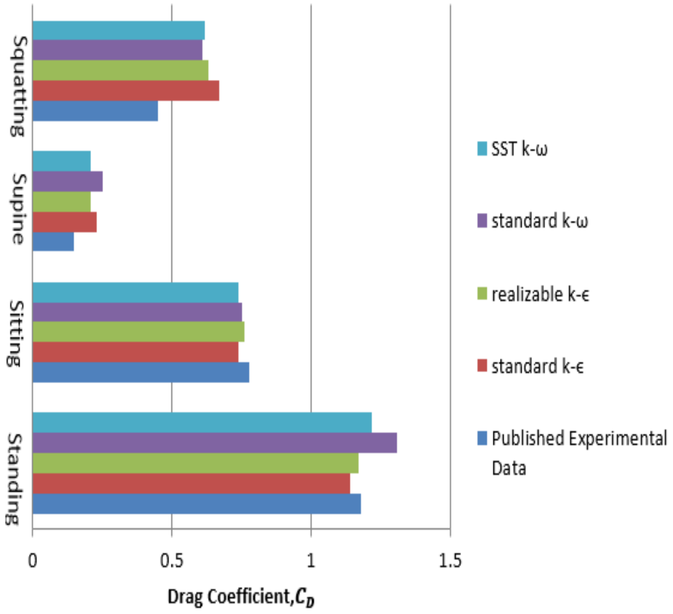

Fig. 3 Drag coefficient of Various Positions with Turbulence Models.

4. Discussion

Figure 3 shows that the supine position gives the lowest drag coefficient while the standing position gives the highest. The drag coefficient of various positions from lowest to highest value in ascending: supine, squatting, sitting and standing. It also shows that the lesser projected frontal area can greatly reduce the drag coefficient. Since the input boundaries of velocity inlet, air viscosity, air density and flow direction are the same for 4 positions; the only factor to affect the changes in drag coefficient is the frontal area. In others words, a less frontal area means the body expose lesser external flow to the wind. As the standing position has the highest projected frontal area, it exerts more forces due to the pressure and skin friction drag on the frontal area on the human opposite the wind direction. While the supine position has the lowest projected frontal area because the exposed area in this position is less and thus the skin friction drag is less as well.

In other hand, the research also carries out using different turbulence models. For squatting and supine positions, the values between the four turbulence models are very close. However, it has huge differences between the experimental data and numerical simulation data. This may due to the simplified human body model as the projected frontal area is not the same as the real human sample carry out by Schmitt [3]. The geometry of the upper body of the simplified human body is too wide and therefore it has higher drag coefficient. The difference of percentage errors for supine and squatting is relatively high, from 35% to 67%. For standing and sitting positions, the values between the experimental data and numerical simulation data are very close, the maximum error differences is only approximately 11%, which is still in the accepted range. The difference values of each turbulence model may occur due to the input method of the computational domain and boundary condition at the set-up. Each turbulence model has their own limitations when solving the same condition study; therefore, it may produce the different final values.

Table 1. Percentage Error between Published Experimental Data and Numerical Simulation Data

	Percentage of Error (%)			
Positions	standard k-ϵ	realizable k-ϵ	standard k-ω	SST k-ω
Standing	3.3	0.008	11.1	3.3
Sitting	5.1	2.5	3.8	0.05
Supine	44.4	40	66.7	40
Squatting	48.9	40	35.6	37.8

5. Conclusion and Recommendations

In conclusion, the standing position gives the highest value of drag coefficient while supine gives the lowest drag coefficient. To improve the accuracy, the modeling of the human body cannot be too simplified as the sometimes the real body do not generate the same projected frontal area as the simplified model. The input method and meshing may affect the accuracy too. Further study on these options need to be carried out more critically. However, although the accuracy of the wind tunnel and CFD are not totally the same, CFD still can be used to study in high speed application sports like running, swimming, etc. to optimize the body configuration as it gives detailed flow for every single study. In the other hand, the results presented in the current study are part of the ongoing study. Investigation on apply velocities are considered such as average of walking speed, running, skiing and etc. Angle of attack is also one of the parametric to be considered in the overall studies.

Acknowledgment

Appreciation to Taylor’s University School of Engineering for the funding and equipment support of this project.

References

1. Defraeye, T., Blocken, B., Koninckx, E., Hespel, P., and Carmeliet, J. (2010). Aerodynamic study of different cyclist positions: CFD analysis and full-scale wind-tunnel tests. *Journal of Biomechanics*, 43(7), 1262-1268.
2. Anderson, John D. Jr. (2000). *Introduction to Flight.* Fourth Edition, McGraw Hill Higher Education, Boston, Massachusetts, USA.
3. Schmitt, T. J. (1954). *Wind Tunnel Investigation of Air Loads on Human Being.* Virginia, USA.
4. Hoerner, S. F. (1965). *Fluid Dynamic Drag.* Midland Park, New Hersey, USA.
5. Cengel, Y.; Cimbala, J.; Turner, R. (2012). *Fundamentals of Thermal Fluid Sciences.*
6. Chowdhury, H.; Alam, F. and Subic, A. (2010). An Experimental Methodology for a Full Scale Bicycle Aerodynamics Study. *Inter-national Conference on Mechanical, Industrial and Energy*, Khulna, Bangladesh.
7. Defraeye, T., Blocken, B., Koninckx, E., Hespel, P., and Carmeliet, J. (2010). Computational fluid dynamics analysis of cyclist aerodynamics: Performance of different turbulence-modeling and boundary layer modeling approaches. *Journal of Biomechanics*, 43(12), 2281-2287.

Mechanical Stability of Ca-alginate Beads as Support for Yeast Cell

N. F. H. Fadel [1*], M. M. Shamel [2], M. M. Zain [3]

[1, 2, 3]*Chemical Engineering Department, Taylor's University, Malaysia,*
**nurulfarhana.hamdanfadel@sd.taylors.edu.my*

Abstract—**Rising of interest in encapsulation by Ca-alginate is the main reasons to explore different concentration and physical condition of ca-alginate beads. The long term mechanical stability of alginate beads is a critical factor to study in a reactor operating condition. This study was carried out to investigate the mechanical stability in term of shear force impact to the beads in fluidized reactor condition. By producing different concentration of alginate beads, the operation of reactor was executed using distilled water and glucose solution as medium. Different flow rate was applied and the effect of beads diameter was observed. Alginate beads basically are strong enough to endure shear stress impact by water and glucose solution as medium.**

Keywords— Ca-alginate beads, Encapsulation, Immobilization, Mechanical stability, shear stress

1. Introduction

In recent years, the fermentation process is considered as an alternative to many chemical processes in industry for the production such as enzymes, flavors, fragrances and medicine. High yield value is essential for process economics and it is also desirable to have a rapid fermentation with high alcohol levels to minimize capital costs and separation energy [1], [2]. The efficiency of the production processes depends on several aspects; operational simplicity, productivity, product concentration in the fermentation and product recovery. In fermentation process, the productivity is proportional to the yeast cell concentration, and technique to retain the cells in the fermentation section must be maximized [2], [3].

Encapsulation is defined as a process of confining active compound within a matrix in particulate form to achieve one or more desirable effects [4]. Alginate is widely used for encapsulation in the last thirty years. In the bioengineering field, the mechanical stability of alginate will be a critical factor to study especially under reactor operation such as operating temperature, volumetric flow rate and solvent properties. Long term stability of the gel material will be an important parameter in application of biocatalyst gel particles in bioreactor system [5].

In this study, the research will be focused on the forces that are applied on the beads by the reactor. This article is intended to investigate the mechanical stability of Ca-alginate beads for yeast immobilization for ethanol fermentation. By using different concentration of Ca-alginate, range of beads were produced and tested for different applied shear force. Distilled water and glucose solution were used as medium. A special attention is also paid to the stability of the beads and response of the beads to shear forces in term of mechanical stability.

2. Methodology

2.1. Chemical, apparatus and devices

Peptone (R&M Chemicals, UK), yeast extract (BD Bacto, France), D(+)-Glucose (R&M Chemicals, UK) sodium alginate powder (R&M Chemicals, UK), calcium chloride (R&M Chemicals,UK), sodium chloride (R&M Chemicals,UK), *Saccharomyces Cerevisiae* yeast (Mauripan instant yeast), optical microscope (M10 Series, Swift, USA), peristaltic pump (77200-50, Mastreflex, USA), Creep Testing Machine (WP600, Gunt Hamburg, Malaysia), Incubator refrigerator (BCR240, Bio Concept, France), Autoclave, (WAC 60, Wise Clave, Korea), centrifuge (Zentrifugen, Universal 32R, Germany).

2.2. Formation of calcium alginate beads with dripping technique

2.2.1. Un-loaded Ca-alginate beads formation

Sodium alginate solutions with concentration of 1%, 2%, 3% and 4% (w/v) were prepared by diluting sodium alginate powder in distilled water. By using dripping technique, 100 ml of sodium alginate solution was titrated into $CaCl_2$ gelling solution. After the titration process is finished, 1 hour is spent for hardening process.

2.2.2. Cell-loaded Ca-alginate beads formation

A gram and a half of *Saccharomyces Cerevisiae* (Mauripan instant yeast, Malaysia) was mixed with distilled water to made 50 ml yeast solution. Then, the yeast solution was mixed with 500 ml YPD (Yeast extract-peptone-dextrose) medium with 0.2 gL^{-1}, 0.1 gL^{-1} and 0.2 gL^{-1} concentration respectively. The yeast + YPD solution was incubated at 30°C for 8 hours before centrifuge. The precipitate was separated and diluted with distilled water to make an active yeast solution. Then, yeast solution was mixed together with same amount of alginate solution (50 ml) before titrated into gelling solution.

2.3. Bead size analysis

The diameter of beads had been analyzed using optical microscope (M10 Series, Swift, USA). The image of beads was capture and the diameter was determined. For beads size analysis, the beads assumed to be sphere. Sample sizes of 100 beads were taken for each type of beads.

2.4. Mechanical Stability Testing

2.4.1. Water properties

The weight of individual bead was measured using weighing balance for 10 samples. Using the same sample of beads, the bead was compressed with weight load 10N to deform using third class lever mechanism by Creep Testing Machine Gunt WP600. After permanent deformation, the weights of beads were measured again to see the amount of water loss after deformation. Water properties was measured based on percentage of beads weight.

2.4.2. Shear force test

25 gram of beads measured and installed inside the column with the dimension of 26 mm inner diameter and 290 mm length. For cell loaded alginate beads, YPD medium contained 0.2 gL^{-1} concentration of glucose was used as reactor medium while distilled water medium applied on unloaded beads. Constant flow rate of 187.5 ml/min and 377.36 ml/min was applied using 25 tubing size. Physical appearance and beads diameter was measured based on average of 10 samples of beads for every an hour or two hours interval.

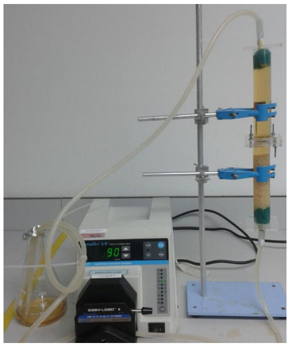

Fig. 1: Shear force experimental setup

3. Results and discussion

3.1. Distribution of beads size

For 3% (w/v) alginate beads, average diameter size of unloaded beads is 4.364 mm which is bigger compare to cell loaded beads which give the average size 3.814 mm. 1% (w/v) alginate beads gave smaller diameter with 3.501 mm mean size. Standard deviation for 1% (w/v) and 3% (w/v) cell loaded beads were 0.250 and 0.148 respectively which explained the uniformity of higher concentration beads was better compare to lower concentration beads.

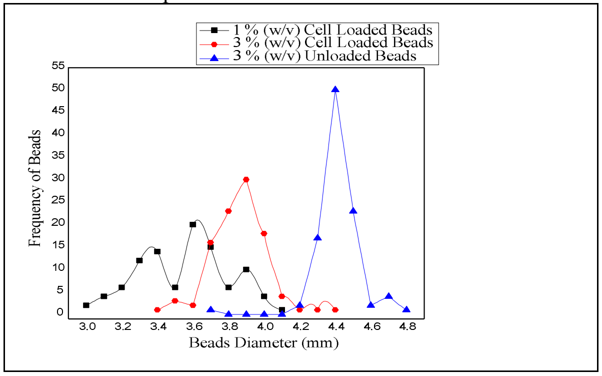

Fig. 2: Size distribution of beads (mm)

3. 2. Water Properties

For water properties analysis, the water loss was measured based on difference weight of beads before and after deformation. With constant value of 10 N weight load applied using third class lever mechanism, the beads with 1% (w/v) and 3% (w/v) concentration is compared.

Table 1: Percentage of water loss based on weight of beads before and after deformation

Types of beads	Initial weight of beads (g)	Weight of beads after deformation (g)	Percentage of water loss (%)
1% unloaded	0.023	0.020	13.04
3% unloaded	0.038	0.034	10.53
3% cell loaded	0.032	0.028	12.50

3% (w/v) cell loaded beads loss more water compare to 3% (w/v) unloaded beads. Lower concentration of beads will loss more water compare to higher concentration. This response is due to higher amount of polysaccharide will increase the number of junction zones between alginate chains in the polymer network [6]. Because of this reason, alginate beads are strong enough to retain water properties with the strength. To loss more water especially for high concentration of beads, higher value of load must be applied.

3.3. Shear force test

Due to mechanical properties of the beads, unloaded beads will be more stabilize since the elastic properties decrease with the addition of yeast suspension [5]. However, with 187.5 ml/min and 377.36 ml/min flow rate applied, there was no shear force impact to the beads even though with lowest concentration. It proved that alginate properties were actually strong enough to support the beads from shear force impact by water and glucose solution. Based on the result obtained, changes of beads diameter due to reaction occurrences and compatibility had a very small significant to the shear force impact by medium.

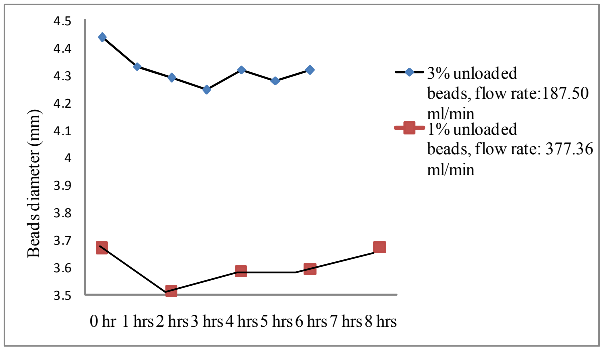

Fig 3:1% and 3% unloaded alginate beads diameter size (mm) using distilled water as medium

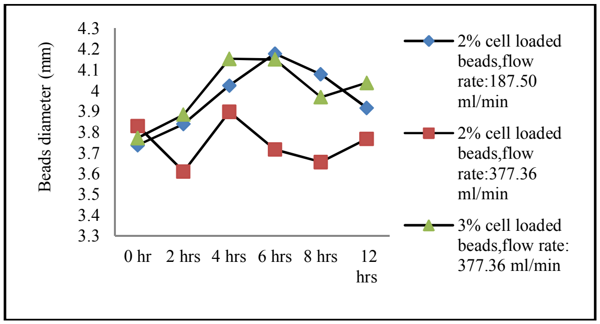

Fig 4: 2% and 3% cell loaded alginate diameter size (mm) using glucose solution as medium

4. Conclusion

Higher concentration of alginate gave higher standard deviation value therefore better size uniformity achieved. High concentration of alginate can retain water properties due to junction zones between alginate chains in the polymer network. Unloaded and cell loaded alginate beads can endure shear force impact in water and glucose solution with 187.50 ml/min and 377.36 ml/min flow rate. Further study of shear force impact on alginate beads should be carried out with method modification by considering reactor operating parameters such as temperature and oxygen supply to enhance the productivity.

Acknowledgment

Special thanks to School of Engineering Taylor's University, Marwan and Masniroszaime throughout finishing this project.

References

[1]Llewellyn, B. Edwin, G. (1984). *Biotechnology and Bioengineering,* 26, 1492-1497.
[2]M. Roehr (2001). *The Biotechnology of Ethanol, Classical and Future Applications,* WILEY-VCH Verlag GmbH, Weinheim
[3]Groot, W.I, van der Lans, R.G.J.M.,Luyben, K.C.A.M. (2009). *Application Biochem and Biotechno*, 28/29, 539-547
[4]Chan,E-S.,Lee,B.-B.,Ravindra, P.&Poncelet. (2009). Prediction models from shape and size of calcium-alginate macrobeads produced through extrusion technique. *Journal of Colloid and Interface Science,* 338, 63-72
[5]Georgi Kostov, Mihail Angelov, Ivan Mihaylov, Denis Poncelet. (2010). Mechanical properties of Ca-alginate beads for ethanol fermentation with immobilized yeast. *Reveu de Genie Industriel*, ISN 1313-8871
[6]G.-A.Junter, D.T.Bui, F.Vinet. (2009). Tensile Properties of yeast cell-loaded Ca-alginate gel layers. *Chemical Engineering Journal* 152, 297-300

Optimisation the Concentration of Thymol from Dried *Plectranthus amboinicus* leaves

Kuok Loong Ng, Puteri Farah Wahida, Chien Hwa Chong

School of Engineering, Taylor's University, Lakeside Campus

No 1, Jalan Taylor's, 47500 Subang Jaya, Selangor, Malaysia

Abstract— *Plectranthus amboinicus* (PA) is one of the herbal plants that traditionally used to cure asthma, coughs and diseases affected by virus and bacteria. The objectives of this study were to extract essential oil from the leaves of the plant and optimise the extraction parameters using Research Surface Methodology (RSM). The PA leaves were dried using a convection air drying method and followed by extraction using a Soxhlet method. Design Expert 6.0.8 was used to design the experiments based on Box-Behnken Design with three parameters to control. It was found that higher concentration of thymol was observed in the oil extracted using ethanol. The optimum extraction conditions were 6 hr with ratio of solid to solvent of 1:30.

Keywords — *Plectranthus amboinicus*, essential oil, soxhlet extraction, gas chromatography analysis, research surface methodology (RSM)

1. Introduction

Treatment for chronic diseases with modern medicine or drugs might have various and severe adverse effect on patient's body. Therefore, people nowadays are looking for naturally originated agents with very little side effects to substitute chemical therapeutics. PA leaves are considered as one of the medicinal herbs. PA plant is a type of plant belongs to family of Lamiaceae which is known as borage in English [1]. PA leaves have been widely used traditionally for various purposes such as medical treatment for cough treatment, cephalagia, otalgia, anorexia, diarrhea, cholera, chronic asthma malarial fever and cathartic [2]. The principal component of the oil is Thymol [3-4].

Essential oil is the essence from a plant [5] which is important for pharmaceuticals. Thus, the concentration is a vital element in this study. An appropriate solvent is needed to maximize the amount of oils extracted. Due to this, the less polar solvent like ethanol, non-polar like hexane and diethyl ether were used to extract the targeted compound in the PA leaves which is polar [6]. Throughout the research on essential oil from herbal leaves, the optimisation of the concentration of main active compounds from *Pletranthus amboinicus* using Research Surface Methodology (RSM) has not been reported yet. Therefore, the aims of this project were to analyse the concentration of the extracted essential oil from different extraction parameters using Gas Chromatography (GC) and to optimise the extraction parameters using the RSM method.

2.0 Methodology

2.1 Project Description

In this project, the fresh plucked leaves were dried using a convective air drying method. These dried leaves were sent for Soxhlet extraction. The solvents selected for the Soxhlet extraction were diethyl ether, hexane and ethanol. The main reason to select these solvents was based on their polarity which is less polar and non-polar and as well based on the targeted compound, thymol, is a polar compound. The extracts was analysed by using GC.

2.2 RSM – Box Behnken Design

Design Expert version 6.0.8 was used to optimization on concentration of the main active compounds from the essential oil extracted. Box-Behnken Design (BBD) was selected as it demonstrated a more efficient design in optimisation [7]. There were 17 runs with different setting of parameters generated from the Design Expert (Version 6.0.8, Stat-Ease Inc., Minneapolis) statistical software.

2.3 Convection Air Drying

Conventional oven (FAC-350, PROTECH, USA) was used to dry the leaves at low temperature, 50˚C for 72 hours in order for it to completely remove the moisture. The moisture loss of these leaves was found to be 94.6%.

2.4 Soxhlet Extraction

In this extraction method, solvents such as ethanol, diethyl ether and hexane were used. The main active compounds, thymol was found to be polar [6]. The grinded dried leaves weighted about 6 g was placed in a cellulose thimble and inserted into the Soxhlet apparatus with 250ml flasks. The 17 runs designed by the Design Expert 6.0.8 were performed based on the extraction time, ratio of solid to liquid and types of solvents designed for each run by the software. The solvent was added to the flask and heated and maintained in continuous reflux process. The following step was the extracts were concentrated by using a rotary evaporator (RV 10, IKA, USA) to separate the solvent from the essential oil. The essential oil was stored at 3˚C in universal bottle until being analysed.

2.5 Gas Chromatography

GC (Clarus 500, Perkin Elmer, USA) analysis were carried out on Elite-5 MS capillary column (30m x 0.25mm x 0.25 μm of cross-linked Phenyl-Methyl Siloxane) equipped with flame ionization detector (FID). The initial column temperature was programmed at 60°C. It was raised at a rate of 10 °C/min to 180 °C for 12 minutes. The injector and detector temperatures were programmed at 260 and 280 °C respectively. Nitrogen was used as carrier gas with the flow rate at 2 ml/min.

2.6 Statistical Analysis

Analysis of Variance (ANOVA) was used to test the significant terms in the model for each response and significant was judged by the F-statistic calculated from the data. Values of 'Prob > F' less than 0.05 indicate model terms are significant whereas values greater than 0.1 indicate the model terms are not significant.

3.0 Results and Discussion

In this study, the independent variables set were types of solvents (x1), extraction time (x2) and ratio of solid to solvents (x3). The response was the concentration of main active compounds, Thymol, extracted from different extraction conditions. The concentration of thymol from PA leaves is shown in Table 1. The highest concentration of thymol was obtained by ethanol (6 hours, ratio of 1:35). Thymol is a phytochemical that provides antioxidant activity and effective antimicrobial activity against food pathogens [8-9]. The experimental conditions for diethyl ether did not show good results in terms of concentration of thymol could be due to diethyl ether has a low boiling point (34.6˚C), so the evaporation rate is faster than its condensation rate and this has caused losses of diethyl ether vapor to the environment. So the extraction rate is lesser than other solvents. Extraction from ethanol for 6 hr exhibited high concentration compared with the time of 4 hr. Soxhlet extraction using ethanol yielded higher phenolic compounds concentration with the increase of the extraction time [10].

Table 1: Composition (%w/w) of main active compounds of *Plectranthus amboinicus* oils obtained by Soxhlet

Time (Hour)	Ratio of solid to liquid	Extraction Concentration (ppm)		
		Ethanol	Hexane	Diethyl Ether
		Thymol	Thymol	Thymol
4	1:30	1866.28	-	-
	1:35	1351.81	-	202.50
	1:40	1562.98	-	-
5	1:30	3339.40	-	376.57
	1:35	-	2209.91	-
	1:40	3616.28	-	210.57
6	1:30	-	2445.78	-
	1:35	3796.56	-	560.75
	1:40	-	2635.75	-

The model suggested by the Design Expert 6.0.8 was calculated using the statistical software. This result is shown in **Table 2**. In the fit summary result, quadratic model is suggested for this experiment and cubic model will not be considered as it is aliased. In choosing the right model, the probability (PROB > F) needs to be examined, if the Prob > F falls below 0.05 then it should give the best model.

Table 2: Summary table of Sequential Model Sum of Squares

Source	Sum of squares	DF	Mean Square	F value	Prob >F
Mean	64116217.56	1	64116217.56		
Linear	16936330.02	3	5645443.34	22.65	< 0.0001
2FI	1198235.06	3	399411.69	1.96	0.1846
Quadratic	1371026.23	3	457008.74	4.77	0.0408
Cubic	663550.57	3	221183.52	126.88	0.0002
Residual	6972.89	4	1743.22		
Total	84292332.33	17	4958372.49		

The quadratic model as suggested also shows a low standard deviation, high R-squared value and low PRESS value shown in **Table 3**.

Table 3: Model Summary Statistics

Source	Std. Dev.	R-Squared	Adjusted R-Squared	Predicted R-Squared	PRESS
Linear	499.21	0.8394	0.8024	0.6814	6.429E+006
2FI	451.84	0.8988	0.8381	0.5528	9.023E+006
Quadratic	309.50	0.9668	0.9240	0.4733	1.063E+007
Cubic	41.75	0.9997	0.9986		

By applying multiple regression analysis on the experimental data, the concentration and the test variables are related by the following second-order polynomial in equation 1.

$$Y = 209.91 + 556.91A_1 + 1344.21 B_2 - 0.31C_3 - 245.01A_1^2 - 487B_2^2 + 162.79C_3^2 + 521.63A_1B_2 + 123.32A_1C_3 + 110.72B_2C_3 \quad (1)$$

The result obtained from the Table 1 could only show the best result. So it is further analysed to determine the optimise result. The optimisation result is shown in **Table 2**.

Table 2: Optimisation result of Thymol concentration based on optimise numerical setting

Run	Extraction Time (hour)	Types of solvents	Ratio of solid to solvent	Concentration of thymol (ppm)	
1	6	3	1	3804.4	Selected
2	6	3	3	3828.11	
3	6	3	1	3805.57	
4	6	3	3	3955.5	
5	6	3	1	3806.97	
6	6	3	2	3844.06	
7	6	3	2	4001.31	
8	6	3	1	3798.45	
9	6	3	3	3900.1	
10	6	3	2	3812.09	

It was found that the Run 1 was selected by the software as it has the optimum extraction parameters and gives 3804.40 ppm. Even though, Run 7 gives the highest concentration of thymol, 4001.31 ppm, but it was not selected by the software. This could be due to the insignificant increase of thymol concentration as the difference among them is 196.91ppm. By selecting Run 1, it can save the amount of solvent used by 37ml or 21% and thus bring economic benefit to the project in term of low solvent usage and low waste produced.

4.0 Conclusions

It is concluded that the Soxhlet extraction method applied in this study was promising and the extracted oil showed a high ppm of thymol. Data obtained from this study indicate application of RSM could optimise the concentration of thymol.

Acknowledgment

We acknowledge the support from School of BioSciences, Taylor's University.

References

[1] Kirtikar K.R. and Basu B.D. Indian Medicinal Plants. Vol.3. International Book Distributors, Dehradun, India; 1999. p. 1970-71.

[2] Roshan P., Naveen M., Manjul PS, Gulzar A., Anita S., Sudarshan S. (2009) Plectranthus Amboinicus (Lour) Spreng: An Overview, Sudarshan Publication, Sudarshan Institute of Technical Education Pvt. Ltd. 4; 01-15

[3] Uma M., Jothinayaki S., Kumaravel S.and Kalaiselvi P. (2011) ' Determination of Bioactive Components of *Plectranthus amboinicus L*our by GC–MS Analysis' New York Science Journal, 2011;4(8): 66-69]. (ISSN: 1554-0200).

[4] Chiu Y.J., Huang T.H., Chiu C.S., Lu T.C. and Chen Y.W. (2012) 'Analgesic and Antiinflammatory Activities of the Aqueous Extract from Plectranthus amboinicus (Lour.) Spreng. Both In Vitro and In Vivo' Evidence based complementary and Alternative Medicine 2012:508137.

[5] Damain P. and Damian K. (1995) Aromatherapy: Scent and Psyche. Inner Traditions International. pg 161-163

[6] Soumya E.A., Saad I.K., Hassan L., Ghizlane Z., Hind M. and Adnane R. (2011) *Carvacrol and thymol components inhibiting Pseudomonas aeruginosa adherence and biofilm formation*. Vol. 5(20), pp. 3229-3232

[7] Carasek E., Martendal E., Budziak D.and Chromatogr J. A 1148 (2007) 131.

[8] Delfine S., Loreto F., Pinelli P., Togntti R., Alvino A., Isoprenoids content and photosynthetic limitations in rosemary and spearmint plants under water stress, Agric. Ecos. Environ. 106, 243-252 (2005).

[9] Nazer A.I., Kobilinsky A., Tholozan J.L., Dubois F. -Brissonnet, Combinations of food antimicrobials at low levels to inhibit the growth of Salmonellasv. Typhimurium: a synergistic effect? Food Microbiol. 22, 391-398 (2005).

[10] Lapornik B., Prosek M. and Wondra A.G., Comparision of extracts prepared from plant by-products using different solvents and extraction time, J. Food Eng. 71, 214- 222 (2005).

CFD Simulation of Natural Ventilation and Pollution Dispersion in Taylor's Lakeside Campus

N. S. Virik[1*], S. M. Salim[1]

[1] *School of Engineering, Taylor's University, Malaysia*

**nivenvirik@yahoo.com*

Abstract— **The analysis of natural ventilation and air pollution dispersion in an urban environment can be immensely beneficial in the field of building design. Numerical analysis using Computational Fluid Dynamics (CFD) is done based on the prevailing conditions on Taylor's University campus which itself represents an urban surrounding. The study is done parametrically by varying the wind direction and speed affecting the campus. This is to determine the optimal campus orientation that enhances natural ventilation and minimizes pollution accumulation.**

Keywords— Air pollution dispersion; Computational Fluid Dynamics (CFD); Natural ventilation

1. Introduction

Urban areas that utilize the occurrence of natural ventilation well are susceptible to good levels of thermal and wind comfort, reduced energy costs, and sustainable development [1]. Exploiting this natural occurrence has become an important strategy in building design. Air pollution dispersion on the other hand is directly influenced by the direction and airflow pattern determined by natural ventilation [2].

Taylor's University campus presents itself as an appropriate example of an urban site. Minimizing pollution dispersion caused by traffic and amplification of ventilation around the campus is important in providing a comfortable environment for its occupants. Similar numerical studies on campuses have been done [2]-[4] evaluating the pedestrian wind comfort, the effects of change in the structure's orientation, and the dispersion of traffic pollution within the campus. Such investigations can be applied and adapted in Malaysia reaping benefits such as saving time and cost, providing powerful visualization capabilities, and allowing for parametric studies. This consequently leads to the increase in confidence in the use of CFD.

3D numerical simulations were carried out by means of CFD using ANSYS FLUENT to model the natural air ventilation and pollutant dispersion in the campus with consideration of prevailing meteorological conditions. This study serves as a tool to increase confidence in using CFD building design whilst laying the foundation for a potential future micro-scale study.

2. Methodology

The analysis of the natural ventilation is done by simulating two wind directions which represent the highest and lowest average wind speeds obtained from meteorological data. Variations are done on the wind speed and direction in order to determine the optimal airflow pattern that enhances the natural ventilation within the campus. Steady-state RANS turbulence model, namely k-epsilon (k-ε) is employed. The convergence criterion is set to 1×10^{-6} for all flow properties with the SIMPLE scheme chosen. For simplification purposes, the dimensions of the domain are measured in terms of H which represents the height of the tallest building as shown in Figure 1. The domain is discretized using hexahedral and tetrahedral elements. A mesh with a total cell count of 1.87 million is incorporated wherein 0.95 million cells are within the sub-domain. The natural ventilation setup is summarized in Table 1.

Table 1. Summary of Natural Ventilation Analysis

Wind Direction Analyzed	Average Wind Speed	Wind Rose	Turbulence Models
South-Southeast (SSE)	6 Knots (3.0867 m/s)	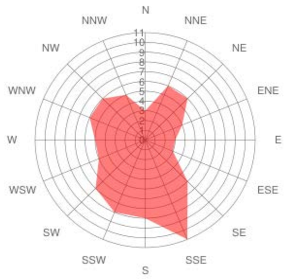	k-epsilon (*k*-ε)
North	4 Knots (2.0578 m/s)		

The investigation on the campus is followed by analyzing the air pollution dispersion. Sulphur hexafluoride (SF_6) is used as a tracer gas to mimic traffic pollution occurring around the campus. It is difficult to quantify the emission rate as it varies with the number of cars, type of cars, and even the day of the week. However, the emission rate, Q is maintained at 10 g/s to replicate the study done by Salim et al. [5]. The turbulence model used was Large Eddy Simulation (LES) with the dynamic Smagorinsky-Lily sub-grid scale chosen.

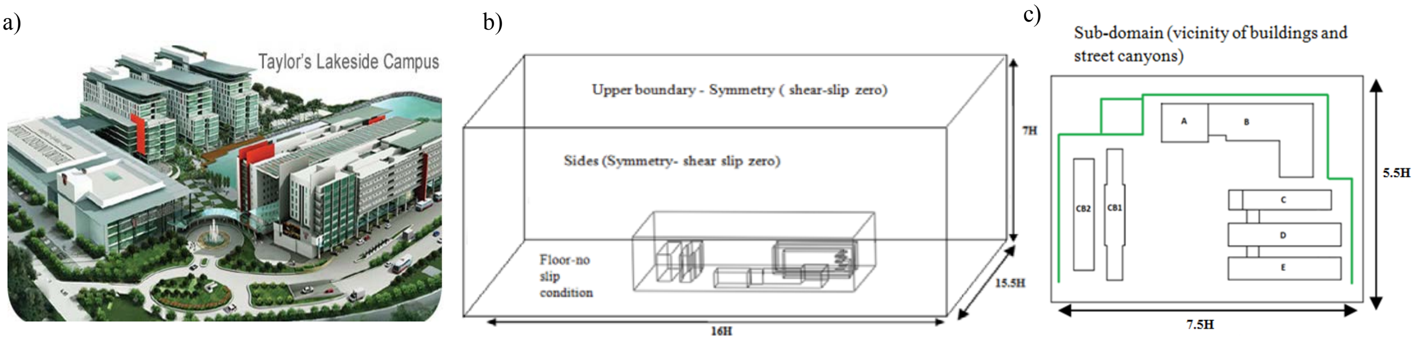

Fig. 1 a) Physical domain b) Computational domain and boundary conditions c) Pollution source region

Second order upwind discretization schemes are used for species and energy transport equations to increase the accuracy and reduce numerical diffusion [6].As for pressure and pressure-velocity coupling, PRESTO! and SIMPLEC are employed. The scaled residual criteria for all flow properties are set at 1 x 10^{-3} with a dimensionless time-step of 0.001.The dispersion modeling is summed up in Table 2.

Table 2. Summary of Pollution Dispersion Analysis

Wind Speed	Wind Direction	Pollutant	Turbulence Models
6 Knots (3.0867 m/s)	South-Southeast (SSE)	Sulphur Hexaflouride, SF_6	Large Eddy Simulation (LES)

3. Results & Discussions

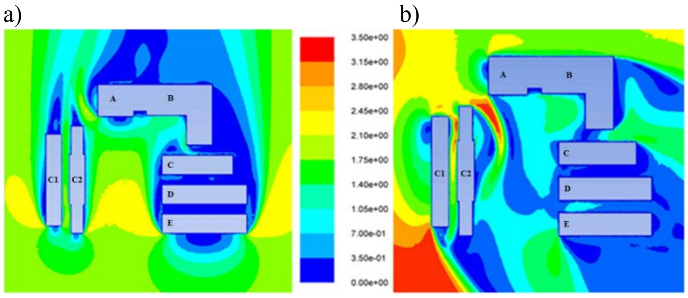

Fig. 2 Wind velocity distribution with a) wind velocity of 2.0578 m/s in the north direction and b) wind velocity of 3.0867 m/s in the SSE direction

The arrangement of tall building structures in the campus heavily influences the airflow pattern and wind velocity occurring at the ground level. Strong winds aloft interact with these buildings causing it to be pushed down to the surface. Based on Simiu et. al [6], wind speed accelerates when channeling between large buildings and at building corner streams which is noticeable in Figure 2. Vortex flows are also observed at the two street canyons created by building block C, D and E.

In Figure 2, when the air flows from the SSE direction, the highest noticeable wind velocity arising within the campus occurs at the channel between block A and the second commercial block. This stream of wind conjured from the channels has a velocity of between 3.15 m/s to 3.5 m/s. Referring to the study done by Penwarden [7], at velocities within that range, wind is prominently felt on the faces of pedestrians and causes cloths to flap and hair to be disturbed. Velocities within the range of 1.6 m/s to 3.3 m/s is referred as 'light breeze' where the wind is felt on the skin leading to desired wind comfort. Wind velocities in the range of 0.4 m/s to 1.5m/s are instead labeled as 'light airs' with the wind being unnoticeable. As majority of the flow in the campus falls beneath 1.5 m/s, the natural ventilation within the campus is considered to be poor.

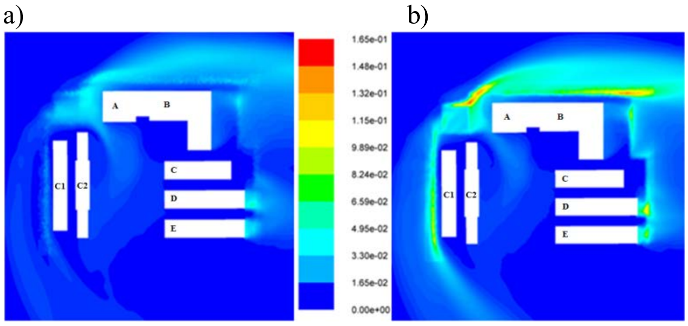

Fig 3. Mean mass fraction of SF_6 with wind velocity of 3.0867 m/s and airflow from the SSE direction at a) height z = 5m and b) height z = 1m

In the case of wind blowing from the SSE direction at 3.0867 m/s in reference to Figure 3, the highest air pollution is observed at the roundabout and roads located at the east side. The high pollution presence at the roundabout is due to the emission being more concentrated than roads surrounding the campus. The high pollution presences towards the east roads on the other hand are due to airflow restrictions in that area. Without proper ventilation, pollutants emitted become concentrated posing a health risk to passersby.

As the height from the ground increases, pollutant concentration is observed to decrease as well. However, the most vulnerable areas susceptible to high pollution concentration remains the same. This investigation also leads to the predicted conclusion that pollution will disperse more thoroughly with lower concentrations at higher wind speeds.

4. Conclusions

In reality, the concept of natural ventilation and pollution dispersion in a real urban environment is a complex one. Emission rates are not evenly distributed and cannot be accurately predicted due to the number of moving cars. The phenomena happening in the campus is also affected by external factors. By comparing the results obtained between the two different wind directions in Figure 2, it is conclusive that the campus is better ventilated when the wind blows from the SSE direction. Better ventilation will then lead to greater pollution dispersion with lower pollutant concentration.

References

[1] Y. Jiang, C. Allocca, and Q. Chen, "Validation of CFD Simulations for Natural Ventilation," International Journal of Ventilation, vol. 2, p. 12, 2004.

[2] B. Blocken, T. van Hooff, and W. D. Janssen, "CFD simulation for pedestrian wind comfort and wind safety in urban areas: General decision framework and case study for the Eindhoven University campus," Environmental Modelling & Software, vol. 30, pp. 15-34, 2012.

[3] N. Zhang and Q. Meng, "Digital Simulation of Outdoor Wind Environments and Energy Consumption for Rebuild Campus," International Journal of Energy Engineering vol.1, pp. 77-81, 2011.

[4] N. Nikolopoulos, A. Nikolopoulos, I. Papadakis, and K.-S. P. Nikas, "CFD Applications in Natural Ventilation of Buildings and Air Quality Dispersion," CFD Applications in Energy and Environment Sectors: International Energy and Environment Foundation, vol. 1, pp 53-100, 2011.

[5] S. M. Salim, R. Buccolieri A. Chan, and S. D. Sabatino, "Numerical simulation of atmospheric pollutant dispersion in an urban street canyon: Comparison between RANS and LES," Journal of Wind Engineering and Industrial Aerodynamics, vol. 99, pp. 103-113, 2011.

[6] H. K. Vesteeg, and W. Malalasekera, "An Introduction to Computational Fluid Dynamics: The Finite Volume Method," Harlow, Pearson Education Limited, ch. 5, 2007.

[7] E. Simiu, and R. H. Scanlan, "Wind effects on structures," 3rd Ed.,Wiley, New York, 1996

[8] A. D. Penwarden, "Acceptable Wind Speeds in Towns," Building Science, vol.8, pp. 259-267, 1973

Peak Demand Analysis for the Look-ahead Energy Management System: A Case Study at Taylor's University

Nadarajan[1], Aravind CV[2*]

[1]*Applied Electromagnetic and Mechanical cluster,*
Computer Intelligence Applied Group, Taylor's University, Malaysia
**aravindcv@ieee.org*

Abstract— **To derive an energy management for sustainable energy usage the peak demand analysis is highly critical. This paper presents the investigations on the peak demand analysis for the existing power system network at Taylor's University. From the analysis it is inferred that the average peak demand of 3000kW could be managed with proper kilowatt management. The analysis pertaining to the computations of power analysis and a proposed framework to support the analysis is presented. Further to stabilising the load requirement, equally the economics of the system is improvised by about 7.33%.**

Keywords— peak demand, energy management, economics

1. Introduction

The most common factor influence the energy management is the active energy consumption (KWh), the reactive energy consumption (KVARh) and the peak demand (KW). Conventionally the utility system put their effort on the reduction of KWh consumption and on addressing the reactive energy demand to improvise the power factor. However for the medium voltage and high voltage consumers' proper KW demand management implies to reduce the use of contracted power, adjusting to the new requirement and avoiding the demand limit penalties [1]. Figure 1 shows the concept in the power management. As can be seen the power management is interlinked and the possible energy management between the KW and KVAr the net power consumption can be reduced. In order to find the demand requirement to propose new system architecture to address the demand requirement the peak demand analysis is to be investigated. Peak demand is the power consumed over a predetermined period of time, typically between 8 to 30 minutes. The power is calculated using a power demand meter, which records the highest KW value in the period of measurement, over a month's time. The purpose of demand control is not to exceed the contracted maximum demand limit. The common way is to isolate the non-critical load during peak hours. A number power demand modeling and analysis, towards optimization of demand curve [2] as well as forecasting [1] are the subjects of interest in recent years. However, accuracy and resolution of the model are important [3]. We have utilized the data on energy management from the Taylor's University, Malaysia laced at latitude of 3°07'51.99"N and longitude of 101°59'11.77"E. The demand analysis is based on the utilized power between Jan 2011 till April 2013. Our initial study is to derive the average peak demand requirement and suggest a KW management system for energy sustainability. From our study a detailed proposal on the energy management by suggesting a KW framework is to be presented towards the end of this research work.

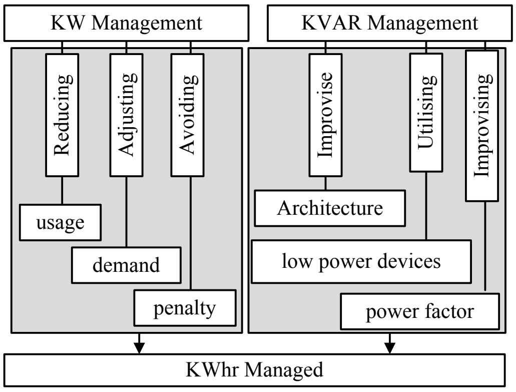

Figure 1. KWhr Management Strategy

2. Methodology

The methodology involved in this investigations is as shown in the Figure 2 and the power system architecture is as shown in Figure 3. The computation procedure for the demand analysis and the net KW demand computation is as below. Let the contracted power be (P_C), the maximum demand is (P_D) then the power used in excess (P_E) is computed as

$$P_E = P_C - P_D \tag{1}$$

where P_{Dm} is the actual peak demand value from the maximum demand meter and K_d is the demand factor

$$P_D = P_{Dm} X K_d \tag{2}$$

The penalty by the supplier to the utility is computed as

$$P_P = (P_C - P_D) X K_P \tag{3}$$

where K_P is the penalty factor. Therefore the actual KW value (P_A) computed is given by

$$P_A = [(P_C - P_D) X K_P] + [P_{Dm} X K_D] \tag{4}$$

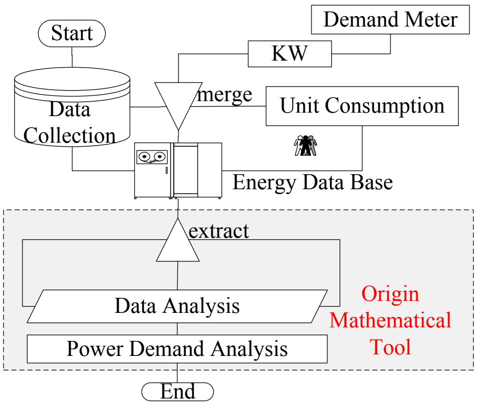

Figure 2. Methodology Employed

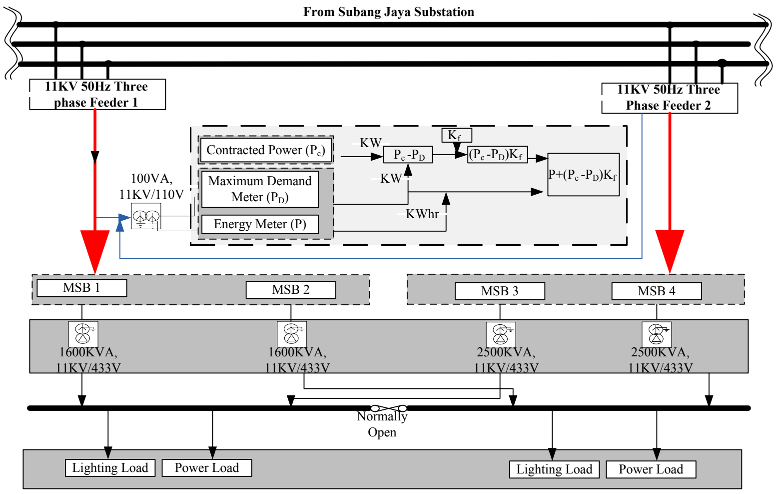

Figure 3. Power System Architecture for the Peak Demand Computations

3. Results and Discussions

Table 1 shows the percentage share of the pay bill to the Tenaga nasional. As can be seen the average peak demand (PD) is about 20.87% and the KWh utility is about 78.77% for the three year period. If the average peak demand is catered through a energy management system the power system network ideally becomes sustainable. Figure 4 shows the unit consumption and during the second quarter the unit consumption is predominantly high and at the same time the peak demand (as in Figure 5) is critically very high. The peak demand is addressed through the design of a renewable structure and reconfigures the existing power system architecture in our further investigations.

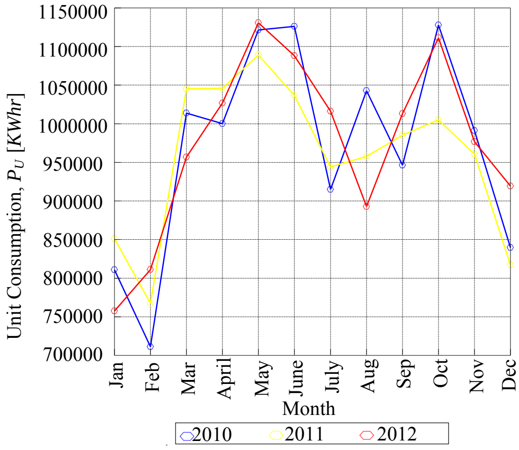

Figure 4. Unit Consumption of Energy

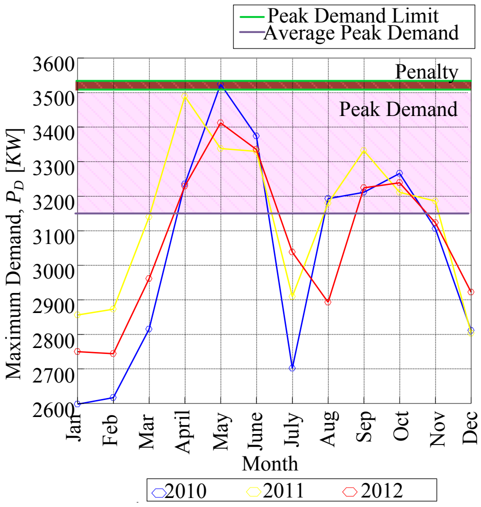

Figure 5. Power Demand Analysis

4. Conclusions

The initial investigations on the power demand curve analysis for the look-ahead energy management system is presented in this work. It is inferred that about 20.87% of the pay bill accounted to the peak demand requirement. A sustainable framework based on this analysis would be further investigated.

5. References

[1] García-Ascanio and C. Maté, “Electric power demand forecasting using interval time series: A comparison between VAR and iMLP,” Energy Policy, vol. 38, no. 2, pp. 715-725, Feb. 2010

[2] N. Li, L. Chen, and S. H. Low, “Optimal demand response based on utility maximization in power networks,” in 2011 IEEE Power and Energy Society General Meeting, 2011, pp. 1-8

[3] J. Widén and E. Wäckelgård, “A high-resolution stochastic model of domestic activity patterns and electricity demand,” Applied Energy, vol. 87, no. 6, pp. 1880-1892, Jun. 2010.

Table 1. Percentage of Pay Bill Ratio at Taylor’s University

Year	KWh	PD	Renewable	Penalties
2010	79.38	20.64	0	0.01
2011	78.58	21.35	0.07	0
2012	78.37	20.63	0.09	0

Energy Efficient Measures in Cement Production

Nawoor Ilshad*, Satesh Navasivayam

School of Engineering, Taylor's University, Selangor, Malaysia

**Corresponding author: ilou786@hotmail.com*

Abstract— **the purpose of this feasibility study is to appraise the energy savings, cost and carbon dioxide emission reduction associated with the implementation of a number of technologies and measures applicable to the cement production process. The information presented is based on publicly available reports, magazines, journal articles and case studies from applications of technologies around the world. According to these sources, the cement production is comprised of many theories such as physics law, theoretical calculation, chemical reaction and mechanical properties. After analysing these theories, new idea and theory are utilized to come up with reduction of harmful gases emission and also less energy consumption. The outcome of this project shows that energy consumption in cement production can be reduced significantly by applying latest technology. The statistic used is to gain better understanding of influence of operating conditions on energy consumption in cement plant.**

Keywords— energy, measures, cement, gas

1. Introduction

The cement industry is a resource intensive, energy consuming and vital industry for sustaining infrastructure of nations. The global cement market, while establishing a small share of world industry production, has been growing at an increasing pace in recent years. Many cement manufacturers face a lot of difficulties as there is an increase of competition in the business environment globally. This has created a concerning pattern on economic efficiency. Therefore they seek opportunities to reduce production cost without negatively affecting product yield or quality. And also with the growing concern of cleaner production, manufacturers have to focus on the energy efficient technologies in a greener way that is reducing the emission of harmful gases during the production [1].

2. Literature Review & Methodology

The study was introduced by emerging individual analytical models to evaluate performance in energy management, technical practices and energy efficiency. This present work is based on 5 main energy efficiency technologies and measures in cement production:

2.1. Use Scrap Tires as Alternative Fuels

Scrap tires are tires that are no longer adequate or authorized to use due to damage, brittleness and low tread depth. Tires lose 20% of their mass after it has been used. Around 1 billion tires are being sold every year worldwide. Weight of a normal used car tire is around 6.5 kg. Thus availability of tire is easy and massive [2]. On the other hand, the calorific value of a fuel plays an important role since it is the quantity of heat produced by its combustion (operated at constant pressure and under normal conditions). The calorific value of tires is between 6450kCal/kg and 8000kCal/kg where as coal is between 5900kCal/kg and 6100kCal/kg. (1 kcal/kg = 4.1868 kJ/kg) [3].

2.2. Indirect Firing System

Indirect firing system does not fed the kiln with air and coal directly. All moisture from the combustion of the fuel is vented to the exhaust and the thrashed fuel is transported to storage via bag filters. Thrashed fuel is then densely transported to the burner with a primary transport air. As the primary air supply is decoupled from the fuel mill in multi-channel designs, the percentages of primary air will be reduced gradually at certain percentage of 5 to 10 % of its initial [4]. In other word, the heat input, Q_{in} is less. Agreeing to thermal efficiency (η) equation 1, work out (W_{out}) is the same, the efficiency is higher.

$$\eta = \frac{Wout}{Qin} \times 100 \qquad (1)$$

If the thermal efficiency is greater mean less fuel is needed to combust for same amount of work output. This help in reducing CO_2 emission also as CO_2 is formed during combustion [4].

2.3. Addition of Pre-Heaters

Pre heaters are used mainly to heat up the limestone to a high optimum temperature by using the high temperature gas from the rotary kiln. Multi stages of pre heaters help to reduce heat loss in a way. Part of the heat from the hot gases, which come from the kiln, will heat up the limestone. The rest will be lost to the wall or surrounding. As soon as the hot limestone enters the kiln, the reaction will be faster. Therefore a shorter kiln can be used as a shorter time is needed for the reaction, thereby reducing radiation loss [1].

$$Q_{radiation} = (T_1 - T_2) \text{ x } A \qquad (2)$$

Where:
T_1: body radiation at the inside temperature of the kiln
T_2: radiation at the ambient temperature
A: effective area of the kiln

2.4. Wet Process Conversion to Semi-Dry Process

In the wet process, the slurry before entering the kiln consists of 40% of water. This amount of water needs an extra heat value to evaporate. Thus lead to a more energy consuming kilns [5]. On the other hand, if semi dry process is implemented, a slurry drier used the waste heat from kiln to dry the slurry material before its being fed to the kiln. As the slurry doesn't contain water in the kiln, no extra energy is needed [6].

$$\text{Energy} = \text{power x time} \qquad (3)$$

Energy is dependent on power and time. Change in power will result in change of energy.

$$\eta = \frac{Wout}{Qin} \times 100 \qquad (4)$$

Power is the same as Q_{in} which affect thermal efficiency in a way.

2.5. Effect of Secondary Shell

Heat losses to the surrounding from the kiln shell by radiation and convection are a significant source of energy loss in cement kilns. These losses can be reduced by using a secondary shelf. The idea is to cover the kiln shelf with another metallic shelf having low surface emissivity and thermal conductivity [1].

$$Q_{radiation} = \varepsilon\, \sigma\, T^4 A \qquad (5)$$

Where:
ε = emissivity of the shell
σ = 5.6703 10-8 (W/m2K4) The Stefan Boltzmann Constant
T = absolute temperature Kelvin (K)
A = area of the emitting body (m2)

3. Result & Discussion

3.1 Tires

Mass of 1 billion car tires collected per year = 6.5×10^8 = $6.5{*}10^9$ kg ≈ $6.5{*}10^6$ tons.
1 kg of tire can produce 6450 x 4.1868 kJ of heat (energy).
1 kg of coal can produce 6100 x 4.1868 kJ of heat.
$6.5{*}10^9$ kg of car tire combustion can produce ($6.5{*}10^9$ x 6450 x 4.1868) = $1.75{*}10^{14}$ kJ
$6.5{*}10^9$ kg of coal combustion can produce ($6.5{*}10^9$ x 6100 x 4.1868) = $1.66{*}10^{14}$ kJ
% heat of coal combustion to tire = ($1.66{*}10^{14}$ / $1.75{*}10^{14}$) x 100 = 94.8%
To substitute 1 ton of coal around 0.76 - 0.95 tons of scrap tires is needed. The result shows that scrap tires have better combustion efficiency than coal in term of heat energy.

3.2 Indirect Firing

Assumed a reduction of 10% excess primary air is achieved, means that 90% of the heat input, Q_{in} is needed.
Supposed to get a work output of 190kBtu/ton, heat input of 250kBtu/ton is needed.

Thermal efficiency of direct firing = $\frac{190}{250}\, x\, 100 = 76\%$

Thermal efficiency of indirect firing = $\frac{190}{225}\, x\, 100 = 84.4\%$

According to equation 1, the thermal efficiency for indirect firing is higher by 8.4% than direct firing system.

3.3 Pre Heaters

The length of the kiln is shortened; therefore the area will be reduced. Base on radiation loss equation 2, if the area decreased, there will be a net decreased in the heat radiation loss also. Hence energy consumption is less and the raw material temperature entering the calciner will be higher too as shows in figure 1 below.

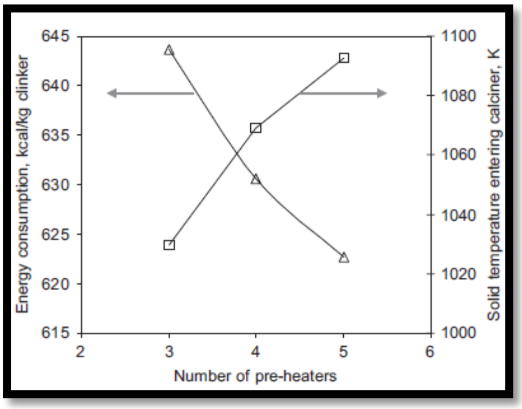

Fig 1: Raw material temperature and energy consumption versus number of pre heaters [1].

3.4 Semi-Dry process

For comparison, a kiln consumes an amount of energy for evaporation, while increasing electricity use. Evaporation energy needs can be cut down by a certain amount using a slurry drier, reducing fuel consumption. Equation 3 shows that if less energy is required, therefore less power is needed. Power required reduced mean that less heat input. Thus from equation 4, the thermal energy again is increased significantly.

3.5 Secondary shell

The emissivity of the shell means the amount of its ability to emit radiation energy in comparison to a blackbody at the same temperature. Using a secondary shell with lower emissivity will surely lessen the heat loss by radiation referring to equation 5. If the heat loss is less, the thermal efficiency within the kiln will be higher. The use of secondary shelf is a promising way for reducing net energy consumption in the clinker manufacturing process. This recuperated heat loss can be used in other cement process such as pre heaters and clinker.

4. Conclusions

The report focuses on the detailed analysis of energy use and reduction of carbon dioxide emissions by process, specific energy efficiency technologies and measures. Energy effectiveness is clearly shown that it is more efficient with the use of new technologies and the fraction of production of harmful gases is reduced in the cement industry.

Around the world, only few cement plants use these technologies. Therefore it is very important for the cement industry to implement these latest technologies as it really shows up many advantages. Verily it requires a high initial cost but long life running will result in more profit to the company and in a greener way operation.

5. Acknowledgment

Express the deepest appreciation to Dr Satesh Navasivayam, Deputy Dean of school of engineering department at Taylor's University, for his constant encouragement.

6. References

[1] Kaustubh Mujumdara∗. (2007). Rotary Cement Kiln Simulator (RoCKS): Integrated modeling of pre-heater, calciner, kiln and clinker cooler. "*Chemical Engineering Science" 62 (2007)*

[2] Asthana & Patil. (2006). Use of alternative fuels in Indian cement industry. "*Advances in Energy Research (AER)".*

[3] Environmental Protection Agency, Office of Solid Waste (1991). "*Markets for scrap tires" United* States, EPA.

[4] E.Deborah, "A life-cycle assessment of Portland cement manufacturing," *Journal of Cleaner Production,* 2009.

[5] Ernst Worrell (2008). Energy Efficiency Improvement Opportunities for the Cement Industry. "*Environmental Energy Technologies Division & Lawrence Berkeley National Laboratory".*

[6] Matthias Mersmann, KHD Humboldt Wedag AG. (2002, April). "*Dry Changes – Switch to Dry Process"* Paper presented at the PetroCem Conference 2002, St. Petersburg, Russia.

Removal of Zn^{2+} from Wastewater Using Membrane Electrolysis

Ng Kah Kit, Nurhazwani Ismail, TVN Padmesh

School of Engineering, Taylor's University, Malaysia

**Corresponding author email: kahkit.ng@sd.taylors.edu.my*

Abstract— Performance of electrolysis with carbon electrode on waste water that contains heavy metal ions (Zn^{2+}), has been studied. Parameters such as metal ion concentration and temperature were studied to achieve higher removal rates of heavy metals from the waste water. The research shows that electrolysis perform the best when the pH is kept at neutral conditions. Besides that, the removal efficiencies of metal ions is highest at 45°C. The research shows that the use of membrane electrolysis has a removal efficiencies of 99.6%.

Keywords— Electrolysis; Heavy Metals; Membrane; Anion; Cation

1. Introduction

Heavy metals are metals that contains more than five times of specific gravity (SG) compare to SG of water [1]. Heavy metals are harmful to human's body when they are not processed and they will start gather in the human tissue. Heavy metals may enter the human body through digestion, ingestion, inhaling, exposure to skin and eye [2]. There are a few sources of heavy metals that can leach in to the ecosystems such as industrial discharges, domestic discharges and ore mining activities. Rapid industrialization had also increased the demand for heavy metals and causes them to leach into the ecosystem. Unlike organic substances, heavy metals are not degradable through process such as biological process [3]. Therefore, treatment of heavy metals wastewater are required before discharging. There are a few treatment process can be done to the wastewater however most of them results in the loss of valuable metals. The ideal way to remove the heavy metals and recovered them back to usable metal is electrolysis. Electrolysis wasn't the common method used to remove heavy metals due to its low-mass transfer rate between metal ions and cathode surface when the metal ions are in low concentrations. However this can be solved by combining the use of an anion membrane, stirrer and also increase in temperature in order to speed up the rate of reaction. Extraction of heavy metals using electrolysis is selected due to the process does not generate sludge, low operating cost, no reagents are needed for the process and precious heavy metals can be preserve and recycle [4].

2. Methodology

The research is separated into two parts. The first part of is to study the optimum parameters for electrolysis of the heavy metals wastewaters. 6 x 200 mm of carbon electrodes purchased from Japson, India is used in the experiment. Reagents used to prepare the synthetic wastewater (Zinc Sulfate Heptahydrate) is supplied by Bendosen, Malaysia. Main parameter that need to be considered is the metal ions concentration, initial pH of the electrolyte, temperature of the electrolyre and the current density of the electrolysis process. After the parameters are being optimized, the second part of the research is to use the anion membrane in the electrolysis method and a comparison is made between the conventional electrolysis method and the anion membrane electrolysis method.

2.1. Reagents

All of the solutions used in the experiment is prepared in room temperature with distilled water. Reagents that used to prepare the stock solutions are all under analytical grade and used without purification. The apparatus used in the experiments are all washed and rinsed with distilled water.

Stock synthetic wastewater solution of Zinc Sulfate Heptahydrate ($ZnSO_4.H_2O$) were prepared by dissolving required amount of $ZnSO_4.H_2O$ powder with distilled water. Further dilution were done for lower concentration of the synthetic wastewater.

The pH of the synthetic wastewater were adjusted to pH 7 by using 1 M of Hydrochloric Acid and Sodium Hydroxide. It is proven by the previous study that the most effective removal capacity were achieved in between pH values 4-8.

2.2. Experimentation

Electrolysis was carried out in a laboratory scale setup. The experiment is carried out in a 250ml container. Two carbon electrodes which acted as the anode and cathode were dipped in the synthetic wastewater. The electrodes are supplied with a D.C. current using a laboratory power supply (Meguro Model: MP302-3). Samples of 3.2ml of the electrolyte were taken periodically and the samples were put in the spectrophotometer in order to determine the residual of the metal ions concentrations. The optical densities of the residual were measure at wavelength, λ=391nm.

The optimum temperature of the electrolyte, initial pH of the electrolyte and metal ions concentration are subjected to the next analysis which is to determine the effect of addition of anion membrane in the electrolysis process.

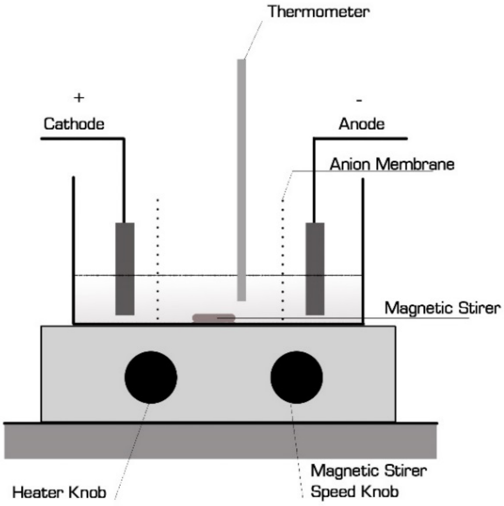

Figure 1 shows the experimental setup of the analysis.

Performance of electrolysis the synthetic wastewater is studied in a range of pH from 4 to 8 while keeping the concentration of the metal ions in 100mg/L. The current density is kept at 0.8A as previous research shows that at 0.8A, the removal efficiencies of heavy metal ions can reach up to 99% [5]. The optimum temperature for electrolysis had been studied by conducting the experiment in a range of temperature from 25°C to 45°C. The experiment repeats by changing the concentration of the heavy metal ions in between the range of 100mg/L to 500mg/L. The optimum parameters will be then used for the experimentation of the membrane electrolysis.

3. Results and Discussion

Studies shows that initial pH of the electrolyte will directly influence the results of the electrolysis. In order to determine the optimum pH value, the experiment of effect of pH value on removal of metals in electrolysis is conducted under 25 °C. Figure 2 shows that the removal efficiencies of the metal ions achieved 98.5% at pH 6 which is slightly acidic.

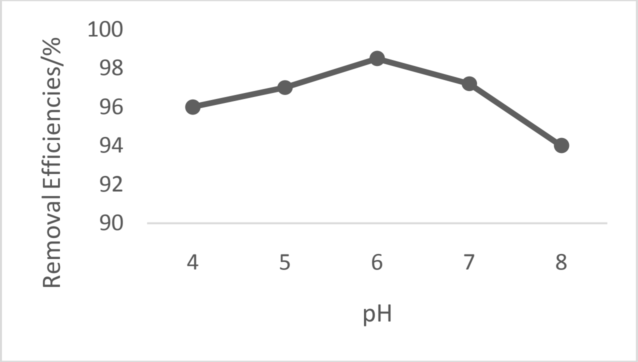

Figure 2 Effect of pH on removal efficiencies of Zn^{2+}

From figure 3, results shows that the optimum temperature for electrolysis is 45°C. Studies shows that high temperature electrolysis are more efficient and cost effective. High temperature electrolysis is favorable from a thermodynamic point of view because the heat energy can transfer to the metal ions and the activation barrier is lowered [6]. However, there is only a slight increase of removal efficiencies between 40°C and 45°C. Considering more cost is needed to increase the initial temperature of the electrolyte, hence 40°C is set to the optimum temperature for the membrane electrolysis.

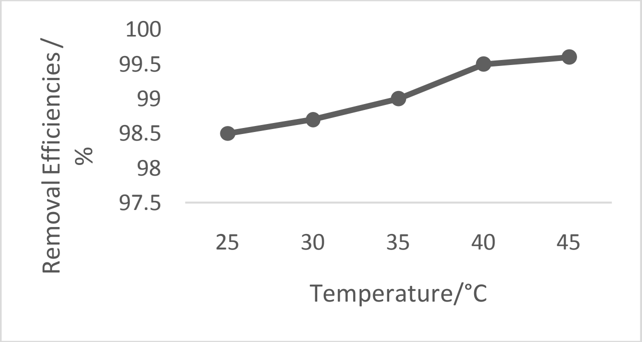

Figure 3. Effect of initial temperature of electrolyte on removal efficiencies of Zn^{2+}

Figure 4 shows that the initial concentration of the metal ions will affect the rate of removal of metal ions. The lower the initial concentration of the metal ions, the rate of removal metal ions will be higher. Therefore, 100mg/L of initial concentration of the electrolyte is selected as the optimum concentration for electrolysis process.

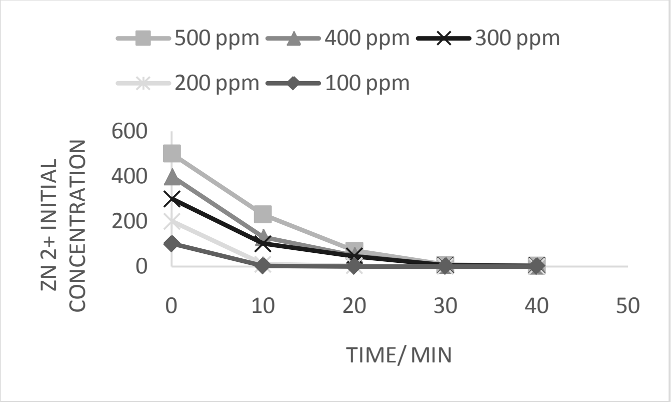

Figure 4. Effect of initial concentration of Zn^{2+} on removal efficiencies.

4. Conclusions

The research proceeds by perform experiment using membrane electrolysis under the optimum parameters such as pH6, temperature at 40°C and the initial concentration are kept at 100 mg/L. The removal efficiencies has achieved 99.6% with the use of membrane electrolysis.

This research shown the applicability of removal of zinc metal ions by using electrolysis. This method is suitable to remove and preserve precious heavy metal ions from wastewater. The performance of the experiments achieved a percentage of 99.6 when it is perform under the optimum parameters. The use of membrane electrolysis is to ensure the anion flows in one direction in order to increase the treatment rate and treatment efficiency.

Acknowledgment

First and foremost, I would like to express my sincere appreciation to my supervisor, for constantly guiding and encouraging me throughout the research module. Besides that, I would like to acknowledge School of Engineering for their support in providing complete facilities to carry out this research. In addition, I would like to thank my co-supervisor for supporting me in the project by giving me useful advice and information. His technical efforts and suggestions helps me manage to reach the goals of the project. Besides that, I would like to thank the lab assistant that helps me on the project.

References

[1] Anne Marie Helmenstine, Ph.D. Heavy Metal Definition from http://chemistry.about.com/od/chemistryglossary/g/Heavy-Metal-Definition.htm

[2] Howard Hu, M.D., M.P.H., Sc.D. (2002) Human Health and Heavy Metals Exposure

[3] John H. Duffus (2002), "Heavy metals" a meaningless term? (IUPAC Technical Report)" Pure and Applied Chemistry, Vol. 74.

[4] Robert W. Peters and Young Ku (1985). Evaluation of recent techniques for removal of heavy metals from industrial wastewaters.

[5] J. Mater. Chem., (2008) Highly efficient high temperature electrolysis

[6] Nafaaˆ Adhoum, Lotfi Monser, Nizar Bellakhal, Jamel-Eddine Belgaied (2004). Treatment of electroplating wastewater containing Cu2+, Zn2+ and Cr(VI) by electrocoagulation

[7] Soha A. Abdel-Gawad1*, Amin M. Baraka,Kawther A. Omran,Mohamed M. Mokhtar (2012) Removal of Some Pesticides from the Simulated Waste Water by Electrocoagulation Method Using Iron Electrodes

Automatic Car-plate Detection and Recognition System

Ng Simin[1*], Florence Choong Chiao Mei[2]

[1]*Electrical and Electronic Engineering, Taylor's University, Malaysia,* [2]*Electrical and Electronic Engineering, Taylor's University, Malaysia*

[*]*simin_ng@hotmail.com*

Abstract— **Automatic number plate recognition (ANPR) is a system where car plate is recognized and identified automatically. This project focuses on processing the image in Matlab software for number plates in Malaysia. The algorithm constructed is to target field programmable gate array (FPGA) as its end product. First, the number plate area is detected using edging, and then the characters are identified using optical character recognition (OCR) with correlation approach. The algorithm is successfully constructed with sample of images correctly identified.**

Keywords— ANPR, OCR, edge detection, correlation, Matlab

1. Introduction

ANPR as stated in the name recognises the number plate automatically. When a car is detected, the camera takes a picture of the car. The picture is then sent to a chip to filter unwanted image, leaving the characters of the number plate. The characters can then be identified using optical character recognition (OCR) [1], [2].

With number plates coming in various shapes, sizes, fonts and colours, the algorithms needs to be refined to increase its efficiency. Another aspect is so that the ANPR can process at break-neck speeds. Most of the research on ANPR system targets hardware that uses C language such as microprocessors. FPGA should take into consideration as the program runs concurrently unlike C language that runs sequentially. This will speed up the process of recognition.

Even though ANPR system is available in other country, research still needs to be done as the style and font of number plate in Malaysia is different [3]. The project is further extended to target FPGA.

2. Objective

The aim of the project is to analyse and create image processing algorithm for ANPR system that takes in consideration of number plates in Malaysia. Simplicity is reflected in the algorithm as the end product targets FPGA.

3. Theoretical Framework

The Basic flow of ANPR algorithm is as shown in Fig. 1.

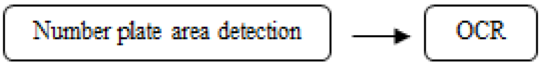

Fig. 1 Basic flow chart of ANPR algorithm

Many approaches have been researched in this area. Table 1 and Table 2 illustrates the few methods that are used

Table 1 Number plate area detection methods

Methods	Description	Disadvantage
Edge detection	Number plate has high magnitude in edges [4]	Background interference creates high magnitude in edges
Colour contrast	Black and white number plate has high colour contrast [5]	Not applicable for number plates with colours

Table 2 OCR methods [6]

Methods	Advantage	Disadvantage
Correlation [6]	Straight forward and reliable	- Not tolerant to font difference and tilt - Huge storage is needed to store all templates
Structure analysis [7]	tolerant to font difference and tilt	Complex analysis is needed to differentiate all characters
Neural-network [8]	tolerant to font difference and tilt	High investment to train system

4. Methodology

This project aims to focus on the image processing algorithm in ANPR system which is simulated in Matlab software. Images that are taken should be clear enough to be processed and should not contain any defects in the number plate for example missing characters.

Number plate area is identified using colour contrast method. This is because number plates in Malaysia are in black and white. First, the upper half of the image is removed as it is found out that the number plate occurs at the bottom half of the image. By comparing the neighbouring pixels horizontally and vertically, the summation of difference between neighbouring pixels for each column and row is computed. These signals are then passed through a filter that removes values that are less than the average of the signal. Few candidates for the number plate area are then detected. The area with the highest contrast is then identified as the number plate area. The area is then cropped out.

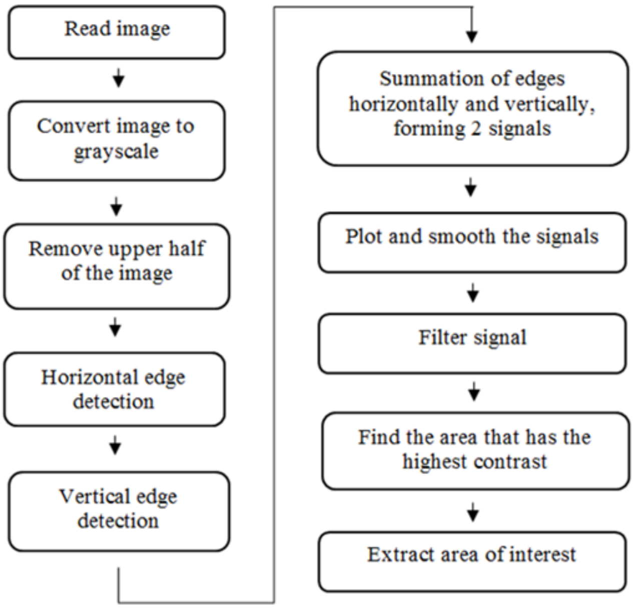

Fig. 2 Flow chart of number plate area detection

After segmenting the number plate area, the characters are then recognized through OCR by correlation method. This is because correlation is straight forward and cheaper. First, the image is converted to black and white. Then, objects that are bigger or smaller than the characters in the number plates are removed. The characters are then separated individually. Each character is then compared with a set of template shown in Fig 3 using correlation. The template with the highest correlation coefficient corresponding to the image defines its identity.

Fig. 3 Template used for OCR

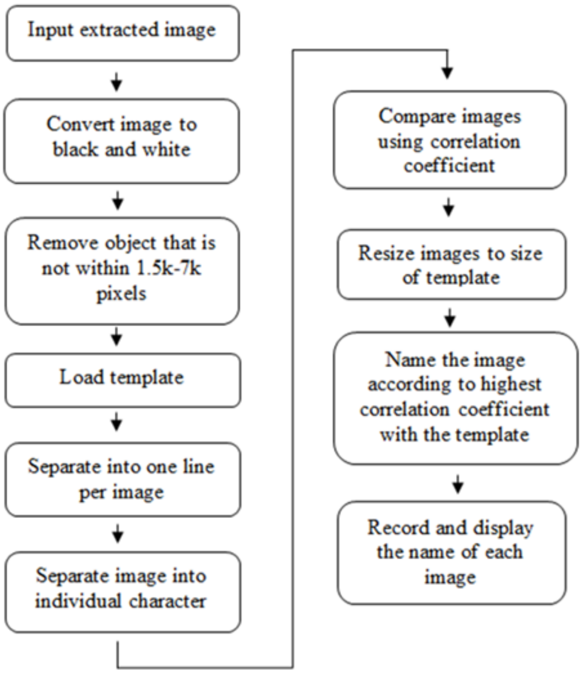

Fig. 2 Flow chart of OCR

5. Results

5.1. Number Plate Area Detection

Fig. 5 shows that the number plate area is detected and cropped.

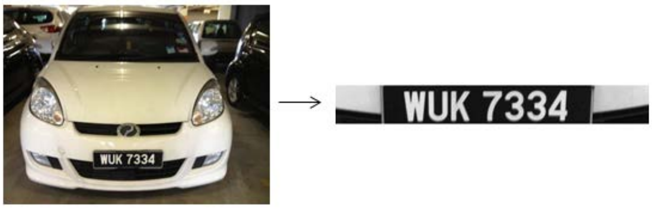

Fig. 3 Number plate area segmented

The number plate area detection algorithm is simulated with several pictures and the result is recorded in Table 3.

Table 3 Data collected for number plate area segmentation

Total samples	50
Correctly segmented samples	21
Incorrectly segmented samples	29
Accuracy percentage	42%

Unsuccessful number plate area detection is due to background interference and radiator design of the car which has high contrast.

5.2. OCR

Fig. 6 demonstrates that number plate is correctly identified

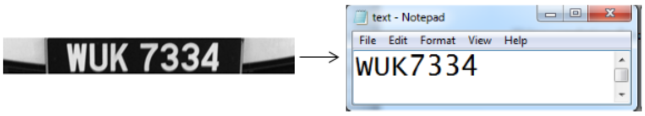

WUK7334

Fig. 4 Characters identified

The 21 samples that are correctly identified from number plate area detection code are inputted into the OCR algorithm.

Table 4 Data collected from OCR

Total samples	21
Correctly identified samples	11
Identified samples with errors	10
Accuracy percentage	52.4%

The different font and special wordings in number plate in Malaysia, for example: Putrajaya and Proton, contribute to errors Other than that, skewed pictures is also an issue.

6. Conclusions

The basic structure of the code, the number plate area segmentation and OCR code is constructed. The project is then extended to target FPGA for future works.

Acknowledgment

I would like to express my utmost gratitude to my supervisor who guided me from the start to the end of this project.

References

[1] Leonard. G. C. H. & Colin P. (2005), *Automatic Number Plate Recognition for Australian Conditions*, Macquarie Park, New South Wales: Macquarie University.

[2] Ondrej M. (2007), *Algorithmic and Mathematical Principles of Automatic Number Plate Recognition Systems*, Brno, Czech Republic: Brno University of Technology.

[3] Norfaeza N. M. (2006), *License Plate Recognition using Kohonen Neural Network Algorithm, Shah Alam*, Selangor: University Tecknology MARA.

[4] Karim M.R., Abdullah A.S. & Yasin A.M. (2009), Travel Time Measurement in Real-Time using Automatic Number Plate Recognition for Malaysian Environment. *Journal of the Eastern Asia Society for Transportation Studies*, vol. 8.

[5] Naikur B. G. (2010), *Car License Plate Detection, Sacramento*, California: California State University.

[6] Kapadia P. S. (2010), *Car License Plate Recognition using Template Matching Algorithm*, *Sacramento*, California: California State University.

[7] Nelson L. J. (2007) Plate Recognition. Retrieved December 5, 2012, From http://www.photocop.com/recognition.htm

[8] Nagare A. P. (2011), License Plate Character Recognition System using Neural Network, *International Journal of Computer Applications*, vol. 25.

Bed Massage: Automated Heating and Cooling Cycle for Muscle Recovery

Nor Syazwani Mohd Yasin[1*], Mohamed Nassir[2]

[1]*School of Engineering, Taylors' University, Malaysia,* [2]*School of Engineering, Taylors' University, Malaysia*

syazwani.yasin90@gmail.com

Abstract— **Human muscle experiences fatigue and discomfort after reacting to activities. A comprehensive study for anatomy of the muscle and nervous system is carried out. New proposed technique which is using cycles of heating followed by cooling to the painful areas where we expect drastic change in the effectiveness of the massage afterwards. This research brings further improvement in therapeutic process hoping to set the ideal heating and cooling temperature which results in optimum result.**

Keywords— Human muscle, temperature, thermoelectric, nerves system, muscles therapy, heating and cooling.

1. Introduction

Recovery of human muscle is extremely important as human muscle is being used in every daily life activities which most of the activities are possible to cause sudden muscle ache or discomfort. Simple, fast, and safe recovery method is highly recommended without involving any chemical medicine. Physical therapy, based on temperature manipulation, has being used commonly for centuries [1] in which heating or cooling cycle is used for treatment ranging from headache to muscle spasm. Both hot and cold therapies are proven to prevent from further muscle injuries and successfully aiding recovery process. New idea came to combine these two processes in an alternate periodical sequence. The ideal frequency rate and the temperature being used of each cycle is a subject to studies and investigation so that the optimum muscle recovery can be achieved. This new idea, expectedly, will solve the problem of traditional physical therapy efficiently which includes, but not limited to, late recovery and more time for treatment. This project, upon completion, provides answers to most important concerns: optimum temperature and the period of treatment.

2. Thermal Manipulation Therapy

Historically, the oldest thermal therapy was reported around 3000 BC [1] where the temperature used for the therapy cannot be controlled. The treatment then was simply carried out as a cold or hot pack which needs to be applied to the ill part of the body for certain time until recovery or sign of recovery is achieved. Since that time (5000 years ago) until now, thermal therapy is still considered as an effective option for muscle treatment because of the limitation of the conventional method (drug, massage, surgery, etc). Recently, due to the significant attentions and interest, thermal therapy has been improved by researches and medical members especially in the field of hot and cold application [2] [3] [4].

Some therapeutic treatments use hot pack; others use cold pack. Previous research has been proven that hot pack can improve blood circulation under the muscle [1] and, in addition, relaxing the muscle [5] as part of the muscle recovery process.

Different for cold therapy, result on the research done for cold therapy show slightly different effect on muscle. In low temperature condition, muscle tissue is thought to stimulate receptors and this will reduce the swelling and inflammation effects after the injury [6]. Not only that, low temperature also can reduce the pain and bleeding after the muscle injury [5], [7], [8]. Even the reaction of the muscle towards both cold and hot condition is different; both reactions are the process experienced by the muscle in order for it to recover after being treated with thermal therapy.

The issue of alternating hot and cold therapy is subject to debate amongst researchers regarding the beginning of this therapy. What reported is the results summarized by Calder [9] [10] which suggest that several research have shown that the contrast hot–cold water technique could recover the muscle much faster by stimulating the central nervous system. Calder further added that blood flow is enhanced by this technique. Not only that, this technique also slow down the energy released by the muscle, reducing the muscle activities and allows recovery process to occur more rapidly thus revitalizes and energizes the muscle physical condition [11]. Contrast hot-cold is a bathing technique which the hot baths temperature ranging from 37 to 43°C and for cold baths, the temperature ranging from 12 to15°C. Duration ratio of warm to cold water for injury treatment ranges between 3:1 to 4:1 [12] [13] [14] [15]. Usually the cycle is applied for 20 to 30 minutes and it is believes that it is better if we end the therapy with hot bath and it is highly recommended if the process is repeated twice daily [16]. Currently, the hot-cold cycle is conducted using two separate baths. In this project, the treatment will be conducted in a continuous cycles which allow a smoother and more effective temperature change.

3. Methodology and Data

A 5x5-cm 'p' and 'n' type semiconductor material layered by a 5mm-thickness ceramic material and enclave in a plastic envelop. The semi-conductor material (see Fig. 1) is connected to an adjustable power supply of 15 volts and 1.5 amperes. By adjusting the power supply, the current flows in the semi-conductor material changes and heating the ceramic materials. The power supply serves as dual purposes by heating the semi-conductor or, upon reversing the current, cooling it. Currently, at this early stage of designing this pad, the current could reverse manually which results generating the heating/cooling cycle. This device is easy to handle, to maintain, and due tits durability it can be used to attach to any part of the body. Also, by adjusting the current and the current direction, we may make one surface of the ceramic surface cold and, at the same time, the other surface hot. Under this circumstance, we can apply the cycle with the ability of the therapist based on the need of the treatment.

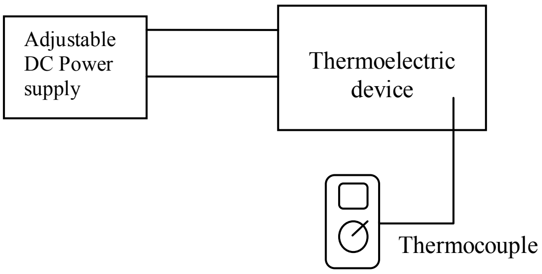

Figure 1 – experiment setup for thermoelectric

By using thermoelectric device, the prototype of heating and cooling device is made for the purpose of introducing a new heating and cooling mechanism for treating the muscle strain. By using thermoelectric device, the complication of contrast bath can be eliminated as a totally different concept is used in this prototype.

The experiment was run in order to determine the amount of current needed to produce desired temperature for muscle therapy. The setup of the experiment is shown in the figure 1 and the result is recorded. The prototype will be built and run using the amount of current obtained from the experimental result.

4. Result

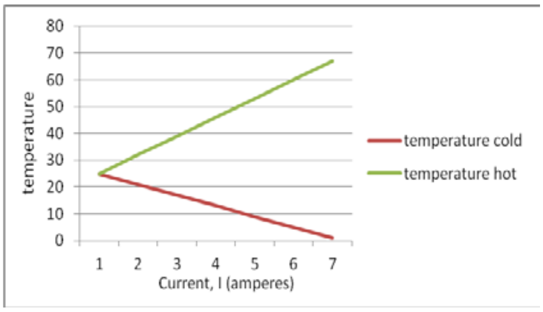

Figure 2 shows the theoretical relation of temperature, t, and current, I [17].

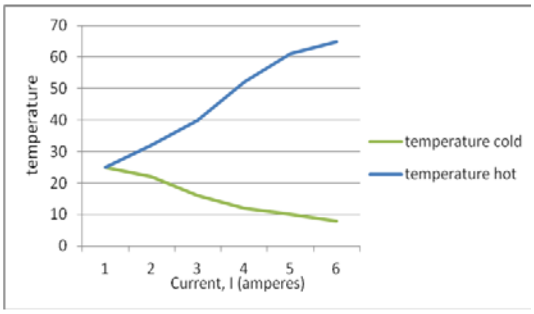

Figure 3 shows the experimental relation of temperature, t, and current, I.

5. Discussion

Experimentally, the temperature is inconsistent due to the heat loss to the surrounding. The maximum temperature reached by the thermoelectric is too high for the therapy application. Same goes to the minimum level which too cold. The current input need to be adjusted in order to adjust the output temperature as the ideal temperature is 37 to 43 $^{\circ}$C for hot and 12 to15 $^{\circ}$C for cold. Based on the experimental and theoretical results, the amount of current which produces the desired temperature range is around 3amps. More than that, it can cause burn sensation to the skin surface. From the graph, the cold temperature when current is 3 amps is around 15° meanwhile, the hot temperature for the same amount of current is around 40°. Thus, the thermoelectric device will be run using 3 amps current. The main disadvantage of thermoelectric is the high cost because it is not widely used.

For the muscle respond, the rate of muscle recovery is expected to increase about 15% from rate of normal muscle recovery using hot pack or cold pack. It is a conflicting issue on what parameter should be taken to measure the rate of recovery of the human muscle. However, based on the theoretical framework, the alternating hot and cold method is definitely enhancing the recovery rate of muscle. By improving and smoothing the muscle treatment system, the rate of muscle recovery is expected to improve along with it even the prototype cannot run exactly as the expected design due to the limited budget.

6. Conclusion

As conclusion, thermoelectric semiconductor device is applicable for the usage of thermal therapy for its ideal specifications. The quantitative effectiveness of alternate hot and cold cycles is still under investigation while, qualitatively, its effectiveness is highly reliable amongst the medical field personnel.

Acknowledgment

Thank you to School of Engineering of Taylors' University for provides me for this research and thank you to Dr. Mohamed M. Nassir for the guidance and supports throughout this research.

Reference

[1] W. R. Habash, B. Rajeev, D. Krewski and T. A. Hafid, 2006 "An Introduction to Thermal Therapy," *Thermal Therapy, Part 1,* no. 34, pp. 459-489.

[2] P. R. Stauffer and S. N. Goldberg, 2004, "Int J Hyperthermia," in *Introduction: Thermal Ablation Therapy*, pp. 7:671-7.

[3] J. G. Short and P. F. Turner, 1980, Physical Hyperthermia and cancer therapy., pp. 68: 133-42.

[4] A. Y. Cheung, 1987, Microwave hyperthermia for cancer therapy, pp. 34: 493-522.

[5] J. Lehmann and B. de Latuer, 1999, "Ultrasound, shortwave, microwave, laser and superficial eat and cold in the treatment of pain. In:," in *Textbook of Pain*, 4th ed., Edinburgh, Churchill Livingstone, pp. 1383-1397.

[6] C. Enwemeka, C. Allen, P. Avila, J. Bina, J. Konrade and S. Munns, 2002, "Soft tissue thermodynamic before, during, and after cold pack therapy," in *Medicine and Science in Sport and Exercise*, pp. 45-50.

[7] D. J. Dandy and D. J. Edward, 1999, Essential Orthopaedics, 4th ed., Edinburgh: Churchill Livingstone, pp. 273-281.

[8] R. M. Linchitz and P. J. Sorrel, 2003, "Physical Therapy Techniques," in *Pain Medicine: A Comprehensive Review*, Philadelphia, Mosby, pp. 327-333.

[9] A. Calder, 1996, "Recovery Training," in *Training for Speed and Endurance*, , Sydney, Allen and Unwin.

[10] A. Calder, 2001b, Personal Communication.

[11] D. J. Conchrane, 2004, "Literature review: Alternating hot and cold water immersion for athlete recovery: a review," *Physical Therapy in Sport 5,* pp. 26-32.

[12] A. T. Bell and P. G. Horton, 1987, "The uses and Abuse of Hydrotherapy in Athletics : A review," *Athletic Training 22,* no. 2, pp. 115-119.

[13] J. W. Myrer, D. O. Draper and E. Durrant, 1994, "Contrast therapy and intramuscular temperature in the human leg," *Journal of Athletics Training 29,* no. 4, pp. 318-322.

[14] P. Brukner and K. Khan, 2001, Clinical Review of Sport Medicine, Roseville, NSW: McGraw-Hill.

[15] G. A. Halvorson, 1990, "Therapeutic heat and cold for athletic injuries," *Physician and Sportsmedicine 18,* no. 5, pp. 87-92. See also page 94,.

[16] D. Higgins and T. W. Kaminski, 1998, "Contrast therapy does not cause fluctuation in human gastrocnemius intramuscular temperature.," *Journal of Athletic Training 33,* pp. 191-201.

[17] Technical Data Sheet, TM-127-1.4-8.5, Thermoelectric Module, ADVANCED THERMOELECTRIC, Nashua, New Hampshire.

Motorized Bat Wing

Raynon Po, Mohammad Hosseini Fouladi,
Paul Ratnamahilan Hoole, Aravind. C. V
School of Engineering, Taylor's University, Malaysia

The purpose of the research is to display the motion of bat wing with mathematical modeling. To obtain the flight feature of a bat, several theses is studied. These include the studies of aspect ratio, wing loading, population analysis, wing tip cycle, wing contraction rate, wind tunnel analysis and twisting angle. By using the information found, some sketches are made, equations are modeled. The features are compiled with a curve fitting tool. The bat wing is initially segregate into 2 part, and then further improve by introducing one additional part. The pattern shows persist but lack of accuracy plot compare to the benchmarks. The next stage of the research is to model the bat wing in higher speed and fabricate it.

1. Introduction

Human have display their hunger to fly. For the first five hundred years of flapping flight history, a few notable people perform their studies for flight transport (Lynn Harmon ,2008). In modern days, the ideaof flight machine is shifted tocapablilities on speed hight and size. (Lynn Harmon, 2008). This become one of the enlightenment to deal with Motorized Bat Wing due to bats are mammals and their hand profile looks similar to human.

The understanding of the difference and behavior of bats are vital. It has a shorter humerus, which direct the tip, longer finger for maneuver purpose, and radius which connect both the fingers and the humerus. Each of its joints rotates independently and their combination forms a flight pattern, which is the main concern in this paper. Most of the critical information such as the rotation angle and flight pattern is obtained. The main objective is to make use of these properties and form a prototype that correlates the flight pattern. The information obtain are listed below.

1.1. Literature review

Colorado, J. et al. (2012)., provide DoF analysis. He also provides the dimension of bat wing as a reference for the wing frame. This thesis is more closely related to the field of interest. However it has 3 critical weaknesses: complicated, expensive and time consuming. It uses specialized material that is not relevant to the project.

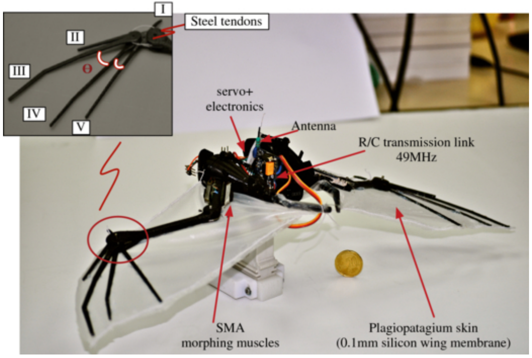

Figure 1. Biomechanics of morphing wings in a Bat-robot actuated by SMA muscles. [1]

Von Busse. et al (2012), produces experiment and analyze the bat wing pattern. This paper provides varies of crucial flight angles and pattern generated by the joints. The information is grouped into 3 different forward flight speed (not to confuse with flapping speed), 0m/s (maintaining same height), 3m/s and 7m/s. This information is a good stepping stone to start the project by analyze the joints and its rotation. It is one of the bench marks for the result.

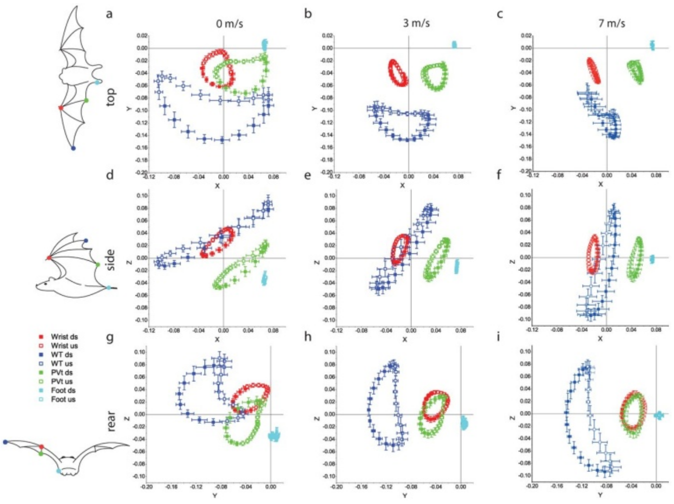

Figure 2. Flight pattern of a bat [2]

Lynn Harmon, R. (2008), In this Book, some unique properties of bat wing compare to other animals such as birds and other flying animal are found. It helps us to analyze the joints and links on a bat, simulate it as it is a crank mechanism. The prototype is then segregate into fingers, radius and humerus based on Figure 3.

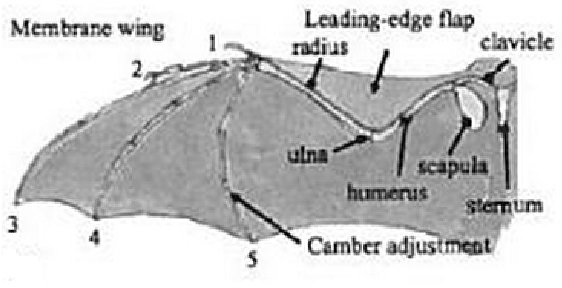

Figure 3. Bat wing profile [3]

2. Methodology

2.1. Geometry construction and simplification

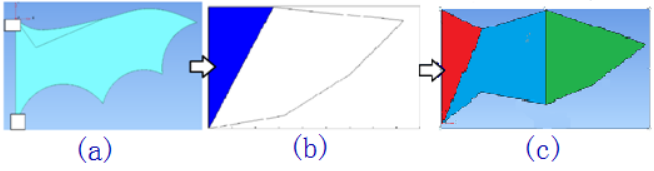

Figure 4. Evolution of bat wing frame, (a) Initial frame with Powershape drawing, (b) simplified model with Matlab(2 joints), (c)simplified model with Matlab(3 joints),

A rough bat wing model is generated; (refer to Figure 4a). The pattern is generated according to the literature reviews. While simulate the bat wing in matrix form, simplification is needed. It is simplified into two section initially, with humerus represented by a triangle, where the fingers and radius is combined and drawn in an irregular pentagon (refer to Figure 4b). Then the simplification is improved by separate the finger with radius.

2.2. Curve fitting

With a 0.5mm error and rounded number, the information is extracted from the literature review and curve fit with Matlab extension function: “cftool”. Just like generating trend line and obtain equation of a scatter plot in Ms Excell, “cftool” is a curve fitting tool that is specialized on perform varieties of curve fitting such as weibull, rational and inverse function. One of the most important functions provided by “cftool” is the sum of sine curve. It fit the scatters to the sum of sine curves and provides equation. According Von Busse. et al (2012), the curve that relates the angle changes to time shares similar pattern to the sine curveand proven that the regression is more than 90%. To simplify the equation, the sine equation is limited up to 2 degree.This allow the equation that relates angle and time modeled in sum of sine curve.

2.3. Rotation Matrix

Consider the leg of the bat as the origin, the entire bat body is represented by *z-axis.* The bat has a height of 9cm where the head of the bat locate on (0, 0, 90). To display the rotation in Matlab simulation, rotation matrix is studied. The bat humerus rotates around the bat body (z-axis) where the rotating angle is found from Von Busse’s thesis.. The full span of the wing occupies the x-z plane. The rotation motion of the wing is obtained by multiply the geometry matrix, to the rotation matrix. Let [S] be the geometry matrix, the resultant geometry matrix [S’], $[T]$ is the rotation matrix. The next wing position is:

$$[S'] = [S][T] \qquad (1)$$

With this equation, the matrix $[S']$ is changing with respect to $[T]$, $[T]$ is changing with respect to angle, angle is changing with respect to time, which is obtained from 2.1 .The rotation matrix $[T]$ stays in the form of:

$$\begin{bmatrix} 1 & 0 & 0 \\ 0 & cos\emptyset & -sin\emptyset \\ 0 & sin\emptyset & cos\emptyset \end{bmatrix} \qquad (2)$$

The Equation of the radius and finger deals with an arbitrary axis. The rotation is performed by introduce a new rotation matrix. Let [Rx], [Ry],[Rz] be rotation about *x-axis*, *y-axis* and *z-axis*, where [Rx], [Ry] is dealing with the arbitrary axis and [Rz] is dealing with the angle of interest. The equation of the rotation about an arbitrary axis is:

$$[T] = [Rx]^{-1}[Ry]^{-1}[Rz][Ry][Rx] \qquad (2)$$

3. Result (Matlab simulation) and discussion

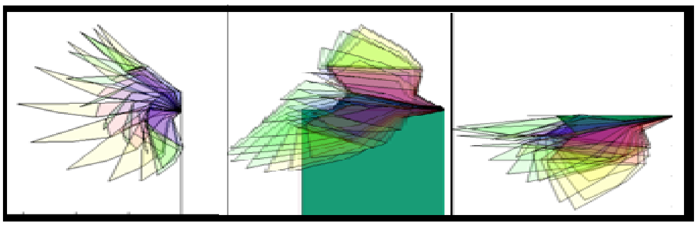

(a) (b) (c)

Figure 5. Matlab simulation for bat wing model (3 parts) in Figure 4c, wing movement at 0m/s(maintain height). (a) front view (b) side view, (c) top view

To allow the wing pattern to visualize clearly without animated, the movement is freeze and the object body is made transparent. The expansion and contraction while up stroke and full length down stroke are clearly shown in the simulation. As the bat is speeding up the wing contract lesser and tend to flap their wing at a higher frequency, then it flap for a larger span at a higher speed. The angle of forward stroke is approximately45 degrees, which is also shown in the picture. However the pattern form from the wing tip and the joints are not correlated.

3. Conclusions and Future works

The simulations produced manage to explain how the bat flaps their wing while staying on same position and speeding up., however it is still considered as an infant stage. The model hardly represents the actual bat wing profile.

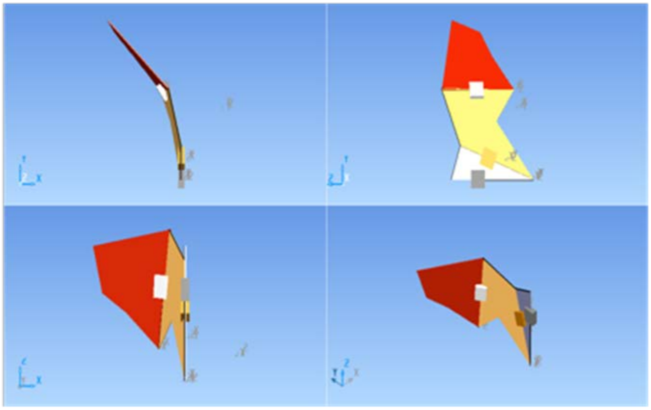

Figure 6. Psmodel of physical prototype from left to right: Top view, Front view, Side view, Iso view

For future work, to correctly simulate the bat wing motion, the bat wing tip is further analyzed. The other bat wing speed must be modeled. Besides that, fabrication is another vital step. The design of the wing looks like what is shown in figure 7. The square boxes shown in the figure are the servo motors location. The first motor (attached on the triangle plane) is going to attached on a fixed support to ensure the flapping is stable.

References and Acknowledgement

[1] C. J., "Biomechanics of Smart Wings in Bat Robot: Morphing Wings Using SMA Actuators," Center for Automation and Robotics, Spain, 2012.

[2] V. B. R, "Kinematics and wing shape across flight speed in the bat," Biology open, Berlin, Germany, 2012.

[3] H. R.L., Aerodynamic modeling of a flapping membrane wing using motion tracking experiment, College Park, Maryland, United States: ProQuest, 2008.

[4] B. E., "Flight Style in Bats as Predicted From Wing Morphometry: The Effect of Specimen Preservation," *Journal of Zoology,* vol. 234, 2009.

[5] Iriarte-Diaz.J, "Kinematics of slow turn maneuvering in the fruit bat Cynopterus brachyotis," *Journal of Experimental Biologist,* vol. 211, no. 21, pp. 3478-3489, 2008.

[6] N. U. M, " Echological Morphology and flight in bats(Mammalia; Chiroptera): wing adaptions, flight performance, foraging strategy and echolocation," *Philosophical Transactions of the Royal Society of London Series B Biological Science,* pp. 335-427, 1987.

[7] Unknown, "Rotation about an Arbitrary Axis(line)," 1986. [Online]. Available: www.engr.uvic.ca/~mech410/lectures/4_2_RotateArbi.pdf. [Accessed 28 February 2013].

Developing an Integrated Approach for Experimental Modal Analysis of Multi-Bent Copper Phosphorous Tubes

P. Kamalanathan[1*], M. Hosseini Fouladi [1], K. H. Yap[2]

[1]*School of Engineering, Taylor's University, Malaysia,* [2]*Panasonic Appliances Air-Conditioning R & D Malaysia Sdn Bhd, Shah Alam*

**Corresponding author's e-mail: prashanth77@live.com*

Abstract— **Modal Analysis provides valuable information about a structure in terms of its dynamic properties. In this study, an Experimental Modal Analysis (EMA) procedure was developed for the testing of a suction tube under "free-free" boundary conditions to validate the dynamic properties obtained from the Finite Element (FE) Modal Analysis method. Modal Indicator Functions (MIF) and parameter estimation algorithms were used to extract the dynamic properties of the suction tube.**

Keywords— Dynamic properties, Modal parameter estimation, Mode indicator function, Suction tube, Stability Diagram

1. Introduction

The tubes in an air conditioning outdoor unit are constantly subjected to external excitations which vary from the vibrations caused by the compressor, and during the transportation of the air-conditioning outdoor unit. Coincidence and prolonged exposure of these excitations with the natural frequencies of the tube will result in resonance leading to a shortened lifespan of the tube due to fatigue failure. Current design validation processes of new tubes designs are based on prototype testing which is both time consuming and costly. The outcomes of the study will act as a platform to assist air-conditioning manufacturers in validating new tube designs in a cost effective, yet efficient manner without the need for prototype fabrication. In this study, Experimental Modal Analysis (EMA) is used to determine the dynamic properties (natural frequencies, damping ratio, mode shape) of a 2.0 Hp suction tube with a mass of 0.197 kg and a wall thickness of 0.7 mm. EMA is a technique where an external excitation is applied onto a structure using an impact hammer or a shaker and the response of the structure is measured via accelerometers mounted on the structure. The empirical data from EMA are then analyzed using various computational algorithms to give the dynamic properties of the structure. The objectives of this study are; 1) to develop and validate a complete EMA testing procedure on multi-bent copper phosphorous tubes, 2) to validate the dynamic properties from the Finite Element (FE) Modal Analysis under "free-free" boundary conditions with the dynamic properties obtained from EMA, and 3) to determine the damping ratio of the suction tube to update the FE model. The damping ratio can only be determined using the EMA procedure and is used to update the FE model for a more robust computation, hence justifying the sheer importance of EMA. Reference [1], shows a study done on a suction and discharge tube attached to a compressor under fixed boundary conditions. The distinguishing factor in this study compared to the previous study is that in this study, EMA is carried out on a suction tube under "free-free" boundary conditions as the measurements obtained are very reliable, suitable in cases where correlation is required and the configuration is easily achieved [2], [3].

2. Theoretical Overview

In EMA, the "free-free" boundary condition is normally achieved by suspending the structure using elastic cords as shown in Fig. 1. The empirical data obtained from EMA are called Frequency Response Functions (FRF). These FRFs are a ratio of the response of the structure measured via an accelerometer over the excitation applied onto the structure at a particular point [4]. The FRF is computed using an algorithm called the Fast Fourier Transform (FFT), commonly implemented in FFT analyzers [2]. In order to extract the dynamic properties of the structure from the FRFs, Modal Indicator Functions (MIF), and modal parameter estimation are utilized. The MIF is an algorithm that assists in the mode shape identification process via the selection of poles from an FRF plot, where the mode shapes are the deformation of a structure at a particular natural frequency [4], [5]. Rigid body modes on the other hand are similar to mode shapes except that they do not deform elastically and occur at a near zero natural frequency. The highest rigid body mode in an EMA test can serve as a validation tool for the "free-free" boundary condition of the experimental setup [6]. The modal parameter estimation process comprises of various advanced algorithms which locally or globally curvefits an analytical function to the FRF data while creating a stability diagram containing poles [2]. The selection of stable poles from the stability diagram provides the dynamic properties of the structure. Exponential windowing functions applied to the response spectrum in the time domain to reduce leakage adds artificial damping to the response spectrum which has to be accounted for in order to obtain the accurate damping percentage of the structure at its natural frequencies [6].

3. Research Methodology

The frequency range of interest in this study is between 0 to 200 Hz. The integrated process begins with the meshing of the suction tube on the ANSA software by βETA CAE using a shell mesh with an element size of 0.5 mm and 142 200 elements. The loadcase setting for the NX Nastran solver was set on ANSA based on the Lanczos method and the loadcase file was exported to NX Nastran 8.5 Enterprise by Siemens PLM for Modal Analysis solving. A wireframe of the suction tube was used as the geometry for the EMA procedure on MTC Hammer by Brüel & Kjær. A roving hammer test was carried out based on 34 measurement points with 4 single-axial accelerometers by Brüel & Kjær which is attached to the suction tube using beeswax as an adhesive. The FRF data from MTC Hammer was exported to PULSE Reflex by Brüel & Kjær which facilitated the collaborative usage of the modal parameter estimation process, MIF and a stability diagram to obtain the dynamic properties of the suction tube. The correction of damping was then carried out, and the results from both methods were exported to μETA by βETA CAE to obtain the frequency difference and visualize the mode shapes.

Fig. 1 The "free-free" boundary condition set-up for EMA

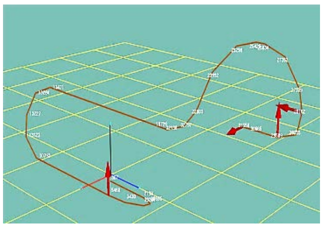

Fig. 2 The positioning of the 4 single-axial accelerometers

4. Results and Discussions

In this study, the Complex Mode Indicator Function (CMIF) and the Rational Fraction Polynomial-Z (RFP-Z) algorithm were used to extract the dynamic properties of the suction tube from the raw FRF data generated by the FFT analyzer. The four plots shown in Fig. 3 are the CMIF plots where the first plot from the top is the primary CMIF plot. The numerous shapes on the stability diagram are called poles which are generated from the RFP-Z modal parameter estimation algorithm. The coincidence of the poles with the peaks of the primary CMIF plot assists the user in selecting stable poles which corresponds to the dynamic properties of the structure.

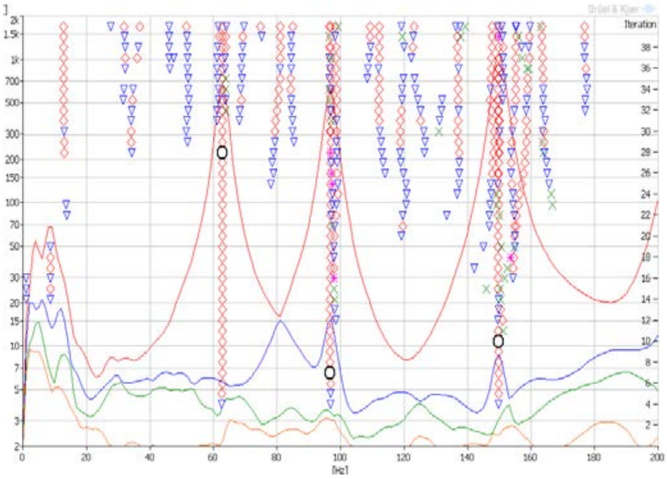

Fig. 3 The stability diagram used in this study

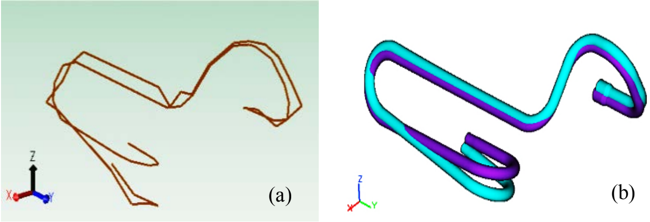

(a) (b)

Fig. 4 Visual comparison of the experimental mode shape (a) and simulated mode shape (b) for Mode 1 at 62.8 Hz

Three different natural frequencies were observed in the frequency span of 0 to 200 Hz. The FE Element Modal Analysis was able to accurately compute the natural frequencies and the deformation of the mode shapes as compared to the results from EMA whereby the highest percentage difference observed in terms of the natural frequency was 1.9 %. The percentage error can be seen in Table 1 and the visual comparison of the mode shapes is shown in Fig. 4. The reason for error could be due to the material properties used in the loadcase setting on ANSA, especially the density of the material. Since the natural frequency is a function of mass and mass is directly proportional to density, it is highly possible that the variation in the natural frequency could be due to the density of the material used in the loadcase setting. The first peak observed on the primary CMIF plot occurs at a frequency of 3.1 Hz which indicates the presence of a rigid body mode. The "free-free" boundary conditions of the experimental setup can only be valid if the natural frequency of the rigid body mode is less than 15 % of the first natural frequency [6]. In this case, the rigid body mode is 4.9 % of the first natural frequency indicating that the "free-free" boundary condition is valid. The highest response in terms of the CMIF peak and the lowest damping ratio occurs at Mode 3 indicating that the greatest possibility of fatigue failure due to resonance will occur at Mode 3.

5. Conclusion

Three different natural frequencies were identified for the 2.0 Hp suction tube in a frequency span of 0 to 200 Hz where the FE Element Modal Analysis was able to accurately determine the natural frequencies of the suction tube and the deformation of the mode shapes compared to experimental results from EMA. The progressively decrease in damping indicates that fatigue failure will occur most readily at a frequency of 149.7 Hz due to the low level of damping. The validation of the "free-free" boundary condition justifies the reliability of the experimental setup and the integrated usage of the CMIF and the RFP-Z algorithm to extract the dynamic properties of the suction tube via selection of stable poles on the stability diagram is highly recommended for future EMA procedures on suction tubes. Future developments could incorporate the usage of mode shape validation in terms of vector analysis to ensure accurate validation of mode shapes. This study will benefit the air-conditioning industry as it is able to reduce cost and time in terms of validation of new tube designs compared to prototype testing.

Acknowledgment

The author would like to thank his supervisors, Mr. Low Lee Leong, and his family members for their continuous support and help. The author would also like to extend his gratitude to Mr. Cheng Chee Mun for the approval and opportunity to use the software and equipment available at PAPARADMY1 and to Mr. Low Seng Chok for the approval of the copper tube specimens used in the study.

References

[1] S. K. Loh et al.,(2011). Vibrational characteristics of piping system in air conditioning outdoor unit, *Science China Technological Sciences, 54*(5), 1154-1168.

[2] Brandt, A. (2011). *Introduction, in Noise and Vibrational Analysis: Signal Analysis and Experimental Procedures.* Chichester, UK: John Wiley & Sons, Ltd.

[3] Perinpanayagam, S., & Ewins, D. J. (2003, February). *Free-Free, Fixed or Other Test Boundary Conditions for the Best Modal Test?.* Paper presented at the IMAC-XXI: Conference & Exposition on Structural Dynamics, Kissimmee, Florida.

[4] Ewins, D. J. (2000). *Modal Testing: Theory, Practice, and Application.* Baldock, Hertfordshire: John Wiley & Sons, Ltd.

[5] Dimitrijević, J. (2005). Complex mode indicator function to find repeated roots or closely coupled modes. *Scientific-Technical Review,* (3-4), 50-58.

[6] Giorelli, M. (2002). *Methodology for Correlating Experimental and Finite Element Modal Analysis on Valve Trains.* M.S Thesis, Worcester Polytechnic Institute, Worcester, United States.

Table 1. Simulation and Experimental Dynamic Properties of the 2.0 Hp Suction Tube in a Frequency Span of 0 Hz to 200 Hz

Mode	Experimental (EMA)			Simulation (FE)	Percentage Error (%)
	Natural Frequency ω_n	Uncorrected Damping D_e (%)	Corrected Damping D_c (%)	Natural Frequency ω_n	
1	62.8	3.547	3.481	64.0	1.9
2	96.8	2.398	2.355	95.2	-1.7
3	149.7	1.623	1.595	151.4	1.1

Solar Drying of *Polygonum minus* Huds

Puong Wee Lau[1], Puteri Farah Wahida[1], Chien Hwa Chong[1]

[1]*School of Engineering, Taylor's University, Taylor's Lakeside Campus, No.1 Jalan Taylor's, 47500 Subang Jaya, Malaysia*

**ChienHwa.Chong@taylors.edu.my*

***Abstract*— The objective of this study is to design and fabricate a solar dryer to dehydrate medicine herbs. In addition, drying kinetics of solar drying was compared with natural sun drying. Average temperature and relative humidity of *P.minus* were 41 ℃ ± 5 ℃ and 30% ± 0.5% respectively. Lewis models, Henderson and Pabis models, Logarithm models, Page model and Midilli et. al model were used to determine the best fit models. The effective diffusivity for D_{nbnc}, D_{hbc}, D_{abc}, D_{abnc} and NSD processes varied from 0.608E-10 m^2/s to 1.722E-10 m^2/s.**

Keywords— thin layer modelling, indirect forced convection solar drying, moisture content, herbs

1. Introduction

Polygonum minus Huds (*P.minus* Huds) originated from Southeast Asia [1]. This plant belongs to the Polygonaceae family [1]. *P.minus* Huds leave was widely used in Malaysia cooking as flavoring ingredient and can be used to treat digestive disorders and dandruff [1].

In recent years, solar energy was concerned as an alternative energy to replace the fossil fuel in energy consumptions. Solar drying using different solar dryer and natural sun drying would be studied [2]. The natural sun drying was abundant and free pollution whereas the solar drying improves the drying quality from hygiene and reduce drying time. Mathematical modeling and experimental studies had been conducted on thin layer drying process of mint, parsley leaves [2] by using different type of solar drying system.

The main objective of this study is to study and compare the thin layer drying characteristics of *P. minus* Huds leaves in the newly designed solar dryer and natural sun drying.

2. Materials and Experimental set – up.

The drying chamber was constructed by aluminum sheet. In order to enhance radiation, the outer surface was painted matte black. One drying tray was placed inside the drying chamber. The circulate fan (12 V, 25W) which powered by two solar panel in parallel connection was located under the drying chamber in order to suck the hot air from solar collector to drying chamber. The solar panel and collector were oriented towards the sun with the angle of 20□.

The solar collector constructed from aluminum tray with its interior layered with matted black painted stainless steel sheet (thickness 0.5 mm). A glass cover was placed on the aluminum tray, allowing a space of 0.5 mm above the stainless sheet in order to trap more heat in the collector due to greenhouse effect. Insulation material of calcium silicate (thickness 0.5 mm) was placed at the bottom of aluminum tray in order to minimize the heat loss from side of collector.

2.1. Experimental procedure

Solar drying experiments by indirect forced convection solar dryer and natural sun drying were performed in open area from 11 am to 2pm as shown in Fig.1. The experiment of natural sun drying of *P.minus* Huds was conducted on stainless steel sheets under direct sun. The oven – drying experiment of equilibrium weight samples was conducted on oven (Protech Model FAC-350) for 24h at 105 ℃ to determine the moisture content according to AOAC method [3].

The temperatures of tray, temperature of inlet collector, temperature of outlet collector were measured using Data Logger (Delta Ohm DO2003) with hot probe wire (Thermocouple type K). Both the relative humidity and air velocity were measured using the data logger with hot probe wire (capacitive Mk-33 sensor and NTC thermistor sensor respectively). The weight of the sample was measured every 5 minutes using weighing balance (AND Model EK-610i).

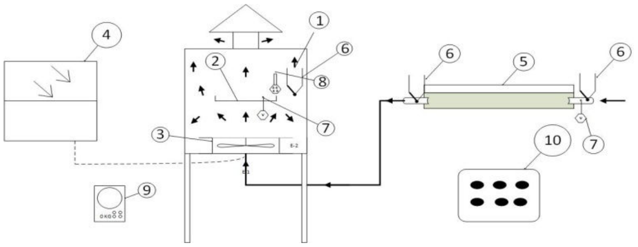

Fig 1. Schematic view of experimental set up: (1) Drying Chamber (1000 mm x 1000 mm x 800 mm), (2) Tray(1000 mm x1000 mm) , (3) Circulation Fan, (4) Solar Panel (290 mm x 385 mm) (355 mm x 700 mm), (5) Solar Collector (712 mm x 470 mm), (6) K – type thermocouple, (7)Thermistor sensor, (8) Capacitive Mk-33 sensor, (9) Weighing balance, (10) Natural Sun Drying.

2.2. Mathematical modeling of drying curves

The moisture ratio [4], moisture content [3] and drying rate [4] of *P.minus* Huds leaves were calculated as equations below:

$$\text{Moisture content (dry basis)} = \text{MC} = \frac{M_t - M_d}{M_d} \quad (1)$$

$$\text{Drying Rate} = \text{DR} = \frac{M_{t+dt} - M_t}{dt} \quad (2)$$

$$\text{Moisture Ratio} = MR = \frac{M_t - M_e}{M_0 - M_e} \quad (3)$$

The thin layer drying equations which shown in Table 1 were used to select the best model for describing the drying curve equation of *P.minus* Huds using solar dryer and under natural sun .

Table 1. Thin layer modelling

Model Name	Model	Reference
Lewis	$MR = \exp(-kt)$	[5]
Page	$MR = \exp(-kt^n)$	[6]
Henderson & Pabis	$MR = a\exp(-kt)$	[7]
Logarithmic	$MR = a\exp(-kt) + b$	[8]
Midilli et. al	$MR = a\exp(-kt^n) + bt$	[9]

Data evaluation of drying curves based on the value of R^2, RMSE and χ^2 is calculated as equation below [4]:

$$\textit{Correlation Coefficient} = R^2 = 1 - \frac{\sum_{i=1}^{N}\left(MR_{exp,i} - MR_{pre,i}\right)^2}{\sum_{i=1}^{N}\left(MR_{exp,i} - MR_{mean,i}\right)^2} \quad (4)$$

$$\textit{Root mean square}\ \text{error} = RMSE = \sqrt{\frac{\sum_{i=1}^{N}\left(MR_{pre,i} - MR_{exp,i}\right)^2}{N}} \quad (5)$$

$$\textit{Reduced Chi-square} = \chi^2 = \frac{\sum_{i=1}^{N}\left(MR_{exp,i} - MR_{pre,i}\right)^2}{N - z} \quad (6)$$

2.3. Effective diffusivity

Effective diffusivity of product was estimated from analytical solution of Fick's diffusion equation [4] and shown as equation below.

$$MR = \frac{M - M_e}{M_0 - M_e} = \frac{8}{\pi^2} \exp\left(\frac{-\pi^2 D_{eff} t}{4d^2}\right) \qquad (7)$$

2.4. Efficiency of solar collector

The instantaneous efficiency in % for the application experimental was as shown below [10].

$$\eta_{co}(\%) = \frac{\dot{q}_{co} \rho_w C_p (T_{outco} - T_{inco})}{G_T A_{co}} \qquad (8)$$

3. Results and Discussion

3.1. Drying curves

The tray temperature for experiment D_{abc} D_{hbc} D_{nbnc} D_{abnc} and NSD were 45.84℃, 43.07℃, 32℃, 44.62℃ and 35℃ respectively. Fig.2 shows that experiment D_{abc} gives the highest drying rate as the solar collector built up temperature of 66℃. At the same time, four-sided black surface of drying chamber radiates more heat compared to D_{hbc} and D_{nbnc}. The drying rate for natural sun drying was higher than D_{nbnc} because the *P.minus* Huds leaves were dried on stainless steel sheets under direct sun light. For experiment D_{nbnc}, the ambient air flow through the fan into drying chamber, thus no temperature build up inside the drying chamber. The tray temperature for D_{nbnc} was similar to ambient air temperature. The silver grey surface on the aluminium drying chamber had lower spectrum-absorptance product compared to black surface, thus minimal of heat radiation pass through the grey colour aluminum drying chamber.

Fig.3 illustrates the relationship between dimensional moisture ratio and drying time. Drying curves for D_{hbc} and D_{abc} are overlapped. Experiment D_{abc}, D_{hbc} and D_{abnc} required same duration of 70 min to reach equilibrium moisture content. Duration required for experiment D_{nbnc} was 180 min, while the drying time required for a natural sun drying experiment was 105 min.

Experiments using solar dryer with solar collector require less time to achieve equilibrium compared to natural sun drying [2,4] Presence of solar collector cause temperature builds up in the drying chamber during experiment D_{abc} and D_{hbc}. Efficiency of collector for D_{abc} and D_{hbc} varied from 27.5 – 44.9% and 28.5 – 59.2% respectively. Heat radiate through four-sided black surfaces of a drying chamber during experiment D_{abnc}, however the temperature on tray for NSD highly depend on the ambient air.

The five thin layer modelling equations were fitted to the drying curve. The best fit models shows highest value of R^2, low value of RMSE and χ^2.The results showed that Page model was the best fit model for describing drying curve of D_{nbnc}, D_{hbc} and D_{abc} whereas Midilli et. al model was the best fit model for describing drying curve of D_{abnc} and NSD.

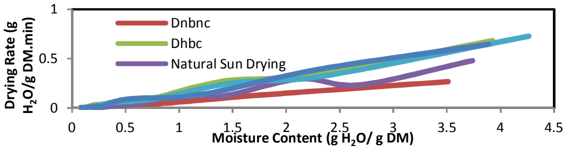

Fig.2 Relationship between drying rate versus mositure content.

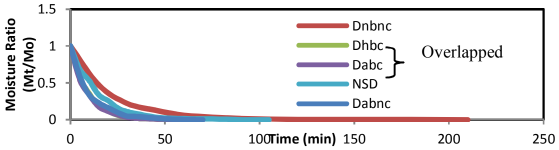

Fig.3 Relationship between moisture ratio versus time.

4. Conclusions

Page model was the best fit model for describing drying curve of D_{nbnc}, D_{hbc} and D_{abc} whereas Midilli et. al model was the best fit model for describing drying curve of D_{abnc} and NSD. Value of R^2, RSME and χ^2 for Page model is varied from 0.9993 to 0.9998, 0.00046E-05 to 9.6E-05, 0.23E-04 to 0.85E-04 respectively. For Midilli et. al model, value of R^2, RSME and χ^2 is varied from 0.9981 to 0.9989, 5E-05 to 8E-05, 1.60E-04 to 2.70E-04 respectively. Overall, the D_{abc} solar drying system achieves the highest drying rate compared to others.

References

[1] Qader SW, Abdulla MA, Lee SC and Hadden S, "Potential bioactive property of Polygonum minus Huds (kesum) review," *Scientific Research and Essays,* vol. 7, no. 2, pp. 90-93, 2012.

[2] Akpinar EK, "Drying of mint leaves in a solar dryer and under open sun: Modelling performance analyses," Energy Conversion and Management, vol. 51, pp. 2407-2418, 2010.

[3] Reeb J, Milota M, "Moisture content by the oven dry method for industrial testing," May 1999.

[4] Premi M, Sharma HK, Sarka BC and Singh C, "Kinetics of drumstick leaves (Moringa oleifera) during convective drying," African Journal of Plant Science, vol. 4, no. 10, pp. 391-400, 2010.

[5] Lewis WK, "The rate of drying of solid Materials", Journal of Industrial Engineering, vol.13, pp.427-443, 1921.

[6] Page G, "Factors influencing the maximum rates of air drying shelled corn in thin layers", in M.s.c.thesis, Purdue University, Indiana, 1949.

[7] Henderson SM, "Grain drying theory I: Temperature effect on drying coefficient," Journal of Agricultural Research Engineering, vol.6, pp.169-174, 1961.

[8] Yaldiz O, Ertekin C, "Thin layer solar drying of some vegetables," Drying Technology, vol.19, no.3 & 4, pp. 583-597, 2001.

[9] Midilli A, Kucuk H, Yapar Z, "A new model for single – layer drying," Drying Technology, vol.20, no.7, pp. 1503-1513, 2002.

[10] Kadam DM, Samuel DVK, "Convective Flat plate Solar Heat Collector for Cauliflower Drying," Biosystems Engineering, vol. 93, no. 2, pp. 189-198, 2006.

Nomenclature

M_0	Initial moisture content	t	Drying Time
M_e	Equilibrium moisture content	MR_{mec}	Mean value of experimental moisture ratio
M_d	Final moisture content	MR_{exp}	Experimental moisture ratio
M_{t+dt}	Moisture content at time $t + dt$	MR_{pre}	Predicted moisture ratio
M_t	Moisture content at time t	D_{eff}	Effective Diffusivity
dt	Time interval	d	Half thickness of leaves
a,b,k,n	Constants	N	Number of observations
D_{nbnc}	Drying Chamber in no black surface without solar collector	D_{abnc}	Drying chamber in four-sided black surface without solar collector
D_{abc}	Drying chamber in four-sided black surface with solar collector	D_{hbc}	Drying chamber in two-sided black surface with solar collector
NSD	Natural Sun Drying	$\dot{q}_{co}$	fluid flow in solar collector
ρ_w	density of air	C_p	specific heat capacity of air
T_{outco}	Temperature of collector outlet	T_{inco}	Temperature of collector inlet
G_T	Solar irradiance of sloped plane	A_{co}	collector aperture area

Adsorption of Gaseous Pollutants (SO_2 & CO) onto Palm Shell Activated Carbon

Ralina Shirin Akbar*, Christopher M. K. Chew·Nurhazwani Ismail, TVNPadmesh

School of Engineering, Taylor's University, Malaysia

**Corresponding author email: ralinashirin.akbar@sd.taylors.edu.my*

Abstract— **Gaseous pollutants namely, Sulphur dioxide, (SO_2) and Carbon monoxide (CO) have adverse effects on environment and the human health. An adsorption column with activated carbon packing is used to remove these pollutants. Activated carbon (AC) samples are prepared from palm shells and their efficiencies are compared with commercial activated carbon. The optimal conditions for adsorption of CO and SO_2 onto the palm shell based activated carbon removed 75% of CO and 100% of SO_2.**

Keywords— Activated carbon, Adsorption, Gaseous Pollutants, Palm shell, Commercial Activated Carbon

1. Introduction

In Malaysia the air pollution comes mainly from land transportation, industrial emissions, and open burning sources [1]. All natural and anthropogenic emissions into the air can be termed as air pollution, because they alter the chemical composition of the natural atmosphere [2] The major sources that contribute to air pollution in Malaysia are mainly from land transportation, industrial emissions, and open burning sources [3].The Clean Air Act has identified six common air pollutants. These commonly found air pollutants are also known as "criteria pollutants" namely particulate matter, ground-level ozone, carbon monoxide, sulphur oxides, nitrogen oxides, and lead [4].Adsorption is a process of preferential removal of gas or liquid by adsorbing it on the surface of a solid. Activated carbon (AC) is a favoured adsorbent for removal of gaseous pollutants from mobile and stationary sources [5].Variety of AC can be prepared from different waste materials both conventional as well as non-conventional wastes.The abundance of palm shells in Malaysia makes it a cheap and better alternative for the activated carbon production. Palm shell is converted into activated carbon using chemical activation followed by physical activation [6].

A lab-scale batch adsorption experiment is conducted to identify the removal efficiency for Sulphur dioxide (SO_2) and Carbon Monoxide (CO). Then the adsorbent is used and its performance is compared with commercial activated carbon. The absorbent bed height and gas flow rates are varied to study the adsorption characteristics of activated carbon on SO_2 and CO.

2. Methodology

Palm shells used in this research were obtained from Banting Palm Oil Mill, Selangor, Malaysia. The palm shells were dried in the oven for 24 hours at 110^0C [7]. Then the shells were crushed and sieved to obtain the size in the range of 1.0–2.0mm.

2.1. Preparation of Activated Carbon

Palm shell based AC was prepared through chemical activation followed by physical activation.The pretreated palm shells were carbonized in a furnace under purified nitrogen gas at 700 °C [8] for 2 h, with constant nitrogen gas flow rate. The resulting char was soaked in 0.1M Potassium Hydroxide (KOH) solution with an impregnation ratio of 1:1 [8]. The mixture was then dehydrated in the oven at 105 °C for 24 hours. The activation process succeeded the dehydration, under the same condition as carbonization but to a final temperature of 850°C [8]. Finally the activated carbon sample was cooled down to room temperature.

3. Experimentation

3.1. Setup

A batch adsorption experiment was conducted to identify the best activated carbon adsorbent for SO_2 and CO removal. Then the identified best adsorbent was used in the continuous system in which parameters such as adsorbent bed height and gas flow rates were varied and the resulting removal efficiency was studied. Adsorption of the gaseous pollutants was conducted in a Perspex column as shown in Fig. 1 filled with palm shell-based activated carbon. A cloth mesh was used to hold the activated carbon granules at the bottom of the column.

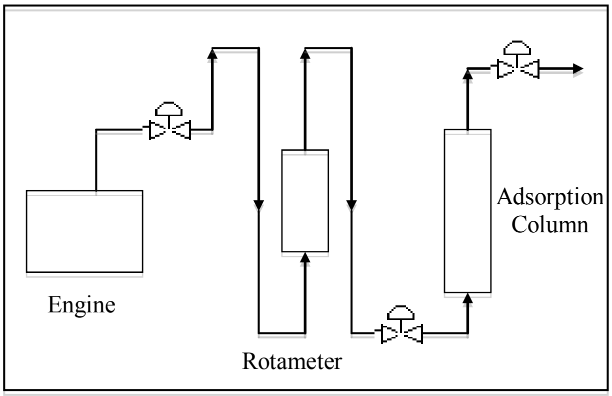

Fig. 1. Experimental Set-up of the adsorption system

Up-flow mode was used to operate the adsorption column.The experiment was conducted at room temperature of 25^0C and ambient pressure of 1bar. The petrol engine exhaust gas containing SO_2 and CO was introduced into the inlet of the adsorption column. The amount of sulphur dioxide and carbon monoxide in the exhaust gas at the inlet of the adsorption column and at the exit of the column was measured continuously at constant intervals using a gas analyser (BTU 4400 Gas Analyser). The experiment was conducted for 30 minutes.The gas flow rate was varied from 5L/min to 15L/min. The gas flow rate was controlled by a flow meter. The adsorbent bed height was varied from 5cm to 30 cm. The adsorption efficiency of different samples were observed and collected.

4. Results and Discussions

4.1. Effect of types of Activated Carbon

The comparative results between the palm shell-based activated carbon and the commercial activated carbon is shown in Fig. 2. and Fig. 3.Palm shell-based AC adsorbed more gaseous pollutants compared to the commercial AC. Commercial AC removed 55% of CO whereas palm shell-based AC removed 75% of CO. This implies that the palm shell-based activated carbon adsorbed the gaseous pollutants more effectively than commercial AC.

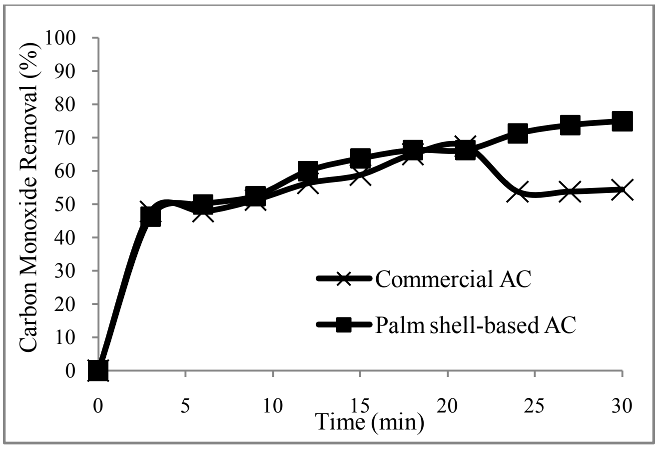

Fig 2. Carbon Monoxide adsorption using Commercial AC and Palm shell based AC

The differences in the performance of both activated carbons were probably due to their different internal pore structures [7] since they have similar particle sizes and the experiments were done under the same operating settings.

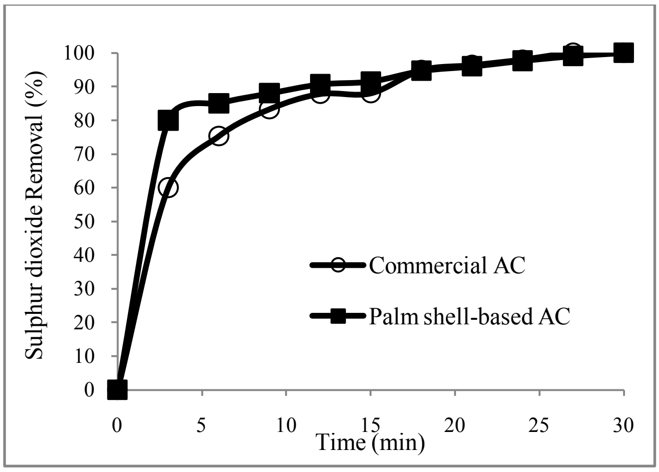

Fig 3. Sulphur dioxide adsorption using Commercial AC and Palm shell based AC

4.2. Effect of flow rates

In this study the flow rates of $5\ \mathrm{L/min}$, $10\ \mathrm{L/min}$, and $15\ \mathrm{L/min}$were investigated while the bed height was fixed at 30 cm. As the gas flow rate increases, lesser amount of gaseous pollutants is adsorbed.Guo J. and Lua. A [7] also observed this trend and this is as expected because at higher flow rates the contact time between CO and SO_2 gases and the adsorbent decreased. Hence it reduced the amount of exhaust gas treated and adsorbed. Increasing the flow rates, decreased the amount of pollutants adsorbed on the palm shell-based AC.

4.3. Effect of bed heights

For the palm shell-based activated carbon and at a fixed flow rate of $5\ L/min$, increasing the adsorbent bed height increased the amount of pollutants adsorbed in 30 minutes. Similar trend was found in another adsorption study using palm shell based AC [7]. At 30 cm bed height and $5\ L/min$ the adsorption system adsorbed the highest amount of pollutants as seen in Table 1.75% of CO gas while 100% of SO_2 gas was removed from the exhaust gas.

Table 1. Percentage removal of pollutants using the adsorption system

Flow rate (L/min)	Bed height (cm)	CO removal, %	SO_2 removal, %
5	5	11	100
5	15	73	100
5	30	75	100
10	30	63	96
15	30	49	98

5. Conclusions

The performance of the palm shell-based activated carbon can be compared to that of the commercial activated carbon and the former exhibited a better performance. Commercial activated carbons are mainly produced from coal whereas in this project activated carbon precursors are from agricultural wastes. Therefore, this cheap and abundant palm shell wastes can be utilised properly and can be converted into something beneficial. This system can be further improved by employing multiple fixed beds of adsorbents so that it can function continuously.

Acknowledgment

First and foremost, I thank God for endowing me with health, patience, and knowledge to complete this research. I would like to thank my family and friends for their never-ending support.

References

[1] RafiaAfroz,M.N. Hassan, N. A. brahim, “Review of air pollution and health impacts in Malaysia” Department of Environmental Sciences, Faculty of Science and Environmental Studies, University Putra Malaysia, 2002.

[2]Daly, A. and Zannetti, P. (2007) An Introduction to Air Pollution – Definitions, Classifications, and History.. CA (USA): The Arab School for Science and Technology (ASST) and The EnviroComp Institute.

[3] Afroz, R., Hassan M.N., & Ibrahim N. A. (2003) Review of air pollution and health impacts in Malaysia. Environmental Research, 92 p.71–77.

[4] Department of Environment (DOE) Malaysia (2012) Air Quality Trend Department of Environment Malaysia.

[5] Nevers, N. (2000) Air Pollution Control Engineering. Singapore: McGraw -Hill International Editions.

[6] Da̧browski, A., 2001.Adsorption from theory to practice. Advances in Colloid and Interface Science, 93, 135–224.

[7] Guo , J. and Lua, A. (2003) Adsorption of sulphur dioxide onto activated carbon prepared from oil-palm shells with and withoutpre-impregnation. Separation & Purification Technology, 30 p.265-273.

[8] Tan, I., Ahmad, A., &B.HHameed. (2009) Fixed-bed adsorption performance of oilpalm shell-based activated carbon for removal of 2,4,6-trichlorophenol. *Bioresource Technology*, 100 p.1494-1496.

Digital Power Control Supply for Critical Systems

Saniy Azman[1], Aravind CV[2*]

[1,2]*Applied Electromagnetic and Mechanical Cluster,*
Computer Intelligence Applied Group, Taylor's University, Malaysia
**aravindcv@ieee.org*

***Abstract*— Digital power control supply is designed from the first principles of electrical engineering. The objective of this investigation is to develop a precise digital power control supply that is essential for critical systems. The digital control power provides an output for the supply ranging from 0V-24V with maximum current of 2A.**

Keywords— power supply, digital control, critical power

1. Introduction

Analogue control power supply is favourable compare to digital control power supply in the sense of robustness and fast transient response. However, in the era of digital control communications, an adaptive power supplies regulation becoming a point of interest in building such a low power digital systems [1]. Based on [2], a lot of industries already implemented digital control but not in a sense of accuracy and stability compared to scientific applications where such elements are very important in order to have a consistent results and observations. Furthermore due to some instability and inconsistency of a power supply, the lifespan of any hardware will eventually become deteriorate. Therefore the capability and ability to provide such an accurate and stable power supply lies on the development of digital control power supply. Conventional analogue power supplies in most research laboratory have low reliability, bulky and sophisticated [3]. Additionally, those kinds of power supplies are not equipped with safety mechanism and the selection of desired output is based on switch band and potentiometer where accuracy is not applicable. Therefore in order to overcome this, a single chip had been design to control the power output and safety mechanism digitally where a typical analogue cannot. By going digital, the system can be optimized based on the functionality desired. Explained in [4] an on-chip digital power supply control had been used for system-on-chip (SoC) systems. The design provides a local adaptive control of power and energy per Voltage Island, integrated power switch gating in sleep mode, simple digital control and low overhead in silicon area as compared to typical DC to DC converters.

2. Methodology

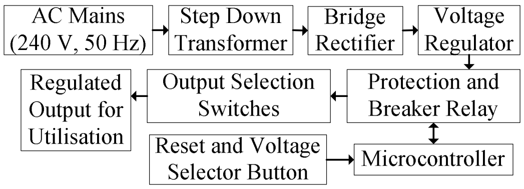

Figure 1: Block diagram of the system.

Based on Figure 1, the system consists of basic components of electrical engineering devices such as transformer, rectifier and regulator. The protection also essential to make sure the circuit is safe under short circuit condition. The output is selected based on stages such that it goes from 0V, 5V, 9V, 12V and 24V. Figure 2 shows how the system is constructed using a simulation software. The circuit was being tested and simulated in certain number of times until the output produced is based on the sequence mentioned earlier.

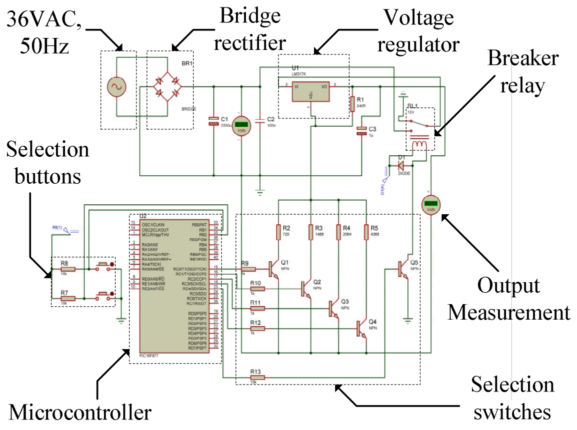

Figure 2: Circuit diagram of the system.

Figure 3 explains how the processes of the design and development stages are being carried out. The flowchart describes the initial study of the main components of the system followed by a few sessions of simulations and troubleshoots. Prior to fabrication, the prototype must complete another test which combines all the components into one system.

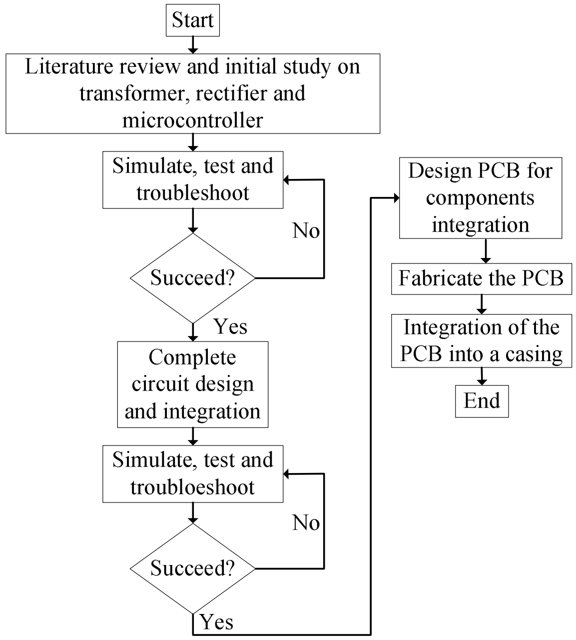

Figure 3: Design and development methodology.

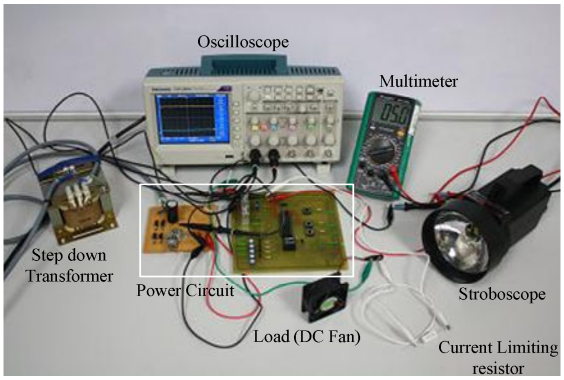

Figure 4: Experimental setup.

3. Results and Discussions

An experiment was performed in order to test the performance of the output produced by the power circuit in Figure 4. Based on Figure 4, the input of the DC Fan which its current is being limited by a current limiting resistor is increased in a specific sequence and the speed is being measured using a laboratory stroboscope. The results of the experiment are shown in Figure 5 (a) and Figure 5 (b). The trend describes that the speed of the DC fan is linearly proportional to the increment of the voltage input. But as the input voltage of the DC fan or output voltage produced by the power circuit increasing, the ripple voltage is increasing as well. Figure 6 (a) and Figure 6 (b) show how the trend of the input voltage of the regulators in power circuit changes.

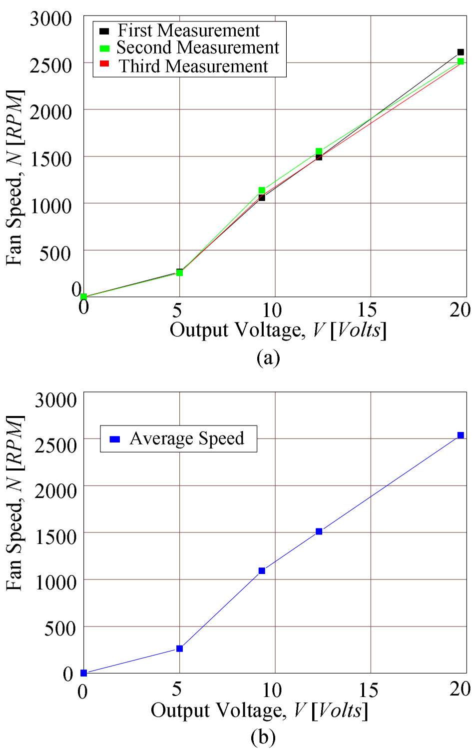

(a)

(b)

Figure 5: The results of the experiment.

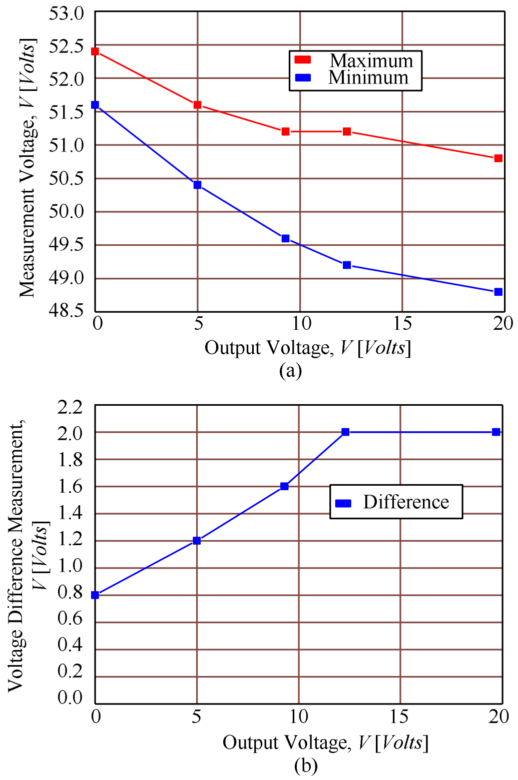

(a)

(b)

Figure 6: The comparison between the minimum and maximum voltage measured.

4. Conclusion

The output of the power circuit is stable and can be used in laboratory experimental setup and at the same time the range of the output is typical voltage range that can be found in standard electronics and electrical devices.

Acknowledgement

I would like to express my greatest gratitude to the school laboratory assistants for providing me the accessibility and tools for the design and development stages.

References

[1] K. Jaeha and M. Horowitz. "An Efficient Digital Sliding Controller for Adaptive power Supply regulation". *Symposium on VLSI Circuits Digest of Technical Papers*, pp. 133-136, 2001.
[2] W. Renso, W. Hei, B. Stefan, F. Long and G. Ronnie. "Digital Power Supply Controller for Control of Extremely Precise Power Supply". *IEEE*, pp. 1-6, 2006.
[3] W. Hengyu, T. Minli and H. Ling. "The Design And Facture Of A Digital Control DC Regulated Power Supply Based On Single Chip". *IEEE*, vol. 1, pp. 749-751, 2009.
[4] M. Maurice, J.P. de Gyvez and O. Ralph. "On-Chip Digital Power Supply Control For System-On-Chip Applications". *IEEE*, pp. 311-314, 2005.

Heat Transfer Enhancement using CNT Nanofluids in a Turbulent Flow Heat Exchanger – An Experimental Study

Seik San Ong[1], Rashmi Walvekar.[1*]

[1] *Department of Chemical Engineering, Taylor's University Lakeside Campus, Malaysia.*
**Corresponding author email:rashmi.walvekar@gmail.com*

Abstract— **Suspensions of nano-sized particles (<100 nm) in base fluid are termed as Nanofluids, which are believed to be the promising coolant in heat transfer applications due to their enhanced thermal conductivity. In this study, the enhancement in heat transfer of CNT nanaofluids under turbulent flow conditions was investigated experimentally. Carbon nanotube (CNTs) nanofluids of 0.051-0.085 wt%, stabilized by optimum concentrations of gum Arabic were used as hot fluid in a concentric tube turbulent flow heat exchanger. The flow rates of cold fluid (water) was varied from 1.7 - 3 L/min and flow rates of the hot fluid (nanofluid) is varied between 2 - 3.5 L/min. Thermal conductivity, density and viscosity of the nanofluids were also studied as a function of temperature and CNT concentration. Enhancements in the heat transfer were validated with conventional heat transfer correlations for turbulent flow available in the literature. Results showed an enhancement in heat transfer range between 9 - 67% as a function of temperature and CNT concentration.**

Keywords— Nanofluids, Carbon nanotubes (CNT), gum Arabic, heat transfer enhancement, heat exchanger

1. Introduction

In the past decade, researchers had discovered the techniques to disperse ultrafine particles or nano-sized particles in conventional base fluids.. Examples of nanoparticles are metals, metal oxides, graphene and CNT [1, 2]. Presence of these nanoparticles with high thermal conductivity enhanced the thermal properties of conventional heat transfer fluid/coolant such as water, ethylene glycol (EG) and oil, eliminating the need of increasing the power or extending the heat transfer surface. Nano-sized particles are preferable compared to micro-sized particles which are prone to clogging, erosion, and sedimentation.

2. Experimental

2.1. Preparation of Nanofluids

Three different concentrations (0.051 wt%, 0.068 wt%, and 0.085 wt%) of CNT nanofluids stabilized with optimum concentration of gum Arabic (GA) as dispersant are used in this experimental study. Nanofluids were homogenized for 10 minutes using a high speed homogenizer (IKA-T18, ULTRA-TURRAX, Germany) and sonication of 4 hours in a ultrasonic bath (Crest Ultrasonics, USA) to obtain stable suspensions.

2.2. Thermophysical Properties

Convective heat transfer performance is related to the thermophysical properties of nanofluids. The thermal conductivity, viscosity, and the density of nanofluids were studied with respect particle concentration and temperatures (25 to 55 °C). Thermal conductivity was measured using a thermal conductivity meter (KD2 Pro, Decagon device, USA). A viscometer (DV-11+Pro, Brookfield, USA) was used for viscosity measurement. Density of nanofluids were measured using a density meter (DA-130N, Kyoto Electronics, Mexico).

2.3. Convective Heat Transfer Experimental Setup

Experimental studies of convective heat transfer were carried out in a concentric tube heat exchanger as shown in Fig. 1. Inlet of cold fluid (tap water) is connected to the water tap and outlet is left to drain, whereas the hot fluid (nanofluid) is stored in a built-in reservoir. Flow rates of both cold and hot stream were controlled by two built-in flow meters. Setup consists of six thermometers mounted on the inlet, middle, and the outlet of both cold and hot tubes. Experiments were carried out with respect to concentration by varying the flow rates of cold and hot fluids from 1.7 L/min – 3 L/min and 2 L/min – 3.5 L/min, respectively.

3. Results and Discussion

3.1. Thermophysical Properties

(a) Thermal Conductivity

Fig. 1 below shows the thermal conductivity ratio of nanofluids to base fluid water with respect to temperatures at three different CNT concentrations. It can be concluded that thermal conductivity increases with increasing temperature and CNT concentration. Thermal conductivity enhancement of 69 – 250% is observed compared to water, mainly due to the presence of high thermal conductivity of CNT nanoparticles.

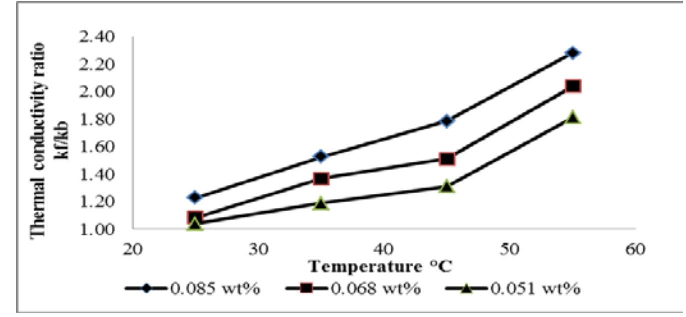

Fig. 1: Thermal conductivity ratio of nanofluid to water with respect to temperature and particle concentrations.

(b) Viscosity

From Fig. 2 below it is observed that viscosity decreases with increasing temperature. Viscosity is slightly higher for higher concentration nanofluids, however viscosity of nanofluids are significantly higher when compared to water due to presence of nano-sized particles. At higher temperatures, the forces between the CNT nanoparticles and the base fluid weakened, causing a decrease in viscosity value [1].

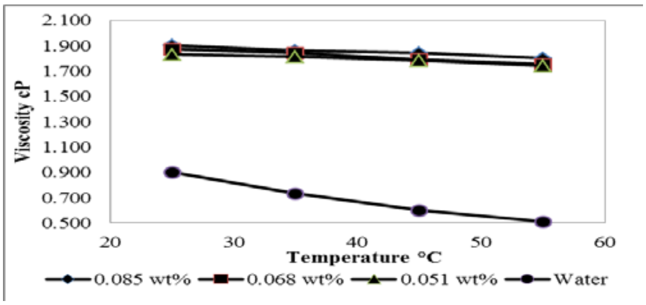

Fig. 2: Viscosity of nanofluid and water with respect to temperature and particle concentrations at shear rate of 100/s.

(c) Density

Referring to Fig. 3 below, there is a negligible decrease in density with temperature. Nanofluids have slightly higher density than water due to the presence of low concentration of CNT nanoparticles and GA.

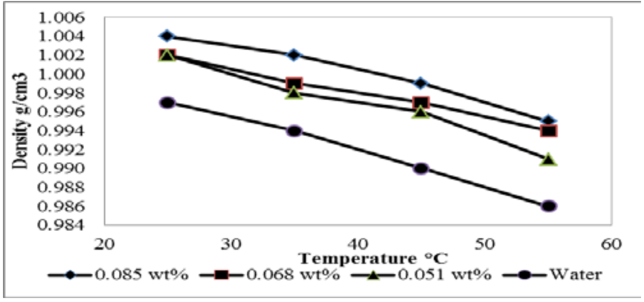

Fig. 3: Density of nanofluid and water with respect to temperature and particle concentrations.

3.2. Convective Heat Transfer Experiment

Prior to conducting heat transfer studies using nanofluids, experimental results conducted using water is compared to the theoretical Gnielinski correlation [3] to determine the reliability of the experimental set-up. Analysis is performed by comparing the Nusselt number between the experimental values and theoretical values obtained from Gnielinski correlation. An acceptable error within 15% is observed as shown in Fig. 4.

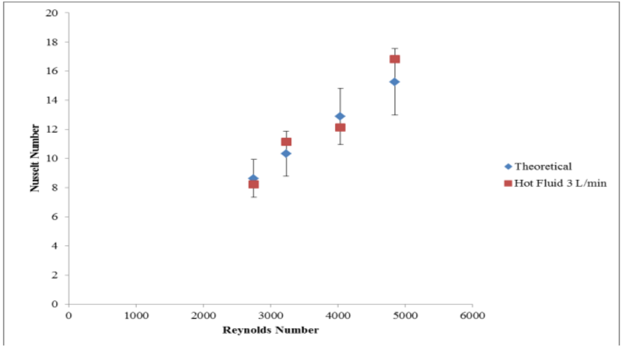

Fig. 4: Comparison between Nusselt number calculated from experimental values and theoretical correlation at hot fluid rate of 3 L/min. (Figure at hot fluid rate of 2, 2.5, and 3.5 are not shown)

An overall enhancement of 9 – 67% in heat transfer rate is achieved for the three nanofluid concentrations at 0.085, 0.068 and 0.051 wt%. Fig. 5 shows that Nusselt number increases with increasing Reynolds number and nanofluid concentrations. Enhancement of heat transfer can be associated with the enhancement of thermal conductivity.

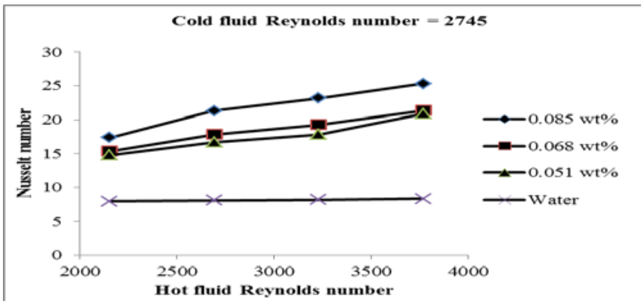

Fig. 5: Relationship between Nusselt number and hot fluid Reynolds number for three different nanofluids concentration at cold fluid results number of 2745. (Figure at cold fluid Re = 3230, 4087, and 4845 are not shown)

3.3. Theoretical studies

Referring to Fig. 7 below, experimental Nusselt number obtained showed a good agreement with the Gnielinski [3] and Pak & Cho [4] correlation, but differs significantly when compared with Duangthongsok and Wongwises [5] correlation. Differences can be explained by the effect type nanoparticles, shape of nanoparticles, as well as the range of temperature measured [1].

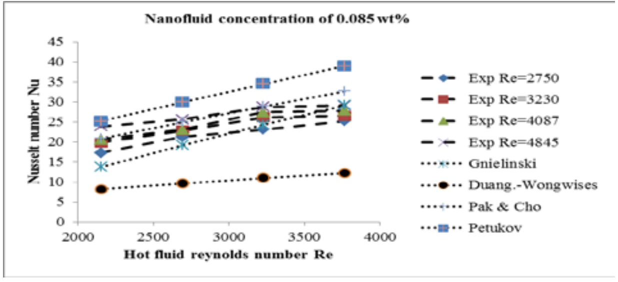

Fig. 7: Validation of experimental Nusselt number taken from nanofluid concentration of 0.085 wt% with Nusselt number obtained from Gnielinski correlation, Duangthongsok and Wongwises correlation, and Pak and Cho correlation. (Figures at nanofluid concentration of 0.068% and 0.051% are not shown)

4. Conclusion

Stable CNT nanofluids were prepared using GA as a dispersant. An overall enhancement of 69-250% in thermal conductivity was observed as a function of CNT concentration and temperature compared to water. However, viscosity increases due to presence of nanoparticles and GA. Negligible increase in density is observed. 7-202% enhancement in heat transfer is observed using CNT nanofluids compared to water. Experimental results validated with available correlation showed good agreement.

References

[1] Rashmi G.W. (2012). *Experimental and Theoretical Studies on Convective Heat Transfer of CNT Nanofluids stabilized by Gum Arabic*, Ph.D. dissertation, Dept. Biotechnology Eng., International Islamic University Malaysia. Give ref to my paper rather than thesis.

[2] Ozerinc S. (2010). *Heat Transfer Enhancement with Nanofluids*. M.S thesis, Dept. Mechanical Eng., The Graduate School of Natural & Applied Science of Middle East Technical University.

[3] Gnielinski, V. (1976). New equations for heat and mass transfer in turbulent pipe and channel flow. *International Chemical Engineering* 16, pp. 359–368.

[4] Pak B.C. and Cho Y.I. (1998). Hydrodynamic and heat transfer study of dispersed fluids with submicron metallic oxide particles. *Experimental Heat Transfer* vol. 11(2), pp. 151-170.

[5] Duangthongsuk W. and Wongwises S. (2010). An experimental study on the heat transfer performance and pressure drop of TiO2-water nanofluids flowing under a turbulent flow regime. *International Journal of Heat and Mass Transfer*, vol. 53, pp. 334-344.

Numerical Study of Pollutant Dispersion Within Urban Canyons

S.S.Tan*, S.M. Salim

School of Eng,Taylor's University, Malaysia

**E-mail: tan.soonsien@sd.taylors.edu.my*

Abstract— **The purpose of this paper is to simulate different idealized configuration of Malaysian's urban canyon to evaluate and determine which layout has the best natural ventilation .It is found that the porous region of the tree crown acts as obstacles that restrict air flow, preventing air pollutant to disperse into the above-roof environment and hence reducing the air quality within the urban canyons.**

Keywords— Pollution dispersion, Computer simulation, Urban streets, Natural ventilation

1. Introduction

Natural air ventilation of urban canyons is becoming one of the most important factors to ensure a healthy air quality of urban canyon. The main source of air pollution in urban canyons is the ongoing traffic exhaust gas emitted from ground vehicles [1]. As the number of ground vehicles increases every year, the amount of air pollution emitted also increase drastically.

Therefore to ensure good air quality of those urban canyons, many studies have been done experimentally and numerically to determine the best natural ventilation of urban canyons and provide solutions to improve the air quality. For example, research done by Zajic, *et al.* illustrates the wind flow through an idealized urban canyons of different building height and distance between the buildings [2]. In his study, the vortex regimes formed in between different layout of idealized urban canyons are presented in Fig. 1a.

However, those studies fail to take into consideration the aerodynamics effect of tree crown [1]. Alternatively in studies done by Salim [1], number of simulation done numerically have provided evidences that due to the porous nature of tree crowns, air pollutions which suppose to disperse into the atmosphere, are trapped and accumulated instead. In his simulations, European layout – equivalent in height of the trees and buildings, was chosen to be his case for simulation as shown in Fig. 1b.

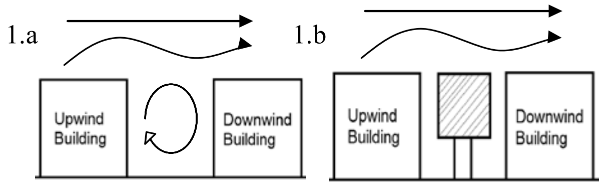

Fig. 1. Examples of European Urban Canyon Configuration (a and b)

In this paper, numerical simulations are done to study the aerodynamic aspect of Asian urban configuration which is referring to a Kuala Lumpur urban canyon shown in Fig 2. With the tree are much higher than the building, a study regarding if the height different between European and Asian trees configuration will affect the dispersion of air pollution within urban canyon.

After the simulations are done, recommendations are provided to improve the air ventilation of the urban canyons.

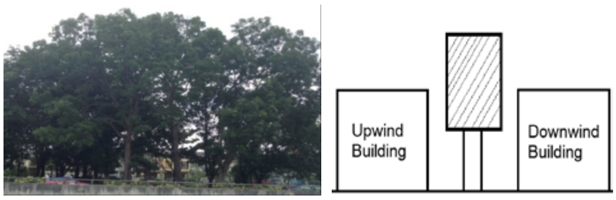

Fig 2. Typical Asian Urban Canyon and an idealized 2D drawing of Asian urban canyon

2. Methodology

An explanation of the meshing of computational domains and the different boundary conditions (with pollution emission) are shown and discussed in this section.

2.1 Boundary Condition

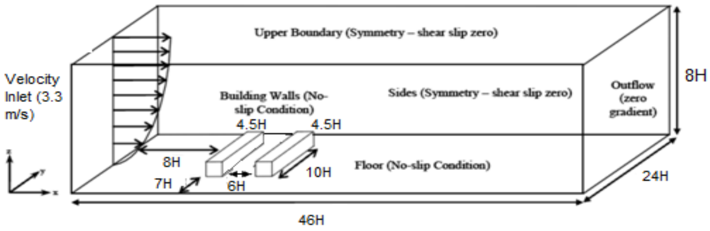

Fig. 3. Computational domain of Fig. 1.c [4]

By referring to wind tunnel measurement data (CODASC data base,) [3] and research paper done by Salim [1] as benchmark, the computational domain of the area of interest has been designed as shown in Fig. 3 .To enable the dispersion of air pollution to be capture easily, sulphur hexafluoride (SF6) was chosen as the "air pollutant" since its used as a tracer gas [1]. The figure below shows the meshes of the boundary condition. While the rectangle region represent trees species of *Acaia Mangium* [5], it is clear that most of the meshes focus around the building area. To determine whatever Asian trees are able to prevent the dispersion of air pollution, the pollutant concentration of the windward building are recorded and compare with 2 configurations, urban canyon with trees and another is without trees.

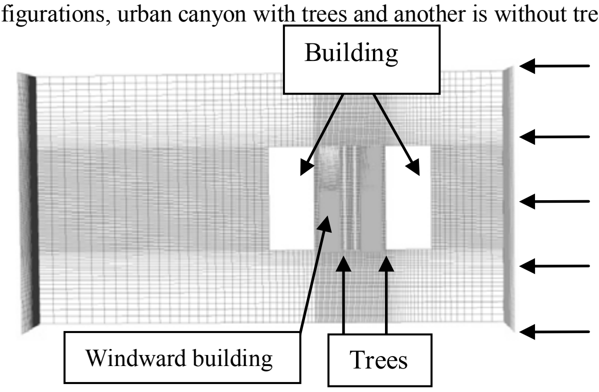

The table below summarizes the boundary condition of this paper.

Table 1. The Boundary Condition of the Computer Simulation [5]

Parameters	**Values**		
Inlet Velocity (ms^{-1})	User Defined Function (UDF)		
Roughness Length, Z_0 (m)	0.007		
Turbulence Model	Reynolds Stress Model (RSM) and Large Eddy Simulation (LES)		
Pollutant Used	Sulphur Hexafluoride, SF6		
Urban Canyon Configuration	Pressure loss coefficient ,$\lambda(m^{-1})$	Tree Height, (m)	Porosity, P_{vol} (%)
Without Trees	-	-	-
European Trees	200	13	96
Malaysia Trees	200	33	96

2.2. User Defined Function

Therefore to increase the realism of the simulation, not only the meshes must be fine at the near-wall region, *User Defined Function* (UDF) is used to create a velocity profile. The profile is plotted by using power law equation:

$$\frac{u(z)}{u(z_{ref})} = \left(\frac{z}{z_{ref}}\right)^{\propto} \quad (1)$$

Where u(z) is the mean velocity at height of z (m) while $u(z_{ref})$ is the mean wind speed at a certain reference height, z_{ref} and $\propto$ represent a constant of 0.3. [6]

3. Result and Discussion

Fig. 5. demonstrate the velocity contour of Large Eddy Simulation (LES) of the Asian urban canyons. As wind passes through obstacle such as buildings and porous region of the tree crown, the aerodynamic drag forces of those obstacles will causes the flow to lose its kinetic energy as work [7] as its used to overcome the aerodynamic drag force and shown in fig.6. By comparing the result, it is clear that the porosity of the trees diverged wind flow away from the building, causing a low velocity flow at the windward building. Due to this, the air pollutions emitted in between the building are trapped and hence cannot disperse into the atmosphere. This proves that even Asian trees prevent the dispersion of air pollutions.

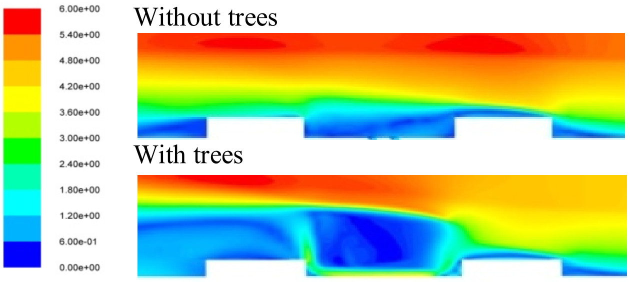

Fig. 5: The velocity contour of LES simulation

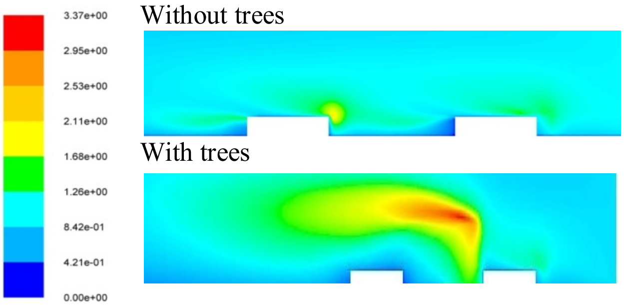

Fig. 6: The Turbulence Kinetic Energy (*TKE*) contour of the simulation

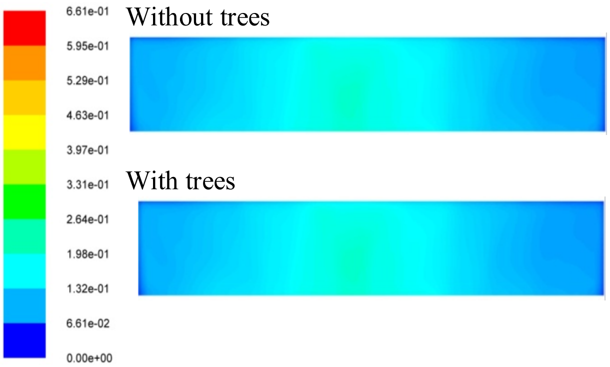

Fig. 7. The Mass Concentration of SF_6 at Windward Building

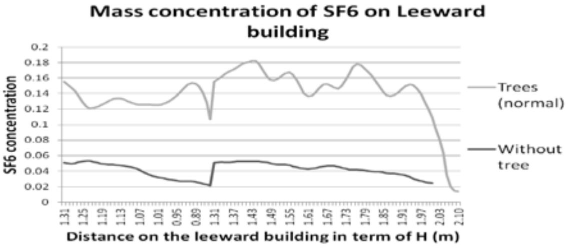

Fig.8. The Graphs of SF6 Concentration

Fig 7 and 8 display the pollutant concentration on the windward buildings. By comparing the diagram and the graphs, it is clear that the amount of pollutant trapped on the windward building of the urban canyons with Asian trees are much more higher compared to urban streets without the present of tree.

4. Conclusion

The aerodynamic of the trees have direct impact on the natural ventilation of urban canyons. The porous region of the trees will act as an obstacle, directing air flow away from the urban canyons into the above-roof region and hence restricting the dispersion of air pollution. Therefore, tree-free urban canyons are much more likely to have a good quality of air compared to urban canyons with trees.

References

[1] Salim.M.Salim, "Computational Study of Wind Flow and Pollutant Dispersion Near Tree Canopies", University of Nottingham, PhD Thesis,2011.

[2] Zajic.D. Fernaando. H.J.S.Calhoun. Princevac R,M., Brown M.J., and Pardyjak E.R.. "Flow and Turbulance in an Urban Canyon". Dept of Mech and Aero Eng. 31 Aug 2010.

[3] CODASC "*Concentration Data of Street Canyons*". Laboratory of Buildingand Environmental Aerodynamics, IfH, Karlsruhe Institute of Technology.2008

[4] Salim, S. M., Ong, K. C. and Cheah, S. C., "Comparison of RANS, URANS and LES in the prediction of airflow and pollutant dispersion," *Proceedings if the World Congress on Engineering and Computer Science, volume 2,* 2011.

[5] Sahri M, Ashaari Z, Kader R, Mohmod A. Physical And Mechanical Properties of Acacia mangium and Acacia Auriculiformis from Different Provenances. *Pertanika Journal Of Tropical Agricultural Science* [serial online]. 1998;21:73-82. Available from: British Library Document Supply Centre Inside Serials & Conference Proceedings, Ipswich, MA. Accessed June 20, 2013

[6] Hersteeg, H.K. and Malalasekera, W. "Turbulence and its modeling" in *An introduction to Computational Fluid Dynamics: the Finite-Volume Method*,2nd edition, Pearson, 2007, pp. 98-109.

[7] Carpman.N, *Turbulence Intensity in Complex Environments and its Influence on Small Wind Turbines*. Uppsala, Sweden , 2011.

Blind Signal Separation Implementation on Power Systems

Tan Yen Choung

School of Engineering, Taylor's University Lakeside Campus, Malaysia

tanyenchoung@gmail.com

Abstract— **The ability to detect power load remotely that are connected to one power system may lend us a hand in analysing the entire system. This work is able to detect and separate a number of independent signals from the random mixture of itself. The signals are also identified as individuals.**

Keywords— independent signals, power load, power system, signals separation, blind signals

1. Introduction

Using the Blind Source Separation (B.S.S.) [1], signals that are mixed up without a clear trace of its origins are separated again to its formal individual signals. This concept was developed by the team that created FastICA[2]. By separating the signals into individuals, it is easier to analyse the type of appliances that are connected to the system. This work takes the concept to a higher level by categorizing the individual signals into specific appliances.

2. Theoretical Background

There are many ways to conduct Blind Source Separation, such as Principal Component Analysis [3], Singular Value Decomposition [4], Independent Component Analysis [5], Dependent Component Analysis [6], Non-negative Matrix Factorization [7], Low-complexity coding and decoding [8], Stationary subspace analysis [9], and Common Spatial Pattern [10]. In this project Independent Component Analysis (ICA) is the main technique used for blind source separation.

As stated in the Independent Component Analysis, first of all the components has to be certified as "independent". A component is independent only when it is different from other sources[11]. And by that the sources have to be real existing signals. ICA can differentiate signals that are real and contains differentiating factor among other signals. In a more general mathematical concept, if a signal is more non-Gaussian then the signal can be considered as more independent. In ICA a mathematical formulation such as kurtosis is used to measure the non-Gaussianity of a signal.

2.1 Kurtosis

Kurtosis is the fourth moment. The first moment is the Ensemble Mean, also known as mean value. The second moment, also known as second Central moment is the variance of values. The third moment is known as Skewness[12]. Kurtosis in a mathematical formulation, would analyze the random value that contains in a set of values, thus giving us the most non-Gaussian value and it is assumed as the independent component that exists in the set of value. [13]

$$kurt(y) = E\{y^4\} - 3(E\{y^2\})^2 \qquad (1)$$

The above equation (1) states the mathematical expression of kurtosis. The 4th moment is stated as $E\{y^4\}$, while $3(E\{y^2\})^2$ states the Gaussian of the fourth moment.And so if the 4th moment $E\{y^4\}$ is Gaussian , the answer would be zero.

2.2 Cross-Correlation

Initially before cross-correlating, discrete Fourier Transform is used to change signals from the Frequency-domain into Time-domain, the purpose is to simplify signal processing. By cross-correlating a signal with another signal, it provides information on the type of signal inside another digital signal.In this work, cross-correlation helps in identifying the type of signal that has been separated previously by ICA.

Convolution has a similar mathematical expression towards cross-correlation. Cross-correlation visually follows the convolution mathematical formula except the difference that one of the Fourier Transforms has been complex conjugated[14].

$$f * g = \int_{-\infty}^{\infty} f(u)g(x-u)du \qquad (2)$$

Shown above is the formula representation of convolution for function *f* and function g.

$$H = \int_{-\infty}^{\infty} \bar{f}(u)g(u+x)du \qquad (3)$$

Shown above equation (3) H is the cross-correlation representation for cross-correlating function f and function g. The cross-correlation functions in a way that it gives a result of how correlated it can be when two functions come together. In this work, the separated independent signals are cross-correlated with the original load signals to identify the appliance to that signal.

3. Methodology

Initially, current signal from multiple appliances are sensed. The signals are sensed through a current transducer, also known as a hall-effect current sensor. In this work the LTS-25NP was chosen as the current sensor. Current signal produces specific harmonics and so it is best chosen for Independent Component Analysis. Different appliances contain individual current harmonics as most power loads contain individual reactance causing distortion in alternating waveform signal. The harmonic signal is then transferred to the Data Acquisition Card (DAQ) system for data acquisition. The DAQ used in this work is the NI-USB6008, a National Instrument DAQ board to convert information from the sensor into the computer.

The signal that goes into the computer is just one harmonic signal that was sensed through one current sensor, thus the challenge is to identify the signals that consist in this one particular sensed current signal.

Once the signals are successfully separated it is then sent for cross correlation with signals that were previously saved. These saved signals are the original individual signals that were recorded and named as individual existing real signals.

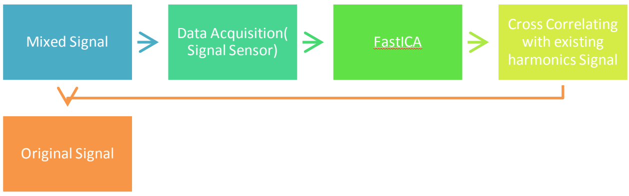

Fig.1:Design Methodology

4. Main Results

The first experiment was done by simulating with basic waveforms such as sine and cosine waveform with a specific valued frequency. The waves can be mixed with different coding, as long as the mixed signal is shown in a one line continuous random amplitude waveform.

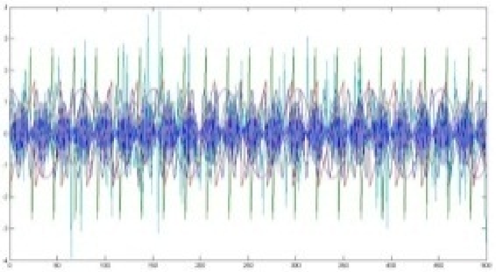

Fig.2a: Eight Signals Stacked

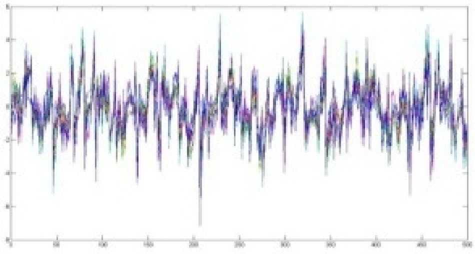

Fig.2b:Eight Signals Mixed

The mixing of signals has to be done correctly in the simulation with basic signals. As shown in Fig.2a the signals are not correctly mixed but rather just stacking on top of each other. The correctly mixed signals such as shown in Fig.2b can be separated using the FastICA algorithm.

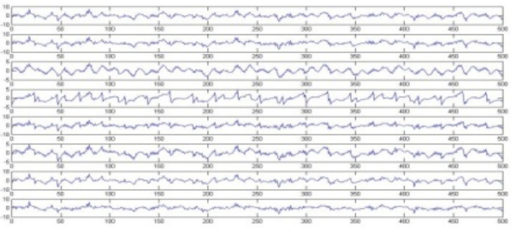

Fig.3a: The Mixed Signals presented in Eight Rows

Fig.3a shows eight rows of signals assembled in a way that is easy for us to identify the number of signals that consists inside the mixed signal. However the amount of signals that were mixed is known by the user. The challenge is to separate the signals to its original form.

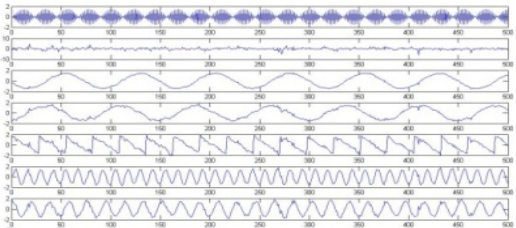

Fig.3b: Separated Mixed Signals

The signals were successfully claimed to its original forms before being mixed. However the signals are not perfectly similar, as there is still a gap in precision and the signals are displayed in a different order in Fig.3b.

5. Conclusions

The signals that were mixed are separated into individual original signals. The final stages of this work still needs some progress in cross-correlating signals.For a general user, it would ease the hassle on identifying appliances in the system manually, and therefore contributing in the field of power analysis. The drawback of separating the signals is that the number of signals that are mixed was unable to identify, due to lack of differentiating factor information. The number of appliances connected to the grid is set on approximation. The number of appliances may be denoted if the amplitude of the separated signals were maintained.

Acknowledgment

A debt of gratitude will be hard to repay towards my supervisor Dr. Pirapaharan for giving me step by step procedure to ensure the progress of my project.

I am particularly grateful for the founder of Quantum Engineering Solutions Sdn. Bhd. Mr.QuanTeng Zee for providing importantly useful information to ensure the successful conduction of this project. The kick-off of this project was mainly the contribution of Mr.QuanTeng Zee.

References

[1] A. Cichocki. (2007). *ICALAB for Signal Processing* Hirosawa Wako Saitama, Japan: John Wiley and Sons.

[2] Fabian J. (2005). *A Short Tutorial on Blind Source Separation*, Tokyo: University of Regensburg, Institute of Biophysics.

[3] H., Abdi. & Williams L.J. (2010). Wiley Interdisciplinary Reviews: Computational Statistics *Principal Component Analysis, 5,* 443-459. Retrieved July/August, 2010, from http://onlinelibrary.wiley.com/doi/10.1002/wics.101/full

[4] T.L.N. & B.3.David (1997) *Numerical Linear Algebra* Philadelphia: Society for Industrial and Applied Mathematics.

[5] Pierre Comon (1994). Signal Processing- Special issue on higher order statistics *Independent component analysis, a new concept?: Vol. 36.* pp. 287-314. The Netherlands: Elsevier North-Holland, Inc.

[6]T. Lillesand & R. Kiefer & J. Chipman (2004). *Remote Sensing and Image Interpretation Fifth edition* United States, America: John Wiley & Sons, Inc.

[7] J. Shen&G.Israel (1989) Atmospheric Environment. *A Receptor Model Using a Specific Non-negative Transformation Technique for AmbientAerosol*23(10):2289-2298.DOI:10.1016/0004-6981(89)90190-X pp.2289-2298

[8]S. Hochreiter & J. Schmidhuber (1997). *Low Complexity Coding and Decoding*, Germany:TechnischeUniversityat Munchen

[9] Sawyer, S., & Tapia, A. (2009). American Physical Society's New Journal *Finding Stationary Subspaces in Multivariate Times Series, Phys.Rev.Lett.*

[10]Z. J. Koles, M. S. Lazaret and S. Z. Zhou (1990). Brain Topography *Spatial Patterns Underlying Population Differences in the Background EEG,* Vol. 2(4) pp. 275-284

[11]A. Hyvarinen & J. Karhunen & E. Oja, (2001). *Independent Component Analysis*Brisbane, Australia: John Wiley and Sons Inc.

[12] P. T. v. Hippel, (2005) *Mean, Median, and Skew: Correcting a Textbook Rule* Ohio: Journal Statistics Education.

[13] A. Hyvarinen,(1999) *Fast and Robust Fixed-point algorithms for Independent Component Analysis* IEEE Transactions on Neural Networks

[14] Simon Rozman. (2011). *Computing Block-Wise Cross Correlation.* Retrieved April 12th 2011from http://simon.rozman.si/computers/dsp/block-wise-cross-correlation

Analysis and Positioning of Blade Structure for the Maglev Assisted Vertical Axis Wind Turbine

S.C Tay[1], Aravind CV[1, *], Rajparthiban R[2]

[1]Applied Electromagnetic and Mechanical cluster,
Computer Intelligence Applied Group, Taylor's University, Malaysia
[1]University of Nottingham, Malaysia
**aravindcv@ieee.org*

Abstract— **Vertical Axis Wind Turbine is more commonly employed for the standalone and low power generation applications. Design of the blade and the angle of attack influences heavily the power generating capability. The efficiency of the VAWT is highly affected by the design of the blades as the cut-in speed is proportional to the amount of wind generated. With proper design of the blade, it will improve the efficiency of VAWT thus generating more power at low wind speed. Preliminary investigation on three different wind profiles and the suitable airfoil for the vertical axis wind turbine is reported in this paper. The degree of impact at angle of 30^0 is found to have the highest lift coefficient.**

Keywords— CFD, VAWT, Maglev, ML-VAWT, Airfoil

1. Introduction

The wind strength Malaysia experience annually is about 2-3m/s with highest being 7m/s at Mersing [1]. The use of horizontal win turbine is less significant as it requires wind speed of about 8-15m/s [1]. However vertical axis type wind turbine generates electricity even at low wind speed [3], typically low power utility. The efficiency of such type of turbine is highly influential with optimizing the blades as the cut-in speed is proportional to the amount of wind power generated. With the current improvement in technologies and the decrease of price material such as magnets, maglev-assisted turbine offer great advantage in the market [4]. The maintenance is also easier as there are less movable parts [5]. This research investigates the use of magnetic levitation for the designed VAWT. By replacing the bearing in the VAWT with maglev, it can reduce the vibration losses due to the mechanical movement of the bearing. With further improvement on the rotor blade of the VAWT, it can increase the wind harvest thus increases the efficiency of the VAWT. This paper reports the preliminary work in the design of the blade structure and the choice of angle of attack for the blade design using finite element analysis tool.

2. Design Methodology

There are three different types of blade shapes namely NACA0012, NACA4212 and NACA8612 are simulated and compared in this paper. Those blades are. Simulation is done on these 3 blades to obtain the lift force and coefficient of the blades. The lift force produced by the blade is given in Eq. (1).

$$L = \frac{1}{2}\rho u^3 A C_L \qquad (1)$$

where C_L is the lift coefficient, ρ is air density [kg/m^3], A is the area of blade [m^2], and u is wind speed [m/s].

The lift force can be seen that it depends on the size of the blade, wind speed and the lift coefficient. Computational Fluid Dynamic (CFD) analysis is done on all three blades. Two different models are used to generate the flow across the airfoils which are K-Epsilon and Spalart-Allmaras. Spalart-Allmaras to give a more accurate result as this model is made to analyze airfoils. Table 1 shows a comparison of three blade structure for an angle of attack of 16^0. Figure 1 shows the comparison of lift coefficient versus angle of attack, α. It is shown that NACA 8612 produces the highest lift coefficient compare to NACA 0012 and NACA 4212. The lift coefficient of NACA 0012 and NACA 4212 is declining when α>11°. It is shown that the lift coefficient is changing when α changes.

Table 1 Airfoil profile at 16^0 angle of attack

Model	Airfoil Profile	Lift Coefficient
NACA0012	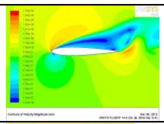	0.7276253
NACA4212	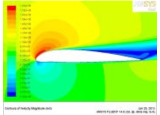	1.0528769
NACA8612	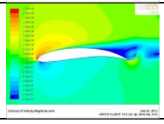	1.7929726

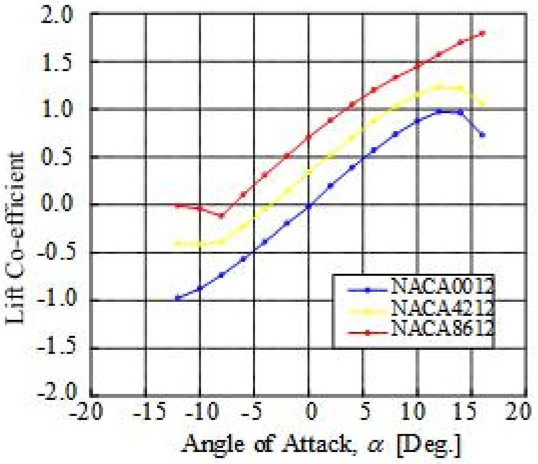

Fig. 1 Lift Coefficient of NACA 0012, NACA 4212 and NACA 8612

A five blade structure is used for the analysis to determine the best position of the blade structure. Figure 4 shows the simulation of angle of attack at various degree of impact (θ). It is observed that at 30° is the most suitable because of the highest lift coefficient. In order to have the airfoil to have a high lift coefficient the pressure below the airfoil has to be larger than on the top of the airfoil [7]. Figure 5 shows the lift coefficient at various degree of impact.

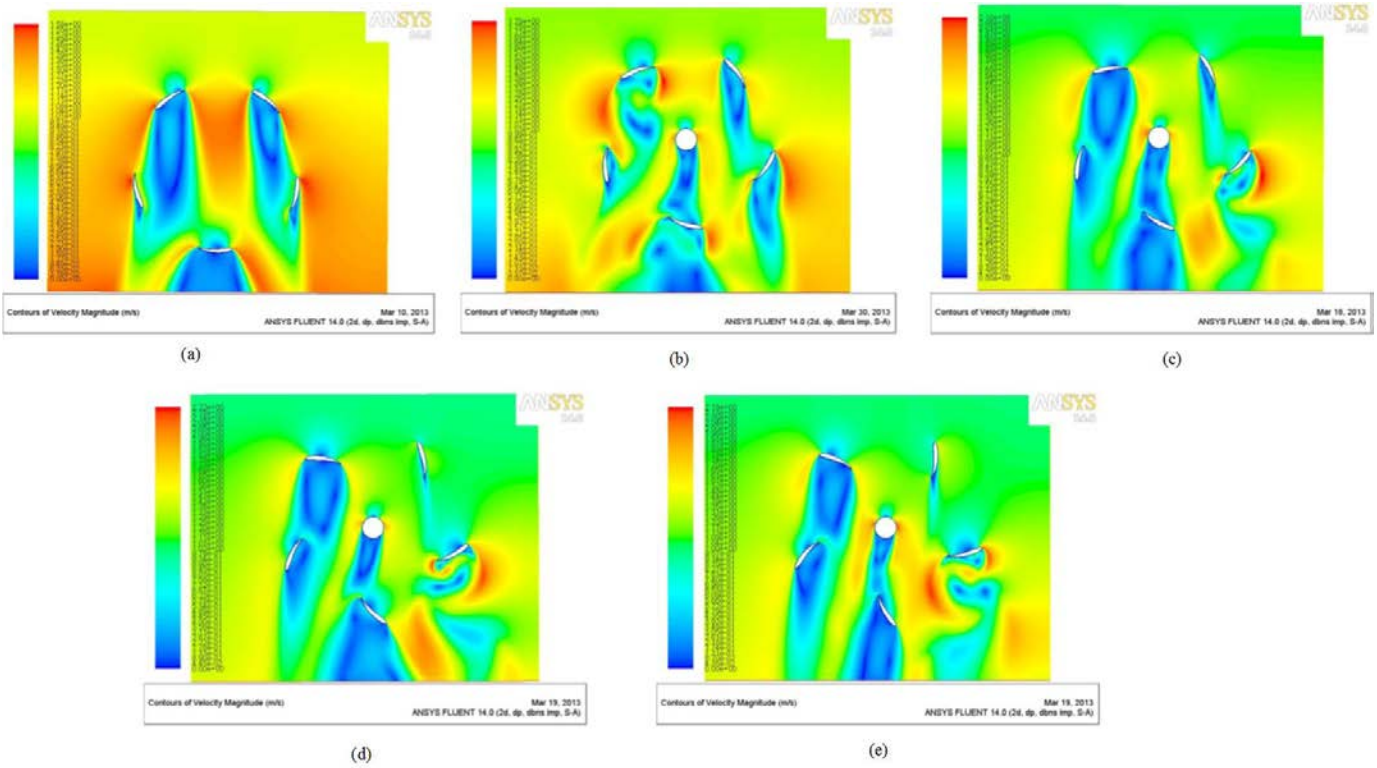

(a) (b) (c)

(d) (e)

Fig. 4 Angle of Attack at five blades (a) 0^0 (b) 18^0 (c) 30^0 (d) 45^0 (e) 60^0

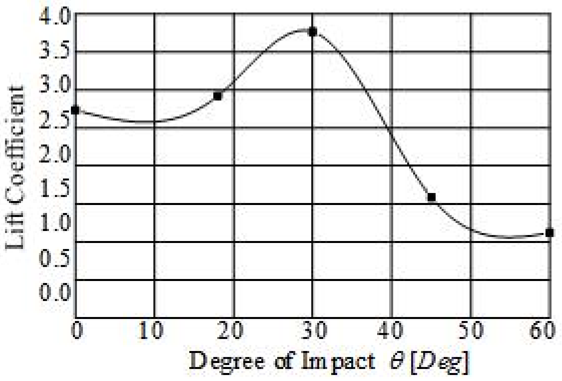

Fig. 5 Lift co-efficient based on degree of impact

3. Conclusions

The lift force of the blade is an important factor to extract the maximum power from the wind turbines. Different shape and angle of attack develop different power output. It is inferred from this initial investigation that the air profile NACA8612 is able to generate the highest lift coefficient. The angle of attack for the proposed five blade structure reveals the positioning of the blades at the angle of 30^0 evolves the highest lift coefficient. The design simulation results are to be used for the design and application in the development of the VAWT that would be reported in future.

References

[1] A.A.Wahab, S.Mohd, M.N.Dahalan, S.Mat, W.T.Chong, M.H.Ismail, M.F.Abas & R.Muslimen. “Eqwin Turbine – The breakthrough for wind energy implementation in Malaysia” in Proc. ICME,1986

[2] M.R.S Siti, M. Norizah & M. Syafrudin. “The Evaluation of Wind Energy Potential in Peninsular Malaysia” International Journal of Chemical and Environmental Engineering, vol. 2, pp 4-5, Aug. 2011

[3] C. Rigoberto, G. Samuel, T. Joseph. “Wind Power Technologies: A Need for Research and Development in Improving VAWT’s Airfoil Characteristics” Journal of Industrial Technology, vol. 27, pp 4, Jan. 2011

[4] P. Bhatta, M. A. Paluszek, J. B. Mueller. “Individual Blade Pitch and Camber Control for Vertical Axis Wind Turbines” Princeton Satellite Systems, 2008

[5] E. Sandra, B. Hans& L. Mats. “Evaluation of different turbine concepts for wind power” Renewable and Sustainable Energy Reviews, vol. 12, pp 10-11, May 2006

[6] C. Eamonn, “Modeling Flow around a NACA 0012 Foil” Curtin University, 2011

[7] S. Alex. “Aerodynamic Forces Acting on an Airfoil” The College of Wooster, May 2010

[8] A.L. Olimpo, J. Nick, E. Janaka & et.al. “Electricity Generation from Wind Energy” in Wind Energy Generation, UK: A John Wiley and Sons,Ltd, 2009

A Structural Investigation of an Electric Car Chassis

R.Y. Teh*, Douglas K.T. Tong

Mechanical Engineering, Taylor's University, Malaysia

**Corresponding author: tehrenyu@gmail.com*

Abstract—**this analysis focussed primarily on the main frame and suspension arm. There were two concepts each for both the chassis and the suspension arm. These concepts were simulated to determine the optimum balance between weight and rigidity. Torsional rigidity was analyzed for the chassis while static force, braking torque test and cornering test were performed for the suspension arm. The results showed that the stressed skin chassis concept and three tube suspension arm had higher rigidity.**

Keywords— Finite Element Analysis, light weight, SolidWorks, limited resources, good strength to weight ratio

1.0 Introduction

The structural investigation of this electric car chassis was conducted to produce a lightweight electrical vehicle for competition purpose. Two concepts of chassis namely stressed skin chassis and triangulated chassis were investigated. The stressed skin concept gained popularity in recent years especially in FSAE competitions around the globe due to its effectiveness in increasing chassis rigidity without significant weight increase. The stressed skin concept is extremely popular in motorsports but still new in the electric car chassis design. The objective was to determine whether the stressed skin chassis was suitable for an electric car chassis. An additional objective was to analyze two concepts of suspension arm design to determine which was safer under loading.

2.0 Research Methodology

2.1 Torsional Rigidity Testing on Chassis

Fig. 2.1a and Fig. 2.1b show two different approaches of chassis design, namely the stressed skin chassis and the triangulated chassis. The size and shape of both chassis were kept the same. The stressed skin chassis shown in Fig. 2.1a is 4.1% lighter than the triangulated chassis shown in Fig. 2.1b.

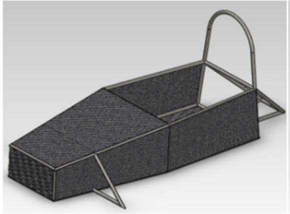

Fig. 2.1a Stressed Skin

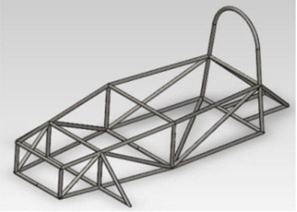

Fig. 2.1b Triangulated

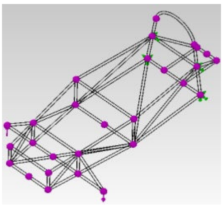

Fig. 2.1c F.T Test

Frame torsion test was used to study torsional rigidity [1]. Fig. 2.1c shows the setup of the frame torsion test where the green dots represent the fixtures and purple arrows represent the loads applied to the chassis [1]. With this setup, a torque was applied to the arms of the chassis. The torque was determined from equation (1),

$$T = F\ell \qquad (1)$$

The angular displacement was then obtained from equation (2),

$$\vartheta = \tan^{-1} {(\mathrm{Y1} + \mathrm{Y2})} / {2\mathrm{L}} \qquad (2)$$

Torsional rigidity was obtained by dividing the torque by the angular displacement as shown in equation (3) [2],

$$K = {T}/{\vartheta} \qquad (3)$$

2.2 Testing for Suspension Arm

Fig. 2.2a shows the arm design which uses two tubes while Fig. 2.2b shows arm design uses three tubes. Both designs utilized the flexibility provided by the rod end bearing to provide flexibility for the suspension arm. The difference is in the number of tubes used which affects the weight of the suspension arm and the alignment of the front rod end bearing which connects the upright. Three tests – static force, braking test, and cornering test – were conducted to compare both designs to determine which design is safer under operating condition by withstanding higher loads. Both suspension arms were constructed using tube size of 17mm. The 2 tube arm weighed 360g while the 3 tube arm weighed 460g.

Fig. 2.2a Two-tube suspension arm

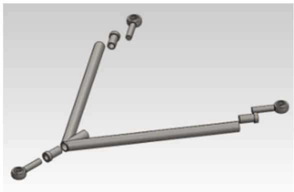

Fig. 2.2b Three-tube suspension arm

3.0 Results and Discussion

3.1 Chassis

The stressed skin concept was more effective as it provided 119% more rigidity to the chassis despite being 4.1% lighter. Its rigidity was the result of the external skin performing structural duties. It linked all structural elements together to form a "closed" structure. This fully utilized the surface area of the frame for the purpose of stiffening and strengthening [3]. The stressed skin chassis was lighter because it was made of Carbon Fiber, Thornel Mat VMA sheet which is 293% lighter than the steel tubes of the triangulated frame.

The maximum displacement in the Y axis was used to calculate the torsional rigidity. Fig. 3.1a shows the stressed skin chassis had lesser deflection compared to the triangulated chassis. The stressed skin chassis had 54.7% less deflection compared to the triangulated chassis. The torsional rigidity of both designs is shown in Table 1.

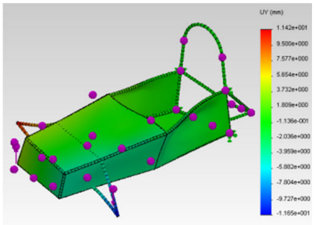

Fig. 3.1a: Stressed Skin Contours

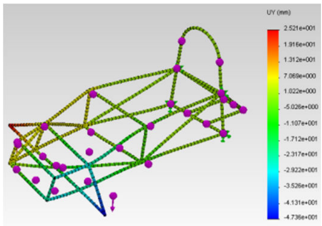

Fig. 3.1b: Triangulated Contours

Table 1 Torsional Rigidity Comparison

Chassis	**Torsional Rigidity, Nm/Degree**
Triangulated	342
Stressed Skin	749.77

3.2 Suspension Arm

3.2.1 Static force on Lower Suspension Arm

The maximum weight for this vehicle was limited to 210kg and supported by 3 wheels. Hence the weight per wheel was 70kg≈687N. With a recommended Factor of Safety of 4 [4], the total force per wheel was 2746.8N≈2747N. This force was acting upwards at the rod end bearing of the bottom suspension arm.

The results are shown in Fig. 3.2.1a and Fig. 3.2.1b.

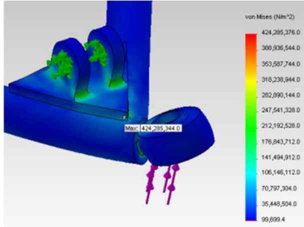

Fig. 3.2.1a Max Stress of Two-tube

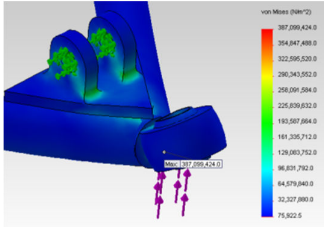

Fig. 3.2.1b Max Stress of Three-tube

3.2.2 Braking Test on Lower Suspension Arm

The average travelling speed for an electric car was 30km/h = 8.33m/s. The car was required to stop in 1 second, the average deceleration, a_d is 8.33m/s^2 . From Newton's Law of Motion,

$$F = ma \tag{4}$$

F=1749.3 $N \approx 1750N$. The radius of the wheel was 0.2286m from a standard road bike which was 18 inches in diameter, hence

$$BrakingTorque = F \times wheel.radius = 400Nm \tag{5}$$

With a safety factor of 4 [4], the final braking torque was 1600Nm and it was applied at the top and bottom arm at the same time.

The results are shown in Fig. 3.2.2a and Fig. 3.2.2b.

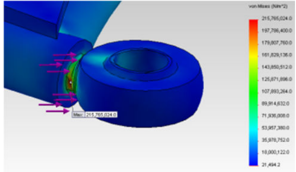

Fig. 3.2.2a Max Stress of Two-tube

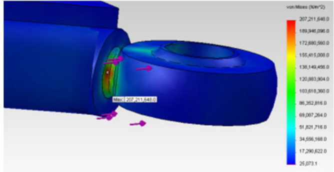

Fig. 3.2.2b Max Stress of Three-tube

3.2.3 Cornering Test on Lower Suspension Arm

Assuming the vehicle is entering a 21.3m radius corner which is the tightest corner in Sepang International Circuit with a speed of 30km/h. From Newton's Second Law, the centripetal force

$$F = {mv^2}/{r} \tag{6}$$

F= 684N≈285N and with a Safety Factor of 4 [4], the total centripetal force acting on the lower suspension arm was 2736N.

The results are shown in Fig. 3.2.3a and Fig. 3.2.3b.

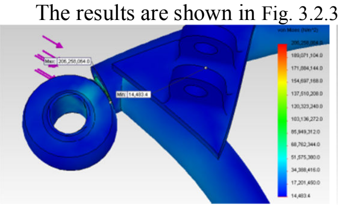

Fig. 3.2.3a Max Stress of Two-tube

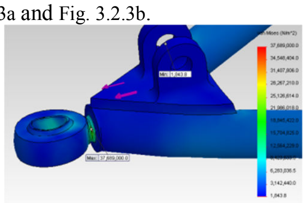

Fig. 3.2.3b Max Stress of Three-tube

3.2.3 Analysis of Suspension Arm

Table 2 shows three-tube suspension arm design has a lower overall maximum stress compared to the two-tube design as the force is shared by three tubes. The location of maximum stress for the three-tube design was at the threaded shaft of the rod end bearing as shown in Table 2. This was due to stress concentration at the threads. In many situations involving notched parts, the notch not only increased the primary stress but also caused one or both of the other principal stress to take nonzero values [4]. Fig. 3.2.1a shows the maximum stress on the tube inclusive of safety factor exceeded the yield strength of the tube material of 180MPa hence it was unsafe. The maximum stress and maximum displacement of both designs in cornering test shown in Table 2 and Table 3 showed significant differences between both designs. This was due to the placement of the rod end bearing of the two- tube suspension arm. Unlike the rod end bearing placed in the three-tube suspension arm which was parallel to the force direction, the two tubes rod end bearing was placed 57^o off the force direction due to the design of the two-tube lower arm design which was inevitable. This created a moment force pivoted at the notch which contributed to the extra stress on the bearing

Table 2 Maximum Stress Comparison

Test	**2-Tube Max Stress, (Mpa)**	**3-Tube Max Stress, (Mpa)**	**Location of Maximum Stress for 2 Tubes**	**Location of Maximum Stress for 3 Tubes**
Static force	424	387	Arm	Bearing
Braking Test	215	207	Bearing	Bearing
Cornering Test	206	37	Bearing	Bearing

Table 3 Maximum Displacement Comparison

Test	**2 Tubing's Max Displacement, (mm)**	**3 Tubing's Max Displacement, (mm)**
Cornering Test	0.0067	0.063

4.0 Conclusions

To obtain maximum energy efficiency for an electric car, weight reduction is crucial. The obvious way to reduce weight is to reduce the material usage without compromising the safety of the driver. The above analyses were conducted to determine the optimum balance between weight and rigidity. Composite material such as carbon fiber used in the analysis for stressed skin chassis design provided better strength to weight ratio. This analysis has also shown that the 2 tubes suspension arm design should be avoided despite the weight and manufacturability advantages.

Physical testing such as frame torsion test on the chassis and braking test for suspension arm designs are crucial and will be done in the future as any results obtained from the CAD software needs validation.

.

References

[1] H. Adams, Chassis Engineering, New York: Penguin Group, 1993.
[2] W. B. Riley and A. R. George, "Design, Analysis and Testing of a Formula SAE Car Chassis," *SAE Technical Paper Series,* 2002.
[3] "Research on Stressed Skin Construction for Chassis," ScholarBank@NUS, Singapore.
[4] R. C. Juvinal and K. M. Marshek, Machine Component Design, John Wiley & Sons, INC, 2012.

An Application of Research Methodology Framework Relating Cognitive Ergonomics to Sport Science

Terence Foo Kai Wai, Praveena Nair Sivasankaran

School of Engineering, Taylor's University, Malaysia

Fookaiwai@gmail.com

Abstract— **Golf is considered among the most difficult sports to master as it does not only require physical capabilities, but also mental abilities. Therefore, mental behaviour will play a vital role in affecting a golfer's performance. Factors such as mood, nutrition, lifestyle, course layout, game skills and club selection were categorized to study the impact on each individual factors and how it influence a golfer's mental processing during the game.**

Keywords— Cognitive ergonomics, mental behaviour, stress, golf performance, optimization techniques, design of experiment, response surface methodology.

1. Introduction

Ergonomics is defined as a system-oriented discipline that applies theory, principles, data and design methods to optimize human well-being and the overall performance of a system. Ergonomics is categorized into many different sub-categories such as physical ergonomics, cognitive ergonomics, neuroergonomics and organizational ergonomics [1]. For this research, cognitive ergonomic will be the main interest of study as it is highly correlated with golf. Golf is a slow pace game which involves not only physical abilities, but also mental abilities. During a golf game, mental abilities are very crucial as golfers often deal with attention distribution, decision making, concentration, mental stress, and mental processes. Therefore, the mental behaviour is a determinant key which affects the outcome of golf performance. The experimental factors involved for this research are categorized as

a) mood
b) nutrition
c) lifestyle
d) course layout
e) club selection
f) game skill

A number of junior male elite golfers were selected to participate in a specially designed questionnaire to study the behaviour of each golfer towards the experimental factors. Later on, the data were collected and analyzed using optimization techniques. Optimization techniques were performed using Stat Ease design expert software with response surface method (D-optimal) to provide an optimal solution based on the experimental result gathered [2]. The optimal solution was obtained based on the combination of numerical and categorical factors induced in the software stimulation. Hence, the optimal solution provides a prioritize factor which a golfer can improve on it. By improving the proposed optimal factor, it also improves decision making, concentration and ability to handle stress. Thus, it improves a golfer's performance and scores with a better mental behaviour.

2. Research Methodology

This research study consists of experimental and computational/numerical nature where results will be obtained through experimental questionnaire follow by statistical analysis using State-Ease software for design of experiment (DOE). A number of participants with category of junior male elite golfers were selected to participate in a specially designed questionnaire. Information of participants will be stated as anonymous and the results will be handling with care to protect the privacy of participants. This research study will be conducted with ethical guideline from American Psychological Association's 2002 Ethical Principles of Psychologists and Code of Conduct [3]. Data from the questionnaire were then computed and analyzed with Stat-ease software. D-optimal analysis consists of 2 primary grouping, which is categorical and numerical factor. A categorical factor is qualitative value which has a fixed and non absolute measurement where numerical factor is a quantitative value with absolute measurement. Thus the entire sub category has been input according to numerical and categorical as shown in Fig. 1.

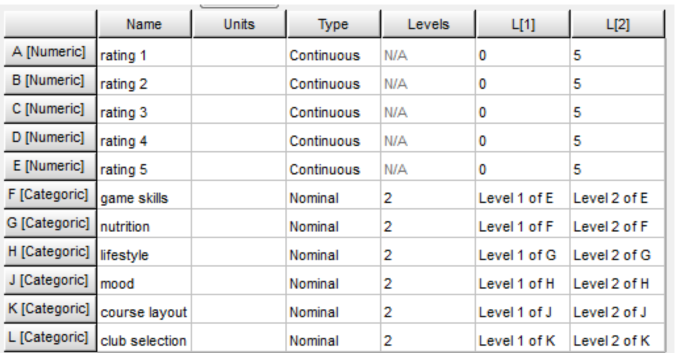

	Name	Units	Type	Levels	L[1]	L[2]
A [Numeric]	rating 1		Continuous	N/A	0	5
B [Numeric]	rating 2		Continuous	N/A	0	5
C [Numeric]	rating 3		Continuous	N/A	0	5
D [Numeric]	rating 4		Continuous	N/A	0	5
E [Numeric]	rating 5		Continuous	N/A	0	5
F [Categoric]	game skills		Nominal	2	Level 1 of E	Level 2 of E
G [Categoric]	nutrition		Nominal	2	Level 1 of F	Level 2 of F
H [Categoric]	lifestyle		Nominal	2	Level 1 of G	Level 2 of G
J [Categoric]	mood		Nominal	2	Level 1 of H	Level 2 of H
K [Categoric]	course layout		Nominal	2	Level 1 of J	Level 2 of J
L [Categoric]	club selection		Nominal	2	Level 1 of K	Level 2 of K

Fig. 1 Numerical and Categorical Factors for D-optimal design

The outcome of this stimulation provides an optimal solution with an overlay plot describing the importance of each categorical factor affecting the golfers. Other than that, ANOVA table will be presented with F values to represent the significance of the inputs variable. ANOVA simply means analysis of variance where it computes all the statistical data to study the variation of different factors. It is a significant study as it provides an understanding of interaction between each numerical and categorical factor. Hence, when the F value is determined from the software, level of significance of each factor can be prioritize. The theoretical calculation of F value is usually presented in a ratio where

$$F = \frac{SS_{model}\ /df_{model}}{SS_{error}\ /df_{error}} \qquad (1)$$

$$F = \frac{MS_{model}}{MS_{error}} \qquad (2)$$

The initial calculation for F value is the sum of mean square over the degree of freedom shown in equation 1 [4]. Thus it can be simplified to the ratio of mean square of model over the error as shown in equation 2 [4].

3. Results and Discussion

Table. 1 ANOVA table with F value for nutrition factor

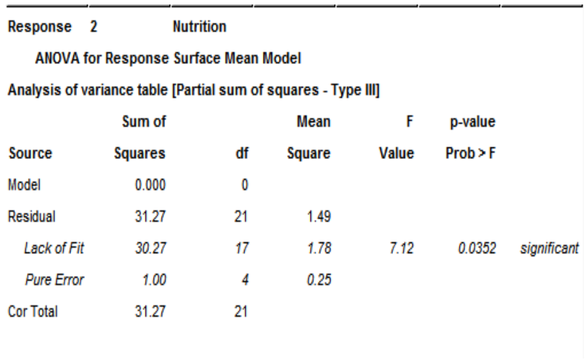

Response 2 Nutrition

ANOVA for Response Surface Mean Model

Analysis of variance table [Partial sum of squares - Type III]

Source	Sum of Squares	df	Mean Square	F Value	p-value Prob > F	
Model	0.000	0				
Residual	31.27	21	1.49			
Lack of Fit	*30.27*	*17*	*1.78*	*7.12*	*0.0352*	*significant*
Pure Error	*1.00*	*4*	*0.25*			
Cor Total	31.27	21				

Table1 shows the ANOVA table computed using response surface method D-optimal mode. F value computed by the software is calculated using the theoretical equation shown in equation 1 and 2. Table 1 indicates F value of 0.352 which is considered significant. This can also be interpreted that the questionnaire survey shows participants are fair enough in giving a significant amount of attention to nutrition which results in nutrition not being a point to be considered for optimizing purpose. Hence , it can be conclude that participants is aware of nutrition factors such as the amount of food and water consumed during the golf game as well as supplements and nutritious food consumed in their daily life which helps to maintain a healthy physical build. Therefore, nutrition is the least likely factor to affect the golfer's performance.

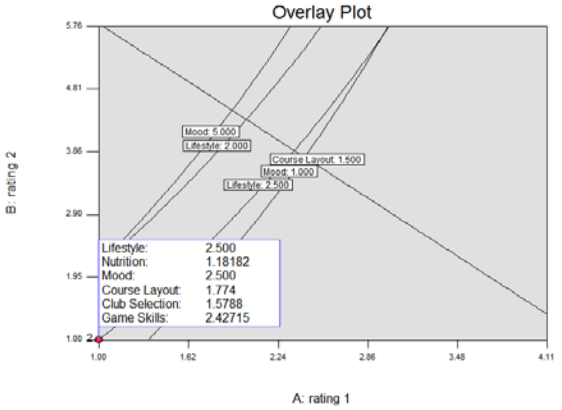

Fig. 2 Overlay Plot shows the level of significance between each categorical factor

The overlay plot indicates the interaction and priority sequence of all the categorical factors. Mood and lifestyle has the highest value of 2.5 as shown in figure 2. This indicates that these 2 factors have the highest priority for optimization. The value on the plot shows the sequence of significance level needed for optimization. Nutrition was not fitted into the graph because it is the least important factors and not required for optimization. Therefore, mood and lifestyle has the highest influence to a golfer's performance and it is required to be improved.

Table. 2 questionnaire survey for mood factor

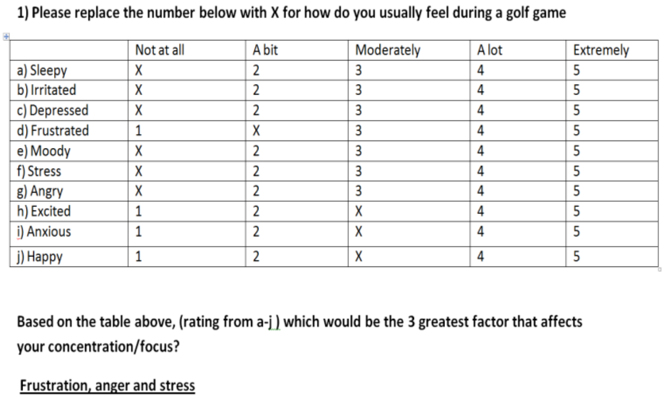

1) Please replace the number below with X for how do you usually feel during a golf game

	Not at all	A bit	Moderately	A lot	Extremely
a) Sleepy	X	2	3	4	5
b) Irritated	X	2	3	4	5
c) Depressed	X	2	3	4	5
d) Frustrated	1	X	3	4	5
e) Moody	X	2	3	4	5
f) Stress	X	2	3	4	5
g) Angry	X	2	3	4	5
h) Excited	1	2	X	4	5
i) Anxious	1	2	X	4	5
j) Happy	1	2	X	4	5

Based on the table above, (rating from a-j) which would be the 3 greatest factor that affects your concentration/focus?

Frustration, anger and stress

Results from the questionnaire indicated that majority of the golfer is having difficulty in handling stress and often feel frustrated during the game. This is a significant contribution to the poor performance of a certain golfers as mental behaviour plays an important role to the outcome score. On the other hand, lifestyle also has a vital impact to cognitive behaviour. Results show that majority of the golfers do not have enough rest as they often engage with training. This will lead to exhaustion of physical which indirectly affecting mental processes as well. Hence the overlay plot produced an accurate result for optimization as compared to actual experimental data.

4. Conclusions

In summary, Overlay Plot and ANOVA table provides a clear picture of the importance and significance level of each categorical factor. The results obtained from the software clearly reflect the general behaviour and response of the participants as compared to the experimental result gathered. Hence, golfers can improve on the suggested significant factor. By overcoming the usual behaviour, golfers will also improves their mental abilities such as better stress management, proper planning and effective decision making during their game. Thus, when golfers have good mental processes, his golf performance will surely improve as well.

Acknowledgment

I would like to appreciate and thank my supervisor Ms Praveena for supporting me with this research. Other than that, I would like to thank all the participants who took part in the questionnaire survey in order to make this research happen.

References

[1] Jose. Canas, Boris B. Velichkovsky and Borris M. Velichkovsky, "Human Factors and Ergonomics", pp.3-4, University of Granada, Spain, KurchatovReasearch Institute, Moscow, Russian Federation, Dresden University of Technology, Germany.

[2] Maters Raymond H.& D.C. Montgomery, "Response Surface Methodology: process and product optimization using designed experiment" A Wiley-Interscience Publication, 2002

[3] Bill Altermatt, "Ethical Responsibilities to Participants", updated on November 2011

[4]Paul J.Holmes, "The ANOVA table", MARK5000 Statistical Methods in Marketing.

Maximum Power Point Tracking in Domestic Application

Trinetra Sundrasagra[1], Mohammad Taghi Hajibeigy [2*]

[1]School of Engineering, Taylor's University, Malaysia, [2] School of Engineering, Taylor's University, Malaysia
*Corresponding author: Mohammadtaghi.hajibeigy@taylors.edu.my

Abstract— **This paper explains the operation of the Maximum Power Point Tracking (MPPT) system which harnesses the maximum possible power from available sunlight through photovoltaic system. The aim of this research is to develop a system using cost effective components that can be used in simple domestic application to charge a load. The MPPT system uses the Perturb and Observe (P&O) algorithm as a method to compute and regulate power derived. The proposed method was evaluated to observe the voltage and current output and the results are presented. The strengths of the system were identified.**

Keywords— Maximum Power Point Tracking (MPPT), solar energy, renewable energy, photovoltaic (PV) systems, solar charging system

1. Introduction

The search for an alternative and potential source to replace the exhaustive resources such as crude oil is a continuous effort. One of the identified and preferred renewable resources is solar energy. Photovoltaic (PV), cells are devices that convert the solar energy of into direct current (DC) electric energy [1]. The mechanism of PV cells is based on semiconductor principles, that when light strikes the silicon surface its electrons are released, to generate an electric current.

The power generated by the PV cells depends on irradiance, temperature, and cloud conditions. The power generated at each instance has a Maximum Power Point (MPP) which is never constant over time. MPPT should be used to track its changes. An MPPT tracks the highest current level in these conditions at a particular power rating level available and directs it to load [2]. In this paper, the MPPT is applied to simple charging application to demonstrate the effectiveness of the system to supply the load with more current.

2. Methodology

This is a quantitative study. The MPPT is used to bridge the PV array and the load to be charged, under sunlight. The MPPT's embedded algorithm computes the available power MPP and draws maximum current to charge the load. The reading is taken from solar panels with power rating of 130W under variable weather conditions.

2.1. System Design and Modeling

This section describes the typical layout of the system. The MPPT controller consists of voltage and current sensor which calculate the voltage at which the module is able to produce maximum power. The Current sensor determines the current that can be drawn at identified MPP[3].

A high efficiency DC-to-DC power converter converts voltage level at the PV module to the microcontroller and battery. A microcontroller is integrated circuit to read voltage and current signals from the sensors and the MPPT system samples the output of the PV cells using a voltage and current sensor and affects the proper resistance by microcontroller to obtain maximum current from available voltage level.

Fig. 1[6] shows the block and flow diagram of the MPPT system implemented using sensors and microcontroller.

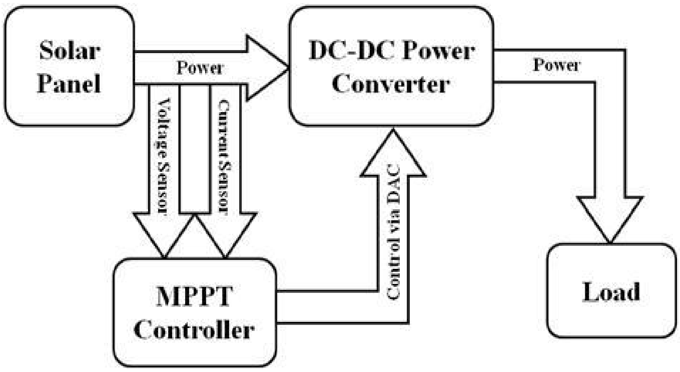

Fig. 1 MPPT Block and Flow Diagram [6]

The design implements the Perturb and Observe (P&O) method which is convenient for its simplicity and lesser time delay. The P&O algorithm increases the operating voltage until the power and current level begin to decrease as shown in Fig. 2. When MPP drops, the voltage is decreased to get back towards the MPP [4].

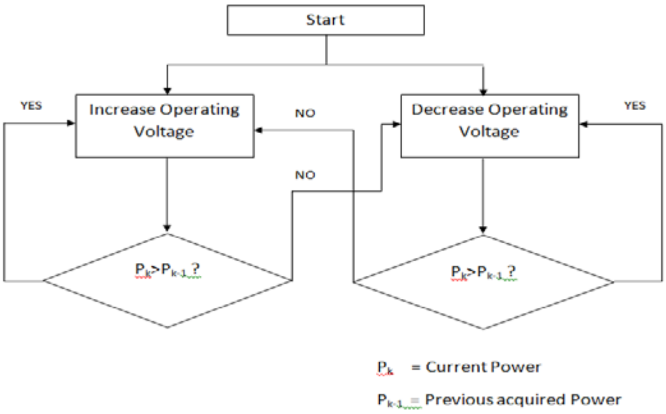

Fig.2 Flow diagram of the P&O algorithm implemented

2.2 Data Collection and Testing

The PV module is placed outdoors under direct sunlight during varying weather conditions. A constant is used by measuring the output of the PV module without MPPT implementation versus the PV module using MPPT system. This test commenced when the system was completely built, from 27th April to 16th May 2013 during the daylight hours from 8 am to 5 pm for a total of 9 hours.

A multimeter is used to measure the voltage across the MPPT module and towards the load (battery). The embedded current sensing circuit paved a way for the highest detected current to flow towards the load. The battery's remainder voltage capacity is measured from time to time to prove the charging of the load via PV and MPPT.

This test is carried by connecting one set of solar panel to load without MPPT and another similar set but consisting of the MPPT. The readings gathered will illustrate the actual efficiency of the MPPT system

3. Results

The performance of the PV module with rating 12 Watts to charge the given load is tested using one set with MPPT system and another without. The testing is carried out for two light intensity conditions namely sunny and cloudy. The results obtained are tabulated in Fig. 2 and Table 1.

Fig. 3 shows the graph of voltage levels of the PV system without MPPT implementation for sunny conditions.

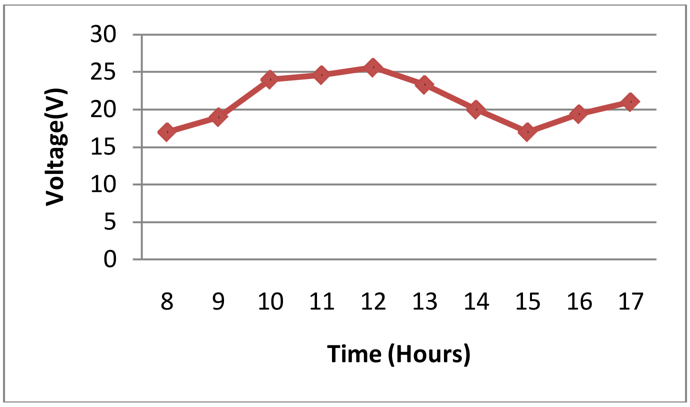

Fig.3 Voltage of PV Module with Respect to Sunny Condition at Different Daylight Hours without MPPT Implementation

Table 1 tabulates the reading obtained for the PV module's output voltage level with the implementation of MPPT.

Table 1 Voltage and Current of PV Module with Respect to Weather Condition at Different Daylight Hours with MPPT

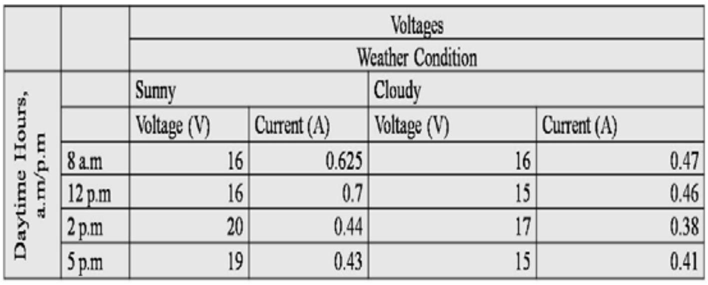

		Voltages			
		Weather Condition			
Daytime Hours, a.m/p.m		Sunny		Cloudy	
		Voltage (V)	Current (A)	Voltage (V)	Current (A)
	8 a.m	16	0.625	16	0.47
	12 p.m	16	0.7	15	0.46
	2 p.m	20	0.44	17	0.38
	5 p.m	19	0.43	15	0.41

4. Discussion

The availability of sunlight enables the strongest reaction of irradiance between semiconductor materials in PV cell to generate free moving electrons, therefore higher current [5].

However, the highest efficiency of the MPPT is during early midday (11 a.m) when voltage levels are high and the panel is not heated up.

The P&O algorithm can convert the voltage level to a lower one to obtain a higher current level at the power produced by the PV cell.

It is shown through comparison that the voltage level in the MPPT system is adjusted to a lower one so that more current is drawn to charge the load. The controller detects the MPP at a given time, then increases the voltage until the MPP is observed to decrease. Then the controller responds by decreasing the voltage level to re-obtain the MPP with the maximum current level. The given power rating of the solar panel is 12W.

The MPP can be evaluated by using the power formula, P = V.I [5]
Based on Table 1 at 12 p.m it is observed that the voltage level is given as 16 V. To obtain the power in Watts, the current obtained is multiplied with the voltage.

$$P = V \times I$$
$$16\ \text{V} \times 0.7\ \text{A} = 11.2\ \text{W}$$

Thus, the MPP at 12 p.m is 11.2 W which is close to the PV module power rating of 12 W.

5. Conclusion

Renewable energy sources, like solar energy, are suitable for residential and industrial applications. MPPT could increase the energy delivery by up to 24% on a solar day and in increase of 25% on cloudy days. The MPPT can regulate occurrence of battery overcharge protection, saving the cost of maintenance.

The future work proposed for this project details in programming an algorithm that combines the P&O algorithm and Incremental Conductance to detect rapid changes in light intensity. One could also integrate the use of Pulse Width Modulation PWM or fuzzy logic control to determine the state of weather and use a higher clock speed microcontroller such as 120MHz to decrease time delay computation.

Acknowledgment.

I would like to thank Dr.Florence for keeping me updated on my performance and academic requirements.

References

[1] Adedamola O., (2006). Thesis of Analysis, Modeling and Simulation of Optimal Power Tracking of Multiple-Modules of Paralleled Solar Cell Systems. The Florida State University.
[2] David C. H. and Yan H. L., (2000). Simple maximum power point tracker for photovoltaic arrays.Electronic Letters, Vol. 36, No. 11.
[3] Liu Y. H., Huang J. W. (2011). A fast and low cost analog maximum power point tracking method for low power photovoltaic systems. Solar Energy, 85, 2771-2780.
[4] K. Hussein, I. Muta, T. Hoshino, and M. Osakada (2006), "Maximum Photovoltaic Power Tracking: An Algorithm for Rapidly Changing Atmospheric Conditions", IEEE Proceedings. Generation, Transmission and Distribution, 1995, **142**, (1), pp. 59-64
[5] D. Hohm and M. Ropp, (2008) "Comparative Study of Maximum Power Point Tracking Algorithms", Progress in Photovoltaics: Research and Applications, 2003, **11**, pp. 47-62
[6] Buckley Bryan (2011) Maximum Power Point Tracking from http://bama.ua.edu/~bwbuckley/projects/mppt.html

Microwave Assisted Infrared Drying of Mango (Mangifera Indica L.)

Wai Lik See[1*], Chien Hwa Chong[1], Chung Lim Law[2]

[1]*School of Engineering, Taylor's University, Lakeside Campus, No1, Jalan Taylor's, 47500 Subang Jaya, Malaysia*

[2] *Department of Chemical and Environmental Engineering, University of Nottingham Malaysia Campus, Broga Road, 43500 Semenyih, Selangor Darul Ehsan, Malaysia*

**Corresponding author: see.wailik@sd.taylors.edu.my*

Abstract – Mango were dried using microwave, infrared-microwave, microwave-hot air and microwave-infrared-hot air methods. This research aims to reduce drying duration, retained vitamin C and total phenolic content (TPC) of mango. Samples were dried at different microwave power levels (50W, 310W, 380W) and temperature (60°C and 70°C). It was found out that microwave-infrared drying had reduced in drying period but the quality of the samples was not able to retain. To neutralise the defect, microwave-infrared-hot air drying was performed. It was found that this method has a positive impact in retaining TPC and vitamin C of samples.

Keywords: Tropical Fruits; Drying; Microwave; Moisture Content; Total phenol content; Infrared

1. Introduction

The foremost purpose in drying agricultural products is to reduce the moisture content in fruits or vegetables to a level such that safe storage over an extended period is allowed. Also, it brings about substantial reduction in weight and volume, minimising packaging, storage and transportation cost [1].

Microwave produces electromagnetic energy which will be absorbed by water molecules in the body of the samples. Water molecules then agitate and create heat around the body which will then lead to moisture removal [2]. Infrared on the other hand applies almost comparable drying mechanisms as microwave drying. Infrared source also creates a high ambient temperature in drying environment. Moisture is removed from the inner body via microwave radiation and surface moisture dissipates through temperature gradient in the drying environment; consequently improving the drying rate.

The objective of this study is to investigate the drying kinetics and retention of d TPC and vitamin C of dried mango. Materials and methods

1.1. Materials

Fresh elephant tusk mangoes (Mangifera indica L.) were supplied by K.P Mak Trading. Fresh mangoes were sliced into the thickness of about 5 mm before drying.

1.2. Drying Equipment

Infrared-microwave drying was performed with domestic analogue microwave oven (Electrolux EMM 1908S, Malaysia) with 20L inner volume. It can operate at 50W, 310W, 380W, 540W and 700W power levels. A ceramic infrared heater (ISH 70355, Vitar, 240VAC) with 2.0W/mm of heating length was acquired from Vitar VBC Electro-Heat Sdn. Bhd. Hot air convective oven (PROTECH, FAC-350) was also used in microwave combined hot air drying and also microwave-infrared combined hot air drying (hybrid drying).

1.3. Drying Methods

About 50 g of sliced mango samples were weighed using a 2 decimal place electronic balance (Ohaus Pioneer) and then placed in the microwave oven to dry at 50 W, 310 W and 380 W. At time interval of 1 min, the weight of the samples was recorded until a constant weight was found. Similar methods were practiced in infrared-microwave drying.

Products formed after microwave and microwave-infrared drying did not seem to meet the required quality due to charred and darkening, hybrid drying was introduced. In hybrid drying, samples with similar thickness and weighs were pre-dried in the microwave oven (either with or without the presence of infrared source) until the colour of the samples started to change. The samples then were placed in the hot air oven to continue drying process at 60°C and 70°C until an equilibrium weight was reached.

1.4. Drying Kinetics

Parameters such as moisture content, MC_d (dry basis), moisture ratio, MR and drying rate, DR best describe the drying kinetics. Referring to Ekechukwu (1996) and Fatouh et al (2006), these parameters can be determined as below [3,4]:

$$MC_d = {(m - m_{bd})}/{m_{bd}} \tag{1}$$

$$MR = {(MC_d - MC_{d.final})}/{(MC_{d.initial} - MC_{d.final})} \tag{2}$$

$$DR = -\left(MC_{d,t} - MC_{d,t+1}/{\Delta t} \right) \tag{3}$$

where m represents instantaneous weight while m_{bd} is the bone dry weight.

1.5. Total phenol content analysis

Concentrations of phenolic content in the dried samples were determined via absorbance method using UV spectrophotometer (Dynamica, HASA RB-10, Switzerland) at 725nm wavelength. This was conducted after extraction process using 50% ethanol solution. A gallic acid calibration curve was also produced to illustrate the concentration of phenolic compound expressed in gallic acid (mg/L).

1.6. Vitamin C analysis

Vitamin C determination was conducted using a titration method. Extracted vitamin C (5% trichloroacetic acid) from dried mango samples were titrated against 2,6 dichlorophenolindophenol (DCPIP) solution [5].

2. Results and Discussion

Fig. 1 indicates that it took almost 4 times faster for the sample to reach moisture content at 0.1 moisture ratio in 380W (t=10min) power rating compared to 50W (t=40min) power level. Increasing power level will escalate the intensity of microwave energy, at which water molecules absorbs the high intensity electromagnetic wave and vaporise rapidly as agreed by Soysal (2004) [6].

Presence of infrared reduced the time spent to reach equilibrium moisture content as shown in drying curve. However, the increase in drying rate is not significant for high microwave power level. At 310W power level, the time taken for samples to reach moisture ratio of 0.1 only increased by about 5% when infrared source was turned on. At 50W power rating, an increment of about 37% drying rate was recorded.

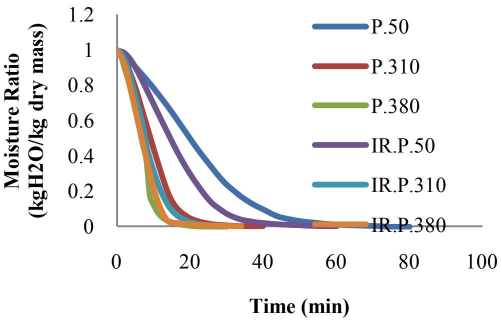

Fig. 1 Drying Rate at Different Settings

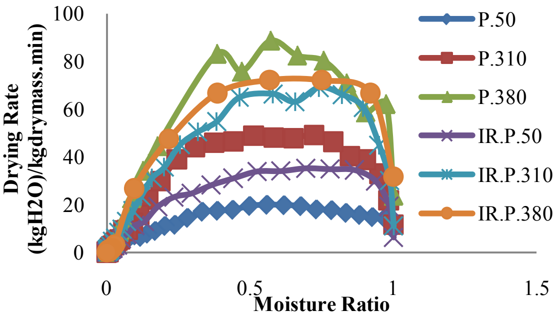

Fig. 2 Drying Rate against Moisture Ratio

The falling period in Fig. 2 indicates that there is moisture removal within the body of the mango samples. This scenario causes the colour of the samples to darken as temperature within the body of mango samples increases. Fig. 2 also showed that the constant rate at lower microwave power rating (50W) is much lengthier compared to 310W and 380W, proving that samples surface drying took longer time at lower power rating. Longer surface drying also means minor temperature change, then less colour and quality deterioration.

Another important parameter to be studied in this research is the total phenolic content loss of the dried samples. Fig. 3 showed hot air drying at 60°C had better TPC retention than at 70°C. Drying at lower temperature had secured the nutrient content of the samples as agreed by Vega-Galvez et al (2009) [7]. In general, when microwave and microwave-infrared pre-drying was performed, drying at 70°C showed lesser TPC percentage loss. This can be explained by the higher efficiency in moisture removal at 70°C, which then retain the nutrient of dried samples. Presence of infrared in pre-drying stage had better TPC retention effect at lower power level (50W). This is because at lower power level, the microwave intensity is much lower, allowing infrared heating to have more effect on the duration of pre-drying stage, at the same time allow better TPC retention.

Referring to Fig. 3, drying at 60°C resulted in higher retention of vitamin C compared to 70°C. The difference is more significant at lower power level (50W) during pre-drying stage because of infrared drying duration.

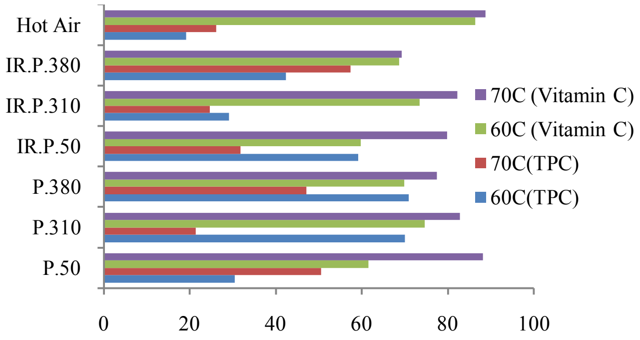

Fig. 3 Percentage Loss in Total Phenolic Content and Vitamin C of Dried Samples

With microwave and microwave-infrared pre-drying stage, the overall duration of drying process was reduced due to the high moisture removal rate at pre-drying stage using microwave and infrared drying. The reduction in drying period subsequently reduces the overall percentage loss of vitamin C compared to hot air drying.

3. Conclusion

Microwave-infrared drying method had been proved to improve drying length especially at low microwave power level. But the presence of high energy electromagnetic wave tends to worsen the nutrition preservation as proposed in the results of this study. To counteract this challenge, microwave-infrared was used as a pre-drying technique to reduce moisture content in the inner body, and then followed up by hot air drying to retain Vitamin C and TPC of mango.

Acknowledgement

I would like to show my gratitude to Vitar Group and Yee Onn Engineering for their contribution in sponsoring partially for the equipment costs.

Reference

[1] I. Doymaz, "Sun Drying of Figs: An Experimental Study," *Journal of Food Engineering*, June 2004.

[2] E.I Goksu, "Fluidized Bed, Microwave and Microwave Assisted Fluidized Bed Drying of Macaroni Beads," Middle East Technical University, Thesis 2003.

[3] OV Ekechukwu, "Review of Solar-Energy Drying Systems I: An overview of drying principles and theory," 1999.

[4] M. Fatouh, M. N. Metwally, A. B. Helali, and M. H. Shedid, "Herbs drying using a heat pump dryer," *Energy Conversion and Management*, vol. 47, pp. 2629-2643, February 2006.

[5] S. S. Nielsen, *Food Analysis Laboratory Manual*, 2nd ed. New York, United State of America: Springer Science, 2010.

[6] Y. Soysal, "Microwave Drying Characteristics of Parsley," *Biosystems Engineering*, vol. 89, no. 2, pp. 167-173, 2004.

[7] A. Vega-Galvez et al., "Effect of air-drying temperature on physico-chemical properties, antioxidant capacity, colour and total phenolic content of red pepper," *Food Chemistry*, vol. 117, pp. 647-653, 2009.

[8] J. Ndawula, J. D. Kabasa, and Y. B. Byaruhanga, "Alterations in fruit and vegetable b-carotene and vitamin C content caused by open-sun drying, visqueen-covered and polyethylene-covered solar-dryers," *African Health Sciences*, vol. 4, no. 2, pp. 125-130, August 2004.

Drying Kinetics and Total Phenolic Content of Dried *Mentha arvensis* Linn Leaves

Siew Fan Wong[1], Dr. Chong Chien Hwa[2*], Puteri Farah Wahida[3*]

[1]*School of Engineering, Taylor's University, Taylor's Lakeside Campus, No.1 Jalan Taylor's, 47500 Subang Jaya, Malaysia*

** ChienHwa.Chong@taylors.edu.my*

Abstract—**The objective of this study is to investigate the effects of sun drying and infrared drying on drying characteristics and total phenolic contents (TPC) of MA leaves. Infrared drying temperature was ranged from 50°C to 80°C; average temperature of natural sun drying and enhanced sun drying was 34 ± 1.2°C and 45.67 ± 0.5°C respectively. To represent the experimental data, five different empirical models (Lewis, Page, Henderson & Pabis, Two-term Exponential and Midilli et. al) were used. The best model was selected based on highest R^2, lowest RMSE andχ^2. TPC of dried leaves was determined and it was found that enhanced sun drying method gave the highest TPC.**

Keywords— Mentha arvensis Linn, thin layer modelling, natural sun drying, infrared drying, total phenolic content

1. Introduction

Mentha arvensis is a type of herb commonly known as "Japanipudina" [1]. This plant is originally from Japan [1]. *M. arvensis* contains menthol (66%), (-)-menthyl acetate (15%) and (-)-menthone (8%) and it also has some phenolic content [2].

Literature review of sun drying and infrared drying on *M. arvensis* leaves were done. These two drying methods were chosen because there was very limited information on drying of MA leaves using these methods. TPC of MA leaves was analysed. Phenolic is a natural antioxidant which very important to human health. The findings will be useful for future scientific interest of processing similar herbs.

The objective of this research is to compare sun drying and infrared drying in term of the drying characteristics and the total phenolic content found in dried *M. arvensis* in this two drying methods.

2. Materials and Methods

M. arvensis leaves were purchased from SS15, Subang Jaya, Selangor, Malaysia.

2.1. Design of Sun Drying Tray

Sun drying tray was built using plywood. The dimension for the tray was 600 mm x 400 mm x 245 mm (L x W x H). Bottom of the tray was covered with aluminium sheet; top of the tray was covered with a wire net; inside of the tray has a portable stainless steel sheet.

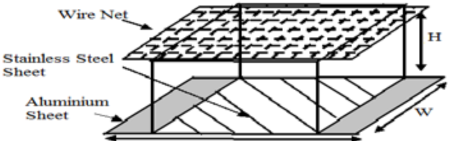

Fig. 1 Sun Drying Tray

2.2. Experimental Procedure

For sun drying, 10 g of freshly washed leaves was put in the designed sun drying tray and exposed to the sunlight. The weight of leaves was measured at 15 minutes time interval until the equilibrium moisture content. Dried leaves were then put into an oven at 105°C for 24 hours.

For infrared drying, 1.0 g of fresh washed leaves was put in a moisture analyser (XM 50; accuracy of ±0.001g; Swiss made). The temperature used was 50°C to 80°C. The weight of leaves was recorded at 1 min time interval until the equilibrium moisture content. Then, dried leaves were left to dry at 105°C (AOAC method 1990).

For determination of TPC, the dried leaves were extracted using diethyl ether. The dried leaves extract was mixed with 1N Folin-Ciocalteu reagent. After 5 min, 4 ml of 7.5% sodium carbonate (Na_2CO_3) and 3 ml of distilled water were added and allowed to react for 2 hours at room temperature. Then, absorbance of the mixture was measured using a UV spectrophotometer (model: HASA RB-10; country: Dynamica, Switzerland) at 765 nm. A standard curve of gallic acid solution of 15000 ppm to 20000 ppm was prepared.

3. Drying Characteristics

3.1. Drying Kinetics and Drying Rate

Drying kinetic process is the process of recording change of the average moisture content against time or the drying rate against moisture content (MC) [3]. MC [4], MR [5], and drying rate (DR) [6] were calculated using Eq. 1, Eq. 2 and Eq. 3 respectively.

$$\text{MC (dry basis)} = \frac{M_t - M_b}{M_b} \tag{1}$$

$$MR = \frac{M - M_e}{M_o - M_e} \tag{2}$$

$$DR = \frac{M_{t+dt} - M_t}{dt} \tag{3}$$

3.2 Mathematical Modelling

Table 1 showed the thin layer modelling used to fit the data from the experiment. The best model was determined for each variables parameters. R^2- [5], $RMSE$- [5] and χ^2- [5] were used to determine the goodness of the data fitted into the thin layer modelling equations and calculated using Eq. 4, Eq. 5 and Eq. 6, respectively.

Table 1. Mathematical Modelling

Model Name	Model	Ref.
Lewis	$MR = \exp(-kt)$	[4]
Page	$MR = \exp(-kt^n)$	[7]
Henderson & Pabis	$MR = a\exp(-kt)$	[8]
Two-term exponential	$MR = a\,exp(-kt) + (1 - a)\,exp(-kat)$	[9]
Midilli et al.	$MR = a\exp(-kt^n)$ +bt	[10]

$$R^2 = \frac{\sum_{i=1}^{N}(MR_i - MR_{pre,i}) \cdot \sum_{i=1}^{N}(MR_i - MR_{exp,i})}{\sqrt{\sum_{i=1}^{N}(MR_i - MR_{pre,i})^2 \cdot \sum_{i=1}^{N}(MR_i - MR_{exp,i})^2}} \tag{4}$$

$$RMSE = \sqrt{\frac{\sum_{i=1}^{N}(MR_{pre,i} - MR_{exp,i})^2}{N}} \tag{5}$$

$$\chi^2 = \frac{\sum_{i=1}^{N}(MR_{exp,i} - MR_{pre,i})^2}{N - z} \tag{6}$$

3.3 Effective Moisture Diffusivity

Eq. 7 was proposed using Fick's second law to calculate effective moisture diffusivity [11].

$$MR = \frac{M-M_e}{M_0-M_e} = \frac{8}{\pi^2}\exp\left(\frac{-\pi^2 D_{eff}\,t}{4d^2}\right) \qquad (7)$$

4. Results and Discussion

As shown in Fig. 2, there was only falling rate period for sun drying. This result was the same as the result obtained by earlier researcher [12]. For infrared drying, there was preheating period, where the leaves were being heated up to heating temperature and falling rate period, where the drying process of leaves took place. Drying rate was increased with temperature. This was because as the temperature increased, more heat was provided to the leaves, led to increase in moisture removal, hence drying rate increased. These results were in good agreement with earlier research on saffron stigmas [13].

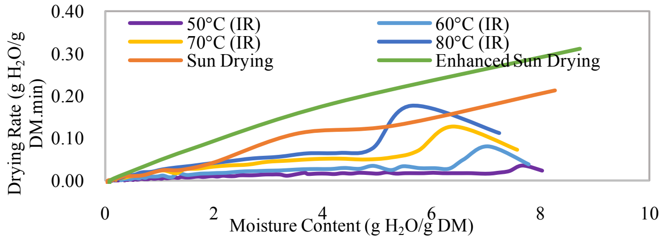

Fig. 2 Relationship between Drying Rate and Moisture Content

Fig. 3 showed MR was plotted against time, for the purpose of curve fitting with 5 drying models. These models were evaluated based on highest R^2, lowest $RMSE$ and lowest χ^2. It was determined that Page was the best descriptive model for IR at 50^{0}C, 70^{0}C, 80^{0}C and enhanced sun drying; Midilli et al. and Page both were the best models for IR at 60^{0}C; Handerson & Pabis model for natural sun drying. The drying time was decreased with the increased of temperature. These results were similar with results in earlier study [13].

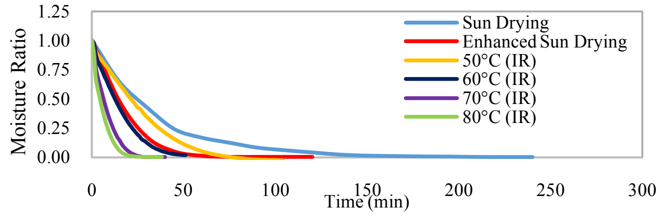

Fig. 3 Relationship between Moisture Ratio and Time

Fig. 4 illustrated the TPC in mint leaves dried using different drying method. TPC determined was between 14.77 mg GAE/g to 16.72 mg GAE/g. Enhanced sun drying (ESD) produced the highest TPC followed by IR-80^{0}C, IR-70^{0}C, IR-60^{0}C, IR-50^{0}C and the least by sun drying. ESD contained highest TPC might be due to there was only natural forces applied on leaves during drying and hence reduce the loss of phenolic. ESD had higher TPC than sun drying because ESD temperature was higher. For IR drying, TPC increased with temperature might be due to less drying time and hence less phenolic loss during drying. One-way ANOVA was used and it was found that the TPC between the extracts were statistically significant (p<0.05).

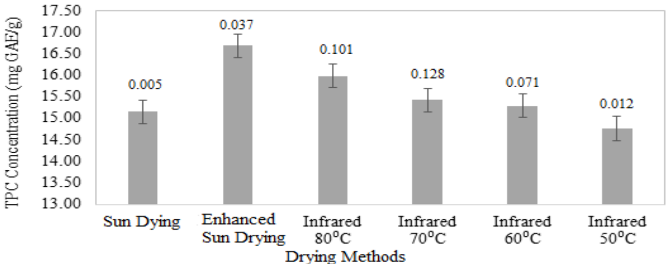

Fig. 4 Comparison of TPC in Different Drying Methods

5. Conclusions

For sun drying, the drying rate decreased with moisture content. For infrared drying, the drying rate decreased with moisture content after the samples were heated up to the desired temperature. Drying time decreased with the increase of temperature. Page was the best descriptive model for IR at 50^{0}C, 70^{0}C, 80^{0}C and enhanced sun drying; Midilli et al. and Page both were the best models for IR at 60^{0}C; Handerson & Pabis model for natural sun drying. Effective moisture diffusivity was in the range of 9.90×10^{-12} to $1.17 \times 10^{-11} m^2/s$. Range of TPC found in mint leaves was between $14.77\, mg\ GAE/g$ to $16.72\, mg\ GAE/g$.

Acknowledgment

My deepest thank goes to my family and friends for their constant support and encouragement. My gratitude for my supervisors' guidance throughout this research.

References

[1] Verma, S. M., Arora, H. & Dubey, R., "Anti-inflammatory and sedative - hypnotic activity of the methanolic extract of the leaves of Mentha arvensis," Ancient Science of Life, 2003.

[2] Suresh, S. N., Rathishkumar, S, Rajeshwari, V., Sagadevan, P., Gayathri1 S., & Eswari1 D. V., "Studies on phytochemical composition and antibacterial potential of methanolic leaf extract of Mentha arvensis. Linn," IJPRD, 2012.

[3] Mujumdar, A. S. & Menon, A. S., "Drying of solids," in Handbooks of Industrial Drying, 1st ed., New York, Marcel Dekker, Inc.

[4] Lewis, W. K., "The rate of drying of solid materials," Journal of Industrial Engineering, vol.13, pp.427-443, 1921, vol. 13, pp. 427-443.

[5] Akpinar, E.K., Bicer, Y., Cetinkaya, F., "Modelling of thin layer drying of parsley leaves in a convective dryer and under open sun," Journal of Food Engineering, vol. 75, pp. 308-315, 2006.

[6] Monica, P., Sharma, H. K., Sarkar, B. C. & Singh, C., "Kinetics of drumstick leaves(Moringa oleifera) during convective drying," African Journal of Plant Science, vol. 4, no. 10, pp. 391-400, 2001.

[7] Page, G., "Factors influencing the maximum rates of air drying shelled corn in thin layers," Indiana, USA, 1949.

8] Henderso,n S. M., Pabis, S., "Grain drying theory I. Temperature effect on drying coefficient," Journal of Agriculture Engineering Research, vol. 6, no. 3, pp. 169-174, 1961.

[9] Togrul, I. T., Pehlivan, D., "Modelling of drying kinetics of single apricot," *Journal of Food Engineering*, vol. 58, no. 1, pp. 23-32, 2003.

[10] Midilli, A., Kucuk, H., & Yapar, Z., "A new model for single layer drying," Drying Technology, vol. 20, pp. 1503-1513, 2002.

[11] Amin, T. G., Shahin, R., Alireza, K., "Study on Effective moisture diffusivity, activation energy and mathematical modeling of thin layer drying kinetics of bell pepper," Australian Journal of Crop Science, 2011.

[12] Akpinar, E. K., "Drying of mint leaves in a solar dryer and under open sun: Modelling, performance analyses," Energy Conversion and Management, vol. 51, no. 12, pp. 2407-2418, 2010.

[13] Akhondi, E., Kazemi, A., Maghsoodi, V., "Determination of a suitable thin layer drying curve model for saffron (Crocus sativus L) stigmas in an infrared dryer," Scientia Iranica, vol. 18, no. 6, pp. 1397-1401, 2011.

Nomenclature

M_0	Initial moisture content	$RMSE$	Root error square error
M_e	Equilibrium moisture content	D_{eff}	Effective moisture diffusivity
M	Moisture content	χ^2	Chi-square
M_t	Weight at time t	d	Half thickness of leaves
M_{t+dt}	Weight at time $t+dt$	$MR_{exp,i}$	Experimental moisture ratio
M_b	Bone Dry Weight	$MR_{pre,i}$	Predicted moisture ratio
dt	Time interval	R	Correlation coefficient
N	Number of observations	k, n, a, b	Empirical constants in the drying models
z	Number of constant		

Investigation of Flow across a Symmetrical Airfoil with Backward Facing Step

Yap Wai Kit*, Mushtak Al-Atabi

Mechanical Engineering, Taylor's University, Malaysia

**yap.kit07@gmail.com*

***Abstract*— Airfoil designers are in continuous pursuit of airfoils with the highest Lift Coefficient. One way to improve the Lift Coefficient is to introduce a backward facing step at the airfoil. This paper reports on a CFD studies to assess the effect of introducing backward facing step in NACA 0012 airfoil. Results show that introducing the backward facing step has improved the Lift Coefficient for Reynolds's number of 500000 over 15AoA. The CFD results were validated by comparing them to available experimental result and good agreement was reported.**

Keywords— Airfoil, Backward Facing Step, Lift Coefficient, CFD, Backward-step Simulation

1. Introduction

If an airfoil with good lift-to-drag ratio is used for an aircraft wing, this will be translated into lower fuel consumption, shorter take-off and landing times, and shorter runways [1]. Airfoils with backward facing step is a novel idea in the pursuit of designing airfoils with high Lift Coefficient [1]. This paper aims to study the flow across a symmetrical airfoil with a backward facing-step and also to determine which backward facing-step design gives the Lift Coefficient. When the fluid flows across the airfoil with a backward facing step, a vortex region which has a lower pressure will be created. This will reduce the wake region of the airfoil. The idea of backward-facing step airfoil originate from the idea of dimples on the golf ball where the dimples induce the creation of small vortex regions and help decrease the wake region of the golf ball. Hence, a golf ball with dimples will have lesser drag than a golf ball without. [2]

2. Methodology

An airfoil with NACA 0012 profile was selected for this study. A backward facing step of depth, *Du* and length, *lu* was introduced as shown in Fig. 1. The airfoil was modelled using the CFD software *ANSYS FLUENT*. The flow field and boundary conditions are shown in Fig. 2. The results from the CFD simulations were used to compute the lift and drag for the three airfoil designs. The three designs were selected based on the experimental result from previous work[1]. A C-domain mesh was used in order to determine the boundary condition whereby it had a velocity inlet and a pressure outlet. Similar results were reported by previous work [1].

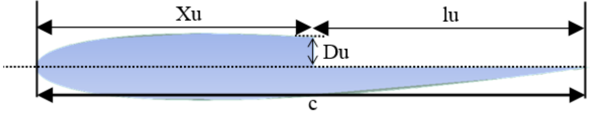

Fig. 1 Geometry Parameter of the airfoil

In CFD, different turbulence models were used in the simulation for the flow across the airfoil. Three models were being tested to investigate the flow. The Spalart-Allmaras tubulence model is an equation model designed specifically for the analysis of airfoils and streamlined bodies. The k-ω SST (Shear Stress Transport) turbulent model is an improved version of the standard k-ω turbulence model which provides more accurate results in near-wall regions [3]. The standard k-ε turbulence model is a model which attempts to solve flow problems through two transport equations which are the turbulent kinetic energy and also the turbulent dissipation rate equations [4]. There is also an improved version of k-ε model which prescribes the tubulent length scales algebraically from medium to high complexity flows [5]. Each of the cases are kept at a constant Reynold's Number, which is 500000, with a velocity inlet of 7.3m/s whereby the working fluid is air. The Reynold's Number is kept at 500000 in order to compare with the experimental result done by Finaish F and .. Witherspoon S [1].

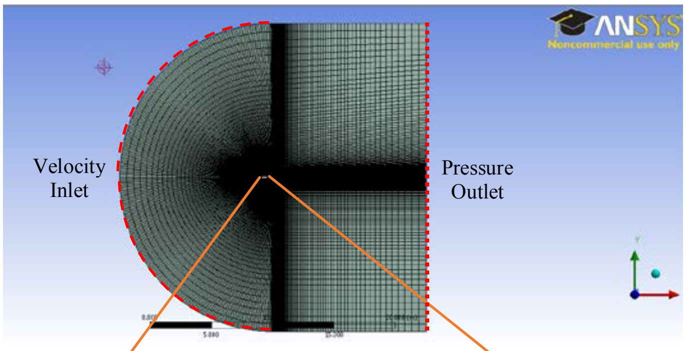

Fig. 2 C-Domain mesh of the computational model

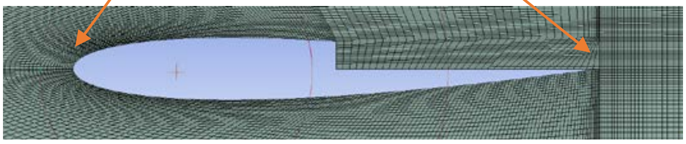

Fig. 3 Close up view of the meshing around the airfoil

3. Result and Discussion

The results are tabulated in a graph and was compared and validated with the experimental result from previous works [2]. Fig. 4 shows the coefficient of lift generated by an airfoil using different turbulence models used in CFD at varying angles of attack (AoA). This simulation is done to determine the best turbulence model before conducting further simulations. It is shown in the Fig. 4 that the k-ω SST turbulence model provides the closest result to the experimental results among all other turbulence models. Thus, k-ω SST turbulence model will be used in generating results for lift and drag coefficients in further simulations.

Fig. 6 shows the changes in Lift Coefficient (C_L) against step depth (Du) when α is 15°. In Fig. 5, it shows that when the airfoil has an AoA of 15° and a step depth of 0.50, the airfoil will have the greatest C_L from experimental data and CFD results.

Fig. 6 and Fig. 7 show the air flow across a NACA 0012 airfoil with 0.5 Du at 15° AoA. In Fig. 7, it shows that the velocity of the air is slower at the backward facing-step region compared to the lower surface of the airfoil. Additionally, a clockwise direction vortex can be observed in the backward facing step region generating lift [6].

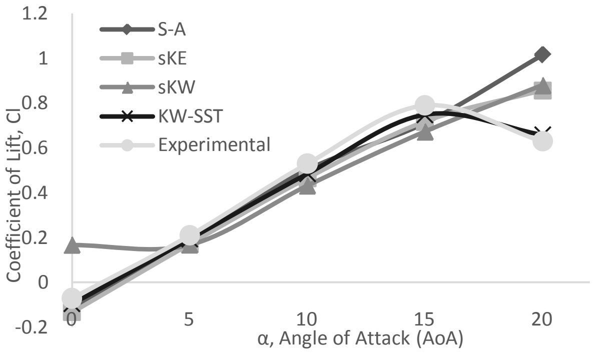

Fig. 4 Effects of turbulence models on C_L at various AoAs.

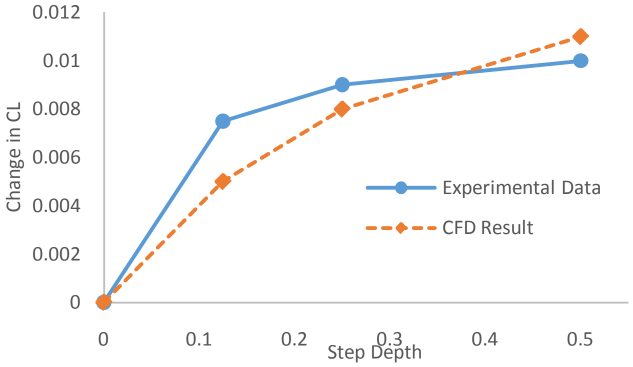

Fig. 5 Graph of change in C_L against Step Depth (Du), α= 15 Degree

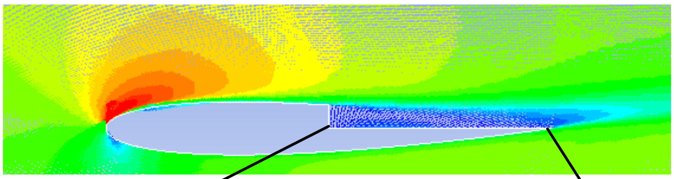

Fig. 6 Velocity Vector plot over Airfoil with 0.5 Du at 15° AoA

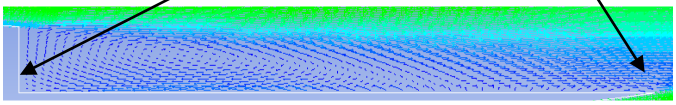

Fig. 7 Velocity Vector plot of Step region of Airfoil.

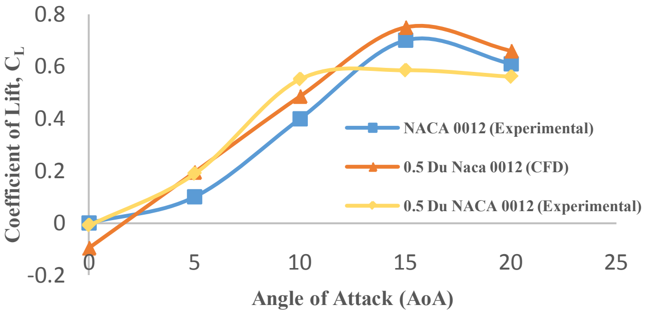

Fig. 8 Lift Coefficient of NACA0012 with and without backward step

The coefficient of lift is proven to be higher for NACA 0012 with backward facing step in Figure 8 and it is validated with the experiment done by Robert E. S. and Paul C. K [7]. At AoA of 10, 15 and 20 degree, it shows that backward facing step on the airfoil will increase the coefficient of lift by 0.05, which proves that the vortices formed at the backward facing step have created lift. The wind tunnel result generated on 0.50 Du NACA 0012 airfoil is also shown in Figure 8. A measurement uncertainties of 14% recorded from the result generated from wind tunnel. It's shown that the result generated from the wind tunnel share the same pattern of graph despite the 14% errors shown.

4. Conclusion

Different CFD turbulent models have been used in order to study the flow and it is found out that k-ω SST turbulent model is the most suitable turbulence model to be used despite Spalart-Allmaras turbulence model being specifically designed for aerospace applications [8]. From the investigation of the flow across NACA 0012 airfoil with backward facing-step, it is concluded that the airfoil with a step depth of 0.50c will generate more lift as compared to step depths of 0.25c and also 0.125c due to the vortex created by the airfoil with 0.50c step depth being greater than that of 0.125c and 0.25c which leads to a greater reduction in wake region. Wind Tunnel studies is proved to be useful in this case whereby the result can be enhanced by using a full-scaled geometry of the airfoil. Hence, airfoil with backward facing step on the upper surface is able to generate a higher lift as compared to the conventional airfoil.

Acknowledgment

We would like to thank Taylor's University School of Engineering for the funding and equipment support of this project.

Nomenclature

c	- Chord length
Du	- Step depth
Lu	- Length of step
Xu	- Distance from leading edge to step leading edge
α	- Angle of Attack (AoA)
C_L	- Coefficient of Lift

References

[1] Finaish F and .. Witherspoon S, "Aerodynamic Performance of an Airfoil with Step-induced Vortex for Lift Augmentation," *Journal of Aerospace Engineering,* vol. 2, no. 1, pp. 9-16, 1998.

[2] C.H. TAI, C.-Y. CHAO, J.-C. LEONG, Q.-S. HONG, "Effects of golf ball dimple configuration on aerodynamics, trajectory, and acoustics," International Conference: BAIL 2006, Boundary and Interior Layers, Computational & Asymptotic Methods, pp. 145-146, 2006

[3] G. Fertis D, "New Airfoil-design Concept with Improved Aerodynamic Characteristics," *Journal of Aerospace Engineering,* no. 7, pp. 328-339, 1994.

[4] W. a. L. B. E. Jones, "The Prediction of Laminarization with a Two-Equation Model of Turbulence," *International Journal of Heat and Mass Transfer,* vol. 15, pp. 301-314, 1972

[5] B. E. a. S. B. Launder, "Application of the Energy Dissipation Model of Turbulence to the Calculation of Flow Near a Spinning Disc," *Letters in Heat and Mass Transfer,* vol. 1, no. 2, pp. 131-138, 1974

[6] P. D. M. al-Atabi, "Flow around Symmetrical Airfoil with Backward Facing Step," in *14th International Symposium on Flow Visualization,* Daegu, South Korea, June 2010.

[7] R. E. S. a. P. C. K, Aerodynamics Characteristic of Seven Symmetrical Airfoil through 180 degree angle of attack for use in Aerodynamic Analysis of Vertical Axis Wind Turbine, Springfield: United States of National Technical Information Service, 1981.

[8] E. D. C., A. T. I. and D. M. P., "Evaluation of turbulence models for the simulation of the flow over a National Advisory Committee for Aeronautics (NACA) 0012 airfoil," *Journal of Mechanical Engineering Research,* vol. 4, no. 3, pp. 100-111, March 2012.

Arsenic Biological Interaction Kinetics in Wastewater

Yee W. See.[1*], Marwan M. Shamel[1]

[1]*School of Engineering, Taylor's University, Malaysia*

**Corresponding author: yee.waisee@sd.taylors.edu.my*

Abstract— **Two microbes species isolated from ash samples obtained from a local coal-fired power plant were experimented in As(V)-infused nutrient broth solution under different growing parameters to study the biological interaction. In four bottles of 250 ml As(V)-infused phosphate buffered broth solution, each microbe species were added into each bottle with dosage 50:1 and 100:1 and incubated at 37 ℃ for 24 hours. The experiment is repeated with 45 ℃ amd 55 ℃ to obtain optimum growing temperature. Samples were collected every 4 hours for absorbance measurement and As(V) analysis. The optimum growing temperature was experiment to be 37 ℃ while dosage is 50:1. However, the species was not able to reduce As(V) concentration in solution due to adsorption inhibition.**

Keywords— Coal-fired power plant, microbiology, fly ash, arsenic, wastewater

1. Introduction

Human activities that reclaim arsenic (As) containing natural resources caused the As compound to be unleashed to the environment. One of the biggest contributors is the combustion of coal in power generation industry. The path of As travels into water starts from the combustion of coal containing As. After burning of coal, As is associated more with fly ash than bottom ash due to its volatility [1]. Moreover, pentavalent arsenic (As(V)) stands a more substantial amount compared to trivalent arsenic (AS(III)) [2]. The fly ash is sent to water impoundment after being separated from the air pollution control equipment. As in the fly ash is then transferred from the coal to the fly ash and at last to the water in the impoundment area. The impoundment water rich with As then posed pollution problem to the environment. There are techniques to treat the As-contaminated water that are generally expensive in terms of capital cost and maintenance including ion exchange [3], reverse osmosis [4] and membrane technologies [5]. This research will focus in developing a technique of microbiological treatment for contaminated water from coal-fired power plant with rather low cost and high efficiency using the strain of microbes isolated from ash samples obtained locally. Microbiological treatment of wastewater containing heavy metals had been proven to be workable in numerous literatures [6, 7]. The mode of biological interaction is also proven to be adsorption by several literatures [8, 9].

2. Experimental Design

2.1. Materials

Ash samples were obtained from a local coal-fired power plant, Jimah Energy Ventures Sdn. Bhd. Agar plates and broth solution were prepared using Nutrient agar (Merck Millipore) and Nutrient broth (Merck Millipore) powder. To maintain the growth of microbes within pH 7, any growth related experiments were conducted in phosphate buffered solution. Phosphate buffered solution consisted of Disodium Hydrogen Phosphate (Na_2HPO_4, Fisher Scientific, A.R. ≥99.5%), Potassium dihydrogen Phosphate (KH_2PO_4, R&M Chemicals, C. P., ≥98%), Sodium Chloride ($NaCl$, R&M Chemicals, A.R., ≥99.5%) and Potassium Chloride (KCl, R&M Chemicals, A.R., ≥99.5%) [10]. Solution that involves arsenic was prepared using Sodium Hydrogen Arsenate Heptahydrate ($NaHAsO_4 \cdot 7H_2O$, R&M Chemicals, A.R., ≥98.5%).

To minimize contamination of assays, preparation of agar and broth not containing As(V) was carried out under ESCO Labculture® Vertical Laminar Flow Cabinet. Sterilization of agar solution and instruments was carried out using Autoclave (WAC-60, Daiman Scientific, Taiwan). However, any preparation of solution involving As(V) was carried out under fume hood equipped with scrubber as a safety measure. Respirator was also required when dealing with As(V) as well as chemical resistant gloves.

2.2. Methods

Preparation of Diluted Ash Sample [11]

One gram of ash sample was added into a beaker filled with 99 ml of distilled water. This forms a diluted ash sample with concentration of $10^{-2}\ g/ml$. Then, 1 ml of the mixture was transferred to a universal bottle filled with 9 ml of distilled water which forms another diluted ash sample of $10^{-3}\ g/ml$. The dilution was repeated until concentration of $10^{-6}\ g/ml$ is obtained. (Serial dilution)

Culturing Microbe with As(V)-infused Nutrient Agar

A stock solution of 10 ppm of As(V) was prepared first by mixing 0.042 g of sodium hydrogen arsenate heptahydrate in 1 L of distilled water. Due to safety reasons, student was allowed to work with maximum concentration of 10 ppm. Subsequently, nutrient agar infused with 10 ppm and 5 ppm of As(V) was prepared by mixing appropriate amount of As(V) stock solution into nutrient agar powder and distilled water. Lastly, solidified agar plates with different concentration of As(V) were streaked with $10^{-6}\ g/ml$ diluted ash sample and placed in incubator (Froilabo, France) at 37 ℃ for 24 hours.

Optimization of Parameters and Growth Curve Determination

Two parameters were studied for the maximum growth of microbe species isolated from the ash sample. Single colony isolated from ash was grown in a mixture solution consisting of nutrient broth, As(V) and phosphate buffer content at 37 ℃, 45 ℃ and 55 ℃ [12] with different ratio of cells which are 50:1 and 100:1 [12]. Data were extracted by measuring absorbance of solution every 4 hours [12] using UV-vis spectrophotometer (Dynamica, RB-10). In parallel, growth curve of species of microbe was determined.

Reduction Kinetics of Isolated Species on As(V)

Microbes isolated from diluted ash sample were grown in a mixture of nutrient broth, phosphate buffered solution and 10 ppm As(V) under optimum parameters including dosage and temperature. Samples were collected every 4 hours. Immediately after collection, samples were acidified and refrigerated. Collected samples were then centrifuged with 15000 rpm for 20 minutes at 4 ℃ [6]. Supernatant was retained for analysis of As(V) concentration using ICP-OES (D7000, Perkin-Elmer).

3. Results and Discussion

3.1 Effect of Concentration of As(V) on Growth of Microbes

There were initially two species of microbes successfully isolated from the ash samples prepared differentiated by colours namely yellow, Y and white, W. In the 5 ppm As(V) agar plate, growth was more compared to agar plate with 10 ppm As(V). This shows that more As(V) in the nutrient agar can restrict the growth of microbes.

The two species of microbes isolated from diluted ash sample are of the same *Burkholderia* genus is as shown in Figure 1.

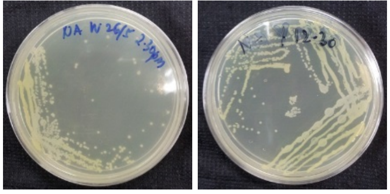

Figure 1: Left: White and Right: Yellow.

3.2 Growth Curve

The growth curve of species W and Y are plotted as shown in Figure 2. Visible light with wavelength 400 nm were used throughout the analysis of absorbance of the solution as the peak of wavelength occurs at this point.

Figure 2 shows the growth of W and Y at 37 °C which was the experimented optimum temperature at different ratio of substrate to biomass 50:1 and 100:1. Here, 50:1 indicates 5ml of microbes stock in the initial volume of mixture solution which is 250 ml, where 100:1 indicates 2.5 ml of microbes stock.

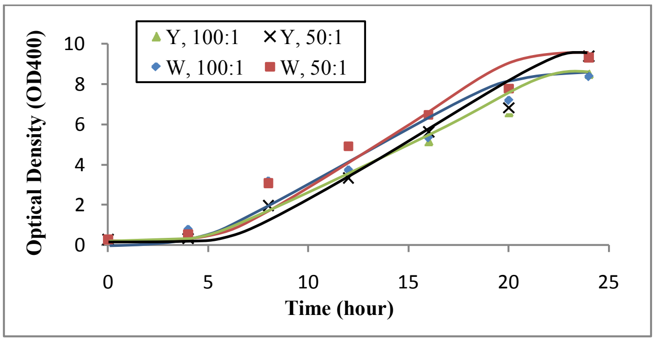

Figure 2: Colony W and Y Growth Curve at 37 °C.

As shown in the growth curve of both colonies, lag phase is overcome within 4 hours' time. Similarly, as presented by Marwan M. S. et al [12], the species of microbe experienced lag phase of 4 hours, and also have the optimum temperature of 37 °C. In the growth curve in Figure 2, both W and Y showed equal growing ability with different ratio of substrate to biomass respectively. It is observed that growth curve with dosage of 50:1 for both W and Y overcame the exponential phase faster than growth curve exhibited in dosage 100:1. However, growth curve for dosage 50:1 reaches stationary phase earlier than 100:1. The different growth curve characteristic shown by different dosage of microbes in the broth solution has its impact on the design of bioreactor in the future. For instance, when the maximum yield of product is not considered and non-productive stages are undesirable, lower dosage of microbes in reactor is preferred. Vice versa, when the highest production rate is concerned, higher dosage is more feasible.

3.3 Reduction of As(V) in Solution

It was intended to utilize the colonies isolated from diluted ash sample to examine their reduction kinetics in the synthetic wastewater. Samples collected each 4 hours which centrifuged and refrigerated are analysed using ICP-OES.

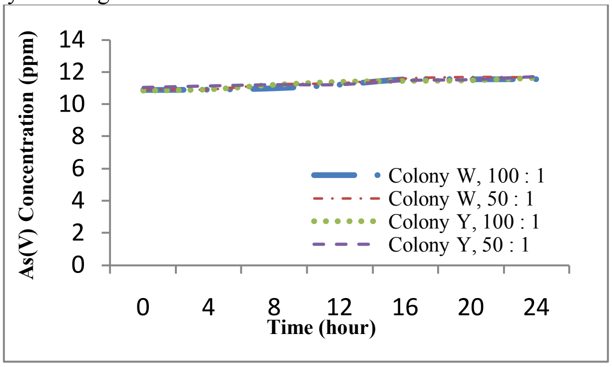

Figure 3: Reduction of As(V) in Samples.

Referring to Figure 3, it is observed that the concentration of As(V) did not reduce as time increases. This situation was investigated to be caused by phosphate originated from phosphate buffered solution. Phosphate is a structural analog with arsenate and resulted in uptake inhibition to the microbes' membrane [13]. The phosphate is loaded into the cell through a membrane-associated phosphate transporter rather than targeted As(V). This has been proven by Slaughter et. al. [13], Harold et. al. [14] and numerous researchers.

4. Conclusion

The research experiments had been conducted under controlled and limited conditions. Two species of bacteria from the same species had been successfully isolated from the ash sample and showed resistant characteristic towards As(V) in the broth solution. They were found growing best under 37 °C and dosage 50:1. However, the kinetics studies were not able to be performed due to adsorption inhibition of As(V) by phosphate originated from buffered solution.

Acknowledgment

I would like to thank Associate Professor Dr. Marwan in guiding me all the way towards the end of the research and also Dr. Kaveh in assisting me to analyse samples containing As(V) using ICP-OES equipment.

References

[1] Y. E. Yudovich and M. P. Ketris, "Arsenic in Coal: a review," *International Journal of Coal Geology,* vol. 61, pp. 141-196, 2005.

[2] F. E. Huggins, J. J. Helble, N. Shah and J. Zhao, "Forms of Occurrence of Arsenic in Coal and Their BBehavior During Coal Combustion," Argonne National Laboratory, Chicago.

[3] C. K. Jain and R. D. Singh, "Technological options for the removal of arsenic with special reference to South East Asia," *Journal of Environmental Management,* vol. 107, pp. 1-18, 2012.

[4] A. H. Malik, Z. N. Khan, Q. Mahmood, S. Nasreen and Z. A. Bhatti, "Perspective of low cost arsenic remediation of drinking water in Pakistan and other countries," *Journal of Hazardous Materials,* vol. 168, pp. 1-12, 2009.

[5] L. M. Camacho, M. Gutierrez, M. T. Alarcon-Herrera, M. d. L. Villalba and S. G. Deng, "Occurrence and treatment of arsenic in groundwater and soil in northern Mexico and southwesthern USA," *Chemosphere,* vol. 83, pp. 211-225, 2011.

[6] E. Chockalingam and S. Subramaniam, "Studies on removal of metal ions and sulphate reduction using risk husk and Desulfotomaculum nigrificans with reference to remediation of acid mine drainage," *Chemosphere,* vol. 62, pp. 699-708, 2006.

[7] K. L. Shuttleworth and R. F. Unz, "Sorption of Heavy Metals to the Filamentous Bacterium Thiothrix Strain A1," *Applied and Environmental Microbiology,* vol. 59, no. 5, pp. 1274-1282, 1993.

[8] N. Yee and J. Fein, "Cd adsorption onto bacterial surfaces: A universal adsorption edge?," *Geochimica et Cosmochimica Acta,* vol. 65, no. 13, pp. 2037-2042, 2001.

[9] M. Monachese, J. P. Burton and G. Reid, "Bioremediation and Tolerance of Human to Heavy Metals through Microbial Processes: a Potential Role for Probiotics?," *Applied and Environmental Microbiology,* vol. 78, no. 18, pp. 6397-6404, 2012.

[10] Cold Spring Harbour Laboratory Press, "Phosphate-buffered saline (PBS)," *Cold Spring Harbor Protocols,* 2006.

[11] M. T. Madigan, J. M. Martinko, D. A. Stahl and D. P. Clark, Brook Biology of Microorganisms, San Francisco: Benjamin Cummings, 2011.

[12] M. S. Shamel, K. C. Ho, Y. K. Fang, F. Ahamed and A. Hartanto, "Treatment of arsenic in the effluent of a coal fired power plant," in *11th International Conference on Sustainable Energy Technologies (SET-2012),* Vancouver, 2012.

[13] D. C. Slaughter, R. E. Macur and W. P. Inskeep, "Inhibition of microbial arsenate reduction by phosphate," *Microbiological Research,* vol. 167, pp. 151-156, 2012.

[14] F. M. Harold and J. R. Baarda, "Interaction of Arsenate with Phosphate-Transport Systems in Wild-Type and Mutant Streptococcus faecalis," *Journal of Bacteriology,* vol. 91, no. 6, pp. 2257-2262, 1966.

The Effect of Synthetic Jet Mixing on Enzyme Activity

Yeong Leong Lim[1*], Marwan M. Shamel[2]

[1,2] Department of Chemical Engineering, Taylor's University, Malaysia.

*lim.yeongleong@sd.taylors.edu.my

Abstract – **Conventional mixing process is normally involved with high shear stresses, which makes the enzyme tend to denaturalize. Enhancement in enzymatic kinetics in batch reactor and power consumption by using novel flow pulsing mechanism termed 'synthetic jet' was studied. The effect of the oscillating frequency and amplitude will be comparing with conventional overhead stirrer on enzyme kinetics and denaturalization. Synthetic jet has proven with higher enzymatic kinetics and lesser enzyme denaturalizes compared with conventional mixer.**

Keywords— Synthetic Jet, Enzyme, Mixing, Denaturalization rate, Kinetics

1. Introduction

Mixing of enzyme and microorganisms [1] is applied in pharmaceutical and biological processes. Conventional mixing process is normally involved with high shear stresses which able to deteriorate the protein structure of enzyme [1]. Besides that, it consumes high electrical power. Other than that, when high shear rates is applied, enzyme and microorganisms tend to denaturalize and degrade, respectively [1].

In engineering fluid systems, researchers investigating the synthetic jet application have been on-going in flow control for different geometries. For example in aircraft aerodynamics, jet flow control can result in improved airframe efficiency and reduced jet noise where the flow control can be active or passive. For jet flows, active flow control traditionally uses mechanical systems such as gimbaled nozzles and movable surfaces. However, there is an advantage for fluidic jet flow control which involves flow field manipulation by zero mass flux if compared with the traditional mechanical actuating methods. These include higher response rates, precise control and improved lifetime [2].. These fluidic systems include synthetic jets, voice coil actuator and piezoelectric actuators [2].

The actuator mounted under the synthetic jet reactor to cause the Polytetrafluoroethylene (PTFE) or Teflon diaphragm that moves oscillating at fixed amplitude and frequency forcing water jet flow through 4mm orifice. In its inward motion, the diaphragm imparts a high-speed jet into the synthetic jet reactor creating a pair of counter-rotating vortices in the surrounding fluid. When retrieving, it draws fluid back into the cavity. The fluid ejected through the orifice and the vortices periodically interrupt and interact in cross-flow manner with the synthetic jet reactor fluid flow. Over one diaphragm cycle, the jet discharges an intense net outflow of fluid momentum into the synthetic jet reactor while the net mass delivered through the orifice is zero as it known as Zero-Net-Mass-Flux jet [3].

In this study, synthetic jet mixer will be used to reduce the external diffusion limitations for an enzymatic reaction. The power consumption, enzyme kinetics and rate of denaturalization of enzyme this mixing method will be compared with conventional overhead stirrer bioreactor, also known as Stirred Tank Reactor (STR), where the applied shear will be applied on the enzyme solution with impeller. This study aims to understand the enzyme kinetics, enzymes' denaturalization and power consumption during the course of mixing using synthetic jet mixers [4]. The other studied parameters will be range of oscillating amplitude and frequency.

2. Materials and Methods

2.1 Materials

Lipase from *Candida* expressed in *Aspergillus* (Lipozyme CALB-L) with activity of 100 kLU/ml is obtained from Novozyme Malaysia Sdn. Bhd.. Besides that, analytical grade of tributyrin oil (98 %) is obtained from Fisher Scientific (M) Sdn. Bhd. Anhydrous glycerin (99.5 v/v%) and sodium hydroxide pellet both with analytical grade is obtained from LGC Scientific Malaysia.

2.2 Substrate Emulsion

Dissolve 8.95 g of NaCl and 0.2 g of KH_2PO_4 in 230 ml distilled water with 270 ml of glycerol. Under vigorous stirring, add 3.0 g of Gum Arabic to the mixture until it homogenizes. Under vigorous stirring, mix 50 ml of emulsifying reagent with 3.0 ml of tributyrin oil and 298.0 ml of distilled water [5].

2.3 Synthetic Jet Mixer

Synthetic Jet Mixer, hereof defined as the assembly of a transparent tube with 150 mm diameter and 170 mm height which made from Poly(methyl methacrylate), a module made with stainless steel 316L with 80 mm diameter and 20 mm height, Polytetrafluoroethylene (PTFE) or Teflon diaphragm with 80 mm diameter and 1 mm thickness as well as the solenoid actuator.

2.4 Enzyme Kinetics

2.00 liters of substrate emulsion solution will be placed in the synthetic jet mixer. 500 µL of pure lipase with 100 kLU/ml was added into the synthetic jet mixer and the actuator will be activated. 20 ml of the samples will be taken every 10 minutes and the sample will be heated with Bunsen burner for 5 minutes. Titration will be done with autotitrator and record the total volume of NaOH (0.05 M) required achieving pH 7.00. The enzyme kinetics will be compared with conventional overhead stirrer mixer [5].

2.5 Enzyme Deactivation

2.00 liters of distilled water will be placed in the synthetic jet mixer. 500 µL of pure lipase with 100 kLU/ml was added into the synthetic jet mixer. The optimum value for oscillating frequency and amplitude of synthetic jet mixer obtained from enzyme kinetics will be implementing on the actuator and measure the activity loss of the enzyme. The result will be compared with conventional overhead stirrer [4] [5].

2.6 Power Consumption

Power consumption is the product of voltage (r.m.s) and current (r.m.s). The measurement of voltage and current is been made with data acquisition device, model name NI USB-6009 from National

Instrument Malaysia, where the device is able to monitor the real time voltage flow. The current flow will be measured with current transducer (HXS 50-NP) from LEM USA. The current transducer is able to convert current flow to analog voltage output. Software programming with National Instrument LabView 2012 is been done with the voltage and current monitoring and the r.m.s value of them.

3. Result and Discussions

3.1 Enzyme Kinetics

The effect of oscillating frequency and amplitude of synthetic jet mixer on total moles of substrate consumed was examined at the range of frequency 5 Hz to 15 Hz as well as 0.5 mm and 1.0 mm of oscillating amplitude. Increasing of frequency will result in reduction of rate of enzymatic reaction. Besides that, increased oscillating amplitude will also have the same result. However, at 5 Hz oscillating frequency, rate of reaction for 0.5 mm oscillating amplitude is more than 1.0 mm amplitude. These results are compared with rate of reaction for conventional overhead stirrer mixer. Table 1, 2 and 3 shows the result of the total substrate consumed with overhead stirrer and synthetic jet mixer. Table 3 shows that synthetic jet mixer at 5 Hz and 1.0 mm oscillating amplitude has the highest enzyme kinetics.

Table 1: Substrate Consumed (Moles) for Overhead Stirrer Mixer

Time (minutes)	Stirrer	
	300 rpm	600 rpm
10	0.00862	0.00611
20	0.01011	0.00990
30	0.01191	0.01189
40	0.01452	0.01393
50	0.01589	0.01587
60	0.01621	0.01628

Table 2: Substrate Consumed (Moles) for Synthetic Jet Mixer at 0.5 mm Oscillating Amplitude

Time (minutes)	Synthetic Jet @ 0.5 mm amplitude		
	5 Hz	10 Hz	15 Hz
10	0.00722	0.00720	0.00674
20	0.00994	0.00986	0.00979
30	0.01250	0.01238	0.01230
40	0.01465	0.01431	0.01400
50	0.01533	0.01502	0.01480
60	0.01598	0.01554	0.01553

Table 3: Substrate Consumed (Moles) for Synthetic Jet Mixer at 1.0 mm Oscillating Amplitude

Time (minutes)	Synthetic Jet @ 1.0 mm amplitude		
	5 Hz	10 Hz	15 Hz
10	0.00721	0.00402	0.00371
20	0.01089	0.00715	0.00697
30	0.01401	0.00943	0.00812
40	0.01515	0.01072	0.00955
50	0.01691	0.01151	0.00999
60	0.01796	0.01220	0.01015

3.2 Enzyme Denaturalization

The effect of synthetic jet mixer and overhead stirrer mixer on the rate of denaturalization of enzyme was investigated for 2.5 hour and the 1 ml of the sample will be taken. Enzyme solution with same concentration without any mixing will be used as the control. Control has 8.10 % activity loss at 2.5 hours) while synthetic jet mixer has the lowest enzyme loss in percentage (10.13 % at 2.5 hours) and overhead stirrer mixer with 600 rpm can contribute the 18.98 % of activity loss at 2.5 hours.

Figure 1: Activity Loss of Enzyme over Time

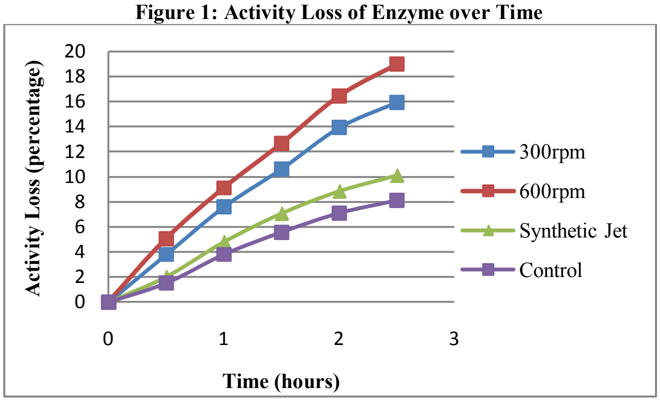

3.3 Power Consumption

The power consumption of the synthetic jet mixer at 5 Hz and 1.0 mm oscillating amplitude is compared with the conventional overhead stirrer at 300 rpm and 600 rpm. Table 4 shows the voltage (r.m.s), current (r.m.s) and power consumption of the mixer.

Table 4: Voltage, Current and Power Consumption of the mixer expressed as Root Mean Square value (r.m.s).

Device	Voltage (V)	Current (A)	Power (W)
Overhead Stirrer @ 300 rpm	240.0	0.094	22.51
Overhead Stirrer @ 600 rpm	240.0	0.111	26.64
Synthetic Jet @ 5Hz, 1.0 mm	11.0	0.350	3.85

4. Conclusion

In overall, the effect of increasing oscillating amplitude has contributed in the reduction of the reaction rate, particularly for frequency at 10 Hz and 15 Hz. However, the effect of increasing oscillating amplitude on 5 Hz had increased the reaction rate. The effect of increasing oscillating frequency for all oscillating amplitude had contributed the reduction of the reaction rate.

As conclusion, synthetic jet mixer has better performance in enzyme kinetics, lower rate of denaturalization of enzyme and lower power consumption compared with conventional overhead stirrer mixer.

Acknowledgment

The authors wish to convey their appreciation to Taylor's University for funding this research project. The author also wishes to acknowledge Dr. Marwan for his supervision and guidance. Additionally, we would also like to acknowledge Professor Mark Simmons of the University of Birmingham for providing the particle image velocimetry apparatus for this project.

Reference

[1] K. Buchhloz, V. Kasche and U. T. Bornsheuer (2005), Biocatalysts and Enzyme Technology, Weinheim: Wiley-VCH Verlag GmbH & Co. KGaA

[2] T. T. Chandratilleke, D. Jagannatha and R. Narayanaswamy (2010), *International Journal of Thermal Science*, vol. 49, pp. 504-513.

[3] N. J. Lawson, M. P. Arruda and M. R. Davidson (2005), "Control of a Submerged Jet in a Thin Rectangular Cavity," *Journal of Fluid and Structures*, vol. 20, pp. 1025-1042.

[4] R. L. Stein, Kinetics of Enzyme Reaction, Hoboken: John Wiley & Sons, Inc, 2011.

[5] S. AL. Zuhair (2006), "Kinetics of Hydrolysis of Tributyrin by Lipase" *Journal of Engineering Science and Technology*, vol. 1, pp. 50-58.

Investigation of Blood Flow through the Mitral Valve

Yvonne H.L. Lim*, Mushtak Al-Atabi

School of Engineering, Taylor's University, Malaysia

*yvonne.limhuili@sd.taylors.edu.my

Abstract — **The mitral valve is located in the heart. It controls the unidirectional blood flow from the left atrium to the ventricle. Due to various reasons, the mitral valve and its chordae may be damaged, causing mitral regurgitation. The purpose of this study is to examine the blood flow through the mitral valve in both experimental and numerical heart models, aiming to develop a reliable protocol to assess the effectiveness of various mitral valves repair methods.**

Keywords — Mitral valve, surgical repair methods, flow visualisation, computational fluid dynamics

1. Introduction

The mitral valve is a heart valve located between the left atrium and left ventricle. It opens when the left ventricle relaxes, allowing blood to flow into the ventricle from the left atrium; it closes when the left ventricle relaxes, preventing blood in the ventricle from flowing back into the atrium. The mitral valve consists of the mitral valve leaflets and the subvalvular apparatus, namely, the chordae tendinae and papillary muscles.

At times, the mitral valve fails due to damaged subvulvular apparatus, such as the loosening of the chordae tendinae, which are the chords preventing the valve from flopping back into the atrium causing a condition known as mitral valve prolapse which causes regurgitation of blood back into the atrium [1].

There are various methods of repairing the mitral valve surgically [2]. Different medical professionals have different opinions of which surgical repair method is most effective. Due to ethical reasons, surgeons cannot test these methods on patients. According to the Hippocratic Oath which states that as medical professionals, they should first do no harm [3], therefore surgeons are not to treat patients with any method that they do not consider the best. There have been attempts to test the effectiveness of surgical repairs in vitro based on pressure drop required to cause mitral valve prolapse which have been carried out by Espino et al [4].

The objective of the study is to develop a platform to visualize the flow structure through a mitral valve, with the aim of further developing it into an effective protocol to assess the effectiveness of mitral valve repair in vitro.

2. Methodology

This research is carried by experimental means. Computational fluid dynamics models are generated and used for validation purposes.

2.1 Experimental

2.1.1 Mitral Valve Extraction

The heart valves were extracted from porcine hearts which were stored in the refrigerator before use. The mitral valve was removed by extracting a section with the mitral valve annulus and the anterior and posterior leaflets papillary muscles.

2.1.2 Experimental design

The mitral valve annulus is sutured onto a ring structure to attach specimen to the experimental set-up. The papillary muscles of the mitral valve specimen are attached to a wire set-up which is connected to the ring structure.

The set-up is shown in the Fig. 1 below. Water is used as the blood analogue fluid. The manometer is used to measure the pressure drop.

The flow of the fluid in the apparatus is visualized using silver coated hollow glass beads at 10µm particles illuminated by a scattered laser beam. A DSLR camera (Nikon D7000) was mounted on tripod. A shutter speed of 1/6s was used with an ISO of 100 and an aperture of f/16.

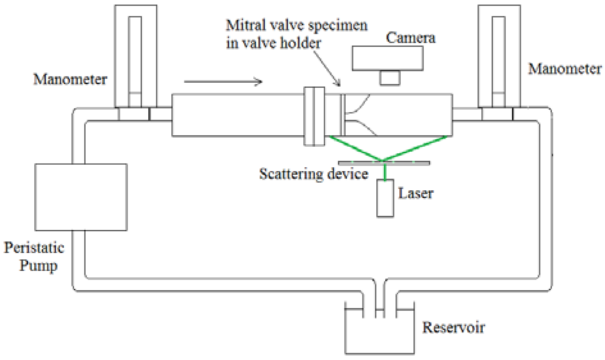

Fig. 1 Experimental Set-up

2.2 Numerical Simulation

Numerical simulation was carried out using computational fluid dynamics is ANSYS FLUENT ©. 2-dimensional geometries of the left atrium and ventricle with opened and closed mitral valve were generated using echocardiographic measurements of the left heart chambers [5]. The open valve is simulated with the inlet at the left atrium and no outlet. The closed valve is simulated with the inlet at the apex and the outlet at the left ventricular outflow tract.

A 2D simulation of the experimental set-up was also performed which is to be evaluated against the experimental results. Half of the geometry was generated and the bottom axis was used as a mirror to reflect the geometry generated to obtain a plane from the experimental results.

A steady-state simulation using glycerin as the fluid was carried out. This is because a solution of glycerin has similar properties as blood. The density and viscosity of glycerin used is $1060 kg/m^3$ and 0.0027Pa.s respectively [6]. The velocity of the fluid flow is 0.12 m/s, representing blood flow through the mitral valve into the left ventricle. No-slip conditions were used for the walls; this includes the walls of the valves. The turbulence model used was realizable k-ε turbulence model. The simulation was carried out using the SIMPLE solver.

3. Results and Discussion

The results from the experimental and numerical simulation are reported.

3.1 Experimental Results

It is seen from the experimental results in Fig. 2 that flow through a healthy mitral valve produces two vortices behind the mitral valve leaflets.

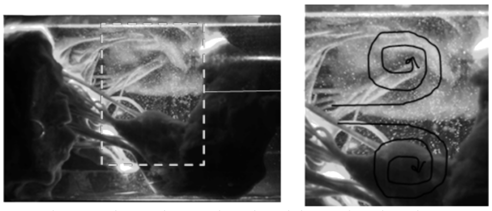

Fig. 2 Flow through a healthy mitral valve

Velocity increases as water passes through the mitral valve annulus. The flow decelerates as the cross sectional area increases when the flow emerges from the annulus. The boundary layer separates when water passes through the leaflets causing flow in opposite directions, thus generating vortices [7]. The formation of vortices is important in the flow of blood in the heart. The energy generated by the swirl helps propel the flow out of the ventricle.

3.2 Numerical Results

The simulation results were compared to the visualization of blood flow through the mitral valve in vivo using various imaging technologies. The result was validated with pathline visualization of 4D velocity mapping using cardiovascular magnetic resonance imaging, CMR [8].

For the opened mitral valve, it can be seen that CMR image of left ventricular during diastasis, the middle stage of the ventricular relaxation; is similar to the numerical simulation results generated. Two vortices are formed in the simulated results, the two vortices are also formed in the heart during diastasis.

(a)

Fig. 3a Velocity vector of simulated flow through an open mitral valve

(b)

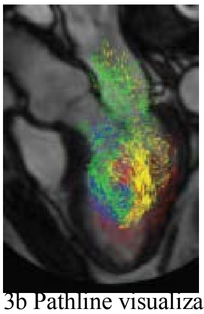

Fig. 3b Pathline visualization of blood flow during left ventricular diastasis [8]

The numerical simulation of the closed mitral valve simulates the period of peak diastole. No vortices are formed inside the ventricle during this stage as seen in Fig. 4a. This is comparable with the CMR image during systole.

(a)

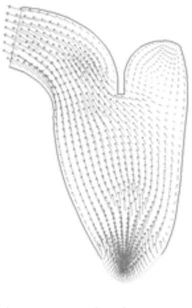

Fig. 4a Velocity vector of simulated flow through a closed mitral valve

(b)

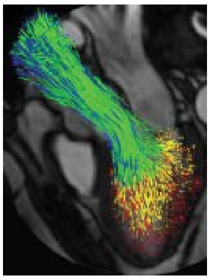

Fig. 4b Pathline visualization of blood flow during peak systole [8]

It is seen that the generated numerical results is comparable to the actual blood flow in the left heart chambers, and therefore can be used as validation for the experimental results.

The numerical simulation of the experimental design is compared to the flow through the experimental design and the CMR images of an opened mitral valve during diastasis. The simulated results of the experimental model shows the formation of vortices as the fluid flows through the opened mitral valve. This is comparable to both the experimental results (Fig.2) and the actual flow through the mitral valve in the human heart (Fig. 3a)

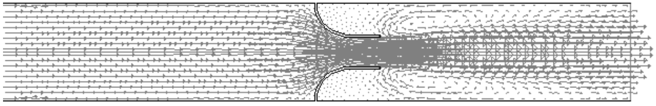

Fig. 5 Velocity vector of simulated flow through a mitral valve in the experimental set-up

It is seen from the simulated results of both the idealized geometry and the experimental based geometry give a flow comparable with the actual flow of blood through the mitral valve. It can therefore be employed as a means for validation for the designed protocol.

4. Conclusions and Recommendation

Flow through a healthy mitral valve produces two vortices. Vortices are important as they help propel the flow from the ventricle. The simulated results of the idealised geometry and the experimental model agree with the experimental result obtained as well as the CMR images. The numerical results can therefore be employed as a tool to be compared with the results obtained from the designed protocol.

The set-up can be further developed to test various mitral valve repair methods and implemented for more personalised healthcare. A patient's mitral valve failure can be evaluated through various medical imaging methods and the data obtained may be used to simulate a physical model which can be used as an analogue to be placed inside the chamber. Various repair methods may be tested on the damaged mitral valve analogue. The method which yields the flow structure closest to a healthy mitral valve will be chosen for the patient.

Acknowledgment

All glory to God. I would also like to thank the school for their support throughout the project. I also express my gratitude to my family and friends who have supported me throughout this project.

References

[1] Drake, R.L., Vogl, A.W. & Mitchell, A.W.M. (2010). *Gray's Anatomy for Students*. 2nd Ed. Churchill Livingstone: Elsevier.

[2] Espino, D.M., Hukins, D.W.L., Shepherd, D.E.T., Watson, M.A. & Buchan, K.G., (2006). Determination of Pressure Required to cause Mitral Valve Failure. *J Medical Engineering and Physics,* 28, 36-41.

[3] Miles, S.H. (2003). *The Hippocratic Oath and the Ethics of Medicine*, New York: Oxford University Press.

[4] Espino, D.M., Hukins, D.W.L. & Buchan, K.G. (2006). Mitral Valve Repair: An In-Vitro Comparison of the Effect of Surgical Repair on the Pressure Required to cause Mitral Valve Regurgitation. *J Heart Valve Disease*, 15(3), 375-381.

[5]Anderson, B., 2007. *Echocardiography: The Normal Examination and Echocardiographic Measurement*. 2nd ed. Manly, Queensland: MGA graphics.

[6] Espino, D.M., Hukins, D.W.L., Shepherd, D.E.T., Watson, M.A. & Buchan, K.G. (2006, November). *Simulation of Blood Flow through the Mitral Vlave of the Heart: A Fluid Structure Interaction Model*. Paper presented at the COMSOL Users Conference, Birmingham, UK.

[7] Sengupta, P.P, Pedrizzetti, G., Kilner, P.J., Kheradvar, A., Ebbers, T., Tonti, G., Fraser, A.G. and Narula, J., 2012. Emerging Trends in CV Flow Visualisation. *J Cardiovascular Imaging,* 5(3), 306-314.

[8] Markl, M., Kilner, P.J. & Ebbers, T. (2011). Comprehensive 4D velocity mapping of the heart and the great vessels by cardiovascular magnetic resonance

Organising Committee

Steering Committee

Conference Chairs
Professor Dato' Dr. Hassan Said,
Vice Chancellor & President

Professor Dr. Mushtak Al-Atabi,
Dean, School of Engineering

Co-Chairs
Associate Professor Dr. Marwan M Shamel
Dr. Edwin Chung Chin Yau
Dr. Satesh Narayana Namasivayam

Treasurer
Dr. Chong Chien Hwa
Dr. Florence Choong Chia Mei
Dr. Mohammad Hosseini Fouladi
Dr. Salim Mohamed Salim

Technical Committee

Chair
Associate Professor Dr. Marwan M Shamel

Members
Dr. Chockalingam Aravind Vaithilingam
Dr. Mohamed H Nassir
Praveena Nair Sivasankaran
Tham Chan Seng

Journal Publication Committee

Chair
Dr. Florence Choong Chiao Mei

Members
Dr. Abdulkareem Sh. Mahdi Al-Obaidi
Dr. Kandasamy Pirapaharan
Alexander Chee Hon Cheong

Organising Committee

Chair
Dr. Padmesh Tirunelveli Narayanapillai

Members
Dr. Suresh Manic Kesavan
Masniroszaime Binti Md Zain
Praveena Nair Sivasankaran
Tham Chan Seng

Graduate School
Kiew Suet Yin
Syafinaz Saifuddin

Marketing & Publicity
Chew Hui Sin
Michelle Tan

TAYLOR'S
UNIVERSITY
Wisdom · Integrity · Excellence

Taylor's University, Lakeside Campus (JPT/BPP(U)1000-801/67/Jld.2(32) KPT/JPS/DFT/US/B21)
No. 1, Jalan Taylor's, 47500 Subang Jaya, Selangor Darul Ehsan, Malaysia
Tel : 603-5629 5000 Fax : 603-5629 5001 E-mail : admissions@taylors.edu.my
Website : www.taylors.edu.my